Ultrasonography in Dentomaxillofacial Diagnostics

Kaan Orhan
Editor

Springer

Ultrasonography in Dentomaxillofacial Diagnostics

Kaan Orhan
Editor

Ultrasonography in Dentomaxillofacial Diagnostics

Springer

Editor
Kaan Orhan
Department of DentoMaxillofacial Radiology
Ankara
Turkey

ISBN 978-3-030-62178-0 ISBN 978-3-030-62179-7 (eBook)
https://doi.org/10.1007/978-3-030-62179-7

This Springer imprint is published by the registered company Springer Nature Switzerland AG
The registered company address is: Gewerbestrasse 11, 6330 Cham, Switzerland

To my family and students,
And to my mentors, Prof. A. Nuri Yazıcıoğlu,
Prof. Candan S. Paksoy and Prof. Souhei Furukawa (RIP).

Foreword

The discovery of X-rays app. 120 years ago changed dramatically the diagnostic capabilities. Since then, there have been many advances in medicine, which have had more of an impact on modern health care. However, the story of ultrasonography started way before X-ray discovery. Lazzaro Spallanzani (1729–1799) was a physiologist, professor, and priest who carried out numerous experiments that led to great insights in human and animal biology. In 1794, Spallanzani performed studies on bats which is now known as echolocation where locations are determined or identified through sound waves being reflected or bounced back from objects in an environment. With these same principles medical ultrasound technology functions today. In the twenty-first century, the first to use ultrasonic waves began to be used as a diagnostic tool which gave tremendous possibility for this noninvasive technology.

Starting in the 1980s, ultrasound technology became more sophisticated with improved image quality and 3D imaging capabilities. These improvements continued into the 1990s with the adoption of 4D (real-time) capabilities. Ultrasound-guided biopsies (endoscopic ultrasounds) also began in the 1990s.

Research on the use of USG in dentomaxillofacial radiology as well as intra-oral use are becoming widespread, and there is a growing demand for the application of USG in DMFR. This book will mainly focus on dental and dentomaxillofacial radiology applications. So far there are books for Head and Neck region, but to the best of my knowledge this book will be the first that specially focuses on dentomaxillofacial radiology. The intra-oral use of USG is underestimated and not well-known by many radiologists and also dental specialists. Thus, this book will focus more on intra-oral and surrounding tissues for the use of USG. The book itself will contain dentomaxillofacial pathologies as mentioned above with intra-oral use of USG. These pathologies are not well-known by the radiologists. Thus, the book itself will give detailed information of intra-oral lesions and USG appearances. It should be emphasized that success is measured by the people's impact on their community and that is the goal; as the editor of this book, I would like to achieve the publication of this book. I would like to remember that the progress of the science and scientific community is a team effort starting from basics to fundamental research to high impact and specified ones. For these

reasons and goals, this book should be regarded a stage in learning and understanding the USG imaging that will stimulate both engineering and medical professions seek a more in-depth appreciation of the subject and its contribution to the scientific community.

Kaan Orhan
Ankara University
Ankara, Turkey
December, 2020

Preface

Accurate interpretation of indications for treatment is the cornerstone of success in medicine. The book examines the relation between clinical features, diagnosis, and choice of minimally invasive technique for a range of dentomaxillofacial disorders and also provides information on post-treatment therapy. It explains how selection of imaging technique is intimately related to clinical and diagnostic aspects and how recognition of this relation forms the foundation for an optimal outcome. In addition to examination of various anatomical regions, careful attention is paid to the role of including the latest imaging techniques on USG. The book will provide detailed discussion of the pathology, treatment, and prognosis of common and rare diseases, congenital/developmental malformations, and more in dentomaxillofacial area which is underestimated and also not well-known by the radiologists. This comprehensive imaging book will help radiologists, dentists in their training and daily practice.

The book will contain updated high-resolution images created on state-of-the-art equipment. Advanced USG imaging introduces readers to current imaging modalities. Pathological descriptions of radiologic diagnoses help clarify the pathophysiology of the disease. Pearls and pitfalls of imaging interpretation for quick reference. Authors are world-renowned dentomaxillofacial radiology experts.

In this book, the chapters fall into several categories: The anatomy, technique, and fundamentals of this imaging modality will be discussed in Chaps. 1–5. Chapters 3–5 briefly reviews general considerations for USG applications in head and neck, physical principles of Doppler and color Doppler ultrasound as well as advanced USG imaging. The rest of the book covers both medical and dental applications of USG in Chaps. 6–21.

This book is an outstanding book for learning and understanding the USG imaging in dentomaxillofacial radiology that will stimulate both radiologists and students to seek a more in-depth appreciation of the subject and its contribution to the scientific community of Radiology. As a result, this book offers a comprehensive review of the state-of-the-art in USG dentomaxillofacial imaging.

Ankara, Turkey
December, 2020

Kaan Orhan

Contents

About the Editor

Kaan Orhan, DDS, MSc, MHM, PhD, BBA is a Professor of Dentomaxillofacial Radiology at Ankara University, Faculty of Dentistry, where he serves as a faculty in Dentomaxillofacial Radiology Department, Ankara University, Ankara, Turkey, and currently also visiting professor at the department of Dental and Maxillofacial Radiodiagnostics, Medical University of Lublin, Lublin, Poland, and also was visiting professor at the OMFS-IMPATH Research Group, Department of Imaging and Pathology, University of Leuven, Belgium.

Dr. Orhan received his dental degree in 1998 and completed his PhD and Maxillofacial Radiology residency studies in 2002 at the Osaka University Faculty of Dentistry in Osaka, Japan, and Ankara University, Faculty of Dentistry. In 2004, he started his academic career in Ankara University as a consultant at the Faculty of Dentistry. Between 2004 and 2006, he worked as Maxillofacial consultant and lecturer in the same University. He became an associate professor in 2006 and a full-time professor in 2012. From 2007 to 2010, he was the founder and the chairman of Dentomaxillofacial Radiology Department, Near East University, Cyprus, and also still continuing as a faculty in Dentomaxillofacial Radiology Department, Ankara University, Ankara, Turkey.

He has over 250 international publications on peer-reviewed journals and received over 3500 citations from his studies with an h-index 33. He particularly made significant contributions in the Maxillofacial Radiology. He has been invited to give many lectures in national and international scientific meetings. He served as the chairman of Research and Scientific Committee, European Academy of Dentomaxillofacial Radiology between 2008 and 2012, and he was elected for the Vice president position (2012–2014) and then as the President for the same academy. He is also serving in the Research and Scientific com in IADMFR, he is fellow of many organizations including Japanese Board of Dentomaxillofacial Radiology, Medical Ultrasonography Society, European Society of Radiology (ESR). He is a fellow of Japanese Board of Dentomaxillofacial Radiology, European Society of Head and Neck Radiology (ESHNR), European Society for Magnetic Resonance in Medicine and Biology (ESMRMB). He is also serving a Board member of specialization committee in Ministry of Health and served as the recognition of Dentomaxillofacial Radiology specialty in Turkey. He is editor of *Oral Radiology*, *BMC Medical Imaging*, and also in the editorial board of many journals including *Clinical Oral Investigations*, *Oral Surgery Oral Medicine*,

Oral Pathology, *Oral Radiology*, *Radiology: Open Access* and *Oral Radiology*, *Journal of Radiation and Radiation Therapy* and also serving as reviewer for more than 50 different journals on his field including Oral Surgery, Oral Medicine, Oral Pathology, Oral Radiology, Dentomaxillofacial Radiology, World Journal of Surgical Oncology, Quintessence International, Journal of Forensic Dental Sciences, Clinical Anatomy. Besides, he is co-author and contributor of eight books both in English and Turkish. His research interests include CT, CBCT, MRI, ultrasonography (USG), head and neck radiology, and Micro-CT.

Introduction to Ultrasonography in Dentomaxillofacial Imaging

1

Kaan Orhan

Contents

1.1 Introduction

Sound is pressure changes or vibrations in the frequency range that are emitted in a certain environment and can be detected by the human ear. The upper limit of the sound that the ear can detect is 20 kHz. Any sound above the audible frequency level is defined as ultrasound (ultrasonic sound wave). Ultrasound imaging (USG) is based on the piezoelectric (pressure-electric) effect that was discovered in 1880 by the brothers Pierre and Jacques Curie. The piezoelectric effect working with the expansion of crystals when electrical energy is given, and thus turn electricity into sound waves. Likewise, the sound waves that were returned back after reflection by the organs converted into electrical energy with the same method.

K. Orhan (✉)
Faculty of Dentistry, Department of Dentomaxillofacial Radiology, Ankara University, Ankara, Turkey

The energy converting materials are called transducers. In USG devices, the transducer is also used as a receiver. Briefly, high sound waves are sent to organs through the skin and each organ reflects these sound waves differently. The reflected sounds are then collected again with the help of the transducer and following a live image is obtained [1]. The transducer in USG imaging is called a probe. The probe produces and emits the ultrasonic waves and transmits to the tissues where the reflected sound waves from the tissue are detected and converted into electrical signals to generate images. High-frequency sound waves lose their energy due to absorption and reflection as they pass through different tissues. Tissue depth is determined depending on the time required for the sound wave to leave and return to the probe [2, 3]. Images are generated according to tissue specifications, depth as well as the amplitude of the echoes returning from the tissues [2, 4]. The rapid vibration, which is transmitted to the patient through a conductive gel, propagates longitudinally into the body as a short, brief series of com-

K. Orhan (ed.), *Ultrasonography in Dentomaxillofacial Diagnostics*,
https://doi.org/10.1007/978-3-030-62179-7_1

pressions (high pressure) and rarefactions (low pressure). Each ultrasound wave is characterized by a specific wavelength (distance between pressure peaks) and frequency (number of pressure peaks per second). The propagation velocity of a sound wave (i.e., acoustic velocity) is fairly constant.

in the human body (c) and is approximately 1540 meters per second. The process of transmission and reception can be repeated over 7000 times a second and, when coupled to computer processing, will result in the generation of a real-time two-dimensional image that appears seamless. The degree to which the ultrasound waves reflect off a structure and return to the probe will determine the signal intensity on an arbitrary grayscale. Structures that strongly reflect ultrasound generate large signal intensities and appear whiter or hyperechoic. In contrast, hypoechoic structures weakly reflect ultrasound and appear darker [5].

Dense and homogenous structures have little attenuation; waves pass through them and do not lose amplitude. For example, fluid-containing structures—such as vessels, distended bladder, and cysts—have minimal wave attenuation due to the fluid's homogeneity and appear hypoechoic (dark gray) to anechoic (black). In contrast, muscle and visceral organs have higher attenuation coefficients as a result of their heterogeneity and appear hyperechoic (light gray to white). The properties of the various media in human tissue and their respective ultrasound appearances are summarized in Table 1.1. [6].

In general, there are currently four modes of ultrasonography imaging: A-mode, B-mode, M-mode (motion), and Doppler. A-mode uses one transducer to "scan a line through the body with the echoes plotted on screen as a function of depth." In B-mode, 2-D images are created using linear transducers that send waves along one plane of the body. M-mode is a series of B-mode images taken in succession, creating moving images. Doppler mode measures the direction and velocity of blood flow, often used in cardiovascular imaging. The Doppler modality is useful in identifying regions of vascularity in lesions to perform fine-needle aspiration biopsies (FNAB) [7].

Advantages of this imaging technique include:

- Noninvasive.
- Nonionizing radiation is used.
- Simple.
- Real-time imaging.
- Portable machine.
- Can repeat and easy to store.
- Less artifacts.

Disadvantages include:

- Operator and equipment dependant.
- Hard tissue cannot be imaged.
- Deep structures cannot be visualized.
- Restricted to the area of the sensor, i.e., lack of imaging of the organ as a whole (tomographic cross-section only).
- Lower resolution than MR and CT [8, 9].

USG was introduced in the medical field in the early 1950s with steady development. The

Table 1.1 Acoustic impedance and attenuation coefficients for various media and their resultant ultrasound appearance (derived from Bakhru and Schweickert, 2013)

Medium	Acoustic impedance (10^6kg/[s × m^2])	Attenuation coefficient (dB/m at 1 MHz)	Ultrasound appearance
Air	0.0004	4500	Hypoechoic (high scatter)
Fat	1.3	60	Hypoechoic
Fluid	1.5	6	Very hypoechoic
Blood	1.7	9	Very hypoechoic
Liver/ kidney	1.7	90	Echogenic
Muscle	1.7	350	Echogenic
Bone	7.8	870	Hyperechoic surface with anechoic posterior shadow

requirement of ultrasound has gained importance in the medical field and slowly its use in dentomaxillofacial and dentistry is also advancing. This method will be a growing imaging modality for these fields because of its advantages such as easy-to-apply, easy to tolerate by patients, includes portable equipment, less artifact, and allows images to be stored.

1.2 What Does the Clinician Need in Terms of USG Imaging in Dentomaxillofacial Diagnostics?

Several different imaging methods have been used in Dentomaxillofacial diagnostics with the progress of technological developments. One of these imaging methods, USG is thought to be having an important potential for maxillofacial region, although not widely used especially intraorally and dentistry [10, 11]. USG is a nonionizing, synchronized, noninvasive, and cost-effective imaging technique used in medical diagnostics and intraoperative guidance in several fields of medicine. Ultrasonography (USG) is also used as a diagnostic imaging modality for the evaluation of head and neck lesions in lymph nodes and salivary glands, as well as facial bone fractures, etc. USG produces dynamic video images depicting muscular dystrophy and denervation in the chewing and striated muscles that produce voluntary contractions, as well as involuntary muscle contractions such as fasciculation [12].

Recently, ultrasound use has a growing demand in dentomaxillofacial area and dentistry for diagnosis and treatment methods. It helps to visualize superficial structures in oral and maxillofacial tissues without ionizing radiation. The anatomy of the head and neck region is complex; therefore, it is necessary to know the normal anatomy very well for the use of ultrasound in this region. Overall, the use of USG in dentomaxillofacial diagnostics are;

- Orofacial swellings.
- Salivary gland disorders.
- Periapical lesions.
- Lymph nodes.
- Intraosseous lesions.
- Temporomandibular joint disorders.
- Examination of chewing muscles.
- Congenital vascular lesions of the head and neck.
- Primary lesions of the tongue.
- Mandibular condyle and ramus fractures.
- Midface fractures.
- Detection of foreign bodies.
- Mandibular bone distraction.
- Suspicious lumps and bumps on the head and neck.

while the therapeutic use of ultrasound in the following areas;

- Myofascial pain.
- Temporomandibular joint dysfunction.
- Treatment of salivary gland stones with baskets and cannulas with/without shock wave lithotripsy.
- Bone healing and osteointegration.
- Oral cancers.
- Treatment of surface skin lesions.

Moreover, USG use in different fields of dentistry is also growing such as in orthodontics. The USG is being used in diagnosis of swallowing models, improvement of orthodontics-induced root resorptions, acceleration of orthodontic tooth movement, and for selection of appropriate mini screw selection in daily clinical applications.

1.3 Conclusion

A close collaboration between clinicians and the radiologists should be made to ensure the correct diagnosis; moreover, standardized terminology and evidence-based guidelines must be taken into consideration for correlation of clinical symptoms and imaging findings in dentomaxillofacial diagnostics. The clinicians should combine the clinical examination and then refer for imaging to the radiologists. The most important part while sending the patient is to provide as much clinical

information to the radiologists which allow both sides to have a proposer diagnosis.

Throughout this book, the applications of USG in dental and dentomaxillofacial radiology diagnostics will be discussed in detail. The use of intraoral use of USG is underestimated and not well-known by many radiologists and also dental specialists. Thus, this book will focus more on intraoral and surrounding tissues for the use of USG. The book will provide a detailed discussion of the pathology, treatment, and prognosis of common and rare diseases, congenital/developmental malformations, and more in dentomaxillofacial area.

The chapters that follow fall into two categories: The fundamentals and clinical applications of USG. The technique and fundamentals of this imaging modality will be discussed in Chap. 2–5. Chapters 2–4 briefly review the fundamentals and general considerations of USG imaging. Chapter 5 will be reviewing recently developed advanced USG imaging. The rest of the book will focus on clinical applications in dentistry and dentomaxillofacial diagnostics.

Acknowledgments Some of the researches in this book were supported by Ankara University Scientific Research Projects Coordination Unit (Grant number: 17B0234004 and 18B0234002).

References

1. Kossoff G. Basic physics and imaging characteristics of ultrasound. World J Surg. 2000;24:134–42.
2. Oyar O, Gülsoy UK. The physics of USG. In: The physics of Medical Imaging. Rekmay: Ankara; 2003. p. 172–82.
3. White SC, Pharoah MJ. Other imaging modalities. Oral radiology: principles and interpretation. 7th ed. St Louis, Missouri: Elsevier; 2014. p. 246–7.
4. Whaites E, Drage N. Alternative and specialized imaging modalities. Essentials of dental radiography and radiology. 5th ed. Edinburgh: Elsevier; 2013. p. 240–3.
5. Sites BD, Brull R, Chan VW, Spence BC, Gallagher J, Beach ML, Hartman GS. Artifacts and pitfall errors associated with ultrasound-guided regional anesthesia. Part I: understanding the basic principles of ultrasound physics and machine operations. Reg Anesth Pain Med. 2007;32(5):412–8.
6. Bakhru RN, Schweikert WD. Intensive care ultrasound: I. Physics, equipment, and image quality. Ann Am Thorac Soc. 2013;10(5):540–8.
7. le Tina KM. Suppl 2: M11: an inventory of current available ultrasound devices for dental use. Open Dent J. 2015;9:319.
8. Essays, UK. (2018). ultrasonography advantages and disadvantages. https://www.ukessays.com/essays/sciences/ultrasonography-advantages-7018.php?vref=1.
9. Tognini F. Comparison of ultrasonography and magnetic resonance imaging in the evaluation of temporomandibular joint disc displacement. J Oral Rehab. 2005;32(4):248–53.
10. Dib LL, Curi MM, Chammas MC, Pinto DS, Torloni H. Ultrasonography evaluation of bone lesions of the jaw. Oral Surgery, Oral Medicine, Oral Pathology, Oral Radiology, and Endodontology. 1996;82(3):351–7.
11. Joshi PS, Pol J, Sudesh AS. Ultrasonography – a diagnostic modality for oral and maxillofacial diseases. Contemp Clin Dent. 2014;5:345–51.
12. Engel-Hoek LV, Lagarde M, Alfen NV. Ultrasound of oral and masticatory muscles: why every neuromuscular swallow team should have an ultrasound machine. Clin Anatomy. 2017;30:183–93.

2 Anatomy for USG Application in Head and Neck

Franciszek Burdan and Jerzy Walocha

Contents

2.1 Introduction

The dentomaxillofacial radiology covers not only stomatognathic system but also surrounding structures including oral and nasal cavity, paranasal sinuses, salivary glands, and a majority of neck structures as well as nerves and vessels that supply them. Their development starts at three and a half weeks of fetal life and is related to ectodermal oral stomodeum that unites with endoderm to form the buccopharyngeal membrane. Its rapture finally connects the future oral cavity with the foregut and at gestational sixth week the dental lamina could be seen and teeth development starts. Connection with pharyngeal arches and cranial bones finally forms a complicated apparatus that highly coordinated mastication, and is also involved in deglutition, phonation, respiration, and other activities. Since the book is dedicated for an ultrasound diagnostic, the anatomical description will focus mostly on soft tissue structures that are important for routine clinical practice. For detailed morphological and topographical explanations, proper anatomical textbooks—used to prepare the current chapter—are recommended [1–5].

F. Burdan (✉)
Department of Human Anatomy, Medical University of Lublin, Lublin, Poland

Radiology Department, St. John Cancer Center, Lublin, Poland

J. Walocha
Department of Anatomy, Jagiellonian University Medical College, Krakow, Poland
e-mail: j.walocha@uj.edu.pl

K. Orhan (ed.), *Ultrasonography in Dentomaxillofacial Diagnostics*,
https://doi.org/10.1007/978-3-030-62179-7_2

2.1.1 The Skeleton of the Head and Neck

Anatomically, the skeleton of the head and neck comprises of the skull, mandible, hyoid bone, and all seven cervical vertebrae. Functionally, the upper part of thoracic cage, including manubrium of the sternum, upper ribs, and thoracic vertebrae as well as the clavicle and scapula are also added due to the close connection with major muscles of the neck. It should be also pointed out, that radiologically the computed tomography (CT) or magnetic resonance imaging (MRI) of the neck always ends on the level of the upper sternal joint (synchondrosis), not only to see the lower attachment of the cervical muscles but also due to the fact that primary lymph nodes of some of the cervical structures are located posteriorly to manubrium of the sternum, in the upper mediastinum (group VII, see below).

Since most elements of the skull and cervical vertebrae are formed by the bones they are not well-visible during the US examination, they will not be explained below. However, during an early period of human life, membranous and cartilaginous structures such as fontanelles allow to exam the neonatal brain and other intracranial elements using the modality. In adults, the access is limited only to selected so-called acoustic windows (i.e., transtemporal, submandibular, transorbital, suboccipital) but such transcranial Doppler ultrasound (TCD) is performed mostly by neurologists [6, 7].

2.1.1.1 Temporomandibular Joint

The only skeletal structure of the head that is routinely examined ultrasonographically is the temporomandibular joint (TMJ). It is a bilateral synovial joint that contains distinguish (articular surfaces, cavity, and capsule) and accessory elements (disc, ligaments). The head of the joint is formed by the head of the condylar mandibular process while (Fig. 2.1) the socket by the mandibular/glenoid fossa and articular tubercle/eminence of the squamous part of the temporal bone (Fig. 2.2). Unlike most of the synovial joints, articular surfaces of TMJ are covered by fibrous not hyaline cartilage. The border of the socket forms also the upper attachment of the capsule. The lower one is located on the neck of the condyle, slightly away from the cartilage. The capsule is formed by the external fibrous layer and internal synovial one, responsible for synovial fluid secretion. The capsule and articular surfaces surround articular cavity that contains synovial fluid and articular disc and some of the intracapsular ligaments. The disc forms a movable socket for the mandible and divides the joint cavity and synovial membrane into upper and lower com-

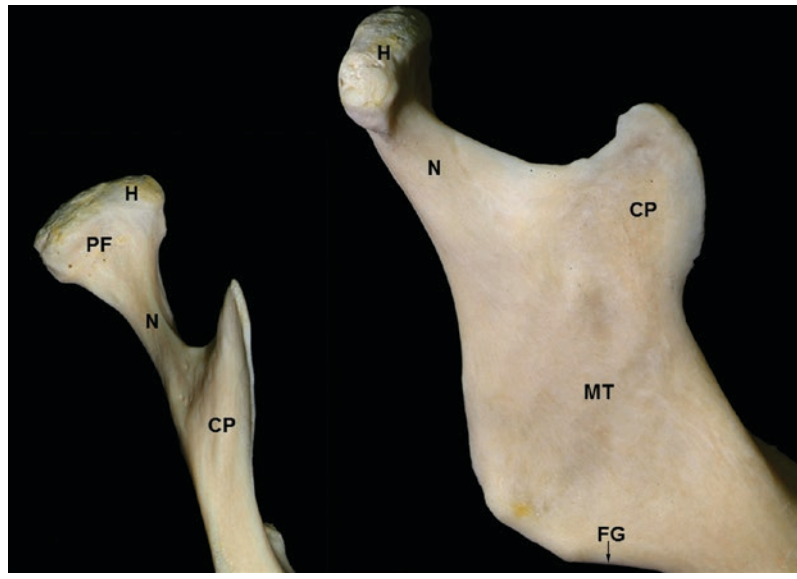

Fig. 2.1 Ramus of mandible. CP—coronoid process, FG—facial grove/incisura, H—head of mandible, MT—masseter tuberosity, N—neck of mandible/condylar process, PF—pterygoid fossa

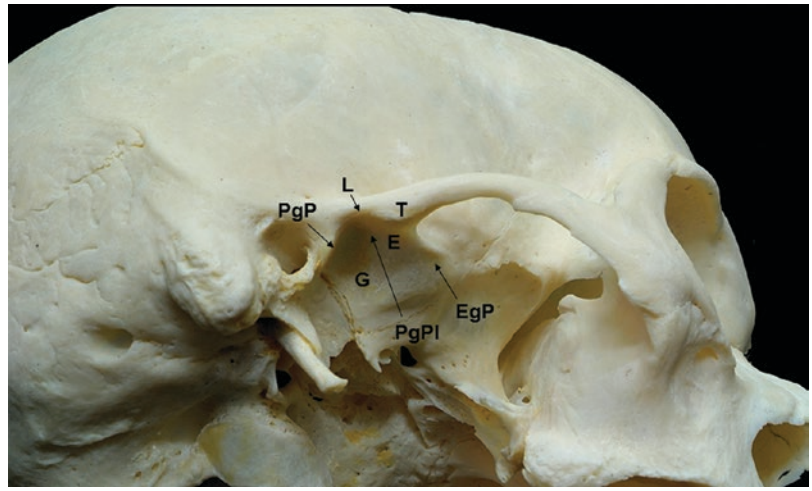

Fig. 2.2 Socket of temporomandibular joint. E—articular eminence (media/anterior root of the zygomatic process), T—articular tubercle, PGP—preglenoid plane, L—lateral border of glenoid fossa, ENP—entoglenoid process, PGT—postgleoid process

partments. The upper one (1.2 cm^3) is responsible for the gliding movements protrusion and retrusion (translation between condyle-disc complex and articulate eminence), while the lower one (0.5–0.9 cm^3) for hinge moments (rotation of the head). The disc itself is an avascular oval (10 × 20 mm) and biconcave fibrous plate (1–3 mm thickness). Its anterior border splits into upper and lower lamellae, that attach to the anterior border of the articular eminence and neck of the condyle, respectively. The space between them is penetrated by the tendineal fibers of the lateral pterygoid muscle. Posteriorly, the disc is attached to the fibrous capsule and limits the retrodiscal region formed by its highly vascular and innervated loose connective tissue. Both, medial and lateral borders of the disc give origin to the medial and lateral disco-condylar ligaments that are attached to proper surfaces/poles of the condylar process and stabilize the disc during protraction and retraction. The joint is also supported by capsular (lateral, medial) and extracapsular ligaments (stylomandibular, sphenomandibular, retinacular). The lateral (temporomandibular) ligament runs from the zygomatic process of the temporal bone and the articular tubercle to the lateral side of the neck of the mandible and mix fibers with fibrous layer of the articular capsule. Due to the fibrous position, it is deviated into an outer oblique portion and an inner horizontal one. It prevents excessive retraction or moving backward of the mandible. The medial ligament is only a developmental variation of the sphenomandibular ligament, that runs from the sphenoid spine bone to the mandible lingula and limits an advanced protrusion. The most medially located fibers may exit the main complex and rich the medial aspect of the condylar process to form the medial ligament that supports the joint capsule. The recently described retinacular ligament arises from the articular eminence of the zygomatic process of the temporal bone and runs to the mandible, mix fibers with masseter fascia and retrodiscal tissue, transverse facial, and wall of superficial temporal veins [8]. It has been postulated that the ligament maintains blood circulation during the masticatory movements. The joint is supplied by the auriculotemporal and masseteric branches of mandibular branch of the trigeminal nerve. The blood comes mostly from the superficial temporal artery or less commonly from deep auricular artery, anterior tympanic artery, ascending pharyngeal artery, and maxillary artery. The blood is collected by the pterygoid plexus.

2.1.2 Muscles and Fasciae of the Head and Neck

Muscles of the head are divided into muscles of the facial expression and masticatory ones (Table 2.1). The first group contains a number of small muscles that coordinate fascial expression/

Table 2.1 Muscles of the head

Muscles of facial/mimic expression (innervated by CNVII)
Muscles of the scalp (epicranius)
– Occipitofrontalis m.
– Temporoparietalis m. (epicranial aponeurosis)
Muscles of the mouth, lips, and cheeks
– Orbicularis oris
– Depressor anguli oris
– Transversus menti
– Risorius
– Zygomaticus major
– Zygomaticus minor
– Lavator labii superior
– Lavator labii superior alaeque nasi
– Depressor labii inferioris
– Levator anguli oris
– Buccinator
– Mentais
– Platysma
Muscles of the orbital opening
– Orbicularis oculi
– Corrugator supercilii
Muscles of the nose
– Procerus
– Nasalis
– Depressor septi nasi
Muscles of the ears
– Auricularis anterior
– Auricularis superior
– Auricularis posterior
Muscles of mastication (innervated by CNV_3)
– Temporal
– Masseter
– Lateral pterygoid
– Medial pterygoid

Table 2.2 Muscles of the neck

Superficial muscles
– Platysma
– Sternocleidomastoid (SCM)
Anterior muscles
Suprahyoid muscles
– Mylohyoid
– Geniohyoid
– Stylohyoid
– Digastric
Infrahyoid muscles
– Sternohyoid
– Omohyoid
– Sternothyroid
– Thyrohyoid
Middle muscles (lateral vertebral muscles)
– Anterior scalene
– Middle scalene
– Posterior scalene
– Minimus scalene
– Rectus capitis lateralis
– Splenius capitis
Posterior/prevertebral muscles (anterior vertebral muscle)
– Longus colli
– Longus capitis
– Rectus capitis anterior

mimic, all are innervated by the facial nerve (cranial nerve VII—CNVII), have at least one attachment in a subcutaneous tissue or skin, and are not covered by the fascia, with exception to the buccinator muscle that is covered by buccopharyngeal fascia. The muscle is also important in a daily ultrasound practice since it is pierced by the parotid duct, just before it empties into the oral vestibule. Anatomically, muscles of mastication contain four muscles that surround TMJ. However, functionally few other muscles, mostly from suprahyoid group of the neck also coordinate movements of the mandible. In the neck, muscles are divided into few groups/layers: superficial, anterior, deep (middle), and prevertebral muscles (Table 2.2). Behind the vertebral column, deep and superficial muscles of the back are located.

As it was pointed above, all muscles except mimic expression ones are surrounded by fascia. Just below the skin there is a superficial cervical fascia formed by the subcutaneous tissue of the neck, that is located between the dermis and the investing layers of the deep cervical fascia. It contains various superficial vessels (arterial, venal, lymphatic), superficial lymph nodes, fat, and platysma. The deep cervical consists of investing/superficial, pretracheal, and prevertebral layers [9]. The most externally located part—investing fascia—is formed by superficial and deep laminas that completely encapsulate trapezius and sternocleidomastoid (SCM) muscles, and unites together between them as well as over their distal (superior nuchal line of the occipital bone, mastoid process of the temporal bone) and proximal attachment (manubrium of the sternum, clavicle, spine and acromion of scapula, spinal processes of cervical vertebrae, nuchal ligament). On the level of infe-

rior border of a mandible, both layers split again and form a capsule for the submandibular and parotid salivary glands. The superficial layer runs over and covers external surface of the masseter muscle (masseter fascia) and on the level of zygomatic arch it changes the name again and become a temporal fascia that covers and forms attachment for the temporalis muscle. Both layers are separated also over the jugular notch of the manubrium of the sternum and surround potential—suprasternal—space. The middle aspect of the investing fascia is attached to the hyoid bone. Much thicker is a pretracheal layer of the deep cervical fascia. On the level of the neck, there is a trapezoid-shape muscular part that runs down from the hyoid bone, surrounds all infrahyoidal muscles, including omohyoid that limits the fascia laterally and visceral layers that surround thyroid gland, trachea, esophagus and extends into the fibrous pericardium and superiorly on the pharynx as a buccopharyngeal fascia. Its fibers bilaterally form small hooks that place the intermediate tendon of the digastric muscle to the hyoid bone, as well as the carotid sheaths that surround the cervical neurovascular bundle (internal jugular vein, common and internal carotid artery, carotid sinus and its nerve, vagus nerve—CNX). The prevertebral layer of the deep cervical fascia contains the cervical part of the sympathetic trunk, and runs from the base to the skull, covers prevertebral muscles of the neck, and unites with the anterior longitudinal ligament on the level of third/fourth thoracic vertebra and laterally with endothoracic fascia. On the cervical level, laterally it forms the axillary sheaths that enclose (subclavian/axillary vessels and brachial plexus). The prevertebral layer forms a posterior wall of the retropharyngeal space, while the anterior one is limited by buccolaryngeal and visceral part of the pretracheal fascia that covers the posterior aspect of the pharynx and remaining cervical viscera. Such potential space is divided into anterior and posterior (Danger) compartments by the alar fascia that runs from the base of the skull to the level of C7 [9, 10]. The alar fascia is formed by fibers of buccopharyngeal fascia that arises from pharyngeal raphe and runs laterally to the carotid sheaths.

Secondary to fascia position, the whole neck and oral part of maxillofacial part of the head and neck are divided into various spaces [10, 11]. From the clinical point of view the most important are (Figs. 2.3 and 2.4):

- Masticatory space that is divided by the zygomatic arch into the supra- and infrazygomatic parts. It contains masticatory muscles, as well as anterior and posterior division of CNV3 (mandibular n.), mandibular and pterygoid part if the maxillary artery, superficial part of pterygoid plexus, ramus and posterior part of the mandibular body, lower dental row. The space is limited anteriorly by the buccal space, posterolaterally by the parotid space, and medially by parapharyngeal space.
- Nasopharyngeal mucosal space is limited to nasal cavity and paranasal sinuses (see below).
- Oropharyngeal mucosal space is limited to oral cavity (see below).
- Pharyngeal mucosal space is limited to the pharynx (see below).
- Retropharyngeal or retrovisceral space as explained above is divided into anterior (proper) and posterior compartment (Danger Space). It is limited anteriorly to the pharyngeal mucosal space, posteriorly by the body of vertebrae C1-Th3/4, anteromedially by the carotid space, posteromedially by the parapharyngeal space. Usually, it is a potential space, but small vessels and lymph nodes could be seen there.
- Parotid space is limited by the parotid capsule and contains the gland, terminal division of external carotid artery, and CNVII—parotid plexus, retromandibular vein, intraparotid lymph nodes. It is located below external acoustic meatus, laterally to the parapharyngeal space, medially to subcutaneous tissue of the cheek, anteriorly to the carotid space and posterior belly of the digastric muscle, posteriorly by the masticator space.
- Carotid space surrounded by carotid sheath that contains internal jugular vein, common and internal carotid artery, carotid sinus and its nerve, vagus nerve—CNX, upper part of glossopharyngeal nerve (CNIX), part of cervi-

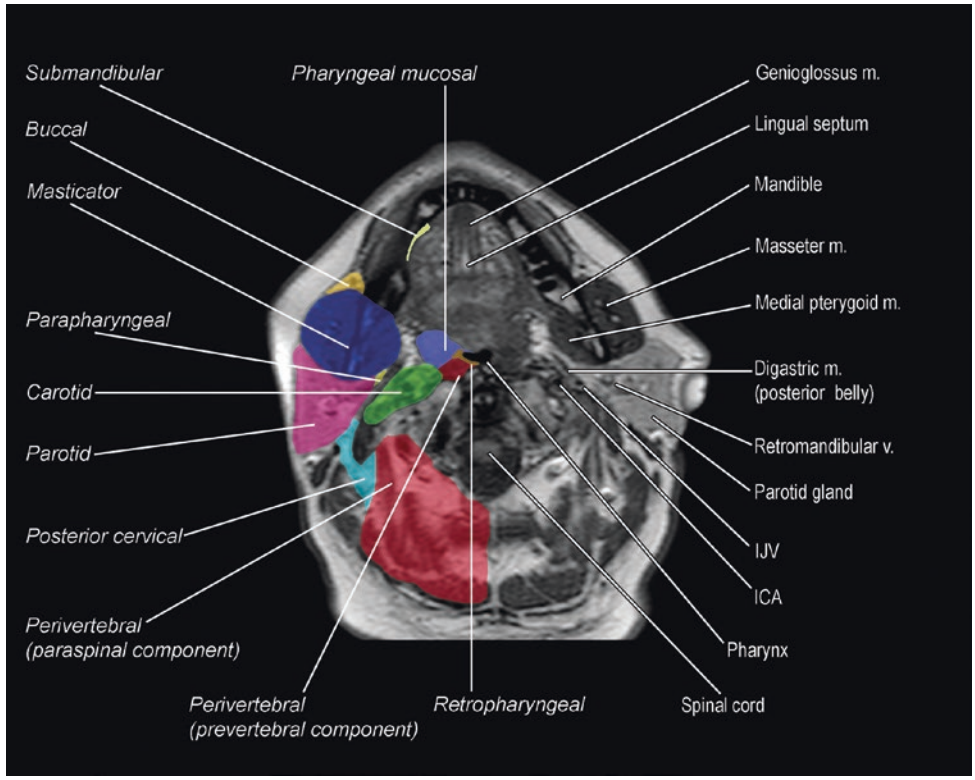

Fig. 2.3 Selected cervical spaces—horizontal section on the C2 level

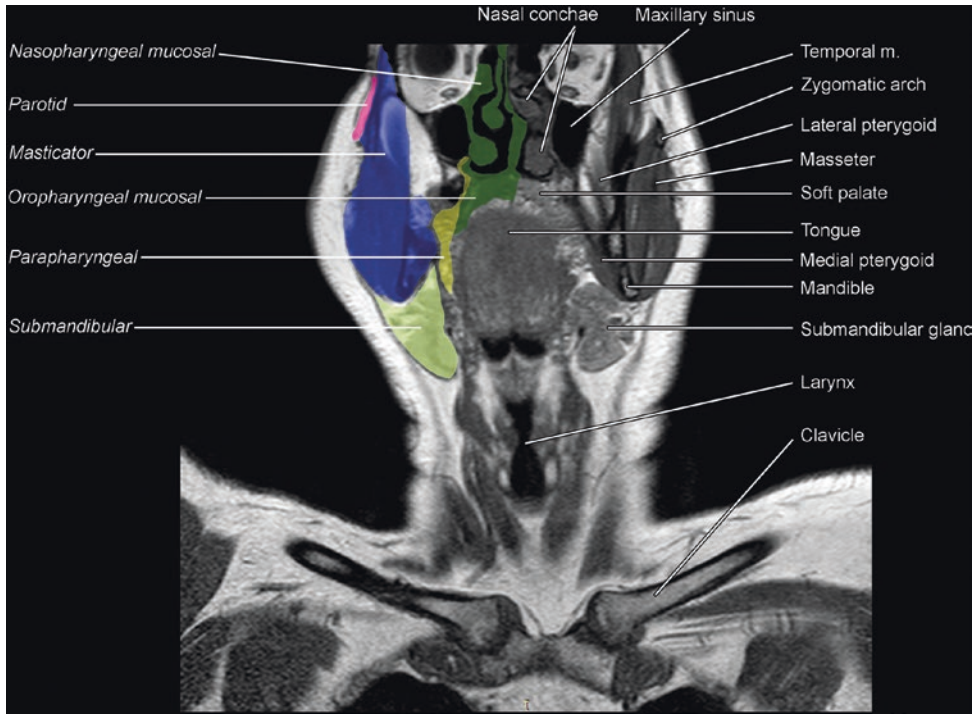

Fig. 2.4 Selected cervical spaces—frontal section

cal neuronal ansa, carotid sympathetic plexus, and some deep cervical lymph nodes (group II, III, IV). The upper part (suprahyoid) is attached anteriorly to the masticator space and parapharyngeal space, laterally to the parotid space, posteriorly to the perivertebral space while medially to the retropharyngeal space. In the lower part (infrahyoid), it is limited anteriorly and laterally by the anterior and posterior cervical space, respectively.

- Submandibular space is limited to the area located between mandible and hyoid bone, surrounded by superficial layer of the deep cervical fascia that forms its floor. It is limited anterolaterally by the mandible, medially by the anterior belly of digastric muscles, posteriorly by muscles of the tongue, superiorly by the mylohyoid muscle, and inferiorly by the hyoid bone. Some authors add submental space to it and in such case the anterior boundary does not exist. The submandibular space contains superficial part of the submandibular gland, submandibular lymph nodes (group Ib), cervical part of the facial artery and vein, hypoglossal nerve, and fat, the upper part of anterior jugular vein, and submental lymph nodes (group Ia) that are visible on the level of submental space.
- Buccal space is located between buccinator, platysma, masticatory muscles, and posterior aspect of the body of the maxilla. It contains retromaxillary fat pat, parotid duct and accessory parotid gland, facial and buccal vessels, buccal branch of the facial nerve (CNVII), buccal nerve of the mandibular nerve (CNV_3).
- Parapharyngeal space is a narrow space located laterally to the carotid sheath, anteriorly to the retropharyngeal space, and anteromedically to masticator space, medially to the parotid space. A lower part of the space may be called a retroesophageal space. It is divided by the rudimentary stylopharyngeal fascia (Zuckerkandl/Testut aponeurosis—band from styloid process to the tensor veli palatini) into pre-styloid and post-styloid parts, that is a synonym of the suprahyoid portion of the carotid space. It contains vagus n. (CNX), upper part of glossopharyngeal (CNIX), accessory (CNXI) with hypoglossal nn. (CNXII), internal carotid artery, internal jugular vein in the carotid sheath, sympathetic trunk and its superior cervical ganglion, ascending pharyngeal artery, deep cervical lymph nodes.
- Perivertebral space is limited anteriorly by retropharyngeal/danger space; posteriorly by thoracolumbar fascia attaches to spinous process and ligamentum nuchae; laterally by posterior cervical space. It is divided into prevertebral and two almost symmetrical paraspinal compartments. The first one is limited anteriorly by prevertebral layer of the deep cervical fascia and contains deep cervical (scalene) and prevertebral muscles, vertebral vessels, phrenic nerve, and supraclavicular part of the brachial plexus. The paraspinal compartments are surrounded by the thoracolumbar fascia and contain deep/intrinsic muscle of the back (some authors include also superficial/extrinsic muscle).
- Posterior cervical space extends from the mastoid process and base of skull to the clavicle. It is located between superficial and deep layer of deep cervical fascia, between SCM and trapezius muscles, limited also by the prevertebral and carotid space. The space contains the external/spinal branch of accessory nerve (CNXI), supraclavicular part of the brachial plexus, dorsal scapular nerve, spinal accessory lymph nodes (group V), and loose connective tissue.
- Anterior cervical space is a small infrahyoid compartment, that is only partially surrounded by fascia and limited posteriorly by the carotid space, medially by the visceral space, and superiorly the hyoid bone and submandibular space.
- Visceral space is divided into upper and lower divisions. The upper one is controversial since contains pharyngeal space, nasopharyngeal and oropharyngeal mucosal spaces. However, since they are partially coved by the deep cervical fascia, some of the scientists regarded them as parts of the visceral cervical space. The proper/lower division is located inferiorly to the hyoid bone and secondarily divided by

the pretracheal layer of the fascia into pretracheal and retrovisceral spaces (anterior and posterior visceral space), limited posteriorly by the alar fascia. The space contains thyroid gland, parathyroid glands, larynx, trachea, hypopharynx, esophagus, their vessels and nerves, recurrent laryngeal nerve, lymph nodes (group VI).

2.1.3 Nerves of the Head and Neck

Muscles, skin, and viscera of the head and neck have a complicated innervation since it comes not only from spinal nerves and autonomic nervous system but also from cranial nerves.

2.1.3.1 Cranial Nerves

Cranial nerves are part of the peripheral nervous system. However, the first two—olfactory and optic ones—are the extra processes of the prosencephalon not proper cranial nerves that arise from the brain stem. The terminal nerve (CN0) is a rudimentary one and usually disappears during fetal period, secondary to physiological in-utero atrophy of vomerovaginal organs. From among 12 cranial nerves, only a few are crucial in a routine dentomaxillofacial practice.

CNI—Olfactory nerves are formed by axons of cell bodies located in the so-called olfactory part of the nasal cavity. They cross the opening of cribriform lamina of ethmoidal bone and reach olfactory bulb—part of rhiencephalon.

CNII—Optic nerve is formed by efferent fibers of ganglionic cell of the retina. They cross optic canal and through optic chiasm and tracts they reach metathalamus.

CNIII—Oculomotor nerve is a mixed nerve. Its motor and preganglionic parasympathetic fibers arise from the midbrain and enter the orbit by the superior orbital fissure to innervate superior, middle, and lower rectus oculi muscles, inferior oblique, and levator palpebrae superioris as well as by ciliary ganglion the ciliary and sphincter pupillae mm.

CNIV—Trochlear nerve is a motor nerve that arises from the midbrain and by superior orbital fissure it reaches the orbit and innervates the superior oblique muscle.

CNV—Trigeminal nerve is a mixed nerve that contains sensory fibers that arise from trigeminal ganglion, located on the top of the pyramid of the temporal bone and motor ones that originate from the nucleus located in the pons. The main sensory trunk splits into three primary branches:

- Ophthalmic nerve (CNV_1) after in pass through the superior orbital fissure innervates the cornea, skin of the forehead, scalp, upper eyelids, nose, and mucosa of nasal cavity and paranasal sinuses, dura mater.
- Maxillary nerve (CNV_2) is also sensory one that through foramen rotundum enters the pterygopalatine fossa where it gives origin for lateral (posterior superior alveolar, meningeal) and terminal branches (zygomatic, pterygopalatine, superior alveolar n.). Both zygomatic and superior alveolar nn. cross the inferior orbital fissure. The first one transmits also autonomic fibers for the lacrimal glands from pterygopalatine ganglion, while the superior alveolar runs in the infraorbital groove and canal, where it gives superior middle and superior anterior alveolar nerves for the upper/maxillary teeth and gum. The distal part of the nerve exits the canal by infraorbital foramen and splits into terminal branches (nasal, palpebral, buccal/zygomatic, and superior labial) that innervate respective parts of the faces. The pterygopalatine nerves form the sensory root of the pterygopalatine ganglion and with their branches innervates mucosa of the nasal cavity, maxillary sinus, palatine, and nasopharynx.
- Mandibular nerve (CNV_3) except sensory fibers contains also motor ones. It exits the middle cranial fossa through the foramen ovale and on the base of skull gives origin to meningeal branch that runs back to the skull by foramen spinosum to innervate the dura matter of the brain. The remaining parts of the nerve split into anterior and posterior division. The anterior contains only one sensory branch (buccal nerve), while the remaining ones are mostly motor and supplies masticatory mus-

cles (deep temporal, masseter, medial, and lateral pterygoid nn.) It has to be mentioned that the medial pterygoid nerve supplies also tensor veli palatine and tensor tympani mm., that have the same developmental origin. From the posterior division of CNV_3, only mylohyoid n. provides motor fibers for mylohyoid and anterior belly of the digastric m. The remaining branches (lingual, auriculotemporal, inferior alveolar nn.) are sensory but mylohyoid may arise from inferior alveolar one. Both, lingual and auriculotemporal branches form sensory roots for parasympathetic submandibular and otic ganglion, respectively. The first one supplies the skin mostly of the external ear while the second one is responsible for the general innervation of mucosa of the anterior two-thirds of tongue and remaining part of the mouth, except palatine and lower/mandibular gum. The inferior alveolar nerve enters the inferior alveolar canal through mandibular foramen (just next to the mandibular lingual) and gives an origin for inferior alveolar branches that supply interior teeth and gum. The distal part of the nerve exits the mental foramen and divides into terminal branches that innervate skin of the lower lips and chin.

CNVI—Abduces nerve is a motor nerve that arises on the junction between pons and medulla oblongata and by superior orbital fissure. It reaches the orbit where it innervates the lateral rectus muscle.

CNVII—Facial nerve emerges from the cerebellopontine angle by two roots: proper (motor fibers) and intermedian nerve (preganglionic parasympathetic and special sensory fibers). It runs across internal acoustic meatus and facial canals where gives origin for the great petrosal n., stapedian n., and chorda tympani. The first after it reaches the base of the skull forms the parasympathetic root of the pterygopalatine ganglion. Stapedial never supplies the stapedius muscle. Chorda tympani after crossing the tympanic cavity exits it through petrotympanic fissure and unite with the lingual nerve. The nerve provides preganglionic parasympathetic fibers for submandibular ganglion that innervates submandibular, sublingual, and small salivary glands of the mouth, as well as special sensory fibers for the anterior two-thirds of the tongue. The extracranial part of the CNVII exits facial canal through the stylomastoid foramen and after giving origin for the digastric (for posterior belly of digastric m.) and posterior auricular branch (for occipital belly of epicranial muscle and posterior auricular mm.), it enters the parotid capsule. On the level of the superficial part of the gland, it divides into five branches (parotid plexus): temporal, zygomatic, buccal, marginal mandibular, and cervical that innervates all muscles of mimic/facial expression, except posterior auricular and occipital belly of epicranial ones.

CNVIII—Vestibulocochlear nerve arises for cerebellopontine angle and is formed only by special sensory fibers from vestibular and cochlear ganglion.

CNIX—Glossopharyngeal nerve emerges from the medulla oblongata and contains motor, sensory, and preganglionic parasympathetic fibers. It exits the posterior cranial fossa through the jugular foramen, where it forms superior and inferior ganglia and give origin of the tympanic nerve that later becomes the lesser petrosal—the parasympathetic root of the otic ganglion that innervates the parotid gland. Then, the main trunk of CNIX enters cervical neurovascular bundle but exits the carotid sheath shortly after, gives sensory branch for carotid sinus and follows stylopharyngeus m. Finally, it splits into terminal branches including branch to stylopharyngeus m., that also supplies superior pharyngeal constrictor as well as palatine tonsil and posterior one-third of the tongue (sensory fibers), sensory branch to the posterior part of pharyngeal plexus and pharyngeal branches for the middle constrictor.

CNX—Vagus nerve like CNX, emerges from the medulla oblongata; contains motor, sensory, and preganglionic parasympathetic fibers. It exits the posterior cranial fossa through the jugular foramen where it forms superior and inferior ganglia. After the nerve enters the carotid sheath, it runs in the groove, behind internal jugular vein and internal/common carotid artery. On the level of the thorax, it splits into few esophageal

branches that mixed together to form esophageal plexus and finally, anterior and posterior vagal trunks that enter the abdominal cavity. On the cranial level, the nerve gives meningeal and auricular branch—the only one that innervates skin (auricular concha and external acoustic meatus). From the cervical part emerge pharyngeal branches for a lower constrictor, superior laryngeal nerve, cervical cardiac branches, and right recurrent laryngeal nerve that gives origin for the inferior laryngeal one (the left one arises from the thoracic part). As it was pointed above motor fibers of the nerve supplies the inferior pharyngeal constrictor, all laryngeal muscle as well as skeletal muscles of the esophagus. Sensory area is much bigger and contains external ear, dura mater of the posterior cranial fossa, taste from the epiglottis and palate, as well as mucosa of the pharynx, larynx, and all thoracic viscera and digested tract until right two-third of the transverse colon. Area of visceral sensation covers also the area of parasympathetic innervation, that also includes spleen, liver, and ovaries/testes.

CNXI—Accessory nerve emerges from medulla (internal) and spinal cord (external root). Both roots unite on the level of jugular foramen then nerve splits again and most of the cranial fibers unites with the vagus nerve, while cervical ones cross the lateral cervical spaces and innervate the trapezius and SCM muscles.

CNXII—Hypoglossal nerve arises from medulla by several roots that unite together and exit the skull by the hypoglossal canal in the base of the occipital condyle. In the canal, the nerve is surrounded by the venous plexus that separates it from bone. Then, it runs inferiorly, surrounds the carotid sheath, where it is united with an upper branch of the cervical ansa. Along the posterior belly of digastric and stylohyoid mm., it reaches the external carotid artery. On this level, the nerve forms an arch and below the intermediate tendon of the digastric m. finally follows hyoglossus and mylohyoid mm. and splits into terminal branches. The nerve supplies all muscle of the tongue including intrinsic and extrinsic ones. Due to the fibrous exchanging with the cervical ansa, it also provides innervation for dura mater of the posterior cranial fossa as well as geniohyoid and thyrohyoid mm.

2.1.3.2 Spinal Nerves

The cervical part of the spinal cord gives origin for eight pairs of spinal nerves, that by the meningeal branches innervate dura mater, by posterior ones the deep muscle and skin of the back, while anterior branches form roots of cervical (C1–C4) and brachial plexus (C5–T1). Only the last nerve (C8) has a typical preganglionic branch; however, the postganglionic ones that connect spinal nerves with ganglia of cervical part of sympathetic trunk are typical for all of them.

The nearby located anterior branches unite together in a prevertebral space and form loops that give origin for sensory/cutaneous as well as short and deep muscular branches. Coetaneous branches after a piercing the prevertebral and superficial layer of the deep cervical fascia arise on the posterior border of SCM muscle on the level of C3 (Erb point) and runs radially:

- Lesser occipital nerve runs posterosuperiorly and innervates the skin of occipital and temporal region, including upper of the middle aspect of the auricle.
- Greater auricular nerve runs anterosuperiorly and innervates the skin of the cheek, lateral aspect of the auricle, and external acoustic meatus.
- Transverse cervical nerve runs anteriorly and horizontally; innervates the skin of anterior cervical triangle, limited by both SCM muscles and body of mandible.
- Supraclavicular nerve run posteroinferiorly and innervate the skin of the deltoid and upper pectoral regions as well as the lateral cervical triangle, limited by SCM, trapezius, and clavicle.

Short muscular branches supply deep muscles of the neck, i.e., anterior and lateral rectal capitis, longus capitis and cervical, levator scapulae, scalene, and anterior intertransversal ones. Long muscular branches include:

- Branch for SCM muscle.
- Branch for trapezius.
- Cervical ansa that, as in was pointed above, joins with CNXII and supplies all anterior cervical muscles (infra- and suprahyoid ones).

– Phrenic nerve on the neck runs on the anterior aspect of anterior scalene muscle and is covered by SCM, then between subclavian vein and artery, it enters the thoracic cage, where it supplies diaphragm, parietal layer of mediastinal and diaphragmatic pleura, pericardium as well as peritoneum that covers abdominal aspect of diaphragm.

Anterior branches of spinal nerves C4-C8 and T1 form a complicated brachial plexus, that in the neck forms superior (C4-C5), middle (C6), and inferior trunks (C7-T1). Each of them, on the level of the posterior scalene fissure, splits into anterior and posterior divisions that enter axilla and units to cords. The supraclavicular/cervical part gives only so-called short branches:

– Long thoracic nerve arises from anterior rami of C5-C7, runs on the lateral aspect of the serratus anterior and supplies it.
– Dorsal scapular nerve arises from anterior ramus of C5 and supplies rhomboid mm.
– Suprascapular nerve arises from superior trunk and supplies supra- and infraspinatus mm.
– Subclavian nerve arises from superior trunk and supplies subclavian m.

2.1.3.3 Autonomic Nerves

The origin of parasympathetic system for head and neck is formed by accessory (CNIII), superior (CNVII), and lower salivary (CNIX), as well as dorsal nucleus (CNX). The preganglionic fibers run, as it was explained above, along branches of mentioned cranial nerves to reach the proper parasympathetic ganglion, that through the postganglionic rami, innervates smooth muscles and glands or various organs.

All the preganglionic sympathetic fibers arise from the intermediolateral nucleus located in a spinal cord on the level C8-L1/2. In case of head and neck, they run from the C8-T6 and through the rami communicantes for the sympathetic cord, they reach cervical sympathetic ganglia: superior, middle, and inferior one. As a variation, an additional vertebral and cervicothoracic/sellatum ones (union between a lower cervical and first thoracic pierced by the subclavian a.) may exist. The cervical part of sympathetic chain runs among prevertebral layer of the deep cervical fascia. Each ganglion gives origin for:

– Postganglionic communication branches for spinal nerves.
– Postganglionic vascular branches that surround nearby located artery and form a periarterial plexus, that later gives sympathetic root for each parasympathetic ganglion of the head and neck.
– Visceral branches—including superior, middle, and cervical cardiac nn. as well as laryngopharyngeal, esophageal, and thyroidal branches, but unlike previous ones they are formed mostly by the preganglionic fibers and reach the ganglia on the level of the proper organ.

2.1.4 Blood Vessels of the Head and Neck

The head and neck are supplied by branches of the common carotid and subclavian arteries. On the right side, both vessels arise from brachiocephalic trunk, while left ones emerge directly from the arch of aorta.

The cervical part of the common carotid artery runs medially to the internal jugular vein and together with vagus nerve form a lower part of the cervical neurovascular bangle, surrounded by the carotid sheath. All structures are located laterally to the trachea/larynx and esophagus/pharynx and separated from them by the thyroid gland (Fig. 2.5). Posteriorly to the bundle, there are posterior processes of the cervical vertebrae (C3/4-C7) and prevertebral muscle. In the carotid triangle (surrounded by SCM, anterior belly of digastric and upper belly of omohyoid mm.), on the level of upper border of thyroid cartilage, the artery splits into external (ECA) and internal carotid arteries (ICA). The internal one replaces the common artery in a bangle and finally throughout the carotid canal enters the middle cranial fossa. Both, common and internal carotid arteries do not give any significant branches on

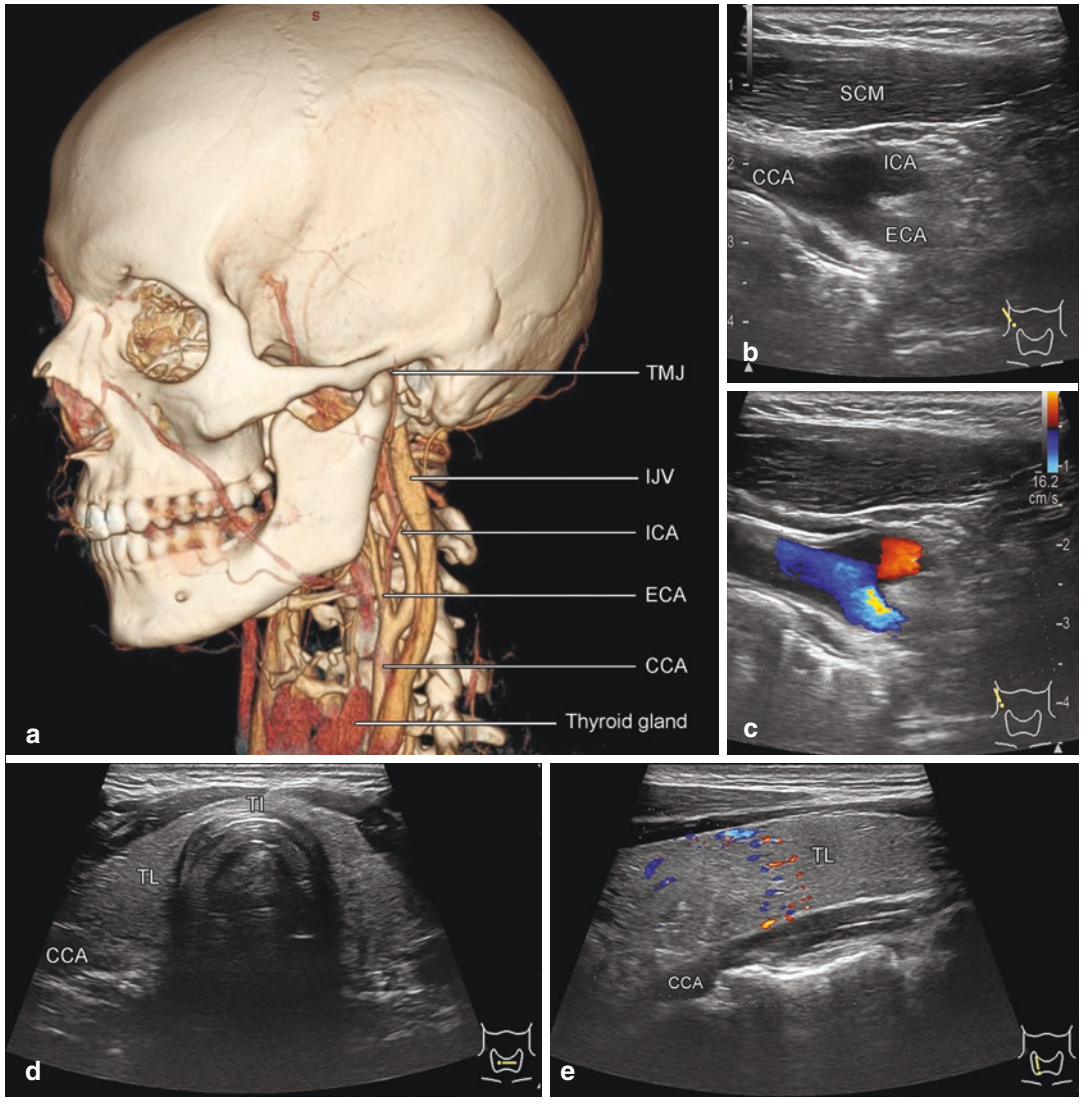

Fig. 2.5 Principal vessels of the neck on computed tomography VR—volumetric reconstruction (**a**) with a common (CCA), internal (ICA) and external carotid artery (ECA) and internal jugular vein (IJV). Ultrasound without (**b**, **d**) and with color Doppler (**e**, **f**) show division of CCA (carotid sinus; **b**, **f**) and relation CCA to the thyroid lobes (TL) and isthmus (TI) on horizontal (**d**) and vertical/lateral view (**e**). SCM—sternocleidomastoid m

the neck. However, the cranial part of ICA before it splits into anterior and middle cerebral arteries, it gives origin for posterior communicating, anterior choroid, and ophthalmic arteries. The second primary branch of the common carotid artery is the external carotid that supplies most of structures of the maxillofacial region and neck. After pricing the carotid sheaths, the artery enters the deep part of the parotid gland and on the level of the mandibular neck, it splits into terminal branches—maxillary and superficial temporal arteries.

Branches of the external carotid artery:

- Superior thyroid a. runs inferiorly for the level of carotid triangle and supplies thyroid gland, upper part of the larynx, and infrahyoid muscles.
- Lingual a. arises on the level of a greater horn of the hyoid bone, runs along the genioglossal

muscle. Before it enters the tongue and changes the name into deep lingual one, the artery gives suprahyoid branch that supplies all muscles of the oral floor (suprahyoid ones).
- Facial a. like the previously described ones arises from the anterior aspect of ECA on the level of carotid triangle. In a cervical part, it crosses the posterior belly of digastric and stylohyoid m., gives the tonsillar branch for palatine tonsil, ascending palatine a. for soft palatine, auditory tube and pharyngeal wall, submental a. for surrounding muscle as well as glandular branches for submandibular salivary gland. After crossing—well palpated facial notch on the base of the mandibular body, just in front of the angle—the artery, enters facial region, forms an arch on the top on the external surface of the masseter and buccinators, and ends in the middle of the orbit by anastomosing as the angular a. with the dorsal nasal a.—the terminal branch of ophthalmic artery. The facial part gives also origin for lower and upper labial branches that supply not only lips and external nose but also muscles of the cheek.
- Ascending pharyngeal a., a small branch that supplies pharyngeal wall, tympanic cavity, and dura mater.
- Occipital a. wings around the terminal part of the SCM, that supplies. It also provides the blood for other muscles of the back on this level, dura matter and auricle.
- Posterior auricular a. supplies auricle, surrounding muscle, tympanic cavity, and mastoid cells.
- Superficial temporal a. is well-visible, runs in front of the auricle and splits into frontal and parietal branches. It supplies auricle, parotid gland, temporalis muscle, frontal and temporal bellies of epicranial muscle as well as adherent scalp structures.
- Maxillary a., the main continuation of ECA, runs medially to the neck of the mandible, between the condylar process and stylomandibular ligament (mandibular part), then between lateral and medial pterygoid muscles (pterygoid part), and finally enters the pterygopalatine fossa, where splits into terminal branches (pterygopalatine part). The first part gives origin into deep auricular a. that supplies TMJ and external acoustic meatus; anterior tympanic a. for tympanic cavity, medial meningeal artery for the dura mater, tympanic cavity, and CNVII; inferior alveolar artery—that between the medial pterygoid muscle and mandibular branch runs inferiorly to reach the mandibular canal. Before entering the mandibular foramen, it gives origin for mylohyoid a., then dental/alveolar branches for teeth and gum, and finally, exits the canal through the mental foramen and divides into few mental branches for the surrounding muscles. The pterygoid part of the maxillary a. supplies mostly the muscles of mastication by the masseter and deep temporal aa., pterygoid branches and buccal a. which supplies muscles of mimic expression and remaining statures of the cheek, including small salivary glands and mucosa. The pterygopalatine part supplies upper teeth and gum by the dental branches of the superior posterior alveolar a., as well as alveolar/dental branches of the suborbital a.. It gives also branches for palatine (descending palatine, great and lesser palatine aa.), pharynx, auditory tube (pterygoid canal a.), nasal cavity, and anterior aspect of the hard palatine (sphenopalatine a.).

The remaining cervical organs are supplied by the branches for the subclavian aa. The cervical part of them forms an arch that runs over the apex of the lung, crosses the posterior scalene fissure (between anterior ad middle scalene mm.) and finally, on the external border of the first rib, changes the name and becomes axillary a. All its branches arise from the proximal ascending part:

- Internal thoracic a. supplies thoracic and abdominal wall and some mediastinal viscera.
- Vertebral a. exits from the upper aspect and along anterior scalene m. and enters the transversal foramen of upper six cervical vertebrae (C1-C6). Between C1 and C2 and over C1 the vessel forms posteriorly pointed arches to reduce the blood pressure before it enters the subarachnoid space by piercing posterior

atlantooccipital membrane. From the spinal canal, it enters the posterior cranial fossa, where right and left vertebral arteries unite together and form the basilar artery, that on the level of the intercondylar fossa, splits into posterior cerebral arteries. The cervical part of vertebral artery gives muscular, spinal, and meningeal branches for deep muscles of the neck and back, spinal cord and spinal nerves as well as meninges of the spinal cord. The intracranial part sends anterior and posterior spinal aa., and inferior posterior cerebellar a.

– Thyreocervical trunk is a short vessel that sends three primary branches: inferior thyroid, suprascapular, and transverse cervical arteries. The two last ones supply mostly muscles of the neck and pectoral griddle. The inferior thyroid a. beside the cervical muscles, dura mater, and spinal cord (ascending cervical a.) provides the blood for pharynx, esophagus, trachea, lower posterior part of the larynx (inferior laryngeal a.), and thyroid gland (glandular branches).
– Costocervical trunk splits into deep cervical and supreme intercostal artery that supplies deep muscle of the back and upper two intercostal spaces, respectively.

Veins of the head and neck have been grouped into (1) cerebral, meningeal, and cranial; (2) superficial; and (3) deep ones. The first group contains superficial and deep veins of the brain that empty into dura mater sinuses as well as small venal trunks that connect sinuses with extracranial veins such as: diploic vv., ophthalmic vv., emissariae vv. as well as venal plexuses of the cranial opening and canals. Among the superficial veins, the most important are facial and external carotid. The root of the facial vein is formed by the angular vein (connection of supraorbital, supratrochlear, and nasofrontal vv.), then it runs as a bowstring of the arch formed by the facial artery, below zygomatic major and over zygomatic minor, and masseter mm. On the mandibular angle, the vein changes the direction, runs horizontally on the superficial part of the parotid gland, where it connects with the retromandibular vein. Finally, in empties into the internal jugular vein. Even as a superficial vessel, it drains the blood from most of the face and some viscera by numbers of tributaries including palpebral, external nasal, deep facial, parotid, submental, and external palatine. The biggest branch is a retromandibular vein that runs inside of parotid gland and is formed by the union of the superficial and middle temporal veins, that receive blood from the scalp and temporalis muscle, respectively. Other tributaries of retromandibular v. are the transvers facial, articular from TMJ, stylomastoid, anterior auricular, parotid, and maxillary bones, that connect the facial vein with the pterygoid plexus. The biggest, well-visible vein of the neck is the external jugular. Its posterior root is formed by the union of the occipital and posterior auricular vein, while the anterior one is a small trunk that arises from the retromandibular vein. The external jugular v. runs between platysma and superficial cervical fascia, crosses the external surface of SCM and slightly over clavicle pierces the superficial and pretracheal layer of deep cervical fascia and finally, empties into the subclavian or internal jugular vein. Beside the root, it receives small suprascapular, transvers cervical veins as well as anterior cervical vein, that collects the blood from the floor of the oral cavity and communicates with the same vein on the other side by two venal arches—prehyoid and suprasternal.

Deep veins are much better developed and grouped into tributaries of pterygoid and vertebral plexus as well as internal jugular vein and brachiocephalic vv. The pterygoid plexus is located in pterygopalatine and infratemporal fossa. It receives the blood from veins that correspond to most of the branches of maxillary artery. The main outflow is by maxillary veins into the external jugular vein.

The vertebral plexus is formed by dens venal network located in epidural space in the spinal canal and outside of the vertebrae, and for this reason, it is divided into external and internal. Both parts are connected by intervertebral veins and basivertebral veins; however, the last ones are usually not seen on the cervical level. The blood flows out mostly by the vertebral and deep cervical vein(s) into brachiocephalic or subcla-

vian vein. Both veins may be plural or multiple superiorly, especially next to suboccipital plexus, but later unite into single trunks.

The biggest vein on the neck is the internal jugular v. (IJV; Fig. 2.5). It is a continuation of the sigmoid sinus, that on the level of jugular foramen, changes the direction and becomes much wider (upper bulb), then the vessel enters the carotid sheath and runs on the later aspect of the carotid arteries, crossing behind the lower mid and lower part of SCM. Posteriorly to sternoclavicular joint, it becomes wider again (lower bulb) and unites with subclavian vein (venal angle) to form the brachiocephalic vein. There are number of cranial (sigmoid, occipital and inferior petrosal sinus, plexus of hypoglossal canal, cochlear canal vein) and extracranial tributaries of IJV, including occipital, facial, pharyngeal, lingual as well as superior, inferior, and lowest/ima thyroid aa. From clinical point of view, it is important to expand data on lingual veins. The main blood flow is into deep lingual veins that follow lingual artery and genioglossus m. and later unite into short lingual vein that empties into IJV. On the dorsal aspect of the lingual root, there is a submucosal venal plexus that drain the blood into dorsal lingual veins. From the inferior aspect of the apex and body blood is collected by the well-visible sublingual veins that run between sublingual gland and genioglossus m. pierce mylohyoid muscle and as vein committing to CNXII empties to the lingual v. or directly to IJV.

2.1.5 Lymphatic System of the Head and Neck

On the level of head and neck, there are a number of organs that do not have lymphatic vessels, i.e., brain, spinal cord, and surrounding meninges, membranes labyrinth, eye, hair, and enamel. All the remaining structures send the lymph to various nodes. Anatomically, there are four groups of lymphatic nodes on the head and numbers on the neck that are grouped into anterior, superficial (posterolateral), and deep cervical ones.

Lymph nodes of the head:

- Occipital ones (n = 2–3) are located on the level of superior nuchal line, receive the lymph from muscles and skin of occipital region and upper back.
- Retromandibular nodes (1–3) are located on the upper attachment of SCM, drain the lymph from middle aspect of the auricle, middle ear including mastoid cavity and cells, and temporal region.
- Parotid nodes (4–6) are divided into superficial and deep ones, that are located outside and inside of the parotid capsule, respectively. They receive lymph from parotid gland, lateral aspect of eyelids, conjunctive, external surface of auricle, external acoustic meatus, and temporal region.
- Buccal/facial nodes (1–2) lie on the buccinators muscle and receive the lymph from the cheek, orbit, nasal cavity, infratemporal fossa, nasopharynx, and palatine.

From all groups, lymph is drained mainly into deep cervical nodes, but parotid and buccal may send also into posterior submandibular ones. A connection between parotid and superficial cervical ones has been also described. Some authors point a separate group—lingual lymph nodes—that is formed by small nodes incorporated into lymphatic vessels between lateral and ventral aspects of the tongue and posterior submandibular lymph nodes.

Anterior cervical lymph nodes drain into deep cervical lymph nodes and contain:

- Submandibular ones (3–8) are located below mylohyoid m., in a submandibular triangle. Secondary to the position to the submandibular salivary gland, they are divided into anterior (1–5), middle (1–3), and posterior group (1–2). The border between the last two is formed by facial artery. The group may be also expanded by small paramandibular nodes (1–2) located inside the submandibular salivary gland The anterior group receives the lymph from lateral part of the lower lip, premolar lower teeth, and

from submental lymph nodes, while middle and posterior ones drain the lymph from middle aspect of eyelids, cheek, external nose, upper lip, hard palatine, maxilla including sinus and upper teeth, submandibular and sublingul salivary glands, lateral and ventral aspect of anterior 2/3 of the tongue. They also receive lymph from parotid lymph nodes by angular tract that runs along retromandibular vein as well as anterior submandibular lymph nodes. Their efferent vessels run along both, facial vein (superficial) and artery (deep) into upper deep cervical lymph nodes.

- Submental lymph nodes (2–8) lie on the level of submental lymph triangle between platysma and superficial cervical fascia, close to mandible (anterior ones) or hyoid bone (posterior ones). They drain the lymph from chin, middle part of the lower lip, canines and incisor, and apex of the tongue. Efferent vessels drain into middle and posterior submandibular lymph nodes or directly into deep cervical lymph nodes, they may also cross midbody line and empty into nodes of opposite side of the body.
- Retropharyngeal (1–3) between nasopharynx and prevertebral layer of deep cervical fascia on the level of C1–C2. The afferent vessels come from nasopharynx, nasal cavity, and auditory tube, while efferent ones drain into deep cervical lymph nodes.
- Infrahyoid nodes (1–2) lie below body of hyoid bone and receive lymph from the laryngeal vestibule, piriform recess, and hypopharynx.
- Prelaryngeal node (1) usually lies on the level of cricothyroid ligament in a midbody line and receive the lymph from hypolarynx.
- Pretracheal nodes (1–3) are located on an anterior aspect of the cervical part of the trachea, below the isthmus of the thyroid gland. They receive lymph from the trachea and thyroid gland. Similarly located nodes on the level of the thorax belong to the right paratracheal lymph nodes.
- Paratracheal nodes (5–6) lie on the lateral aspect of the trachea and grove between it and esophagus. They drain the lymph from the hypopharynx, cervical part of esophagus, thyroid gland, pretracheal lymph nodes, while efferent vessels go into deep cervical or directly into the venal angle by bronchomediastinal lymph duct.
- Suprasternal nodes (1–2) are located in the suprasternal space and receive the lymph from the skin of the anterior cervical triangle, limited by base of mandible and both SCM muscles. Efferent vessels drain directly into the venal angle.

The superficial cervical lymph nodes (4–6) are seen in the upper part of the lateral cervical triangle, along external branch of CNXI, below the superficial cervical fascia. They receive lymph from back and occipital region (including occipital and parotid lymph nodes). The efferent vessels terminate mainly into supraclavicular lymph nodes (8–12), that are located along subclavicular vessels. They receive lymph from axillary and interpectoral lymph nodes, as well as anterior thoracic wall, back and skin of lateral cervical triangle. Efferent vessels form the subclavicular lymphatic duct that empties into the venal angle.

The biggest group on the neck is formed by deep cervical lymph nodes (10–20), that surround the cervical neurovascular bangle. Anatomically, the intermedian tendon of the digastric m. divides them into upper and lower group. From clinical point of view, one node (jugulodigastric) should be pointed out since it receives vessels directly from the root of the tongue. It is located in front of external jugular vein on the level of the great hyoid horn. The deep cervical nodes receive lymph also from most of above-explained groups. Efferent vessels unite together and form the jugular lymphatic duct that empties into the venal angle.

Radiological classification of cervical lymph nodes includes seven principle groups, that partially communicates with anatomical calcification ([12–14]; Fig. 2.6):

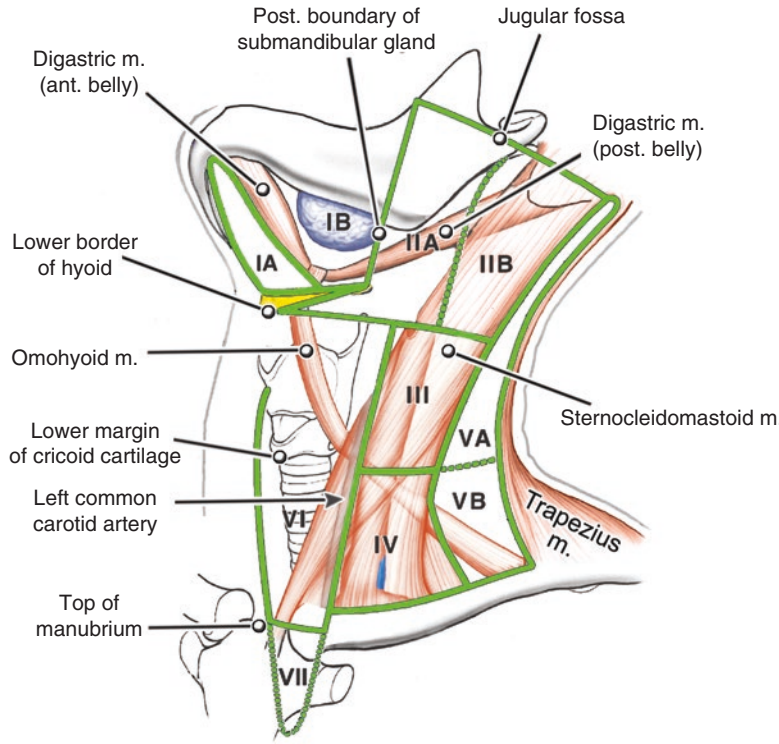

Fig. 2.6 Radiological classification of cervical lymph nodes; based on [13]

- Group IA—submental group.
- Group IB—anterior and middle submandibular group.
- Group IIA—posterior submandibular group (angular mandibular).
- Group IIB—upper deep cervical group (between the TMJ and hyoid bone).
- Group III—mid deep cervical (between the hyoid bone and intermediate tendon of omohyoid m.)
- Group IV—low deep cervical and anterior supraclavicular (below the intermediate tendon of omohyoid m.)
- Group VA—superficial cervical (over the intermediate tendon of omohyoid m.)
- Group VB—superficial cervical (below the intermediate tendon of omohyoid m.) and posterior supraclavicular.
- Group VI—anterior cervical below the hyoid bone.
- Group VII—retrosternal (upper mediastinal).

2.1.6 Oral Cavity

Oral cavity is a true space, beginning of the alimentary system, that contains the tongue. It extends from the inner aspects of the lips and cheeks, starting at rima oris and ends at the fauces, where it continues as oral part of the pharynx (Fig. 2.7). It is usually subdivided into the oral vestibule and the oral cavity proper. The border between these two compartments is the teeth. The hard and the soft palates form the roof of the oral cavity. The oral floor is composed of paired mylohyoid and geniohyoid supported by the anterior bellies of the digastric muscles.

2.1.6.1 Oral Vestibule

The oral vestibule is a narrow gap that extends between inner aspects of the lips and cheeks and the outer surfaces of the upper and lower teeth and gums. It receives drainage from both parotid salivary glands and small labial, buccal, and

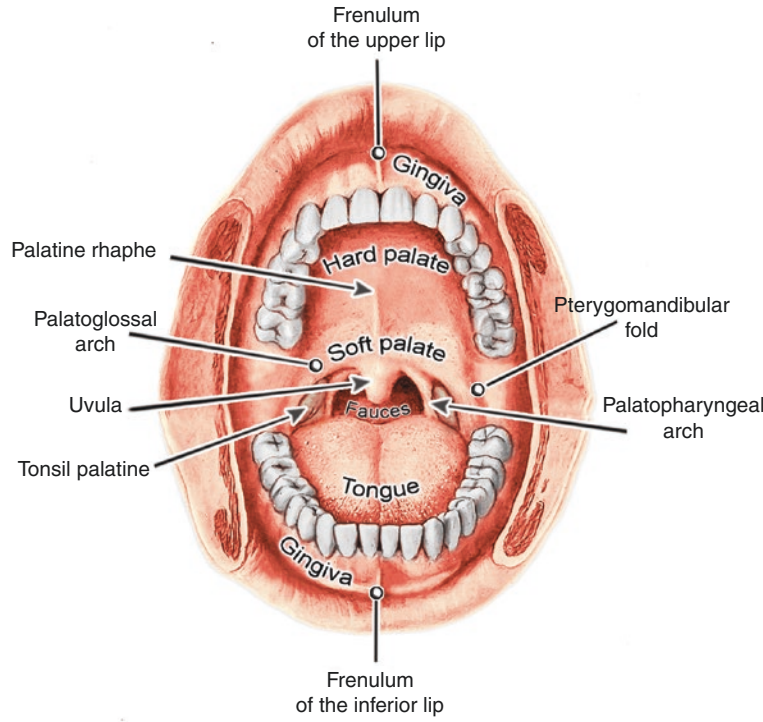

Fig. 2.7 Oral cavity—general view

molar glands. The vestibule communicates naturally with the oral cavity proper through the retrodental space which includes the retromolar triangle, limited by the buccinator crest medially, oblique line laterally, and from anterior by the posterior surface of the last molar tooth.

Lips

There are two lips—upper and lower lip surround the gap called rima oris. The lips are united at both ends by oral angles. The oral angles limit the rima oris from lateral (it extends more or less from left to right canines). The base for the lip is composed of the orbicularis oris muscle. One can distinguish cutaneous, mucosal, and intermediate parts in each lip.

Cheeks—Buccae

The cheeks occupy the region of the face that extends from the oral angle until the auricle and from the zygomatic arch until the lower border of the mandible. Going from the outside one can distinguish the following elements: skin, fat tissue, buccopharyngeal fascia, buccinator muscle, buccal glands, and oral mucosal layer.

Gums

Gums are mucosal structures that adhere to the alveolar processes of the maxillae and alveolar part of the mandible including the neck of teeth.

Blood Supply and Innervation of the Oral Vestibule

Lips are supplied by labial branches of the facial arteries; additionally, the lower lip receives some branches of the mental arteries. The cheek receives arterial supply from the buccal, transverse facial, and infraorbital arteries. Alveolar processes of the maxillae receive blood via superior anterior and posteriori alveolar arteries. Alveolar part of mandible is supplied by inferior alveolar arteries.

Venous blood is drained through the comitant veins to retromandibular and external jugular

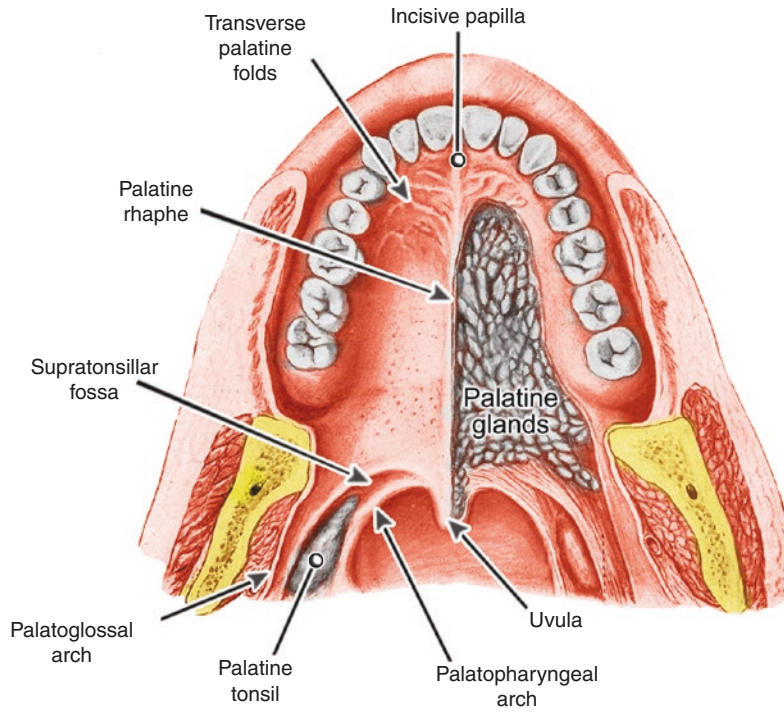

Fig. 2.8 Hard and soft palate—general view

veins. Lymph from the oral vestibule flows into submandibular and submental nodes, as well as directly to the deep cervical.

Motor nerve supply to oral vestibule is derived from branches of the facial nerve. Sensory innervation goes via superior labial branches of the infraorbital nerve and inferior labial branches of the mental nerve. The cheek is supplied with buccal nerve. Alveolar processes of maxillae and alveolar part of mandible are supplied by the superior and inferior dental plexuses, respectively.

2.1.6.2 Oral Cavity Proper

It is a space located internal to the maxillary and mandibular gums and teeth. It is limited from above by soft and hard palates, inferiorly by sublingual region (placed on top of the oral diaphragm), anterolaterally by the alveolar processes of the maxillae and the alveolar part of the mandible with gums and teeth. Posteriorly it communicates with the oropharynx through fauces.

Palate

It is divided into anterior part, that has a bony framework, so-called hard palate and posteriori, which in fact is a fold consisted of mucosa and muscles, so-called soft palate (Fig. 2.8). The hard palate is composed of palatine processes of the maxillae and transverse palatine plates of palatine bones united through median and transverse palatine sutures, respectively. Hard palate is covered with mucosa that adheres to the periosteum directly. It continues anteriorly and laterally into the gums and posteriorly into the mucosa of the soft palate. Palatal glands are located between mucosa and periosteum. Posterior to the incisors the mucosa creates incisive papilla. Posterior to it one can see the palatine raphe with 3–4 transverse palatine folds that extend from the raphe in its anterior portion.

The soft palate is a continuation of the hard one. Its anterior (oral) surface faces the oral cavity proper, and the posteriori (nasal or pharyngeal surface) is directed towards the nasopharynx. Its free concave lower margin forms uvula and laterally it continues in the form of two arches: palatoglossal (anterior) and palatopharyngeal (posterior), with the palatine tonsil in between.

There are five pairs of muscles that constitute the soft palate: tensor veli palatini, levator veli

palatini, palatoglossus and palatopharyngeus muscles, and muscle of uvula. Levator and tensor elevate and tense the soft palate and dilate the auditory tube's orifice. Palatoglossus and palatopharyngeus muscles narrow the fauces and lower the soft palate mm. of uvulae elevates and shortens uvula and the soft palate. Innervation of the tensor veli palatini is derived from the nerve to tensor veli palatini (from mandibular division of trigeminal nerve). Remaining muscles are supplied by pharyngeal rami of glossopharyngeal and vagus nerves (including the fibers of cranial accessory nerve), forming the pharyngeal plexus.

Blood supply of the oral cavity proper is derived from several sources. Alveolar processes of maxillae with their gums and teeth are supplied by the superior anterior and posteriori alveolar arteries, alveolar part of mandible is nourished by inferior alveolar arteries (from maxillary a.). The hard palate receives blood from the greater palatine arteries (of the descending palatine), and the soft palate is supplied by the lesser palatine arteries from descending palatine a. and ascending palatine arteries from facial a.. Sublingual region receives blood from sublingual artery (of the lingual a.).

Venous drainage tends towards the pterygoid venous plexus and the facial veins. Lymphatic flow is analogous to the drainage of the oral vestibule.

Alveolar processes of the maxillary and alveolar part of mandible are supplied by superior and inferior dental plexuses, respectively. Hard and soft palates are innervated by greater and lesser palatine nerves from the pterygopalatine ganglion, while incisive area is supplied by the nasopalatine nerve from the same source as previous nerves. The sublingual region is supplied by the sublingual nerve (from lingual) while fauces receive ramus from facial nerve.

Sublingual Region

The oral floor is created by the sublingual region, that is, based on the oral diaphragm (Fig. 2.9). The diaphragm extends posteriorly till the last molar teeth and is composed of two mylohyoid muscles, supported by geniohyoids and anterior bellies of digastric muscles.

Centrally there is the lingual frenulum with sublingual folds placed laterally, caused by the course of the lesser sublingual glands. Their ducts (ducts of Rivini) open on free margins of these folds. Both sublingual folds unite at the sublingual caruncula. This caruncula serves as a point of exit of two submandibular ducts (ducts of Wharton) and two greater sublingual ducts

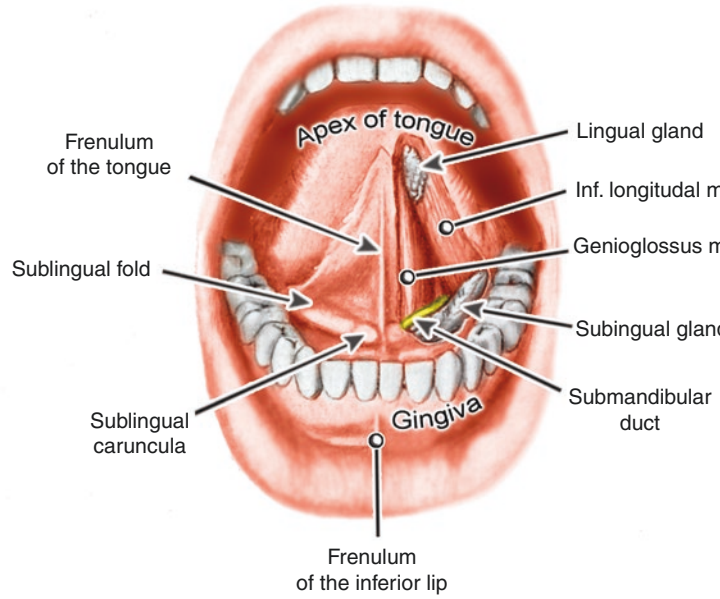

Fig. 2.9 Sublingual region—general view

(ducts of Bartholin). In the inferior aspect of the tongue, one can see the so-called plica fimbriata.

Tongue

The tongue is composed of striated muscles. It is characterized by a relatively large variation of shape and mobility. It is covered with mucosa.

The tongue is divided into the body accounting for anterior 2/3, that narrows to the end and becomes the apex and the root of the tongue that forms posterior 1/3 (Fig. 2.10). Terminal sulcus in the dorsum of the tongue forms a border between the body and the root. V-shaped sulcus faces posteriorly foramen cecum, a visible remnant of the thyroglossal duct. Posterior to the groove one can see the lingual tonsil. Next, the mucosa continues forming medial and two lateral glossoepiglottic folds that border valleculae. Superior surface of the tongue is divided into two symmetric halves by median sulcus. In the horizontal section of the tongue, one can distinguish mucosa, lingual aponeurosis, muscles of the tongue, submucosal layer, and again mucosa. The lingual aponeurosis is a transformed submucosal layer of the lingual dorsum and apex. It joins firmly mucosa and muscles. At right angles to the aponeurosis, one can find lingual septum that separates right and left muscles. It is an incomplete septum that never reaches the surface and the end of the tongue. It is an origin of the transverse muscle of the tongue.

Striated muscles of the tongue have their partial insertions on the bony structures: mandible, hyoid bone, and the styloid process; whereas partially they start from connective tissue elements of the tongue. Muscles of the tongue are divided into intrinsic and extrinsic.

The extrinsic muscles of the tongue by their contractions cause changes of location of the entire tongue, i.e., protrusion and retraction. All these muscles are paired (Figs. 2.11, 2.12 and 2.13). They consist of the following:

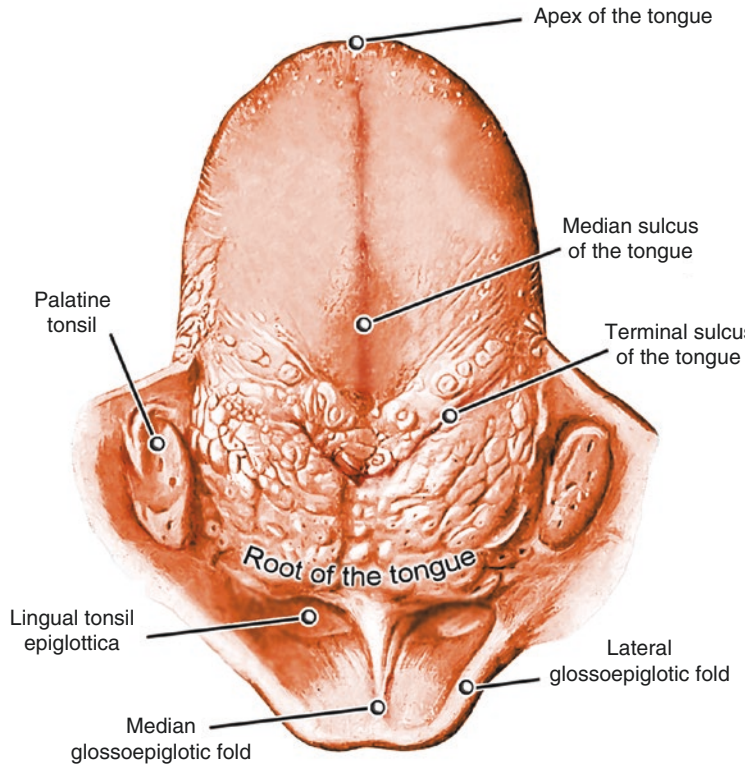

Fig. 2.10 The tongue—view from above

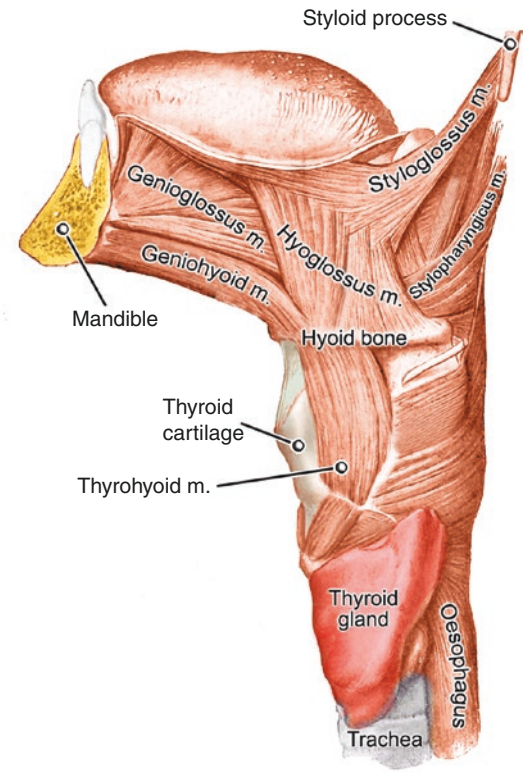

Fig. 2.11 Extrinsic muscles of the tongue—lateral view

- Genioglossus muscle—protrudes the tongue and presses it towards the sublingual region.
- Hyoglossus muscle—retracts the tongue.
- Styloglossus muscle—retracts the tongue.

The intrinsic muscles begin and end within the tongue (Fig. 2.13). They change the shape of the tongue without changing its location or even independently on it (i.e., thickening or flattening of the tongue). The following muscles belong to this group:

- Superior longitudinal—impaired, that shortens and widens the tongue.
- Inferior longitudinal—paired, that shortens the tongue.
- Transverse muscle of the tongue, impaired that flattens the tongue; part of its fibers continue as palatoglossus muscle.
- Vertical muscle of the tongue, paired, that flattens, widens, and elongates the tongue.

Tongue is supplied with the lingual artery and minute branches from facial and ascending pharyngeal. The veins go in company with the arteries, although lingual vein may drain into internal jugular or facial vein (see Sect. 2.1.4). Lymphatic of the tongue joins right and left side. The drainage of the corpus is almost completely separated from the root. Apex of the tongue is drained by the submental nodes, the body by submandibular, and the root by the superior deep cervical (paramandibular lymph nodes). Muscles of the tongue are predominantly supplied by the hypoglossal nerve. The lingual mucosa receives both sensory (touch, pain, temperature, pressure), taste, as well as parasympathetic and sympathetic innervation.

The body of the tongue receives sensory innervation from the lingual nerve (via cell bodies located in the trigeminal ganglion); taste buds of the corpus are supplied by the dendrites of geniculate ganglion that are delivered by chorda tympani that joins the lingual nerve within the infratemporal fossa. Secretomotory fibers (parasympathetic postganglionic) run from the submandibular ganglion, sympathetic accompany the lingual artery (their cell bodies are located in the superior cervical ganglion).

The root of the tongue receives lingual rami of the glossopharyngeal nerve. The mucosa of the regions next to the epiglottis is supplied by internal laryngeal nerve of vagus.

Glands of the Oral Cavity

The mucosa of the oral cavity is lubricated by the saliva produced in and variable large amount of salivary glands, including major (parotid, sublingual, submandibular; Fig. 2.14) and minor ones (buccal, labial, palatal, lingual, molar). The vestibule of the oral cavity drains labial, buccal, molar, and parotid glands. The oral cavity proper drains palatal, lingual, submandibular, and sublingual glands.

Parotid Gland

The gland occupies the parotid space and is divided into superficial and deep parts. Superficial part of the parotid gland is located in the lateral region of the face on the masseter muscle, anterior to the auricle and anterior margin of the sternocleidomastoid muscle, the deep portion is lodged within the retromandibular fossa.

The gland is surrounded by the parotid fascia that is also referred to as parotid capsule. The fas-

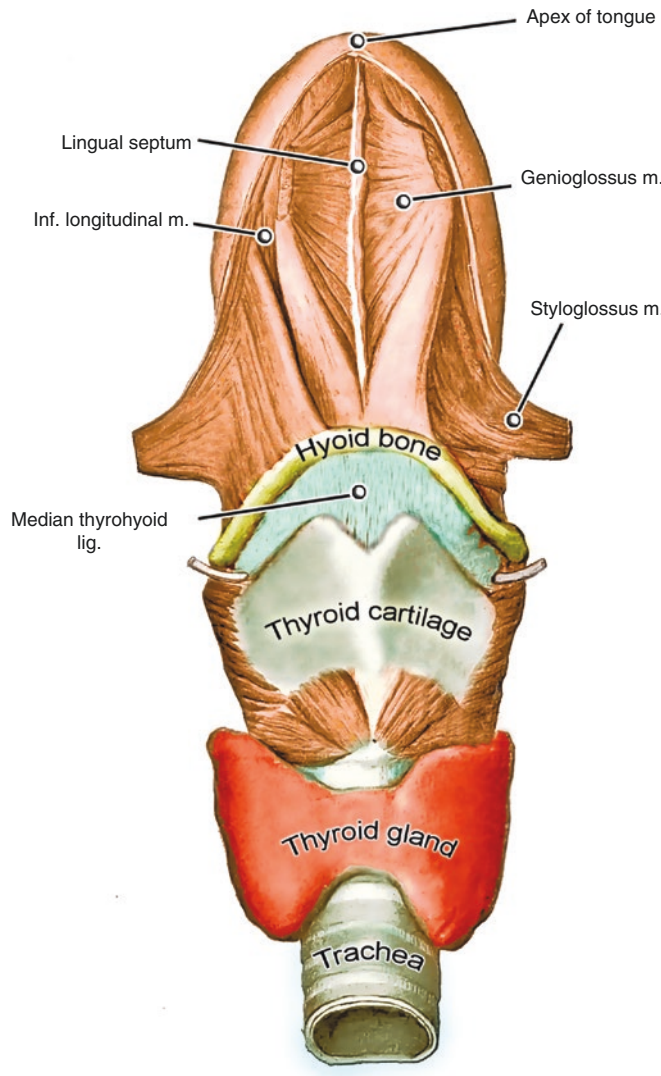

Fig. 2.12 Tongue muscles—view from below

cia continues to the neighboring muscles (i.e., masseter). The capsule encloses a compartment that apart from the gland contains: facial nerve and its branches forming parotid plexus, auriculotemporal nerve, terminal portion of the external carotid artery and its subdivision into maxillary and superficial temporal arteries, posterior auricular and transverse facial arteries, retromandibular vein, lymphatic vessels, and lymph nodes. Superficial to the fascia one can find the superficial parotid lymph nodes and vessels with ramifications of the greater auricular nerve.

Anterior border of the gland gives rise to parotid duct. The duct runs superficially on the masseter muscle, parallel and 1 cm below the zygomatic arch. On the anterior border of the masseter, the duct flexes medially, pierces buccinator muscle, and empties into the oral vestibule on the parotid papilla, located opposite the second upper molar tooth. Right above the duct one can find the transverse facial artery. The superficial temporal artery and the auriculotemporal nerve run between the gland and the external acoustic meatus.

Submandibular Gland

The submandibular gland, divided into superficial and deep parts, is located in the digastric

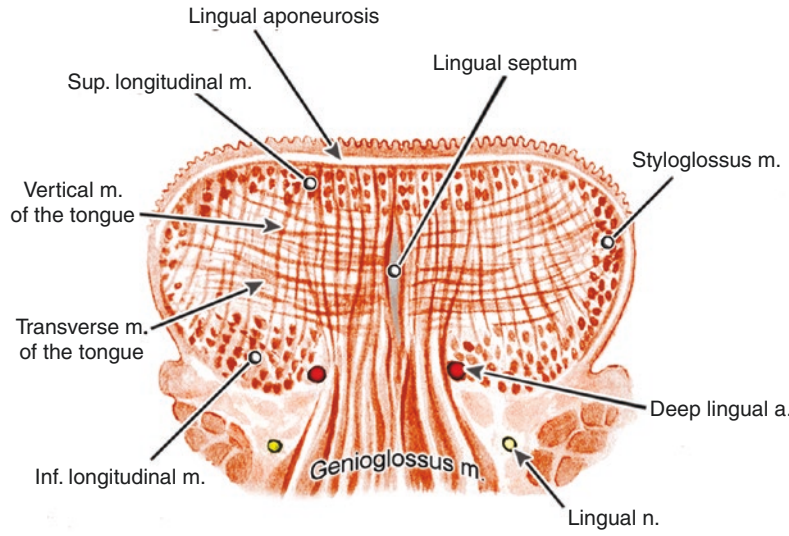

Fig. 2.13 Tongue muscles—frontal cross-section

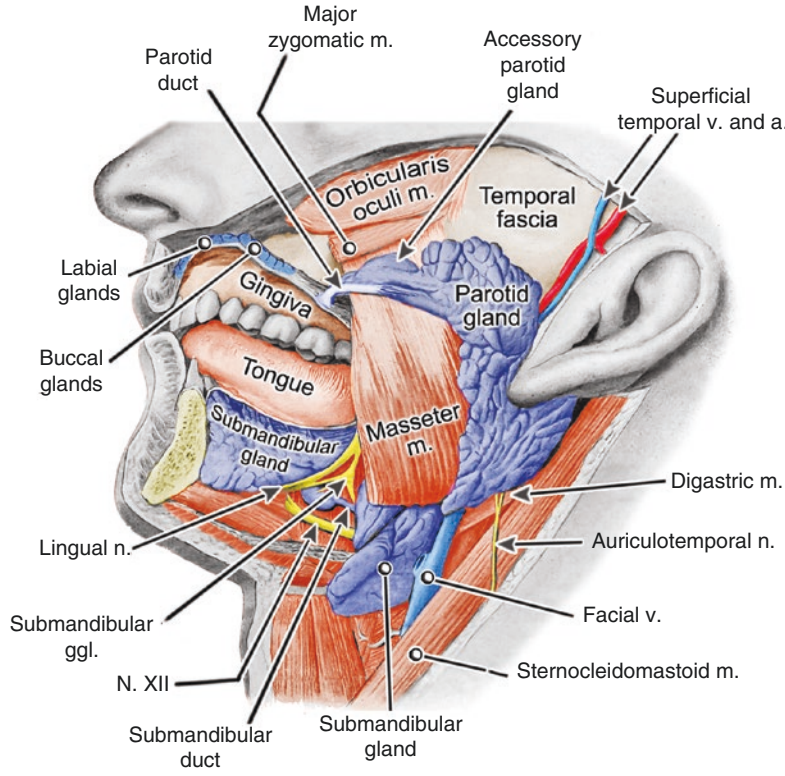

Fig. 2.14 Glands of the oral cavity—general view

(submandibular) triangle. It is separated posteriorly from the parotid gland by the stylomandibular ligament. It neighbors medially to the mandible. The deep portion of the gland lies between mylohyoid, hyoglossus and styloglossus muscles, inferiorly to the lingual and superiorly to the hypoglossal nerves. The submandibular duct traverses the deep part of the gland and bends over the free end of the mylohyoid muscle. It then runs between the mylohyoid and the hyoglossus muscles running between the genioglossus muscle and the sublingual gland. On the

hyoglossus muscle, the duct lies between the lingual and hypoglossal nerves. It opens at the side of the lingual frenulum (sublingual caruncle).

Sublingual Gland

The major sublingual gland is placed on the mylohyoid muscle and is covered with the mucosa of the oral floor thus forming the sublingual fold. It extends between the sublingual fossa of the mandible and the genioglossus muscle. The genioglossus is separated from the gland by the course of the lingual nerve and the submandibular duct. The ducts of the smaller sublingual glands (8–20) open on the sublingual fold or may open into the submandibular duct. Major sublingual duct opens next to the orifice of the submandibular duct. As an anatomical variation a minor sublingual gland on the inferior aspect of the tongue, slightly posteriori to the apex, could be seen.

2.1.7 Nasal Cavity

2.1.7.1 External Nose

One can distinguish the following layers in the external nose: external cutaneous layer, muscular layer, skeleton, and the internal cutaneous layer. Muscular layer comprises nasal muscle, depressor septi, levator labii superioris alaequae nasi, and procerus. The skeleton of the nose is composed of bones, cartilages, and elements of fibrous connective tissue. Bony skeleton consists of nasal bones, nasal part of the frontal, and frontal processes of the maxillae. Cartilaginous skeleton comprises: nasal septal cartilage, lateral nasal cartilages, greater and lesser alar cartilages, vomeronasal cartilage, and accessory nasal cartilages. Fibrous connective tissue is a continuation of the periosteum and perichondrium, that cover bones and cartilages. It unites particular cartilages and cartilages with bony elements. Internal cutaneous layer is a continuation of the external cutaneous layer that through the nares enters the nasal vestibule. The vestibule is separated superiorly from the nasal cavity proper with a visible fold. It is created by the protrusion made by superior margin of the lateral limb of the greater alar cartilage—limen nasi. This ridge is a border between the nasal vestibule and the nasal cavity proper and between the epidermis and mucosa. The nasal septum opposite to limen nasi possesses rich venous plexus—the site of relatively common bleedings—locus Kiesselbach.

Blood supply to the external nose is derived from branches of the dorsal nasal artery (from ophthalmic a.), angular (from the facial a.), and infraorbital (from the maxillary a.). Venous blood flows through the nasofrontal vein to the superior ophthalmic and angular to the facial and mostly to internal jugular vein. Lymph through the parotid and submandibular nodes flows to the superior deep cervical nodes. Muscles of the external nose are supplied by ramifications of the facial nerve. Cutaneous innervation originates from the nasal branches of the anterior ethmoidal and infraorbital nerves.

2.1.7.2 Nasal Cavity Proper

It is limited by internal surface of the external nose and bones covered with mucosa. Anteriorly through the vestibule, nasal cavity opens with nares. Posteriorly it joins the nasopharynx through the choanae. Centrally located nasal septum is composed of the nasal septal cartilage, vomer, and the perpendicular plate of the ethmoid. It divides the nasal cavity into two chambers.

Bony limitations of the nasal cavity are as follows: from above—nasal bones, nasal spine of frontal, cribriform plate of ethmoidal, and body of sphenoid with sphenoidal conchae; from below—palatine processes of maxillae and horizontal laminae of palatine bones; laterally by medial Surface of the frontal process of maxilla, body of maxilla, lacrimal bone, medial wall of ethmoidal labyrinth, inferior nasal turbinate, perpendicular lamina of palatine, and medial pterygoid process.

Nasal septum divides nasal cavity into two compartments. In each of them, one can distinguish superior middle and inferior, middle, superior (sometimes supreme) nasal meatus and sphenoethmoidal recess—placed between the roof of the nasal cavity and the superior nasal concha. Superior nasal meatus is located between the superior and middle nasal conchae. Middle meatus is between the middle and inferior concha, and the inferior meatus is located between the hard palate and the inferior concha. Posteriorly all nasal meatuses join to form common nasopha-

ryngeal meatus that joins with the nasopharynx through the choanae—limited superiorly by the body of sphenoid and wings of vomer, laterally by the medial pterygoid plates, and inferiorly by the transverse palatine plates (Fig. 2.15).

Communication of the Nasal Cavity

The inferior nasal meatus joins with the nasolacrimal canal and duct. Middle meatus communicates with the frontal, maxillary sinuses, and the anterior and middle ethmoidal cells. The superior meatus communicates with the posteriori ethmoidal cells. Sphenoethmoidal recess drains the sphenoid sinuses. The nasal cavity communicates with the pterygopalatine fossa through the sphenopalatine foramen, with the anterior cranial fossa through the cribriform plate of ethmoid, and with the oral cavity through the incisive canal.

Mucosa of the Nasal Cavity

The mucous membrane that lines the nasal cavity is divided into respiratory and olfactory regions. The olfactory region is located on the superior concha, superior meatus, and the adjacent portions of the nasal septum. Axons of the olfactory cells of that area traverse the cribriform plate of the ethmoid entering the anterior cranial fossa, where they reach the olfactory bulb.

Blood Supply and Innervation of the Nasal Cavity

Anterosuperior portion of the nasal cavity and the adjacent fragments of the nasal septum are supplied by the anterior ethmoidal artery (from ophthalmic a.). Posteroinferior part receives branches from the sphenopalatine artery (from maxillary a.). The region next to the sphenoethmoidal recess is supplied by ramifications from the posteriori ethmoidal artery (from ophthalmic). Venous blood flows into pterygoid venous plexus or venous dural sinuses.

Nerves to the anterosuperior part of the nasal cavity are derived from the anterior ethmoidal nerve, while posteroinferior part receives innervation from posteriori nasal branches of the pterygopalatine ganglion. Orbital rami of the pterygopalatine ganglion join the posteriori ethmoidal nerve and supply the mucosa of the sphenoid sinus and posterior ethmoidal cells. Maxillary nerve through the infraorbital n. supplies the maxillary sinus, while the rest of the sinuses are supplied by branches of the frontal nerve.

Paranasal Sinuses

The paranasal sinuses are pneumatic spaces located inside the bones surrounding the nasal cavity (Fig. 2.16). They arise as invaginations of the nasal mucosa that ingrows the neighboring bones.

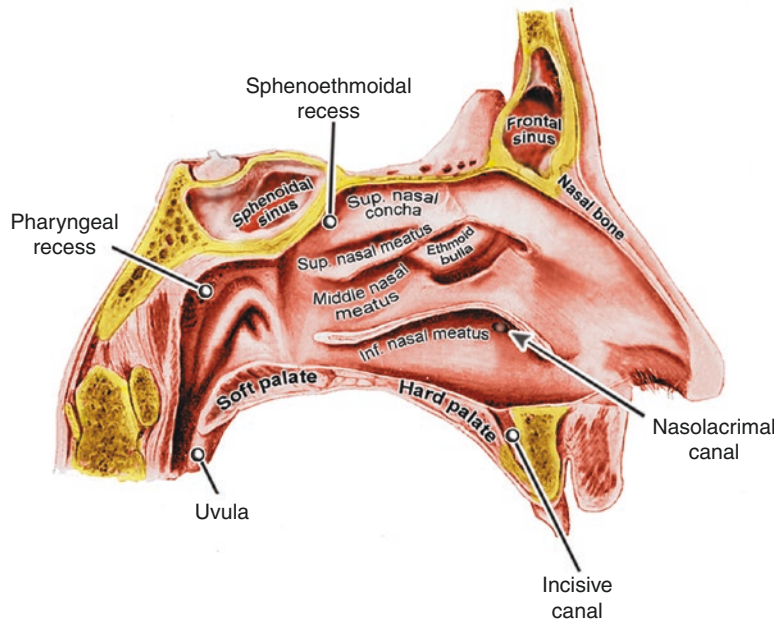

Fig. 2.15 Nasal cavity—sagittal section

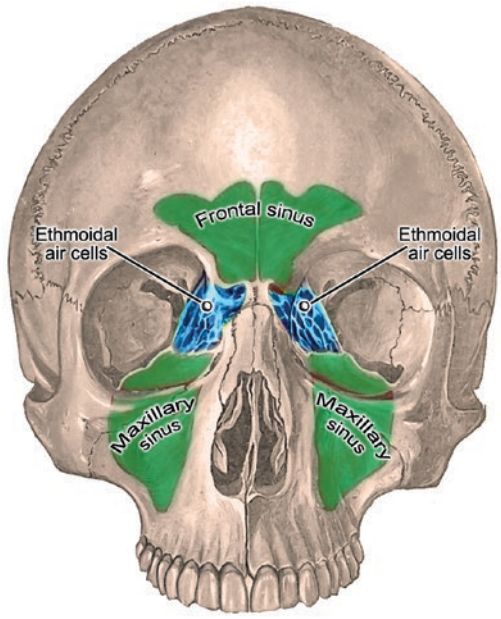

Fig. 2.16 Paranasal sinuses—anterior view

– The frontal sinus is a paired space located in the squamous part of the frontal, at the border between the squama and the orbital part. Its shape resembles the pyramid and its apex is directed upwards. The volume of both frontal sinuses varies from 5–20 cm^3. They develop around 7–8 years and drain into the middle meatus through infundibulum.
– The ethmoidal air cells are located within the ethmoidal labyrinth bilaterally, divisible into anterior, middle, and posterior. Anterior and middle ethmoidal air cells drain into the middle nasal meatus through the infundibulum. Posterior cells empty into the superior meatus. The largest ethmoidal air cell is the ethmoidal bulla that is the largest among the anterior cells. The volume of the cells unilaterally is near 10 cm^3.
– The sphenoidal sinus is located within the body of the sphenoid bone. Its volume reaches 5–6 cm^3. This sinus drains into the sphenoethmoidal recess. It develops around the 3–4. postnatal year.
– The maxillary sinus (sinus of Highmore) is a paired pneumatic space (24 cm^3) that is located in the body of the maxilla. Its shape resembles a pyramid with the apex turned towards the zygomatic bone and the base to the nasal cavity. On the medial surface of the maxillary body, one can see the opening that leads into the sinus. It is so-called maxillary hiatus. This opening is located above the floor of the maxillary sinus. The sinus drains into the middle nasal meatus. Its opening is decreased by the perpendicular plate of palatine from behind, uncinate process of ethmoid bone (from anterior and superior), maxillary process of the inferior nasal turbinate (from below), and the ethmoidal process of the inferior nasal turbinate (in the middle portion). The lumen of the maxillary sinus sends the following recesses:
  - Alveolar—that invaginates in between two laminae of the alveolar process of maxilla.
  - Orbital—that enters the orbital process of palatine.
  - Zygomatic—that penetrates the zygomatic process of maxilla.
  - Infraorbital—that may surround the infraorbital canal.
  - Palatine—that enters the palatine process of maxilla.

2.1.8 Larynx and Other Neck Organs

The larynx is located within the neck, in its central portion, between the pretracheal and prevertebral lamina of the deep cervical fascia. Apart from the larynx, one can find trachea, pharynx, cervical portion of esophagus, thryoid gland, and carotid neurovascular bundles. The larynx is situated below the tongue and hyoid bone, above the trachea. It is covered anteriorly by the sternohyoid, sternothyroid, and thyrohyoid muscles. Posteriorly it neighbors with the laryngopharynx. Information on all these organs is provided by the anatomical textbooks [1–5].

USG Anatomy.

Figures 2.17, 2.18, 2.19, 2.20, 2.21, 2.22, 2.23, 2.24, 2.25 and 2.26 USG image of different anatomical structures.

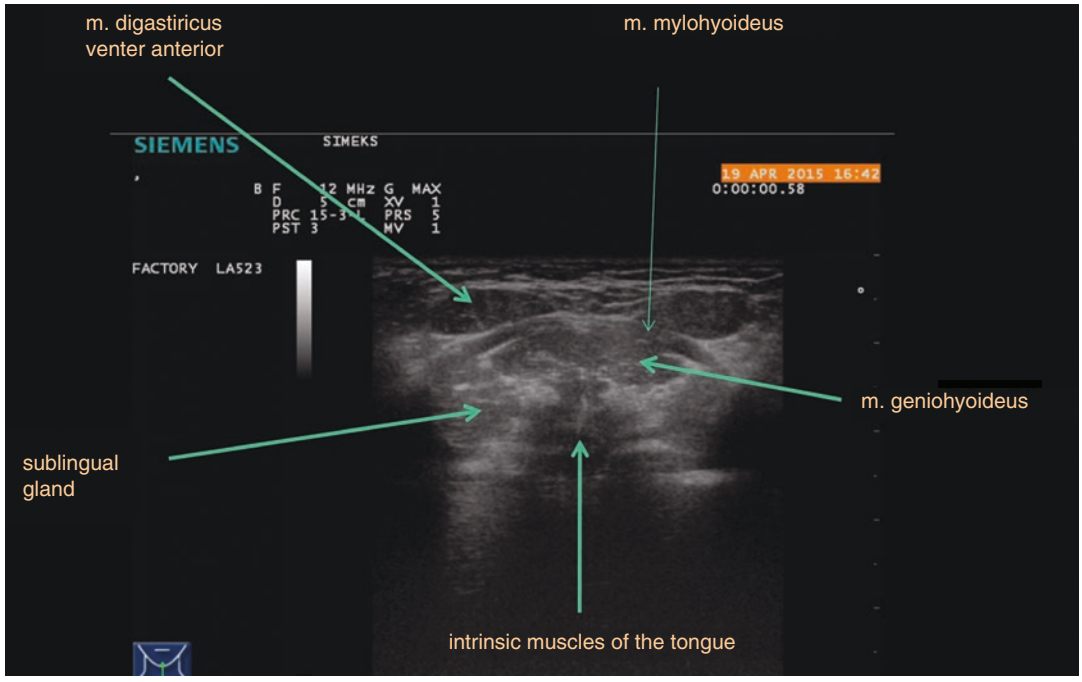

Fig. 2.17 The middle aspect of the floor of the oral cavity on the level of the sublingual salivary gland

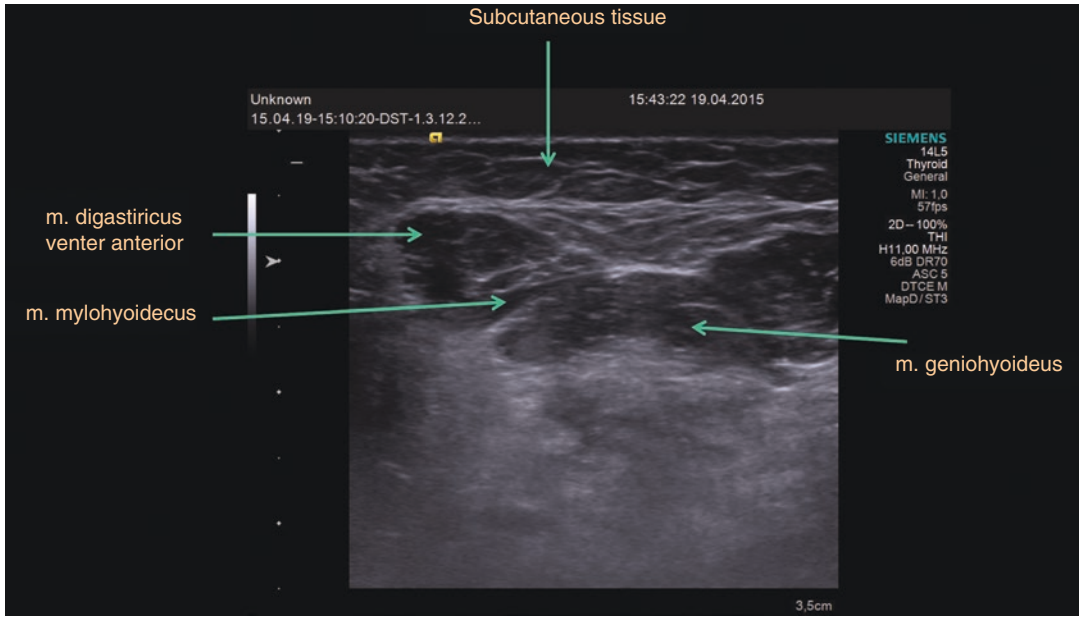

Fig. 2.18 The anterior aspect of the floor of the oral cavity (slightly posteriorly to the mandible body)

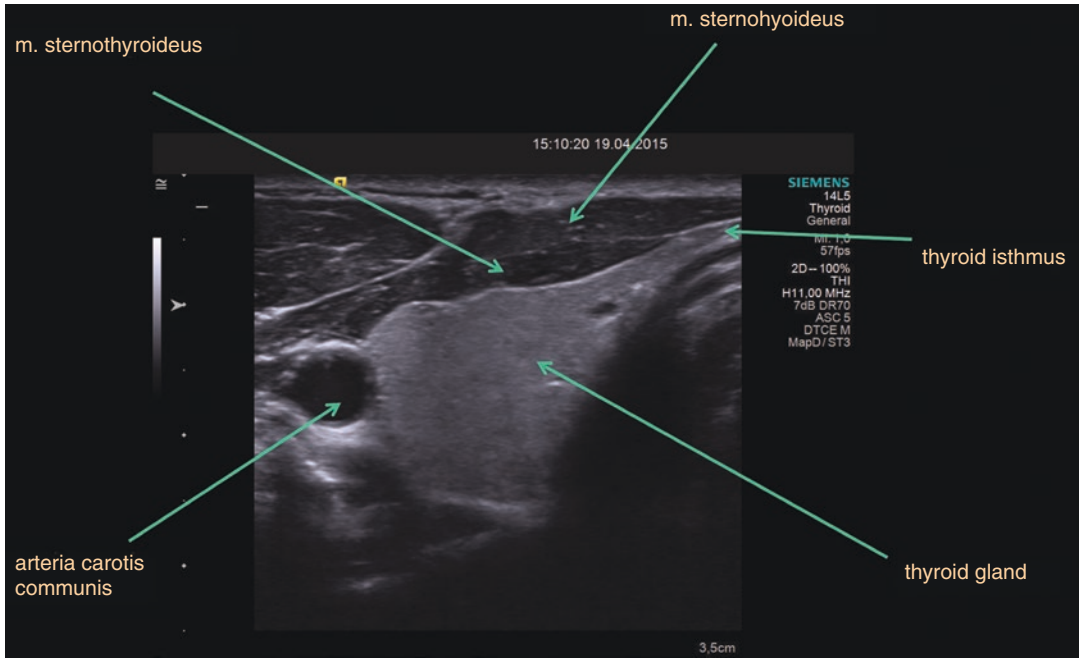

Fig. 2.19 The right thyroid lobe and surrounding structures (A)

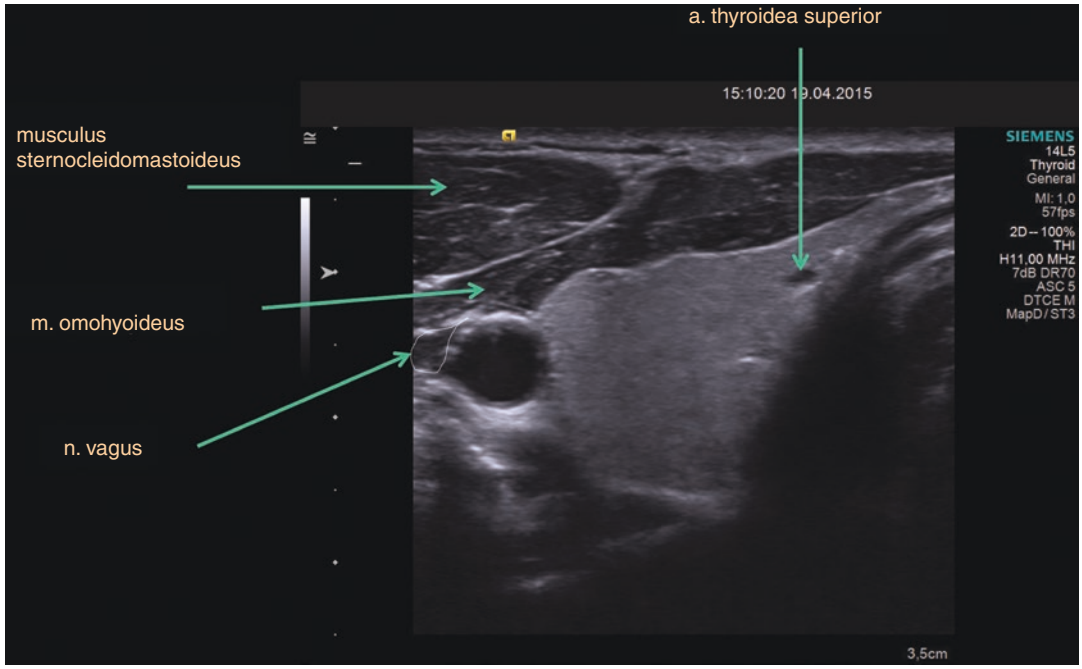

Fig. 2.20 The right thyroid lobe and surrounding structures (B)

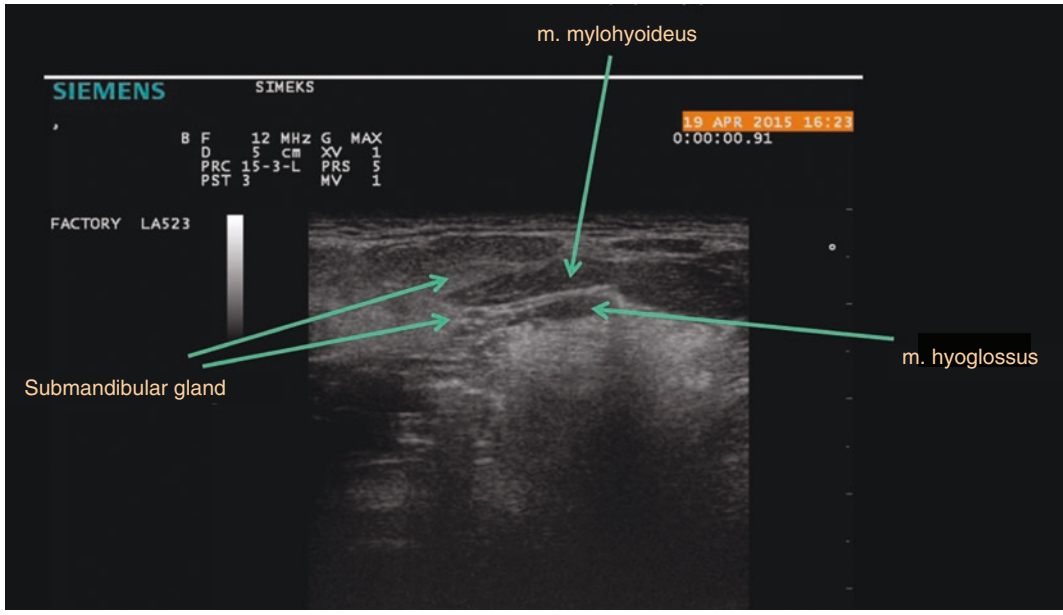

Fig. 2.21 The anterior aspect (main part) of the submandibular salivary gland and surrounding structures

Fig. 2.22 The posterior aspect of the submandibular salivary gland and surrounding structures

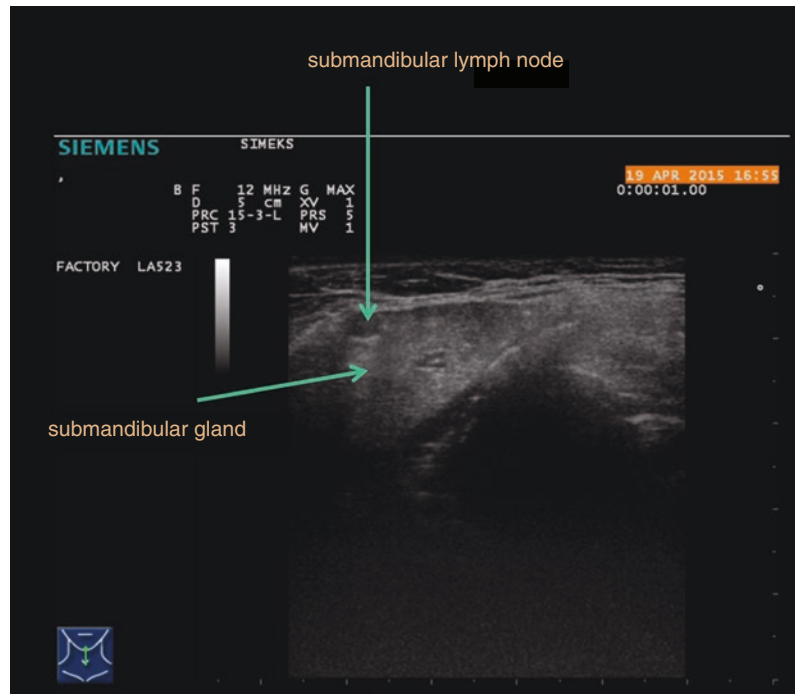

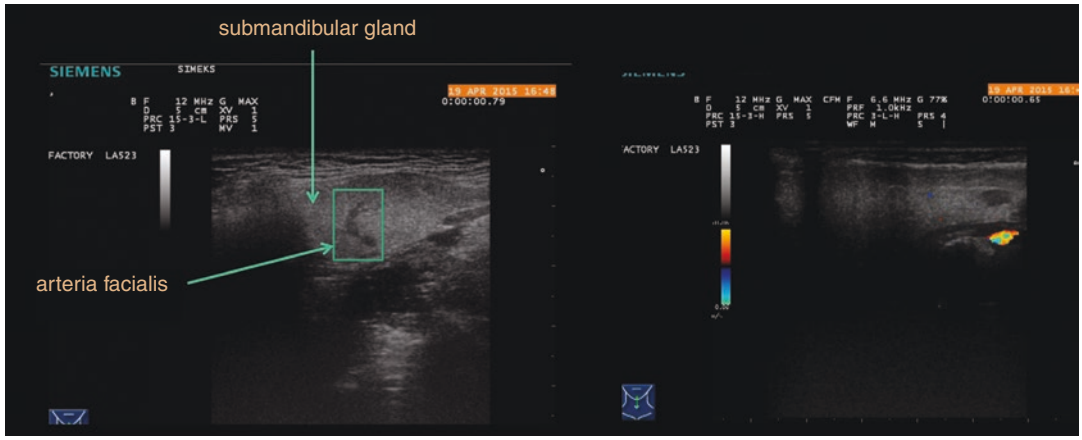

Fig. 2.23 The facial artery in relation to the submandibular salivarty gland. B-mode (A) and Color Doppler examination (B)

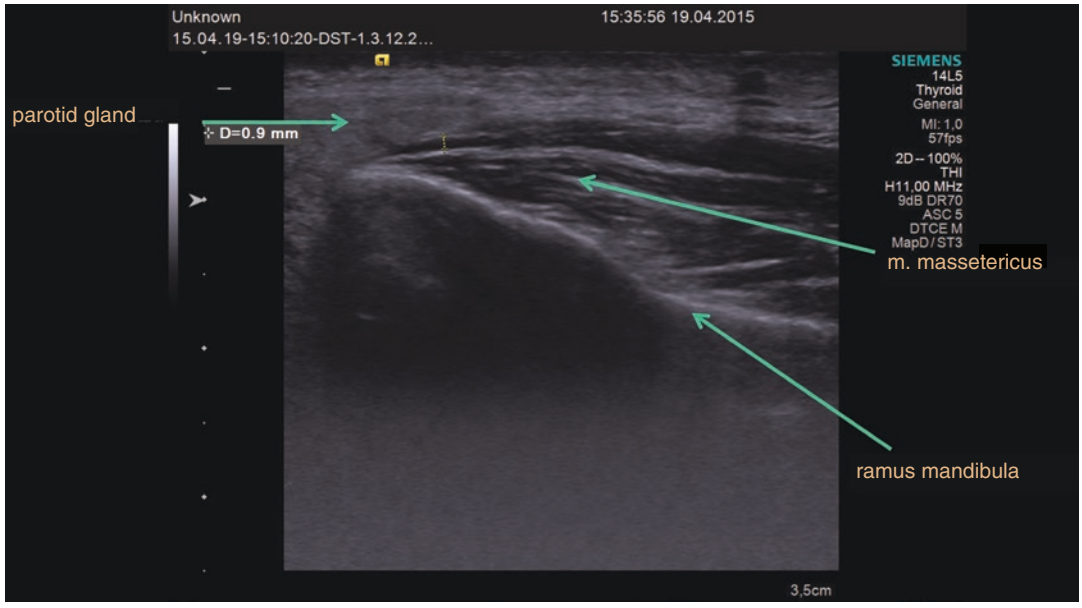

Fig. 2.24 The superficial part of the parotid gland and masseter muscle

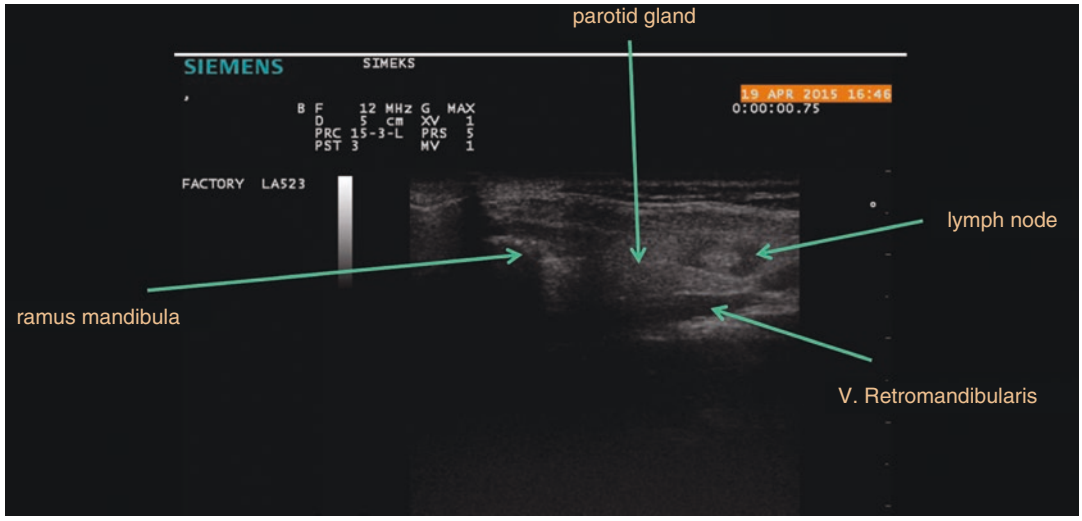

Fig. 2.25 Including: parotid gland, intraglandular lymph node and retromandibular vein

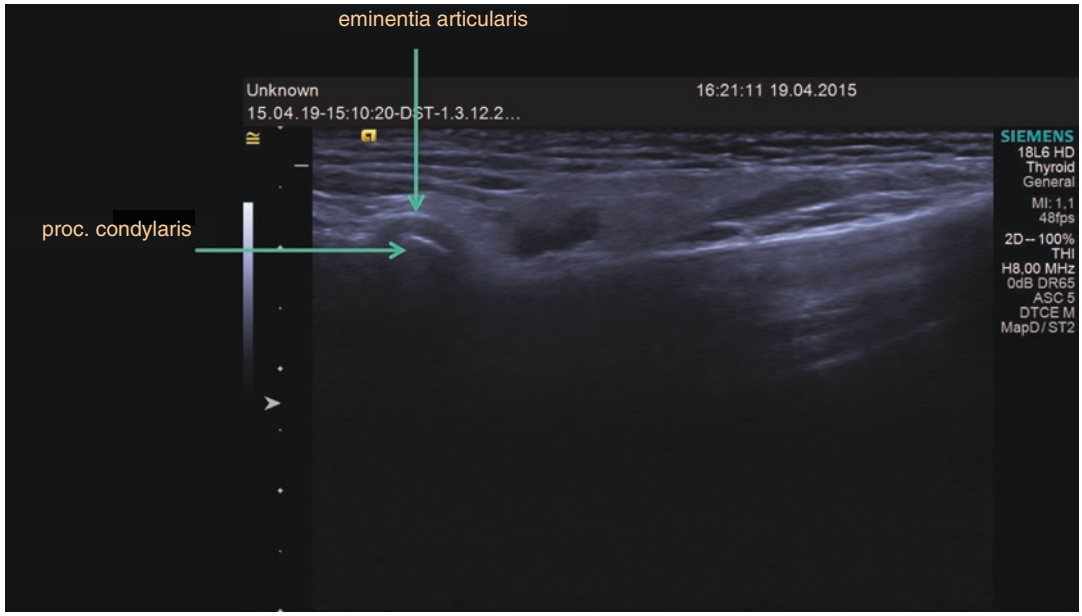

Fig. 2.26 Selected structures of TMJ

2.1.9 Summary

The anatomy of the dentomaxillofacial region is complex due to the number of organs, vessels, and nerves. However, their knowledge is essential for proper diagnosis and treatment. Number of developmental variations may increase the risk of unprecise diagnosis. In such cases, other modalities (MRI/MRT, CT, PET) should be recommended beside the initial ultrasonography.

Acknowledgments Both authors have equal contribution to this chapter. We gratefully acknowledge the support for helping with figures to our friends Jacenty Urbaniak (Jagiellonian University Medical College) and Robert Klepacz (Medical University of Lublin), without which the chapter could not have been completed. Anatomical figures bases on Rauber-Kopsch Lehrbuch und Atlas der Anatomie des Menschen. Band II. Arbeitsgemeinschaft Medizinischer Verlage G.M.B.H. Georg Thieme, Leipzig 1951.

References

1. Bochenek A, Rayher M. Human anatomy (13th eds). Warszawa: PZWL; 2010.
2. Federative Committee on Anatomical Terminology – FCAT. Terminologia Anatomica – International anatomical terminology. Stuttgart: Thieme; 1998.
3. Moore KL, Dalley AF, Argus AMR. Clinically oriented anatomy. 7th ed. Philadelphia: Lippincott Williams & Wilkins; 2006.
4. Rauber A, Kopsch F. Rauber-Kopsch Lehrbuch und Atlas der Anatomie des Menschen. Band II. Arbeitsgemenschaft Medizinischer Verlage G.M.B.H. Leipzig: Georg Thieme; 1951.
5. Standring S, editor. Gray's Anatomy. 41st ed. London: Elsevier; 2016.
6. Naqvi J, Yap KH, Ahmad G, Ghosh J. Transcranial Doppler ultrasound: a review of the physical principles and major applications in critical care. Int J Vasc Med. 2013;2013:629378.
7. Rasulo FA, De Peri E, Lavinio A. Transcranial Doppler ultrasonography in intensive care. Eur J Anaesthesiol Suppl. 2008;42:167–73.
8. Shiraishi Y, Hayakawa M, Tanaka S, Hoshino T. A new retinacular ligament and vein of the human temporomandibular joint. Clin Anat. 1995;8:208–13.
9. Gavid M, Dumollard JM, Habougit C, Lelonge Y, Bergandi F, Peoc'h M, Prades JM. Anatomical and histological study of the deep neck fasciae: does the alar fascia exist? Surg Radiol Anat. 2018;40:917–22.
10. Feigl G, Hammer GP, Litz R, Kachlik D. The intercarotid or alar fascia, other cervical fascias, and their adjacent spaces - a plea for clarification of cervical fascia and spaces terminology. J Anat. 2020;237:197. https://doi.org/10.1111/joa.13175.
11. Guidera AK, Dawes PJ, Fong A, Stringer MD. Head and neck fascia and compartments: no space for spaces. Head Neck. 2014;36:1058–68.
12. Kulzer MH, Branstetter BF 4th. Chapter 1 neck anatomy, imaging-based level nodal classification and impact of primary tumor site on patterns of nodal metastasis. Semin Ultrasound CT MR. 2017;38:454–65.
13. Som PM, Curtin HD, Mancuso AA. Imaging-based nodal classification for evaluation of neck etastatic adenopathy. AJR Am J Roentgenol. 2000;174:837–44.
14. Teymoortash A, Werner JA. Current advances in diagnosis and surgical treatment of lymph node metastasis in head and neck cancer. GMS Curr Top Otorhinolaryngol Head Neck Surg. 2012;11:Doc04.

3 General Considerations for Ultrasound Applications in Head and Neck

Ingrid Rozylo-Kalinowska and Kaan Orhan

Contents

3.1 Basics of Ultrasonography

Ultrasonography (US) is performed using physical properties of ultrasound, i.e., acoustic waves with a frequency above 20,000 Hz (20 kHz) (Fig. 3.1). The normal range of human hearing of a healthy individual is between 16 Hz and 20 kHz. Therefore, ultrasound waves are all acoustic waves with frequency higher than the threshold of human perception of sound. In clinical practice acoustic waves with frequency from 2 to 30 MHz are propagated within a patient's body (Ahuja and Evans, 2013, [1]).

I. Rozylo-Kalinowska (✉)
Department of Dental and Maxillofacial Radiodiagnostics, Medical University of Lublin, Lublin, Poland

K. Orhan
Faculty of Dentistry, Department of Dentomaxillofacial Radiology, Ankara University, Ankara, Turkey

Contrary to electromagnetic radiation such as X-rays, ultrasound waves require an elastic medium for propagation that can be deformed. When oscillation is transmitted, energy transfer occurs.

The source of ultrasound is a probe, also called a transducer, containing piezoelectric elements usually composed of barium titanate or lead zirconate. These crystals or ceramic elements are characterized by special properties, i.e., when electrical current is applied to the piezoelectric element, it contracts and at the same time emits an acoustic wave. The current is proportional to the force of squeezing. Change of the direction and the focus depth of ultrasound wave is adjusted using the phased array techniques. When the piezoelectric crystal is stretched, the voltage turns to the opposite.

The produced ultrasound wave enters the human body then returns from the examined tissues as mechanical oscillations of waves reflected

K. Orhan (ed.), *Ultrasonography in Dentomaxillofacial Diagnostics*,
https://doi.org/10.1007/978-3-030-62179-7_3

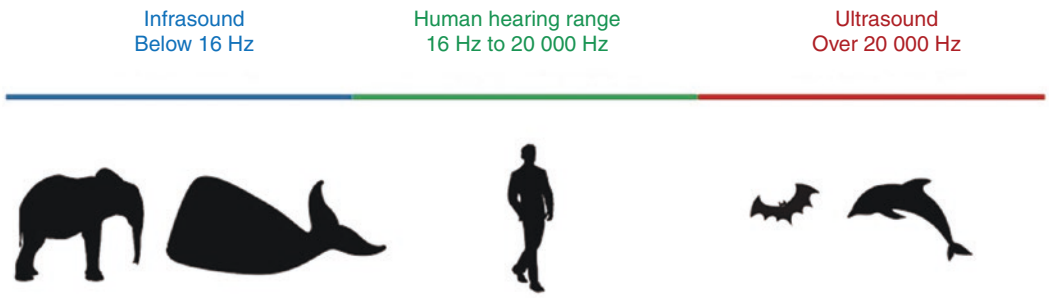

Fig. 3.1 Schematic representation of frequencies of sound related to human and animal hearing range

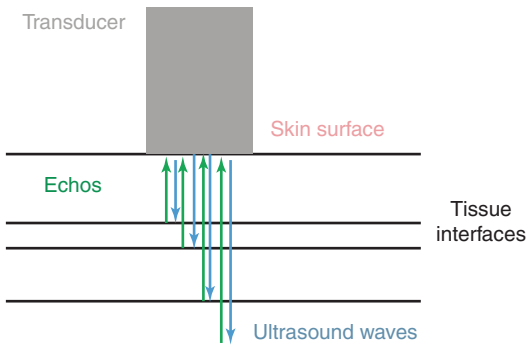

Fig. 3.2 Diagram of fundamentals of ultrasound scanning—echoes return to transducer after bouncing off tissue interfaces at different depths

off the given object, known as echoes (Fig. 3.2). When the wave comes back to the piezoelectric element, it serves as the receiver of acoustic signals producing an electric current. Obviously, the characteristics of the current incurred by returning acoustic wave is different from the initial one.

Acoustic waves are characterized by velocity, wavelength, frequency, and intensity. The velocity equals to the product of multiplication of frequency (in Hertz) and wavelength (in meters). The velocity of ultrasound wave in a human is estimated to be 1540 m/s which is an average value of velocity in tissues, similar to that of an acoustic wave propagated in water. In soft tissues and fluids transmission of ultrasound occurs in the form of longitudinal waves, i.e., the direction of wave propagation is the same or opposite from the direction of the displacement of the medium. In bone, longitudinal wave propagation is accompanied by transverse waves. The velocity of the acoustic wave is characteristic for the medium in which it is propagated therefore when crossing tissue interfaces only wavelength is changed and frequency determined by the source is unaffected [1].

Intensity of ultrasound beam influences the range of examination, i.e., the depth at which imaging still can be performed. Intensity determines the amount of energy transmitted by a wave in one second per unit of area at right angle to the direction of wave propagation.

Ultrasound field generated by a piezoelectric crystal is divided into two parts—near field and far field. In the near field, the width of the beam is constant and the shape of the beam is similar to a cylinder, while in the far field the beam becomes divergent. In the near field, the structure of ultrasound field is not homogenous due to overlapping and interfering of spherical partial waves emitted by different parts of the piezoelectric element. The size of the near field is increased in larger probes, it also increases together with probe frequency.

Since patient tissues are not homogenous, ultrasound encounters different tissue interfaces and various internal structures (fluid collections, calcifications, gas bubbles, discontinuities in tissues). The impedance of tissues is varied, and its values for soft tissues are similar to those of water. The interactions with areas differing in acoustic impedance lead to changes in the returning wave characteristics in comparison with the emitted original ultrasound wave. Inside the examined objects physical phenomena occur—analogical to those applied in optics. These phenomena include reflection, deflection, refrac-

tion, scattering, and absorption with the release of thermal energy (Fig. 3.3). Strong reflections occur when areas very distinct in impedance are imaged such as interfaces between soft tissue and bone as well as between soft tissue and air. Reflection is dependent on the angle of incidence of acoustic wave—when it hits the examined object at right angle, the reflection is strong. On the contrary, lower angulation leads to partial reflection and less echo coming back to the probe. Scattering and absorption result in attenuation of ultrasound wave, which decreases penetration depth of an acoustic wave. Scattering is responsible for creation of internal image of tissues, and more rough surfaces produce more scattering. Refraction is observed in case of differences in velocity of acoustic waves in two areas of the imaged object.

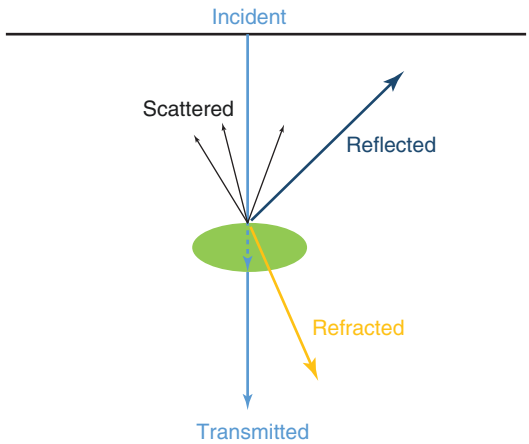

Fig. 3.3 Physical phenomena encountered in propagation of ultrasound waves in examined object

The part of acoustic wave picked up by piezoelectric elements in the transducer acting as the receiver gives rise to electric signal which is presented on screen in real-time as a black-and-white two-dimensional image (B-mode—brightness mode) (Fig. 3.4). Brightness of each pixel in the image on screen depends on the amplitude of the echo. As the sound velocity is assumed to be constant and the time required for the wave to travel forth and back known, it is possible to calculate the depth of tissues where wave reflection occurred. This way the final image in the screen can be compared to a sonar map of the sea bed, where structures located closer to the probe (thus, the surface of skin or mucosa) are visualized on top of the screen, and those lying deeper in scanned tissues further away from the probe towards the bottom of the screen [2].

In the B-mode, the so-called echogenicity is evaluated. An area which produces strong echoes is called hyperechoic (Fig. 3.4), on the other hand areas with no internal echoes are named anechoic. Hypoechoic lesions (Fig. 3.5) are characterized

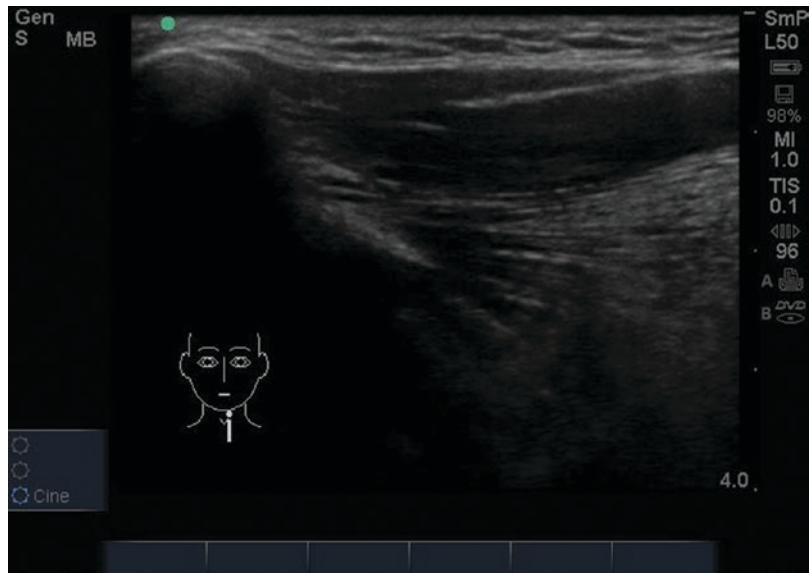

Fig. 3.4 Example of B-mode ultrasound image demonstrating among others hyperechoic outer cortex of mandibular symphysis (top left corner of the image) with post-acoustic shadowing

by echogenicity lower than structures in the vicinity, while areas of the same or comparable echogenicity are called isoechoic. Post-acoustic shadowing occurs when ultrasound beam is completely reflected off the outer surface of a structure such as, e.g., condyle or a very dense lesion, such as calcification (Fig. 3.4). When ultrasound beam travels through a very low-density lesion such as a cyst, the liquid content does not reflect ultrasound thus a bigger portion of the beam reaches tissues located below the fluid collection and more echoes are generated behind the lesion. This appearance is called post-acoustic enhancement (Fig. 3.5).

A-mode (amplitude mode) is more simple than B-mode as it does not depict distribution of echoes over a two-dimensional cross-section but presents them as plotted amplitude of spikes versus time as a function of depth. In this type of presentation, the probe is placed on skin surface and is not displaced during the examination. Therefore, only mobile objects will produce images in the form of amplitude of echoes. This mode is used in ophthalmology for estimation of distances between different parts of the eye [3].

In M-mode (motion mode, also called Time-Motion mode) the probe is also stationary and only a single chosen ultrasound line is emitted and received. All US reflecting objects are displayed on screen along the time axis. In this type of image, echoes are presented as pixels and their brightness corresponds to the magnitude of echo amplitude. Very high sampling rate in this mode is advantageous as it allows detection and quantification of very fast motions. M-mode is mostly used in cardiology.

Tissue Harmonic Imaging (THI) is based on the properties of nonlinear propagation of ultrasound in the examined tissues. The shape of the ultrasound wave is distorted due to uneven velocity of the wave propagation—i.e., faster high-pressure portion of the wave and slower low-pressure part of the beam. The difference in the form of the wave produces the so-called tissue harmonics which are multiples of the frequency—either fundamental or transmitted. Subsequent harmonics are characterized by decreasing amplitude therefore only the second harmonic is sufficient for generation of an image. THI technique increases signal-to-noise ratio, reduces artifacts coming from reverberations, as well as increases resolution, both axial and lateral.

US elastography offers a possibility of evaluation of stiffness of tissues on the basis of analysis of change of their shape when an external stimulus is applied such as exerted pressure (Fig. 3.6) or emission of an acoustic impulse

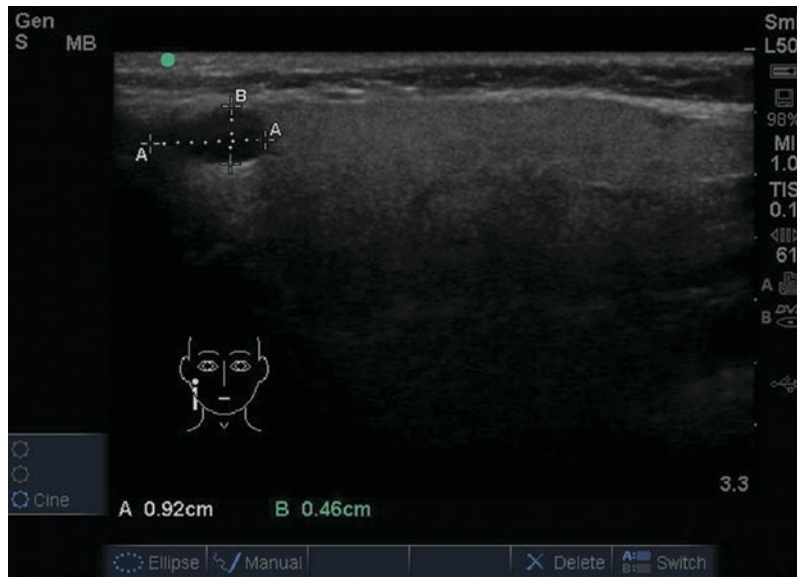

Fig. 3.5 Example of B-mode ultrasound image demonstrating among others a hypoechoic, almost anechoic, intraglandular lymph node (marked with calipers) in right parotid gland, with post-acoustic enhancement

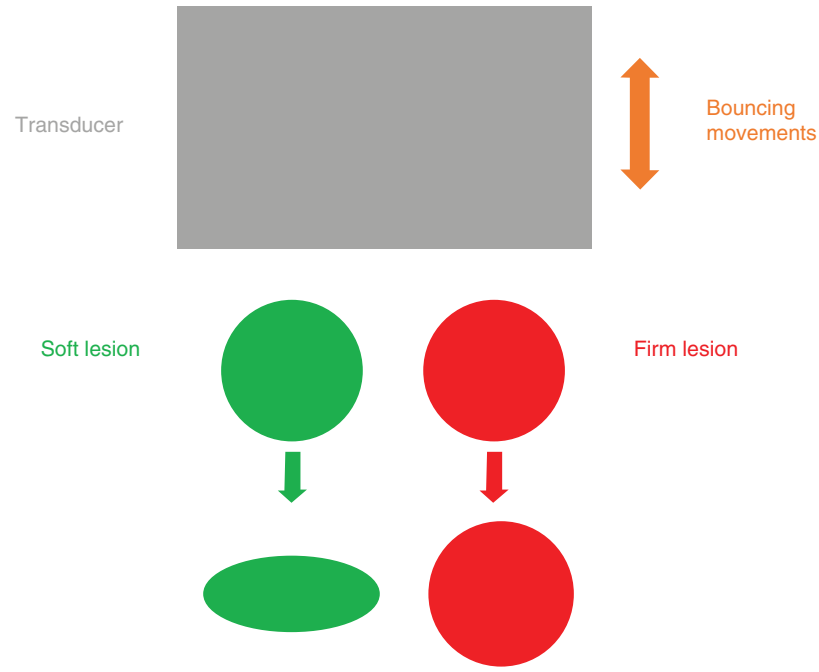

Fig. 3.6 Diagram of strain elastography—during compression exerted by bouncing of the transducer soft lesions change shape, while firm ones are not remodeled

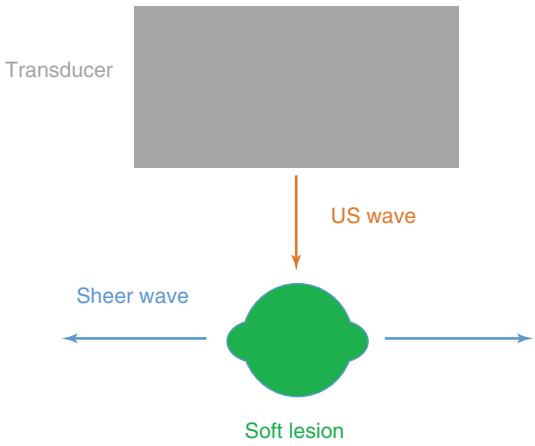

Fig. 3.7 Diagram of shear wave elastography—ultrasound wave impulse remodels a soft lesion which produces shear wave propagated transversely to the original wave

propagated within tissues as the so-called shear wave (Fig. 3.7). A colored map represents areas with higher and lower stiffness in a qualitative manner (Fig. 3.8). In some US machines quantitative assessment is possible in the form of Young's modulus values given in kilopascals (Yuan et al. 2016). Usefulness of the technique is already established for, e.g., breast lesions, thyroid nodules, and musculoskeletal application, and it is being investigated in the maxillofacial area including salivary glands, lymph nodes, muscles of mastication, palatal tumors, tongue carcinoma, and TMJ disk [4–8].

3.2 Ultrasound Probes

There is a large variety of ultrasound units available in the market—from sophisticated machines to portable ones (Fig. 3.9). However, the feasibility of an ultrasound unit depends also on the applied probes (Fig. 3.10). As mentioned before, typically in head and neck applications waves with frequency from 2 to 30 MHz are used. The higher the frequency is, the higher the resolution is, but at the same time penetration depth diminishes. The penetration depth is the highest distance between the probe and the tissues which can still be visualized without image noise. This explains why the highest frequency transducers can be used only for very superficial tissues. On the other hand, mostly higher frequency probes provide higher spatial resolution than lower fre-

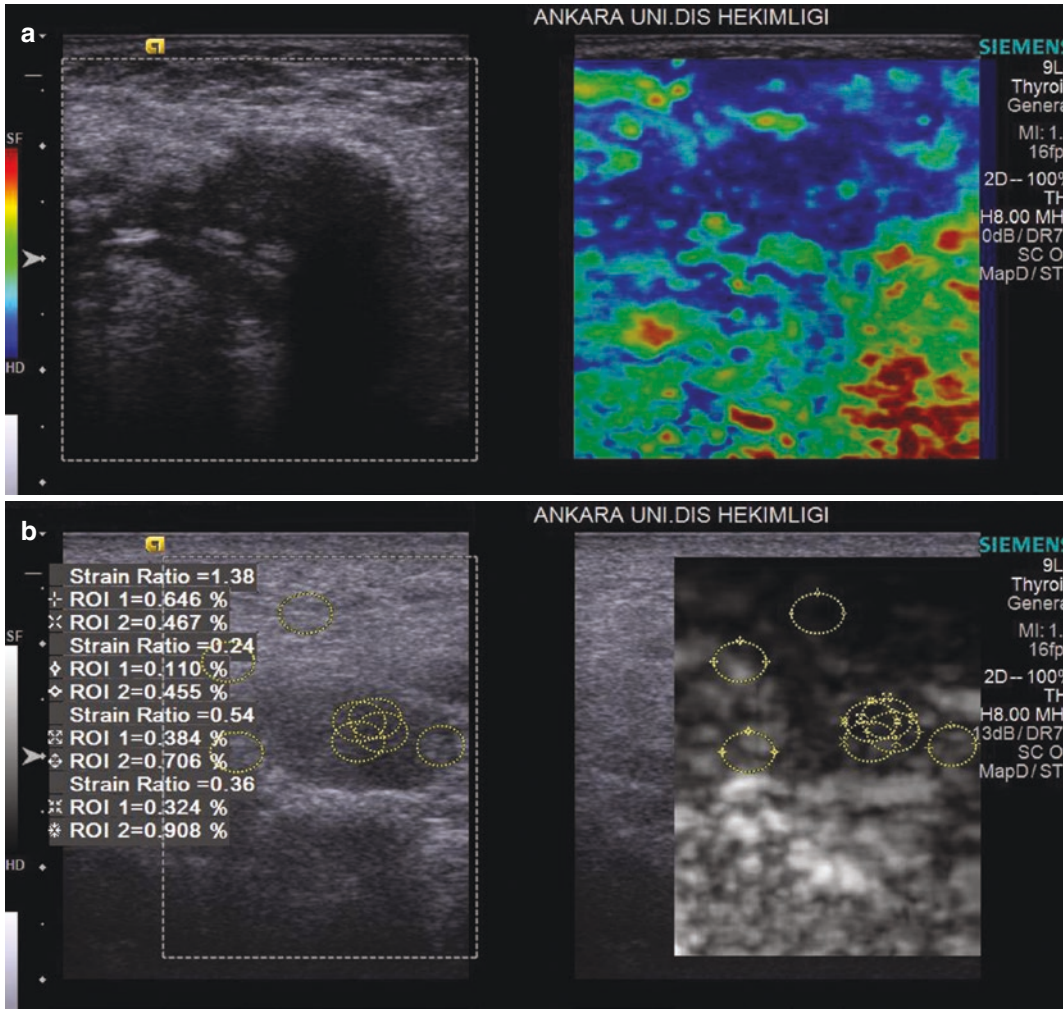

Fig. 3.8 Example of strain elastography. (**a**) color map of elasticity. (**b**) estimation of strain ratios within selected regions of interest

quency transducers. Resolution is the smallest distance between two objects that can be separately discerned in an image. Resolution in the direction of acoustic wave (axial resolution) is higher than the resolution across the direction of the transmission of the wave (lateral resolution). Axial resolution is the smallest distance measured in millimeters between two points located within the axis of ultrasound beam that are visualized as separate. Lateral resolution is the smallest distance between two points placed in equal axial distance from the source of acoustic wave that can be separately discerned. The highest lateral resolution is observed in the focal area of the ultrasound beam. It is estimated that axial resolution is equal to 1.5 of wavelength while lateral resolution is about 7–10 times lower.

Contrast resolution is the ability to discern acoustic impedance of different tissues and depends on the amplitude of echo and attenuation of the ultrasound beam in examined objects.

Shape and size of the probe are also important while scanning. The most common transducer for head and neck application is a linear probe with flat surface. The shape of image obtained from a linear probe will be rectangular, but it can be expanded using the so-called trapezoid mode. Convex probes—the name being derived from

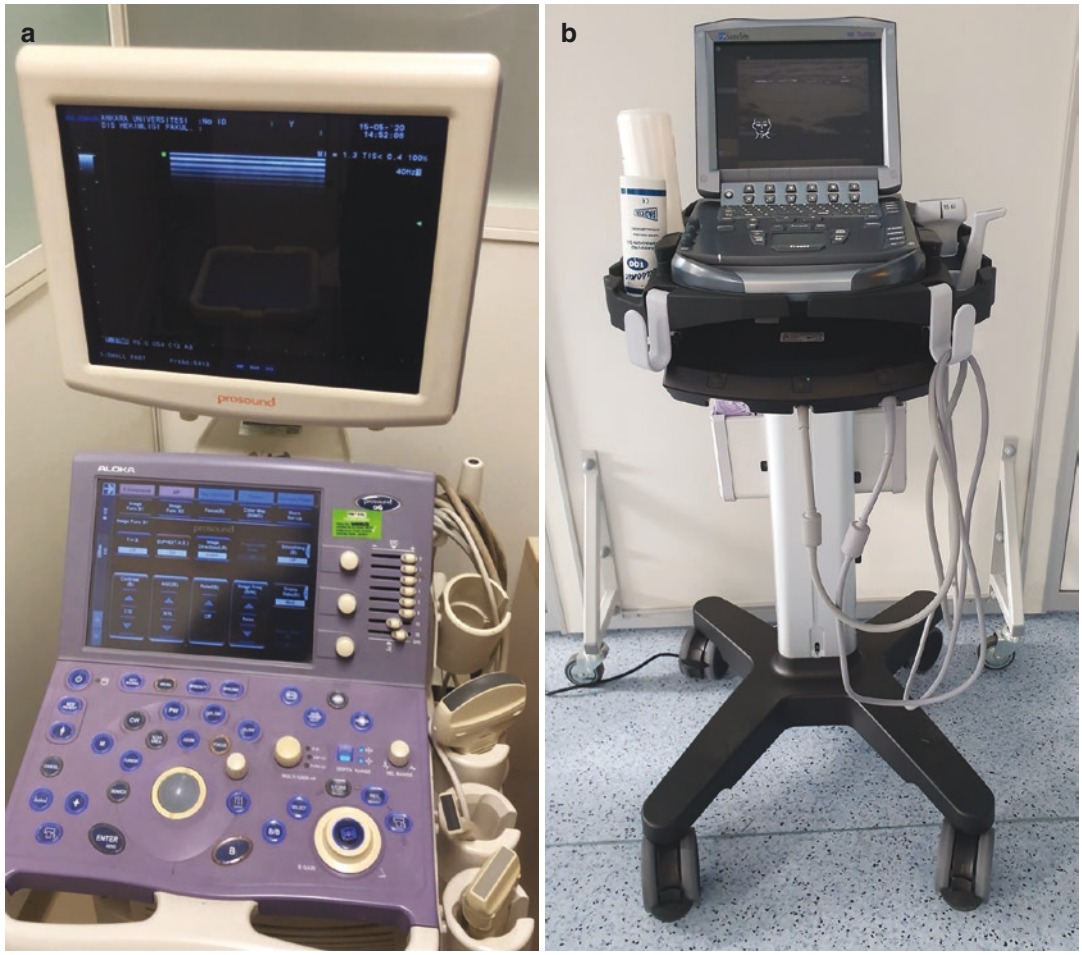

Fig. 3.9 Examples of ultrasound machines. (**a**) Ultrasound scanner. (**b**) portable device

the convex shape—are typically used in abdominal US scanning, but can sometimes be applied in the head and neck for imaging of, e.g., enlarged thyroid gland.

The US probes also differ in sizes of the surface contact area called "footprint" (Fig. 3.11). Larger (longer) footprint will result in the ability to demonstrate more bulky structures in one image, e.g., parotid gland in longitudinal dimension. On the other hand, a probe with a smaller footprint will adapt better to curvatures of the head and neck thus remaining all the time in contact with surfaces of examined areas. Longer, larger probes will have margins "hanging" over curved areas of facial anatomy not producing image in there as contact with the skin will be lost.

Intraoral probes are useful in imaging of tongue, oral floor, gingival lesions, palatal lesions, masticatory muscles, and oropharynx [9]. Dedicated finger probes or finger-tip probes are not widespread and mostly described in research articles [10]. However, an intraoperative "hockey-stick" or a "T-type" probe can be successfully applied instead [11]. Very small intraoperative linear probes are tested for intraoral applications, as well.

Transducers with frequency over 7 MHz are suitable for examinations of superficial organs, often annotated as "small parts" in ultrasound

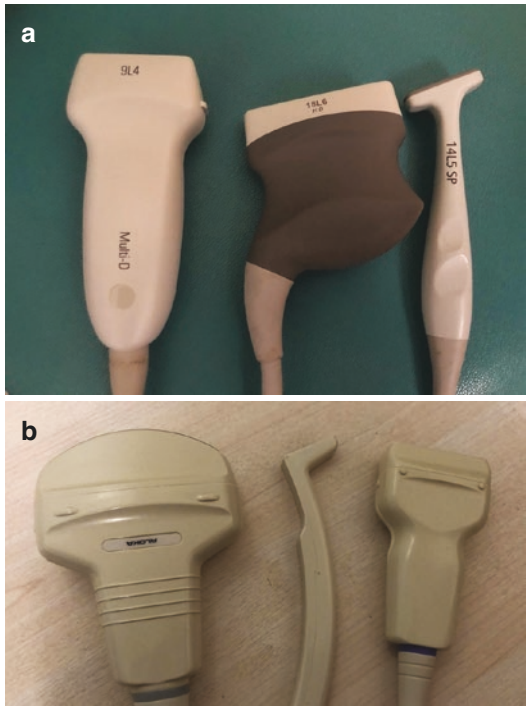

Fig. 3.10 Examples of ultrasound probes. (**a**) Different linear probes, including a T-probe. (**b**) Convex probe, hockey-stick probe, and linear probe

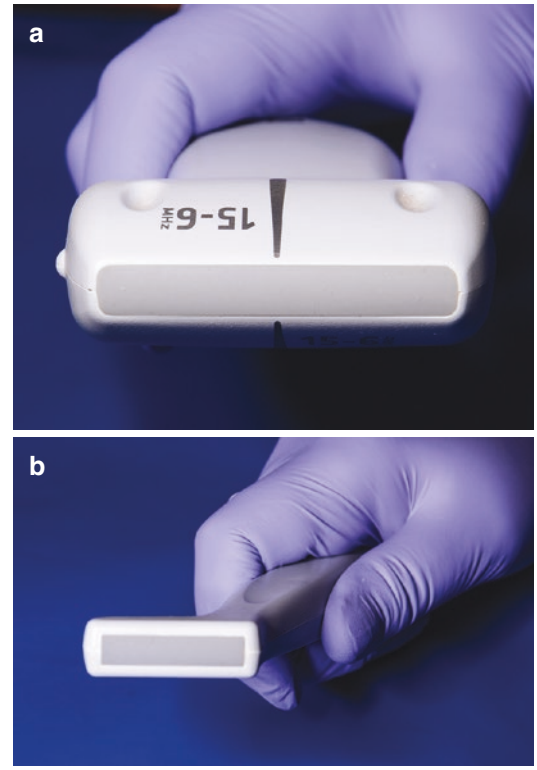

Fig. 3.11 Comparison of footprints of probes. (**a**) linear probe with a larger footprint. (**b**) hockey-stick probe with a smaller footprint

machines. In head and neck applications frequencies typically fall in the range between 7 and 20 MHz. In diagnostics of TMJ high-frequency linear probes (preferably over 12 MHz) with a relatively small "footprint" are applied as they offer high resolution of image with a relatively low penetration depth which is sufficient in examinations of these superficially located joints. A 5 MHz probe may be helpful in imaging of deeper located structures such as deep lobe of the parotid. On the other hand in ultra-high frequency ultrasound (UHFUS) frequencies from 70 to 100 MHz are used in imaging of skin and mucosa allowing for resolution of down to 30 μm but with imaging depth of maximum 10 mm for a 70 MHz probe [12, 13]. Application of a sector probe was described for investigations of oropharyngeal dysphagia [14]. Three-dimensional probes are also available, especially for prenatal diagnosis, which is helpful in the assessment of maxillofacial congenital abnormalities before birth thus allowing referral of the pregnant female to a specialized obstetrics center [15]. Registration of 3-D images is based on tracking of multiple scans acquired during movement of ultrasound probe performed by an operator [16].

3.3 Ultrasound Examination

US scanning of the head and neck is usually performed in a patient lying on an examination bed. It is possible to examine a patient sitting upright, especially for TMJ imaging. However, positioning the patient on an examination bed or chair for majority of examinations is more ergonomic from the point of view of operator as holding the transducer in the air without a stable support for arm of the person performing the exam is exhausting during longer examinations.

Before and during the US scanning water-soluble gel is generously administered on the

patient's skin within the region of interest in order to eliminate air bubbles from between the skin and the probe since ultrasound is strongly reflected by gases (Katzberg 2012, Whaites and Drage 2013). A supply of bed linen and paper towels is mandatory to protect the patient's garments from becoming wet and after the examination to wipe the gel.

Ultrasound scanning is a dynamic procedure as the probe is constantly being swiped over scanned area. Layer of applied gel facilitates performing smooth sliding movements over the skin surface. In case of examinations of oral mucosa use of gel might not be necessary due to presence of saliva in oral cavity already moisturizing the surface of the scanned area. However, a layer of gel (dedicated for mucosa) placed on probe footprint acts as an alternative for a standoff pad. The role of such a spacing device is to increase the distance between transducer and skin or mucosa surface. Otherwise in this near field directly under the probe footprint artifacts appear and decrease image quality. Commercially available ultrasound standoff pads for superficial structures are usually too large for intraoral applications (e.g., 1 cm thick and 6 cm in diameter). Often it is difficult to place them over the scanned area and then maintain in the same position over curvatures of facial features. Yet another solution is application of standoff pads matching the size of transducer footprint and kept in place by means of a dedicated plastic standoff holder adapted to the probe shape and size. New developments in US probe technology offer solutions improving the signal-to-noise ratio thus resulting in high image clarity in both near and far fields.

During examination, the mark on one side of the probe (either a convex dot or a little illuminated spot) and the mark on the US screen should be orientated in the same manner, i.e., with probe transverse, the dot on the probe, and the mark on the screen should be on the same side. When the probe is rotated by 90° to longitudinal position, the dot on the probe should be directed towards the cephalad portions of the examined area then the superior parts of the area will be displayed on top of the screen.

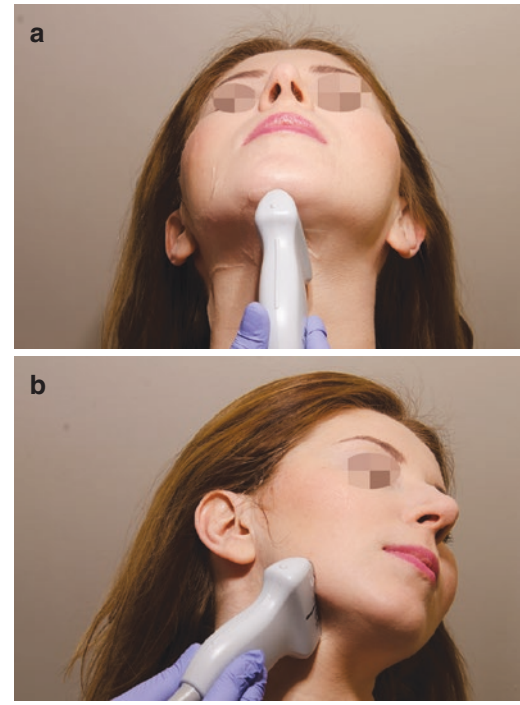

Fig. 3.12 Patient positioning for head and neck ultrasound. (**a**) Head tilted backwards. (**b**) Head turned away from the scanned side

For examination of salivary glands, thyroid gland, submandibular, and neck lymph nodes it is helpful to put a small cushion under the patient's shoulders, ask the patient to tilt the head backwards as well as to the side contralateral to the region of interest in order to better expose the tissues to scanning (Fig. 3.12). Muscles of mastication are examined with teeth clenched and relaxed. TMJ is scanned with mouth closed and mouth open, registration of condylar movement in M-mode is also possible (Ahuja and Evans 2013, [17]).

The whole region of interest must be carefully scanned in all directions on both healthy and diseased sides of the face and neck. It is best if examination is meticulously performed step-by-step so that no organ is missed during scanning. It must be remembered that unlike in CT or MRI once the examination is over and patient is dismissed, it is not possible to review images other than already registered. Just like in other fields of

diagnostic imaging, it is crucial to demonstrate a lesion in at least two planes, possibly at right angle one to another. However, the US images are almost never truly transverse or sagittal (Kundu et al. 2013). This obstacle can be overcome by using a 3-D US probe ([16], Landes et al. 2010).

3.4 Advantages and Disadvantages of Ultrasound Scanning

Advantages of ultrasonography include availability, no ionizing radiation applied thus no harmful effects observed (even in pregnant females and infants), high image resolution, real-time imaging, and a relatively low cost when compared to other diagnostic imaging modalities such as CT and MRI (Ahuja and Evans 2013, Kundu et al. 2013, Whaites and Drage 2013). Smaller US machines are portable, and nowadays instead of a complete ultrasound machine an ultrasound transducer connected with a mobile device such as tablet with installed dedicated software can be used.

One of the disadvantages of US is high dependency on operator's skills and experience (Manfredini and Guarda-Nardini 2009). This can be quickly eliminated when adequate learning curve of an operator is introduced (Ahuja and Evans, 2013).

Another disadvantage of utmost importance in diagnostics of bone and teeth is that it is not possible to demonstrate structures located behind dense objects such as intact cortical bone surface or enamel, as the beam is fully reflected off such structures. For this reason, only a part of TMJ is accessible for US—the articular capsule, the disc, and cortex of laterosuperior aspect of the condyle are visible (Manfredini et al., 2003). The same applies to teeth which are not fully available for ultrasound scanning.

Technical issues in ultrasound scanning include lower intensity range thus lower contrast than in CT, unfavorable signal-to-noise ratio as well as near field artifacts which have been described in the previous subchapter together with solutions for their elimination.

Artifacts appearing in ultrasound scanning can be misleading in interpretation of images. Reverberations are multiple echoes produced by the same structure when sound wave is reflected off the border between two areas characterized by different acoustic properties. Another type of reverberation is mirroring which results in the appearance of a double image being like a reflection in a mirror of the real object.

In case of structures with round or oval limits, complete reflection of acoustic wave can be observed if it hits the boundaries of the object tangentially. This phenomenon occurs in case of, e.g., carotid arteries.

3.5 Indications and Contraindications for Ultrasound

Within the head and neck US is used in diagnostic imaging of salivary glands, thyroid gland, lymph nodes, muscles (masticatory, neck, facial), tongue, oral floor and oropharynx, palate, periodontal tissues, temporomandibular joint (in a limited range), extracranial nerves, paranasal sinuses, large blood vessels, larynx [5, 7, 18–22].

The following pathologies can be investigated by means of ultrasound: inflammations, cysts, primary and metastatic tumors, inborn anomalies, masseter lesions, vascular lesions, peritonsillar abscesses, lichen planus, bullous diseases, some fractures (zygomatic arch, nasal bone) obstructive sleep apnea, oropharyngeal dysphagia (M-mode) as well as identification of foreign bodies [11–14, 23–29].

Ultrasound scanning is also applied as guidance for fine needle aspiration biopsy, core biopsy, abscess drainage, TMJ arthrocentesis, TMJ injections, e.g., with steroids or sodium hyaluronate, intramasseteric injections of botuline toxin for bruxism and/or masseter hypertrophy (Daiysoylu et al. 2013, [17, 30]). Treatment follow-up can be performed using ultrasound, as well.

There are no contraindications for ultrasound scanning apart from lack of cooperation of the examined patient. It can be performed in pregnant females, neonates, and infants as the mean

intensity of emitted acoustic wave usually is lower than 20 mW/cm2, which is considered to be a safe value [1].

References

1. Marotti J, Heger S, Tinschert J, Tortamano P, Chuembou F, Rademacher K, Wolfart S. Recent advances of ultrasound imaging in dentistry – a review of the literature. Oral Surg Oral Med Oral Pathol Oral Radiol. 2013;115:819–32.
2. Iro H, Bozzato A, Zenk J. Atlas of head and neck ultrasound: Thieme; 2013.
3. Carovac A, Smajlovic F, Junuzovic D. Application of ultrasound in medicine. Acta Inform Med. 2011;19(3):168–71.
4. Costa YM, Ariji Y, Ferreira DMAO, Bonjardim LR, Conti PCR, Ariji E, Svensson P. Muscle hardness and masticatory myofascial pain: Assessment and clinical relevance. J Oral Rehabil. 2018;45(8):640–6.
5. Ogura I, Toshima H, Akashiba T, Ono J, Okada Y. Strain elastography of palatal tumors in conjunction with intraoral ultrasonography, computed tomography, and magnetic resonance imaging: 2 case reports. Imag Sci in Dent. 2020;50:73–9.
6. Paluch Ł, Maj P, Pietruski P, Korba M, Noszczyk BH. Shear Wave Elastography in the Evaluation of Temporomandibular Joint Disorders. Ultrasound Med Biol. 2020;46(1):46–54.
7. Shingaki M, Nikkuni Y, Katsura K, Ikeda N, Maruyama S, Takagi R, Hayashi T. Clinical significance of intraoral strain elastography for diagnosing early stage tongue carcinoma: a preliminary study. Oral Radiol. 2017;33:204–11.
8. Zengel P, Schrötzlmair F, Schwarz F, Paprottka P, Kramer M, Berghaus A, Clevert DA. Elastography: a new diagnostic tool for evaluation of obstructive diseases of the salivary glands; primary results. Clin Hemorheol Microcirc. 2012;50(1–2):91–9.
9. Caglayan F, Bayrakdar IS. The intraoral ultrasonography in dentistry. Nig J Clin Pract. 2018;21(2):125–33.
10. Salmon B, Le Denmat D. Intraoral ultrasonography: development of a specific high-frequency probe and clinical pilot study. Clin Oral Invest. 2011;16:643. https://doi.org/10.1007/s00784-011-0533-z.
11. Chammas MC, Macedo TAA, Moyses RA, Gerhard R, Durazzo MD, Cernea CR, Cerri GG. Relationship between the appearance of tongue carcinoma on intraoral ultrasonography and neck metastasis. Oral Radiol. 2011;27:1–7.
12. Izzetti R., Vitali S., Aringhieri G., Caramella D., Nisi M., Oranges, T., Dini V., Graziani F., Gabriele M.: The efficacy of Ultra-High Frequency Ultrasonography in the diagnosis of intraoral lesions. Oral Surg Oral Med Oral Pathol Oral Radiol. 2019. pii: https://doi.org/10.1016/j.oooo.2019.09.012. [Epub ahead of print] (Accessed 09 May, 2020).
13. Izzetti R, Vitali S, Oranges T, Dini V, Romanelli M, Caramella D, Gabriele M. Intraoral ultra-high frequency ultrasound study of oral lichen planus: a pictorial review. Skin Res Technol. 26:200. https://doi.org/10.1111/srt.12777(Accessed 09 May 2020).
14. Hsiao M-Y, Wahyuni LK, Wang T-G. Ultrasonography in assessing Oropharyngeal dysphagia. J Med Ultras. 2013;21:181–8.
15. Lu JW, Lu D, Zhang XL, Bai J. Clinical outcomes of prenatal diagnosis of the fetal micrognathia: a case report. Medicine (Baltimore). 2020;99(4):e18648. https://doi.org/10.1097/MD.0000000000018648. (Accessed 08 May 2020)
16. Landes CA, Goral WA, Sader R, Mack MG. Three-dimensional versus two-dimensional sonography of the temporomandibular joint in comparison to MRI. Eur J Radiol. 2007;61:235–44.
17. Rozylo-Kalinowska I, Orhan K, editors. Imaging of the Temporomandibular joint: Springer; 2019.
18. Benson BW, Flint DJ, Liang H, Opatowsky MJ. Advances in diagnostic imaging for pathologic conditions of the jaws. Head Neck Pathol. 2014;8:383–91.
19. Bhatia KSS, Dai YL. Routine and advanced ultrasound of major salivary glands. Neuroimaging Clin N Am. 2018;28(2):273–93.
20. Iida Y, Kamijo T, Kusafuka K, Omae K, Nishiya Y, Hamagchi N, Morita K, Onisuka T. Depth of invasion of superficial oral tongue carcinoma quantified using intraoral ultrasonography. Laryngoscope. 2018;128:2778–82.
21. Rozylo-Kalinowska I, Kurylo J, Nowak S, Piskorz M, Portka K, Kozek M. Ultrasonographic biometry of soft tissues in patients with gingival recessions. Preliminary report. J Stoma. 2019;72(3):106–11.
22. Zengel P, Schrötzlmair F, Reichel C, Paprottka P, Clevert DA. Sonography: the leading diagnostic tool for diseases of the salivary glands. Semin Ultrasound CT MR. 2013;34(3):196–203.
23. Demiralp KO, Orhan K, Kurşun-Çakmak EŞ, Gorurgoz C, Bayrak S. Comparison of Cone Beam Computed Tomography and ultrasonography with two types of probes in the detection of opaque and non-opaque foreign bodies. Med Ultrason. 2018;20(4):467–74.
24. Froehlich MH, Huang Z, Reilly BK. Utilization of ultrasound for diagnostic evaluation and management of peritonsillar abscesses. Curr Opin Otolaryngol Head Neck Surg. 2017;25:163–8.
25. Hara K, Tohara H, Namiki C, Yamaguchi K, Chantaramanee A, Kobayashi K, Saito T, Nakagawa K, Okumura T, Yoshimi K, Nakane A, Furuya J, Minakuchi S. Relationship between displacement of the masseter muscle during biting and masseter muscle quality and bite force in healthy elderly persons. J Oral Rehabil. 2020;47(4):441–8.
26. Klein Nulent TJW, Noorlag R, Van Cann EM, Pameijer FA, Willems SM, Yesuratnam A, Rosenberg AJWP, de Bree R, van Es RJJ. Intraoral ultrasonography to measure tumor thickness of oral cancer: a

systematic review and meta-analysis. Oral Oncol. 2018;77:29–36.
27. Lee IS, Lee J-H, Woo C-K, Kim HJ, Sol YL, Song JW, Cho K-S. Ultrasonography in the diagnosis of nasal bone fractures: a comparison with conventional radiography and computed tomography. Eur Arch Otorhinolaryngol. 2016;273:413–8.
28. Sahoo BNK, Choudhary MAK, Srinivas BV, Tomar K. Dermoid cysts of maxillofacial region. Med J Armed Forces India. 2015;71:S389–94.
29. Singh M, Tuteja A, Wong DT, Goel A, Trivedi A, Tomlinson G, Chan V. Point-of-care ultrasound for obstructive sleep apnea screening: are we there yet? A systematic review and meta-analysis. Anesth Analg. 2019;129(6):1673–91.
30. Hoffman HT, Pagedar NA. Ultrasound-Guided Salivary Gland Techniques and Interpretations. Atlas Oral Maxillofac Surg Clin North Am. 2018;26(2):119–32.

4 Physical Principles of Doppler and Color Doppler Ultrasound

Ingrid Rozylo-Kalinowska and Kaan Orhan

Contents

4.1 The Doppler Effect

Doppler ultrasound is based on application of the Doppler effect, also called the Doppler shift. This physical phenomenon is related to change in wave frequency that is observed when the wave is moving or when it is reflected off a moving object. The name of the effect comes from the Austrian mathematician and physicist Christian Andreas Doppler.

The most common example of Doppler shift in change in perceived sound of an ambulance siren which is different when the vehicle is approaching and going away (Fig. 4.1). In comparison with the original emitted frequency, the received one is higher when the object is moving towards the source of waves, equal at the moment of passage, while lower when the object is moving away. This is due to change in emission of subsequent waves crests which are first closer to each other, then more and more distant from each other. Consequently, the time required for the wave crest to reach the observer on approach is shorter which results in an increase of frequency. On the contrary, during recession the time is longer thus the frequency is decreased.

The Doppler shift is observed when the source of waves is moving and observer motionless, when it is the observer who is moving and the source of waves constant, finally the medium serving for propagation of sound waves can be mobile. However, light waves and gravitational waves are exceptions as they do not require any medium for propagation.

I. Rozylo-Kalinowska (✉)
Department of Dental and Maxillofacial Radiodiagnostics, Medical University of Lublin, Lublin, Poland

K. Orhan
Faculty of Dentistry, Department of Dentomaxillofacial Radiology, Ankara University, Ankara, Turkey

K. Orhan (ed.), *Ultrasonography in Dentomaxillofacial Diagnostics*,
https://doi.org/10.1007/978-3-030-62179-7_4

In medicine, the ultrasound wave is reflected off the moving objects which are erythrocytes in blood vessels. Instead of change of frequency of wave coming and going, it is the difference in time of returning echoes of subsequent waves (decreased or increased) which is registered as the frequency shift. The bigger the frequency of the transmitted wave, the bigger the frequency shift is. Angulation of ultrasound beam is essential for Doppler measurements. If the angle of incidence equaled 0 and ultrasound wave was parallel to the examined blood vessel, the frequency shift would be the greatest. However, in clinical practice it is not possible to obtain such an angle of incidence therefore angulations between 0 and 60° are applied, and those closer to 60° are preferred as with angulation of 0° no Doppler signal is picked up [1].

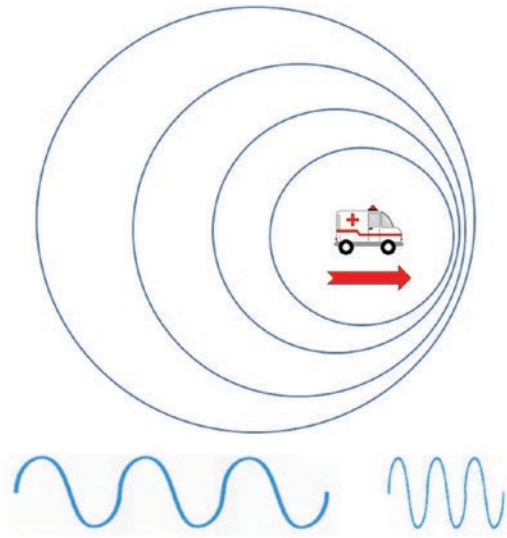

Fig. 4.1 Schematic presentation of the Doppler effect. When the ambulance is advancing, wave frequency is increased. On the contrary, when the ambulance is going away, wave frequency decreases

4.2 Applications of the Doppler Shift in Diagnostic Imaging

The following types of application of the Doppler shift in diagnostic imaging are distinguished:

- Spectral Doppler, including Continuous wave Doppler and Pulsed wave Doppler (Fig. 4.2).
- Color Doppler, also called Color flow Doppler (Fig. 4.3).
- Power Doppler (Fig. 4.4).

In Spectral Doppler imaging velocity of blood flow is represented graphically over time. The

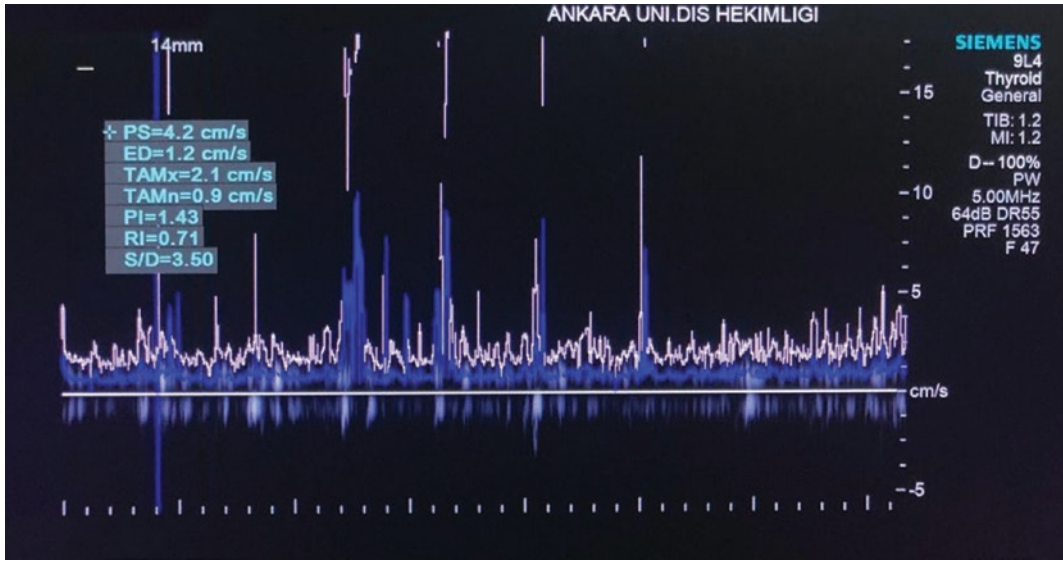

Fig. 4.2 Example of Spectral Doppler examination with measurements of blood velocity and indices

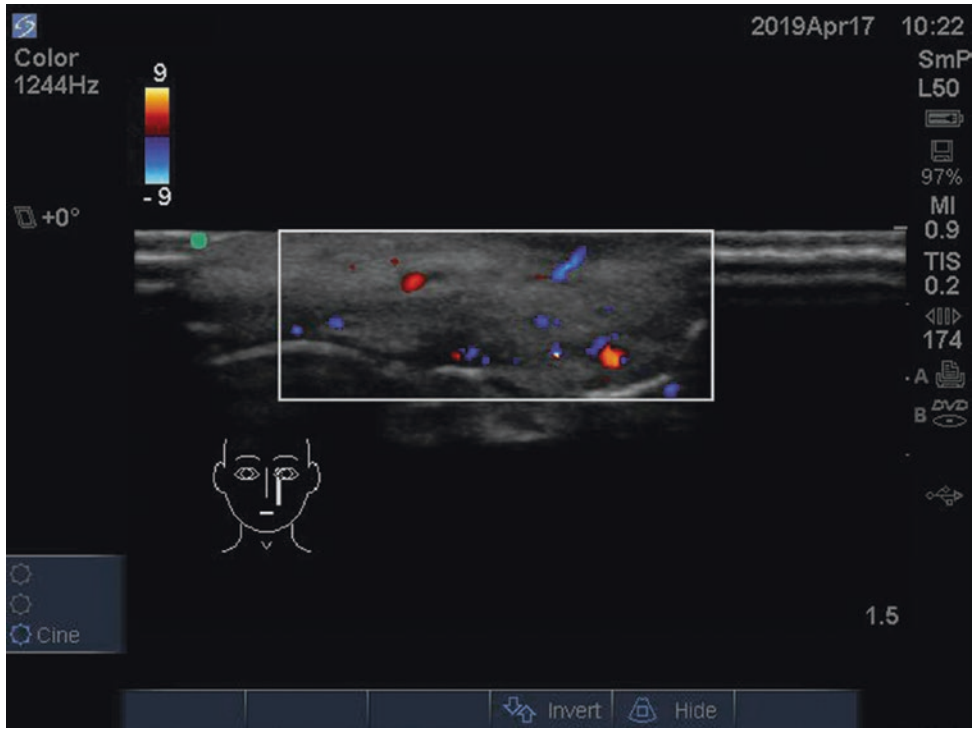

Fig. 4.3 Example of Color Doppler examination of a facial hemangioma

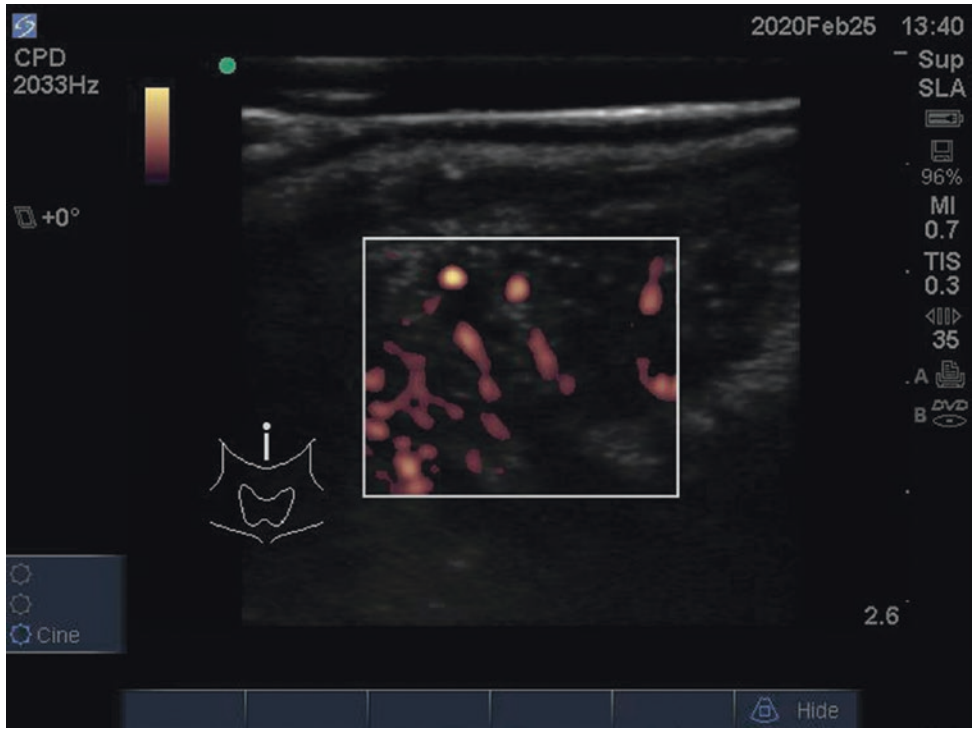

Fig. 4.4 Example of Power Doppler examination of the tongue

name "spectral" comes from the spectrum of Doppler waveforms. During the examination maximum (peak) and minimum blood velocities are measured and mean velocity is calculated on the basis of all velocities. Maximum (peak) velocity is represented as the highest point of the spectral curve, while the minimum one is the opposite. Resistance index (called also resistivity index—RI) is calculated by subtraction of diastolic velocity in a blood vessel from systolic one and dividing the result by systolic velocity. This index is typically used to assess the resistance in small blood vessels located distally to the area of measurement. Pulsatility index (PI) is calculated from the maximum, mean, and minimum Doppler frequency shifts within a cardiac cycle. Just like the RI, PI aids in evaluation of resistance in blood vessels. The shapes of waveforms differ in high and low resistance vessels. In a high resistance vessel, there is a big difference between systolic and diastolic component of the waveform (and in very large vessels the diastolic flow can even be reversed). In a low resistance blood vessel, the diastolic component is relatively large thus the difference in systolic and diastolic velocities is not as great as in high resistance vessels.

Continuous wave Doppler is based on simultaneous emission and receiving of sound waves in separate piezoelectric crystals in transducer along an operator-defined pathway. This modality allows for identification of direction of blood flow and estimation of velocity but does not provide information on depth of the examined blood vessel.

In Pulsed wave Doppler, a certain region of interest usually called "gate" is defined by the operator. Intermittent sampling of ultrasound waves is performed only within this gate which marks the sampling depth, volume, and direction.

Color Doppler mode allows imaging of blood flow with indication of its direction and velocity within a selected region of interest (ROI). In this mode, multiple volumes related to pixels are being sampled along an array of scanned lines. The direction of blood flow in Color Doppler is coded with color, and hence the name of the mode. The blood coming towards the probe is coded in red and blood flowing away from the probe is depicted with blue color. It is a source of common misunderstanding that blood vessels imaged as red are arteries and the ones marked with blue color are veins, which is probably due to traditional presentation of these two kinds of blood vessels in anatomical atlases. However, when the probe is rotated by 180° in relation to the examined blood vessels, color coding will turn to opposite. Consequence in coding of colors aids in avoiding confusion. In Color Doppler mode also blood velocity is indicated with color—the lighter the shades of red and blue are, the higher the blood velocity is. Additionally yellow color serves as indicator of areas characterized by turbulences in blood flow. One of the disadvantages of Color Doppler mode is an artifact called aliasing. It is based on apparent opposite flow direction in relation to the actual one, resulting from crossing a certain limit of frequency, the so-called Nyquist limit (Fig. 4.5).

Power Doppler mode on one hand detects smaller velocities than Color Doppler therefore is characterized by higher sensitivity, but on the other hand it does not assess either direction or velocity of blood flow. The modes elaborated to visualize very small blood vessels with very slow blood flow are differently named by manufacturers (e.g., "e-flow"). One of advantages of Power Doppler over Color Doppler is that aliasing is not observed in Power Doppler mode.

The abovementioned modes are often combined with B-mode presentation as duplex ultrasound, while in triplex mode B-mode, Color Doppler, and Spectral Doppler are simultaneously displayed (Fig. 4.6). This mode allows anatomical identification of a blood vessel using B-mode and color coding which facilitates exact placement of the Doppler gate for the spectral examination in real time. Attention must also be paid to the size of the gate—when too small or too big, the results are affected as the blood flow is faster in the center of a lumen of a blood vessel and slower closer to the walls of the vessel. It is advisable that the gate is placed in the center of the examined blood vessel and its width should be around one half of the lumen of the vessel.

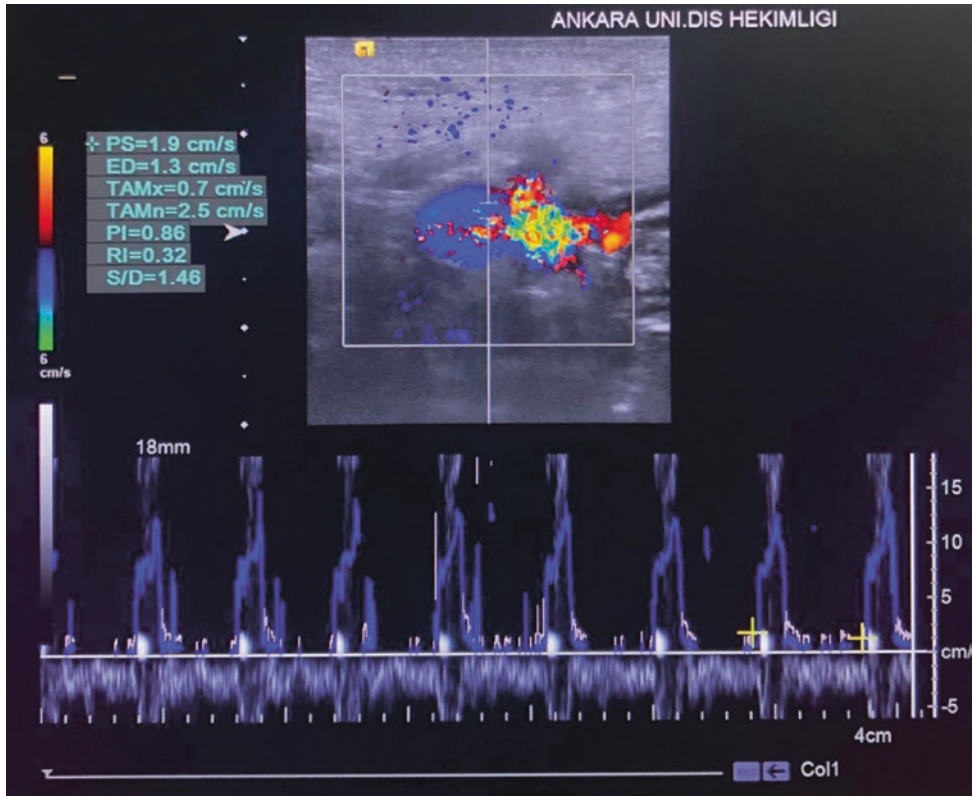

Fig. 4.5 Example of aliasing artifact in Color Doppler in triplex mode

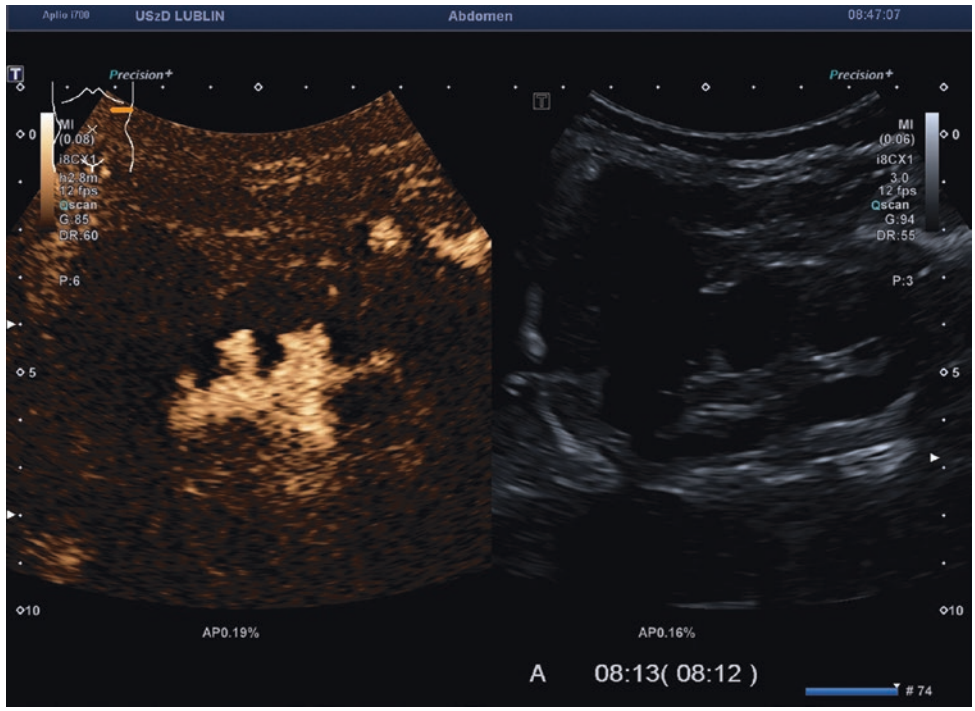

Fig. 4.6 Example of use of US contrast media in vesicoureteral reflux (figure courtesy of Dr. Grzegorz Jedrzejewski)

4.3 Indications for Doppler Examinations in the Head and Neck Region

Applications of Doppler ultrasound within the head and neck region include the following:

- Examination of blood flow in big blood vessels (among others: plaque, stenosis, thrombus, dissection).
- Assessment of vascularization of lesions such as cysts, tumors, and inflammations and vascular lesions such as hemangioma and arteriovenous malformation.
- Assessment of vascular pattern in lymph nodes in differentiating normal, inflamed, neoplastic, and metastatic nodes.

4.4 Limitations of Doppler Examinations

Limitations of Doppler examinations include the following:

1. It is more difficult to depict smaller blood vessels than the larger ones.
2. Blood vessels with a very slow blood flow may be overdiagnosed as completely obstructed if ultrasound device is not sensitive enough to pick up weak blood flow. Slow blood flow not detected by the machine also leads to conclusions that a lesion is completely avascular.
3. Deep vessels are more difficult to be imaged than superficial ones. However, within the head and neck this problem is of lesser importance due to anatomical considerations.
4. If plaques in atherosclerosis are calcified, the post-acoustic shadowing will hamper Doppler examination of this portion of the blood vessel.
5. Aliasing artifact (as discussed above).
6. Just like with other US examinations, patient cooperation is required in order to maintain motionless position during the scan. Otherwise, it will not be possible to perform measurements of blood flow parameters in Spectral Doppler, while in Color and Power Doppler modes patient movement will make tissues falsely coded with color.

4.5 Ultrasound Contrast Agents

Contrast agents are used in medical imaging in order to enhance visibility of certain organs, tissues, and lesions following mainly intravenous administration. Contrast media applied in ultrasound differ considerably from the agents used in CT and MRI as they are composed of microbubbles or nanobubbles of gas. Moreover, due to their composition they are not contraindicated in either patients with allergy to iodine or hyperthyroidism (CT) or with renal failure (MRI). In the first generations of ultrasound contrast agents, the microbubbles of air were present in blood vessels only for a short time as after exposure to acoustic pressure exerted by ultrasound beam they quickly dissolved. In the next generations, gas bubbles are more stable due to the presence of a phospholipid membrane surrounding the gaseous core. The currently applied gases include nitrogen, sulfur hexafluoride, and perfluorocarbon. Microbubbles are smaller than erythrocytes (6 μm vs. 9 μm) which means that they pass easily through capillary vessels of the lungs.

Application of ultrasound contrast media makes dynamic examinations of vascularity feasible, i.e., arterial, venous, and reperfusion phases. The organs most commonly assessed with their aid following intravenous administration are liver and kidney, and bladder after administration through a urinary catheter (Fig. 4.6).

The so far reported indications within the head and neck include:

- Continuous wave Doppler and Pulsed wave Doppler examinations.
- Salivary gland tumors [2].
- Improved visualization of obstructive diseases of salivary glands (alternatively, mixture of air

bubbles and saline can be used for ultrasound sialography) [3].
- Secretory dysfunctions of salivary glands [4].
- Differentiation between benign and malignant thyroid nodules [5].

Contrast-enhanced ultrasound (CEUS) has also been used in imaging of muscles [6] and infantile hemangiomas [7], but not of the head and neck, yet. Ultrasound contrast media are not certified for use in some countries which limits their utility.

Acknowledgments To Dr. Grzegorz Jedrzejewski from the Department of Pediatric Radiology of the Medical University of Lublin, Poland for providing Fig. 4.6.

References

1. Iro H, Bozzato A, Zenk J. Atlas of head and neck ultrasound: Thieme; 2013.
2. Zengel P, Siedek V, Berghaus A, Clevert DA. Intraductally applied contrast-enhanced ultrasound (IA-CEUS) for improved visualization of obstructive diseases of the salivary glands, primary results. Clin Hemorheol Microcirc. 2010;45(2–4):193–205.
3. Oh SH, Kang JH, Choi YJ, Kim BY, Lee SR, Lee SH, Choi YS, Hwang EH. Ultrasound-guided sialo-irrigation with a saline-air mixture as the contrast medium. Oral Radiol. 2019 Jan;35(1):84–9.
4. Zengel P, Berghaus A, Weiler C, Reiser M, Clevert DA. Intraductally applied contrast-enhanced ultrasound (IA-CEUS) for evaluating obstructive disease and secretory dysfunction of the salivary glands. Eur Radiol. 2011;21(6):1339–48.
5. Trimboli P, Castellana M, Virili C, Havre RF, Bini F, Marinozzi F, D'Ambrosio F, Giorgino F, Giovanella L, Prosch H, Grani G, Radzina M, Cantisani V. Performance of contrast-enhanced ultrasound (CEUS) in assessing thyroid nodules: a systematic review and meta-analysis using histological standard of reference. Radiol Med. 2020;125(4):406–15.
6. Fischer C, Kunz P, Strauch M, Weber MA, Doll J. Safety profile of musculoskeletal contrast-enhanced ultrasound with sulfur hexafluoride contrast agent. Ther Clin Risk Manag. 2020;16:269–80.
7. El-Ali AM, McCormick A, Thakrar D, Yilmaz S, Malek MM, Squires JH. Contrast-enhanced ultrasound of congenital and infantile Hemangiomas: preliminary results from a case series. AJR Am J Roentgenol. 2020;214(3):658–64.

5 Advanced Ultrasonography Imaging

Kaan Orhan and Ibrahim Sevki Bayrakdar

Contents

5.1 Introduction

The advancements in computer science provide important developments in imaging technology. In parallel with these developments, significant improvements have occurred in ultrasound imaging over the years. The acceptability of ultrasound imaging is high due to its advantages including ease of use, free of radiation, instantaneous availability of findings, noninvasiveness, low price compared to other imaging methods, and excellent record safety, and so this support the phenomenon of continuous innovation. Various advanced technologies have been presented in recent years for clinical use. Some methods can lead to an innovation almost as valuable as real-time as the real-time imaging, Color Doppler imaging, Tissue Harmonic Imaging, Volumetric ultrasound, con-

K. Orhan (✉)
Faculty of Dentistry, Department of Dentomaxillofacial Radiology, Ankara University, Ankara, Turkey

I. S. Bayrakdar
Faculty of Dentistry, Department of Dentomaxillofacial Radiology, Eskisehir Osmangazi University, Eskisehir, Turkey

K. Orhan (ed.), *Ultrasonography in Dentomaxillofacial Diagnostics*,
https://doi.org/10.1007/978-3-030-62179-7_5

trast-enhanced ultrasonography, and elastography are some of them. All of them have already presented great advancements in diagnostic skills. These will be described below.

5.2 Panoramic Imaging

Ultrasonographic imaging has limited fields of view (FOV) area compared with the other imaging techniques such as Computed Tomography (CT), Magnetic Resonance Imaging (MRI) because the image FOV is restricted by the ultrasound probe width and scanning angle [1, 2]. So, the system cannot show a full view of the complete anatomy and it is difficult to acquire an expanded view of superficial structures. Panoramic imaging is an advance ultrasonographic technic which supplies images with a large FOV which is known also as "ultrasound CT" or "panorama ultrasound." [3] Panoramic imaging provides the transducer to move through the patient's anatomy and combine multiple images to create one long image with an extremely wide field of view. (Figs. 5.1, 5.2 and 5.3) This component uses cross-correlation methods to correlate consecutive images, revolves and fasten them to produce the final image [4]. While, it is maintaining the traditional benefits of sonography including high spatial resolution, low-cost, and lack of ionizing radiation, it gives expanded-view images with lower distortion that has more easiness in real-time practices [4, 5]. Therefore, panoramic ultrasonography technique is promising in clinical applications.

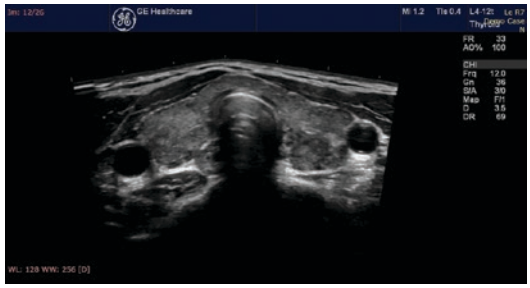

Fig. 5.1 Panoramic imaging of thyroid gland

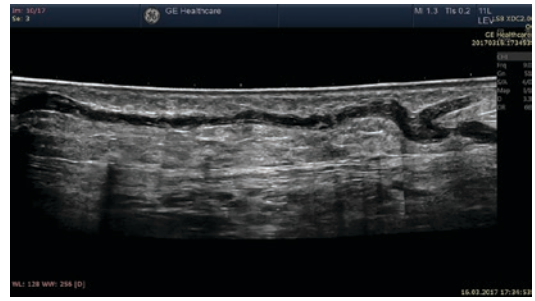

Fig. 5.2 Panoramic imaging of vessel

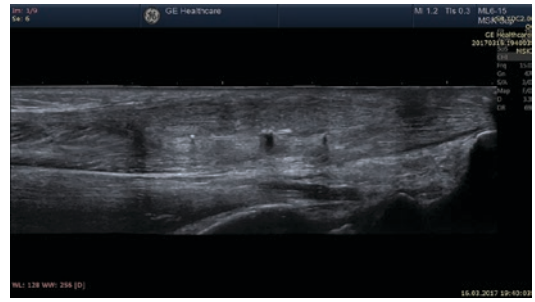

Fig. 5.3 Panoramic Imaging of Superficial Musculoskeletal (MSK) tissues

5.3 Tissue Harmonic Imaging

Various structure layers in the tissue spread the sound wave at different speeds that cause phase shift in the sound wave. The high-pressure part of the sound wave in the tissue moves faster than the low-pressure part which causes an increase in the frequency of the high-pressure part in the waveform. This increase of frequency occuring in the frequency layers of the ultrasound wave are called "Harmonics." [6] Harmonics have been shown by nonlinear propagation in conventional US physics. Tissue Harmonic Imaging (THI) uses nonlinear portions of ultrasound echo signals reflected from tissue for image production [6–9]. THI can supply higher quality images than conventional gray-scale sonography. While the same frequency spectrum is received, which is transmitted to the patient to produce ultrasonographic images in conventional gray-scale sonography,

higher harmonic frequencies produced by the diffusion of ultrasound beam into tissue are used to generate sonograms in THI sonography [6–10] (Fig. 5.4). Many artifacts arise from the interaction of the ultrasound beam with superficial structures are eliminated by using THI sonography. Because the artifact generating signals have no energy to create harmonics, these can be easily filtered while the image is being rendered. THI sonography has many advantages, such as enhanced lateral resolution, diminished side-lobe artifacts, and enhanced signal-to-noise rate. B-mode and Doppler mode of ultrasonography can be used in THI [6–12].

5.4 Real-Time Spatial Compound Imaging

Real-time spatial compound imaging is an ultrasound method which obtain various overlapping scans of an object from different directions and then integrating scans to create a single compound image (Fig. 5.5). In this method, different and

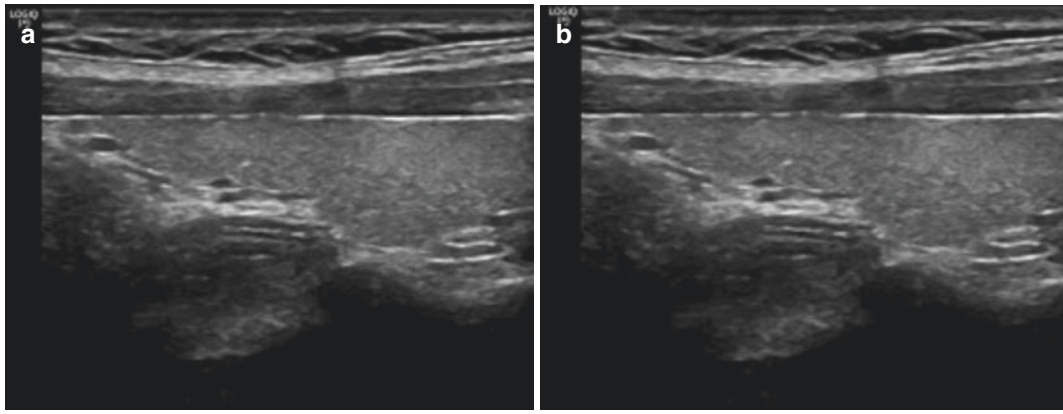

Fig. 5.4 Comparing the images with Tissue Harmonic Imaging (**a**) Tissue Harmonic Imaging—OFF (**b**) Tissue Harmonic Imaging—ON

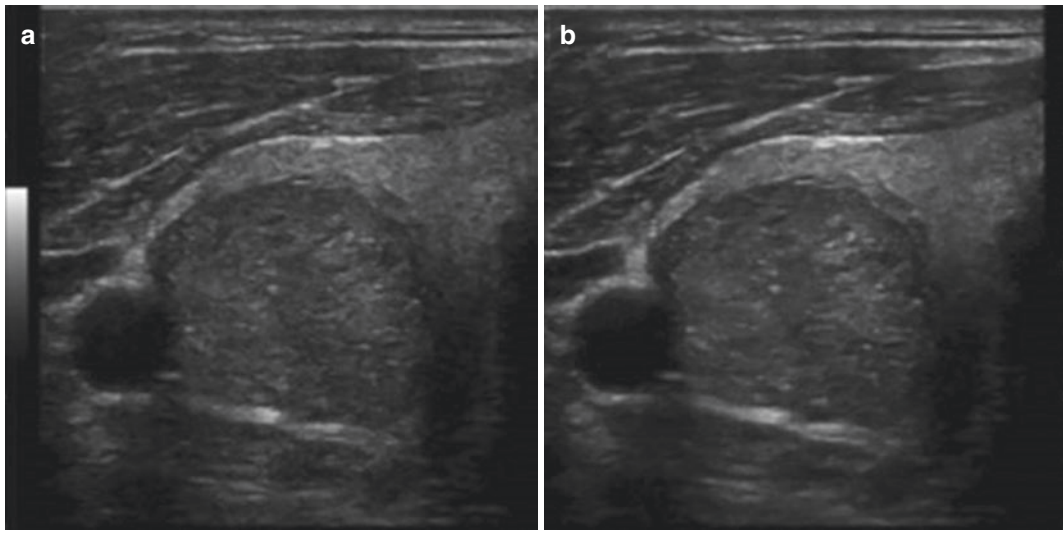

Fig. 5.5 Comparing the thyroid gland images with Real-Time Spatial Compound Imaging mode (**a**) Real-Time Spatial Compound Imaging—OFF (**b**) Real-Time Spatial Compound Imaging—ON

irrelevant artifact patterns were produced because of the scanning from different perspectives using electronic beam steering of a transducer array. So, compound images have low levels of speckle, clutter, and other acoustic artifacts. Averaging distinctive patterns constrain artifacts, and thereby enhancing image quality. Real-time spatial compound imaging has higher contrast resolution and tissue distinction than conventional ultrasound images (Figs. 5.6 and 5.7). [4, 5, 9, 10, 13–15]

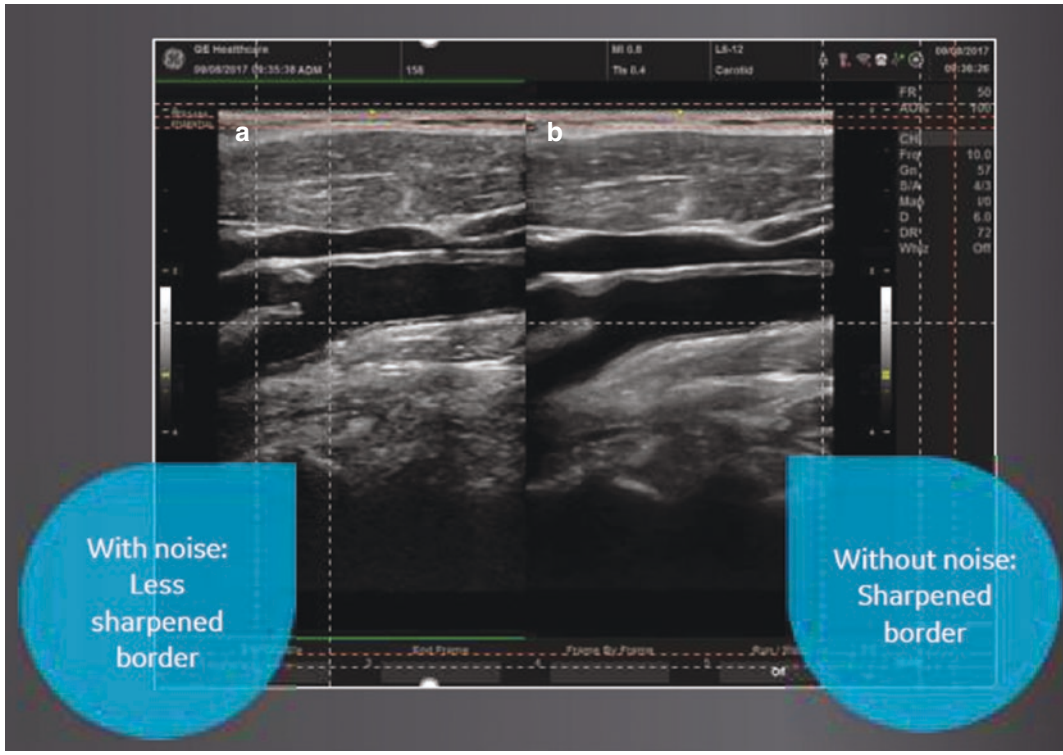

Fig. 5.6 Comparing the images of carotid artery and jugular vein with Real-Time Spatial Compound Imaging mode (**a**) Real-Time Spatial Compound Imaging—OFF (**b**) Real-Time Spatial Compound Imaging—ON

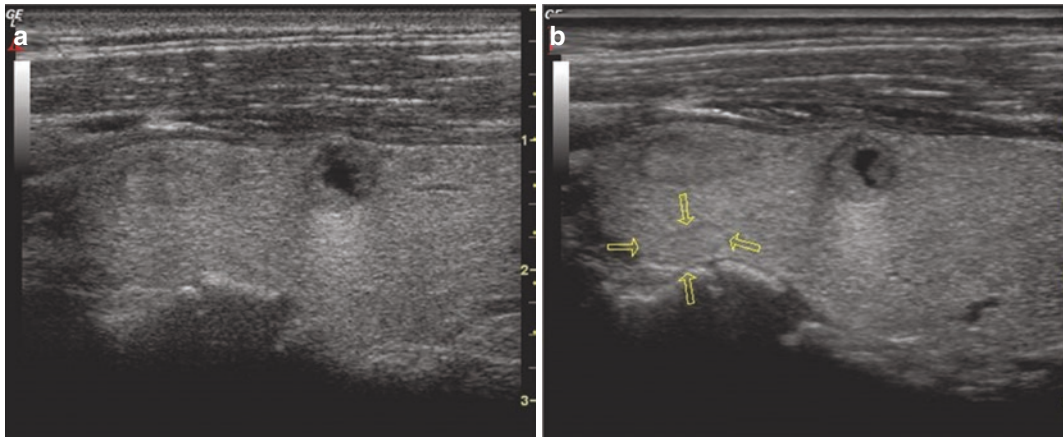

Fig. 5.7 Comparing the images with Real-Time Spatial Compound Imaging mode (**a**) Real-Time Spatial Compound Imaging—OFF (**b**) Real-Time Spatial Compound Imaging—ON

5.5 Chromatic Imaging

Chromatic imaging present shades of a different color than gray in gray-scale examination. No different parameter is used in rendering than the gray-scale display. Chromatic imaging provides enhancement of image clarity, the edge acuity, create a difference in visual perception, and presents detail determination (Figs. 5.8, 5.9, 5.10 and 5.11).

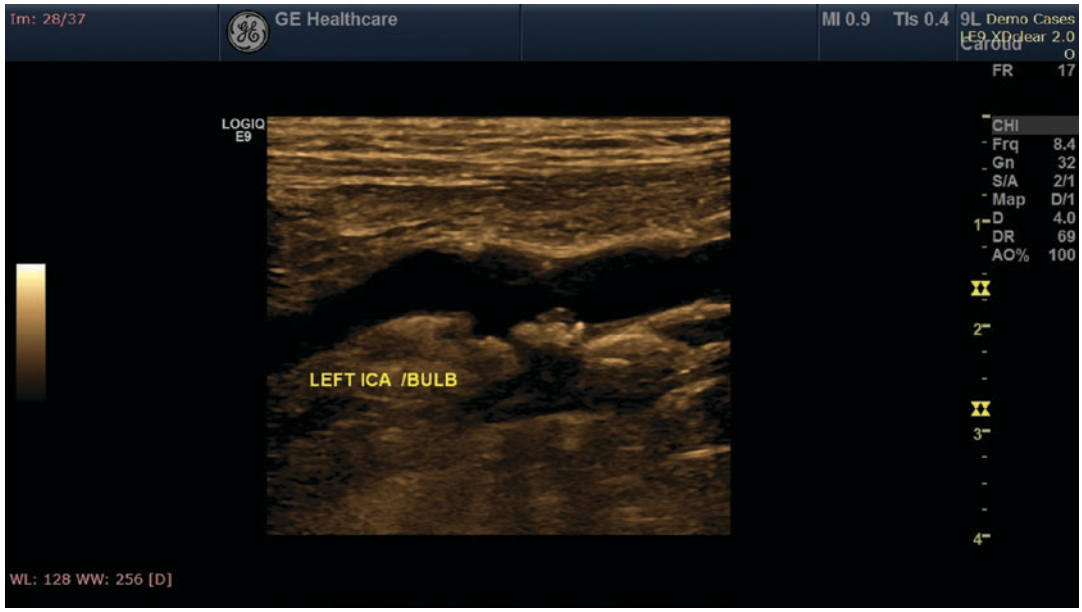

Fig. 5.8 Chromatic Imaging of Internal Carotid Artery (ICA)

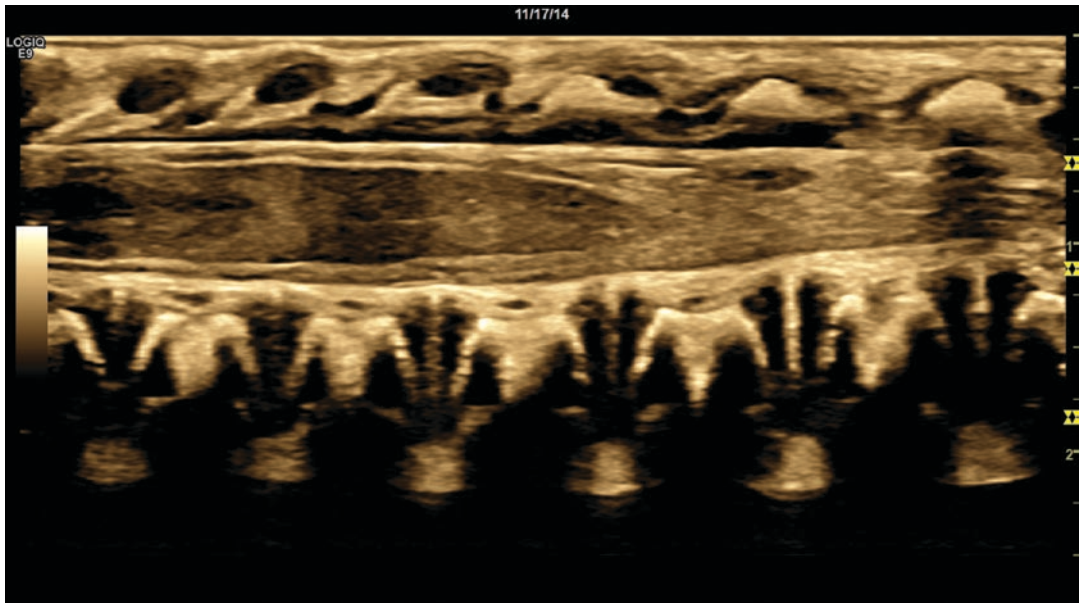

Fig. 5.9 Chromatic Imaging of Spine

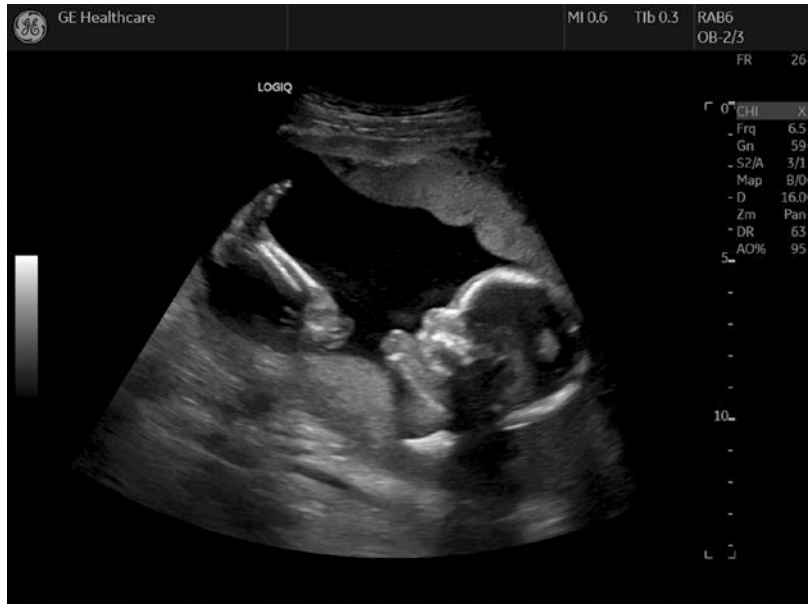

Fig. 5.10 Chromatic Imaging of Fetus

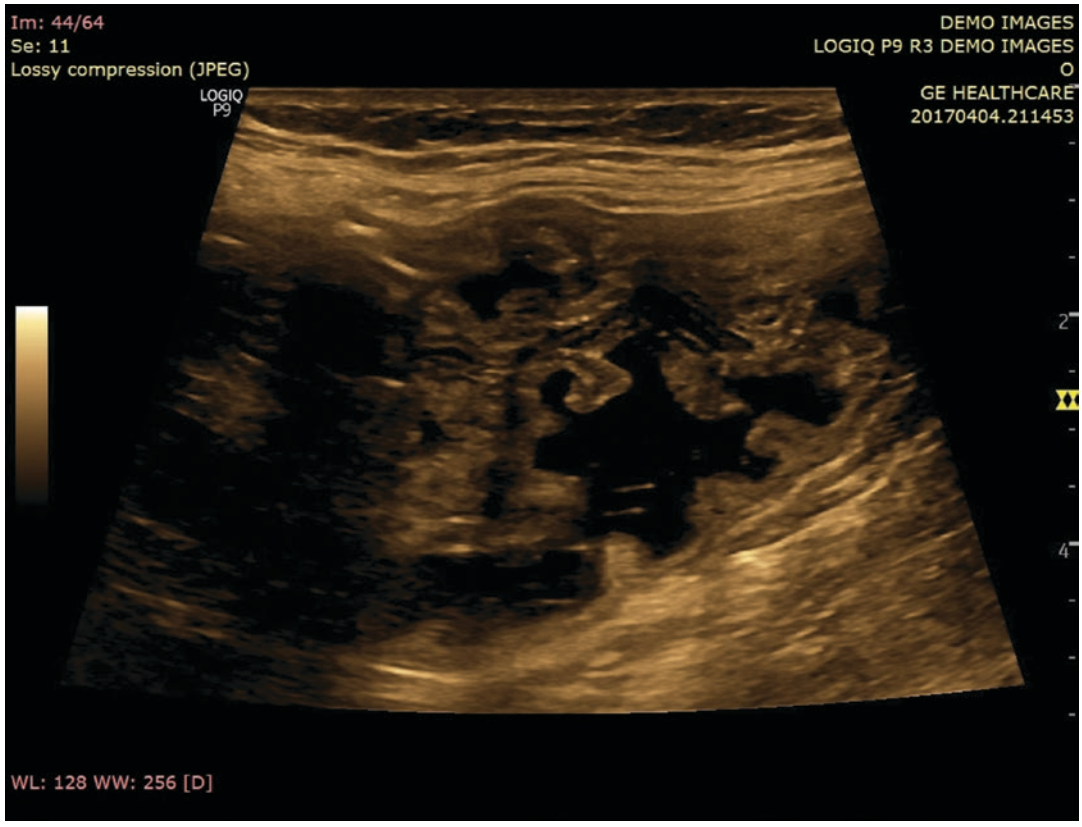

Fig. 5.11 Chromatic Imaging of Bowel

5.6 Volumetric Ultrasound (Three-Dimensional (3D) and Four-Dimensional (4D) Ultrasound Imaging)

Volumetric ultrasound was developed in response to the existing challenges of standard two-dimensional (2D) ultrasound. Volume data acquisition, imaging, and storage capabilities have expanded with advances in high-speed computing technology. Volumetric ultrasonography has proven many advantages with its basic operating principles. It is expected to be a routine part of patient diagnosis and treatment soon [4, 9, 16, 17]. Three perpendicular plans can be displayed simultaneously with this method. Rotating and moving these plans in their circles and moving back and forth to obtain accurate sections for diagnosis and geometric measurement is the greatest advantage of three-dimensional (3D) modality. In this way, 3D ultrasonography combines the advantages of conventional ultrasound (such as safety, ease of application, and low cost) with the advantage of obtaining consecutive sections in an unlimited number and in the desired plane. Sonographic volumes can be stored continuously and used for three-dimensional anatomical reconstructions. In addition, these volumes can be analyzed by examining conventional B-mode planar reformat sections and even images that are not available in routine examinations [4, 9, 16–18] (Figs. 5.12, 5.13, 5.14 and 5.15).

3D ultrasound is introduced as volume rendering of ultrasonographic data and it is also named as four-dimension (4D) when it includes a series of 3D volumes gathered in course of the time. Modern ultrasonography equipment can quickly obtain 3D and 4D data sets thanks to their large computing power. The obtained volume from reconstructed 3D dataset can be presented as different forms including transparent appearance, surface rendering mode or maximum intensity projection (MIP). Furthermore, 3D presentations show topography and volume information [16–20].

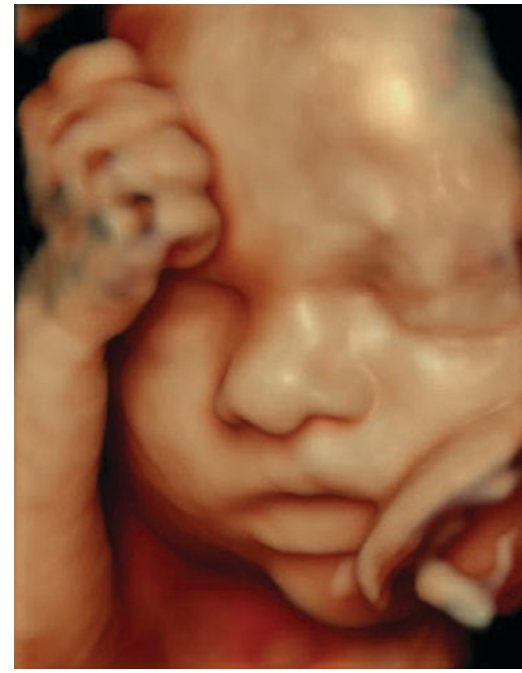

Fig. 5.12 Volumetric ultrasound image of Fetus

5.7 Contrast-Enhanced Ultrasound Imaging

A contrast-enhanced ultrasound imaging (CEUI) is a method which uses specific contrast agents consist of encapsulated microbubbles enhancing the characterization of anatomic structures with the scanning of slight vascular structures [5, 9, 17, 21–24]. Microbubbles make up of a gas core and external shell contributing stability. These are nearly 1–10 mm in size. The main purpose of ultrasonographic contrast agents is to increase the signal intensity returning to the transducer. The primary mechanism of signal increase is the scattering of ultrasound beam caused by microbubbles instead of blood. When the contrast material is used together with harmonic imaging, a significant increase in image quality is achieved. Tissue harmonics formed in tissue are less severe than harmonics formed by microbubbles [5, 9, 17, 21–26]. CEUI is an economical, safe, and efficient

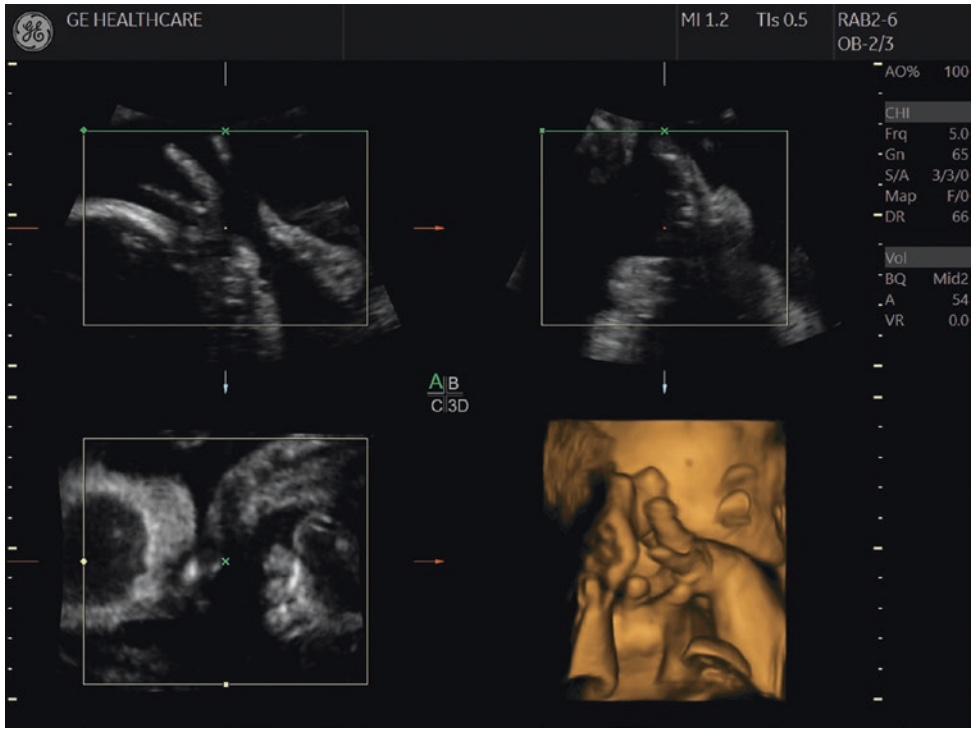

Fig. 5.13 Volumetric ultrasound images of fetus in 3 (Three) views

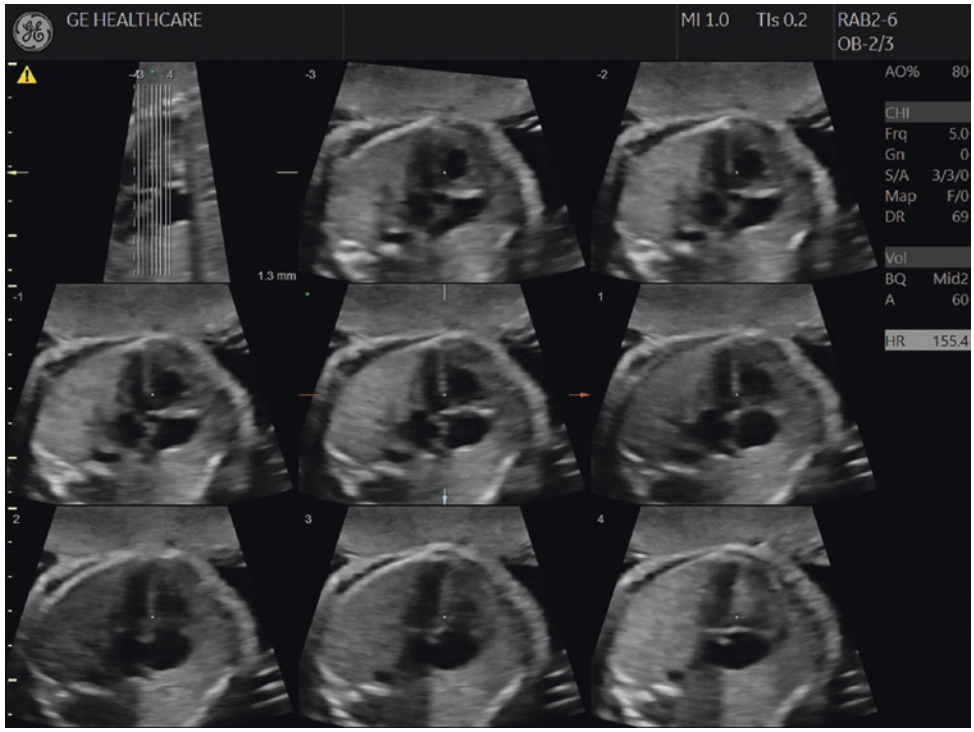

Fig. 5.14 Volumetric ultrasound Tomographic Imaging of Fetal Heart

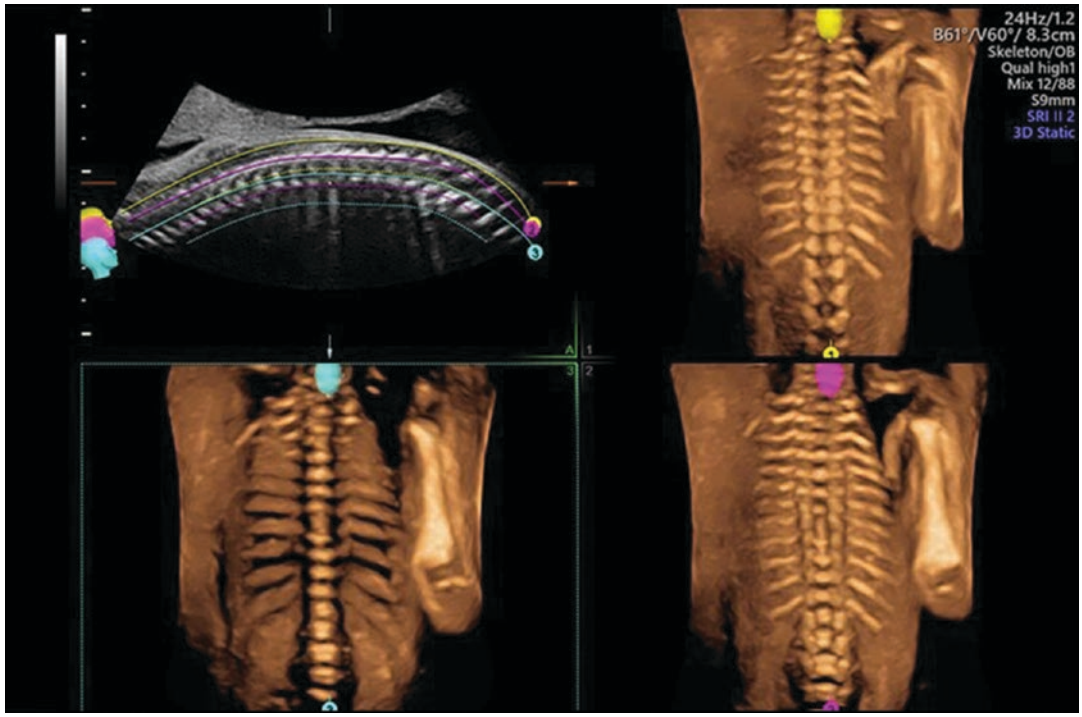

Fig. 5.15 Volumetric ultrasound images of Spine in 3 (Three) views

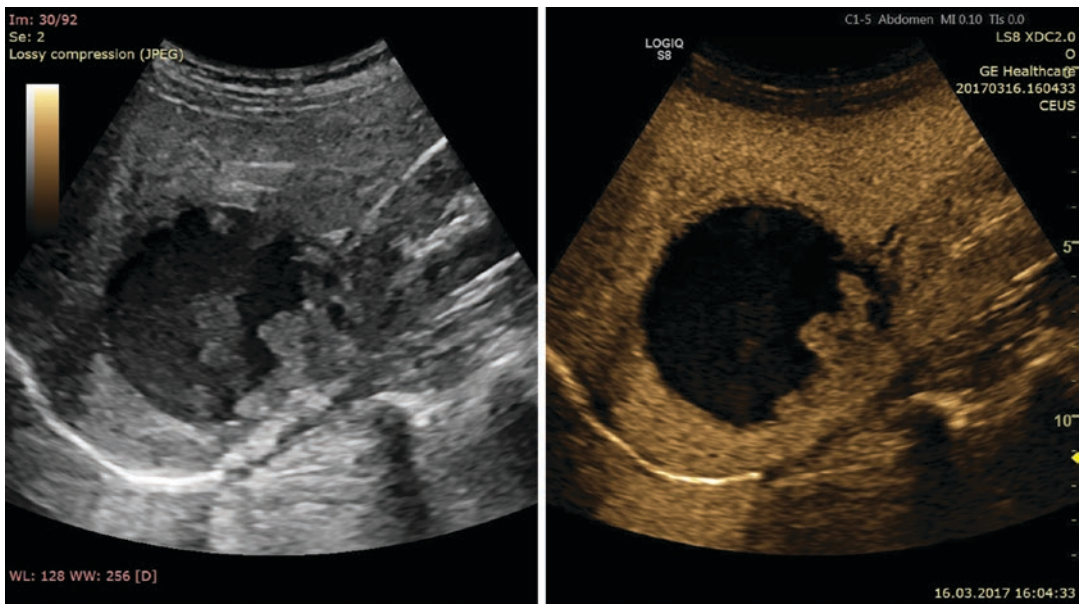

Fig. 5.16 Contrast-enhanced ultrasonography imaging of liver

method with multiple clinical procedures. This technique can be used to characterize different perfusion models that are effective in distinguishing abnormal tissues from normal tissues (Figs. 5.16 and 5.17). CEUI could be a useful tool for evaluation of metastases in lymph nodes, differential diagnosis of benign and malignant thyroid nodules [5, 9, 17, 21–26].

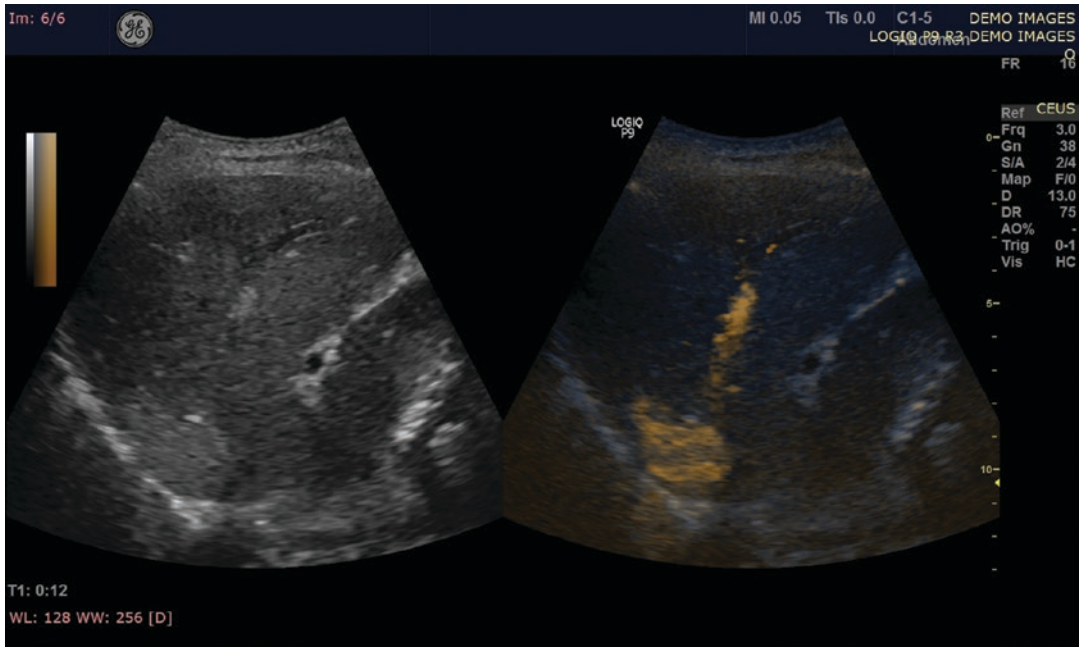

Fig. 5.17 Contrast-enhanced ultrasonography imaging of liver

5.8 Elastography

5.8.1 Strain Elastography

Strain Elastography (SE), also described as compression elastography, sonoelastography, or real-time elastography [27–29], measures tissue stiffness by applying external tissue pressure [30]. The technique is based on low-frequency compression of the tissue, which is usually applied manually via the hand-held ultrasound transducer (free-hand EUS) [31], or in some cases using physiological body movements such as respiration or pulsation [29]. Compression sonoelastography provides a semiquantitative measurement of strain ratio, which shows an index of the relative elasticity between a chosen region of interest (ROI) in the examined tissue and a reference ROI, which is usually in the adjacent subcutaneous tissues [32]. The tissue strain is translated into a color-coded elastogram. The gray or color scale encoding is chosen by the user. Most often warm colors correspond to hard tissues, cold colors to soft ones. [33, 34] (Figs. 5.18 and 5.19) (Table 5.1).

Acoustic radiation force impulse (ARFI) is a type of SE whereby tissue is induced internally by a focused ultrasound pulse, instead of manual or physiological compression. As the ultrasound pulse travels through the tissue, soft tissue experiences larger displacement than hard tissue. After displacement by the pulse, the tissue returns to its original configuration. The tissue displacement by the original push-pulse can be measured using the application of several short-time pulse echoes, which provides data for comparison with the reference image. This method has the advantage of imaging deeper tissue, not accessible by superficial external compression [31] (Table 5.1).

5.8.2 Shear Wave Elastography

Shear wave elastography is another ultrasound-based imaging modality that provides a noninvasive estimate of tissue characteristics by measuring the speed of shear wave propagation through soft tissues (Figs. 5.20, 5.21, 5.22 and 5.23). SWE uses an acoustic radiation force impulse, which specific experience of the exam-

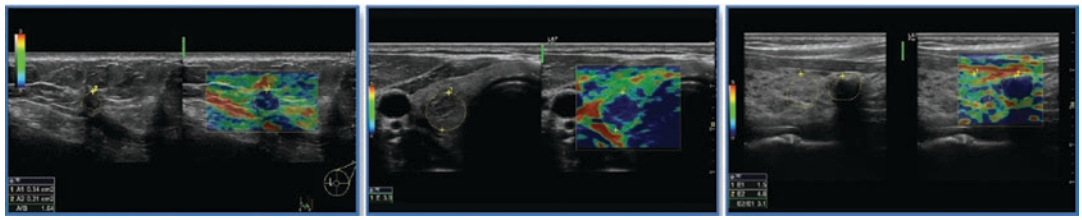

Fig. 5.18 Strain Elastography of thyroid gland

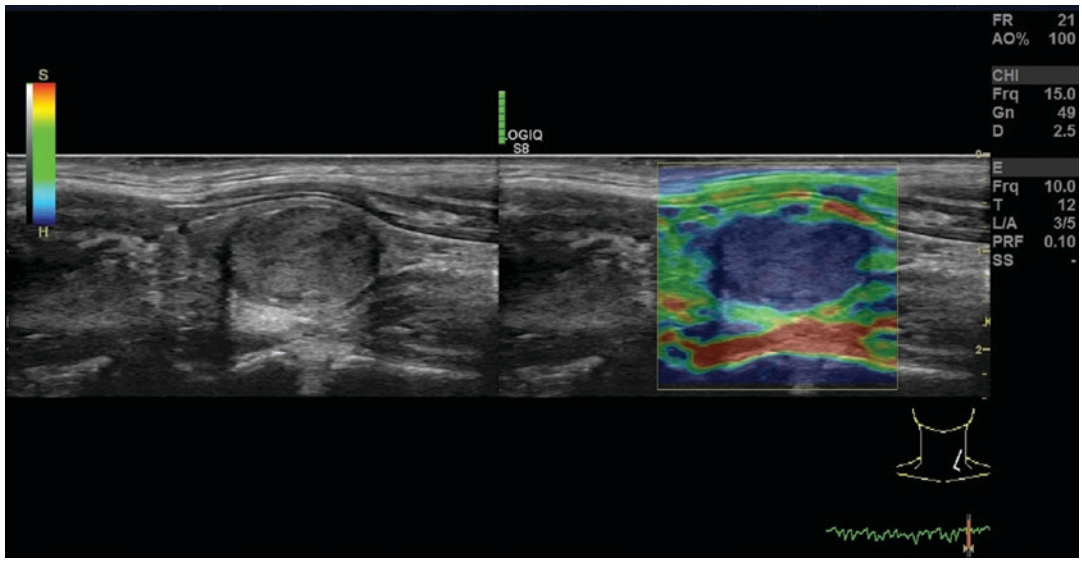

Fig. 5.19 Strain Elastography of thyroid gland

iner is not necessary. SWE is less operator-dependent than strain elastography and represents a reproducible tool for quantifying stiffness [32, 35, 36]. Shear wave propagate perpendicular to the axial displacement caused by the ultrasound pulse and attenuate approximately 10,000 times more rapidly than conventional ultrasound. [31, 37] Speed of shear waves is usually measured to evaluate the tissue stiffness by calculating elastic Young's modulus [32]. This technique provides both qualitative color-coded elastograms and quantitative maps either of elasticity in kPa or of shear wave speed in cms^{-1} [31] (Table 5.1). Shear wave elastography (SWE) has different types which include transient elastography (TE), point shear wave elastography (pSWE), and multidimensional shear wave elastography (2D-SWE and 3D-SWE) [38].

5.8.2.1 Transient Elastography

Transient elastography (TE), also known as vibration-controlled elastography, is usually used in the measurement of regional tissue elasticity with limited depth (Fig. 5.24). This device is designed only for liver elasticity measurement and for use also by persons who are not imaging specialists. Low frequency (50 Hz) induced pulses are used to generate shear waves and the external compression is applied by using a short-tone burst of vibration [31]. TE measures tissue stiffness over a 1 cm diameter–4 cm length region of tissue [30]. This type of elastography evaluates the tissue stiffness only as "soft" and "hard" and requires computing tissue strain. Besides these disadvantages, dynamic tissue motion imaging during real-time is easier with transient elastography [32, 39] (Table 5.1).

Table 5.1 Types of elastography [23, 33]

	Method	Type of force	Applied force	Displayed/ measured	Quantitative	Imaging or measurement	Commercial implementation
Displacement of strain imaging	Strain elastography (SE) and Strain rate imaging (SRI)	Quasi static	Mechanically induced either Active external dispalcement of tissue surface[a] or Passive internal physiologically induced[b]	Strain or strain rate	Qualitative, although tools often provided to analyze image characteristics	Full area image Refreshed at up to the ultrasound frame rate	Esote GE Hitachi Aloka Samsung Medison Siemens Toshiba Ultrasonix Mindra Zonare
	Acoustic radiation force impulse (ARFI) imaging	Dynamic	Ultrasound induced-focused radiation force Impulse at depth	Displacement	Qualitative	Single image within a box	Siemens
Shear wave speed measurement	Transient elastography (TE)[c]		Mechanically induced İmpulse (“thump”) at tissue surface[b]	Shear wave speed[d]	Quantitative	Single measurement, beam-line average	Echosens
	Point shear wave elastography (pSWE), also known as ARFI quantification[c]		Ultrasound-induced focused radiation force impulse at depth	Shear wave speed[d]	Quantitative	Single image within a color box	Siemens
Shear wave speed imaging	Shear wave elastography (SWE)[c]		Ultrasound-induced radiation force focus swept over depth faster than shear wave speed to create a Mach cone	Shear wave speed[d]	Quantitative	İmage within a color box, refreshed at up to several per second[e]	SuperSonic imagine

[a]Palpation, balloon expansion, etc., whether body surface or intracavity

[b]Cardiovascular or respiratory pulsation, or muscular contraction

[c]The term shear wave elastography (SWE) has been used here according to the current literature, where it refers to methods that make images of shear wave speed using radiation force excitation. Thus, it includes 2D-SWE and 3D-SWE. The term point shear wave elastography (pSWE) has been used for the method where a regional average only (no image) of shear wave speed is measured using radiation force excitation. This emphasises that it is essentially a SWE method, even though in the literature it has been referred to as ARFI quantification. Transient elastography (TE) also measures shear wave speed without creating an image but, since it uses a surface mechanical force rather than acoustic radiation force, it has not been classified here under the term SWE

[d]Shear wave speed may be converted to shear modulus or Young’s modulus under assumptions explained in the text and the online appendix

[e]The term “real-time” has been avoided here as, unlike real-time ultrasonography, the elastography systems described in this chapter are not yet suitable for rapid searching through large volumes nor for observing rapid tissue motion within a sequence of elastograms

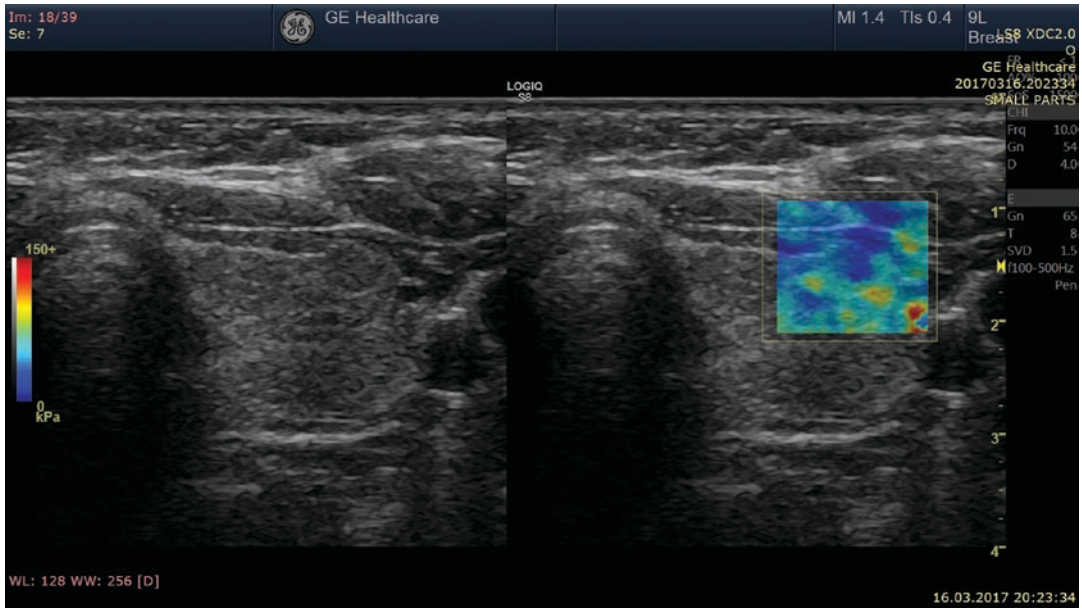

Fig. 5.20 Shear wave elastography of thyroid gland

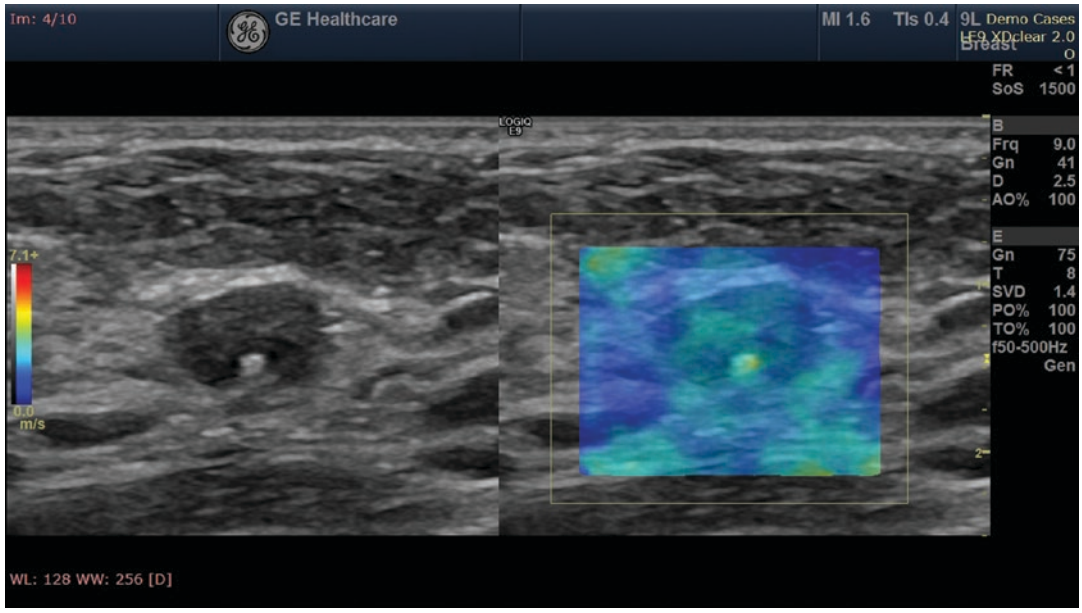

Fig. 5.21 Shear wave elastography of lymph node

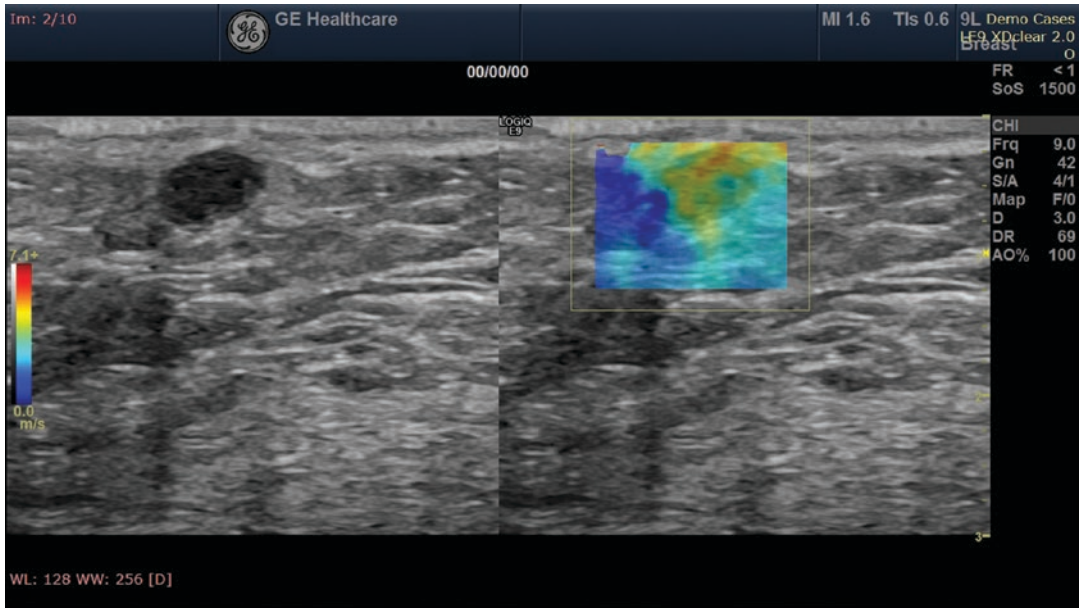

Fig. 5.22 Shear wave elastography of soft lesion

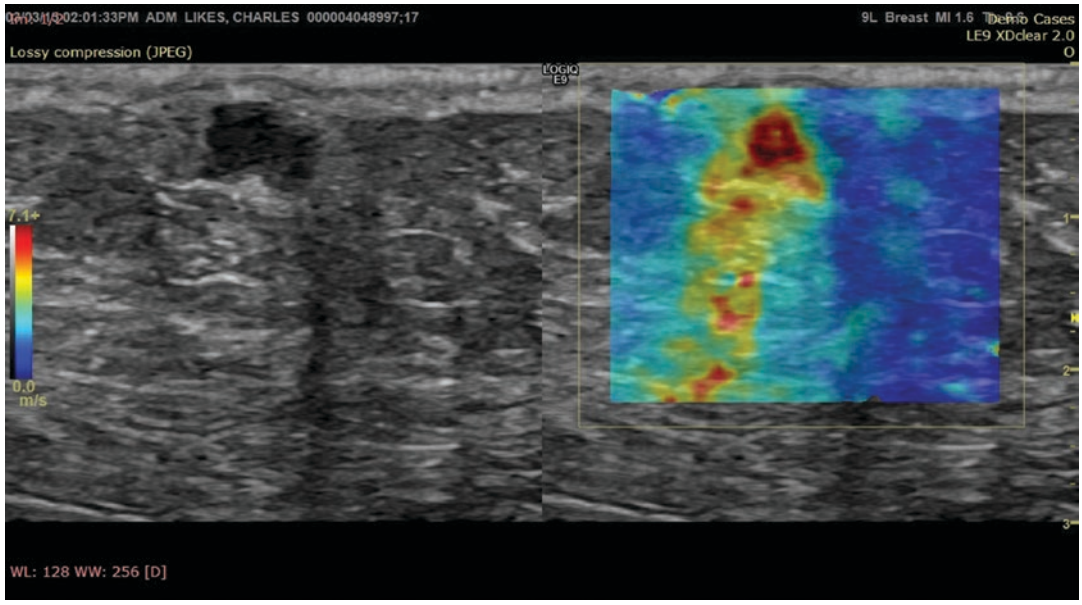

Fig. 5.23 Shear wave elastography of stiff lesion

5.8.2.2 Point Shear Wave Elastography

Point shear wave elastography (pSWE) can be described as a shear wave elastometry at a location in which acoustic radiation force is used to measure the speed of a generated shear wave. Shear wave speed spreads in a large region of interest by placing the ARFI and focus on multiple sequential locations and, at each, it detects the shear wave arrival time at multiple lateral locations. This process creates patches of small SWE images that may be mosaicked to create a large ROI 2D-SWE image [38] (Table 5.1).

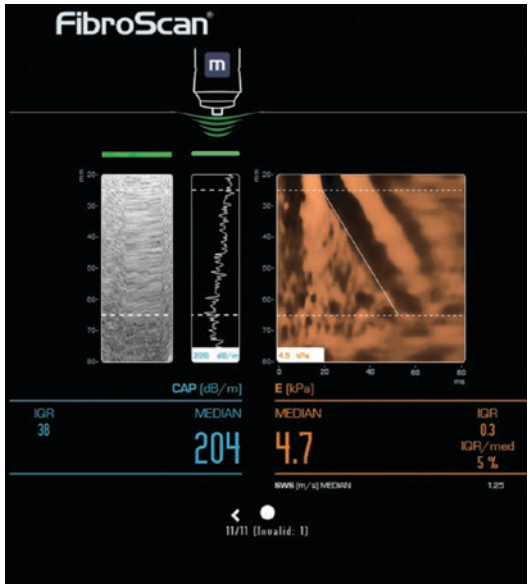

Fig. 5.24 Transient elastography

5.8.2.3 Multidimensional Shear Wave Elastography (2D-SWE and 3D-SWE)

Two-dimensional SWE generates a larger region of interest (ROI) by placing acoustic radiation force impulse foci at multiple sequential locations and acquiring shear wave arrival times at multiple lateral locations. Two-dimensional SWE can provide real-time imaging displayed in both gray scale and color (Fig. 5.25). SuperSonic shear imaging (SSI; SuperSonic Imagine, Aix-en-Provence, France) is the most validated 2D-SWE product for liver applications. SuperSonic shear imaging also has been applied to evaluations of focal breast masses, thyroid nodules, and cervical lymph nodes. Other 2D-SWE systems from different vendors are not widely validated because they have been only recently introduced [40] (Table 5.1).

Recently, usage of SWE is quite common in situations related to physiotherapy which has potential in both research and clinical settings. SWE clearly reveals stiffness changes related to muscle contraction, stretching, and manual therapy in musculoskeletal problems. In the field of biomechanics, SWE of muscle can be used to estimate muscle force during contraction and stretching [36, 41]. In sports, muscle elasticity is a critical determinant of muscle performance, therefore stiffness analysis of muscle could prevent injury and improve training and muscle performance. Consequently, in the field of physiotherapy, SWE may have a promising future in the detection and evaluation of soft tissues that are tender and abnormal to palpation [36].

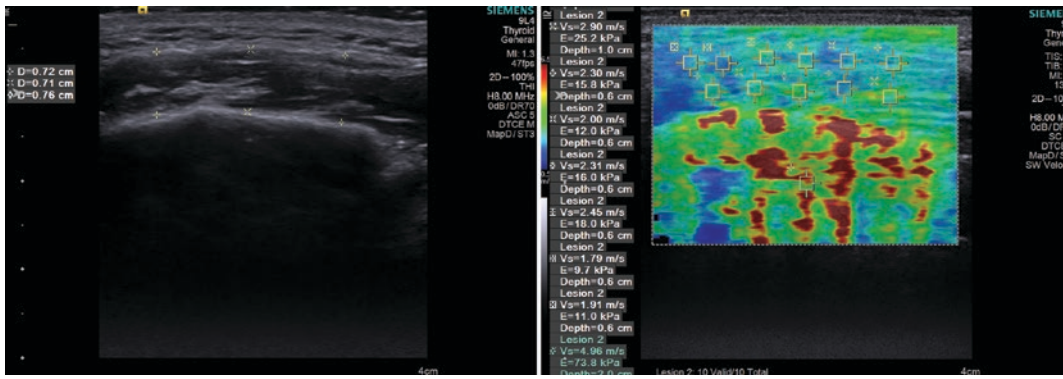

Fig. 5.25 Multidimensional shear wave elastography of masseter muscle

Fig. 5.26 Portable ultrasound system from GE Healthcare

5.9 Portable Ultrasound Systems

Portable ultrasound systems have been developed and available in clinical applications. Portable ultrasound devices have the potential to be a new generation stethoscope in medical departments [4, 17, 42–44]. Patients' anatomical structure can be viewed quickly and practically with a portable ultrasound imaging system. These devices are low cost and can work on laptops or personal computers. In addition, new generation portable ultrasound devices that can work with smartphones have taken their places in the market (Fig. 5.26). Little additional infrastructure is required for portable ultrasound application. This makes it valuable to use in rural areas, disasters, and emergencies. [4, 17, 42–45]

Acknowledgments The USG images in this chapter are courtesy of GE Healthcare, Turkey. The authors would like to thank Ms. Gozde Alpay for sharing the images.

References

1. Weng L, Tirumalai AP, Lowery CM, et al. US extended-field-of-view imaging technology. Radiology. 1997;203(3):877–80.
2. Shapiro RS. Panoramic ultrasound of the thyroid. Thyroid. 2003;13(2):177–81.
3. Rafii-Tari H, Abolmaesumi P, Rohling R. Panorama ultrasound for guiding epidural anesthesia: A feasibility study. In: International Conference on Information Processing in Computer-Assisted Interventions. Berlin: Springer; 2011. p. 179–89.
4. Powers J, Kremkau F. Medical ultrasound systems. Interface Focus. 2011;1(4):477–89.
5. O'Brien RT, Holmes SP. Recent advances in ultrasound technology. Clin Tech Small Anim Pract. 2007;22(3):93–103.
6. Kollmann C. New sonographic techniques for harmonic imaging--underlying physical principles. Eur J Radiol. 2007;64(2):164–72.
7. Uppal T. Tissue harmonic imaging. Australas J Ultrasound Med. 2010;13(2):29–31.
8. Hohl C, Schmidt T, Honnef D, Günther RW, Haage P. Ultrasonography of the pancreas. 2. Harmonic imaging. Abdom Imaging. 2007;32(2):150–60.
9. Abramowicz JS. Technical advances in ultrasound equipment. Clin Obstet Gynecol. 2003;46(4):839–49.
10. Gritzmann NE, Evans DH. New sonographic techniques and applications. Eur J Radiol. 2007;64(2):161–3.
11. Shapiro RS, Wagreich J, Parsons RB, Stancato-Pasik A, Yeh HC, Lao R. Tissue harmonic imaging sonography: evaluation of image quality compared with conventional sonography. AJR Am J Roentgenol. 1998;171(5):1203–6.
12. Shapiro RS, Stancato-Pasik A, Sims SE. Diagnostic value of tissue harmonic imaging compared with conventional sonography. Comput Biol Med. 2005;35(8):725–33.
13. Meuwly JY, Thiran JP, Gudinchet F. Application of adaptive image processing technique to real-time spatial compound ultrasound imaging improves image quality. Investig Radiol. 2003;38(5):257–62.
14. Entrekin RR, Porter BA, Sillesen HH, Wong AD, Cooperberg PL, Fix CH. Real-time spatial compound imaging: application to breast, vascular, and musculoskeletal ultrasound. Semin Ultrasound CT MR. 2001;22(1):50–64.
15. Wortsman XC, Holm EA, Wulf HC, Jemec GB. Real-time spatial compound ultrasound imaging of skin. Skin Res Technol. 2004;10(1):23–31.
16. Claudon M, Tranquart F, Evans DH, Lefèvre F, Correas M. Advances in ultrasound. Eur Radiol. 2002;12(1):7–18.
17. Gummadi S, Eisenbrey J, Li J, Li Z, Forsberg F, Lyshchik A, Lium JB. Advances in modern clinical ultrasound. Advanced Ultrasound in Diagnosis and Therapy. 2018;2(2):51–63.
18. Downey DB, Fenster A, Williams JC. Clinical utility of three-dimensional US. Radiographics. 2000;20(2):559–71.
19. Kwon SH, Gopal AS. 3D and 4D ultrasound: current Progress and future perspectives. Curr Cardiovasc Imaging Rep. 2017;10(12):43.
20. Gebhard RE, Eubanks TN, Meeks R. Three-dimensional ultrasound imaging. Curr Opin Anaesthesiol. 2015;28(5):583–7.

21. Wilson SR, Burns PN. Microbubble-enhanced US in body imaging: what role? Radiology. 2010;257(1):24–39.
22. Chong WK, Papadopoulou V, Dayton PA. Imaging with ultrasound contrast agents: current status and future. Abdom Radiol (NY). 2018;43(4):762–72.
23. Hunt D, Romero J. Contrast-enhanced ultrasound. Magn Reson Imaging Clin N Am. 2017;25(4):725–36.
24. Feinstein SB, Coll B, Staub D, et al. Contrast enhanced ultrasound imaging. J Nucl Cardiol. 2010;17(1):106–15.
25. Gong P, Song P, Chen S. Improved contrast-enhanced ultrasound imaging with multiplane-wave imaging. IEEE Trans Ultrason Ferroelectr Freq Control. 2018;65(2):178–87.
26. Yu D, Han Y, Chen T. Contrast-enhanced ultrasound for differentiation of benign and malignant thyroid lesions: meta-analysis. Otolaryngol Head Neck Surg. 2014;151(6):909–15.
27. Park GY, Kwon DR. Application of real-time sonoelastography in musculoskeletal diseases related to physical medicine and rehabilitation. Am J Phys Med Rehabil. 2011;90(11):875–86.
28. Drakonaki EE, Allen GM, Wilson DJ. Real-time ultrasound elastography of the normal Achilles tendon: reproducibility and pattern description. Clin Radiol. 2009;64(12):1196–202.
29. De Zordo T, Chhem R, Smekal V, et al. Real-time sonoelastography: findings in patients with symptomatic achilles tendons and comparison to healthy volunteers. Ultraschall Med. 2010;31(4):394–400.
30. Ozturk A, Grajo JR, Dhyani M, Anthony BW, Samir AE. Principles of ultrasound elastography. Abdom Radiol (NY). 2018;43(4):773–85.
31. Drakonaki EE, Allen GM, Wilson DJ. Ultrasound elastography for musculoskeletal applications. Br J Radiol. 2012;85(1019):1435–45.
32. Taljanovic MS, Gimber LH, Becker GW, et al. Shear-wave Elastography: basic physics and musculoskeletal applications. Radiographics. 2017;37(3):855–70.
33. Carlsen JF, Ewertsen C, Săftoiu A, Lönn L, Nielsen MB. Accuracy of visual scoring and semi-quantification of ultrasound strain elastography--a phantom study. PLoS One. 2014;9(2):e88699.
34. Ewertsen C, Carlsen JF, Christiansen IR, Jensen JA, Nielsen MB. Evaluation of healthy muscle tissue by strain and shear wave elastography - dependency on depth and ROI position in relation to underlying bone. Ultrasonics. 2016;71:127–33.
35. Eby SF, Song P, Chen S, Chen Q, Greenleaf JF, An KN. Validation of shear wave elastography in skeletal muscle. J Biomech. 2013;46(14):2381–7.
36. Creze M, Nordez A, Soubeyrand M, Rocher L, Maître X, Bellin MF. Shear wave sonoelastography of skeletal muscle: basic principles, biomechanical concepts, clinical applications, and future perspectives. Skelet Radiol. 2018;47(4):457–71.
37. Bercoff J, Tanter M, Fink M. Supersonic shear imaging: a new technique for soft tissue elasticity mapping. IEEE Trans Ultrason Ferroelectr Freq Control. 2004;51(4):396–409.
38. Dietrich CF, Bamber J, Berzigotti A, et al. EFSUMB Guidelines and Recommendations on the Clinical Use of Liver Ultrasound Elastography, Update 2017 (Long Version). EFSUMB-Leitlinien und Empfehlungen zur klinischen Anwendung der Leberelastographie, update 2017 (Langversion). Ultraschall Med. 2017;38(4):e48.
39. Klauser AS, Miyamoto H, Bellmann-Weiler R, Feuchtner GM, Wick MC, Jaschke WR. Sonoelastography: musculoskeletal applications. Radiology. 2014;272(3):622–33.
40. Hwang J, Yoon HM, Jung AY, Lee JS, Cho YA. Comparison of 2-dimensional shear wave Elastographic measurements using ElastQ imaging and SuperSonic shear imaging: phantom study and clinical pilot study. J Ultrasound Med. 2020;39(2):311–21.
41. Hug F, Tucker K, Gennisson JL, Tanter M, Nordez A. Elastography for muscle biomechanics: toward the estimation of individual muscle force. Exerc Sport Sci Rev. 2015;43(3):125–33.
42. Nelson BP, Sanghvi A. Out of hospital point of care ultrasound: current use models and future directions. Eur J Trauma Emerg Surg. 2016;42(2):139–50.
43. Gillman LM, Kirkpatrick AW. Portable bedside ultrasound: the visual stethoscope of the 21st century. Scand J Trauma Resusc Emerg Med. 2012;20:18.
44. Conlon TW, Nishisaki A, Singh Y, et al. Moving beyond the stethoscope: diagnostic point-of-care ultrasound in pediatric practice. Pediatrics. 2019;144(4):e20191402.
45. Wydo SM, Seamon MJ, Melanson SW, Thomas P, Bahner DP, Stawicki SP. Portable ultrasound in disaster triage: a focused review. Eur J Trauma Emerg Surg. 2016;42(2):151–9.

6 Sonographic Anatomy and Pathology: Cervical Lymph Nodes

Antigoni Delantoni and Apostolos Sarafopoulos

Contents

6.1 Introduction

Lymph nodes are small bean-shaped structures that constitute a major part of the body's immune system [1, 2]. Lymph nodes filter substances that travel through the lymph fluid, and contain lymphocytes (white blood cells) that help the body fight infection and disease. There are hundreds of lymph nodes found throughout the body [1, 3]. They are connected to one another by lymph vessels. Clusters of lymph nodes are found in the neck, axilla (underarm), chest, abdomen, and groin [1–4].

A. Delantoni (✉)
Department of Oral Surgery, Implant Surgery and Radiology, School of Dentistry, Faculty of Health Sciences, Aristotle University of Thessaloniki, Thessaloniki, Greece

A. Sarafopoulos
AHEPA General Hospital, Thessaloniki, Greece

6.1.1 Basic Anatomy

Normal lymph nodes are small anatomical oval or kidney-shaped structures with a size ranging from 0.1 to 2.5 cm in size. They are surrounded by a thick connective tissue capsule extending with diaphragms inside the lymph nodes covering multiple compartments [1, 3].

The parenchyma of the lymph nodes is distinguished in the cortical, subcortical, and medullary sections. Enclosed areas of the cortical section form the primary follicles containing a large number of B- and T lymphocytes, mononuclear, and macrophages. B lymphocytes produce antibodies, T lymphocytes destroy antigens, and macrophages perform phagocytosis [1, 3, 4].

A small opening in the middle of the glands creates an area rich in fibrous and fatty tissue designated as the hilum. The medullary section surrounds the hilum and is separated from the cortical section by insertion of the transitional

K. Orhan (ed.), *Ultrasonography in Dentomaxillofacial Diagnostics*,
https://doi.org/10.1007/978-3-030-62179-7_6

zone of the subcortex. The blood supplying artery enters through the hilum and the corresponding vein and the lymph nodes exit through it [1–4].

The accessory lymph nodes collect the lymph from the adjacent tissues and centrally discharge into the capsule of the lymph nodes. The transported lymph infiltrates the lymph nodes, which act as "refineries" of blood, destroying germs, viruses, cancer cells, and harmful foreign substances before eventually entering the venous circulation.

The lymph nodes are innervated by autonomic nervous system fibers and their innervation include the capsule, the inner diaphragms, and the smooth muscle of the blood vessels [1–4].

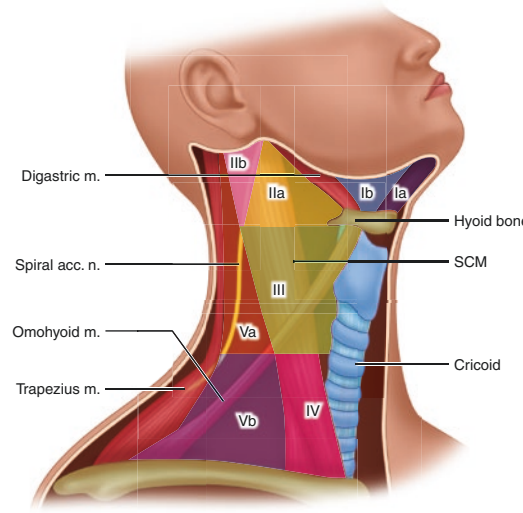

Fig. 6.1 Classification of the neck regions based on lymph node groups. Courtesy of Aikaterini Spanou

6.1.2 Regional and Functional Classification of Lymph Nodes

Based on the older and more recent historical data cervical lymph nodes are classified at least in six different anatomical levels (level I–VI) with different varying subclassifications aiming to the more accurate classification of the pathology, the more detailed surgical planning, and the better programming of the treatment of cervical and even head and neck cancer [5–7].

Figure 6.1 depicts a more current classification of the varying levels and anatomical borders that apply to daily clinical and radiographic treatments, which are analyzed in detail below.

The major lymph node groups of the head region are described together with their topographic location and the structures they drain [5–7].

So basically they are classified according to their drainage and the major divisions are:

- Facial: Skin and mucosa of the eyelids, the nose, the buccal area, the temporal and subtemporal region, and rinopharynx
- Parotid: Skin of the temporal and frontal region. The maxilla, the buccal area, the external acoustic meatus and eardrum, the eyelids, and section of the nose.
- Retroauricular: Side section of the hairy part of the skin behind the ear, the skin at the external acoustic meatus region, and the external ear
- Suboccipital: Posterior section of the hairy part of the head

Cervical lymph nodes are accepted as intermediary stations of the lymph drainage from the head and face lymph nodes groups. They also drain the soft tissues of the region and the organs that are present in the neck area [5, 8, 9]. The most important groups are:

- Submental: Lower lip, tongue tip, gums, and anterior teeth
- Submandibular: Upper and lower lip, intraoral mucosa, tongue, mandible gums, and teeth
- Jugulodigastric: Lingual and pharyngeal tonsils, hard palate, sections of the tongue
- Deep cervical: Larynx, trachea, thyroid gland, parathyroid glands, and upper esophagus
- Supraclavicular: Anterior thoracic wall, armpit region, shoulder, and upper limb
- Superficial cervical lymph nodes are lying on the surface of the sternocleidomastoid muscle, they drain the skin, and the superficial tissues and flow into the deep cervical lymph nodes.

When one is talking about varying levels of classifications, the most frequently followed divisions of the cervical lymph nodes are those

according to the American Academy of Otolaryngology which classifies them as follows:

Level I: Submental and submandibular nodes

- Level Ia: Submental, within the triangular boundary of the anterior belly digastric muscles and the hyoid bone.
- Level Ib: Submandibular triangle—within the boundaries of the anterior belly of the digastric muscle, the stylohyoid muscle, and the body of the mandible.

Level II: Upper jugular nodes (Subdigastric nodes)—around the upper third of the internal jugular vein and adjacent accessory nerve. The upper boundary is the base of the skull and the lower boundary is the inferior border of the hyoid bone. The anterior/medial boundary is the stylohyoid muscle and the posterior/lateral one is the posterior border of the sternocleidomastoid muscle. On imaging, the anterior/medial boundary is the vertical plane of the posterior surface of the submandibular gland.

- Level IIa: Anteriomedial to the vertical plane of the accessory nerve
- Level IIb: Posterolateral to this plane.

Level III: Middle jugular nodes—around the middle third of the internal jugular vein, from the inferior border of the hyoid to the inferior border of the cricoid cartilage. Anteromedially they are bounded by the lateral border of the sternohyoid muscle and posterolaterally by the posterior border of the sternocleidomastoid.

Level IV: Lower jugular nodes—around the lower third of the internal jugular vein from the inferior border of the cricoid to the clavicle, anteromedially by the lateral border of the sternohyoid and posterolaterally by the posterior border of the sternocleidomastoid.

Level V: Posterior triangle nodes—around the lower half of the spinal accessory nerve and the transverse cervical artery, and includes the supraclavicular nodes. The upper boundary is the apex formed by the convergence of the sternocleidomastoid and trapezius muscles, and inferiorly by the clavicle. The anteromedial border is the posterior border of the sternocleidomastoid and the posterolateral border is the anterior border of the trapezius.

- Level VA: Above the horizontal plane formed by the inferior border of the anterior cricoid arch, including the spinal accessory nodes.
- Level VB: Lymph nodes below this plane, including the transverse cervical nodes and supraclavicular nodes (except Virchow's node which is in IV).

Level VI: Anterior compartment nodes—Pretracheal, paratracheal, precricoid (Delphian), and perithyroid nodes, including those on the recurrent laryngeal nerve. The upper border is the hyoid, the lower the suprasternal notch, and the lateral borders the common carotid arteries

The American Joint Committee on Cancer (AJCC) system differs from the above by including Level VII, which is based on the 2002 American Academy system, although the boundaries are defined slightly different [5]

The boundaries are defined as (Superior, Inferior, Anteromedial, Posterolateral)

- Level IA: Symphysis of mandible, Body of hyoid, Anterior belly of the contralateral digastric muscle, Anterior belly of ipsilateral digastric muscle
- Level IB: Body of mandible, Posterior belly of digastric muscle, Anterior belly of digastric muscle, Stylohyoid muscle
- Level IIA: Skull base, Horizontal plane defined by the inferior border of the hyoid bone, The stylohyoid muscle, Vertical plane defined by the spinal accessory nerve
- Level IIB: Skull base, Horizontal plane defined by the inferior body of the hyoid bone, Vertical plane defined by the spinal accessory nerve, Lateral border of the sternocleidomastoid muscle
- Level III: Horizontal plane defined by the inferior body of hyoid, Horizontal plane defined by the inferior border of the cricoid cartilage, Lateral border of the sternohyoid

muscle, Lateral border of the sternocleidomastoid or sensory branches of cervical plexus
- Level IV: Horizontal plane defined by the inferior border of the cricoid cartilage, Clavicle, Lateral border of the sternohyoid muscle, Lateral border of the sternocleidomastoid, or sensory branches of cervical plexus
- Level VA: Apex of the convergence of the sternocleidomastoid and trapezius muscles, Horizontal plane defined by the lower border of the cricoid cartilage, Posterior border of the sternocleidomastoid muscle or sensory branches of cervical plexus, Anterior border of the trapezius muscle
- Level VB: Horizontal plane defined by the lower border of the cricoid cartilage, Clavicle, Posterior border of the sternocleidomastoid muscle, Anterior border of the trapezius muscle
- Level VI: Hyoid bone, Suprasternal notch, Common carotid artery
- Level VII: Suprasternal notch, Innominate artery, Sternum, Trachea, esophagus, and prevertebral fascia

6.2 Cervical Lymph Nodes Pathology

6.2.1 Pathological Swelling of Lymph Nodes Criteria

Normal lymph nodes in healthy individuals are rarely palpable. When they are palpable, they present as small nodular structures that give the impression of sliding at the examiner's fingers. When they are compressed clinically, they give the impression of tension and mild pain [4, 9]. The clinical features of lymph nodes swellings and the type of disease they usually accompany are seen in Table 6.1

Ultrasonographically, normal and reactive lymph nodes are usually found in submandibular, parotid, upper cervical, and posterior triangle regions. On gray-scale sonography, normal and reactive nodes tend to be hypoechoic compared to adjacent muscles, and oval in shape, except for submandibular and parotid nodes, which are usually more rounded. Figure 6.2 depicts a normal cervical lymph node.

Lymph nodes swellings in the head and neck region are usually identified by the patients. The patients usually refer to doctors, for a palpable swelling, painful or not.

The basic clinical characteristics of the pathological swelling of lymph nodes are the following:

- Localized swelling of the soft tissues upon palpation, and in a few cases alterations on the skin color of the area involved in the pathology.
- Single palpable nodule, or multiple in a row, nodules, resembling a pearl necklace. Usually, they are found at the lateral neck borders, with a head-to-tail direction
- Larger and occasionally lobular mass in the event of convergence of multiple nodules, or a nodular group, resulting in the creation of multiple nodules palpable section is often referred to as "block" of lymph nodes.
- Elastic in texture nodes, with free mobility, and sensitivity upon palpation, that often is benign reactive lymph nodes.
- Hard and uncompressed nodules, that present as hard and firm attached often to the regional soft tissues, and the adjacent tissues nodules, without apparent mobility, and painless upon palpation are in the majority of cases malignant in origin.

The major causes of cervical lymph nodes swellings are seen in Table 6.2.

Table 6.1 Lymph nodes clinical characteristics and features according to types of pathology they accompany

Characteristics	Malignant nodes	Benign nodes
Size	>2 cm	<1–2 cm
Texture	Hard, elastic	Soft
Presence (time)	>2 weeks	<2 weeks
Mobility	No	Yes
Adjacent tissues	Attached	Non attached

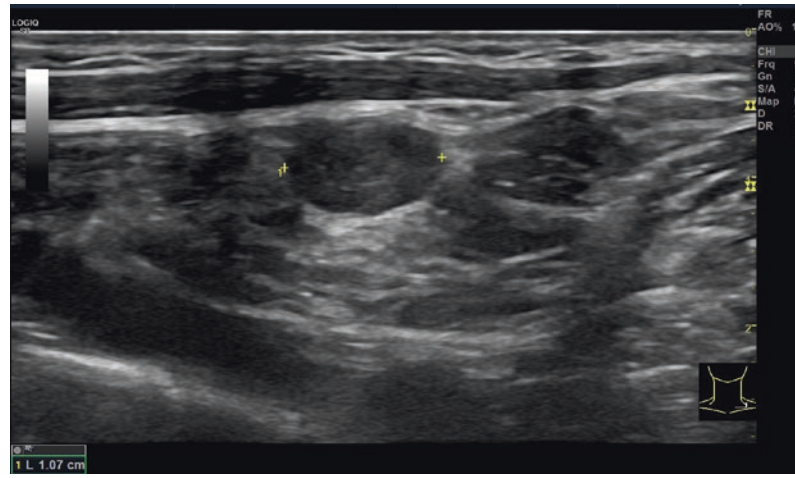

Fig. 6.2 Typical appearance of lymph node, without inflammation, oval shape, and a hilum

Table 6.2 Etiology of lymph nodes neck swelling

Inflammatory causes
Bacterial infections: Streptococcal, staphylococcal, Koch bacilli, etc.
Viruses: Mononucleosis, rhinoviruses, flu, measles, herpes simple type I
Fungal: Candida, Moniliasis
Neoplasma
Primary: Hodgkin and non-Hodgkin lymphomas
Metastatic: Carcinomas of the neck, the upper aerodigestive tract, the thyroid, and salivary glands
Immunological causes
Autoimmune conditions thyroiditis, Behcet syndrome
Immunodeficiency

6.2.2 Ultrasonographic Criteria of Lymph Nodes Pathology

Ultrasonographic control of the head and neck with modern high-frequency probes undoubtedly provides "vivid" high-definition images and offers safer criteria in distinguishing physiological and pathological lymph nodes.

Normal lymph nodes usually have elongated morphology and size not exceeding 1 cm; while, a hypoechoic halo corresponding to the cortex surrounds the ultrasound section of the entry and the medullary complex.

The ultrasonographic findings that characterize swollen and pathological lymph nodes are mentioned [10–12].

In the majority of inflammatory reactive lymph nodes, they appear more rounded and elongated but have a characteristic in many cases halo around them. Benign reactive nodes tend to preserve this shape due to diffuse nodal involvement by pathogens, resulting in diffuse lymphoid proliferation and subsequent cortical widening, while preserving the overall normal shape of the node. Whwn of benignorigin the nodes have been found to have a long-axis diameter at least 2 times the short axis diameter, with a shape index of less than 0.5, corresponding to an oval shape. Typically inflamed lymph nodes are seen and described in Figs. 6.3, 6.4 and 6.5.

The type of inflammation and causes are clearly seen in Table 6.3.

In combination with the patients' history, clinical image, and blood test results, they can be evaluated in the direction of differential diagnosis [13–15]:

- Increase in the size of the lymph nodes with a diameter greater than 1 cm. Regarding the jugulodigastric lymph node, the diameter should not exceed 1.5 cm. the size of a lymph node in the neck may be used for their classification, but this is not without problems due to their anatomical shape (oval/ellipsoid), the node should always be measured in all three planes. A moderate increase in size without alteration of the shape and echo structure of a lymph node is usually due to reactive overfunction.
- "Rounding" of lymph nodes with loss of their normal elongated morphology due to inflam-

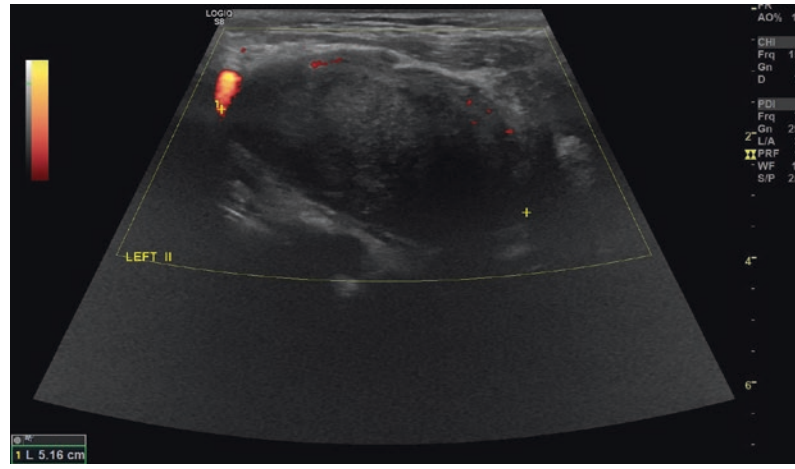

Fig. 6.3 A large lymph node due to inflammation. The node is with ellongated shape and normal texture

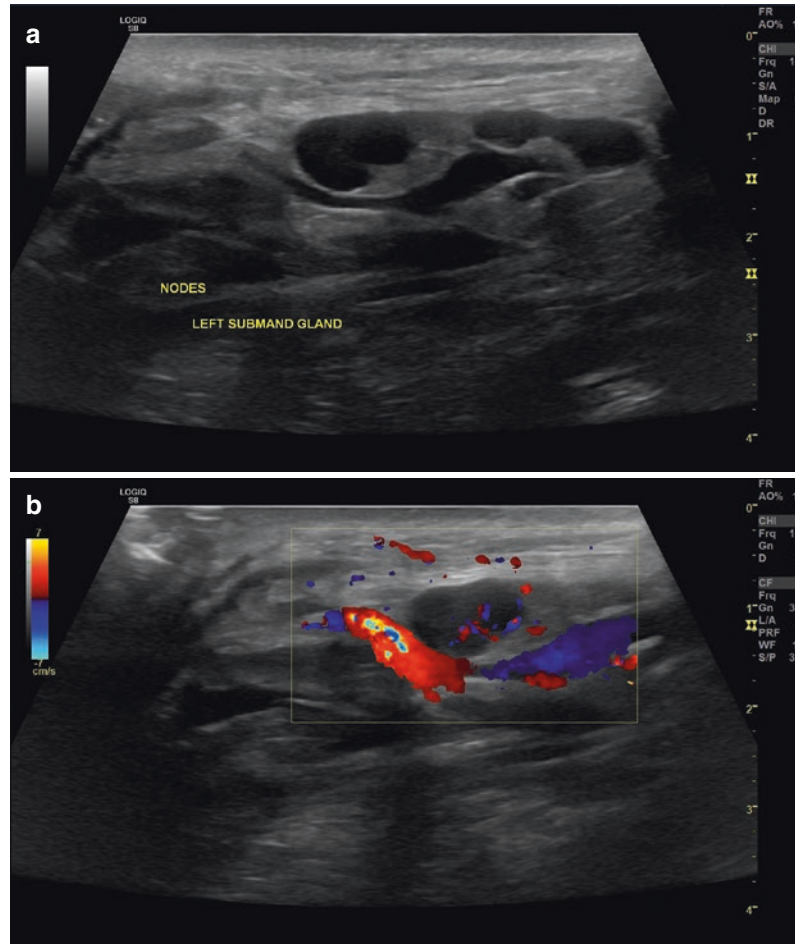

Fig. 6.4 A typically inflamed lymph node. block. Characteristic in the neck region and frequently presenting upon clinical examination. Here is a characteristic appearance with inflammatory response due to infectious mononucleosis

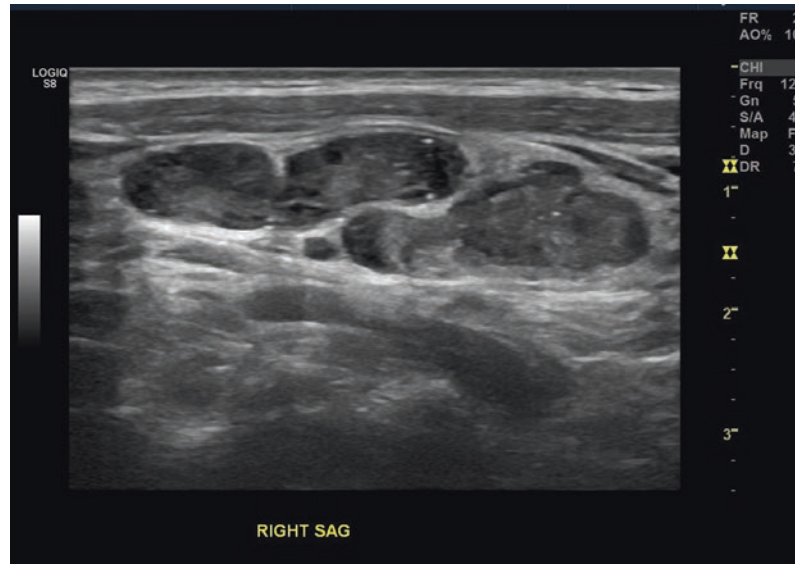

Fig. 6.5 Inflamed reactive lymph nodes of the submandibular region in patient with a tender, painful and palpable lump. The use of Power and Pulse Wave Doppler demonstrates abnormally enlarged nodes with increased vascularity and benign Resistance Index below 0,72

Table 6.3 Ultrasonographic features of nodes based on pathology

inflammatory nodes	• Varying in size, long to short axis ratio ≥2 • Clearly visible lymph node gate
metastatic nodes	• Varying in size, long to short axis ratio <2 • No clear gate imaged, varying vascularity
Primary lymphoma	• Varying in size, long to short axis ratio usually ≤2 • no clear gate imaged,varying echoigenicity, increased vascularity

matory filtration of their parenchyma or an increase in the cell population. The typical rounding of lymph nodes is frequently present in tumor cases as a reactive response initially and as a tumor course directive after. Figure 6.6 shows an extremely enlarged rounded node in the neck of a laryngeal tumor case. Measurable size refers to the reduction of the ratio of diameters of the long-to-short axis below the limit of two (long/short <2/ Solbiati index). Submental lymph nodes are an exception together with most groups of head lymph nodes since they normally exhibit rounded morphology [13, 15] In this rule there are a few exceptions providing a potential pitfall as found in the setting of benign submandibular and parotid nodes, which are often normally round in shape; likewise, tuberculous node

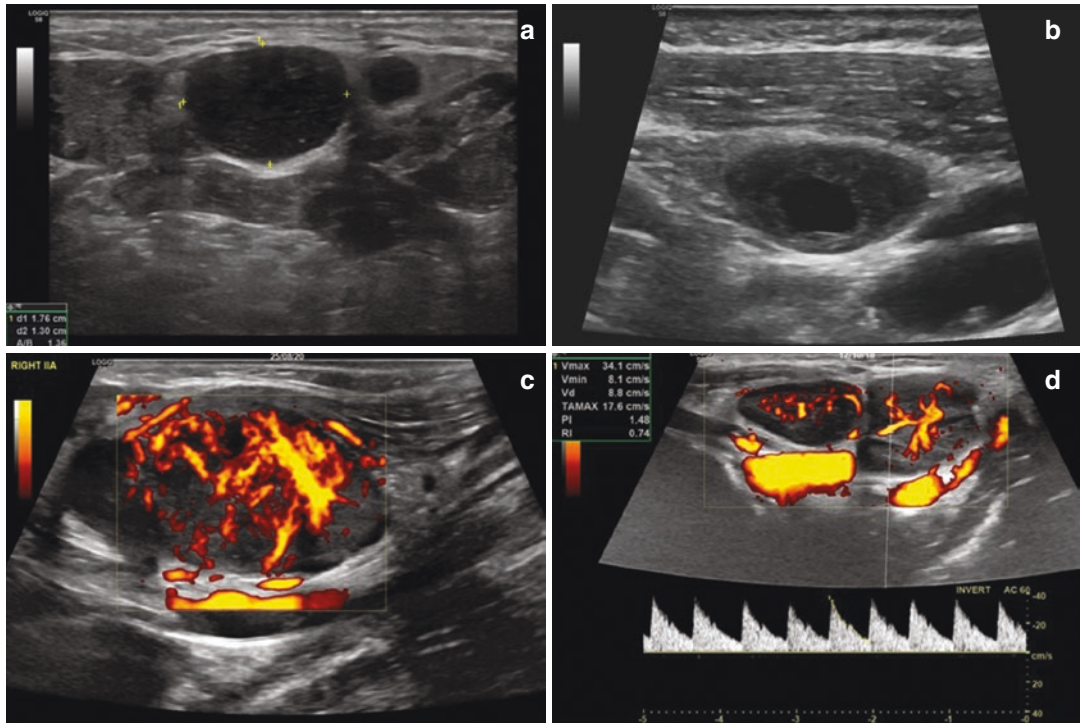

Fig. 6.6 Examples of malignant cervical lymph nodes (**a**) Rounded node with lack of the fatty hilum (**b**) lymph node with anechoic central necrotic like area. (**c**) enlarged node with diffusely increase in the vascularity in the entire parenchymal area (**d**) Acute wave forms with pathological Doppler coloring (Resistance Index >0,72 and Pulsatility Index >1,3)

involvement also tends to be round in shape. Therefore the anatomical and pathological exceptions to the index should be noted.

- In neoplastic lymph nodes, a progressive reduction in size up to and/or even including complete elimination of the nodal hilum is diagnosed due to the replacement of fibroadipose tissue by malignant cells. It is a very important finding, characterized by high sensitivity and low specificity. They typically present with the abovementioned imaging characteristic in lymphoma cases as seen in Fig. 6.7. Similar ultrasonographic images may be observed in benign lymph nodes swellings and in various types of infections such as tuberculosis [10–12].
- Absence of the hyperechoic central structure in the hilar region may be considered as a sign of malignancy (absence of hilar sign).
- Reduction of the echogenicity of lymph nodes and disturbance of their texture in the presence of single or multiple subechoic regions, representing areas of necrosis, melting, or abscesses [19, 20].
- Increased blood perfusion in color Doppler with multiple vascular branches spanning the entire parenchyma, including the periphery of the lymph nodes. In normal and reactive lymph nodes one can depict the nourishing artery and the accompanying vein with small branches that are confined to the area of the node gate and not beyond it [16–18].

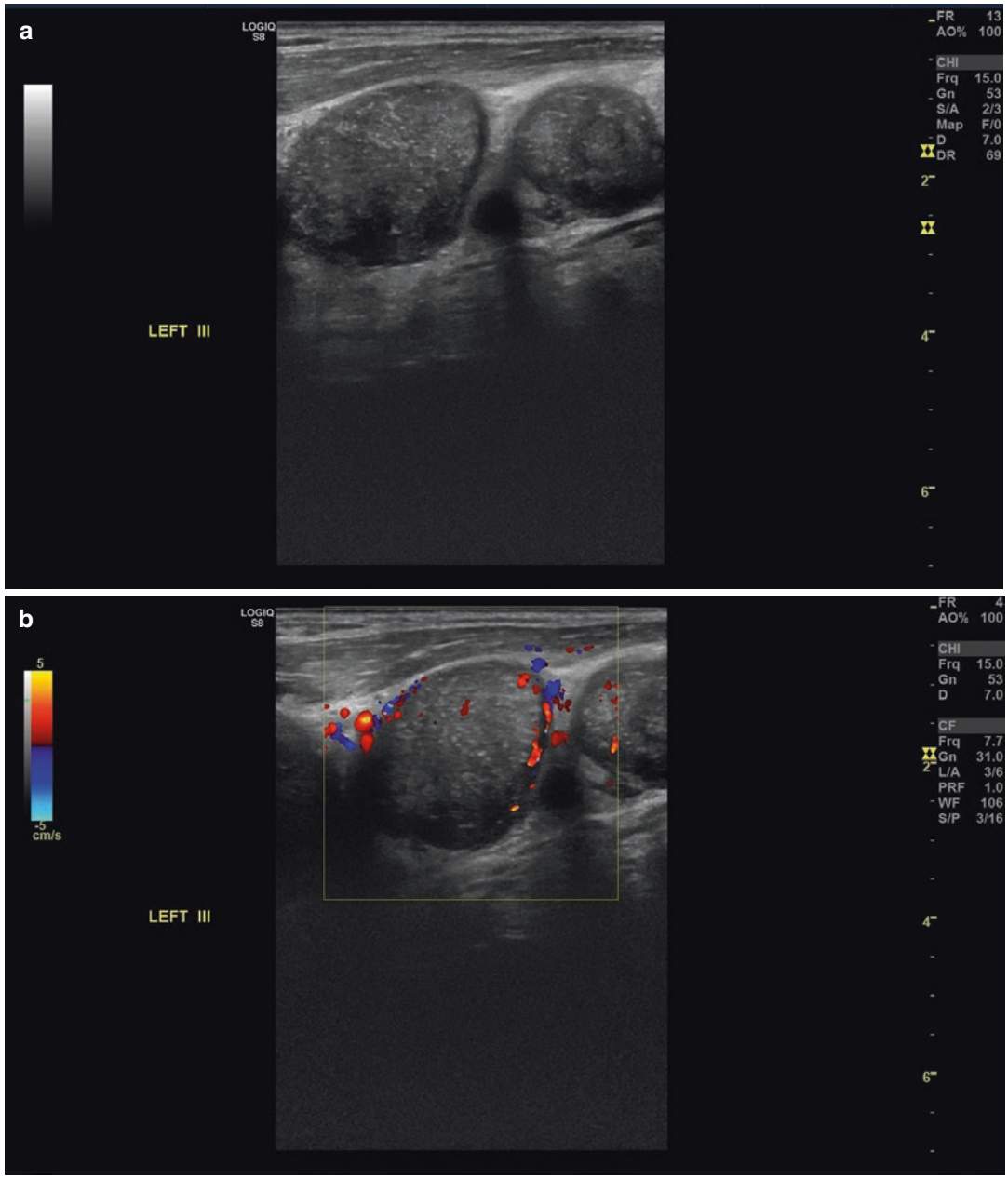

Fig. 6.7 (**a**) Case of a Hodgkin lymphoma with multiple hypoechoic and round shaped nodes. Infiltration of the adjacent fatty tissue is present. (**b**) Same case with peripheral vascularity with the use of color Doppler

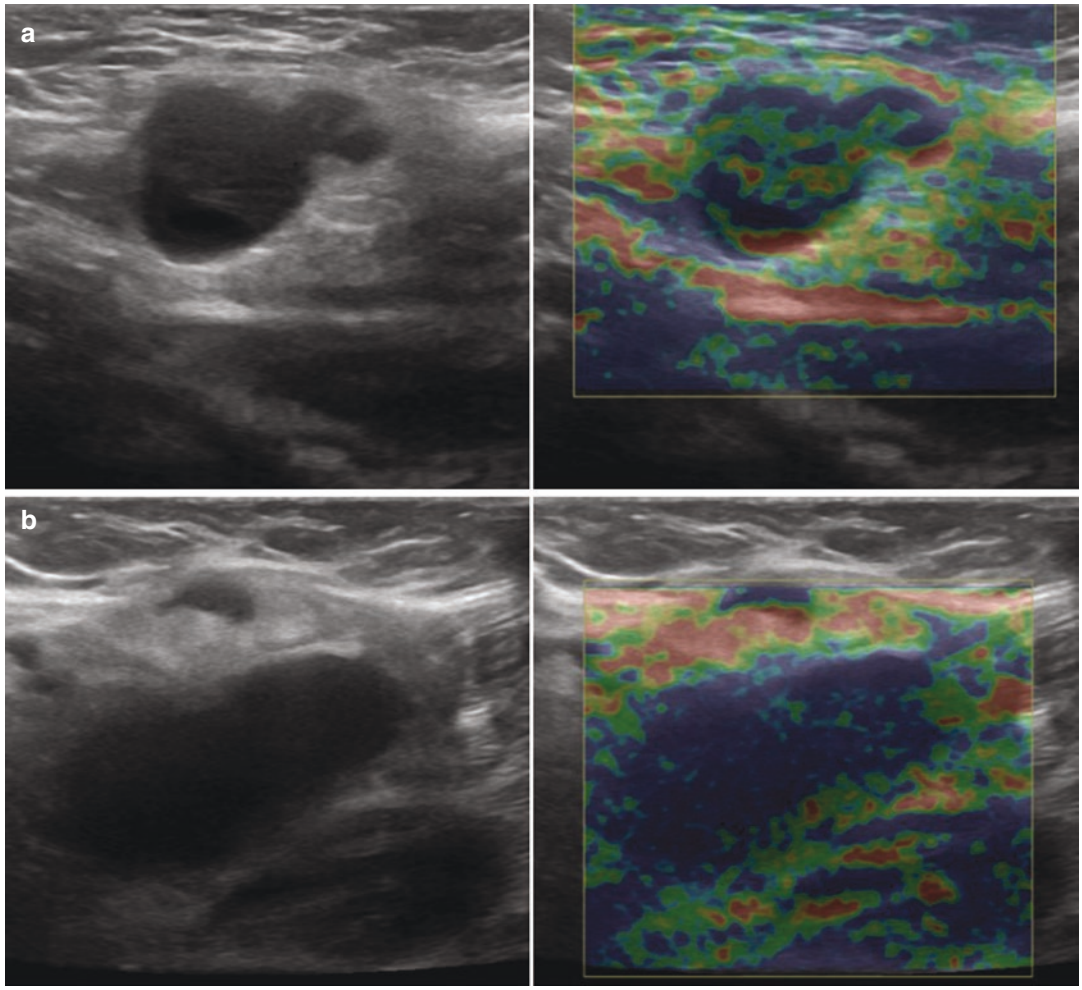

Fig. 6.8 In strain elastography the dark blue color indicates areas of reduced compression of the tissues and the green or red color indicate regions of high elasticity. (**a**) Lymph node with benigh elastographic features and (**b**) Pathological lymph node

- Increase in the resistance index RI bigger than 0.72 and the pulsativity index PI more than 1.3 during examination with the use of Color Doppler. The finding is due to increment of the resistances in the blood circulation caused by the compression of the arteries to the interior of the pathological mostly lymph nodes, and mainly the neoplasmatic ones [19–22].
- High index of rigidity of the pathological lymph nodes, in strain elastography and high units of pressure with the application of shear wave elastography (Fig. 6.8).

Basically, one should always bear in mind the Solbiati index or long-to-short axis ratio which represents the morphology of the nodes and their shape in two dimensions. This index has a cutoff value of 1.5–2 while a node with an index over 2 is highly suspicious for malignancy [15, 21]. Besides the shape and the short to long axis ratio, there are a few other factors one should consider to determine the type of node. These are the presence or absence of the hilum (present in benign lesions), the border type which is irregular in malignant nodes, and thevascularity, since

it has been reported that the use of the vascular pattern in assessing lymph nodes results in a high sensitivity (83%–89%) and specificity (87%–98%) in differentiating malignant from benign nodes [23].

References

1. Susan S. Lymphoid tissues. In: Gray's anatomy: the anatomical basis of clinical practice (41st ed.), vol. 2016. Philadelphia. p. 73–4.
2. Mukherji SK, Londy G, Frank J. A Simplified Approach to the Lymph Nodes of the Neck. Neurographics. 2002;(2)
3. Rouvière H. Anatomie des lymphatiques de l'homme [anatomy of the human lymphatic system, Edwards brothers, Ann Arbor, MI. 1938]. Trans. Morris Jacob Tobias. Paris: Masson; 1932.
4. Willard-Mack CL. Normal structure, function, and histology of lymph nodes. Toxicol Pathol. 2016;34(5):409–24.
5. Som PM, Curtin HD, Mancuso AA. An imaging-based classification for the cervical nodes designed as an adjunct to recent clinically based nodal classifications. Arch Otolaryngol Head Neck Surg. 1999;125(4):388–96.
6. Robbins KT, Medina JE, Wolfe GT, Levine PA, Sessions RB, Pruet CW. Standardizing neck dissection terminology: official report of the Academy's Committee for Head and Neck Surgery and oncology. Arch Otolaryngol Head Neck Surg. 1991;117(6):601–5.
7. Robbins KT, Clayman G, Levine PA, Medina J, Sessions R, Shaha A, Som P, Wolf GT. Neck Dissection Classification Update. Arch Otolaryngol Head Neck Surg. 2002;128(7):751.
8. Young B, O'Dowd G, Woodford P. Wheater's functional histology: a text and colour atlas. 6th ed. Philadelphia: Elsevier; 2013. p. 209–10.
9. Dupont G, Schmidt C, Yilmaz E, Oskouian RJ, Macchi V, de Caro R, Tubbs RS. Our current understanding of the lymphatics of the brain and spinal cord. Clin Anat. 2019;32(1):117–21.
10. Amin MB, Edge SB, Greene FL. AJCC Cancer Staging Manual (Eighth ed.): Springer International Publishing; 2018. ISBN 978-3-319-40617-6
11. Grégoire V, Ang KA. Delineation of the neck node levels for head and neck tumors: a 2013 update. DAHANCA, EORTC, HKNPCSG, NCIC CTG, NCRI, RTOG, TROG consensus guidelines. Radiother Oncol. 2014;110(1):172–81.
12. Edge S, Byrd DR, Compton CC. AJCC Cancer Staging Handbook: From the AJCC Cancer Staging Manual (PDF) (Seventh ed.). New York: Springer; 2011. ISBN 978-0-387-88442-4
13. Eisenmenger LB, Wiggins RH. Imaging of head and neck lymph nodes. Radiol Clin N Am. 2015;53(1):115–32.
14. Chong V. Cervical lymphadenopathy: what radiologists need to know. Cancer Imaging. 2004;4(2):116–20.
15. Chen C-C, Lin J-C, Chen K-W. Lymph node ratio as a prognostic factor in head and neck cancer patients. Radiat Oncol. 2015;10(1)
16. Ishii J, Nagasawa H, Wadamori T, Yamashiro M, Ishikawa H, Yamada T. Ultrasonography in the diagnosis of palatal tumors. Oral Surg Oral Med Oral Pathol Oral Radiol Endod. 1999;87:39–43.
17. Katakai T, Hara T, Lee JH, Gonda H, Sugai M, Shimizu A. A novel reticular stromal structure in lymph node cortex: an immuno-platform for interactions among dendritic cells, T cells and B cells. Int Immunol. 2004;16(8):1133–42.
18. Schulze RK, Curic D, d'Hoedt B. B-mode versus A-mode ultrasonographic measurements of mucosal thickness in vivo. Oral Surg Oral Med Oral Pathol Oral Radiol Endod. 2002;93:110–7.
19. Park CH, Song CM, Ji YB, Pyo JY, Yi KJ, Song YS, Park YW, Tae K. Significance of the Extracapsular Spread of Metastatic Lymph Nodes in Papillary Thyroid Carcinoma. Clin Exp Otorhinolaryngol. 2015;8(3):289–94.
20. Songra AK, Ng SY, Farthing P, Hutchison IL, Bradley PF. Observation of tumour thickness and resection margin at surgical excision of primary oral squamous cell carcinoma–assessment by ultrasound. Int J Oral Maxillofac Surg. 2006;35:324–31.
21. van den Brekel MW, Castelijns JA, Snow GB. The size of lymph nodes in the neck on sonograms as a radiologic criterion for metastasis: how reliable is it? AJNR Am J Neuroradiol. 1998;19(4):695–700.
22. Yuen AP, Ng RW, Lam PK, Ho A. Preoperative measurement of tumor thickness of oral tongue carcinoma with intraoral ultrasonography. Head Neck. 2008;30:230–4.
23. Ahuja A, Ying M, Sonography of neck lymph nodes. Part II: abnormal lymph nodes. Clin Radiol. 2003;58(5):259–66.

Sonographic Anatomy and Pathology Extracranial Nerves

7

Antigoni Delantoni and Apostolos Sarafopoulos

Contents

7.1 General Sonographic Anatomy

The extracranial nerves are only partly available by ultrasonography. The cervical part of the vagal nerve is the only part of the cranial nerves that can be easily identified between the carotid arteries and the internal jugular vein [1].

The vagal nerve exits from the skull base along the lateral wall of the internal carotid artery. The division of the common carotid artery is the landmark after which it runs between the internal jugular vein and the common carotid artery.

A. Delantoni (✉)
Department of Oral Surgery, Implant Surgery and Radiology, School of Dentistry, Faculty of Health Sciences, Aristotle University of Thessaloniki, Thessaloniki, Greece

A. Sarafopoulos
AHEPA General Hospital, Thessaloniki, Greece

The brachial plexus can be seen in level V though it is seldom readily visible by US. It is located laterally to the anterior scalene muscle and often appears as hypoechoic oval structures when displayed obliquely.

Besides the vagus nerve, there are no specific anatomical landmarks for the other cranial nerves, such as the hypoglossal, the accessory, and the facial nerve [2–4].

7.2 Inflammatory Changes

The most common clinical picture of inflammatory changes is the presence of carotidynia, a painful syndrome with pain and tenderness over the carotid areas [5, 6].

Though the condition is doubted by some, the application of ultrasound shows hypoechoic thickening of the wall especially at the bulb level. (Figs. 7.1, 7.2 and 7.3).

K. Orhan (ed.), *Ultrasonography in Dentomaxillofacial Diagnostics*,
https://doi.org/10.1007/978-3-030-62179-7_7

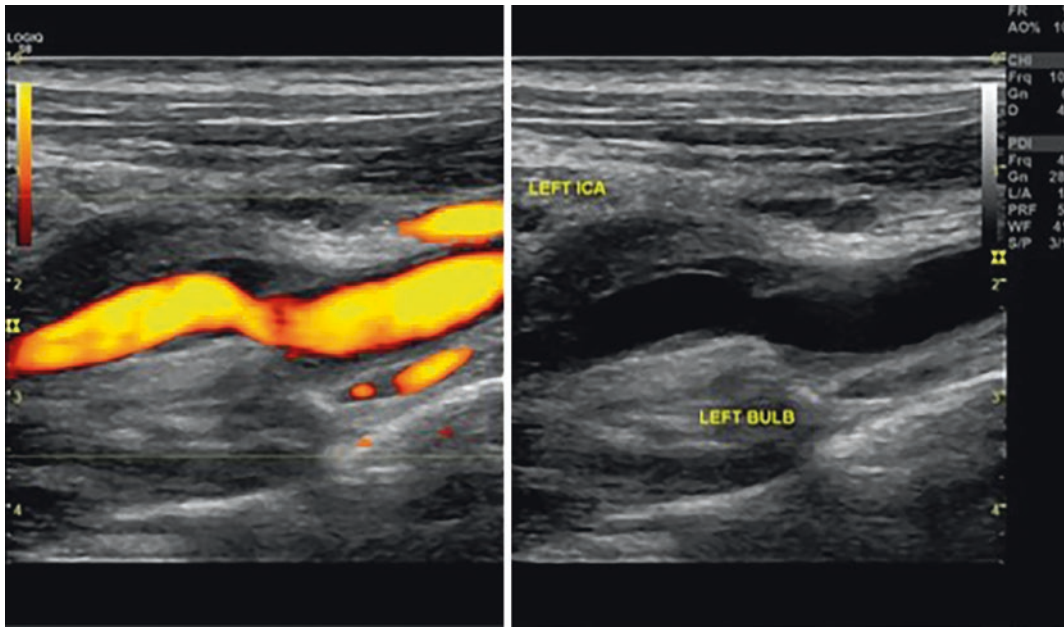

Fig. 7.1 Carotidynia where there are flow disturbances in the section of the carotid that has the problem

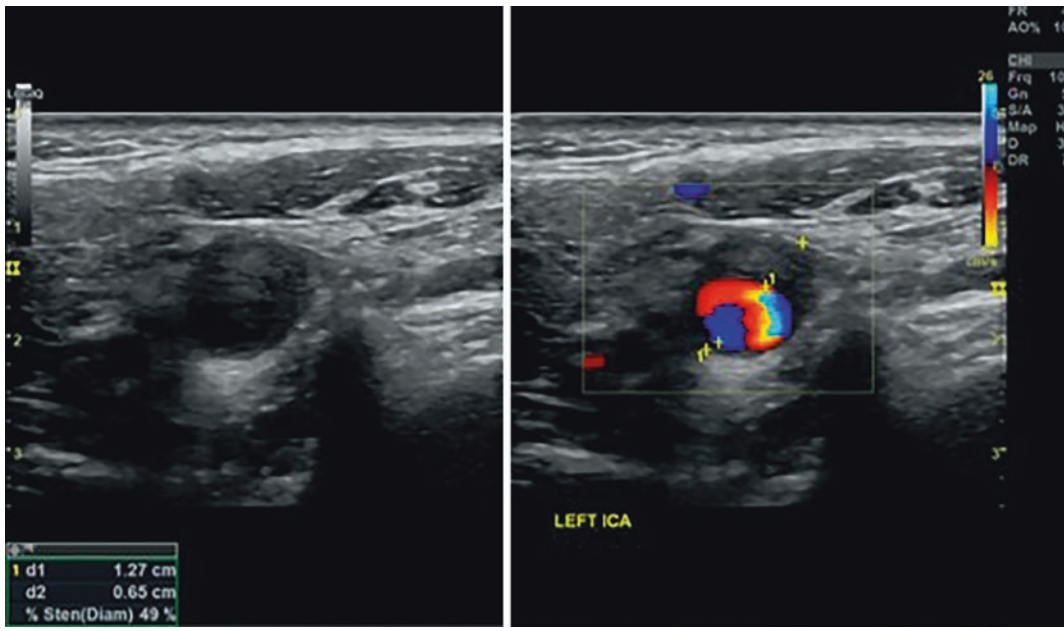

Fig. 7.2 Carotidynia where there are flow disturbances in the section of the carotid that has the problem as seen with the use of color Doppler

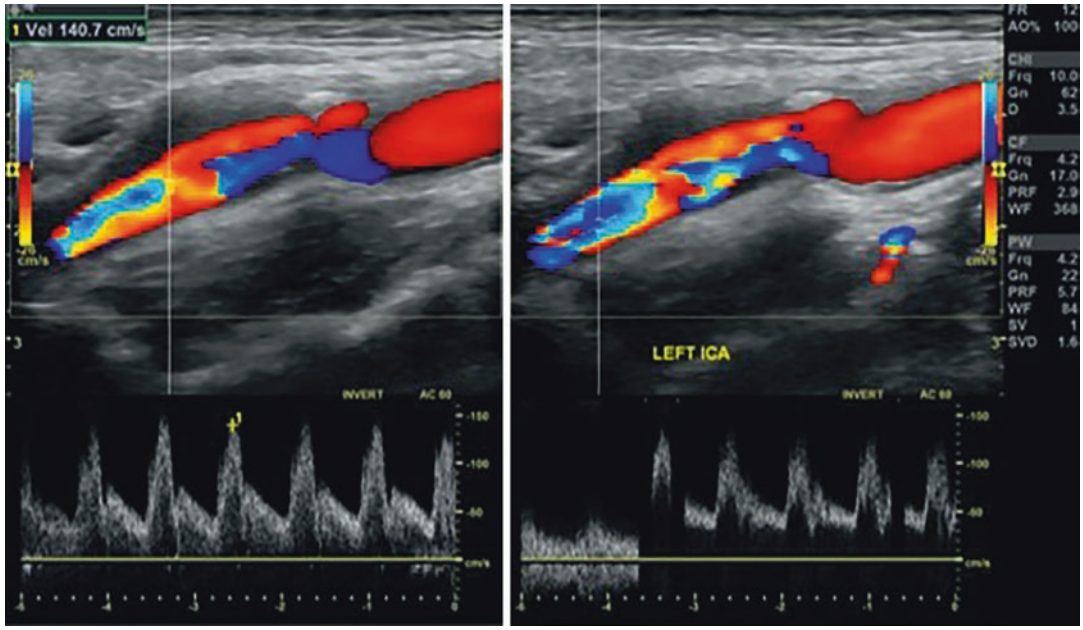

Fig. 7.3 Carotidynia where there are flow disturbances in the section of the carotid that has the problem with the use of color Doppler parallel to the course of the artery

7.3 Benign Tumors

7.3.1 Paragangliomas

Paragangliomas of the autonomous system are rare neuroendocrine tumors that occur due to glomus body hyperplasia or hamartomatous development, and they appear to originate from modified smooth muscle cells [7, 8]. They have a female prevalence of about 3:1 and mainly present in middle-aged people [9, 10]. The initial clinical presentations are insidious even in cases when the tumors reach a large size. Accurate and comprehensive imaging evaluation is the key to their diagnosis. Because they are located in the skull base and are not readily viewed by ultrasound, it is most commonly found by other imaging techniques. The preoperative diagnosis of glomus tumors remains challenging. Inaccurate diagnoses are largely attributed to this tumor's rarity and the lack of distinguishing clinicomorphologic characteristics [11, 12].

Furthermore, such lesions have heterogeneous appearances on radiologic images. A glomus tumor may initially be diagnosed as a salivary tumor, sebaceous cyst, neurofibromatosis, dermoid cyst, developmental tumor, vascular malformation, or another type of mesenchymal neoplasm. Although vascular malformations and cystic soft tissue lesions can usually be ruled out using color doppler ultrasonography, the differential diagnosis of solid tumors remains challenging. Recently, fluorodopa (F-DOPA) positron emission tomography was used for detecting glomus tumors [12, 13]; however, the validity and specificity of this technique for tumors in the head and neck region requires verification. As formal diagnostic guidelines are absent, a thorough radiographic set of examinations and studies may be needed to set the diagnosis but histologic examination and immunohistochemical analysis remain the gold standards [14, 15].

The majority of GT of the neck are most frequently occurring at the carotid bulb and the

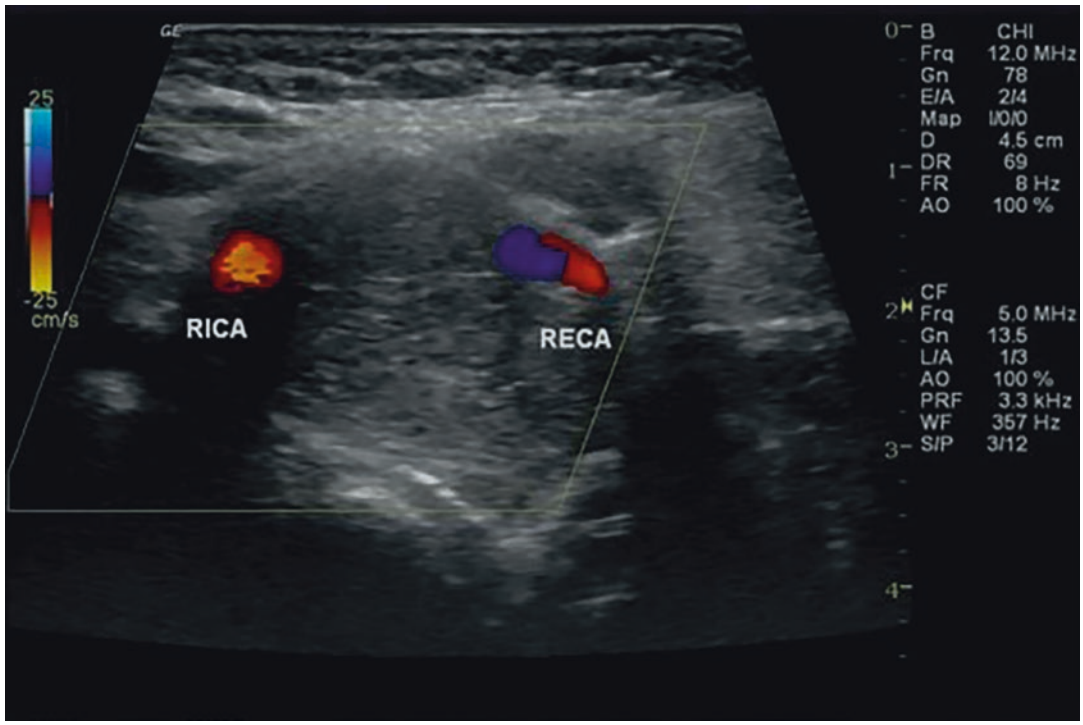

Fig. 7.4 Glomus tumor of the bulb at the level of carotid bulb and the bifurcation area vertical to the arterial flow demonstrating with the use of color Doppler disturances in the arterial flow of the involved artery. Also alterations in the distance of the arterries is prominent

bifurcation area (Figs. 7.4, 7.5 and 7.6) while they are more rare at the level of the vagal ganglion(Figs. 7.7, 7.8 and 7.9). They are most frequent in female patients and in 25% of the cases they are multilocular location [16–18].

In case of carotid bulb paraganglioma, the tumor presents as a pulsating painless swelling at the angle of the mandible, while in the cases of ganglion location they usually present with neuralgic symptoms. A large number of tumors may present with no symptoms at all and appear as incidental findings on US examinations [8, 9].

Color Doppler is an easy, readily available technique that can locate, isolate, and to a certain degree set the diagnosis of neck paragangliomas. The vasculature level of the tumor with Triplex in combination with more detailed imaging techniques such as MRI and MRA set and compose the additional steps to a final definite diagnosis [16, 17, 19].

7.3.2 Neuromas

Though the lesions are very rare they include two types of conditions; neurofibromas and schwannomas [12, 14]. Basically, they are covered under nerve sheath tumors and their subclassification is somewhat confusing. Schwannomas have been termed as neurilemmomas, neuromas, neurinomas, and peripheral fibroblastomas (Fig. 7.10). Additionally, some have applied the term to include both neurilemmomas and neurofibromas, while others include the term schwannoma and neuroma in discussion of neurilemmomas (Fig. 7.10).

Neuromas represent an exaggerated repair response to neuronal injury in which a tangle of regenerative axons, fibrous tissue, and Schwann cells form at the site of a severed nerve.

Neurofibromas are benign peripheral nerve sheath tumors usually solitary and rare; however, there is a strong association with neurofibromatosis type 1 (NF1).

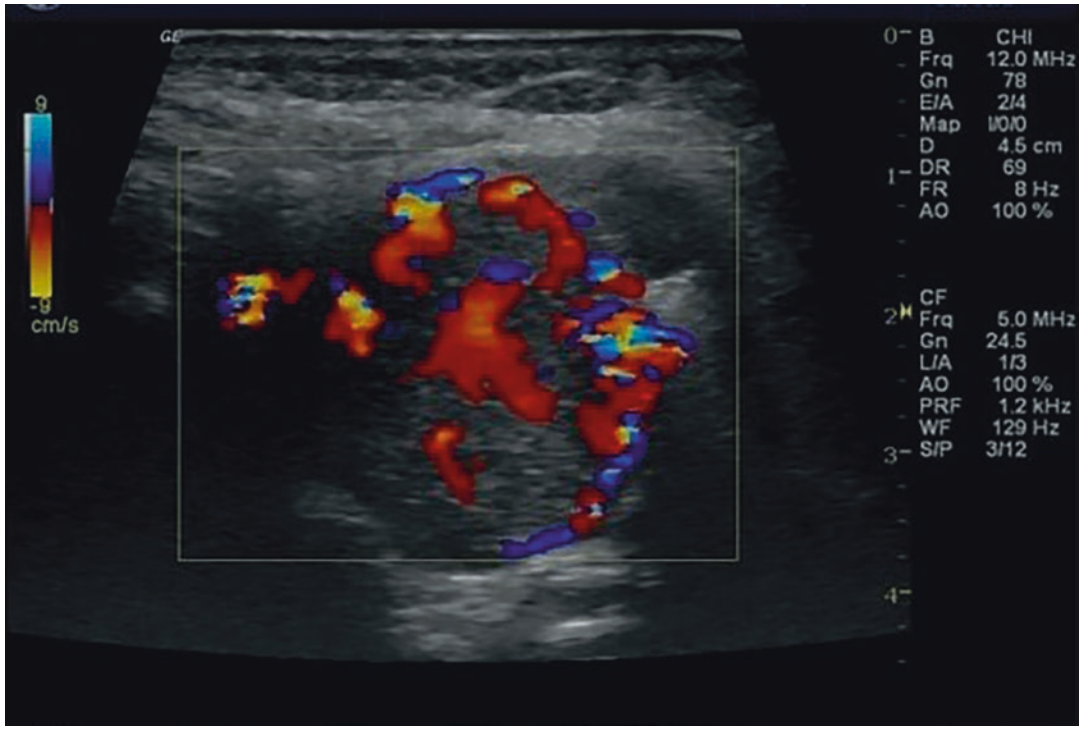

Fig. 7.5 Glomus tumor of the bulb at the level of carotid bulb and the bifurcation area, With the use of color Doppler the variable flow of the lesion is easily noted

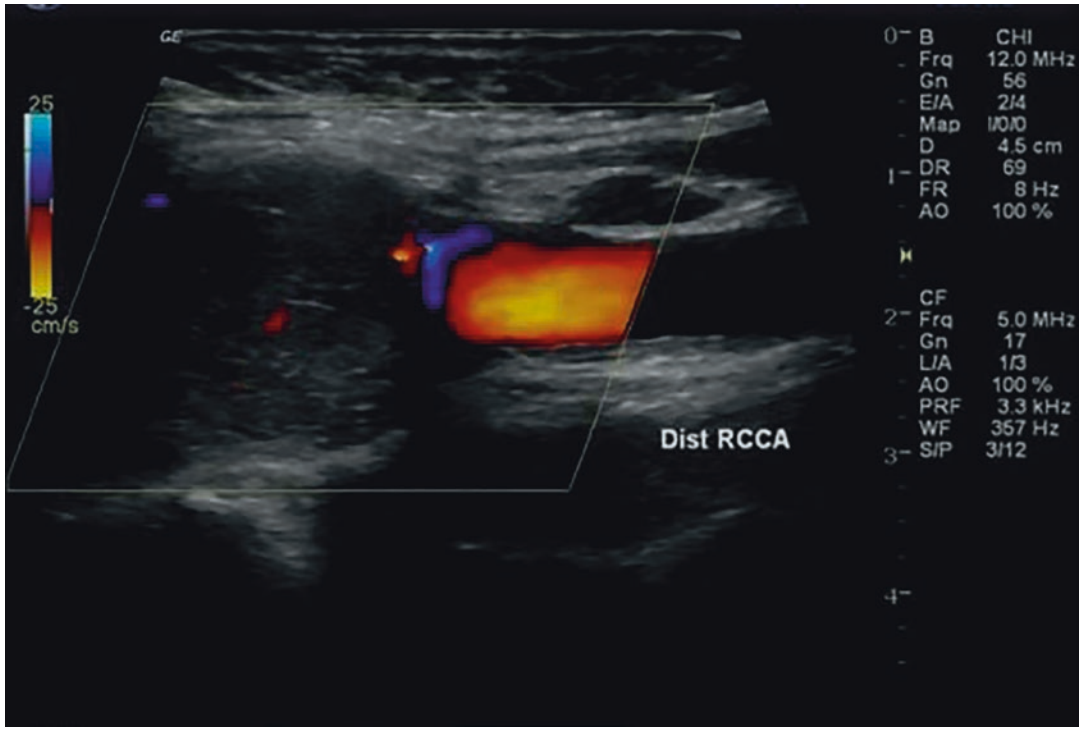

Fig. 7.6 Glomus tumor of the bulb at the level of carotid bulb and the bifurcation area. The pathology is adjacent to the vessel, altering the blood flow in it

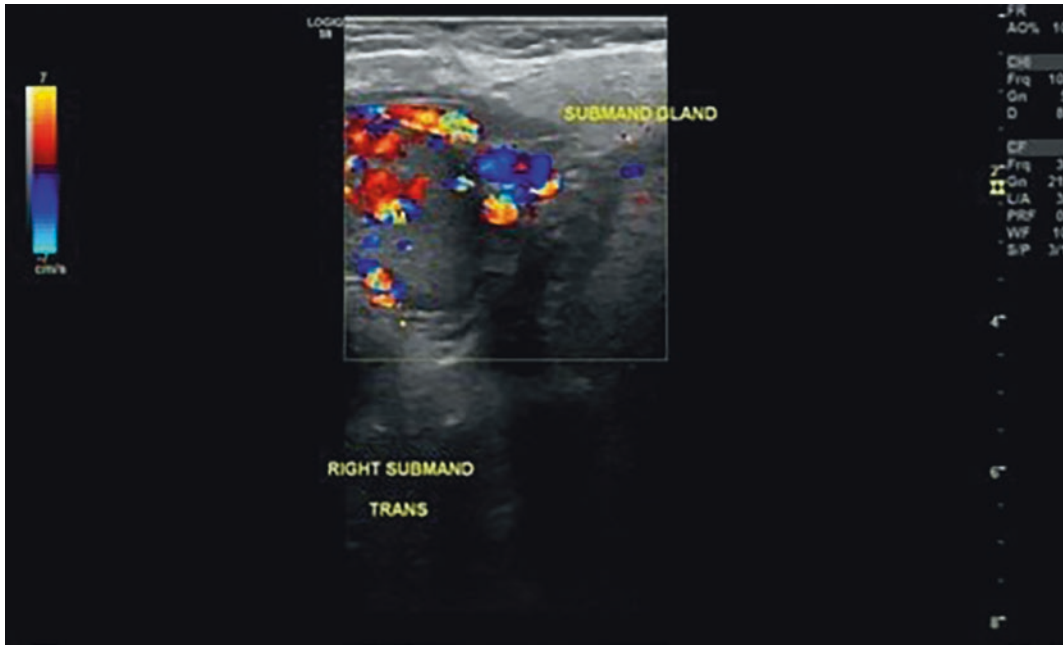

Fig. 7.7 Glomus tumor of the bulb at the level of the vagal ganglion. The lesion is just below the submandibular gland and was diagnosed by a dentist as a cervical swelling

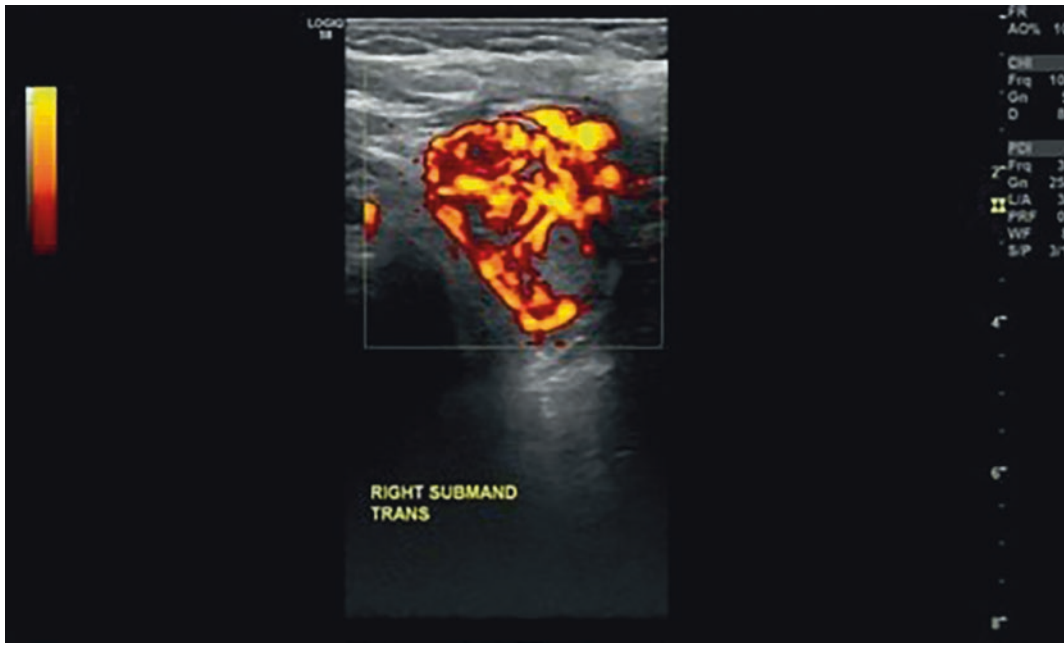

Fig. 7.8 Glomus tumor of the bulb at the level of the vagal ganglion. The same lesion with B flow showing the vascularity of the lesion

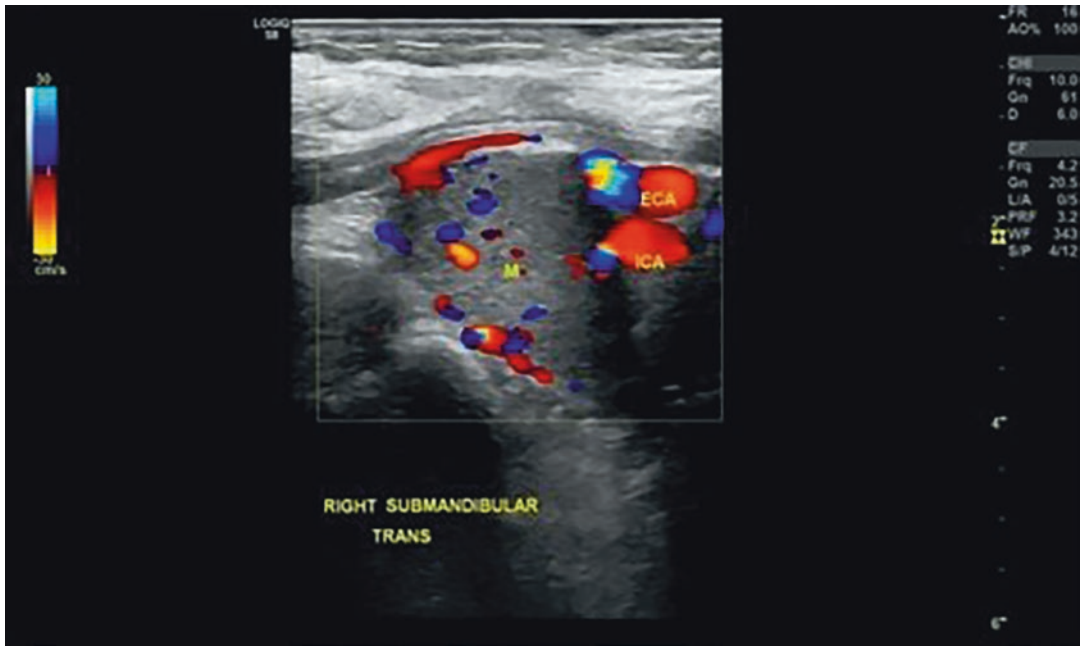

Fig. 7.9 Glomus tumor of the bulb at the level of the vagal ganglion

Localized intraneural neurofibromas are by far the most common form of neurofibroma, representing 90% of these lesions benign peripheral nerve sheath tumors (schwannomas and neurofibromas) and have variable sonographic features.

However, they share the common features of being hypoechoic and homogeneous, with posterior acoustic enhancement and nerve continuity.

Most peripheral nerve sheath tumors are mainly hypoechoic. There are literature references of presentations similar to targets, with a hyperechoic center surrounded by a hypoechoic halo in about 20% of cases. This type of presentation usually sets the diagnosis.

When dealing with schwannomas, they are benign neoplasms of the nerve sheath. They are found in many body sections, the neck being one of them. Approximately, 13% of all schwannomas occur in the extracranial head and neck. They have mild expansions and slow development in the nerve course. They are more frequent in the lateral nerve region with the sympathetic chain being the most common site of origin most schwannomas appear as well-circumscribed homogenous soft tissue density masses on unenhanced CT large lesions may present cystic areas making the diagnosis more difficult [20, 21].

One can therefore claim that nerve tumors are, in the majority of cases, homogenous of hypoechoic structure they follow the course of the nerves and in most cases, they demonstrate posterior acoustic enhancement.

Ultrasonography is not able to set the different features of the different types of nerve tumors of the area; however, the location and course of most tumors usually assist the diagnosis.

7.4 Malignant Tumors

Malignant mesenchymal tumors are the most common malignant entities to affect the cranial nerves. They are usually squamous cell carcinomas, and when they are found in the

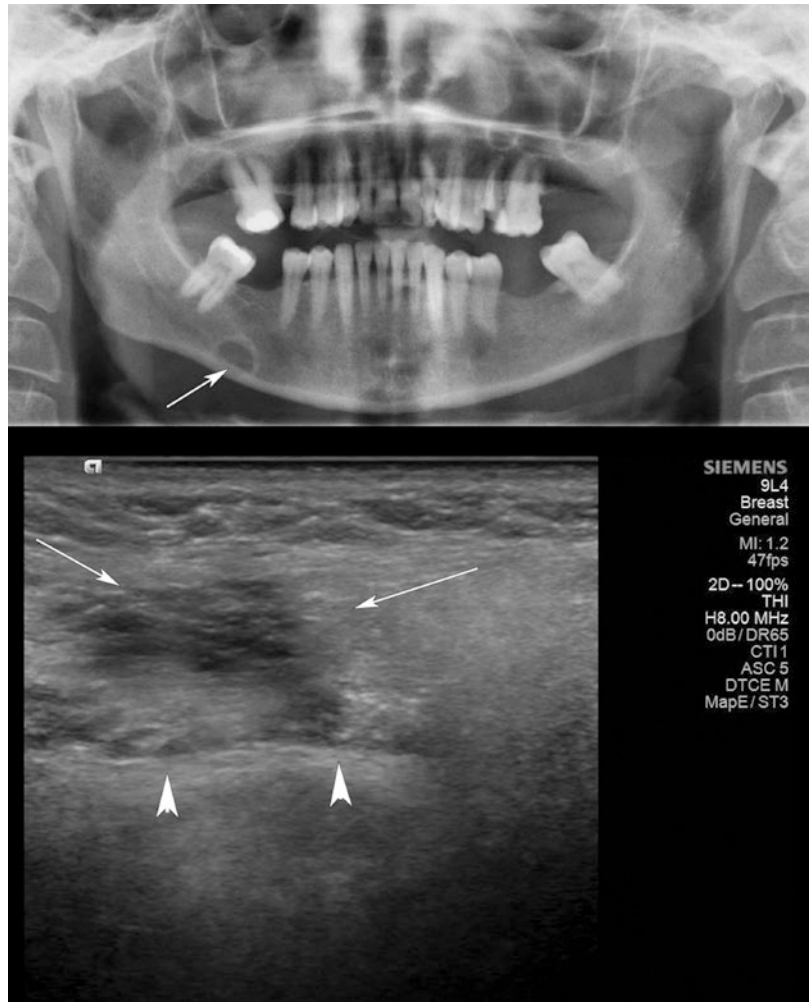

Fig. 7.10 A rare case of Mandibular schwannoma that was expanded through soft tissue (**a**) panoramic radiography of the lesion, (**b**) corresponding B-mode USG image showing hypoechoic lesion (arrows), note the hyperechoic mandibular ramus (arrowhead). Courtesy of Dr. Kaan Orhan

majority of cases they already present with metastases.

Like in the majority of cases the lymph node metastasis can be identified by ultrasonography but they cannot be distinguished or specified to the type of tumor they originate from.

Lymph node imaging is however described in a separate chapter.

References

1. Hafez RF, Morgan MS, Fahmy OM. An intermediate term benefits and complications of gamma knife surgery in management of glomus jugulare tumor. World J Surg Oncol. 2016;14:36.
2. Michael LM 2nd, Robertson JH. Glomus jugulare tumors: historical overview of the management of this disease. Neurosurg Focus. 2004;17:E1.
3. Carlson ML, Sweeney AD, Wanna GB, Netterville JL, Haynes DS. Natural history of glomus jugulare: a review of 16 tumors managed with primary observation. Otolaryngol Head Neck Surg. 2015;152:98–105.
4. Moore MG, Netterville JL, Mendenhall WM, Isaacson B, Nussenbaum B. Head and neck paragangliomas: an update on evaluation and management. Otolaryngol Head Neck Surg. 2016;154:597–605.
5. Murray TJ. Carotidynia: a cause of neck and face pain. Can Med Assoc J. 1979;120:441–3.
6. Kuhn J, Harzheim A, Horz R, et al. MRI and ultrasonographic imaging of a patient with carotidynia. Cephalalgia. 2006;26:483–5.
7. Charrier N, Deveze A, Fakhry N, Sebag F, Morange I, Gaborit B, et al. Comparison of [^{111}In]pentetreotide-SPECT and [18F]FDOPA-PET in the localization of extra-adrenal paragangliomas: the case for a patient-tailored use of nuclear imaging modalities. Clin Endocrinol. 74:21–9.
8. Arya S, Rao V, Juvekar S, Dcruz AK. Carotid body tumors: objective criteria to predict the Shamblin

group on MR imaging. AJNR Am J Neuroradiol. 2008;29:1349–54.
9. Obholzer RJ, Hornigold R, Connor S, Gleeson MJ. Classification and management of cervical paragangliomas. Ann R Coll Surg Engl. 2011;93:596–602.
10. Sajid MS, Hamilton G, Baker DM. Joint vascular research Surg: a multicenter review of carotid body tumour management. Eur J Vasc Endovasc Surg. 2007;34:127–30.
11. van den Berg R, Verbist BM, Mertens BJ, van der Mey AG, van Buchem MA: Head and neck paragangliomas: improved tumor detection using contrast-enhanced 3D time-of-flight MR angiography as compared with fat-suppressed MR imaging techniques. AJNR Am J Neuroradiol 2004, 25: 863–70.
12. Amin MF, El Ameen NF. Diagnostic efficiency of multidetector computed tomography versus magnetic resonance imaging in differentiation of head and neck paragangliomas from other mimicking vascular lesions: comparison with histopathologic examination. Eur Arch Otorhinolaryngol. 2013;270:1045–53.
13. Hoegerle S, Ghanem N, Altehoefer C, Schipper J, Brink I, Moser E, et al. 18F-DOPA positron emission tomography for the detection of glomus tumours. Eur J Nucl Med Mol Imaging. 2003;30:689–94.
14. Carlson ML, Sweeney AD, Wanna GB, Netterville JL, Haynes DS. Natural history of glomus jugulare: a review of 16 tumors managed with primary observation. Otolaryngol Head Neck Surg. 2015;152:98–105.
15. Woolen S, Gemmete JJ. Paragangliomas of the head and neck. Neuroimaging Clin N Am. 2016;26:259–78.
16. van den Berg R. Imaging and management of head and neck paragangliomas. Eur Radiol. 2005;15:1310–8.
17. Lee DW, Yang JH, Chang S, Won CH, Lee MW, Choi JH, et al. Clinical and pathological characteristics of extradigital and digital glomus tumours: a retrospective comparative study. J Europ Acad Dermatol Venereol. 2011;25:1392–7.
18. Delantoni A, Sarafopoulos A, Polanagnostaki A, Orhan K: B-mode and color Doppler imaging of carotid paragangliomas in different neck regions. J Ultrason. 2020;20:e218–e221.
19. Netterville JL, Jackson CG, Miller FR, Wanamaker JR, Glasscock ME. Vagal paraganglioma: a review of 46 patients treated during a 20- year period. Arch Otolaryngol Head Neck Surg. 1998;124:1133–40.
20. Biswas D. Extracranial head and neck schwannomas—a 10-year review. Auris Nasus Larynx. 2007;34(3):353–9.
21. Hanemann CO. News on the genetics, epidemiology, medical care and translational research of Schwannomas. J Neurol. 2006;253(12):1533–41.

8 Sonographic Anatomy and Pathology Floor of the Mouth

Antigoni Delantoni

Contents

8.1 General Anatomy and Ultrasonographic Features

The epithelium of the floor of the mouth varies depending on the area one is studying. There are sections of keratinized and areas of nonkeratinized epithelium. The lateral area of the floor of the mouth contains fat tissue and the sublingual glands as well as other mucous secretion minor salivary glands [1–3].

When it comes to ultrasonographic evaluation of the floor of the mouth there are two ways to perform the exam. The basic and most frequently used way is superficially through the soft tissues of the neck which is done with a typical high-frequency linear transducer (ideally should be over 9 Hz) and the second more difficult to perform is with the use of intraoral probes [4–6]. This can either be done by covering the linear probes and inserting it into the mouth or with smaller "hockey sticks probes" that are easier for the space limitations the exam has.

The most frequently used landmarks in the floor of the mouth examinations are either the hard tissues of the area (mandibular ramus and hyoid bone) or the submandibular gland which helps orientate in soft tissues. The various layers of striated muscles are not easy to separate and identify, and in most cases they are just identified as muscle layers without specifying which ones they are. This is because the muscular layers are very thin and small as regions [3, 6].

A. Delantoni (✉)
Department of Oral Surgery, Implant Surgery and Radiology, School of Dentistry, Faculty of Health Sciences, Aristotle University of Thessaloniki, Thessaloniki, Greece

K. Orhan (ed.), *Ultrasonography in Dentomaxillofacial Diagnostics*,
https://doi.org/10.1007/978-3-030-62179-7_8

The muscles of the tongue however with the use of ultrasound are seen as a whole and they appear homogenous with relatively high echogenicity. Upon examination, particularly in the extraoral ultrasonographic exam, it is important to examine the patient both with longitudinal and transverse views.

The easiest anatomical landmark in the floor of the mouth examination, is the curvature of the tongue's surface. Also important is the determination of the air–tissue interface [3, 6].

Intraoral probes are more useful when we want to examine the tongues surface since they are easier to handle in such a small region.

Also, it is very important to study the entire length of the tongue which can be made by moving the probe beside the floor of the mouth as low as the hyoid bone. The muscles that need to be identified in the exam are the anterior belly of the digastric as well as the geniohyoid, mylohyoid, and genioglossus muscles, though they are not always so easy to identify.

8.2 Inflammatory Changes

Skin and soft tissue inflammatory lesions, including abscesses and cellulitides, are one of the most common problems seen by physicians. The soft tissue infections treatment varies depending on the depth of the infection or the presence of fluid which would require incision and drainage. The evaluation of skin and soft tissue infections can be very eaily performed with ultrasonography, enabling the examiner to diagnose an abscess cavity or deeper infection. The method of ultrasonography has been shown to be more reliable than clinical exam alone. The proper use of ultrasound allows for more appropriate patient care and management of their underlying infection. What is important when dealing with inflammatory changes is the differentiation between an abscess and a simple non developed inflammation.

Simple inflammatory lesions are not clearly delineated and their borders are diffused and hypoechoic. They often appear without clear borders and blurred (Figs. 8.1, 8.2 and 8.3).

Abscesses, on the contrary, have clear borders; they are also hypoechoic lesions and they may have an anechoic central area with acoustic enhancement, or areas of perfusion of the tissue areas (Figs. 8.4, 8.5 and 8.6).

Like all inflammatory lesions there is high vascularity and often swelling of the region involved. Thus as in all inflammations the correlation to the clinical status of the lesion is very important.

8.2.1 Ranulas

Ranulas are a type of mucous cyst, which is characteristic to the floor of the mouth unilaterally [7].

It is included in the inflammatory lesions of the floor of the mouth since it is according to most authors the result of injury of the secretory duct of the sublingual gland, which in many cases

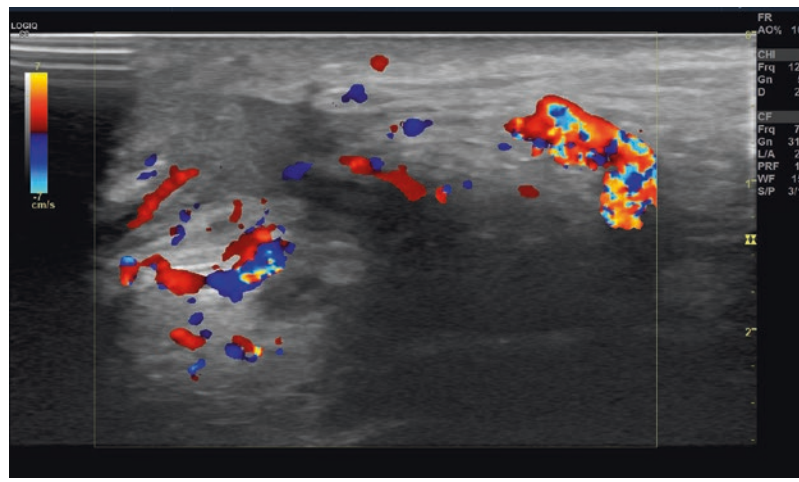

Fig. 8.1 Diffused non specified border inflammatory lesion with increased peripheral vascularity as seen in color Doppler

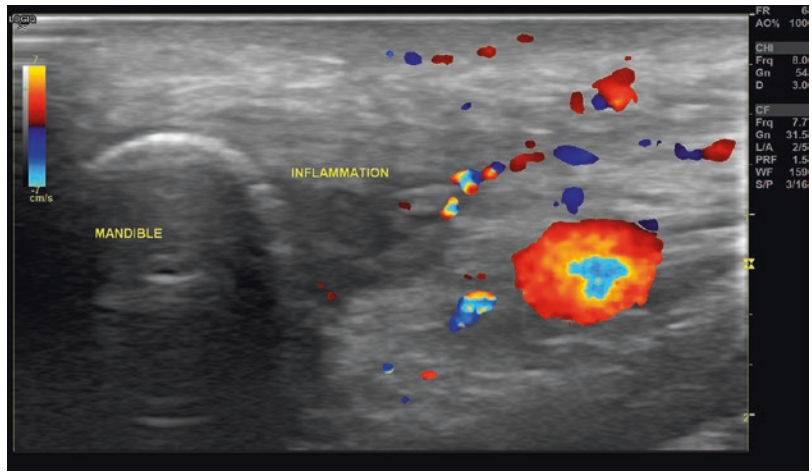

Fig. 8.2 Inflammation adjacent to the mandible again of non-clearly lined borders

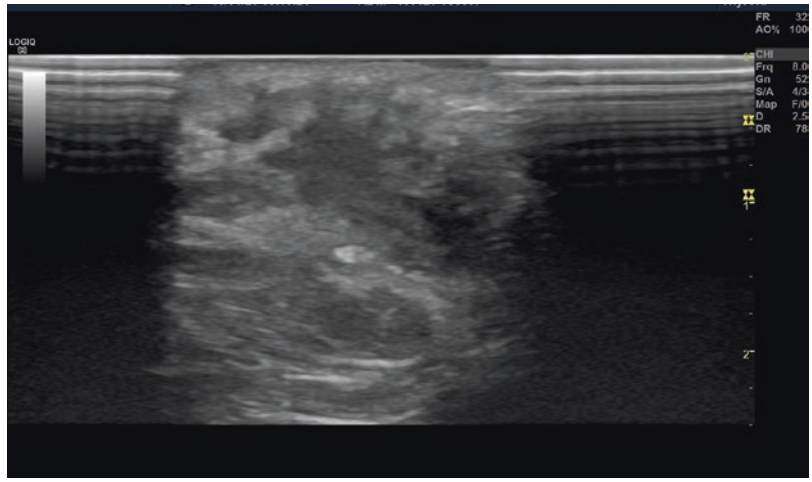

Fig. 8.3 A large lesion of inflammatory origin seen in the submandibular area at the level II of the neck

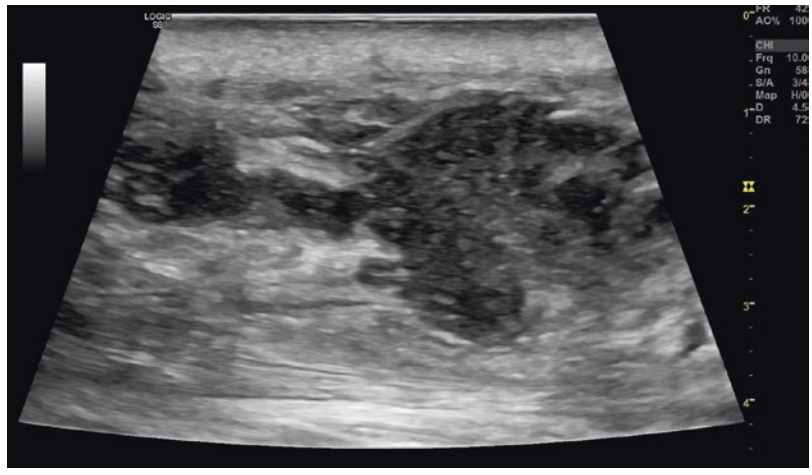

Fig. 8.4 Better defined border of an inflammatory lesion indicating the formation of an abscess

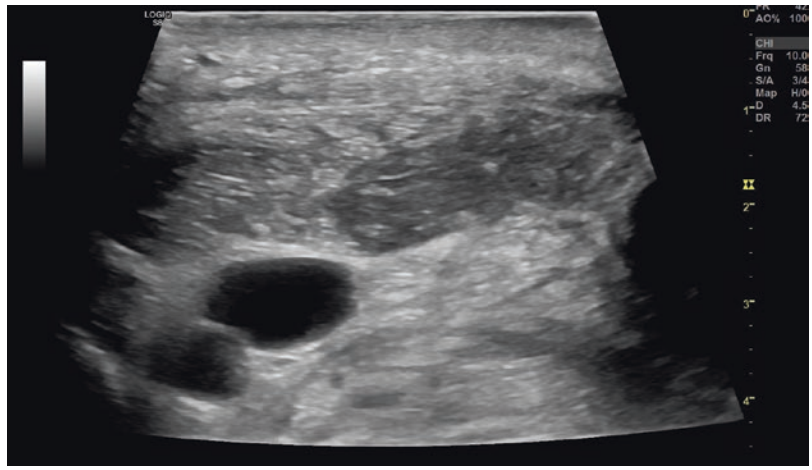

Fig. 8.5 A well defined non clear borders lesion which corresponds to an abscess

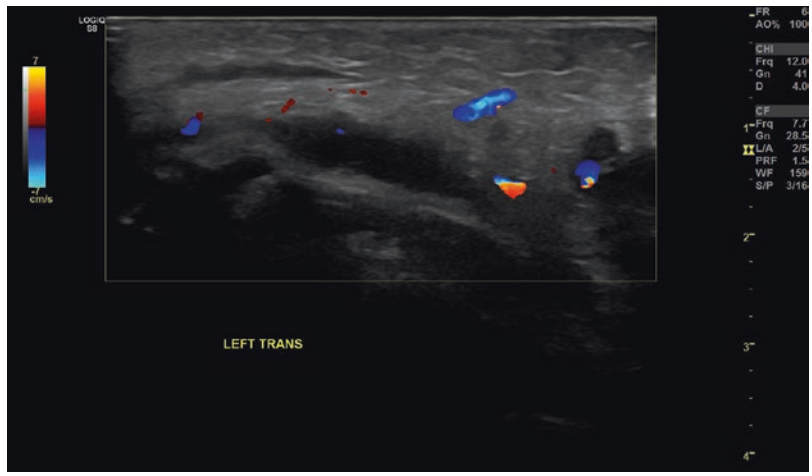

Fig. 8.6 A clear well defined lesion with very clear borders indicating a clear formed abscess

is common to the duct of the submandibular gland while in fewer cases it is from the ducts of minor sublingual glands [8, 9].

A special case of ranula is the diving or plunging ranula, which is considered to appear from a gap between the mylohyoid muscle in which a part of the sublingual gland descends. This leads to the distribution of the saliva through the mylohyoid muscle to the floor of the mouth and submandibular area [10–16].

Clinically, it appears as a semicircular swelling between 1 and 3 cm which is palpating and is located unilaterally in the floor of the mouth. Sometimes when large in size it may force the tongue away from its normal position and cause difficulties in speech, swallowing, and chewing. As with mucous retention cysts, ranulas may burst and reappear at different time frames.

The clinical diagnosis is set from the position and the characteristic image of the lesion [15].

The key to the radiological identification of ranulas is the characterization of the connection to the sublingual space [9–16].

With the use of ultrasound ranulas usually appear are clear hypoechoic lesions, similar to cysts with thin walls [11–13]. Sometimes when infected they may contain fine internal echoes, usually due to the presence of debris from previous episodes of inflammation [14]. A ranula usually appears as a unilocular, well-defined, cystic lesion in the submental region deep to the mylohyoid muscle. For a diving ranula, the bulk of the cystic collection is in the submandibular region, but a small beak may be seen within the sublingual space [12–16]. (Figs. 8.7, 8.8 and 8.9).

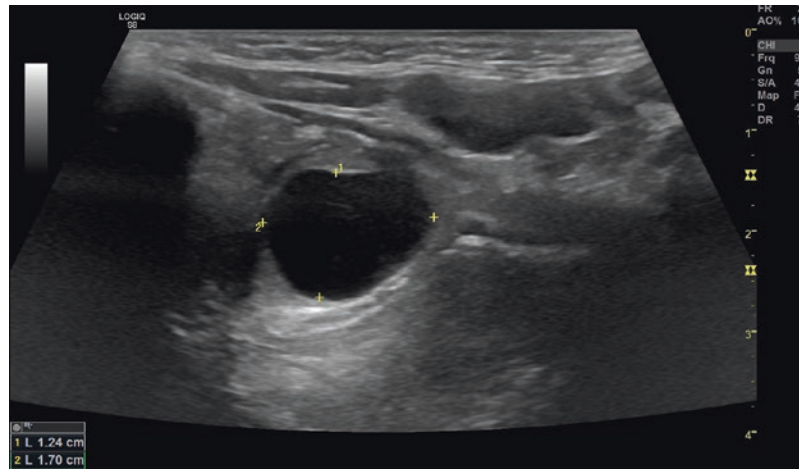

Fig. 8.7 A ranula with characteristic well bordered clear cyst like formation filled with fluid

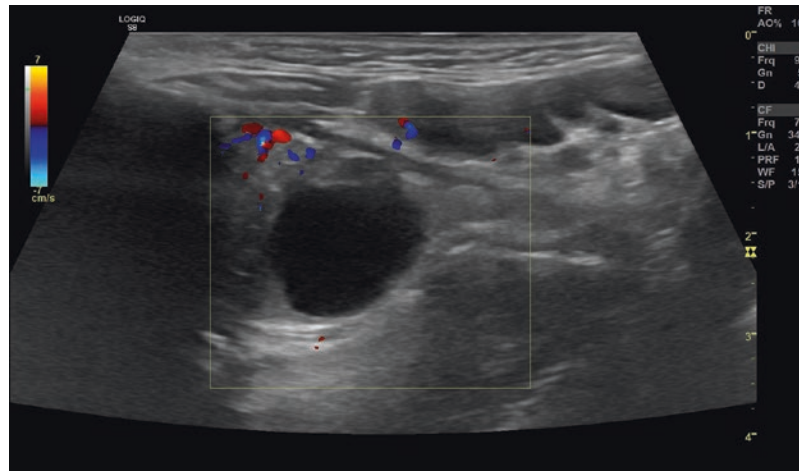

Fig. 8.8 Color doppler of a ranula showing the lack of vascularity in the lesion since it is filled with liquid

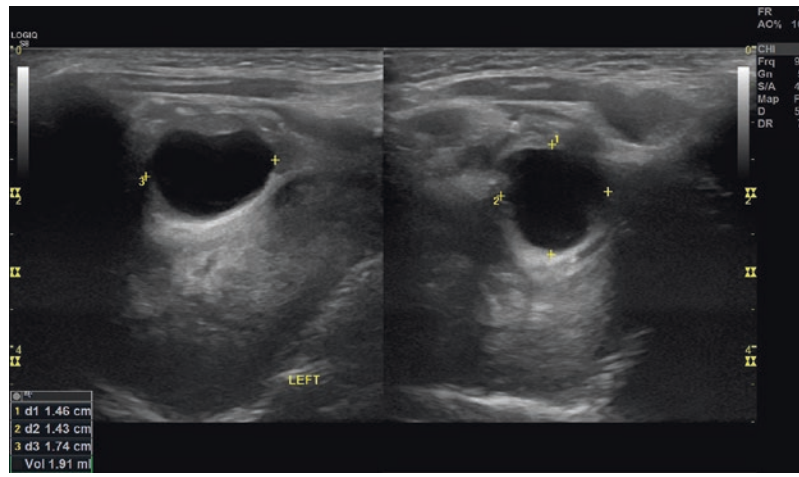

Fig. 8.9 Measurement of the size of the lesion in all three directions and giving the estimate of the volume of the lesion

8.3 Benign Tumors

8.3.1 Branchial Cysts

Branchial cleft cysts arise from incomplete obliteration of any branchial tract, resulting in either a cyst (75%) or a sinus or fistulous tract (25%) and are lying laterally in the neck [17–21].

First branchial cleft lesions are relatively less common and typically closely related to the parotid gland. In these lesions, the cystic appearance is less common when compared to fistulas or sinuses.

The **second** branchial cleft cysts are the most common lesions since the cleft they rise from (pharyngeal cleft) is the largest and longest persisting in embryonic development [19, 21].

Bailey has classified second branchial cleft cysts (BCCs) into four types [21].

- Type-I occurs anterior to the sternocleidomastoid muscle just deep to the platysma muscle;
- Type-II is the commonest type and occurs deep to the sternocleidomastoid and lateral to the carotid space;
- Type-III extends medially between the bifurcation of internal and external carotid arteries to the lateral pharyngeal wall; and.
- Type-IV occurs in the pharyngeal mucosal space medial to the carotid sheath.

Basically, a second branchial cyst can occur anywhere in the lateral aspect of the neck but are most commonly seen at the floor of the mouth in the anteromedial border of the sternocleidomastoid muscle and the posterior margin of the submandibular gland [20, 21].

Upon ultrasonographic examination, the lesion usually lies laterally to the internal jugular vein and caudally to the posterior belly of the digastric muscle. While they are seen as a well-marginated anechoic mass with a thin, well-defined wall [18, 21]. (Figs. 8.10, 8.11 and 8.12).

Malformations of the third and fourth branchial clefts are considerably less common and typically present with continuous and chronic neck inflammations [17, 18].

They are both related to the pyriform sinus with those of the third cleft being above the superior laryngeal nerve and those of the fourth being below the nerve.

Fourth branchial cleft anomalies are generally sinus tracts or fistulae and arise from the pyriform sinus, pierce the thyrohyoid membrane, and descend along the tracheoesophageal groove [17].

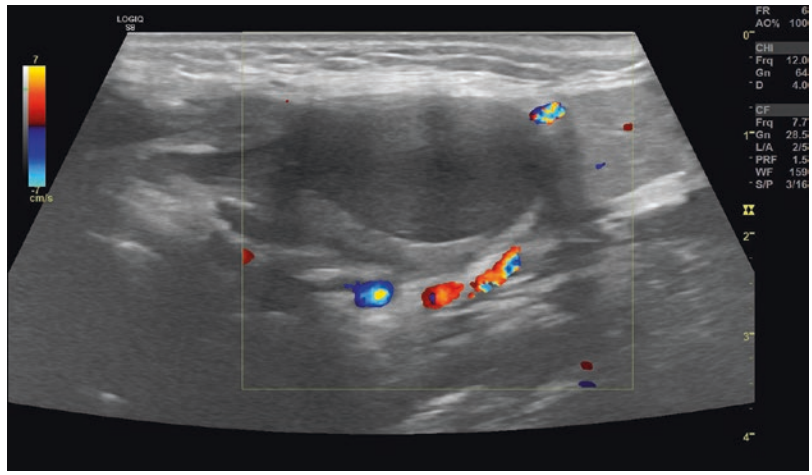

Fig. 8.10 A branchial arch cyst filled with liquid but not as clear as with ranulas

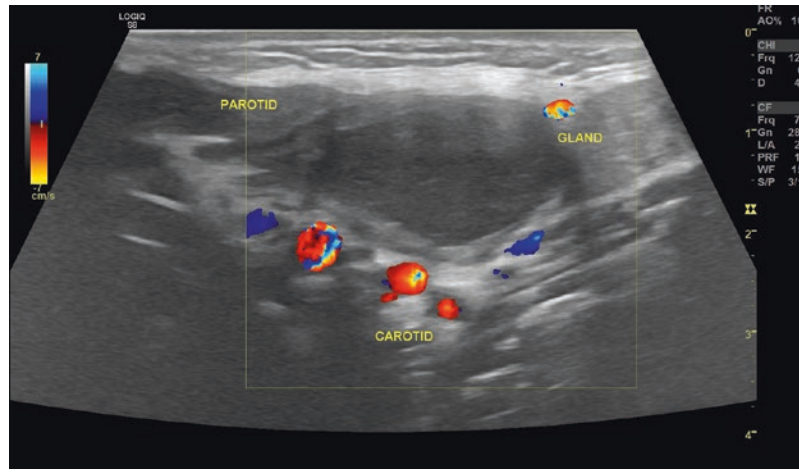

Fig. 8.11 Color doppler of the lesion shows no vascularity since it has liquid. The location of the lesion is at the base of the mandibular angle near the lower border of the parotid gland

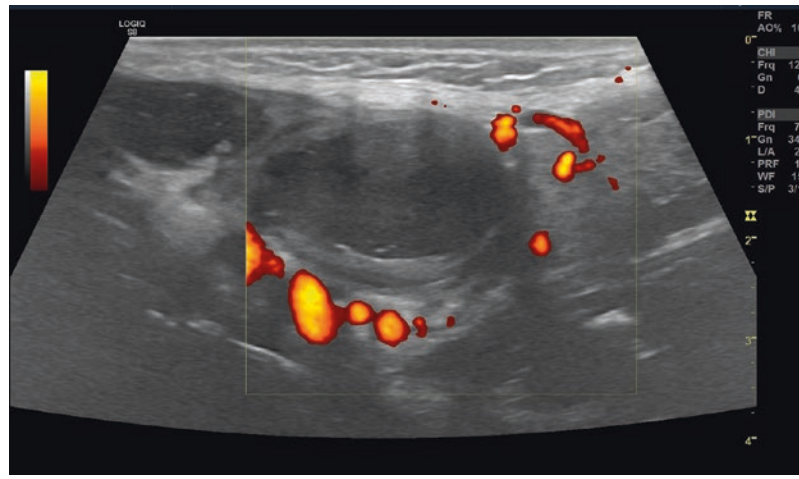

Fig. 8.12 The same lesion with the use of B-flow to give a more accurate image of the vascularity of the area

8.3.2 Thyroglossal Duct Cysts and Fistulas

Thyroglossal duct cysts are the most common midline congenital neck mass accounting for over 70% of all neck congenital pathologies. They are located at the level of the superior thyroid notch and are often noted in close proximity to the hyoid bone [22–25].

The pathogenesis of thyroglossal duct cysts is closely linked to the embryonic development of the thyroid gland in the neck and the cyst occurs along the residual tract left by the thyroid gland after the descent from the foramen cecum at the tongue base to its final position in the visceral space.

They are more frequently seen at the level of the hyoid bone or below it with rarer their presence above it [24, 25].

Upon US examination they appear as highly elastic smooth well-defined and bordered lesion with posterior enhancement in few cases. In the examination, it is highly important to determine the exact location of the lesion and its extent to the base of the tongue. In many cases, they show a hypoechoic pattern with areas of heterogenous echostructure [26–31] (Figs. 8.13 and 8.14).

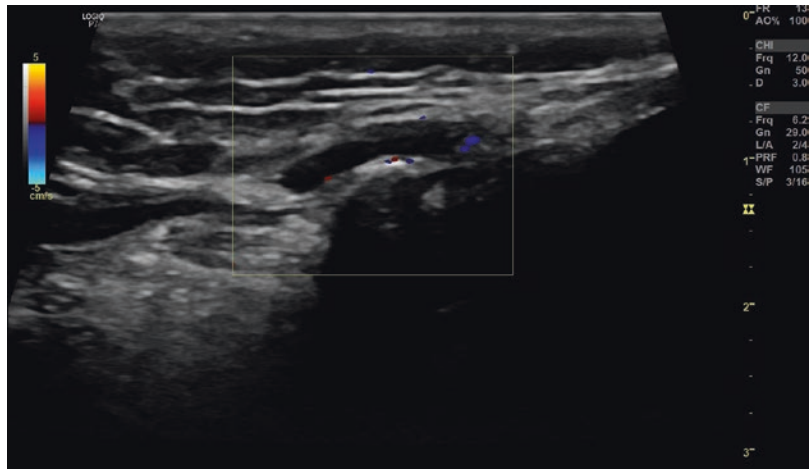

Fig. 8.13 A thyroglossal duct cyst laying adjacent to the hyoid bone

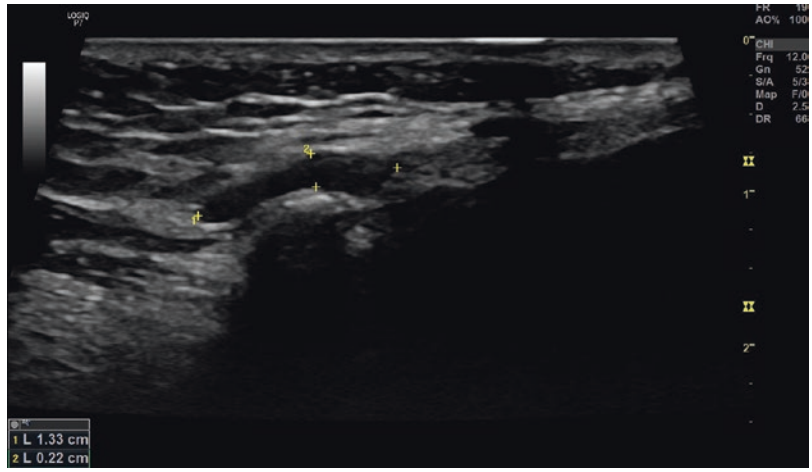

Fig. 8.14 A thyroglossal duct cyst measured in its two axes. The lesion has a characteristic oval shape similar to the curve of the hyoid bone since it lays on it

8.3.3 Dermoid and Epidermoid Cysts

These lesions may occur anywhere in the body with the neck accounting for about 7% of them [32].

When talking about dermoid cysts, they differ from epidermoid cysts in that they contain skin appendages such as sebaceous glands and hair follicles within the cyst wall. Dermoid cysts usually manifest as a slow-growing mass in the submandibular or sublingual space [33–35].

In contrast, epidermoid cysts manifest earlier in life, with most lesions evident during infancy, and are usually seen as well-defined anechoic masses with posterior enhancement in the midline of the neck [35].

Imaging has an important role in confirming the diagnosis and classifying cysts according to their relation to muscle. Ultrasound is the initial imaging modality.

Upon US, they may demonstrate a homogenous structure, though heterogeneous appearance may be seen due to the presence of echogenic fat, osseous, or dental elements [36].

The floor of the mouth lesions typically present as thin-walled, unilocular masses located in the submandibular or sublingual space [36–38].

8.3.4 Other Benign Tumors

Benign tumors of the floor of the mouth, tongue, and oropharynx are no different from the findings for similar tumors elsewhere in the head and neck. Lipomas, hemangiomas, and lymphangiomas can be assessed in relation to surrounding structures. The surgical approach (transoral or transcervical) can be selected on the basis of the findings. The majority of benign tumors of the floor of the mouth are very rare in appearance. They are readily visible upon clinical examination since the tissues of the mouth floor are very thin and easy to access [39–42].

8.4 Malignant Tumors

Malignancies of the oral cavity and the oropharynx represent about 2–5% of all malignancies. The vast majority of the lesions are squamous cell carcinomas which account for about 90% of cases [43–45].

Upon US examination, lesions appear cloud-like, with ill-defined borders. The identification of the exact size of the tumor with US as an initial exam is often required. Also, the relationship of carcinoma of the tongue or floor of the mouth to the midline is important to be assessed by ultrasound as an initial examination [43, 45].

References

1. Smith D. Genetic, embryologic, and clinical aspects. In: Recognizable patterns of human malformation. 3rd ed. Philadelphia: WB Saunders; 1982. p. 472–3.
2. Harnsberger H. Handbook of Head and Neck Imaging. 2nd ed. St Louis, MO: Mosby-Yearbook; 1992. p. 1184–243.
3. Harnsberger HR, Wiggins RH, Hudgins PA, Davidson HC, Macdonald AJ, Glastonbury CM, et al. Diagnostic Imaging Head and Neck. 1st ed. Altona: Amirsys; 2004. p. 30–3.
4. La'Porte SJ, Juttla JK, Ravi K, Lingam RK. Imaging the floor of the mouth and the sublingual space. Radiographics. 2011;31:1215–30.
5. Som P, Curtin HD. Head and Neck Imaging. 4th ed. St. Louis, MO: Mosby; 2002. p. 2006–133.
6. Caglayan F, Bayrakdar IS. The intraoral ultrasonography in dentistry. Niger J Clin Pract. 2018;21(2):125–33.
7. Bouquot, Neville BW, Damm DD, Allen CM, Jerry E. Oral & maxillofacial pathology. 2nd ed. Philadelphia: W.B. Saunders; 2002. p. 391–2.
8. Kerawala C, Carrie. Newlands. In: Oral and maxillofacial surgery. Oxford: Oxford University Press; 2010. p. 199.
9. Hupp JR, Ellis E, Tucker MR. Contemporary oral and maxillofacial surgery. 5th ed. St. Louis: Mosby Elsevier; 2008. p. 410–1.
10. Harrison JD. Modern management and pathophysiology of ranula: literature review. Head Neck. 2010;32(10):1310–20. [3]
11. Suresh BV, Vora KS. Huge plunging ranula. J Maxillofac Oral Surg 2012;11(4):487–90.
12. Mustafa AB, Bokhari K, Luqman M, Hameed MS, Kota Z. Plunging ranula: an interesting case report. Open J Stomatol. 2013;3:118–21.
13. McGurk M, Eyeson J, Thomas B, Harrison JD. Conservative treatment of oral ranula by excision with minimal excision of the sublingual gland: histological support for a traumatic etiology. J Oral Maxillofac Surg. 2008;66:2050–7.
14. De Visscher JG, Vander Wal KG, de Vogel PL. The plunging ranula. Pathogenesis, diagnosis and management. J Cranio-Maxillofacial Surg. 1989;17:182–5.
15. Davison MJ, Morton RP, McIvor NP. Plunging ranula: clinical observations. Head Neck. 1998;20:63–8.
16. Zhi K, Wen Y, Zhou H. Management of the pediatric plunging ranula: results of 15 years' clinical experience. Oral Surg Oral Med Oral Pathol Oral Radiol Endod. 2009;107:499–502.
17. Bailey H. Branchial Cysts and Other Essays on Surgical Subjects in the Facio-Cervical Region. London: Lewis; 1929.
18. Papadogeorgakis N, Petsinis V, Parara E, Papaspyrou K, Goutzanis L, Alexandridis C. Branchial cleft cysts in adults. Diagnostic procedures and treatment in a series of 18 cases. Oral Maxillofac Surg. 2009;13(2):79–85.
19. Muñoz-Fernández N, Mallea-Cañizares I, Fernández-Julián E, De La Fuente-Arjona L, Marco-Algarra J, Algarra J. Double second branchial cleft anomaly. Acta Otorrinolaringol Esp. 2011;62(1):68–70.
20. Thomaidis V, Seretis K, Tamiolakis D, Papadopoulos N, Tsamis I. Branchial cysts. A report of 4 cases. Acta Dermatovenerol Alp Panonica Adriat. 2006;15(2):85–9.
21. Ahuja AT, King AD, Metreweli C. Second branchial cleft cysts: variability of sonographic appearances in adult cases. AJNR Am J Neuroradiol. 2000;21:315–9.
22. Deane SA, Telander RL. Surgery for thyroglossal duct and branchial cleft anomalies. Am J Surg. 1978;136:348–53.
23. Ahuja AT, King AD, Metreweli C. Sonographic evaluation of thyroglossal duct cysts in children. Clin Radiol. 2000;55:770–4.
24. Telander R, Deane S. Thyroglossal and branchial cleft cysts and sinuses. Surg Clin North Am. 1977;57:779–91.
25. Allard RH. The thyroglossal cyst. Head Neck Surg. 1982;5:134–46.

26. Ahuja AT, Wong KT, King AD, Yuen EHY. Imaging for thyroglossal duct cyst: the bare essentials. Clin Radiol. 2005;60:141–8.
27. Kutuya N, Kurosaki Y. Sonographic assessment of thyroglossal duct cysts in children. J Ultrasound Med. 2008;27:1211–9.
28. Wadsworth D, Siegel M. Thyroglossal duct cysts: variability of sonographic findings. Am J Roentgenol. 1994;163(6):1475–7.
29. Ward P, Strahan R, Acquarelli M, Harris P. The many faces of cysts of the thyroglossal duct. Trans Am Acad Ophthalmol Otolaryngol. 1970;74:310–8.
30. Zander D, Smoker W. Imagine of ectopic thyroid tissue and thyroglossal duct cysts. Radiographics. 2012;34:37–50.
31. Zarbo RJ, McClatchey KD, Areen RG, Baker SB. Thymopharyngeal duct cyst: a form of cervical thymus. Ann Otol Rhinol Laryngol. 1983;92:284–9.
32. Sabhalok SS, Shetty LS, Sarve PH, Setiya SV, Bharadwaj SR. Epidermoid and dermoid cysts of the head and neck region. Plast Aesthet Res. 2016;3:347–50.
33. Jham BC, Duraes GV, Jham AC, Santos CR. Epidermoid cyst of the floor of the mouth: a case report. J Can Dent Assoc. 2007;73:525–8.
34. Pereira CM, Gasparetto PF, de Lucena Botelho T. Atypical appearance of epidermoid cyst in tongue's ventral surface. RSBO. 2011;8:240–2.
35. Ibrahim M, Hammoud K, Maheshwari M, Pandya A. Congenital cystic lesions of the head and neck. Neuroimag Clin North Am. 2011;21:621–39.
36. Koeller KK, Alamo L, Adair CF, Smirniotopoulos JG. Congenital cystic masses of the neck: radiologic-pathologic correlation. Radio Graphics. 1999;19:121–46.
37. Tanphaichitr A, Bhushan B, Maddalozzo J, Schroeder JW. Ultrasonography in the treatment of pediatric midline neck masses. Arch Otolaryngol Head Neck Surg. 2012;138:823–7.
38. Voss JO, Buehling S, Thieme N, Doll C, Hauptmann K, Heiland M, Adolphs N, Raguse JD. Sublingual cysts of different entities in an infant - a case report and literature review. Int J Pediatr Otorhinolaryngol. 2018 Oct;113:260–5.
39. Catalano P, Fang-Hui E, Som PM. Fluid-fluid levels in benign neurogenic tumors. AJNR Am J Neuroradiol. 1997;18:385–7.
40. Emery PJ, Bailey CM, Evans JN. Cystic hygroma of the head and neck. J Laryngol Otol. 1984;98:613–9.
41. Friedman ER, John SD. Imaging of pediatric neck masses. Radiol Clin N Am. 2011;49:617–32.
42. Wong KT, Lee YY, King AD, Ahuja AT. Imaging of cystic or cyst-like neck masses. Clin Radiol. 2008;63:613–22.
43. Fernandez JF, Ordonez NG, Schultz PN, Saman NA, Hickey S. Thyroglossal duct carcinoma. Surgery. 2001;110:928–34.
44. Granstrom G, Edstrom S. The relationship between cervical cysts and tonsillar carcinoma in adults. J Oral Maxillofac Surg. 1989;47:16–20.
45. Pound LA. Neck masses of congenital origin. Pediatr Clin N Am. 1981;28:841–4.

9 Sonographic Anatomy and Pathology Salivary Glands

Antigoni Delantoni

Contents

9.1 Introduction

9.1.1 General Sonographic Anatomy

As superficial anatomical structures, the salivary glands are easily accessible to ultrasound. Ultrasound has several advantages that make it the examination of choice in the study of their pathology.

Main advantages are the easy accessibility and the low cost of the method, the safety of technique since radiation is avoided, and the excellent image analysis in real-time with the newer high-frequency transducers used since they provide the details of the superficial structures required for the examination [1, 2].

Although the application of ultrasound is generally accepted in various medical specialties, the

A. Delantoni (✉)
Department of Oral Surgery, Implant Surgery and Radiology, School of Dentistry, Faculty of Health Sciences, Aristotle University of Thessaloniki, Thessaloniki, Greece

K. Orhan (ed.), *Ultrasonography in Dentomaxillofacial Diagnostics*,
https://doi.org/10.1007/978-3-030-62179-7_9

value of the method in assessing and examining salivary glands has emerged over the last two decades with the partial abolition of sialography and its replacement by the use of ultrasound as a noninvasive technique that provides real-time information on their function.

The first papers on the application of ultrasonography on salivary glands pathology goes back to the 70s [3, 4].

Regarding the glands, the superior lobe of the parotid is easily assessed with the use of ultrasonography [2, 3]. However, the deeper lobe is not as easy to access due to the intervention of the ramus of the mandible, which blocks the sound waves.

9.1.2 The Parotid Gland

Anatomically the parotid is the largest of the salivary glands and weighs about 25 gm. It is located in the retromandibular area, with skeletal borders the posterior border of the ramus anteriorly, the mastoid process posteriorly, and the temporomandibular joint and external acoustic meatus superiorly. It has the shape of a three-sided pyramid with its tip inside and base outside with three surfaces. In 20% of patients, a nodule of the accessory parotid gland can be identified on the masseter muscle [4–6].

The *superior surface* includes branches of the facial nerve and superficial intraparotid lymph nodes and more posteriorly the temporomandibular joint.

The *anterior surface* is bordered by the ramus of the mandible and section of the masseter muscle.

The *posterior surface* is related to the mastoid process, the styloid process and its muscles, the sternocleidomastoid muscle, and part of the internal carotid artery.

The parotid gland is assessed in both transverse and sagittal image scans except for the retromandibular section of the gland. The normal parotid gland is homogenous in echostructure and demonstrates medium echogenicity. The borders are clearly demonstrated [5].

Upon ultrasonographic imaging, the tissue layers visible with the probe are the following from the outer surface towards the deeper layers: facial skin, subcutaneous fat, and parotid gland.

Its borders are as follows:

The *anterior border* separates the upper from the anterior surface and is the border that includes the parotid duct, the distal branches of the facial nerve and the vessels that accompany it.

The *posterior border* separates the upper from the posterior inner surface and sits on sternocleidomastoid muscle.

The *inner border* separates the anterior upper surface from the posterior inner surface and is related to the distal part of the pharynx.

Imaging of the parotid should be obtained with a high-frequency transducer due to the superficial structure of the gland. Usually, linear probes of 9–20 MHz are used. The entire gland should be evaluated in two perpendicular planes. The retromandibular vein, which lies directly deep to the facial nerve and lateral to the external carotid artery, is an excellent landmark to separate the superficial and deep lobes.

In the parotid gland, we see branches of the external carotid and the retromandibular vein.

The parotid duct or Stensen's duct may be seen in ultrasonographic examinations as a linear and very thin hypoechoic structure that travel towards the upper mandible from the anterior border of the gland and with a slight low course angulation in the masseter muscle [6]. The end section of the duct corresponds to the second molar and can be visualized with a theoretical line from the inferior part of the tragus to the midsection between the nose and upper lip. (Fig. 9.1).

9.1.3 The Submandibular Gland

The submandibular gland is bordered by the mandible laterally and the mylohyoid muscle superiorly and medially. A small portion of the gland may pass posterior to the mylohyoid muscle to lie within the sublingual area. Note should be taken on the anterior portion of the gland since the area contains lymph nodes [5–7].

Upon US examination of the submandibular gland, the ultrasound probe is placed sideways at the floor of the mouth at each side, parallel to the inferior border of the mandible. Regarding the anatomy of the region the following structures

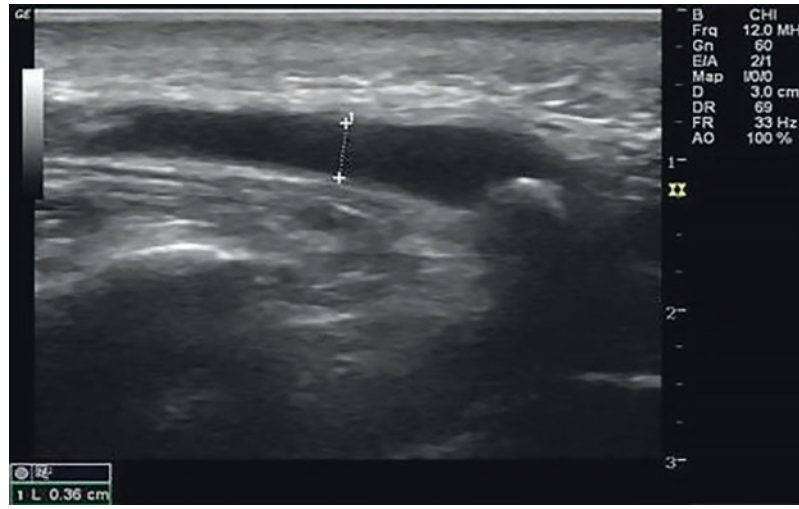

Fig. 9.1 A dilated Stensen duct due to drainage blockage makes it very easy to identify upon ultrasonographic examination the course of the duct

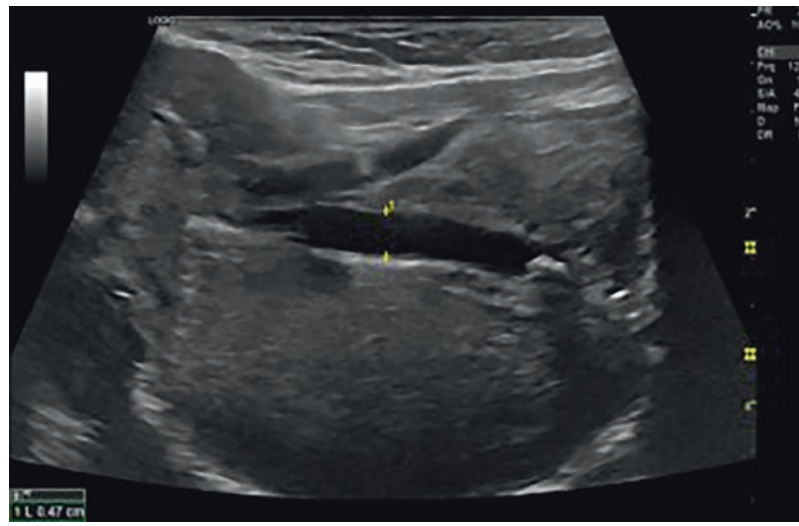

Fig. 9.2 Wharton's duct coursing under the floor of the mouth with dilatation is readily identified

should be noted [6, 7]: The gland itself, the crypts and acini and the main duct.

During ultrasonographic examinations in transverse sections, the gland is depicted with triangular shape. Its crypts are depicted as slightly sub-echoic areas, while the main duct is partially seen inside the glandular parenchyma. (Fig. 9.2).

With the applications of modern ultrasonographic techniques available, many authors claim that ultrasound can help identify inflammatory lesions and differentiate between benign and malignant lesions.

To help differentiate the types of lesions the variations in the shape and borders of the lesions as well as the reflected sound echostructure is studied [3, 5, 6].

Benign lesions are usually tumors with well-defined borders and in majority of cases of homogenous density.

Unlike benign tumors, malignant lesions are depicted with ill-defined borders and an inhomogeneous sound absorption pattern. There have been reported rare cases in the first stages of malignancy with low-grade differentiation where the lesions have well-defined borders.

9.2 Inflammatory Disease

9.2.1 Parotitis

Parotitis which as the name implies refers to glandular inflammation is the most common cause of parotid swelling in developed countries. The most frequent symptom includes noncontinuous pain and fever as well as unilateral or bilateral swelling of the glandular area. The inflammation is limited only to the area of the parotid gland, without involvement of the submandibular or sublingual glands [7]. It is of unknown etiology in a number of cases and the differential diagnosis include mumps or the suppurative parotitis, which is easily excluded from the clinical symptoms (in the case of mumps the glands are involved bilaterally and the skin lesions are prior to the glandular swelling, while in suppurative parotitis, there is unusual secretion from the glandular duct). The majority of cases involve children while there is episode reduction as the children grow, and they cease near puberty or in late adolescence [7, 8]. The male sex is more frequently affected. For the cases of parotitis in the past, sialography was the prime modality for glandular imaging by showing punctate or globular areas of sialectasis. Ultrasound is now the favored imaging approach. Most sonograms of parotitis show the characteristic enlarged parotid glands with multiple round, hypoechoic areas measuring 2–4 mm in diameter, likely representing peripheral sialectasis and lymphocytic infiltration [9–11]. The vascularity of the glands may increase secondary to the inflammation process. (Fig. 9.3, 9.4, 9.5 and 9.6).

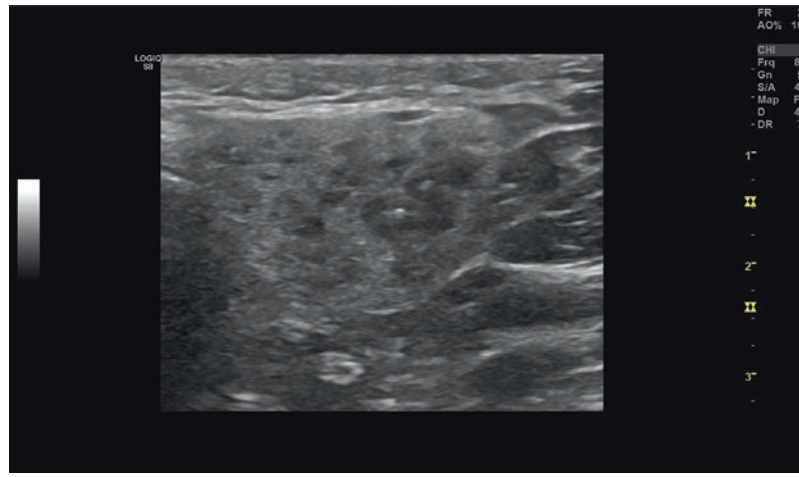

Fig. 9.3 Sialadenitis of the submandibular gland with a very characteristic pattern of inflammation of the acini with a spot-like appearance of the glandular parenchyma

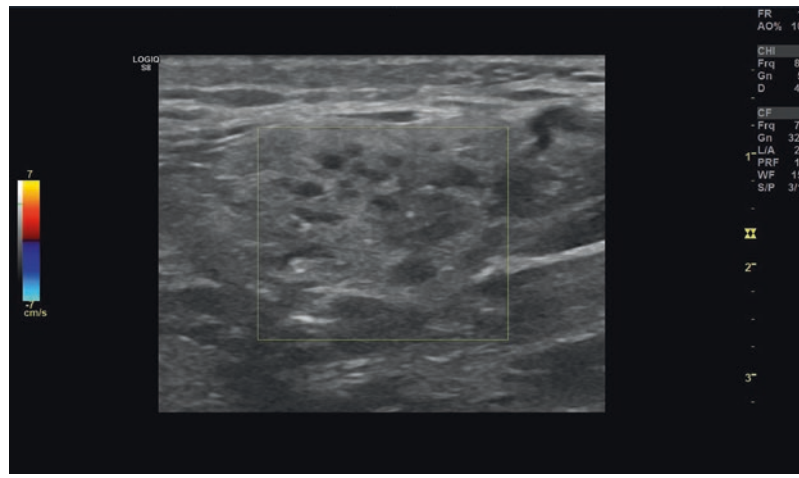

Fig. 9.4 The same lesion with the pattern of spot-like appearance of areas within the glandular parenchyma characteristic of inflammation but with the use of color Doppler. It is readily visible that there is no alterations on the vascularity of the lesion. An intraglandular lymph node is also present

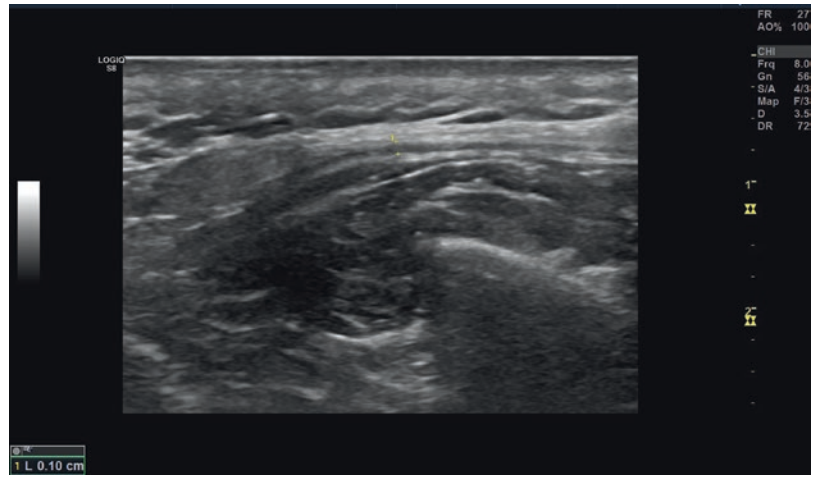

Fig. 9.5 Similar image of the previously inflamed gland showing areas of varying inflammation patterns. Though there are no spot like appearances in the region, inflammatory elements and alterations in the echogenicity of the gland are clearly observed

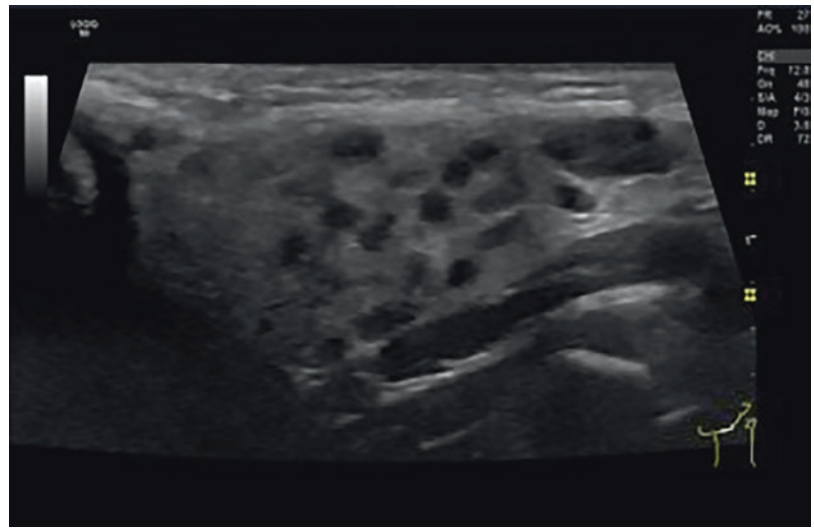

Fig. 9.6 Another case of very characteristic sonographic appearance where the duct of the gland is depicted as dilated due to the existing inflammation

9.2.2 Other Inflammatory Conditions

Chronic sialadenitis may affect all the major glands and is caused by inflammation that is not treated and rests, leading to alterations of the acini and secretory function of the glands. It is attributed to bacterial or nonbacterial inflammations. Clinically, the patients present with swelling and pain. Causes usually include granulomatous conditions such as actinomycosis and histoplasmosis. When of granulomatous etiology, they may appear with less inflammatory image features at ultrasound, and demonstrate a hypoechoic mass with poorly refined margins. Bacterial gland infection is more common, usually presenting at childhood with more common ages from 2–4 years of age. In many cases, abscesses are formed and treatment is required (Figs. 9.7 and 9.8). With the use of color Doppler, abscesses present peripheral blood flow or none at all, due to necrotic debris.

Other inflammatory conditions with similar ultrasonographic features are autoimmune diseases and recurrent sialolithiasis [7–11]. Sjögren's syndrome is an autoimmune disorder that results in inflammation and destruction of the exocrine glands, primarily the lacrimal and salivary glands. To avoid cumulative radiation to the patient at follow-ups it is preferable to monitor them with ultrasound and not with CT scan.

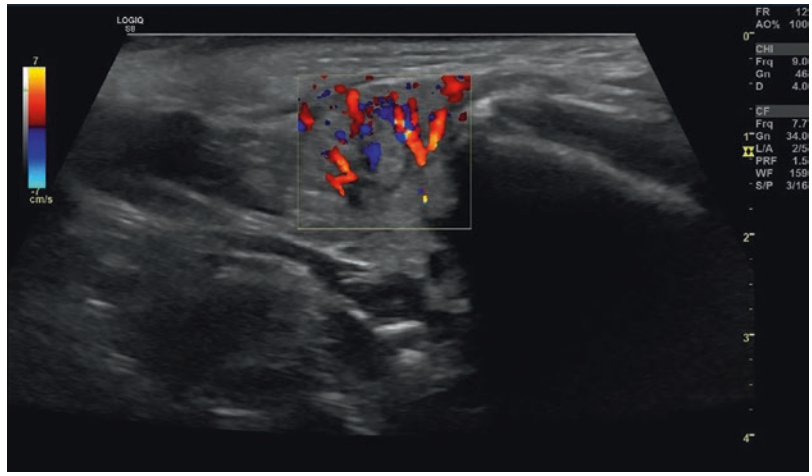

Fig. 9.7 Intraparotid abscess. The inflammation is more diffused and the vascularity of the lesion is very high with the use of color Doppler

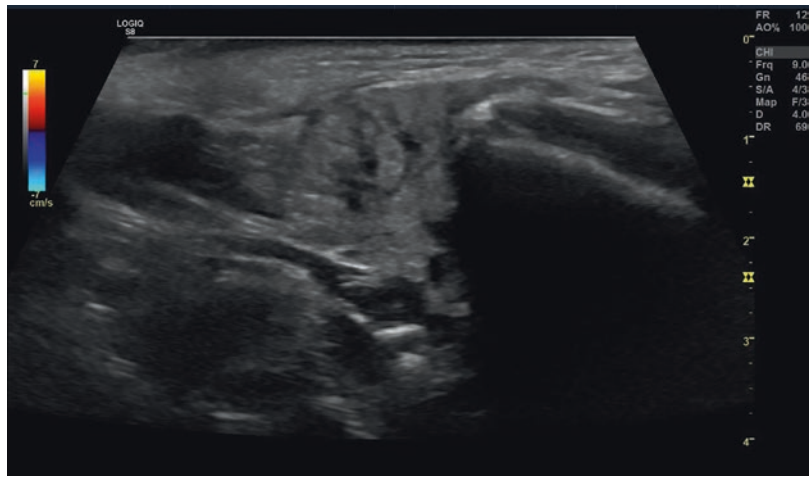

Fig. 9.8 The same abscess of the parotid gland with diffused non-clear borders but characteristic echogenicity of inflammation

9.2.3 Inflammation from Drainage Failure Due to Calcification (Salivary Stone or Sialolithiasis)

The most common reason for inflammation of a single salivary gland is in 80% of cases the presence of a sialolith [7, 12, 13]. Salivary stones form usually within the duct of the glands with more frequent the Wharton's duct of the submandibular gland. They are hard stone-like structures, that form within the gland. They are made of mineral stones, they are slow in development, and they may block the ductal system of the gland. When this happens, the drainage of the gland is blocked, the patient demonstrates pain and swelling and inflammatory features of the glandular system. With the use of ultrasound, the stone may be readily visible, but in many cases the acoustic shadow of the calculi may be all that is visualized. The use of ultrasound is crucial since it visualizes the glandular parenchyma easily [14, 15] (Figs. 9.9 and 9.10).

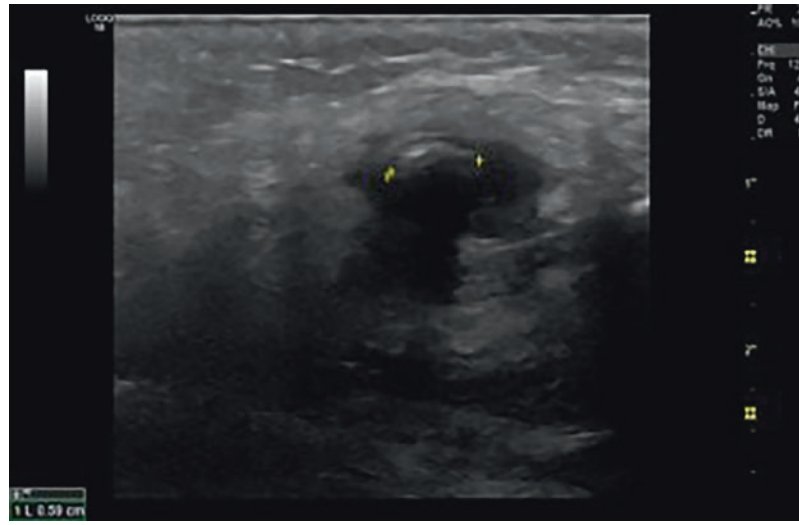

Fig. 9.9 Salivary gland lithiasis. The area measured represents the size of the stone within the gland with the characteristic acoustic shadow behind the stone due to the echostructure of the lesion (black area)

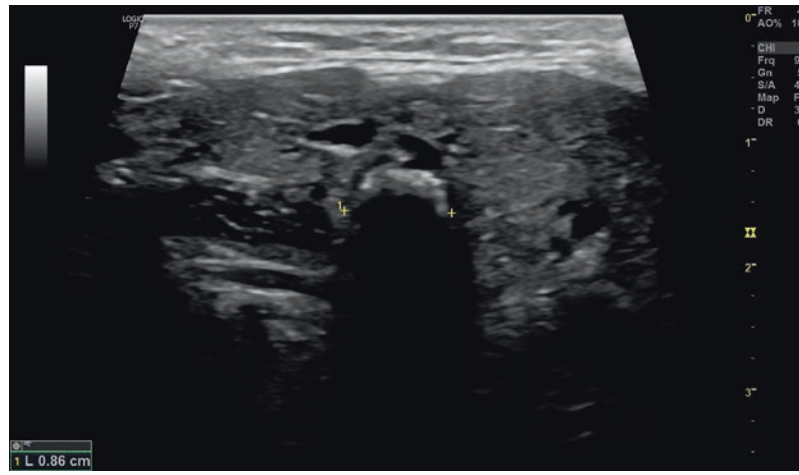

Fig. 9.10 Similar acoustic shadow behind a large salivary stone

9.3 Sjögren's Syndrome

Sjögren's syndrome and other autoimmune diseases, including HIV, are risk factors for primary lymphoma of salivary glands. The syndrome involves all exocrine glands and the primary diagnostic symptoms are usually from the eyes with decrease of lacrimal gland excretions [16]. In the salivary glands involved, ultrasonography, particularly in the acute inflammation phase, demonstrates a diffused enlargement of the gland. Lesions may consist of multiple small, hypoechoic nodules or an irregularly shaped, heterogeneous mass without calcification or anechoic cystic degeneration [17–19]. The imaging features are similar to lymphomas and/or adenitis. Some authors in chronic conditions describe the presence of hypoechoic compartments surrounded by hyperechoic fibrotic tissue, creating a tortoiseshell appearance. Increased color and Doppler flow are typical only in acute phases. Most patients with Sjogren's syndrome have a known autoimmune history. (Figs. 9.11 and 9.12).

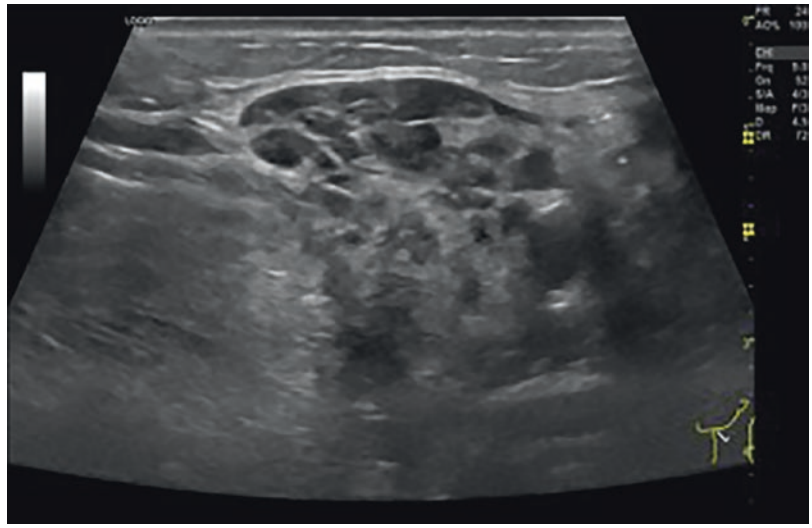

Fig. 9.11 Sjogren syndrome of the submandibular gland with the characteristic similar to inflammation lesions but usually localized bilaterally

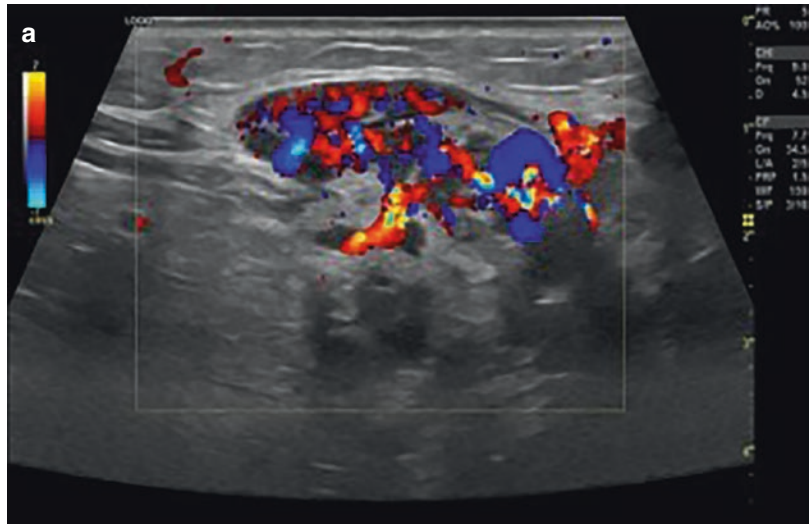

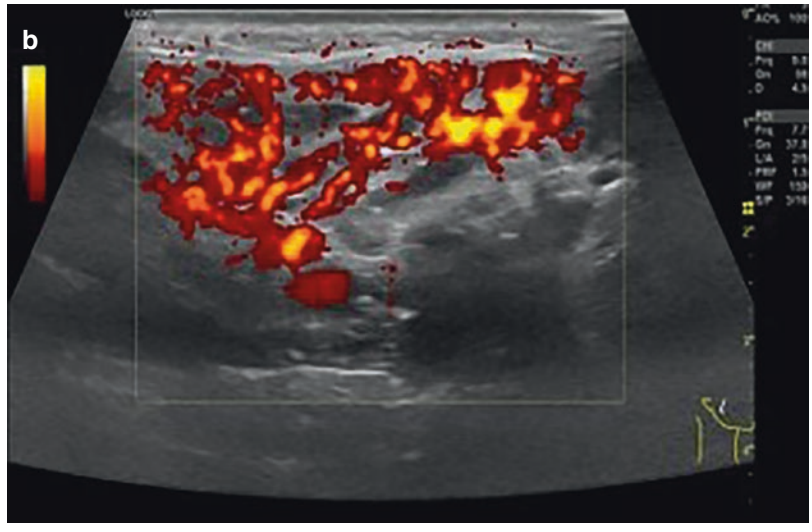

Fig. 9.12 The same submandibular gland of the previous figure with characteristic high vascularity of the lesion in (**a**) which gives higher detail with the use of B-flow in (**b**)

9.4 Neoplasms

Neoplasms of the salivary gland are seen in all age groups and range in frequency according to various authors**.** They constitute about 8% of all primary head and neck tumors, where 90–95% of them occur in the parotid and the rest in the submandibular and sublingual glands. Most masses of the salivary gland are benign and have vascular etiology (about 60%). The majority of cases unfortunately due to the slow and mild swelling which in many cases is painless may not be diagnosed at early stages [20–25].

Ultrasonography is a very useful tool with no radiation and often serves as the initial examination particularly in children. It is extremely useful in the diagnosis and in setting the characteristics of superficial lesions of the glands. With the use of ultrasound 95% of space-occupying lesions are categorized appropriately as benign or malignant and are described. With the proper use of ultrasound, focal from diffuse lesions can be distinguished, high vascularity lesions from low vascularity lesions and solid from cystic masses are well-defined and described [23–25].

9.4.1 Benign Tumors

9.4.1.1 Pleomorphic Adenomas

Pleomorphic Adenomas, also known as benign mixed-cell tumors or multiform adenomas, contain mesenchymal and epithelial originating cells. They are the most frequently occurring neoplasms of benign origin in patients at the fourth or fifth decade of their life and may appear in other age groups. They usually appear as single hard in texture, painless lesions with slow growth rate. The vast majority of the lesions occur in the parotid gland with a range from 60 to 90% while the rest present in the submandibular gland. In the parotid, they are more frequent in the superficial lobe of the gland. Mention should be made that the lesions may present as multiple lesions or bilaterally, though they rarely appear so. With the use of ultrasound, the lesions are lobulated, well-defined, hypoechoic, or sometimes isoechoic to the normal salivary gland. Though the lesion is usually of homogenous echogenicity, there may be cystic completely anechoic areas within the lesion and hyperechoic calcifications with shadowing [23, 25, 26]. Regarding the vascularity of the lesions, they typically demonstrate peripheral blood flow and no central increase. (Figs. 9.13, 9.14 and 9.15).

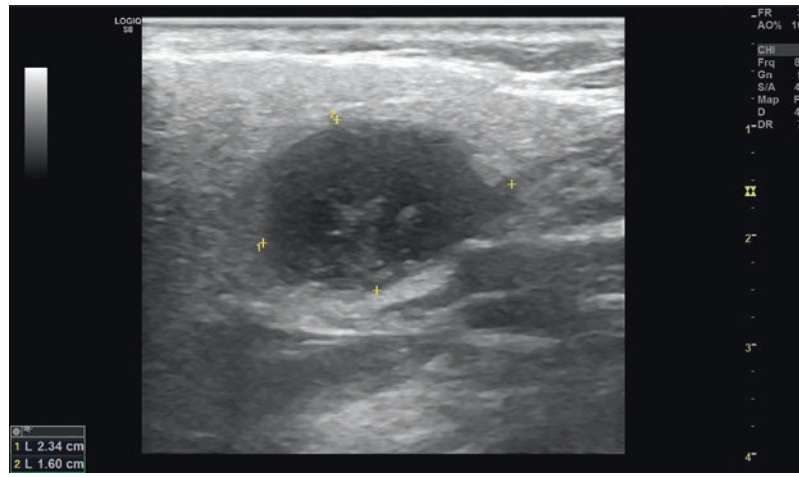

Fig. 9.13 Multiform adenoma of the parotid gland with characteristic single (usually) with clear border lesions similar to a cyst-like structure but with different echogenicity

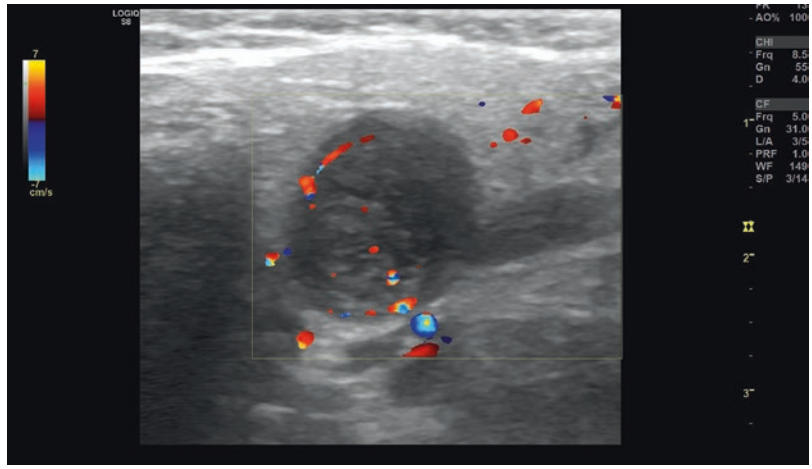

Fig. 9.14 Multiform adenoma with the single lesion with varying echogenicity content and peripheral vascularity

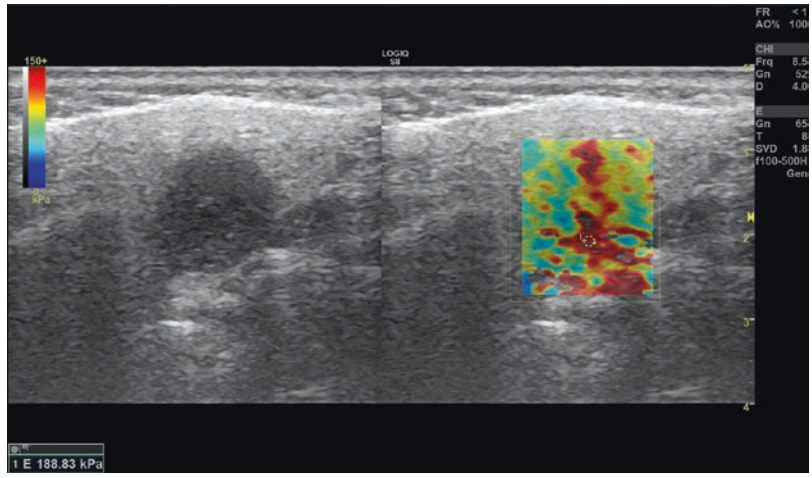

Fig. 9.15 Elastography of a multiform adenoma. The lesions present with varying values of elasticity and characteristic hardness compared to the regular glandular parenchyma

9.4.1.2 Warthin's Tumor

Warthin's tumor or cystic adenolymphoma is the second most common benign salivary gland neoplasm and is almost solely seen in the parotid gland. The lesion is thought to originate from incorporation of lymphatic elements and heterotopic ductal epithelium within the parotid lymph nodes. Typically, the lesion is presented as a painless, solitary, slow-growing mass, which in about 20% of cases is bilateral. With the use of ultrasound, one sees a single or lobulated hypoechoic lesion which is well-defined and often contains microcystic or anechoic areas with a tendency to cystic changes [25, 26]. The lesion has high vascularity with the use of color Doppler. (Figs. 9.16, 9.17 and 9.18).

9.4.2 Malignant Tumors

9.4.2.1 Mucoepidermoid Carcinoma

Mucoepidermoid carcinoma is the most frequently occurring malignant neoplasm in children and consists of cords, sheets, or cystic spaces lined by squamous and mucous cells. They constitute 60% of all malignancies of the salivary glands and about 50% of them arise

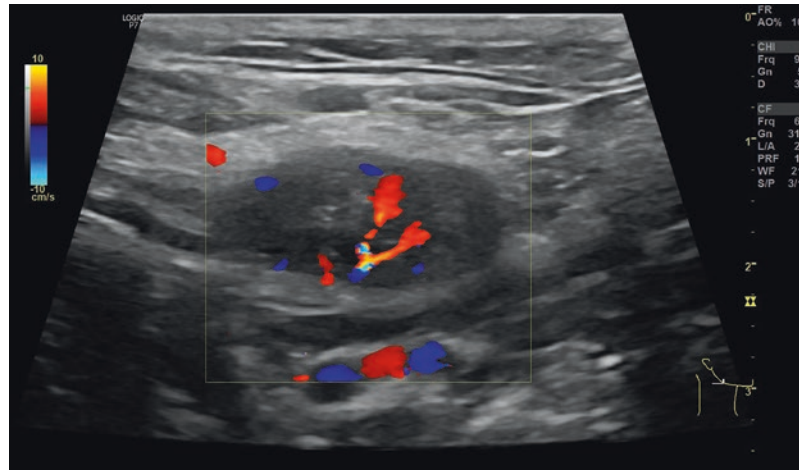

Fig. 9.16 Wharthin's tumor with a varying echostructure lesion and different internal content

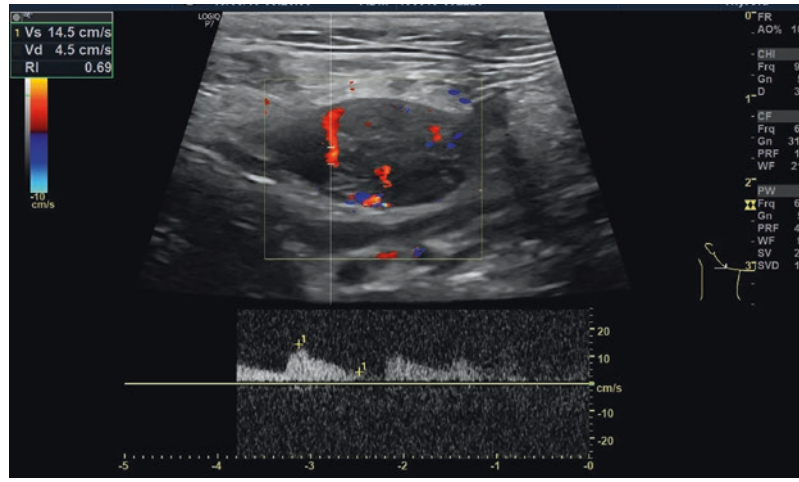

Fig. 9.17 Wharthin's tumor with a vessel checked for the specter of the flow

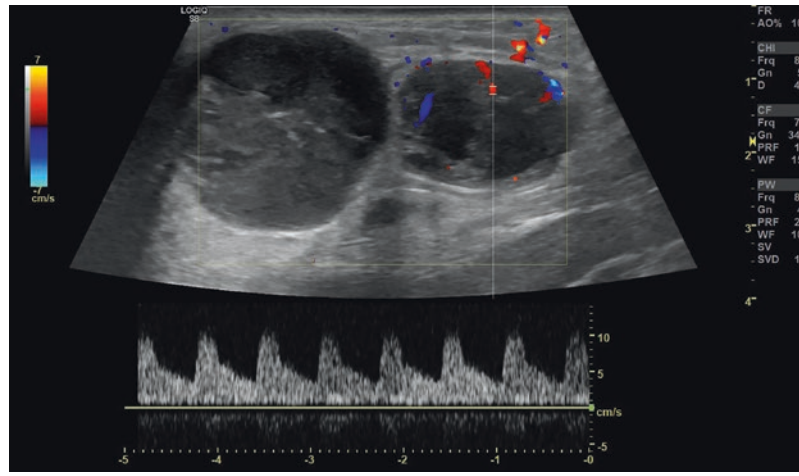

Fig. 9.18 Wharthin's tumor with an abscess adjacent to the tumor. The high vascularity of the second lesion helps differentiate between the two types of lesions

from the parotid gland. They are usually tender lesions in the beginning but they soon turn to palpable hard nonmobile lesions with rapid growth and are often clinically accompanied by facial nerve palsy with local itchiness. The ultrasonographic features depend on the grade of malignancy and the extent of the lesion. In the initial lower grade lesions, the lesion may be homogenous and well-defined, while in later stages higher grade lesions are irregular, poorly defined, with hypoechoic heterogeneous internal architecture [27, 28]. Regarding the use of color Doppler in the initial stages, it is not easy to differentiate benign from malignant lesions, but the appearance of increased intratumoral resistance index (RI) and high peak systolic flow velocity (PSV > 60 cm/s) should increase suspicion for malignancy. Note should be taken on the use of ultrasonography in the differentiation of pathological lymph nodes of the area, in contrast to reactive lymph nodes which may appear as a result of inflammation. The use of ultrasound is to initially differentiate the pathology of the adjacent to the lesion lymph nodes, and help set the final diagnosis. (Figs. 9.19 and 9.20).

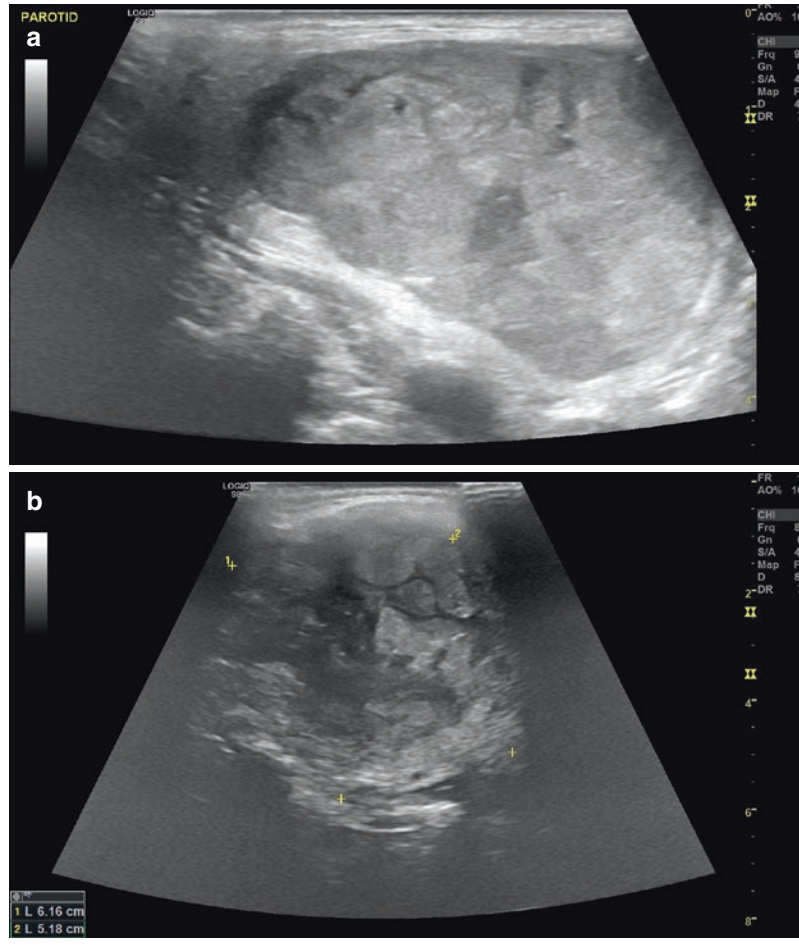

Fig. 9.19 A large mucoepidermoid carcinoma of the parotid.(**a**) the lesion shows varying textures and echostructure and though the borders are clear they appear rugged at areas. (**b**) the two dimensions of the lesions are easily measured

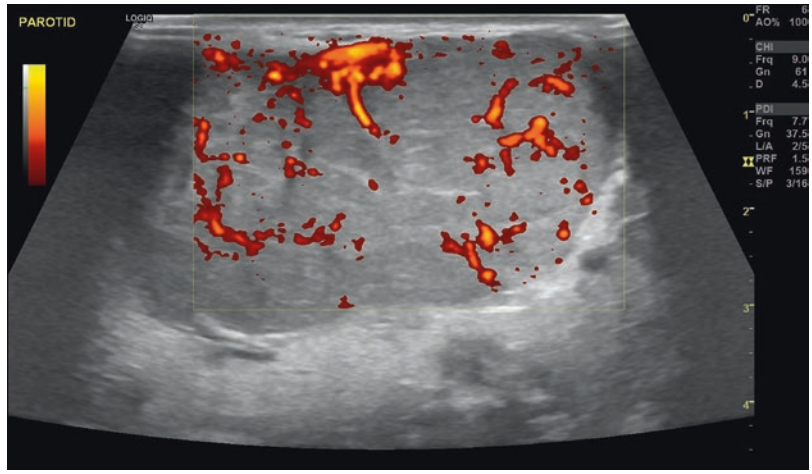

Fig. 9.20 B-flow of a large-sized lesion of the parotid gland. The lesion was of high flow but not very high vascularity

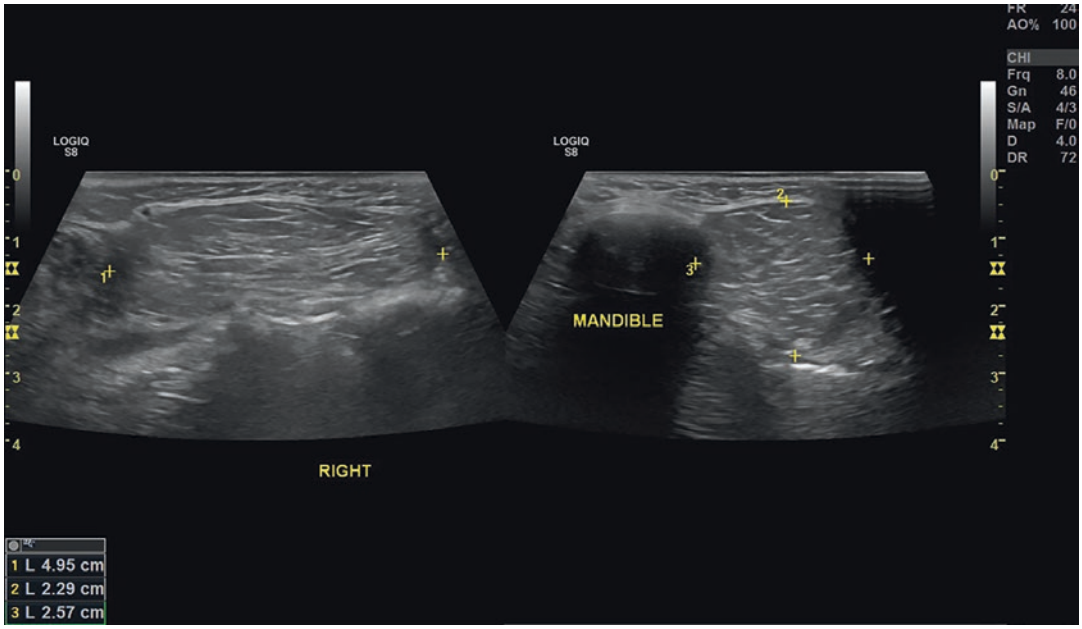

Fig. 9.21 A lipoma of the parotid gland measured in both transverse and sagittal planes

9.4.3 Other Masses

Lipomas represent 1% of parotid tumors; 57% of lipomas in the parotid area arise within the gland. They are compressible, oval, and well-defined. On ultrasound, they contain striped or feathered internal echoes devoid of color and Doppler flow (Fig. 9.21) [27].

Rhabdomyosarcoma occurs 40% of the time in the head and neck and can arise from any muscle. It is the second most common salivary gland malignancy. Salivary gland involvement is frequently by direct extension.

Primary Lymphoma of the salivary glands is termed MALToma, denoting origin from mucosa-associated lymphoid tissue.

Leukemic infiltration is rare, presenting similar to lymphoma on ultrasound.

Metastatic disease is rare in children but would include neuroblastoma, squamous cell carcinoma, melanoma, and thyroid cancer [28].

9.5 Vascular Masses

Hemangiomas are the most common vascular lesions in the salivary gland areas and are more often present in infants and children. They constitute masses that are benign in origin composed of proliferating endothelial cells. Hemangiomas represent 60% of head and neck neoplasms and 60% of all salivary gland neoplasms. Hemangiomas occur three times more often in girls than in boys.

They usually present as painless, movable, slow in growth, and half of them have a bluish or red stain in the skin superficial to the lesion. Hemangiomas are usually visible from birth, but about 95% of the lesions present within the first 6 months of life. They typically have an initial proliferation phase during the first year of life, and after that they usually show spontaneous recession and involution until the age of 6–7 years. Their vast majority present in the parotid area and they are rarely seen in the submandibular area. During an ultrasonographic scan the lesions are usually hyperechoic when compared to the normal parotid gland, and well outlined. There is high vascularity particularly in the first year of life when the lesions increase in size. The vessels that are prominent are both arterial and venous. Since they spontaneously regress, their management usually does not involve surgical excision, but regular follow-up and/or treatment with corticosteroids or in rare cases when the symptoms require it surgical excision.

9.6 Salivary Gland Elastography

Elastography is the newest addition to the various technologies in ultrasound examination. The different existing elastography systems can evaluate histological information by depicting the distribution of tissue stiffness in addition to the more typical differentiation between malignant and benign tissues [26]. This has an effect on the treatment planning and the various therapeutical procedures. It allows for the diagnosis and evaluation not only of masses but also of nonmass lesions.

Since malignant tissues are generally stiffer than benign tumors, sonoelastography has been used in many organs, particularly in the breast and thyroid as well as prostate and lymph nodes, for establishing the differential diagnosis between malignant and benign lesions required [29–32].

In the cases of salivary glands, the gold standard for preoperative procedures is ultrasound-guided fine needle aspiration cytology (FNAC) but it remains invasive, and noninvasive techniques are often preferred thus setting elastography as a method of choice with similar results.

Sonoelastography is very handy in the cases of the major salivary glands, especially in the parotid. Though numerous studies have been written on the use of sonoelastography in salivary glands, the sensitivity of the technique ranges from 40 to 100% and its specificity from 26 to 97%.

The major differences are in the type of elastographic technique used and the probe frequency and depth used [33–39].

False positive results may occur from glands like the parotid which is firmly attached to the mandible and thus does not allow for all lesions to be studied properly with strain elastography, while shear wave elastography provides better results.

In elastography, one should take into account the false positive and negative measurements that may present.

False positive

- Lesions containing calcifications and cystic degeneration or necrosis. For the Strain ratio calculations, we avoid those areas and try to take measurements from the more compound sections of the tumors (as in thyroid, breast).

False negative

- Lobular carcinoma and other soft tissues of the region.
- Cystic carcinoma.
- Deep lesions >4–5 cm (strain elastography).

References

1. Noce JP. Fundamentals of diagnostic ultrasonography. Biomed Instrum Technol. 1990;24(6):456–9.
2. Katz P, Hartl DM, Guerre A. Clinical ultrasound of the salivary glands. Otolaryngol Clin N Am. 2009;42(6):973–1000.
3. Gooding. Gray scale ultrasonography of the neck. JAMA. 1980;243(15):1562–4.
4. Gooding GA. Gray scale ultrasound of the parotid gland. AJR Am J Roentgenol. 1980;134(3):469–72.
5. Gritzmann N. Sonography of the salivary glands. Am J Roentgonol. 1989;153:161–6.
6. Bialek EJ, Jakubowski W, Zajkowski P, Szopinski KT, Osmolski A. US of the major salivary glands: anatomy and spatial relationships, pathologic conditions, and pitfalls. Radiographics. 2006;26:745–63.
7. Yu C, Zheng L, Yang C, Shen N. Causes of chronic obstructive parotitis and management by sialoendoscopy. Oral Surgery, Oral Medicine, Oral Pathology, Oral Radiology, and Endodontology. 2008;105(3):365–70.
8. Mandel L, Surattanont F. Bilateral parotid swelling: a review. Oral Surgery Oral Medicine Oral Pathology Oral Radiology & Endodontics. 2002;93(3):221–37.
9. Baurmash HD. Chronic recurrent parotitis: a closer look at its origin, diagnosis, and management. J Oral Maxillofac Surg. 2004;62:1010–8.
10. Bradley PJ. Microbiology and management of sialadenitis. Curr Infect Dis Rep 2002;4:217–224. [PubMed].
11. Brook I. Acute bacterial suppurative parotitis: microbiology and management. J Craniofac Surg. 2003;14:37–40.
12. Cho W, Lim D, Park H. Transoral sonographic diagnosis of submandibular duct calculi. J Clin Ultrasound. 2014;42:125–8.
13. Joshi AS, Lohia S. Ultrasound indicators of persistent obstruction after submandibular sialolithotomy. Otolaryngol Head Neck Surg. 2013;149:873–7.
14. Caglayan F, Sumbullu MA, Miloglu O, Akgul HM. Are all soft tissue calcifications detected by cone-beam computed tomography in the submandibular region sialoliths? J Oral Maxillofac Surg. 2014;72(1531):e1531–6.
15. Yoshimura Y, Inove Y, et al. Sonographic examination of sialolithiasis. J Oral Maxillofac Surg. 1989;47:907–12.
16. Brito-Zerón P, Baldini C, Bootsma H, Bowman SJ, Jonsson R, Mariette X, Sivils K, Theander E, Tzioufas A, Ramos-Casals M. Sjögren syndrome. Nat Rev Dis Primers. 2016;2:16047.
17. Niemelä RK, Takalo R, Pääkkö E, Suramo I, Päivänsalo M, Salo T, Hakala M. Ultrasonography of salivary glands in primary Sjogren's syndrome. A comparison with magnetic resonance imaging and magnetic resonance sialography of parotid glands. Rheumatology (Oxford). 2004;43(7):875–9.
18. Mansour N, Bas M, Stock KF, Strassen U, Hofauer B, Knopf A. Multimodal ultrasonographic pathway of parotid gland lesions. Ultraschall Med. 2017;38:166–73.
19. Jonsson MV, Baldini C. Major salivary gland ultrasonography in the diagnosis of Sjögren's syndrome: a place in the diagnostic criteria? Rheum Dis Clin N Am. 2016 Aug;42(3):501–17.
20. Bruneton JN, Fenart D, et al. Ultrasonic findings of parotid tumors in 40 patients. J Radiol. 1980;61(3):151–4.
21. Bozzato A, Zenk J, Greess H, et al. Potential of ultrasound diagnosis for parotid tumors: analysis of qualitative and quantitative parameters. Otolaryngol Head Neck Surg. 2007;137:642–6.
22. Badea AF, Bran S, Tamas-Szora A, Floareş A, Badea R, Baciut G. Solid parotid tumors: an individual and integrative analysis of various ultrasonographic criteria. A prospective and observational study. Med Ultrason. 2013;15:289–98.
23. Joshi PS, Pol J, Sudesh AS. Ultrasonography: a diagnostic modality for oral and maxillofacial diseases. Contemp Clin Dent. 2014;5:345–51.
24. Lee YY, Wong KT, King AD, Ahuja AT. Imaging of salivary gland tumours. Eur J Radiol. 2008;66:419–36.
25. Yu J, Du Y, Lu Y, et al. Application of DTI and ARFI imaging in differential diagnosis of parotid tumours. Dentomaxillofac Radiol. 2016;45:20160100.
26. Wakasugi-Sato N, Kodama M, et al. Advanced clinical usefulness of ultrasonography for diseases in oral and maxillofacial regions. Int J Dent. 2010;2010:639382.
27. Luigi S, Vincenzo C. Ultrasonography of the neck. Radiol Clin N Am. 1992;30(5):941–53.
28. Yuasa K, Kawazu T, et al. Computed tomography and ultrasonography of metastatic cervical lymph nodes in oral squamous cell carcinoma. Dentomaxillofac Radiol. 2000;29:238–44.
29. Pinto F, Totaro A, Calarco A, et al. Imaging in prostate cancer diagnosis: present role and future perspectives. Urol Int. 2011;86:373–82.
30. Seitz M, Strittmatter F, Roosen A, Tilki D, Gratzke C. Current status of ultrasound imaging in prostate cancer. Panminerva Med. 2010;52:189–94.
31. Bhatia KS, Tong CS, Cho CC, Yuen EH, Lee YY, Ahuja AT. Shear wave elastography of thyroid nodules in routine clinical practice: preliminary observations and utility for detecting malignancy. Eur Radiol. 2012;22:2397–406.
32. Evans A, Whelehan P, Thomson K, et al. Differentiating benign from malignant solid breast masses: value of shear wave elastography according to lesion stiffness combined with greyscale ultrasound according to BI-RADS classification. Br J Cancer. 2012;107:224–9.
33. Cantisani V, David E, De Virgilio A, et al. Prospective evaluation of quasistatic ultrasound elastography (USE) compared with baseline US for parotid gland lesions: preliminary results of elasticity contrast index (ECI) evaluation. Med Ultrason. 2017;19:32–8.
34. Klintworth N, Mantsopoulos K, Zenk J, Psychogios G, Iro H, Bozzato A. Sonoelastography of parotid

gland tumours: initial experience and identification of characteristic patterns. Eur Radiol. 2012;22:947–56.
35. Wierzbicka M, Kałuzny J, Szczepanek-Parulska E, et al. Is sonoelastography a helpful method for evaluation of parotid tumors? Eur Arch Otorhinolaryngol. 2013;270:2101–7.
36. Celebi I, Mahmutoglu AS. Early results of real-time qualitative sonoelastography in the evaluation of parotid gland masses: a study with histopathological correlation. Acta Radiol. 2013;54:35–41.
37. Altinbas NK, Anamurluoglu EG, Oz II, et al. Real-time sonoelastography of parotid gland tumors. J Ultrasound Med. 2017;36:77–87.
38. Bhatia KS, Rasalkar DD, Lee YP, et al. Evaluation of real-time qualitative sonoelastography of focal lesions in the parotid and submandibular glands: Applications and limitations. Eur Radiol. 2010;20:1958–64.
39. Herman J, Sedlackova Z, Vachutka J, et al. Differential diagnosis of parotid gland tumors: role of shear wave elastography. Biomed Res Int. 2017;2017:9234672.

10 Sonographic Anatomy and Pathology: Temporomandibular Joint

Kaan Orhan and Ingrid Rozylo-Kalinowska

Contents

10.1 General Consideration for Application of Ultrasound in TMJ Diagnostics

In diagnostics of TMJ high-frequency linear probes (preferably over 12 MHz) with a relatively small "footprint" are used as they offer high resolution of image with a relatively low penetration depth which is sufficient in examinations of these superficially located joints. Intraoral

K. Orhan (✉)
Faculty of Dentistry, Department of Dentomaxillofacial Radiology, Ankara University, Ankara, Turkey

I. Rozylo-Kalinowska
Department of Dental and Maxillofacial Radiodiagnostics, Medical University of Lublin, Lublin, Poland

K. Orhan (ed.), *Ultrasonography in Dentomaxillofacial Diagnostics*,
https://doi.org/10.1007/978-3-030-62179-7_10

probes are useful in imaging of masticatory muscles, instead of infrequent finger probes or finger-tip probes, an intraoperative "hockey stick" probe can be successfully applied.

US scanning of TMJ is performed in a patient lying on a special examination bed or sitting upright. A water-soluble gel is generously administered on the patient's skin within the region of interest in order to eliminate air bubbles from between the skin and the probe since ultrasound is strongly reflected by gases [1, 2]. The transducer is then placed parallel to the Frankfurt horizontal plane and at 60–100° to the plane, parallel to the ramus of mandible, both in open and closed mouth position (Fig. 10.1a–d). However, it must be remembered that since US is a dynamic real-time examination, during the study the probe has to be moved gently over the studied area. Therefore the US images are never truly transverse or sagittal [3]. This obstacle can be overcome by using a 3D US probe [4, 5]. During the examination, multiple images are captured and the condyle movement range can be registered as well. Complementary US scanning of masticatory muscles may be performed.

One of the disadvantages of US is high dependency on operator's skills and experience [6]. Another disadvantage of the utmost importance in diagnostics of TMJ is that it is not possible to demonstrate structures located behind the intact bone surface, as the beam is fully reflected off dense outer cortex. Therefore, only a part of TMJ is accessible for US—the articular capsule, the disc, and cortex of laterosuperior aspect of the condyle are visible [7]. Another limitation of TMJ US imaging is osteoarthritis with reduction of joint space width and formation of bony spurs further decreasing area available for penetration with an ultrasound beam [1]. All this discourages

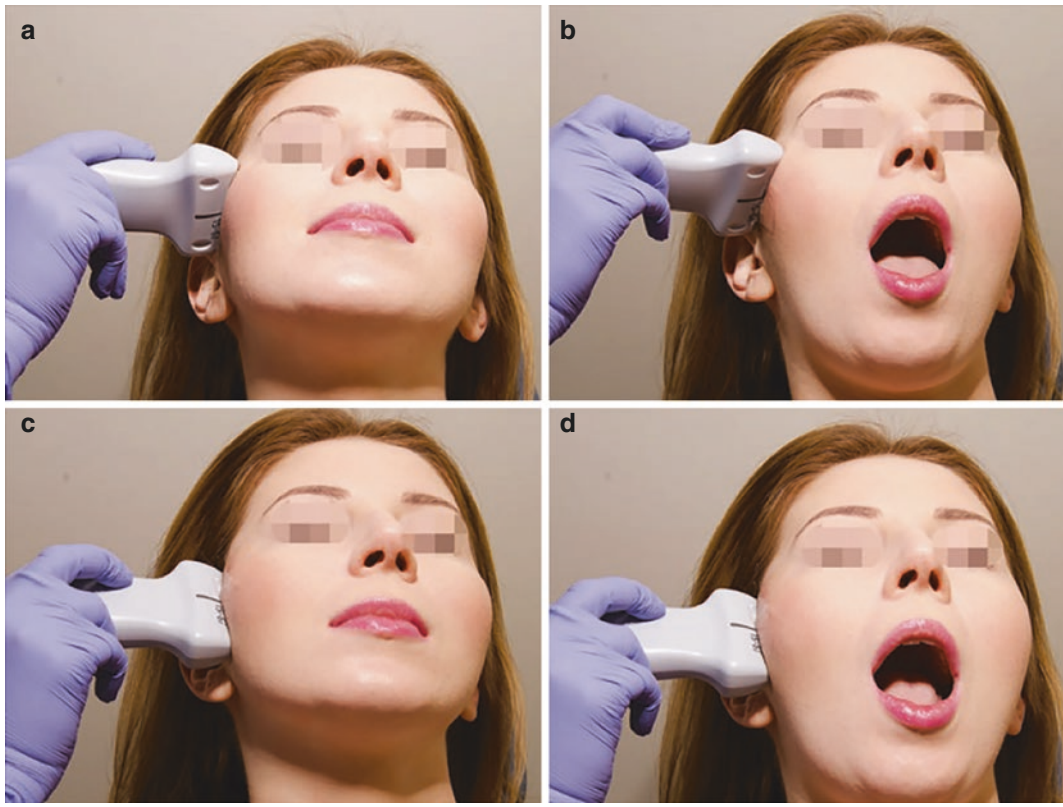

Fig. 10.1 Ultrasound examination of the right TMJ. The transducer is placed parallel to the Frankfurt horizontal plane in closed (**a**) and open (**b**) mouth position as well as at 60–70° to the plane, parallel to the ramus of mandible, both in closed (**c**) and open (**d**) mouth position

some operators from using US in this joint at all, and MR is preferred for that purpose [8].

Reported sensitivity, specificity, and accuracy values of ultrasound vary in broad ranges, e.g., according to Melis et al. [9] sensitivity of US in assessment of disc displacement falls between 13 and 100%, specificity from 62 to 100% and accuracy in the range of 51.8 to 100%. In a meta-analysis by Dong et al. [10] comprising 1096 subjects from 11 studies, for anterior disc displacement with reduction, the pooled sensitivity and specificity were 83% and 85%, respectively while for the anterior disc displacement without reduction the weighted sensitivity and specificity values were 102% and 90%, respectively.

10.2 Indications and Contraindications for TMJ Ultrasound

As far as TMJ is concerned, the following applications were described:

- Joint effusion [11, 12].
- Internal derangement [13] and disc displacement, mainly anterior with and without reduction [5, 7, 14–18]; no studies reported data on lateral or posterior disc displacement [19].
- Osteoarthrosis including condylar erosion [4, 6, 20, 21].
- Rheumatoid, psoriatic, and juvenile idiopathic arthritis with TMJ involvement as well as polyarthritis [12, 22–26].
- Joint function basing on condylar translation range [27–32].
- Condylar movement using Duplex Doppler [33].
- Intraarticular TMJ dislocation [34].
- Guidance in fine needle aspiration cytology (FNAC).
- Guidance for TMJ arthrocentesis [35].
- Guidance in TMJ injections, e.g., with steroids.
- Soft tissue masses around TMJ (Fig. 10.2).

There are neither contraindications for ultrasound scanning nor special patient preparation required.

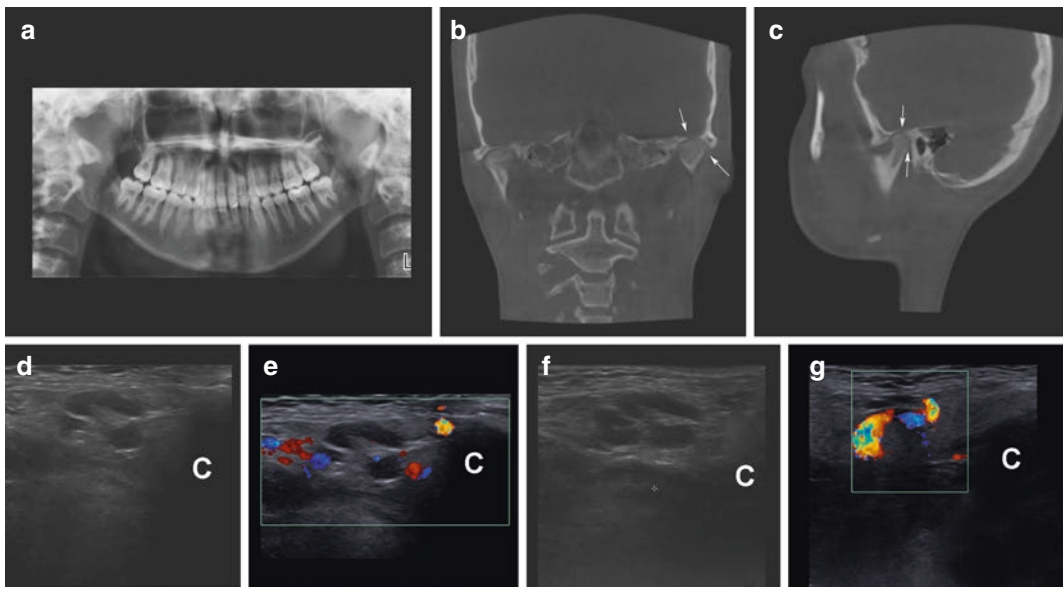

Fig. 10.2 A case of fibrosarcoma around TMJ (**a**) Panoramic radiography shows no abnormality due to superimposition in the left TMJ area, (**b**–**c**) Coronal and Sagittal CBCT images show irregularity and erosive area in the fossa of TMJ (arrows), (**d**, **f**) USG imaging showing hypoechoic area in transversal and longitudinal position, (e.g.) the lesion showing irregular hypoechoic vascularized mass around TMJ which was confirmed. C symbols TMJ condyle

Use of a gel stand-off pad may be necessary in case of very superficially located lesions, but a thick layer of gel with limited pressure on the probe may be applied in its stead (Ahuja and Evans 2013).

10.3 Normal Anatomy of TMJ in Ultrasound

Normal anatomy of TMJ in ultrasound is presented in Figs. 10.3, 10.4, 10.5, 10.6, 10.7 and 10.8.

10.4 Ultrasonography-Guided Invasive Procedures

10.4.1 Fine-Needle Aspiration Biopsy

The golden standard for diagnosis of pathologies concerning the temporomandibular joint is histopathological evaluation. In literature, fine needle aspiration biopsy is a proven method for obtaining pathological specimen and continuing histopathological evaluation.

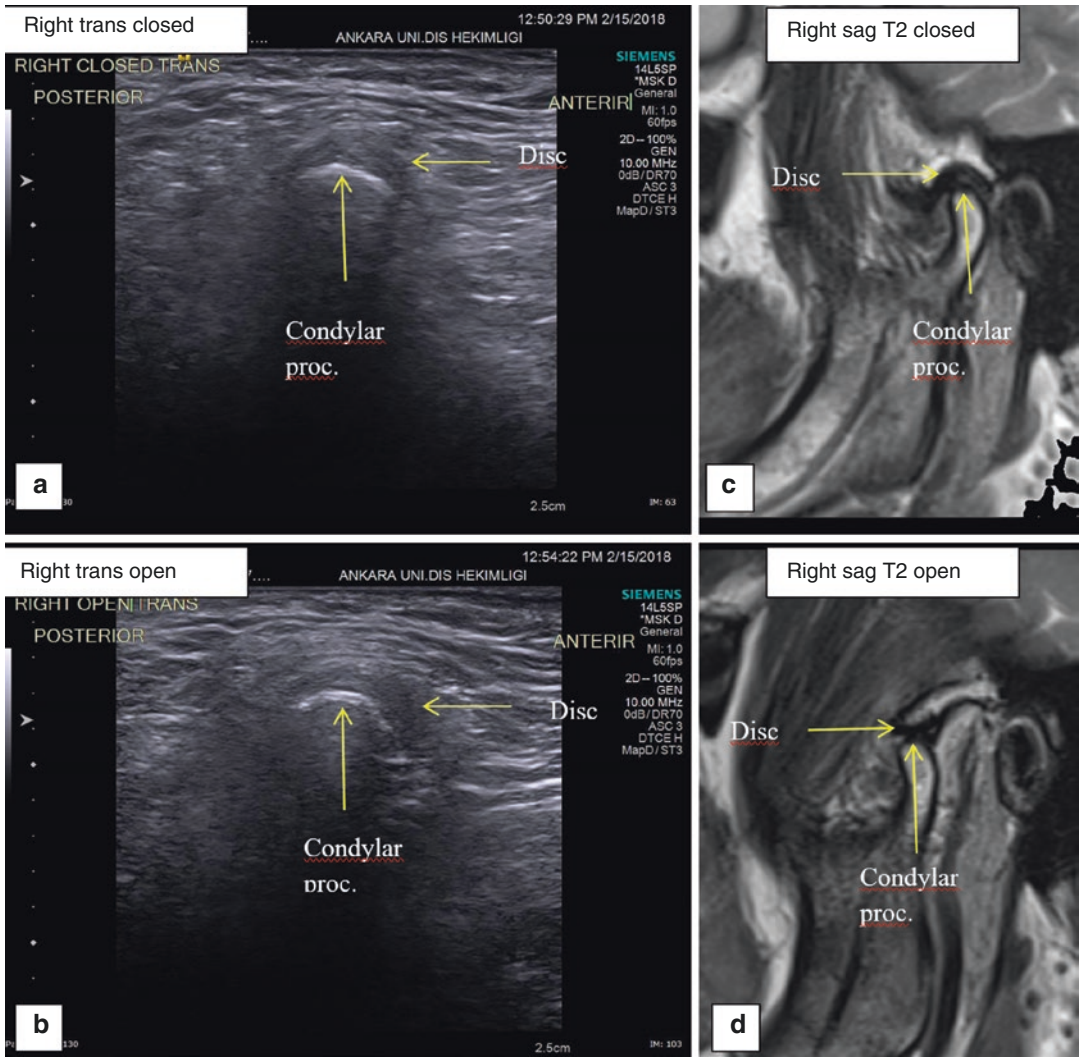

Fig. 10.3 (**a**) closed mouth; (**b**) open mouth, US (transducer placed transversally and MRI (sagittal plane) (**c**) closed mouth; (**d**) open mouth images showing right TMJ with normal disc position

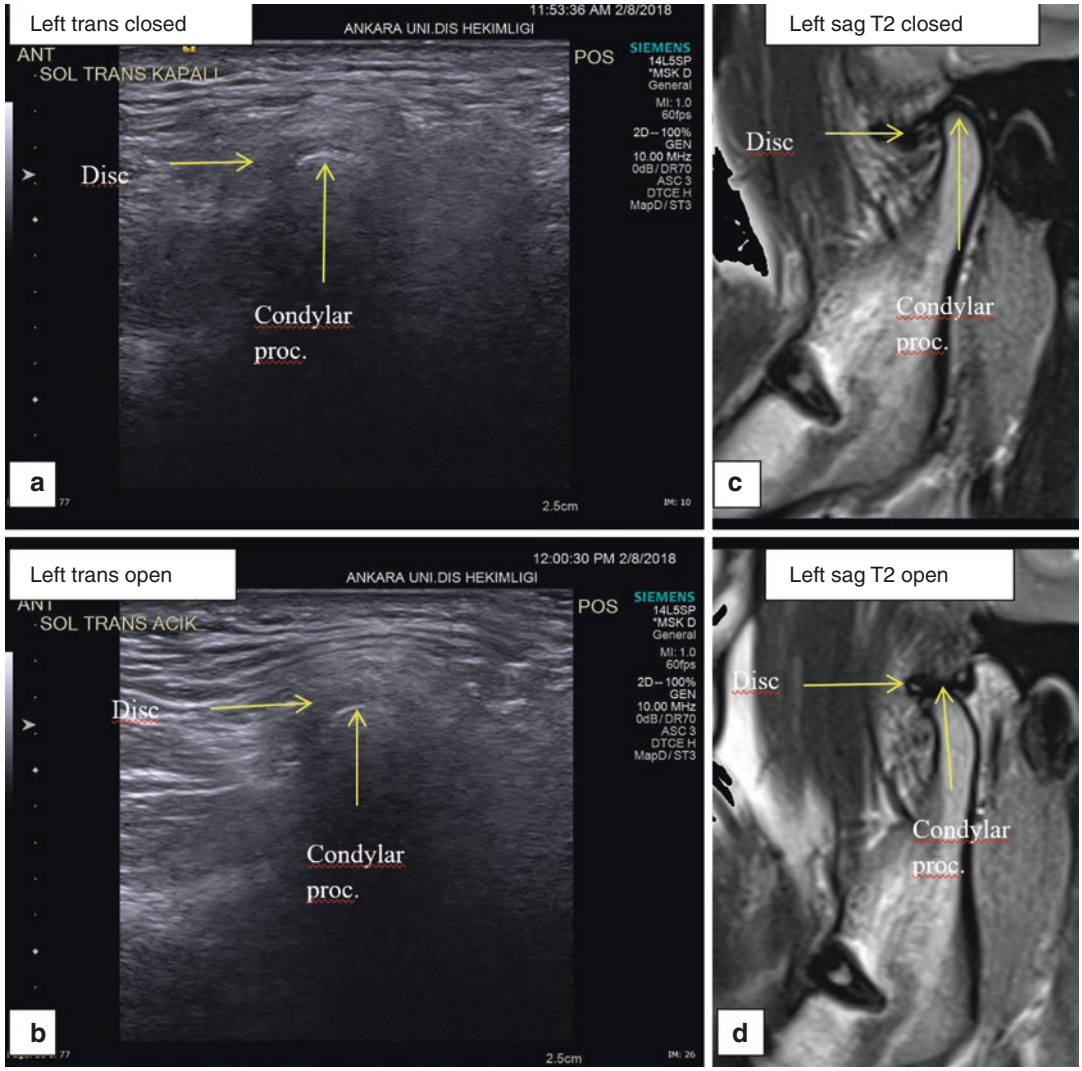

Fig. 10.4 (**a**) closed mouth; (**b**) open mouth, US (transducer placed transversally and MRI (sagittal plane) (**c**) closed mouth; (**d**) open mouth images showing left TMJ with disc displacement with reduction

Ultrasonography guidance while reaching the pathology is one of the primary methods that will ensure results that are more accurate. Features like easy access to this technology, ease of use for the radiologist, being a noninvasive procedure, and easily tolerated by the patients have made this technology a routine while performing fine needle aspiration biopsy.

Ultrasonography guided fine needle aspiration biopsy is a minor invasive procedure which can take place in an ambulatory setting, the patient can be discharged the same day and go back to the daily routine.

10.4.2 Ultrasonography-Guided Fine Needle Aspiration Biopsy

Being an invasive procedure fine needle aspiration biopsy should be planned under sterile conditions. Preparations should be made and checked before biopsy. As a minimal invasive method,

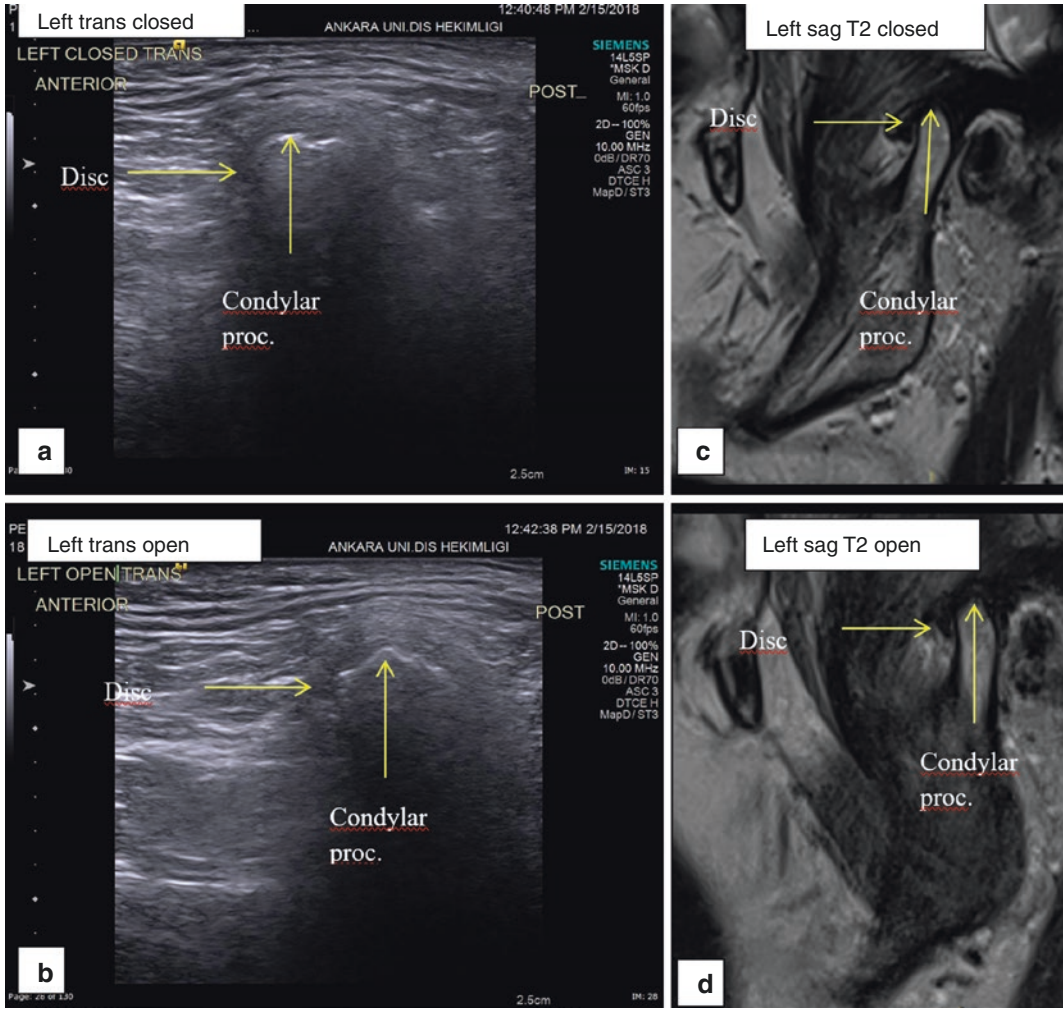

Fig. 10.5 (**a**) closed mouth; (**b**) open mouth, US (transducer placed transversally) and MRI (sagittal plane); (**c**) closed mouth; (**d**) open mouth images showing left TMJ with disc displacement without reduction

ultrasonography-guided fine needle aspiration biopsy could be realized with only one operator, while two operators are commonly preferred. One operator to perform the ultrasonography and guide the procedure while the other performs biopsy.

Before passing on to the procedure the anatomy of the region and pathology should be thoroughly examined with ultrasound by both the operators. This will give both the operators advantage before performing the biopsy. The area should then be wiped from the ultrasonography gel.

Sterile gloves should be worn and the region should be cleaned with skin disinfectants to achieve antisepsis. A local anesthetic solution containing 1:100.000 epinephrine should be carefully and slowly injected inside the temporomandibular joint capsule using a 210-gauge needle. This careful and slow application of local anesthetic should prevent any discomfort during the procedure.

After local anesthetic injection, the region must be palpated and "manually sensed." During palpation of the region, the patient should be instructed to slowly open and close the jaws. This

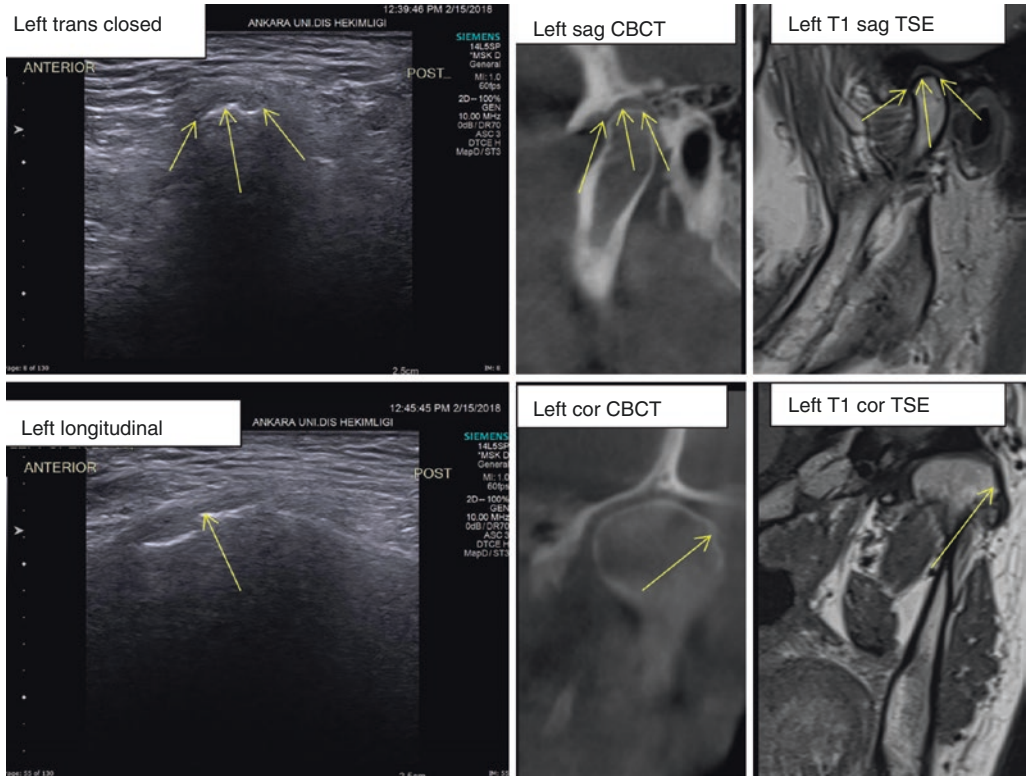

Fig. 10.6 Closed mouth US, CBCT, and MRI of the same patient with degenerative bone changes of left TMJ

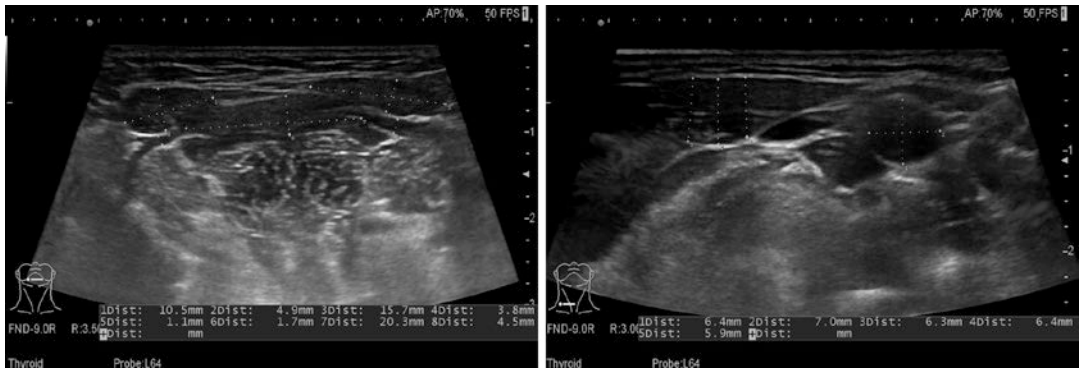

Fig. 10.7 US showing the measurements for anterior belly of digastric, geniohyoid complex, mylohyoid thickness as well as sternocleidomastoid muscle

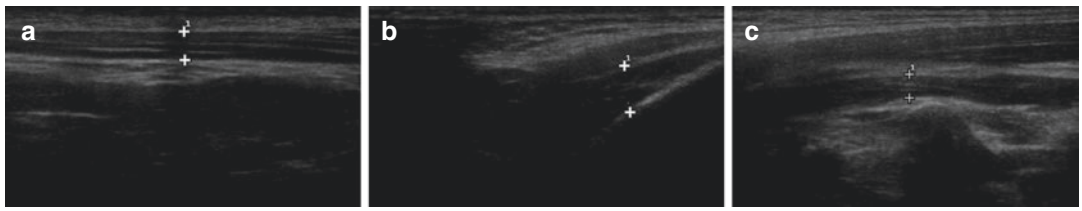

Fig. 10.8 US showing the measurements for posterior belly of digastric muscle, mylohyoid thickness as well as sternocleidomastoid muscle

motion will be helpful for detecting the zygomatic arch and mandibular condyle.

To identify the entrance point of the needle a soft ruler and dermal pen can be used. The ruler should be directed from the outer cantus of the eye to the tip of the outer ear tragus. On this imaginary line, a mark should be made 10 mm away anteriorly from the tragus tip. Another mark should be made on a second imaginary line parallel to the first one just 2 mm below the first mark. This second mark will be the entrance point of the needle. There will be approximately 25 mm from the skin mark to the temporomandibular joint.

A 23- or 210-gauge needle should be preferred. To increase the joint space patient should be instructed to open the jaws widely. The radiologist should then position the ultrasonography probe anterior to the entrance point. This settlement will ensure a comfortable procedure for the operator performing the biopsy. After visualization of the temporomandibular joint structures and associative pathology, the needle should be inserted from the specified mark with the bevel facing the temporomandibular joint. After some advancement, the tip of the needle should be recognized through ultrasonography. The needle should be then advanced into the structures in a posterior and superior route, into the pathology (Fig. 10.9).

Coordination between the two operators is essential during this phase. The ultrasonography operator should help the other operator channel the needle in the correct direction. After access to the pathology, the needle should be advanced to the center of the lesion. Under mild vacuum applied with the plunger, biopsy specimen should be obtained with light forward-backward movements of the needle. The needle should then be removed while mild vacuum continues and the specimen should be spread on a lamella. The specimen should then be sent for histopathological evaluation.

Following biopsy, the area should be closed with a sticking plaster with slight pressure, to prevent hematoma formation. Intermittent cold-pack applications and anti-inflammatory medication will be useful during the postoperative period.

10.4.3 Core Biopsy

Core biopsy is an invasive method, in need of special equipment. While soft tissue core biopsy needles measure around 1 mm, hard tissue core biopsy needles may measure up to 2 mm diameter. The core biopsy needle, produced especially for this procedure, enters the lesion while its blade is closed; when it is triggered the blade opens and closes at high-speed, obtaining the specimen. The specimen with an approximate length of 1 cm is then extracted. This large tissue is very valuable for a correct histopathological diagnosis. Thus, the most important advantage of core biopsy is that chance of accurate histopathological diagnosis is higher and additional biopsy procedures are needed less. Nevertheless, hemor-

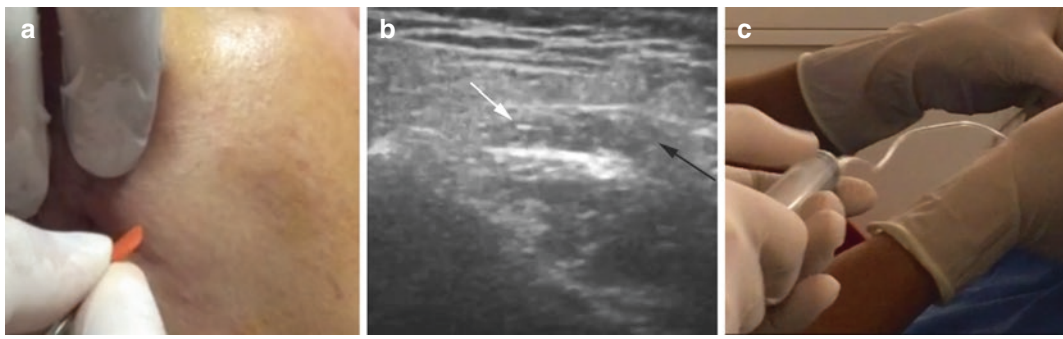

Fig. 10.9 Fine needle Aspiration Biopsy of TMJ mass (**a**) the entrance of needle, (**b**) US image showing needle (white arrow) and the mass (black arrow), (**c**) two hands technique

rhage may occur more frequently during this procedure.

10.4.4 Ultrasonography-Guided Core Biopsy

Preoperative preparation and technique are similar to those of fine needle aspiration biopsy. However, postoperative complications such as pain and edema will be more excessive since wider needles are used, the entrance port is larger and larger amount of tissue is incised.

Core biopsy under ultrasonography guidance will reduce the reliability of the procedure, lower the need for additional biopsies, and shorten operation time while reducing patient comfort.

10.4.5 Intraarticular Sodium Hyaluronate Injection

Sodium hyaluronate is a material similar to the synovial fluid produced in the temporomandibular joint. It serves as a lubricant and absorber of traumas. It is commonly used to treat temporomandibular joint osteoarthritis. It is an agent effective in decreasing temporomandibular joint pain associated with intraarticular derangements unresponsive to conservative treatments.

10.4.6 Ultrasonography-Guided Sodium Hyaluronate Injection

Preoperative preparation and technique are similar to those of fine needle aspiration biopsy. The procedure should be planned under sterile conditions. Preparations should be made and checked before biopsy. As a minimal invasive method, ultrasonography-guided sodium hyaluronate injection could be performed by one operator only, while two operators are commonly preferred.

Before passing on to the procedure, the anatomy of the region and pathology should be thoroughly examined with ultrasound by both the operators. This will give both the operators advantage before performing the procedure. The area should then be wiped from the ultrasonography gel.

Sterile gloves should be worn and the region should be cleaned with skin disinfectants to achieve antisepsis. A local anesthetic solution containing 1:100.000 epinephrine should be carefully and slowly injected inside the temporomandibular joint capsule using a 210-gauge needle. This careful and slow application of local anesthetic should prevent any discomfort during the procedure.

After local anesthetic injection, the region must be palpated and "manually sensed." During palpation of the region, the patient should be instructed to slowly open and close the jaws. This motion will be helpful for detecting the zygomatic arch and mandibular condyle.

To identify the entrance point of the needle a soft ruler and dermal pen can be used. The ruler should be directed from the outer cantus of the eye to the tip of the outer ear tragus. On this imaginary line, a mark should be made 10 mm away anteriorly from the tragus tip. Another mark should be made on a second imaginary line parallel to the first one just 2 mm below the first mark. This second mark will be the entrance point of the needle. There will be approximately 25 mm from the skin mark to the temporomandibular joint.

To increase the joint space patient should be instructed to open the jaws widely. The radiologist should then position the ultrasonography probe anterior to the entrance point. This settlement will ensure a comfortable procedure for the operator performing the biopsy. After visualization of the temporomandibular joint structures and associative pathology, the needle should be inserted from the specified mark with the bevel facing the temporomandibular joint. After some advancement, the tip of the needle should be recognized through ultrasonography. The needle should be then advanced into the structures in a posterior and superior route, into the pathology. Sodium hyaluronate preparations are usually present in ready-to-use syringes. If such syringes are used the presented needles should be used. If no needle is present, a 19-gauge needle can be used (Fig. 10.10).

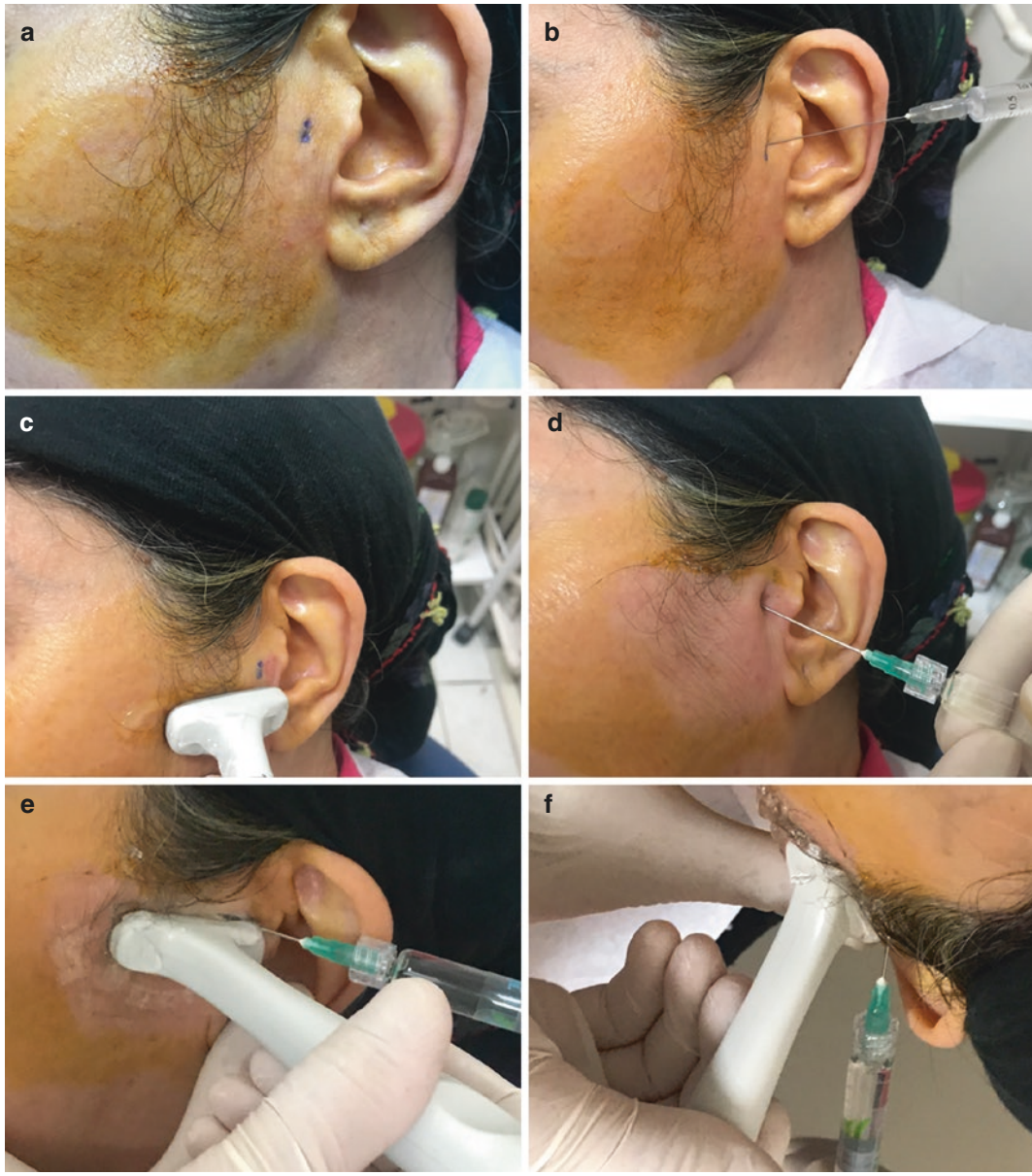

Fig. 10.10 Intraarticular sodium hyaluronate injection procedure, (**a**) identifying the entrance of the needle, (**b**) local anesthesia application, (**c**) US examination before the entrance, (**d**) the entrance of the needle, (**e**, **f**) US-guided intervention

Coordination between the two operators is essential during this phase. The ultrasonography operator should help the other operator channel the needle in the correct direction. After access to the upper temporomandibular joint space, the preparation should be slowly injected. A 1 mL volume is proved efficient for small joints such as the temporomandibular joint, repetitive applications can be made (Fig. 10.11).

Following injection, the area should be closed with a band-aid with slight pressure, to prevent hematoma formation. Intermittent cold-pack applications and anti-inflammatory medication will be useful during the postoperative period.

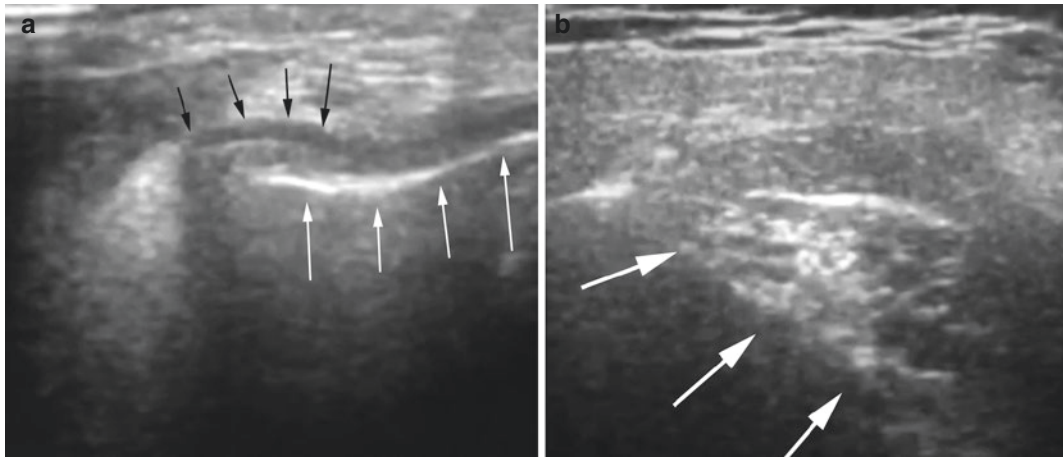

Fig. 10.11 (**a**) US image before Intraarticular sodium hyaluronate injection, black arrows show TMJ disc, white arrows show the needle. Note that the needle is entering lower compartment of the TMJ, (**b**) US image shows the hyperechoic areas after injection

Temporary pain or swelling of the affected joint may occur after injection.

10.4.7 Arthrocentesis

Arthrocentesis is an invasive procedure commonly preferred in conditions of internal derangements of the temporomandibular joint, opening intraarticular cohesions, painful clicking not responsive to conservative treatments, and disc displacement without reduction. It is an ambulatory service, which can be applied in hospital or office settings, under general anesthesia, sedation, or local anesthesia.

The aim of this invasive procedure is to reduce inflammation by washing out demolished tissue products present in the articular joint. This washing out procedure can be performed with sterile solutions such as sodium chloride or lactated Ringer's solution. During the operation, two needles are used; while one needle is used to inject the preferred solution into the articular joint the other needle serves as an exit port for the solution along with tissue demolition products. Afterwards, decrease in pain, increase in maximum mouth opening, and long-term relief of symptoms are expected.

This procedure is commonly performed "blind" using anatomic landmarks.

10.4.8 Ultrasonography-Guided Arthrocentesis

Ultrasonography-guided arthrocentesis essentially leans on the same principles with those of fine needle aspiration biopsy. The technique starts off with the radiologists and surgeons' detailed ultrasonography evaluation of the related temporomandibular joint.

Sterile gloves should be worn and the region should be cleaned with skin disinfectants to achieve antisepsis. A local anesthetic solution containing 1:100.000 epinephrine should be carefully and slowly injected inside the temporomandibular joint capsule using a 210-gauge needle. This careful and slow application of local anesthetic should prevent any discomfort during the procedure.

After local anesthetic injection, the region must be palpated and "manually sensed." During palpation of the region, the patient should be instructed to slowly open and close the jaws. This motion will be helpful for detecting the zygomatic arch and mandibular condyle.

To identify the entrance point of the needle a soft ruler and dermal pen can be used. The ruler should be directed from the outer cantus of the eye to the tip of the outer ear tragus. On this imaginary line, the first mark should be made 10 mm away anteriorly from the tragus tip and just 2 mm below on a second imaginary line parallel to the first one. This mark will be the entrance point of the first needle. There will be approximately 25 mm from the skin mark to the temporomandibular joint. The second mark should be made 20 mm away anteriorly from the tragus tip and just 10 mm below on a second imaginary line parallel to the first one. This mark will be the entrance point of the second needle.

Two 19-gauge needles should be preferred. To increase the joint space patient should be instructed to open the jaws widely. The radiologist should then position the ultrasonography probe anterior to the entrance point. This settlement will ensure a comfortable procedure for the operator performing the biopsy. After visualization of the temporomandibular joint structures, the first needle should be inserted from the specified mark with the bevel facing the temporomandibular joint. After some advancement, the tip of the needle should be recognized through ultrasonography. The needles should be then advanced into the structures in a posterior and superior route, into the upper temporomandibular joint space.

Coordination between the two operators is essential during this phase. The ultrasonography operator should help the other operator channel the needle in the correct direction. After the correct settlement of the needles, 300 mL of the preferred solution should be slowly injected while exiting from the second needle. Thus, the "washing out" of the joint space is verified.

Following the procedure, the area should be closed with a band-aid with slight pressure, to prevent hematoma formation. Intermittent cold-pack applications and anti-inflammatory medication will be useful during the postoperative period.

10.4.9 Intramasseteric Botulinum Toxin Injections for Bruxism

The Botulinum Toxin (BT) is a neurotoxin produced by the Clostridium botulinum bacteria. When this toxin is injected into the muscles, it prevents neurotransmission and the muscle fails to contract. It is commonly used in facial esthetics to prevent wrinkles. In our healthcare area, it is commonly used to prevent bruxism, by affecting the masseter muscle. This procedure is a simple and fast ambulatory application. The effect of BT is temporary, and thus repetitive applications are required.

The masseter is a bulky muscle, and the needle must deliver the BT deeper into the muscle to achieve optimal effect. The muscle is covered with a dense fascial layer, so if the injections are made superficially under this layer the optimal effect will not be achieved. The needle must penetrate this fascia and deliver the BT within the body of the muscle. While this procedure is commonly applied "blinded," ultrasonography-guided applications ensure the BT is injected in the correct depth, it increases the effect of the BT and lowers the number of repetitions (Figs. 10.12, 10.13).

10.4.10 Ultrasonography-Guided Intramasseteric Botulinum Toxin Injections

Desired decrease in bruxism is usually achieved with 20 units of botulinum toxin administered per each side. Additional units may have to be administered to achieve the optimal effect, and the amount is estimated according to the achieved response to the initial treatment.

Being an invasive procedure intramasseteric botulinum toxin injection should be planned under sterile conditions. Preparations should be made and checked before biopsy.

Before passing on to the procedure the anatomy of the region and the masseter muscle should be thoroughly examined with ultrasound by both

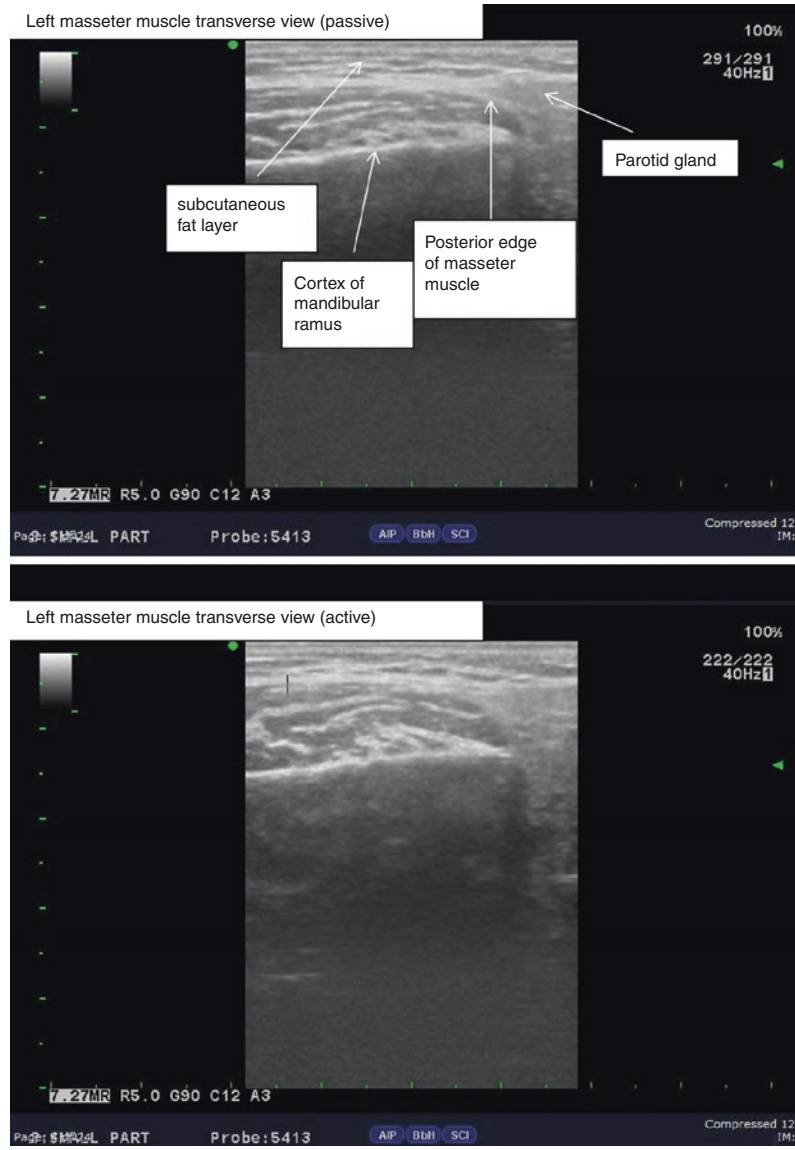

Fig. 10.12 Left masseter muscle transverse view passive and active USG images

the operators. This will give both operators an advantage before performing the injections. The area should then be wiped from the ultrasonography gel.

The masseter muscle should be palpated while the patient should be instructed to relax and bear down the jaw to determine the muscle. A line from the corner of the mouth up to the ear tragus should be traced with a dermal pen. Additionally, the anterior and posterior borders are designated and marked with a line. This defined area should not be crossed during injections. This way the risorius muscle and the zygomaticus major muscles will be protected. Protecting these muscles is important in protecting the patient's smile (Figs. 10.14, 10.15 and 10.16).

Sterile gloves should be worn and the region should be cleaned with skin disinfectants to

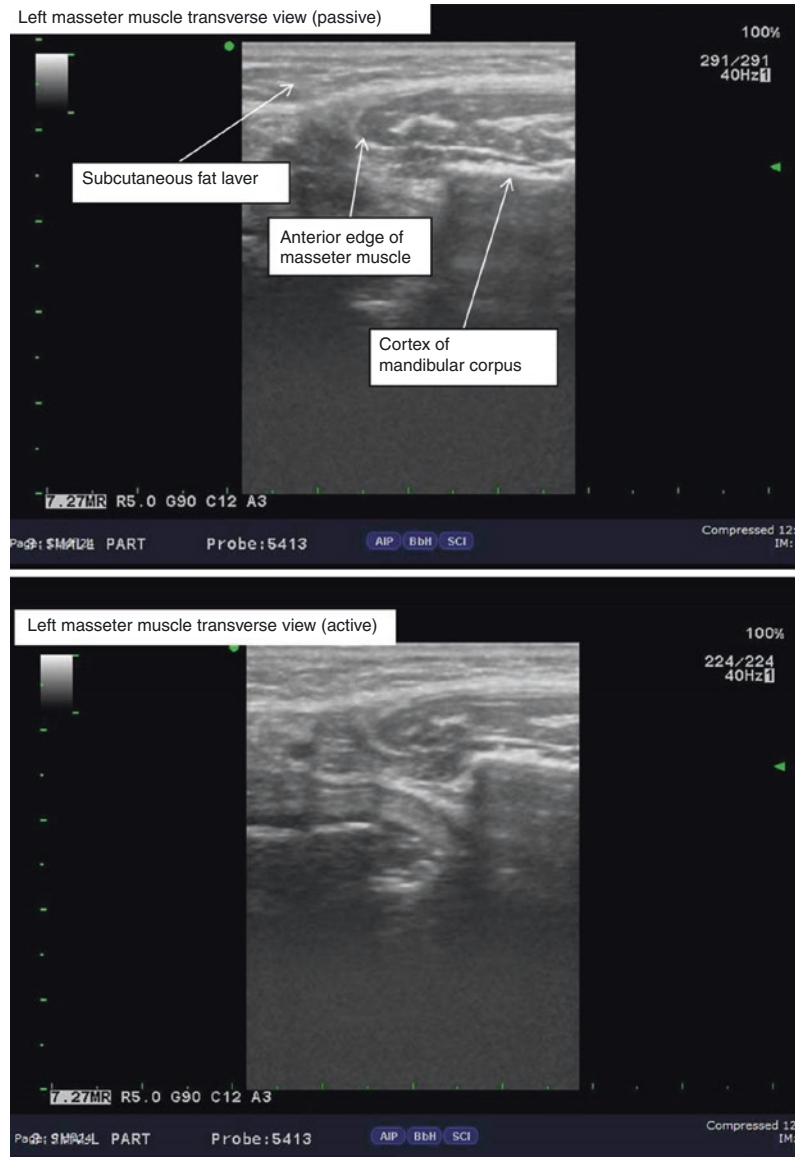

Fig. 10.13 Left masseter muscle transverse view passive and active USG images

achieve antisepsis. The radiologist should then position the ultrasonography probe anterior to the anterior border of the muscle. This settlement will ensure comfort for the operator performing the injection. After visualization of the masseter muscle, the needle should be inserted and after some advancement, the tip of the needle should be visualized by means of ultrasonography. The needle should be then advanced into the structures to enter into the deeper tissues of the masseter muscle. Once the appropriate depth is reached, the injection should be made. Usually, 3–4 injection points will be sufficient (Fig. 10.17).

Cold-pack application is recommended during the first 2–3 hours after treatment. Full effect may be noticed after 3–4 days or even later. The results may last from 3 to 4 months on average but sometimes up to 6 months. Afterwards, the patient will start to experience bruxism-related pain and reapplication will be required (Fig. 10.18).

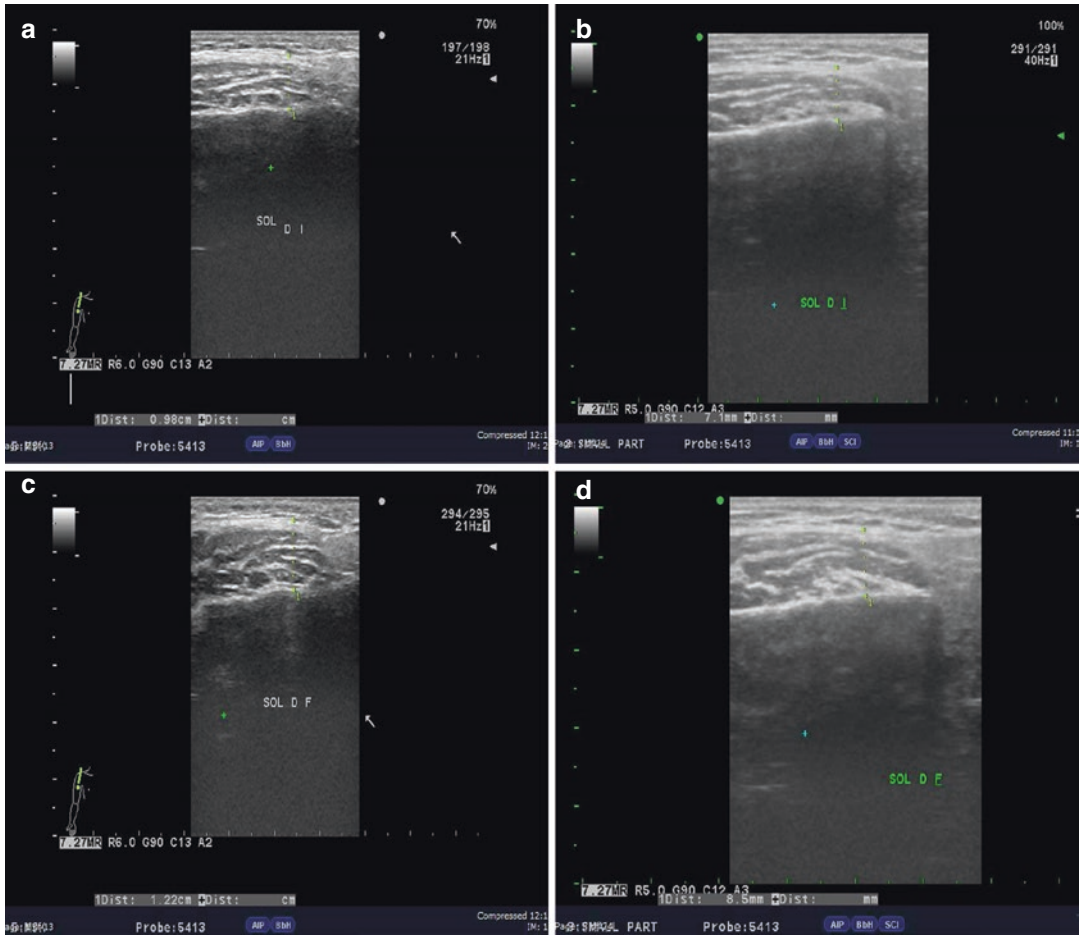

Fig. 10.14 US images show (**a**) thickness of distal edge of left masseter muscle (passive—before injection), (**b**) thickness of distal edge of left masseter muscle (passive—2 months after injection), (**c**) thickness of distal edge of left masseter muscle (active—before injection), (**d**) thickness of distal edge of left masseter muscle (active—2 months after injection)

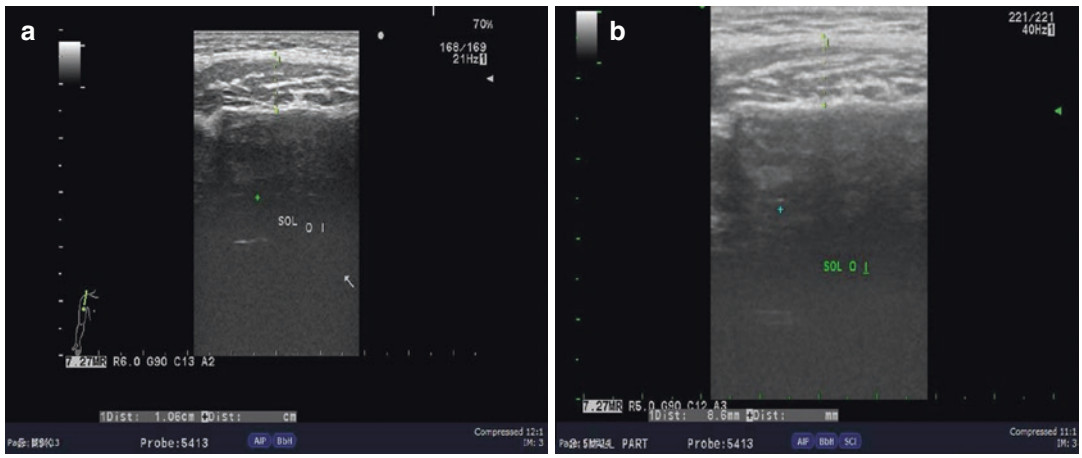

Fig. 10.15 US images show (**a**) thickness of middle portion of left masseter muscle (passive—2 months after injection), (**b**) thickness of middle portion of left masseter muscle (passive—before injection), (**c**) thickness of middle portion of left masseter muscle (active—2 months after injection), (**d**) thickness of middle portion of left masseter muscle (active—before injection)

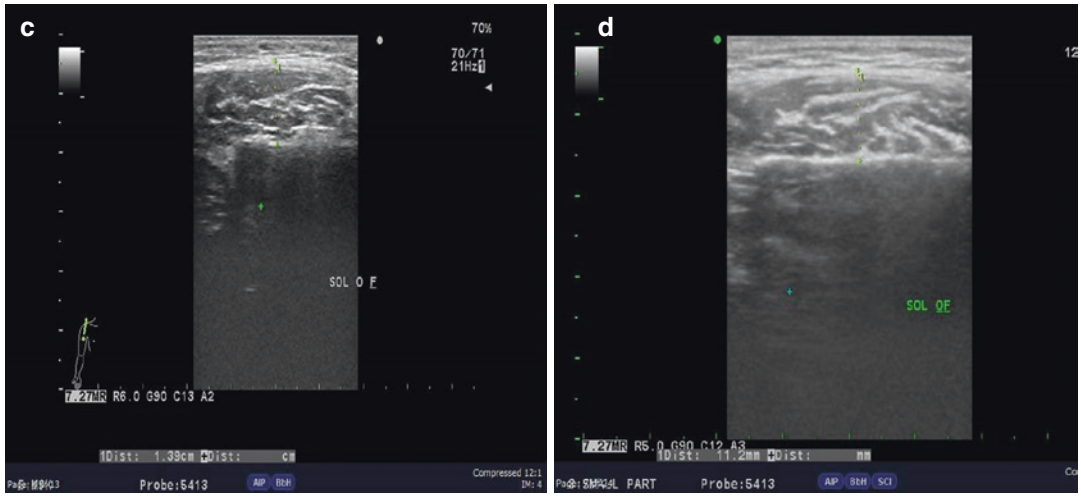

Fig. 10.15 (continued)

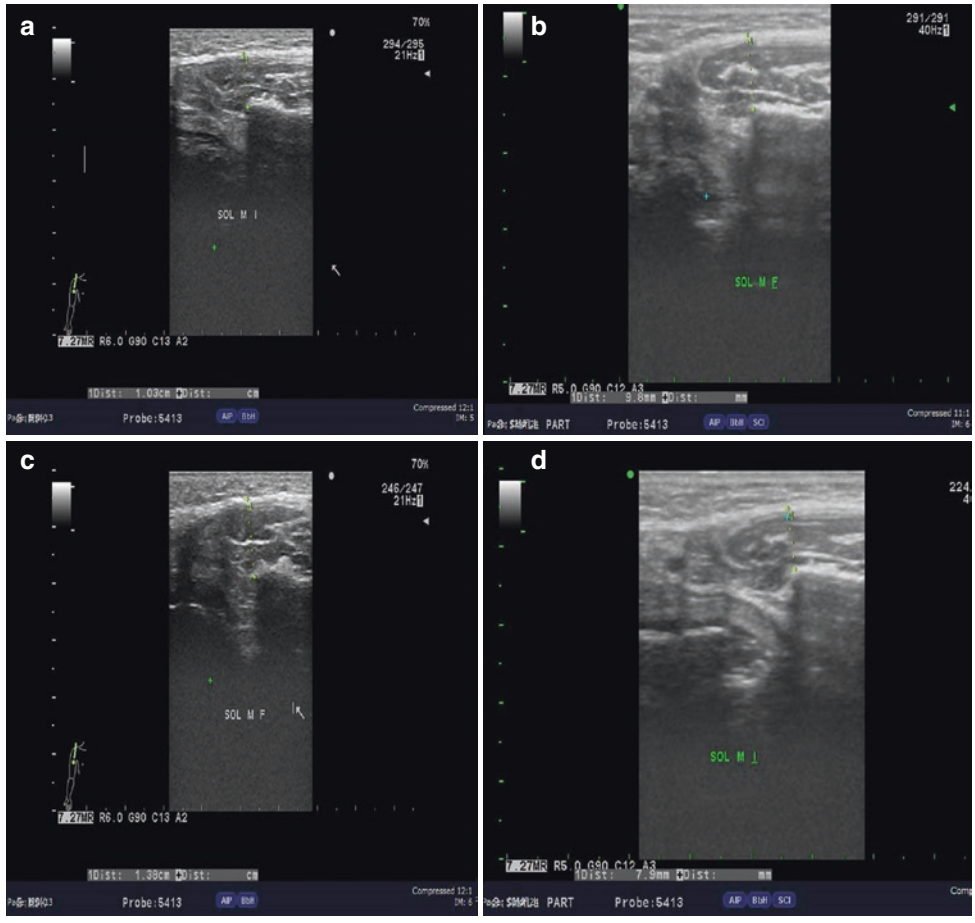

Fig. 10.16 US images show (**a**) thickness of mesial edge of left masseter muscle (passive—2 months after injection), (**b**) thickness of mesial edge of left masseter muscle (passive—before injection), (**c**) thickness of mesial edge of left masseter muscle (active—2 months after injection), (**d**) thickness of mesial edge of left masseter muscle (active—before injection)

Fig. 10.17 Lateral photo showing the application and US image after injection of botulinum toxin into masseter muscle (transverse view)

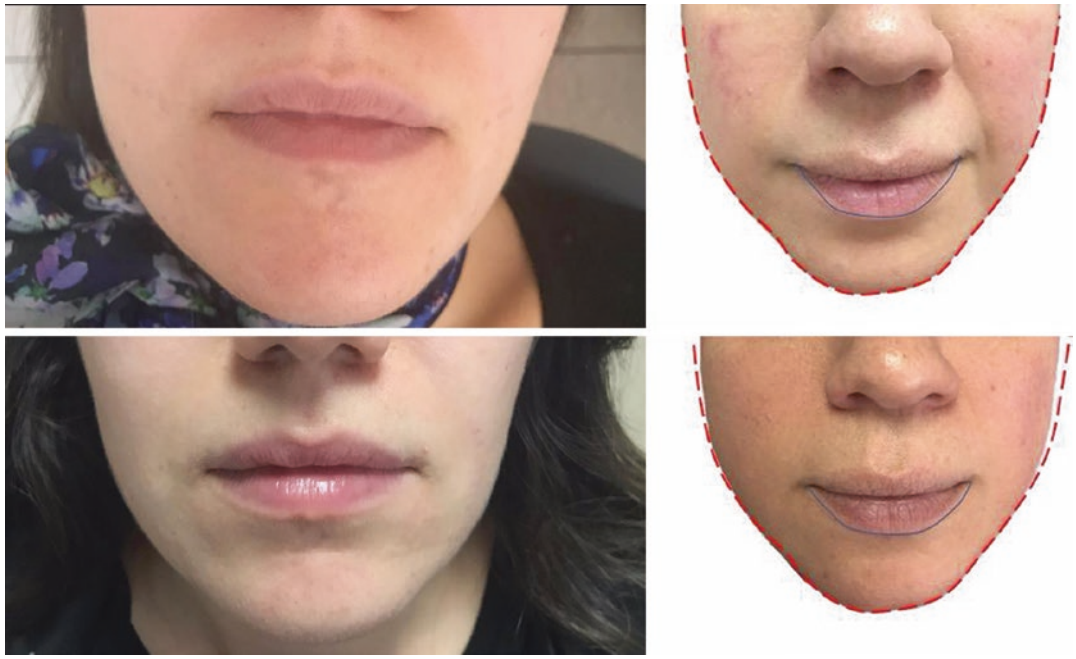

Fig. 10.18 Profile photos demonstrated a decrease in masseter muscle hypertrophy after injection of botulinum toxin in comparison with the baseline status

10.5 The Use of Ultrasonography in Combination with Electromyography and Joint Vibration Analysis

As stated above, US produces dynamic video images depicting muscular dystrophy and denervation in the striated muscles, including muscles of mastication, that produce voluntary contractions, as well as involuntary muscle contractions such as fasciculation (Engel-Hoek LV et al., 2017). On the other hand, electromyography (EMG) is a muscle examination method in which extracellular signals generated by muscle fibrils and transmitted through tissues are recorded, and the electrical activity of the muscles is contracted, monitored, and interpreted. EMG is an effective method for diagnosing sleep bruxism and assessing changes induced by oral devices used for bruxism treatment [36]. US and EMG data are important for measuring the strength, endurance, and structural characteristics of the masticatory muscles in individuals with temporomandibular disorders, which can aid in diagnosis and treatment planning [37].

EMG has been applied in dental research since the late 1940s. It has been used to study asymptomatic and dysfunctional muscles in both static and dynamic modes. The muscle parameters frequently examined by means of EMG have included the "rest" or postural activity and the maximal and clenching activity [38]. When well-standardized protocols are used, surface EMG of the head muscles has been reported to be an effective method for the functional assessment of the stomatognathic apparatus with a good repeatability [39].

The combined application of EMG and US has also been tested in bruxism. Bruxism is defined as the clenching and/or grinding action performed on the teeth without a functional purpose such as chewing and crushing [40]. In its etiology, morphological, psychological, and parafunctional factors are generally found accountable. Bruxism is reported to be associated with TMJ diseases (Peña-Durán et al., 2017). In literature, it has been reported that parafunctional habits cause mechanical stress on the condyle which is can trigger condylar resorption or accelerate already progressing resorption [41].

Combined use of US and EMG has been proved to be an easy and reproducible method in assessing the parameters of masticatory muscles function and by measuring muscle thickness an essential tool for analyzing functional efficiency of jaw elevator muscle contraction during dental clenching [42].

In previous studies, EMG activity and the thickness of the masseter and temporal muscles using US were evaluated in patients with bruxism and healthy control. It was concluded that individuals with bruxism demonstrated decreased EMG activity in the masticatory muscles. Significant changes both for EMG and US measurements were found in different types of treatment modalities (Marcelo [43]). Moreover, there were also studies evaluating TMD patients and healthy controls using EMG and US by the assessment of the differences in thickness and function of masticatory muscles. EMG and US (applied for measurement of muscle thickness) data were similar in the controls and TMD patients. It was also suggested that US can be used to assess muscle activity together with EMG [37]. This approach can be applied in children, as well. EMG activity and muscle thickness with real-time US of masseter and anterior temporalis muscle examinations were reported in children with unilateral posterior cross-bite. A positive correlation was found between the ultrasonographic cross-sectional thickness of the masseter muscle and the EMG amplitude [44].

Finally, US can also be used in combination with Joint vibration analysis (JVA). This analysis is a variant of electromyography based on spectral analysis that was developed to record and analyze TMJ sounds. Using JVA, it is possible to identify vibrations produced by joint tissues during opening and closing movements, visualize the wave types, and calculate the frequencies, as well as the amplitude of the vibrations.

The following seven parameters can be analyzed for joint vibration analysis under the control of US:

Fig. 10.19 The application of joint vibration analysis with EMG

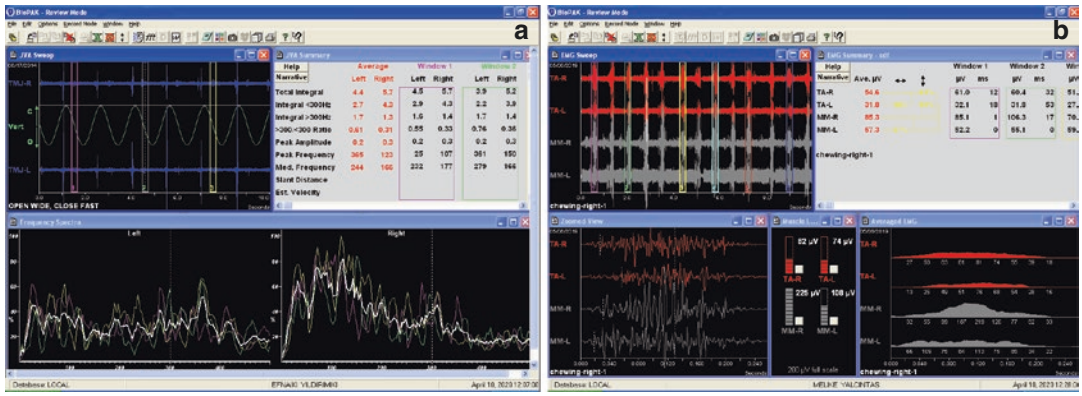

Fig. 10.20 (**a**) Joint vibration analysis and (**b**) EMG recordings

- Total integral (Ti)—the measure of the total amount of energy in the vibration.
- i > 300 Hz—the amount of energy in the vibration that is above 300 Hz.
- i < 300 Hz—the amount of energy in the vibration that is below 300 Hz.
- i > 300 Hz/i < 300 Hz—the ratio of high-frequency to low-frequency energy.
- Peak Amplitude (PA)—indicates the highest intensity of the vibration.
- Peak Frequency (PF)—the frequency at which the highest intensity of the vibration occurred.
- Median Frequency (MF)—the frequency that divides the frequency spectrum into two regions with equal power (MF) (Figs. 10.19, 10.20).

Acknowledgments The authors would like to thank Associate Prof. Dr. Nilsun Bagis, Dr. Poyzan Bozkurt, Dr. Dilek Yılmaz, Dr. Leszek Szalewski, Dr. Bora Akat, Dr. Ayben Bayrak for their contributions to this chapter. Informed consents were obtained from all patients whose pictures are shown in this case series.

References

1. Katzberg RW. Is ultrasonography of the temporomandibular joint ready for prime time? Is there a "window" of opportunity? J Oral Maxillofac Surg. 2012;100(6):1310–4.
2. Whaites E, Drage N. Essentials of Dental Radiography and Radiology. 5th ed: Churchill Livingstone; 2013.
3. Kundu H, Basavaraj P, Kote S, Singla A, Singh S. Assessment of TMJ disorders using ultrasonography as a diagnostic tool: a review. J Clin Diagn Res. 2013;10(12):3116–20.
4. Landes CA, Goral W, Mack MG, Sader R. 3-D sonography for diagnosis of osteoarthrosis and disk degeneration of the temporomandibular joint, compared with MRI. Ultrasound Med Biol. 2006;32(5):6210–32.
5. Landes CA, Goral WA, Sader R, Mack MG. Three-dimensional versus two-dimensional sonography of the temporomandibular joint in comparison to MRI. Eur J Radiol. 2010;61(2):235–44.
6. Manfredini D, Guarda-Nardini L. Ultrasonography of the temporomandibular joint: a literature review. Int J Oral Maxillofac Surg. 2009;38(12):1229–36. https://doi.org/10.1016/j.ijom.2009.010.014. Epub 2009 Aug 22

7. Manfredini D, Tognini F, Melchiorre D, Zampa V. Bosco M: ultrasound assessment of increased capsular width as a predictor of temporomandibular joint effusions. Dentomaxillofac Radiol. 2003;32:359–64.
8. Weiss PF, Arabshani B, Johnson A, Bilaniuk LT, Zarnow D, Cahill AM, Feudtner C, Cron RQ. High prevalence of temporomandibular joint arthritis at disease onset in children with juvenile idiopathic arthritis, as detected by magnetic resonance imaging but not by ultrasound. Arthritis Rheum. 2008;58(4):1189–96. https://doi.org/10.1002/art.23401.
9. Melis M, Secci S, Ceneviz C. Use of US for diagnosis of temporomandibular joint disorders: a review. Am. J. Dent. 2010;20:103–8.
10. Dong XY, He S, Zhu L, Dong TY, Pan SS, Tang LJ, Zhu ZF. The diagnostic value of high-resolution ultrasonography for the detection of anterior disc displacement of the temporomandibular joint: a meta-analysis employing the HSROC statistical model. Int J Oral Maxillofac Surg. 2015;44:852–8.
11. Bas B, Yılmaz N, Gökce E, Akan H. Ultrasound assessment of increased capsular width in temporomandibular joint internal derangements: relationship with joint pain and magnetic resonance grading of joint effusion. Oral Surg Oral Med Oral Pathol Oral Radiol Endod. 2011;112(1):112–7.
12. Tognini F, Manfredini D, Mechiorre D, Zampa V, Bosco M. Ultrasonographic vs magnetic resonance imaging findings of temporomandibular joint effusion. Minerva Stomatol. 2003;52:365–3102.
13. Uysal S, Kansu H, Akhan O, Kansu O. Comparison of ultrasonography with magnetic resonance imaging in the diagnosis of temporomandibular joint internal derangements: a preliminary investigation. Oral Surg Oral Med Oral Pathol Oral Radiol Endod. 2002;94(1):115–21.
14. Brandlmaier I, Rudisch A, Bodner G, Bertram S, Emshoff R. Temporomandibular joint internal derangement: detection with 12.5 MHz ultrasonography. J Oral Rehabil. 2003;30(8):796–801.
15. Emshoff R, Bertram S, Rudisch A, Gassner R. The diagnostic value of ultrasonography to determine the temporomandibular joint disc position. Oral Surg Oral Med Oral Pathol Oral Radiol Endod. 1997;84:688–96.
16. Emshoff R, Jank S, Bertram S, Rudisch A, Bodner G. Disk displacement of the temporomandibular joint: sonography versus MR imaging. AJR Am J Roentgenol. 2002a;178(6):1557–62.
17. Kaya K, Dulgeroğlu D, Unsal DS, Babadağ M, Tacal T, Barlak A. Diagnostic value of ultrasonography in the evaluation of the temporomandibular joint anterior disk displacement. J Cranio-Maxillofac Surg. 2010;38:391–5.
18. Tognini F, Manfredini D, Mechiorre D, Bosco M. Comparison of ultrasonography and magnetic resonance imaging in the evaluation of the temporomandibular joint disc displacement. J Oral Rehabil. 2005;32:248–53.
19. Li C, Su N, Yang X, Sh Z, Li L. Ultrasonography for detection of disc displacement of temporomandibular joint: a systematic review and meta-analysis. J Oral Maxillofac Surg. 2012;100(6):1300–9.
20. Emshoff R, Brandlmaier I, Bodner G, Rudisch A. Condylar erosion and disc displacement: detection with high-resolution ultrasonography. J Oral Maxillofac Surg. 2003;61(8):877–81.
21. Rudisch A, Emshoff R, Maurer H, Kovacs P, Bodner G. Pathologic-sonographic correlation in temporomandibular joint pathology. Eur Radiol. 2006;16(8):11050–6.
22. Assaf AT, Kahl-Nieke B, Feddersen J, Habermann CR. Is high-resolution ultrasonography suitable for the detection of temporomandibular joint involvement in children with juvenile idiopathic arthritis? Dentomaxillofac Radiol. 2013;42(3):20110379.
23. Emshoff R, Jank S, Rudisch A, Walch C, Bodner G. Error patterns and observer variations in the high-resolution ultrasonography imaging evaluation of the disk position of the temporomandibular joint. Oral Surg Oral Med Oral Pathol Oral Radiol Endod. 2002b;93(3):369–75.
24. Hechler BL, Phero JA, Van Mater H, Matthews NS. Ultrasound versus magnetic resonance imaging of the temporomandibular joint in juvenile idiopathic arthritis: a systematic review. Int J Oral Maxillofac Surg. 2018;47(1):83–9.
25. Jank S, Zangerl A, Kloss FR, Laimer K, Missmann M, Schroeder D, Mur E. High resolution ultrasound investigation of the temporomandibular joint in patients with chronic polyarthritis. Int J Oral Maxillofac Surg. 2011;40(1):45–9.
26. Melchiorre D, Calderazzi A, Maddali BS, Cristofani R, Bazzichi L, Eligi C, Maresca M, Ciompi M. A comparison of ultrasonography and magnetic resonance imaging in the evaluation of temporomandibular joint involvement in rheumatoid arthritis and psoriatic arthritis. Rheumatology. 2003;42:6103–6.
27. Cakir-Ozkan N, Sarikaya B, Erkorkmaz U, Aktürk Y. Ultrasonographic evaluation of disc displacement of the temporomandibular joint compared with magnetic resonance imaging. J Oral Maxillofac Surg. 2010;68(5):1075–80.
28. Gateno J, Miloro M, Hendler BH, Horrow M. The use of ultrasound to determine the position of the mandibular condyle. J Oral Maxillofac Surg. 1993;51:1081–6.
29. Jank S, Emshoff R, Norer B, Missmann M, Nicasi A, Strobl H, Gassner R, Rudisch A, Bodner G. Diagnostic quality of dynamic high-resolution ultrasonography of the TMJ - a pilot study. Int J Oral Maxillofac Surg. 2005;34(2):132–7.
30. Jank S, Rudisch A, Bodner G, Brandlmaier I, Gerhard S, Emshoff R. High-resolution ultrasonography of the TMJ: helpful diagnostic approach for patients with TMJ disorders? J Craniomaxillofac Surg. 2001;29(6):366–71.
31. Landes CA, Sader R. Sonographic evaluation of the ranges of condylar translation and of temporo-

mandibular joint space as well as first comparison with symptomatic joints. J. Craniomaxillofac. Surg. 2010;35:3104–381.
32. Landes CA, Walendzik H, Klein C. Sonography of the temporomandibular joint from 60 examinations and comparison with MRI and axiography. J Craniomaxillofac Surg. 2000;28(6):352–61.
33. Stagnitti A, Marini A, Impara L, Drudi FM, Lo ML, Lillo OG. Duplex Doppler ultrasound study of the temporomandibular joint. J Ultrasound. 2012;15(2):111–4.
34. Çil AS, Bozkurt M, Bozkurt DK. Intrauterine temporomandibular joint dislocation: prenatal sonographic evaluation. Clin Med Res. 2014;12(1–2):58–60.
35. Dayisoylu EH, Cifci E, Uckan S. Ultrasound-guided arthrocentesis of the temporomandibular joint. Br J Oral Maxillofac Surg. 2013;51(7):667–8.
36. Nishi SE, Basri R, Alam MK. Uses of electromyography in dentistry: An overview with meta-analysis. 2016;10(3):419–25.
37. Strini PJ, Strini PJ, Barbosa Tde S, Gavião MB. Assessment of thickness and function of masticatory and cervical muscles in adults with and without temporomandibular disorders. Arch Oral Biol. 2013;58(9):1100–8.
38. Suvinen TI, Kemppainen P. Review of clinical EMG studies related to muscle and occlusal factors in healthy and TMD subjects. J Oral Rehabil. 2007;34:631–44.
39. Tartaglia GM, Moreira Rodrigues da Silva MA, Bottini S, Sforza C, Ferrario VF. Masticatory muscle activity during maximum voluntary clench in different research diagnostic criteria for temporomandibular disorders (RDC/TMD) groups. Man Ther. 2008;13(5):434–40.
40. Firestone AR. Orofacial pain: guidelines for assessment, diagnosis, and management. Eur J Orthod. 1997;19(1):103–4.
41. Arnett G, Milam S, Gottesman L. Progressive mandibular retrusion—idiopathic condylar resorption. Part I. Am J Orthod Dentofac Orthop. 1996;110(1):8–15.
42. Göller Bulut D, Avcı F, Özcan G. Ultrasonographic evaluation of jaw elevator muscles in young adults with bruxism and with and without attrition-type tooth wear: a pilot study. Cranio. 2018;28:1–8.
43. Palinkas M, Bataglion C, de Luca CG, Machado Camolezi N, Teixeira Theodoro G, Siéssere S, Semprini M, Hallak Regalo SC. Impact of sleep bruxism on masseter and temporalis muscles and bite force. Cranio. 2016;34(5):309–15.
44. Andrade AS, Gaviao MB, Derossi M, Gameiro GH. Electromyographic activity and thickness of masticatory muscles in children with unilateral posterior cross-bite. Clin Anat. 2009;22(2):200–6.

11 Sonographic Anatomy and Pathology: Facial Soft Tissues Including Muscles

Husniye Demirturk Kocasarac, Dania Tamimi, and Mehtap Balaban

Contents

H. Demirturk Kocasarac (✉)
School of Dentistry, Department of General Dental Sciences, Division of Oral and Maxillofacial Radiology, Marquette University, Milwaukee, WI, USA

D. Tamimi
Oral and Maxillofacial Radiology, Private Practice, Orlando, FL, USA

M. Balaban
Faculty of Medicine, Department of Radiology, Yıldırım Beyazıt University, Ankara, Turkey

K. Orhan (ed.), *Ultrasonography in Dentomaxillofacial Diagnostics*,
https://doi.org/10.1007/978-3-030-62179-7_11

11.1 Anatomy

A large part of the head and neck structures and their related pathologies are located less than 5 cm beneath the skin and thus can be visualized by ultrasonography (USG) [1].

The sonographic appearance of muscles, ducts, and blood vessels is hypoechoic (fairly dark) relative to fat that is hyperechoic or echogenic. Mucosa appears hyperechoic as well and can be simply distinguished from the hypoechoic muscle which it normally covers. The surface of the mandible near the salivary glands presents as hyperechoic linear line and precludes visualization of the parotid gland's deeper portions [1–3].

11.1.1 Parotid Gland

The hypoechoic masseter muscle with its pinnate reflection form is a key landmark in the transverse view of the parotid area. Ultrasound easily demonstrates whether pathology is inside or outside of the salivary gland. Typically, the parotid gland has a homogeneous echotexture on ultrasound (Fig. 11.1). The superficial lobe of the parotid is seen superficial to the well-visualized retromandibular vein which acts as a surrogate indicator for the more superficial intra-parotid facial nerve. In the axial plane, the Stensen duct (parotid duct) can be visualized as paired and parallel echogenic lines 3 mm apart, lying superficially to the masseter muscle but is generally only detectable as a hypoechoic/anechoic structure when it is obstructed (Fig. 11.2) [4, 5]. Stensen duct travels medially and anteriorly, then at the border of the masseter, makes a steep right turn to cross the buccal fat pad and hypoechoic buccinator muscle opening into the vestibule of the mouth, opposite to the second maxillary molar [5].

11.1.2 Muscles

US examination can be performed reliably for some facial expression and masticatory muscles

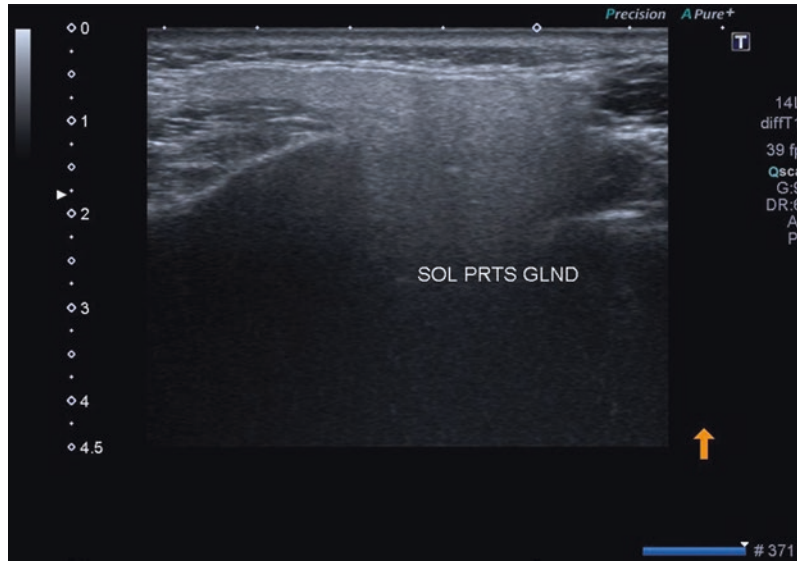

Fig. 11.1 Ultrasonographic view of normal left parotid gland shows a normal parotid gland with homogenous parenchyma and smooth contour in the preauricular region

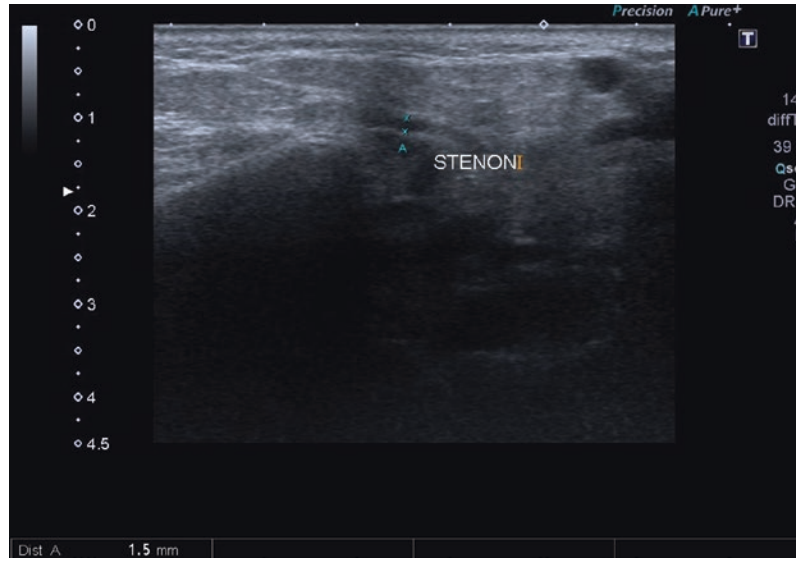

Fig. 11.2 US image of smooth duct ectasia of the Stensen's duct shows a smooth dilated view of the duct in the medial aspect of the left parotid gland superficial lobe. There is a lack of vascularization on color Doppler USG

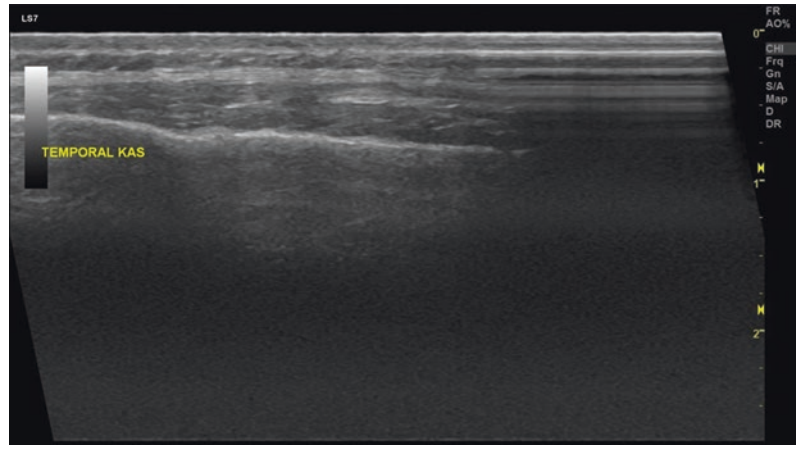

Fig. 11.3 USG view of a normal left temporalis muscle in a healthy young female

including: frontalis; orbicularis oculi; depressor labii inferioris; depressor anguli oris; orbicularis oris; mentalis; temporalis; and masseter (Figs. 11.3, 11.4, 11.5). Other facial muscles may not always be evaluated in all cases or with adequate reliability. Echo intensity is negatively related to muscle strength, particularly in advanced ages. In patients with chronic facial palsy, echo intensity in mimic muscles increases during denervation and decreases (restoration of baseline values) during reinnervation. Echo intensity and muscle size of some masticatory muscles (masseter and temporalis) appear not to be affected by the facial palsy [6].

11.1.3 Lips

Based on the USG characteristics of skin, muscle, and subcutaneous tissue, the normal upper lip tissues can be divided into five layers from superficial to deep. The first layer is a continuous dense hyperechoic line created by the epidermis of the skin and ultrasonic coupling agent. The second layer is somewhat hyperechoic and include superficial muscle fibers of the orbicularis oris muscle, the right and left philtrum columns, philtrum dimple, and skin connection. The third layer is a cord-like hypoechoic area formed by deep fibers of the orbicularis oris. The fourth layer is a slightly

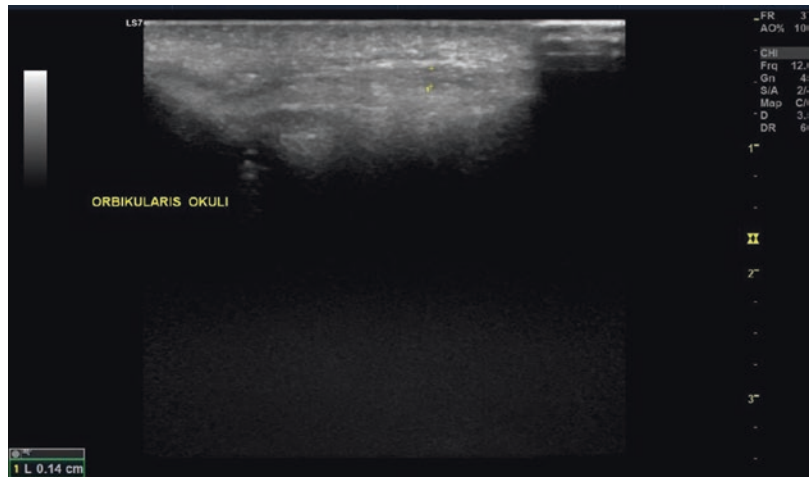

Fig. 11.4 USG view of normal left orbicularis oculi muscle in a healthy young female

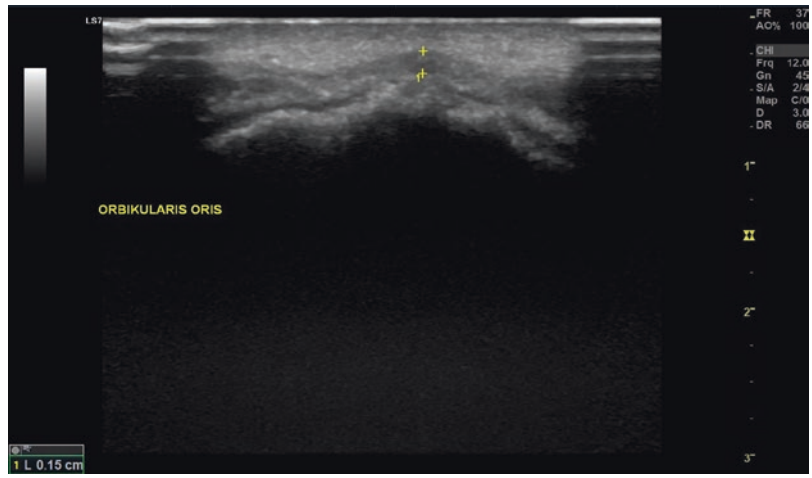

Fig. 11.5 USG view of normal orbicularis oris muscle

hyperechoic region generated by submucosa of the orbicularis oris, upper lip artery, and glandular tissue. The fifth layer is a slightly hyperechoic line created by the mucous layer of the upper lip [7].

11.1.4 Masseter Muscle

Masseter muscle lies on the ascending mandibular ramus (echogenic reflection with distal acoustic shadowing) and is anterior to the parotid gland with its distinctive pinnate reflection pattern. The scan plane for masseter muscle is perpendicular to the muscle's anterior border and to the surface of the underlying ramus. It is close and approximately parallel to the occlusal plane in the thickest part of the muscle (region with the most lateral distention) [8]. A healthy masseter muscle has a relatively smooth internal texture of moderate echogenicity on USG images and is visualized to abut right against the ramus of mandible (Fig. 11.6). It can be displayed on USG both in relaxation and maximum contraction. Generally, large white shadow on the top represents the skin echo. The masseter muscle mass appears hypoechoic beneath the skin. Normal masseter muscle has a heterogeneous speckled look in cross-sectional USG images due to hyperechoic bands that are possibly internal fascia [9]. These bands abate or get lost in presence of inflammation; therefore, this is an essential structural index of masseteric infection [10]. The deep part of the

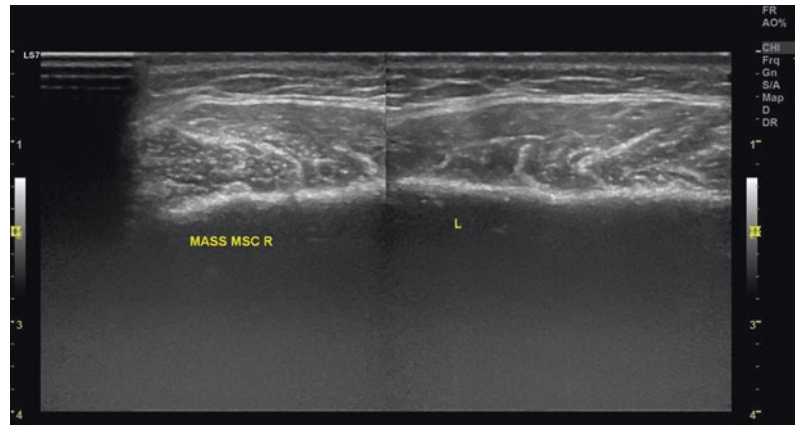

Fig. 11.6 USG view of normal right and left masseter muscles in a healthy young female

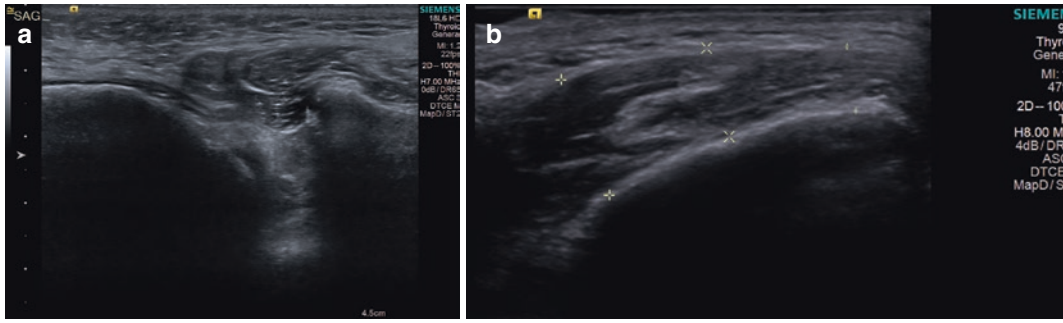

Fig. 11.7 (**a, b**) USG image shows the masseter muscle hypertrophy. Cases courtesy of Dr. Kaan Orhan

masseter can be at its optimum length and clearly portrayed in the USG scan when the patient is in dental intercuspal jaw position [11]. In case of unilateral swelling of the cheek barring parotid gland pathology, masseter hypertrophy due to occlusal parafunction should be considered (Fig. 11.7a, b). USG with a narrow-surfaced probe is effective to diagnose the condition and assess whether the hypertrophic part is in the lower, middle, or upper third of the masseter muscle [12].

11.1.5 Temporomandibular Joint (TMJ)

USG imaging of the temporomandibular joint (TMJ) is also possible with the availability of higher resolution devices and higher frequency probes. With ultra-higher resolution devices (>15 MHz), contrary to probes of 12–15 MHz, TMJ structures, lower and upper joint compartments, some temporomandibular disorders (i.e., dislocation) can be demonstrated reliably with higher sensitivity and accuracy [13].

11.2 Diseases of Facial Soft Tissues and Muscles: Brief Review of Typical USG Aspect of the Most Frequently Encountered Pathologies

11.2.1 Inflammatory Changes

11.2.1.1 Furuncle

A furuncle is a localized infection of the hair follicle with reaction of the immediate tissue. It can arise in any hair-bearing area of the skin. Patients generally exhibit painful swelling in the affected

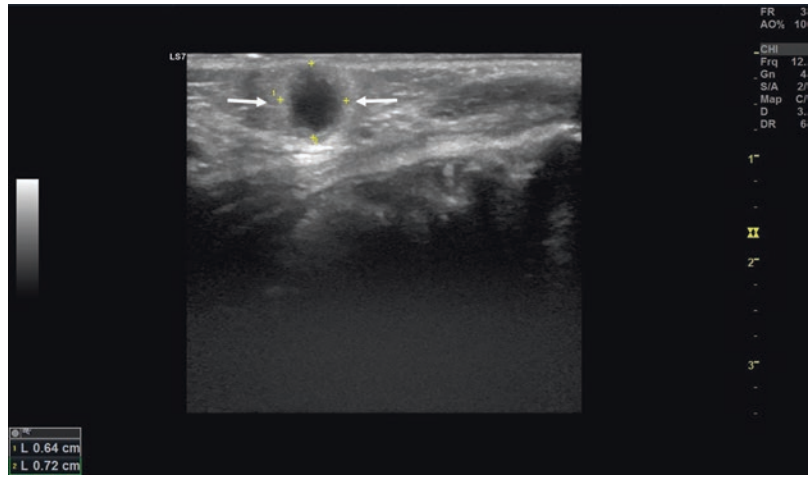

Fig. 11.8 USG view of a furuncle in the buccal (cheek) region shows a collection area with minimal irregular contours within the skin and subcutaneous soft tissue in the right buccal area compatible with the furuncle. Note the accompanying increase in adjacent soft tissue echogenicity (white arrows)

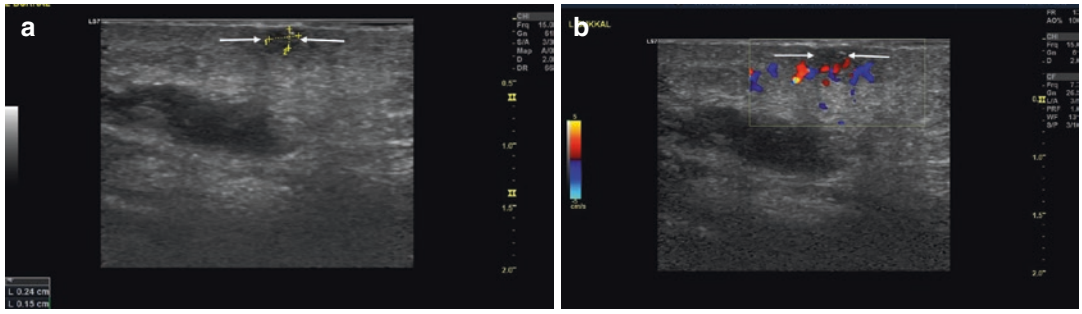

Fig. 11.9 (**a**) USG view of an abscess (white arrows) in the left malar region shows a collection area with irregular contours and dense content, compatible with an abscess within the subcutaneous soft tissue in the left malar region. (**b**) Color Doppler view of the marked increase in peripheral vascularization accompanying the abscess (white arrows) in the left malar region

skin which is red and tense, and a boil may be visible. If not treated appropriately, complications such as facial cellulitis and cavernous sinus thrombosis, which presents with chemosis, headache, fever, proptosis, and cranial nerve III, IV, V, and VI palsies might develop [14, 15]. USG typically displays a star-shaped, hypoechoic, loosely organized lesion on the skin (Fig. 11.8). The extension of the inflammation into the deeper structures may be evaluated without difficulty.

11.2.1.2 Abscess

On USG, abscess formation appears as heterogeneously hypoechoic or anechoic areas with distal acoustic enhancement (Fig. 11.9a). A thick and irregular border indicates hyperperfusion (increased peripheral blood flow) on color Doppler USG (Fig. 11.9b) [16, 17]. Pus within the abscess might initially seem hyperechoic or isoechoic with the adjacent lymph node and becomes anechoic or hypoechoic when antibiotic therapy is administrated [16]. Gas within the tissues such as an abscess leads to ultrasonic scatter that produces a "white out" appearance [4]. Movement of the infected fluid can be detected with a real-time USG examination [16].

Image Interpretation Pearls

Doppler sonography or color duplex evaluation of the angular vein is needed for furuncles superior to the oral fissure. The presence of venous thrombosis indicates a risk for intracranial spread [5].

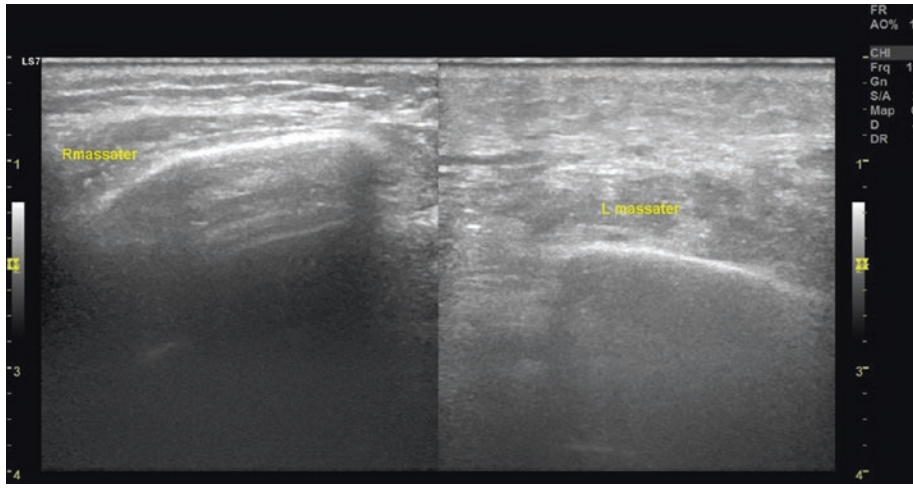

Fig. 11.10 USG image of masseter muscle (Massater) myositis shows diffuse heterogeneous echogenic thickened appearance in the left masseter muscle (L massater) compatible with myositis in the USG examination of an immunosuppressed female case. There are diffuse echogenicity and minimal edema appearance compatible with inflammation in adjacent skin-subcutaneous soft tissue accompanied by effacement of the contours

11.2.1.3 Myositis

Myositis is an immune-mediated inflammatory muscle disease with clinical signs of a palpable mass, localized pain, and tenderness. Typical US features of myositis involve intramuscular spindle-shaped mass, thickened perimysium with a honeycomb pattern (in the axial plane), hypervascularity, and loss of normal fibrillar echotexture. In the acute phase, myositis shows heterogeneous higher echogenicity (hyperechoic) and increased muscle thickness. In the chronic stage of myositis where there are fibrosis and fatty replacement, USG shows higher echogenicity (hyperechoic) with decreased muscle thickness (Fig. 11.10) [18].

11.2.1.4 Mastoiditis

Subcutaneous painful retro-auricular swelling with clinical signs of inflammation is suggestive of mastoiditis. USG or color duplex (duplex or Doppler?) sonography of the temporal bone may reveal subcutaneous, inhomogeneous, poorly demarcated, irregular, poorly (or not at all) perfused, hypoechoic lesion, defect in the cortex of the mastoid process, elevation of the outer periosteum by a hypoechoic underlying layer of purulent material between the periosteum and cortex, a vascular periphery in the retro-auricular area, and signs of intracranial extension through this external cortical defect. Utilization of color duplex sonography might identify inflammation-related hyperemia around periosteum and nearby soft tissue abscesses. Exclusion of temporal bone erosion by USG can be beneficial to differentiate between an inflammatory mastoid process and retro-auricular lymph node, retro-auricular erysipelas or dermoid cyst with presence of inflammation [19].

11.2.1.5 Preauricular Sinus

Preauricular sinus (PAS) is a congenital malformation which is seen as small opening in the external ear, frequently adjacent to the anterior limb of the ascending helix, and may have a fistula aimed towards the external auditory canal. Assessment of preauricular sinus and fistula can be hard with a US transducer, so a fair amount of gel should be used to have a clear USG image. On a USG image, the sinus or fistula seems to emerge from the skin orifice and fistula can reach the external auditory canal. The sinus is generally short and narrow; hence, USG might be able to demonstrate the entire sinus and tract [20].

Image Interpretation Pearls
If the fistula may be probed, a contrast material application, i.e., hydrogen peroxide, can be tried to demarcate the pathology more clearly in the deeper tissues [5].

11.2.1.6 Sialadenitis

Sialadenitis is inflammation of the salivary glands, the most common being the parotid gland, followed by submandibular and sublingual glands (Figs. 11.11a, b, 11.12). It may be acute or chronic. In the acute form, the affected gland is enlarged, hyperemic, and hypoechoic [21]. In chronic sialadenitis, the affected gland may be atrophic and diffusely hypoechoic with irregular borders resembling the sonographic appearances of a cirrhotic liver [22]. In recurrent sialadenitis there may be sialectasis.

11.3 Benign Lesions: Cysts, Cyst like Lesions, and Tumors

For solid tumors, USG can demonstrate the lesion size, its content, and the presence of a fracture or other abnormalities in the surrounding structures. Solid tumors with intrinsic perfusion are apt to be heterogeneously echoic or hypoechoic. Based on sonographic palpation and its echogenicity, the density of the pathology may also be predicted with USG examination. (Figs. 11.13, 11.14, 11.15) [5].

11.3.1 Mucocele and Ranula

The term "mucocele" when used in the floor of the mouth may indicate either mucous retention cysts and mucous extravasation cysts. Mucous retention cysts are lined with ductal epithelium; however, mucous extravasation cysts do not have an epithelial lining and mucous extravasates into the tissues. A ranula is a mucous extravasation cyst frequently originating from the sublingual salivary gland and is classified as simple (intraoral) and deep (plunging). Ranula comes from the Latin word "rana", due to its similarity to the underbelly of a frog [23]. USG appearance of mucocele and ranula is well-demarcated, avascular, hypoechoic to anechoic, sono-compressible lesions, as is the case in cavities filled with viscous mucus, with posterior acoustic enhancement directly medial to the mandible (Figs. 11.16, 11.17) [5, 24].

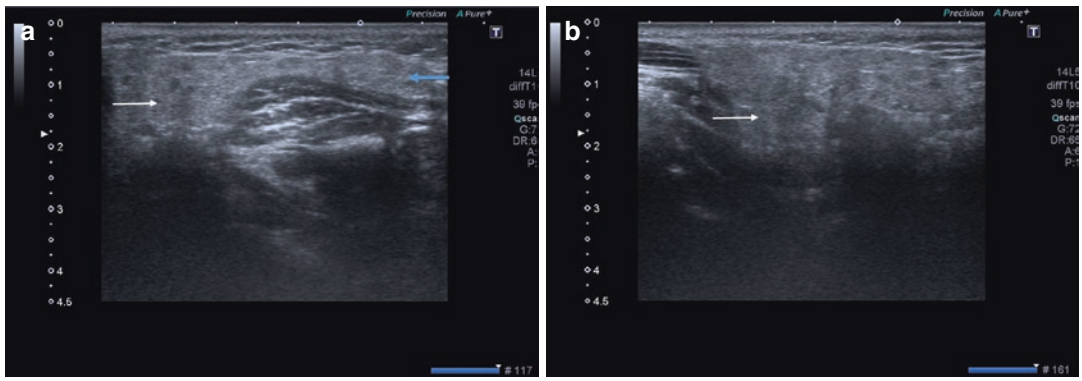

Figs. 11.11 (**a**, **b**) US image of recurrent sialoadenitis in the right parotid gland shows heterogeneity in the gland parenchyma, minimal decrease in echogenicity, and multiple millimetric hypoechoic areas within the gland. An isoechoic accessory lobe (blue arrow) of the parotid gland (variant of normal) continuous with the superficial lobe (white arrow) is seen extending to the malar region

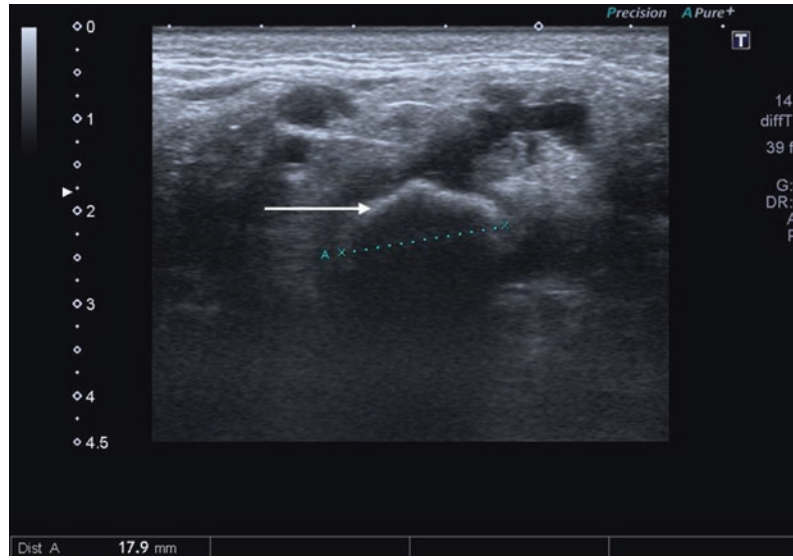

Figs. 11.12 (**a**, **b**) US image of sialolithiasis and concomitant sialoadenitis in the submandibular gland shows heterogeneity in the gland parenchyma, decrease in echogenicity, and irregular sialectasis. Echogenicity is compatible with sialolithiasis (white arrow) with intraductal convex surface and evident acoustic shadow

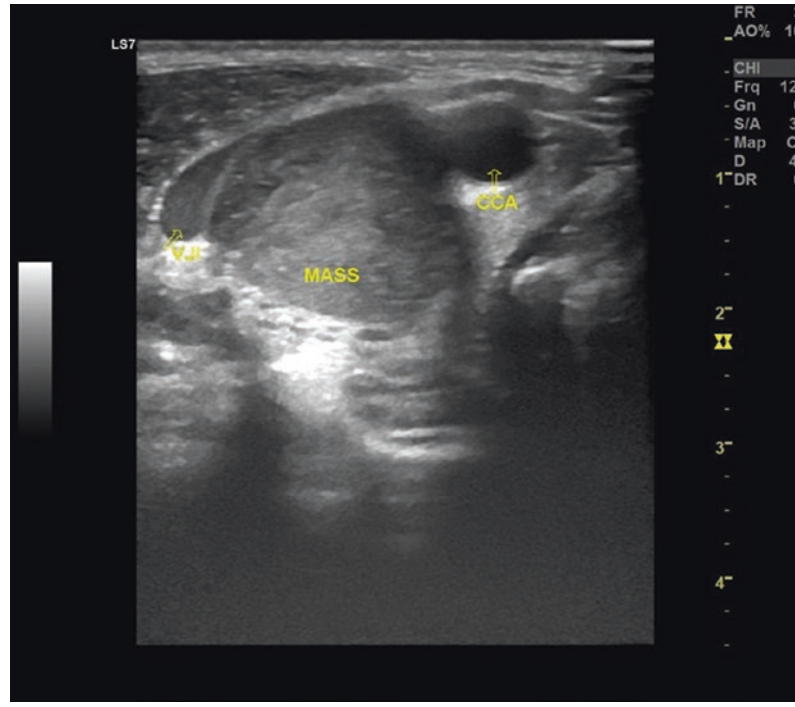

Fig. 11.13 USG view of smooth contoured hypoechoic solid neurofibroma mass located between internal jugular vein and common carotid artery in the neck in a Neurofibromatosis type 1 case

11.3.2 Dermoid and Epidermoid Cyst

Dermoid and epidermoid cysts are ectoderm-lined inclusion cysts which are thought to develop as a consequence of the persistence of ectodermal structures at neural tube and suture closure sites Dermoid cysts comprise of both ectoderm and skin elements (squamous epithelium, sebaceous glands, and hair), while epidermoid cyst comprises solely ectoderm. On USG, dermoid and epidermoid cysts are usually well-circumscribed, inhomogeneous, avascular, and hypoechoic compared to the subcutaneous fat (Figs. 11.18, 11.19, 11.20, 11.21). They infre-

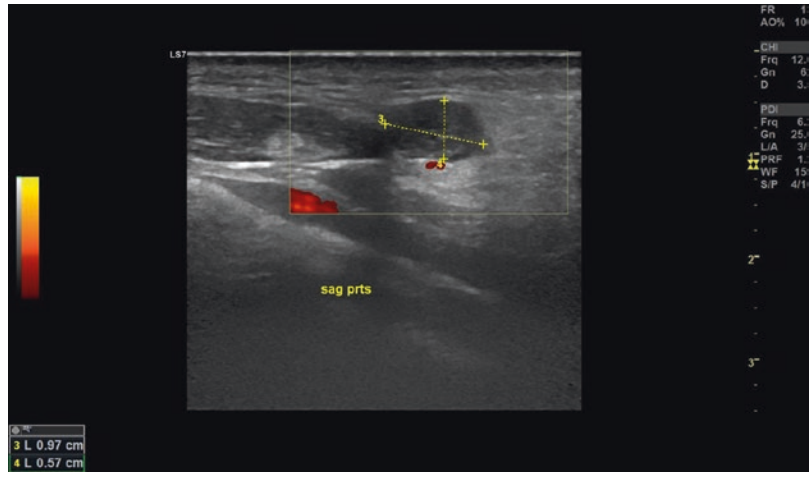

Fig. 11.14 USG image of Pleomorphic adenoma shows heterogeneous hypoechoic and smoothly contoured solid lesion within deep lobe of the right parotid gland (sag prts) with slight peripheral vascularization on color Doppler USG

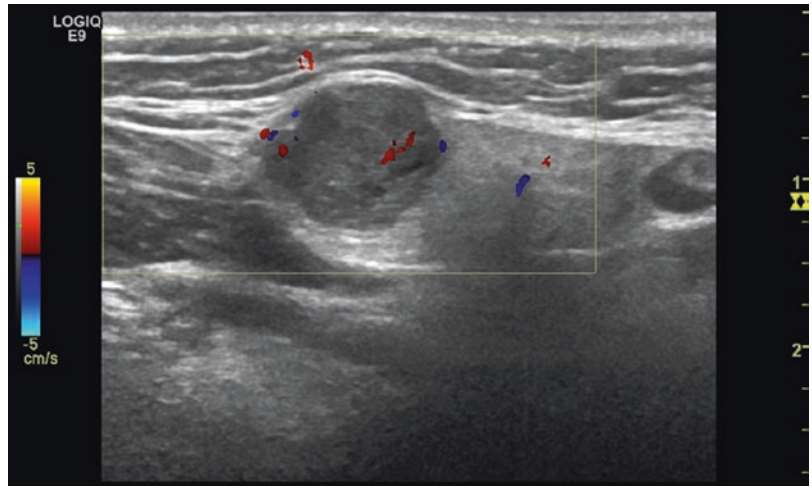

Fig. 11.15 USG view of Pleomorphic adenoma shows heterogeneous hypoechoic and smoothly contoured solid lesion in the left submandibular gland with slight vascularization on color Doppler USG

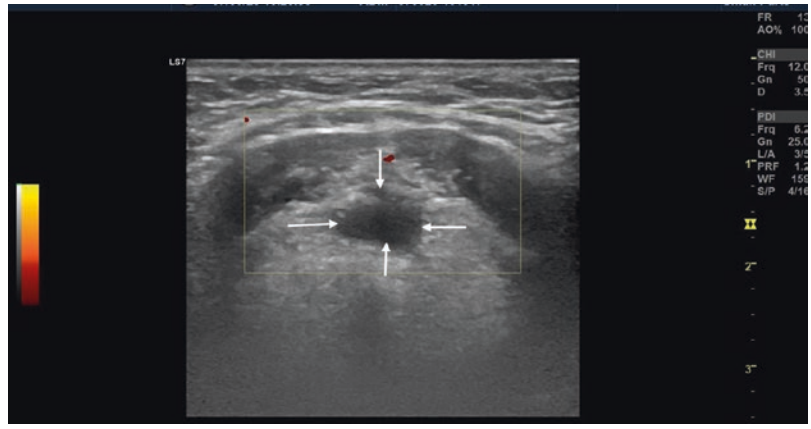

Fig. 11.16 USG view of a mucocele shows anechoic cystic lesion (white arrows) with lobular contours in the midline sublingual region, without vascularization on the color Doppler USG examination

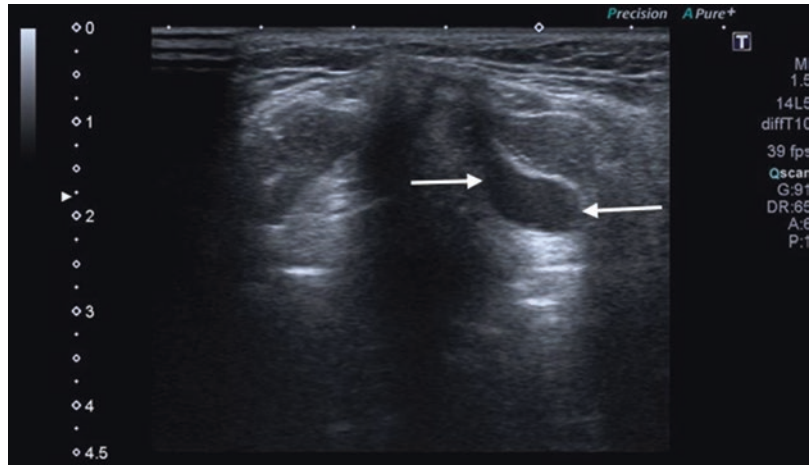

Fig. 11.17 USG view of a ranula shows anechoic cystic lesion (white arrows) with smooth contours and without internal septa in the left sublingual region. No vascularization is noted on the color Doppler USG

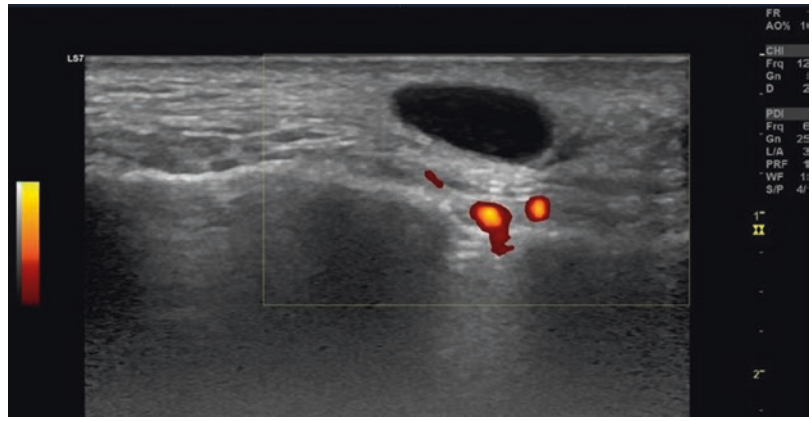

Fig. 11.18 USG view of a dermoid cyst shows an anechoic cystic lesion with smooth contours within the subcutaneous soft tissue in the infraorbital region

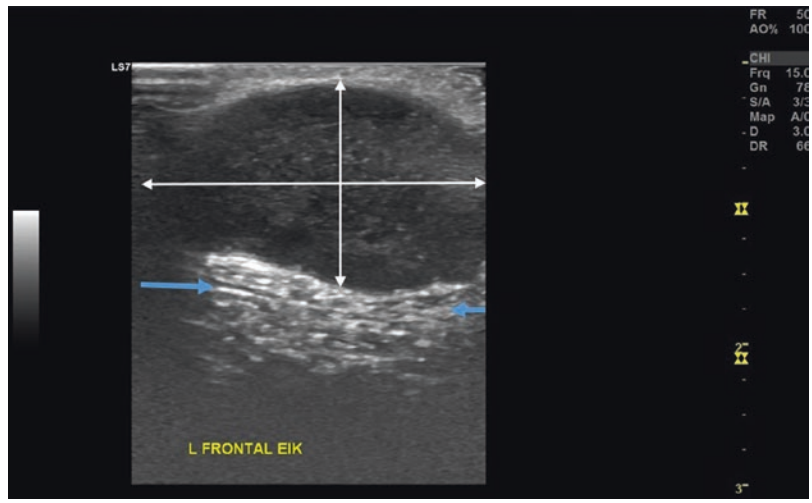

Fig. 11.19 USG image of an epidermoid cyst (EIK) shows a cystic lesion (white double-headed arrows) with smooth contours and dense content within the skin-subcutaneous soft tissue in the left frontal region (L FRONTAL), causing thinning of the skin anteriorly. Note the posterior acoustic enhancement (blue arrows)

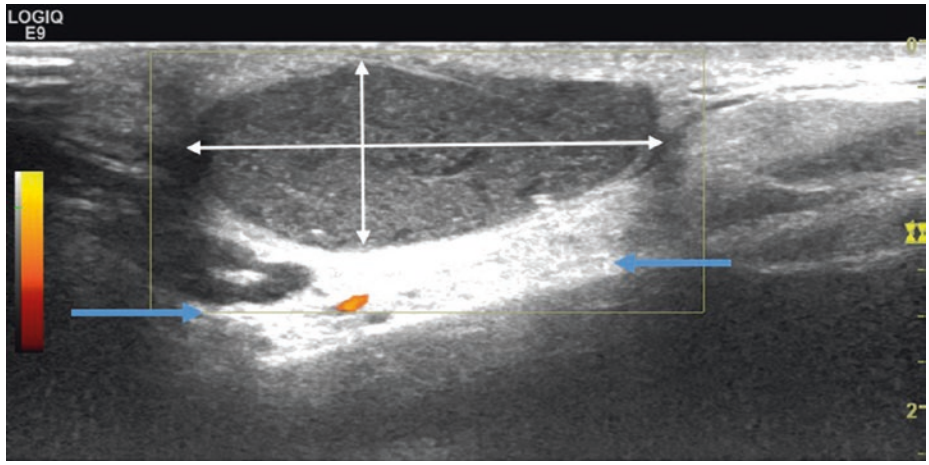

Fig. 11.20 USG image of an epidermoid cyst shows a cystic lesion (white double-headed arrows) with smooth contours and dense content within the skin-subcutaneous soft tissue in the left malar region, causing thinning of the skin anteriorly. Note posterior acoustic enhancement (blue arrows). No vascularization is noted on color Doppler USG

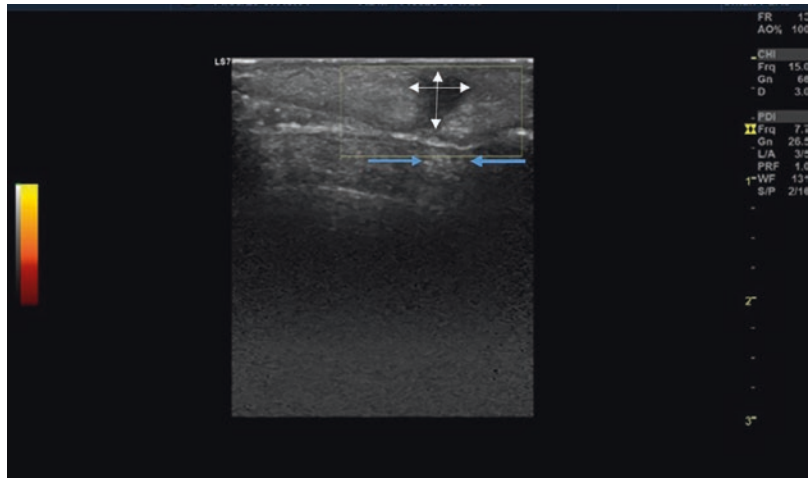

Fig. 11.21 USG image of an epidermoid cyst shows a cystic lesion (white double-headed arrows) with lobular contours and dense content within the skin-subcutaneous soft tissue in the proximal region of the left pinna, causing thinning of the skin anteriorly. Note posterior acoustic enhancement (blue arrows). No vascularization is noted in the color Doppler USG

quently have hyperechoic foci due to the presence of fat, calcification, soft tissue, or mucoid and/or purulent material [16].

11.3.3 Branchial Cleft Cyst

Branchial cleft cysts (BCCs) are commonly acknowledged as deriving from embryonic remnants of branchial pouch. BCCs arise from incomplete obliteration of the branchial arches which stay dormant until they are stimulated to undergo cystic degeneration. They occur in the upper neck, anterior to the sternocleidomastoid muscle.

On USG, they can be unilocular and sharply demarcated thin-walled cyst, but they frequently present a pseudo-solid appearance due to infection causing thickening of the cyst wall, hemorrhage, or debris (Fig. 11.22). This makes it impossible to differentiate BCCs from a necrotic metastatic squamous-cell carcinoma (Fig. 11.23) [4]. Their echogenicity varies from anechoic (most common) to different degrees of heteroge-

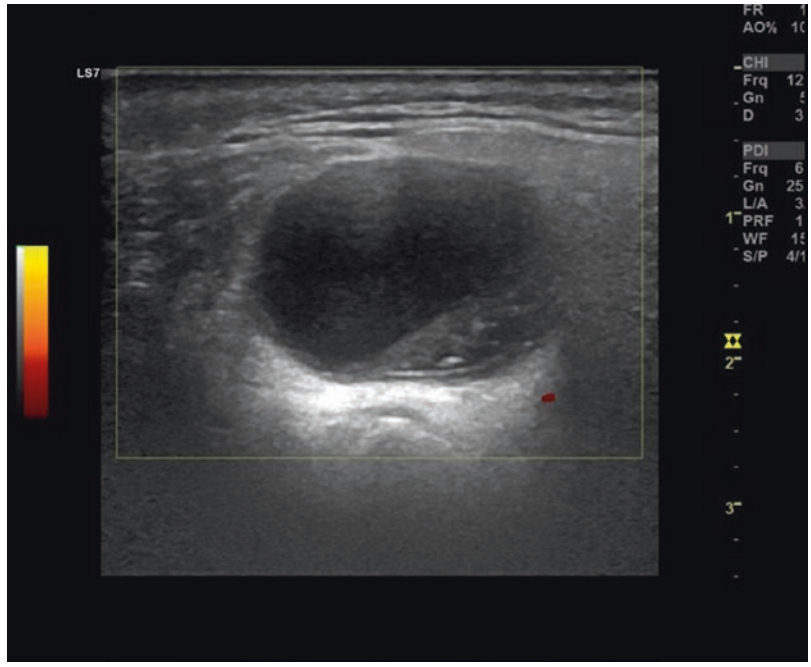

Fig. 11.22 USG image of a branchial cleft cyst shows an anechoic cystic lesion with smooth contours, dense content, and internal leveling (fluid-fluid) within the parotid gland

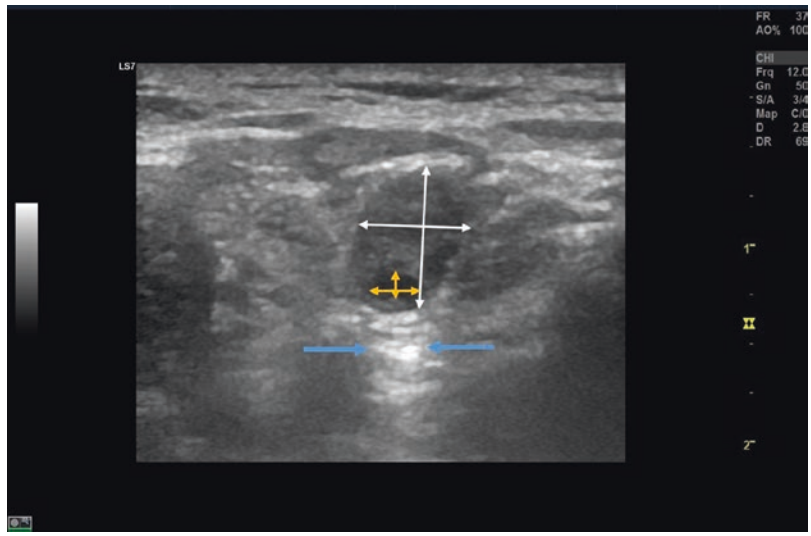

Fig. 11.23 USG image of necrotic metastatic lymphadenopathy (white double-headed arrows) of a postoperative squamous cell carcinoma case with cortical necrosis (orange double-headed arrows) in the left cervical chain, accompanied by acoustic enhancement (blue arrows) in the neighborhood of necrosis

neity depends on the internal debris. When infected, sonographic features of parotitis might be seen. Cystic lesions may show thin septa fed by vascular pedicles [25]. There might be a sinus with drainage to the external ear or skin, generally inside or near to the external auditory canal or parotid gland.

Image Interpretation Pearls

A branchial sinus can reach the lateral pharyngeal wall and carotid artery. Cross-sectional imaging should be performed prior to the removal of any BCCs [4].

11.4 Vascular Lesions

Vascular lesions vary in appearance and can frequently arise in the head and neck region. They have a wide pathological spectrum which comprise several types of malformations and tumors from simple capillary anomalies to complex pathologies including arteries, veins, and lymphatics [26].

Different vascular malformations usually present with alike US characteristics in B-mode scans; thus, to differentiate between them is hard at the first sight. They exhibit a loosely arranged, compressible, honeycomb echo pattern which is partially hypoechoic and partially echogenic (Fig. 11.24) [5].

11.4.1 Hematoma

A hematoma can occur due to vascular malformations (i.e., hemangioma and aneurysm), vessel injury, postoperative bleeding, trauma, or can be idiopathic. It appears as an irregularly defined, hypoechoic to moderately echogenic, space-occupying lesion with no intrinsic perfusion until it is organized [5]. The echogenicity decreases significantly as the hematoma resolves [16].

11.4.2 Hemangioma

Hemangiomas are congenital neoplasms which contain endothelial cell lined vascular channels [17]. On USG, they are seen as discrete cutaneous or subcutaneous soft tissue lesions which have evident internal vascularity. They have inhomogeneous echogenicity which is hypoechoic with the presence of sinusoidal compartments. (Fig. 11.25a, b) [5]. Arterial and venous flow may be shown inside the lesion, with high-velocity arterial waveforms and low-resistance venous waveforms [16, 27]. Phleboliths (venous calcification) can be detected as hyperechoic, shadowing foci [5].

11.4.3 Vascular Malformations

Vascular malformations are congenital abnormalities which are present at birth and that grows as the child grows. They are divided into four categories. Simple malformations involve capillary, lymphatic, venous, arteriovenous malformations (AVM), and arteriovenous fistulas. Combined malformations contain more than one kind of malformation, i.e., lymphatic-venous, capillary-venous. Major vessel malformations and malfor-

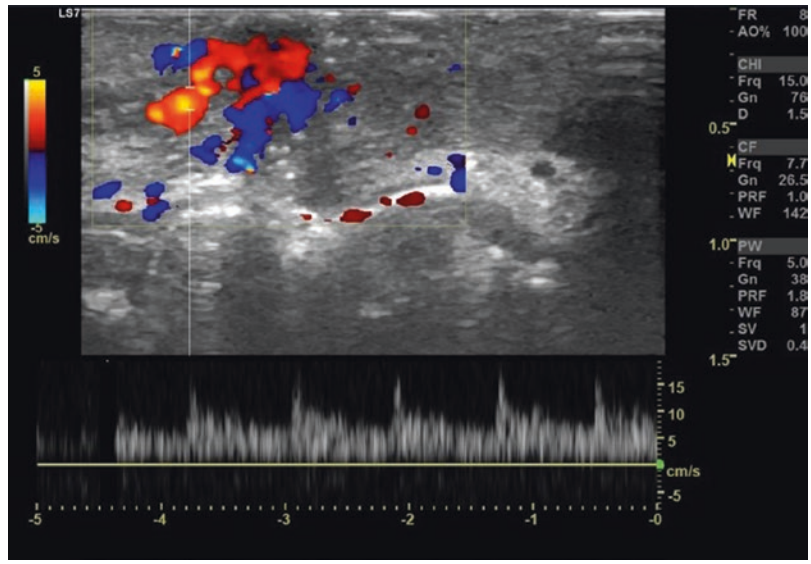

Fig. 11.24 USG image of vascular malformation in right oral commissure shows heterogeneously hypoechoic lesion within the skin-subcutaneous soft tissue containing internal anechoic tubular structures is seen in images taken with a 5–11 MHz linear probe. Note extensive vascularization on color Doppler USG

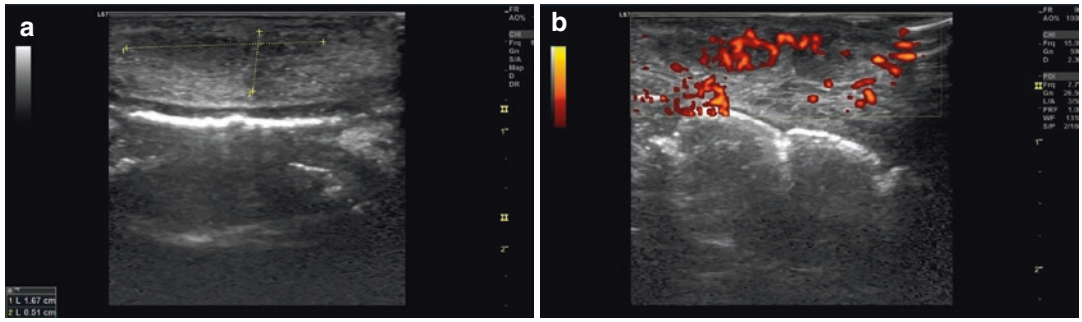

Fig. 11.25 (**a**, **b**) USG image of hemangioma in the tongue shows slightly hypoechoic solid lesion with mild internal arterial and venous vascular areas on the distal aspect of the tongue

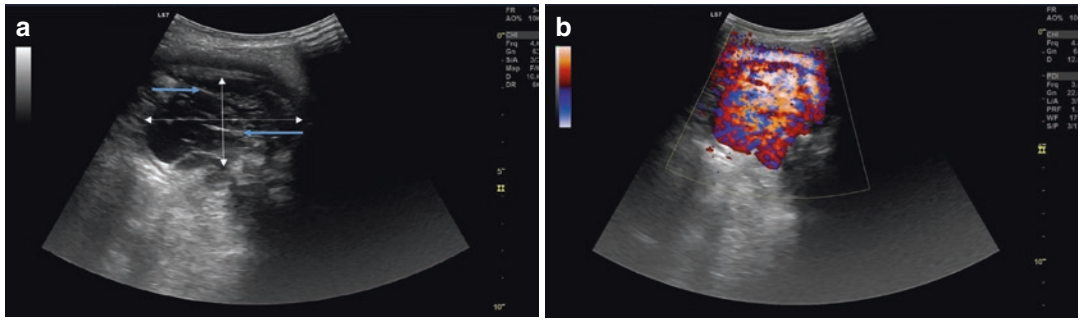

Figs. 11.26 (**a**, **b**) USG image of a vascular malformation using a 3–7 MHz convex probe image in B-Mode and color Doppler USG showing arteriovenous malformation (white double-headed arrows) on the left of the neck. Note extensive vascular anechoic lesion with internal multiple septa (blue arrows)

mations seen with other anomalies constitute the other two classes [26].

Capillary malformations are isoechoic and confined to the dermis on USG imaging. **Venous malformations** constitute most slow flow lesions. On USG, these lesions seem as multiple tubules/vascular channels which might be compressed, have phleboliths, and may or may not have visible flow owing to low velocity. **Lymphatic malformations** are seen as cystic structures with no flow. These cystic structures may be macrocytic (greater than 2 cm) or microcystic (less than 2 cm). On USG, the microcystic form might be seen as hyperechoic as a result of several interfaces of the cyst wall. **Arteriovenous malformations and fistulae** are high-flow anomalies which have a direct connection between arteries and veins and lack the normal capillary bed between these vessels. The USG appearance of AVMs is assortments of numerous tortuous vessels that are not organized as a soft tissue mass. These lesions exhibit high-velocity low-resistance arterial flow with a direct connection between the arterial and venous system on Color Doppler USG. It might be hard to detect the arterial origin or venous drainage of these anomalies (Fig. 11.26a, b) [16, 17, 26, 28].

Lymphangiomas are congenital anomalies of the lymphatic system and are composed of different volume cystic spaces [27]. Lymphangiomas are divided into three categories based on the lymphatic cavity size and their characteristic feature loculated appearance: cystic lymphangioma, capillary or microcystic lymphangioma, and cavernous or macrocystic lymphangioma. On USG, lymphangiomas are usually seen as multilocular cystic masses with the presence of different thickness internal septa (Fig. 11.27). The cystic content might be anechoic or hyperechoic if infection, internal hemorrhage, or elevated lipid content

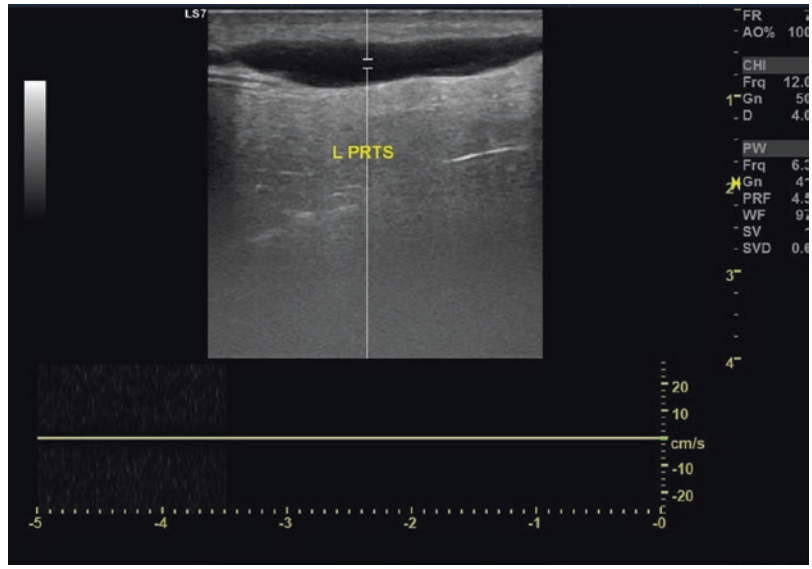

Fig. 11.27 USG image of a lymphangioma shows extraglandular anechoic and lobular cystic lesion with smooth contours containing thin internal septa on the anterior aspect of the left parotid gland (L PRTS). The lesion has a horizontal course. No vascularization is present on color Doppler USG

accompanies [16, 27]. They are easily compressible, generally do not generate any Doppler signal or color flow but sometimes arterial or venous flow might be seen in the septa [5, 16, 17].

11.5 Malignant Lesions

USG and Doppler USG are helpful in preoperative diagnosis of malignant potential or type of tumor in the facial soft tissues although it is not possible to definitively distinguish benign from malignant. The presence of irregular margins, inhomogeneous echogenicity, and abnormal vascularity together with necrotic or enlarged adjacent lymph nodes are indicative of malignant lesions (Figs. 11.28, 11.29). Some malignant tumors exhibit increased vascularity and high systolic peak flow rate while some exhibit high intra-tumoral vascular resistance (Fig. 11.30, 11.31). Bleeding within the tumor can produce heterogeneous solid and cystic looking zones [24]. The sensitivity of imaging tumor vascularity is increased with the application of US contrast enhancement [4]. The capability to palpate with the US probe gives unique information about a lesion's stiffness or compressibility not offered with magnetic resonance imaging and computerized tomography. This "objective" palpation is very helpful in differentiating benign from malignant pathology [29].

11.5.1 Metastasis

The proper lymph node evaluation is crucial, as it is the potential site for regional metastasis [5]. Normal lymph nodes appear as a well-defined, fusiform, kidney-bean shape with a low to intermediate reflectivity, homogeneous cortex, and a hyperechoic linear fatty hilum (highly reflective central hilus). A width-to-length ratio more than 0.5 indicates a rounded pathologic lymph node, and the more rounded a lymph node, the more likely it is a metastasis. In color Doppler, benign node flow is characteristically hilar or central in circulation. Pathologic lymph nodes have a propensity to lose their central echogenic hilum and tendency to be "black" or hypoechoic with thickening of their cortex (Figs. 11.32, 11.33). Subcapsular or peripheral vessels are a robust indication of malignancy. Lymphoma infiltrated lymph nodes are typically seen rounded, but frequently maintain a central hyperechoic hilum, and look hypoechoic (pseudocystic) and homogeneous which makes it difficult to differentiate from benign nodes. Color Doppler usually displays an excessive benign blood flow form (Fig. 11.34) [4].

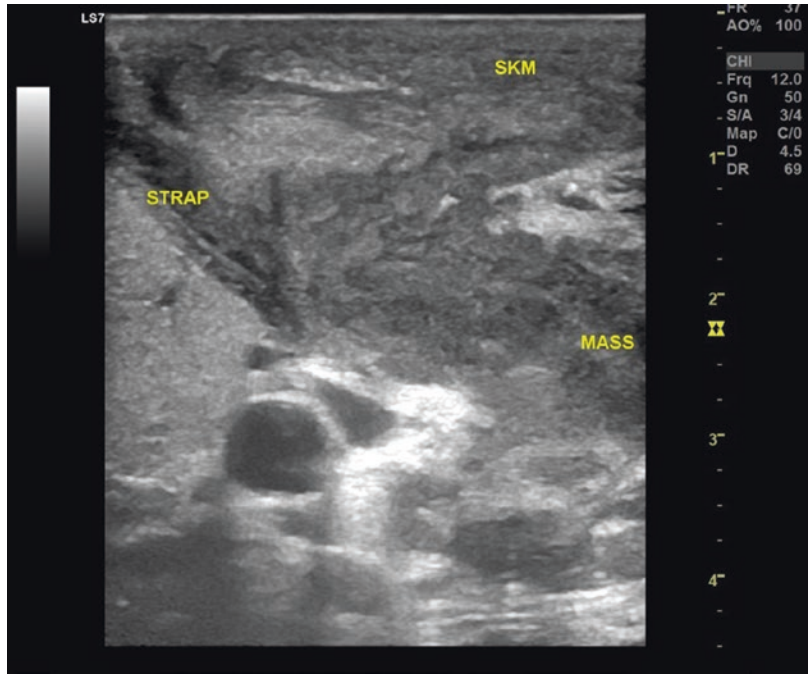

Fig. 11.28 USG image of a nodular sclerosing type Hodgkin lymphoma (HL) mass on the left of the neck shows heterogeneously hypoechoic solid lesion with irregular contours, invading sternocleidomastoid (SKM) and strap (STRAP) muscles and adjacent soft tissues

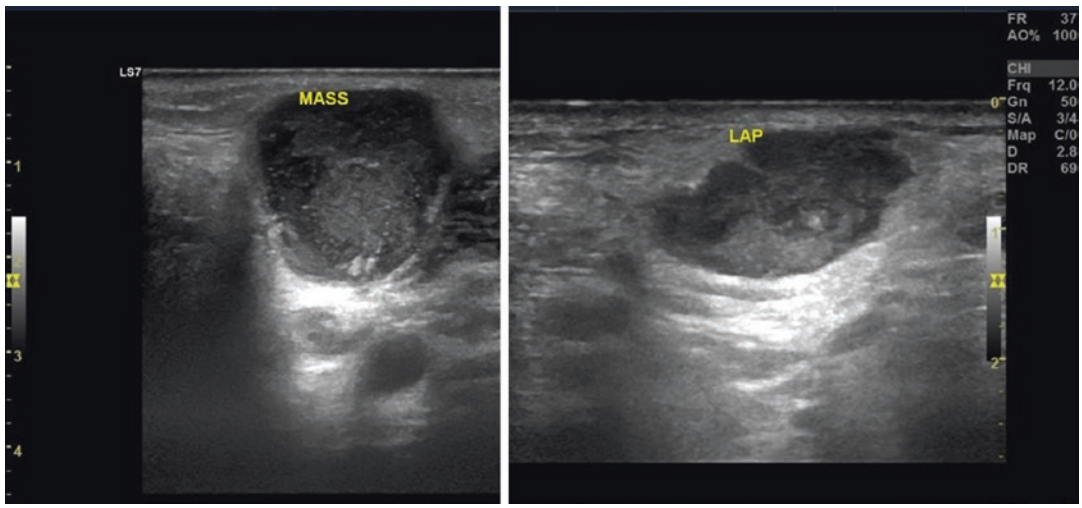

Fig. 11.29 USG image of metastatic lymphadenopathy (LAP) in a mucoepidermoid carcinoma (MASS) of the parotid gland and concomitant metastatic LAP

Image Interpretation Pearls

In patients suspicious of malignancy, related lymphatic drainage systems have to be examined properly for the detection of abnormal nodes and their anatomic sites [5].

11.5.2 Lymphoma

In lymphoma, USG usually shows enlarged, round, hypoechoic to anechoic lymph nodes with an absent or eccentric echogenic hilum and a tendency to form masses (Fig. 11.34). There is increased diffuse central and peripheral hypervascularity [30].

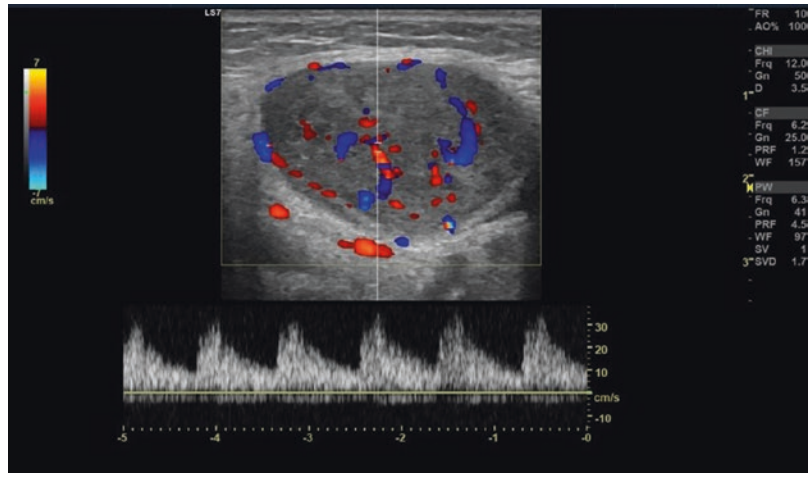

Fig. 11.30 USG image of a malignant mass in the left submandibular gland shows a hypoechoic, heterogeneous solid mass with internal and peripheral hypervascularization consistent with malignancy within the submandibular gland

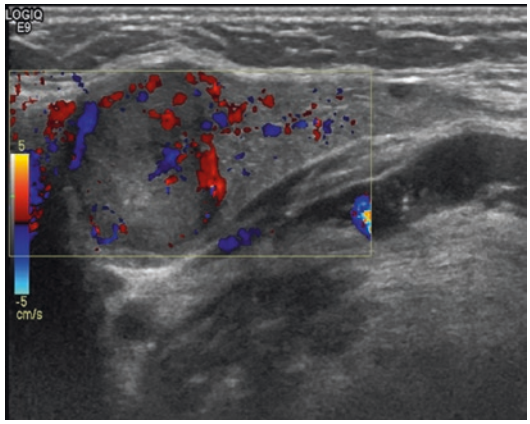

Fig. 11.31 USG image of a metastatic renal cell carcinoma mass in the submandibular gland. Irregularly contoured, hypoechoic, heterogeneous intraglandular solid lesion. The mass has internal and peripheral intermittent hypervascularization on the color Doppler USG

Lymphomatous nodes may demonstrate internal reticulation, resulting in micronodular manifestation, along with high pulsatility index and resistive index values at spectral Doppler USG [16, 30].

11.5.3 Leukemia

In leukemia, enlarged nodes are arranged in large clusters. The shape of lymph nodes may be preserved, but confluent lymphadenopathy simulating lymphoma may be seen. Due to the mass effect, an eccentric hilus indicative of nodal infiltration may be present (Fig. 11.35) [31].

11.6 Systemic Diseases

11.6.1 Sjogren's Syndrome

Sjögren's syndrome (SS) is a systemic autoimmune disorder characterized by lymphocytic infiltration and then destruction of the exocrine glands (especially the salivary and lachrymal glands) resulting in dry eye and mouth [32, 33]. SS frequently accompanies other immune system diseases, such as rheumatoid arthritis and lupus, and might also be seen with serious systemic diseases such as lymphoma. The common USG features are parenchymal inhomogeneity with several, scattered, small, oval, hypo-anechoic or hyperechoic areas (due to multiple cysts or calcifications, respectively), decreased echogenicity, generally well-defined, peri-intraglandular lymph nodes, glandular margin irregularities, and hypervascularity (Figs. 11.36, 11.37) [32]. Glandular hypervascularization might cause decrease in the resistive index (RI) of the transverse facial artery (Fig. 11.38) [33].

Image Interpretation Pearls
USG (B-mode, color, and spectral Doppler of transverse facial artery) and sonoelastography are complementary tools to each other for the evaluation of salivary gland involvement in SS [33].

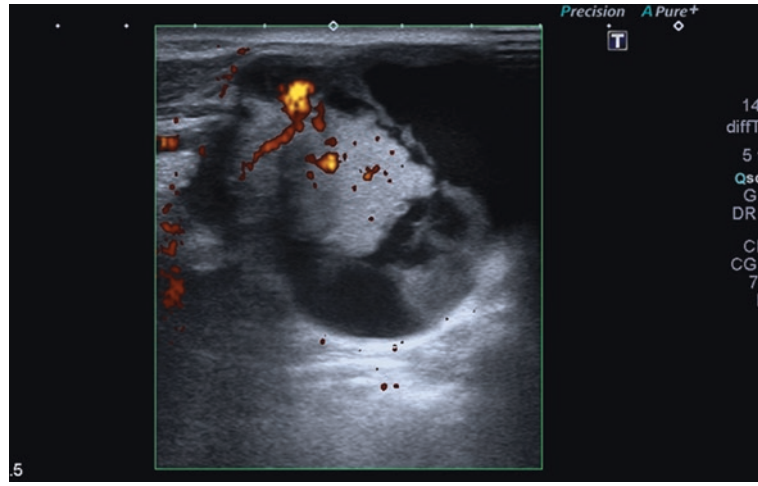

Fig. 11.32 USG image of metastatic lymphadenopathy (LAP) shows metastatic, necrotic cervical LAP of thyroid gland papillary carcinoma

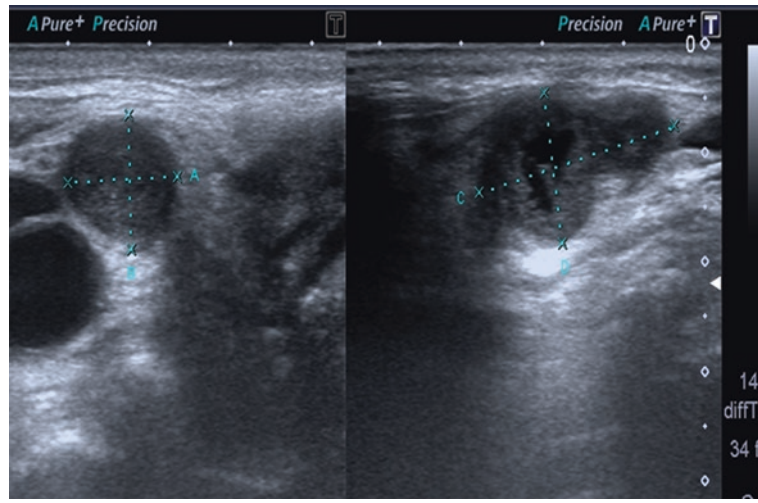

Fig. 11.33 USG image of metastatic lymphadenopathy (LAP) shows cervical metastatic LAPs of epithelial malignant tumor

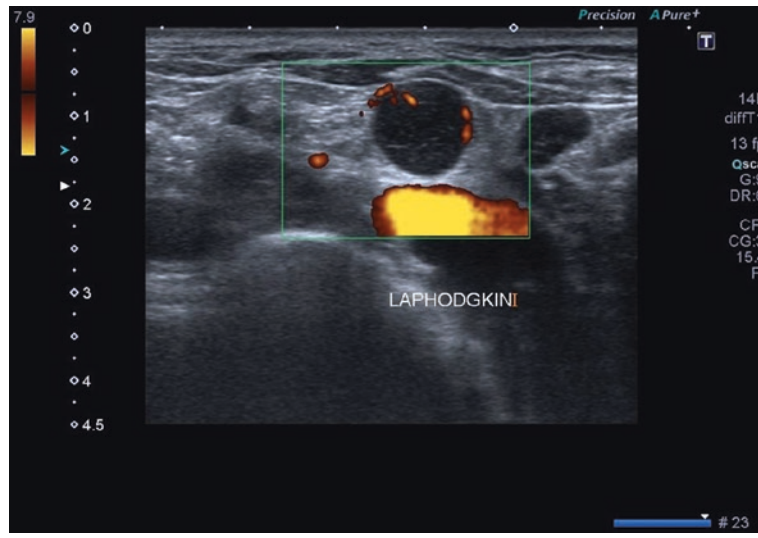

Fig. 11.34 USG image of spherical lymphadenopathy (LAP) with hypoechoic cortex and an effaced hilum in a Hodgkin lymphoma (HL) case. Peripheral vascularization is seen on color Doppler USG

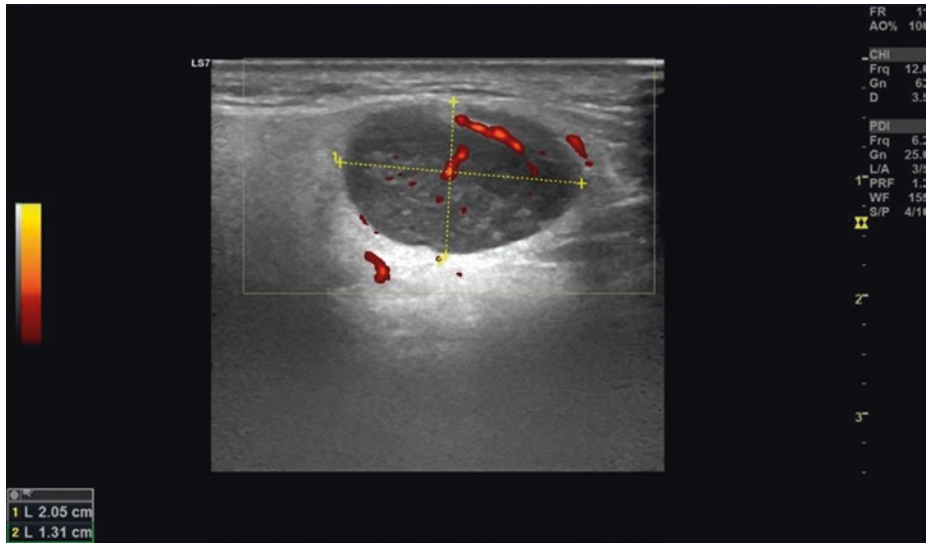

Fig. 11.35 USG image in a patient with leukemia shows intraglandular lymphadenopathy (LAP) with asymmetric heterogeneous thick cortex in the right parotid gland. Hilar cortical and peripheral vascularization is seen

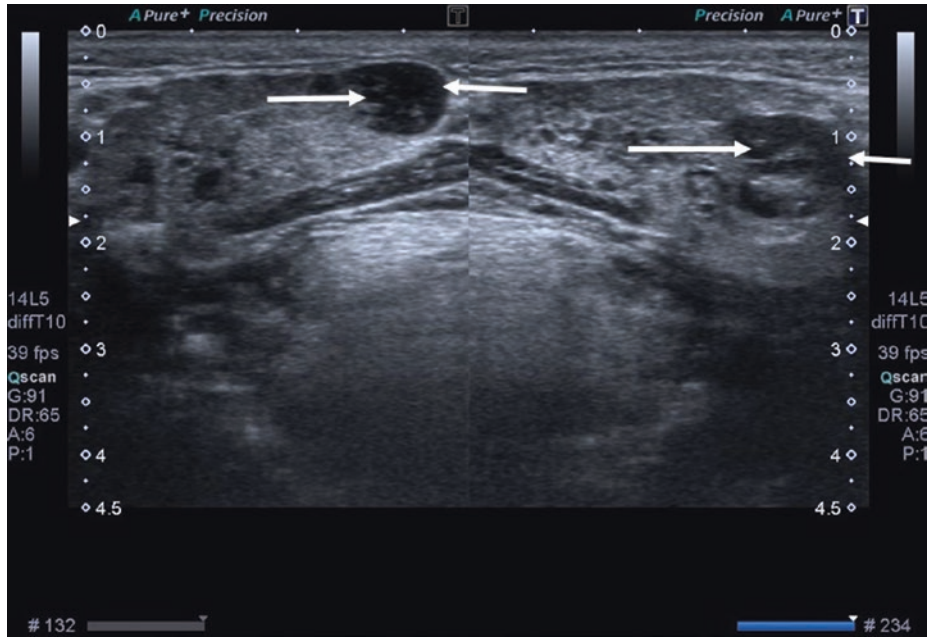

Fig. 11.36 USG image in Non-Hodgkin lymphoma (NHL) in bilateral submandibular glands of a patient with Sjogren's syndrome shows glands that exhibit internal, multiple, millimetric hypo-anechoic micronodular appearances, evident parenchymal septa, decreased echogenicity, and heterogeneous appearance. Extensive, hypoechoic, patchy-pseudonodular NHL involvement areas (white arrows) are present within the glands

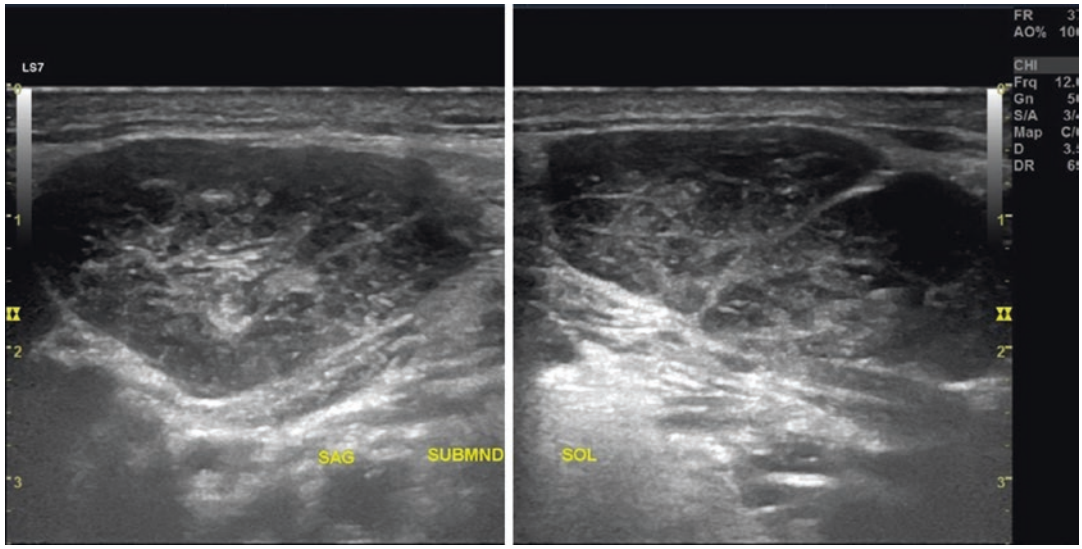

Fig. 11.37 USG image of right (SAG) and left (SOL) submandibular gland (SUBMND) involvement of a patient with Sjogren's syndrome shows glands that are heterogeneous in appearance with decrease in echogenicity, multiple millimetric patchy-micronodular hypoechoic appearances, and evident parenchymal septa

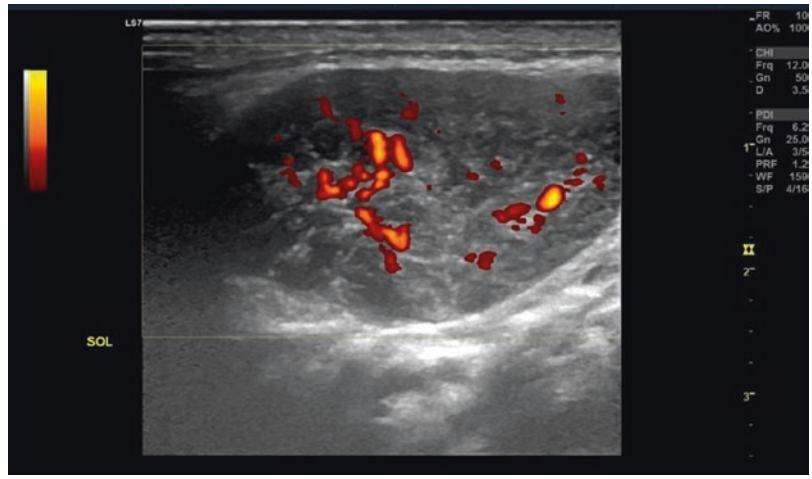

Fig. 11.38 USG image of bilateral submandibular gland involvement in a patient with Sjogren's syndrome shows an increase in gland vascularization on color Doppler USG

References

1. Kotecha S, Bhatia P, Rout PG. Diagnostic ultrasound in the head and neck region. Dent Update. 2008;35(8):529–30. 33-4
2. Klem C. Head and neck anatomy and ultrasound correlation. Otolaryngol Clin N Am. 2010;43(6):1161–9. v
3. Demirturk Kocasarac H, Angelopoulos C. Ultrasound in dentistry: toward a future of radiation-free imaging. Dent Clin N Am. 2018;62(3):481–9.
4. Oeppen RS, Gibson D, Brennan PA. An update on the use of ultrasound imaging in oral and maxillofacial surgery. Br J Oral Maxillofac Surg. 2010;48(6):412–8.
5. Iro H, Bozzato A, Zenk J. In: Iro H, Bozzato A, Zenk J, editors. Atlas of head and neck ultrasound. 1st ed. New York: Thieme Medical Publishers, Inc.; 2013.
6. Volk GF, Pohlmann M, Sauer M, Finkensieper M, Guntinas-Lichius O. Quantitative ultrasonography of facial muscles in patients with chronic facial palsy. Muscle Nerve. 2014;50(3):358–65.
7. Zhang WH, Chen YY, Liu JJ, Liao XH, Du YC, Gao Y. Application of ultrasound imaging of upper

lip orbicularis oris muscle. Int J Clin Exp Med. 2015;8(3):3391–400.
8. Serra MD, Duarte Gaviao MB, dos Santos Uchoa MN. The use of ultrasound in the investigation of the muscles of mastication. Ultrasound Med Biol. 2008;34(12):1875–84.
9. Kiliaridis S, Engvall M, Tzakis MG. Ultrasound imaging of the masseter muscle in myotonic dystrophy patients. J Oral Rehabil. 1995;22(8):619–25.
10. Ariji E, Ariji Y, Yoshiura K, Kimura S, Horinouchi Y, Kanda S. Ultrasonographic evaluation of inflammatory changes in the masseter muscle. Oral Surg Oral Med Oral Pathol. 1994;78(6):797–801.
11. Goto TK, Langenbach GE, Hannam AG. Length changes in the human masseter muscle after jaw movement. Anat Rec. 2001;262(3):293–300.
12. Sano K, Ninomiya H, Sekine J, Pe MB, Inokuchi T. Application of magnetic resonance imaging and ultrasonography to preoperative evaluation of masseteric hypertrophy. J Craniomaxillofac Surg. 1991;19(5):223–6.
13. Surej Kumar L, Zachariah GP, Chandran S. Ultrasonography: a step forward in temporomandibular joint imaging. A preliminary descriptive study. Clin Pract. 2019;9(2)
14. Lipschitz N, Yakirevitch A, Sagiv D, Migirov L, Talmi YP, Wolf M, et al. Nasal vestibulitis: etiology, risk factors, and clinical characteristics: a retrospective study of 118 cases. Diagn Microbiol Infect Dis. 2017;89(2):131–4.
15. Sakat MS, Kilic K, Ucuncu H. Nasal vestibular Furunculosis presenting as the Rudolph sign. J Craniofac Surg. 2015;26(6):e545–6.
16. Bansal AG, Oudsema R, Masseaux JA, Rosenberg HK. US of pediatric superficial masses of the head and neck. Radiographics. 2018;38(4):1239–63.
17. Friedman ER, John SD. Imaging of pediatric neck masses. Radiol Clin N Am. 2011;49(4):617–32. v
18. Reimers CD, Fleckenstein JL, Witt TN, Muller-Felber W, Pongratz DE. Muscular ultrasound in idiopathic inflammatory myopathies of adults. J Neurol Sci. 1993;116(1):82–92.
19. Mantsopoulos K, Wurm J, Iro H, Zenk J. Role of ultrasonography in the detection of a subperiosteal abscess secondary to mastoiditis in pediatric patients. Ultrasound Med Biol. 2015;41(6):1612–5.
20. Hosokawa T, Takahashi H, Miyasaka Y, Ohira K, Tanami Y, Sato Y, et al. Ultrasound evaluation of dermal sinuses/fistulas in pediatric patients. J Ultrasound Med. 2019;38(12):3107–22.
21. Alyas F, Lewis K, Williams M, Moody A, Wong K, Ahuja A, et al. Diseases of the submandibular gland as demonstrated using high resolution ultrasound. Br J Radiol. 2005;78(928):362–9.
22. Ahuja A, Richards P, Wong K, King A, Yuen H, Ching A, et al. Kuttner tumour (chronic sclerosing sialadenitis) of the submandibular gland: sonographic appearances. Ultrasound Med Biol. 2003;29(7):913–9.
23. Diom ES, Fagan JJ, Bolding E. Intralingual mucous extravasation cyst: an uncommon lingual cyst. Ear Nose Throat J. 2019;98(5):E21–e3.
24. Orloff LA, Hwang HS, Jecker P. The role of ultrasound in the diagnosis and management of salivary disease. Oper Tech Otolaryngol Head Neck Surg. 2009;20(2):136–44.
25. Upile T, Jerjes W, Al-Khawalde M, Kafas P, Frampton S, Gray A, et al. Branchial cysts within the parotid salivary gland. Head Neck Oncol. 2012;4:24.
26. Brahmbhatt AN, Skalski KA, Bhatt AA. Vascular lesions of the head and neck: an update on classification and imaging review. Insights Imaging. 2020;11(1):19.
27. Fefferman NR, Milla SS. Ultrasound imaging of the neck in children. Ultrasound Clin. 2009;4(4):553–69.
28. Donnelly LF, Adams DM, Bisset GS 3rd. Vascular malformations and hemangiomas: a practical approach in a multidisciplinary clinic. AJR Am J Roentgenol. 2000;174(3):597–608.
29. Holtel MR. Emerging technology in head and neck ultrasonography. Otolaryngol Clin N Am. 2010;43(6):1267–74. vii
30. Ahuja AT, Ying M. Sonographic evaluation of cervical lymph nodes. AJR Am J Roentgenol. 2005;184(5):1691–9.
31. Restrepo R, Oneto J, Lopez K, Kukreja K. Head and neck lymph nodes in children: the spectrum from normal to abnormal. Pediatr Radiol. 2009;39(8):836–46.
32. Lee KA, Lee SH, Kim HR. Ultrasonographic changes of major salivary glands in primary Sjogren's syndrome. J Clin Med. 2020;9(3)
33. Caraba A, Babalic FC, Iurciuc S, Iurciuc M. The utility of major salivary gland Ultrasonographic parameters in the diagnosis of Sjogren syndrome. Dis Markers. 2019;2019:1716848.

12 Sonographic Anatomy and Pathology: Paranasal Sinuses and Midface

Husniye Demirturk Kocasarac, Dania Tamimi, and Mehtap Balaban

Contents

12.1 Anatomy

As a result of developments in ultrasound (US) technology and high-resolution ultrasonography (USG), US is now used in the examination and diagnosis of bone pathology of the paranasal sinuses and midface [1]. USG may be performed as a screening tool and to get a preliminary diagnosis even though a negative result does not certainly eliminate the possibility of pathology of the paranasal sinuses and midface. Because it is radiation-free, it may be recommended as a first

H. Demirturk Kocasarac (✉)
School of Dentistry, Department of General Dental Sciences, Division of Oral and Maxillofacial Radiology, Marquette University, Milwaukee, WI, USA

D. Tamimi
Oral and Maxillofacial Radiology, Private Practice, Orlando, FL, USA

M. Balaban
Faculty of Medicine, Department of Radiology, Yıldırım Beyazıt University, Ankara, Turkey

K. Orhan (ed.), *Ultrasonography in Dentomaxillofacial Diagnostics*,
https://doi.org/10.1007/978-3-030-62179-7_12

step for the examination of pregnant women, young women, and children [2].

B-mode US images might be generated by mechanically moving an US probe on a trajectory, (i.e., a line), receiving RF-echo traces from each probe position, and then reconstructing the US image following numerous signal processing stages. A-mode USG is the most basic display mode right after plotting the RF-signal and it is progressively being substituted by B-mode USG in diagnostic imaging of the paranasal sinuses and midface [2, 3].

The frontal and maxillary sinuses are easier to visualize with USG owing to their superficial location. Sound waves penetrating through the anterior wall of the frontal and maxillary sinus are reflected by the air in the sinus, as the healthy sinuses are filled with air [4, 5]. However, in the presence of fluid or mucus inside the sinus cavity, sound waves can pass to the posterior wall of the sinus, thereby creating an ultrasound image of the sinus. The first layer is the skin and subcutaneous tissue in the US image of the healthy sinus. The second layer is the anterior wall of the maxillary sinus which is observed as well-defined, hyperechoic lines (Fig. 12.1) [5, 6]. The greater the volume of the mucosal thickening or fluid, the greater the visibility of the US wave [7].

Normal and pathological structures in the eyeball can be visualized with USG (Fig. 12.2). The eyeball is also fluid-filled which allows the imaging of tissues posterior to it such as orbit and ethmoid air cells [8]. However, the ultrasonic acoustic barrier prevents visualization of bony details and deep anatomic tissues, as is the case for posterior ethmoid air cells and sphenoid sinus [9].

Hockey stick and linear probes are preferred for imaging of the maxillofacial region [4–6]. When performing ultrasonographic examination in the paranasal sinuses, the upper body should be in an upright position with the head slightly tilted forward to obtain the appropriate image. Hyperextension or anteflexion of the head can

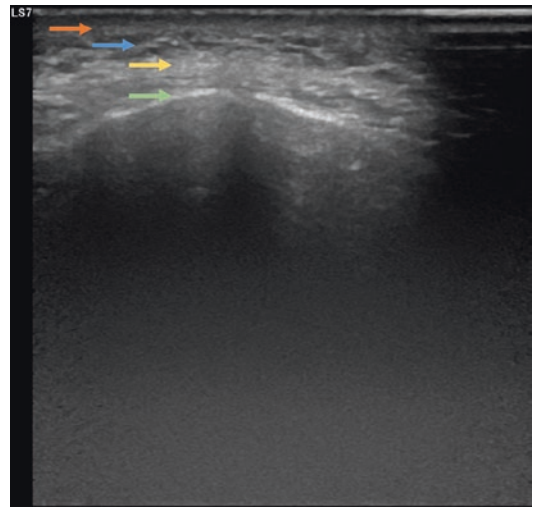

Fig. 12.1 Normal maxillary sinus US image obtained with a 5–11 MHz linear probe. From outside to inside; mildly hypoechoic epidermis (orange arrow), subcutaneous adipose tissue (blue arrow) with hypoechoic lobule appearance, mildly hyperechoic soft tissue (yellow arrow), and hyperechoic maxillary anterior wall (green arrow) with smooth convex surface

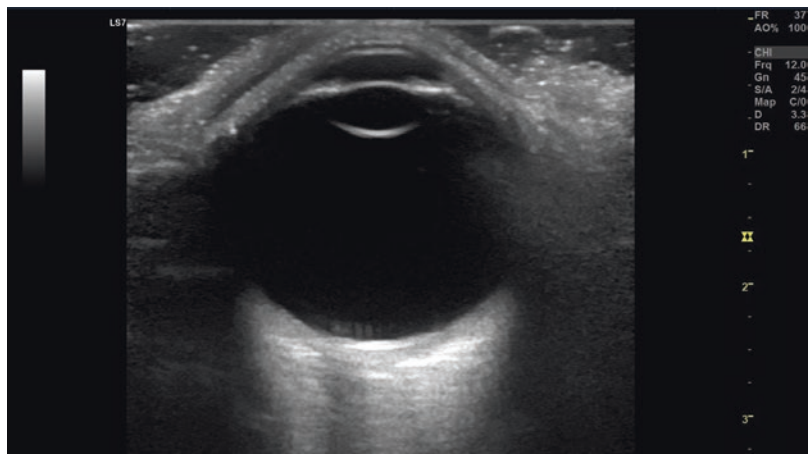

Fig. 12.2 US image of a normal globe

differentiate effusion or fluid from other pathologies [4, 8].

The examination of the frontal and maxillary sinuses is always carried out in longitudinal and transverse planes. It is important to compare the patient's right and left side findings. To evaluate the maxillary sinus, the probe is placed at the level of the infraorbital nerve on the anterior wall of the maxillary sinus (Figs. 12.3 and 12.4). The region is examined by moving the probe in the craniocaudal and mediolateral directions. Positioning the probe at different angles allows a full examination of the area of interest. During the ultrasonographic evaluation of the frontal sinus, the probe must be positioned between and just above the eyebrows (Figs. 12.5 and 12.6). High gain, a penetration depth of ±60 mm, and as low insonation frequency as possible should be adjusted in advance [8].

Fig. 12.3 Photograph showing patient and ultrasound probe positioning for maxillary sinus examination

Fig. 12.5 Photograph showing patient and ultrasound probe positioning for frontal sinus examination

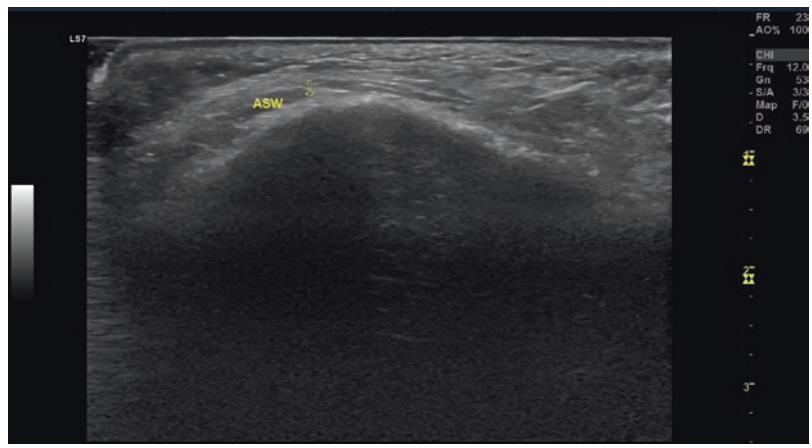

Fig. 12.4 US image of normal maxillary sinus. ASW: Anterior sinus wall

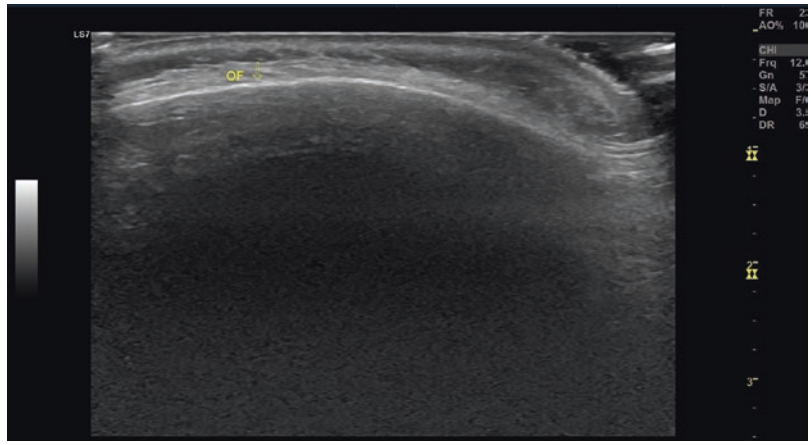

Fig. 12.6 US image of normal frontal sinus of frontal bone

12.2 Diseases of Paranasal Sinuses and Midface: A Brief Review of Typical USG Aspect of the Most Frequently Encountered Pathologies

12.2.1 Inflammatory Changes

12.2.1.1 Sinusitis

US has a significant value in the evaluation of sinusitis of maxillary sinuses, especially acute sinusitis as maxillary sinuses are generally affected. The normal sinus can be accurately diagnosed as healthy because of the total reflection of the air-filled normal sinus [2].

When the sinus is filled with fluid material such as secretion, pus or mucus, sound waves passing through these inflammatory products are reflected by the posterior wall of the sinus cavity giving a visible "posterior wall echo." The posterior wall echo, which is observed in the echogram, indicates that there is a pathological condition in the sinus. When there is fluid collection (i.e., sinusitis) in the paranasal sinus, anechoic to hypoechoic with scarce isolated internal echoes, homogeneous or heterogeneous, well-defined, triangle shape (maxillary sinus) is observed in the image, whereas in case of mucosal thickening, hypoechoic to echoic, non-triangular shape image with unclear boundaries is observed [4–6, 8].

The USG examination is done while the patient is sitting in an upright position, with the head at an angle of 90 degrees flexion to concentrate any fluid characteristics of the sinusitis on the anterior sinus wall (Figs. 12.7 and 12.8) [4, 10]. Swelling of adjacent soft tissues, following interruption of bony structures in pres-

Fig. 12.7 Photograph showing patient and ultrasound probe positioning for frontal sinus examination in presence of fluid collection (i.e., sinusitis). The patient is in a seated position and the neck is anteriorly flexed to concentrate any fluid characteristics of the sinusitis on the anterior sinus wall. The 5–11 MHz linear probe is placed in the medial part of the orbit and angled to the proximal part of the nasal region

Fig. 12.8 Photograph showing patient and ultrasound probe positioning for maxillary sinus examination in presence of fluid collection (i.e., sinusitis). The patient is in a seated position and the neck is anteriorly flexed to concentrate any fluid characteristics of the sinusitis on the anterior sinus wall. Maxillary sinus is visualized from the anterior wall with a 5–11 MHz linear probe

ence of aggravated inflammatory process, can be seen [8].

12.3 Benign Lesions

12.3.1 Paranasal Sinuses

Generally, benign tumors display homogeneous internal echoes, round or oval shape, and clear margins [9]. The visualization of the tumor is not dependent on the head position. If the USG performed while moving the patient's head at different angles shows that the sinus content does not change in thickness; this implies the existence of a solid hypoechoic lesion [4, 10]. In the presence of a lesion in the paranasal sinuses and nasal cavity, the surrounding bone and air improve the contrast of the hypoechoic mass significantly, that facilitates defining the margins of the masses [9].

When a mass is in contact with the anterior wall of the paranasal sinus, US waves continuously propagate to extend to the posterior wall of the sinus. In this case comparison with the contralateral side may exclude the probability of pansinusitis [4, 10]. Since mucous retention pseudocysts often originate from the floor of the maxillary sinus, they will not be detected by USG unless the pathology contacts with the anterior wall of the maxillary sinus [11]. Mucus retention phenomenon and the more aggressive but less common mucoceles that are in contact with the anterior wall might be visualized as space-occupying round lesions. Structures located posterior to the air-filled regions are not observable and an isolated pathology on the posterior wall of the air-filled sinus will not be detected [8].

Benign lesions of the paranasal sinuses like adenoma or mycetoma can be seen on USG in some particular cases and may be difficult to differentiate from inflammatory process. Several heterogeneous reflecting structures neighboring the anterior wall and probably reaching the posterior wall of the sinus might be detected. The intense, irregular echo form differentiates these lesions from mucus retention pseudocyst, mucocele, or effusion that has distinct US features extending from anterior to the posterior wall. The multiple reflections are a strong indication of a solid lesion in the paranasal sinuses [8].

12.3.2 Midface

12.3.2.1 Pilomatrixoma

Pilomatrixoma, also called pilomatricoma, is a benign skin neoplasm thought to originate from hair follicle matrix cells. It occurs as a purplish or single skin-colored lesion on the head and neck region. It is characterized by calcification inside the lesion resulting in hard and bony feeling and frequently appears as angulated shape (tent sign) [12]. USG typically demonstrates target-like lesions with a hypoechoic rim, hyperechoic center, and, frequently, with internal hyperechoic

dots consistent with calcium deposits (Figs. 12.9a, b and 12.10a, b) [13].

12.3.2.2 Lipoma

Lipoma is a common benign neoplasm originating from mature adipose tissue and often develops in subcutaneous tissues where fat is normally present. They frequently present as mobile, subcutaneous, painless masses. Lipoma has classic US features that are hyperechoic linear internal streaks perpendicular to the US beam, compressibility, and absence of internal vasculature on color Doppler imaging (Figs. 12.11, 12.12, 12.13, and 12.14a, b). Intramuscular lipoma (i.e., muscles under the trapezius) may imitate muscles and be difficult to delineate with USG [14].

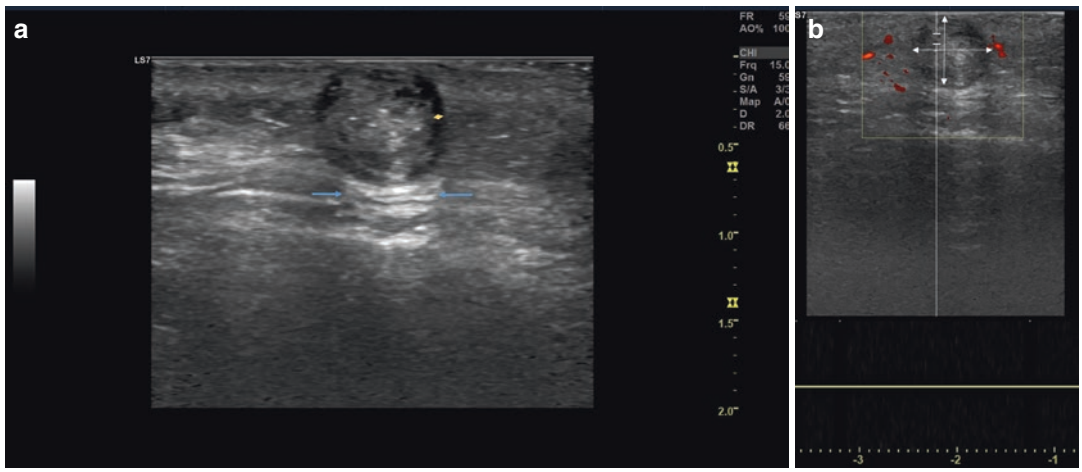

Fig. 12.9 (**a**) and (**b**) US image of a pilomatrixoma shows a heterogeneous hypoechoic, dense cystic lesion (white double-headed arrows) in the right zygomatic region containing micro-echogenicities compatible with internal microcalcifications. There is a smooth thin hypoechoic halo (yellow diamond), posterior acoustic strengthening (blue arrows), and lack of vascularization on color doppler USG

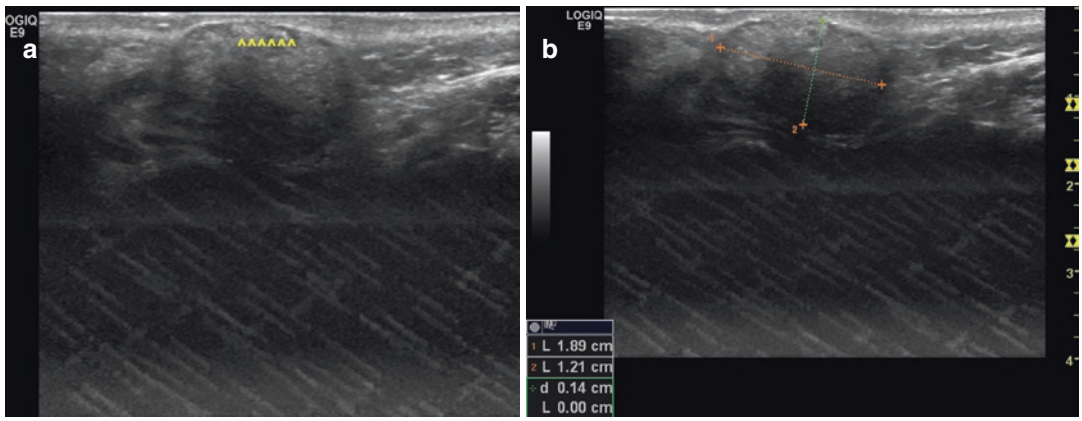

Fig. 12.10 (**a**) and (**b**) US image of a pilomatrixoma shows a dense cystic lesion within the skin and subcutaneous soft tissue in the posterior neck. It has a thin smooth hypoechoic halo which contains internal cluster-like microcalcifications superiorly. The lesion causes thinning of the skin anteriorly and does not show vascularization on color doppler USG

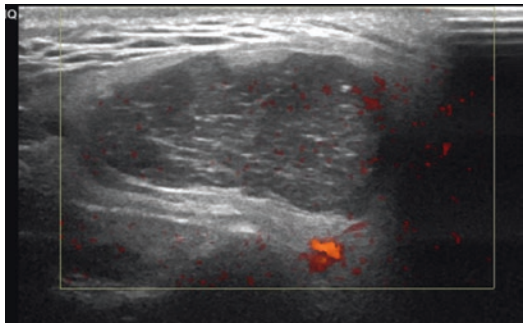

Fig. 12.11 US image of an intraparotid lipoma shows a hypoechoic, compressible, solid lesion in the left parotid gland superficial lobe with smooth contours and internal linear echogenicities and lack of vascularization on color doppler USG

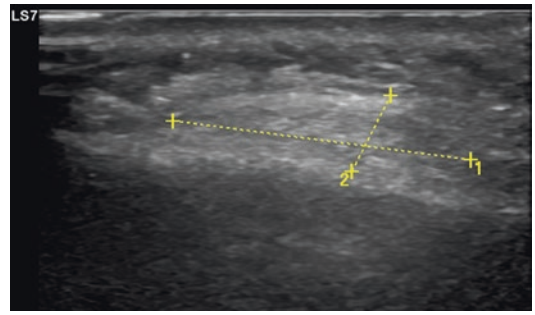

Fig. 12.12 US image of a subcutaneous lipoma in the frontal region shows a compressible solid lesion within the subcutaneous adipose tissue with hyperechoic smooth contours compared to the adjacent adipose tissue. It shows lack of vascularization on color doppler USG

Fig. 12.13 US image of a lipoma shows a compressible solid lesion within the subcutaneous adipose tissue in the frontotemporal region. It is iso-hyperechoic with adipose tissue and shows lack of vascularization on color doppler USG

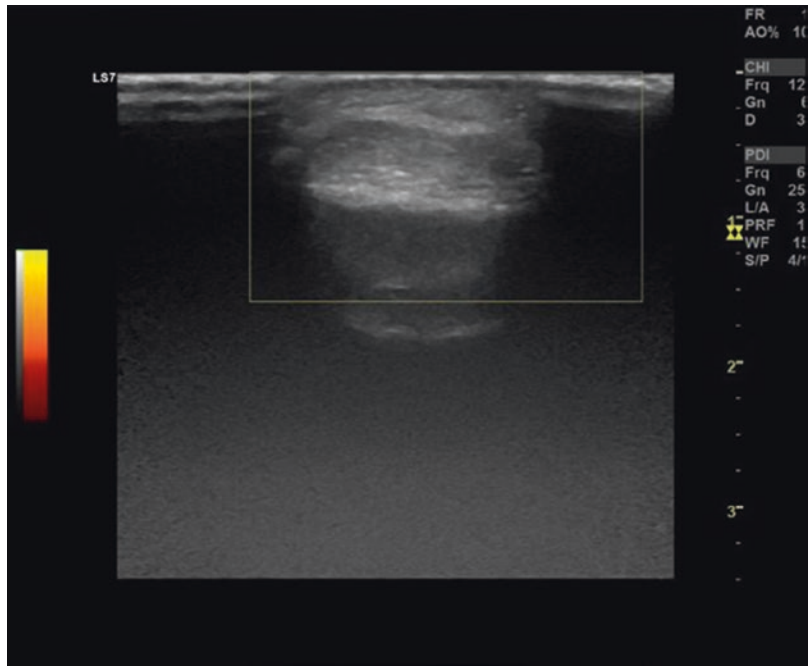

12.4 Malignant Lesions

Malignant tumors exhibit heterogeneous internal echoes, irregularity, unclear margins, bone invasion, diffuse irregular perfusion in the tumor, and calcification (Figs. 12.15 and 12.16). They have more blood flow and a higher resistive index than benign tumors in color Doppler images [9, 15, 16]. It is vital to check the tumor's vascular pattern, as it alerts the surgeon about possible hemorrhage and the necessity for blood transfusion in the surgery [9].

In the presence of suspicious sinonasal and midface lesions, a detailed cervical lymph node examination is crucial [8]. When tumors of the paranasal sinuses and nose metastasize to cervical lymph nodes, there is a higher probability of malignancy [9]. USG has high accuracy in distinguishing benign from metastatic lymph nodes [9, 17].

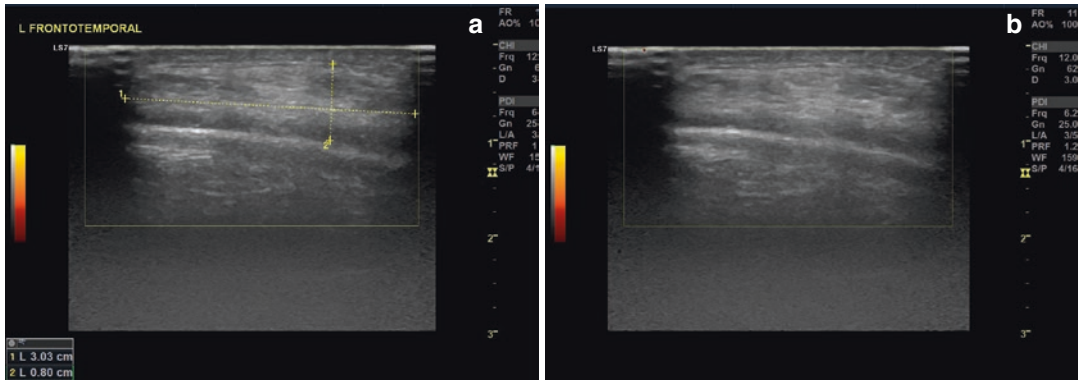

Fig. 12.14 (**a**) and (**b**) US image of a lipoma in the frontotemporal region shows a compressible solid lesion within the subcutaneous adipose tissue. It is isohyperechoic with adipose tissue and shows lack of vascularization on color doppler USG

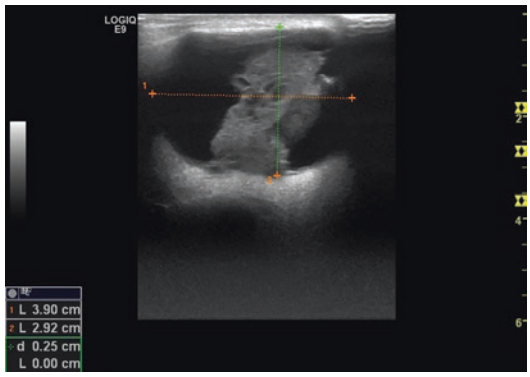

Fig. 12.15 US image of a parotid gland squamous cell carcinoma shows a cystic lesion with heterogeneous solid components and internal irregular contours in the left parotid gland, accompanied by sudden intermittent arterial vascularization on color doppler USG

On USG, normal and reactive lymph nodes have a tendency to be hypoechoic with an echogenic hilum compared to the neighboring muscles and oval (short axis–to–long axis ratio (S/L) < 0.5) excluding parotid and submandibular nodes, that are generally round (S/L ≥ 0.5) (Figs. 12.17, 12.18, and 12.19) [18, 19]. 8 mm is accepted as the upper border for minimum axial diameter of normal and reactive cervical lymph nodes with the exception of the submandibular and subdigastric nodes in which 9 mm is the upper limit of normal [19, 20]. Normal cervical lymph nodes demonstrate hilar vasculature or seem avascular, while reactive lymph nodes mostly demonstrate hilar vasculature on color Doppler, power Doppler, and 3D USG (Fig). Normal and reactive lymph nodes generally have low vascular resistance on spectral Doppler USG [18, 19].

Metastatic lymph nodes are generally round, and hypoechoic with no echogenic hilum at USG (Figs. 12.20, 12.21, and 12.22). Lymph nodes showing cystic necrosis indicates malignancy. In Hodgkin's and non-Hodgkin's lymphoma, lymph nodes have a tendency to be hypoechoic and round, with no echogenic hilum and present intranodal reticulation (Figs. 12.23 and 12.24). Lymph nodes in tuberculosis seem round and hypoechoic, with neighboring soft tissue edema, intranodal cystic necrosis, and no echogenic hilum (Fig. 12.25). Metastatic lymph nodes frequently have mixed (Fig) or peripheral (Fig) vascular pattern on color Doppler, power Doppler, and 3D USG. Malignant lymph nodes have a tendency for high vascular resistance on spectral Doppler USG [19].

12.4.1 Image Interpretation Pearls

When the gray scale USG is ambiguous, color or power Doppler sonography is crucial and beneficial to differentiate benign lymph nodes from malignant [19].

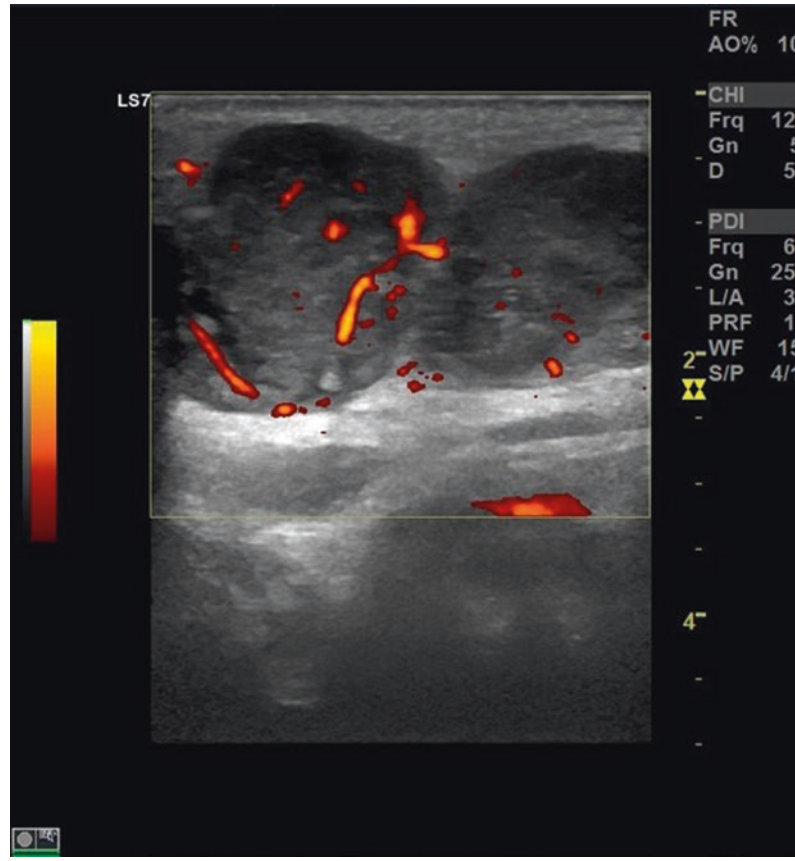

Fig. 12.16 US image of a left parotid gland mucoepidermoid carcinoma shows a multifocal, irregular lobulated, heterogeneously hypoechoic intraglandular solid lesions accompanied by internal arterial vascularization that ends abruptly on color doppler USG

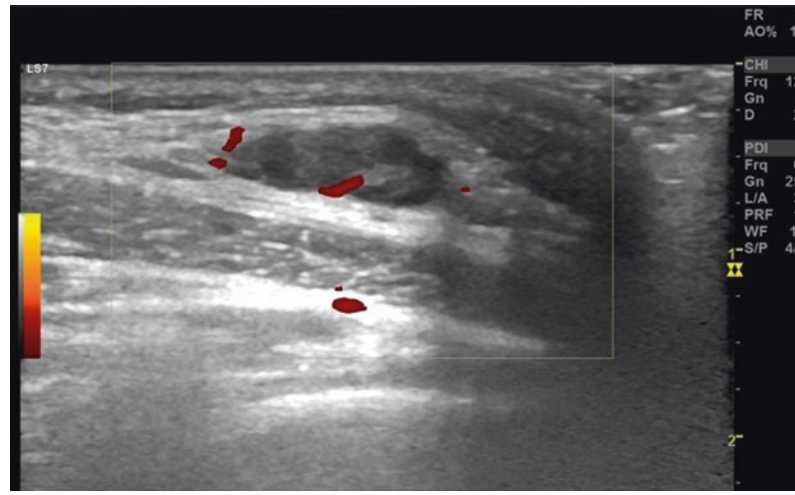

Fig. 12.17 US image of a benign reactive lymph node shows an ovoid-shaped reactive lymph node in the right retroauricular region with an echogenic fatty hilum and hilar vascularization on color doppler USG

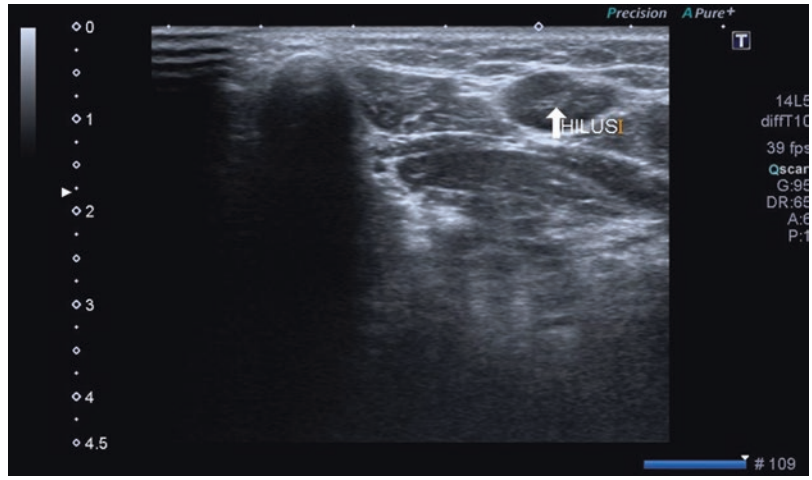

Fig. 12.18 US image of a benign reactive lymph node shows an ovoid-shaped reactive lymph node in the left submandibular region with an echogenic fatty hilum (HILUS)

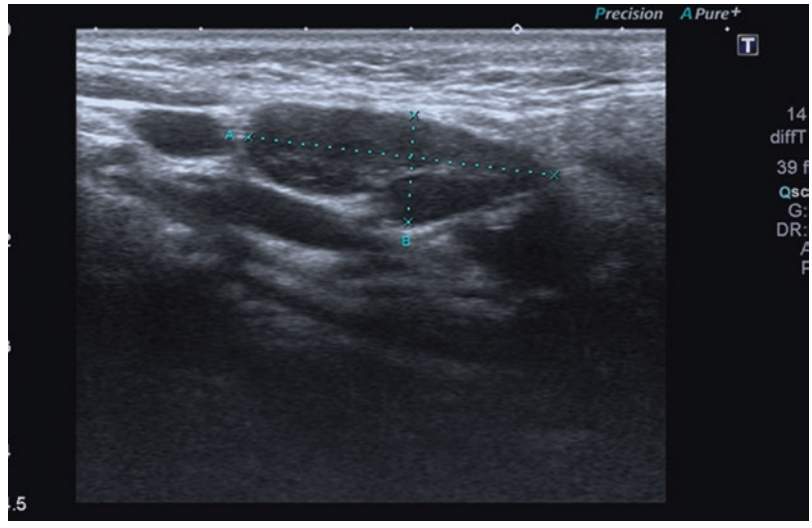

Fig. 12.19 US image of a benign reactive lymph node shows an ovoid-shaped reactive lymph node in the right submandibular region with an echogenic fatty hilum

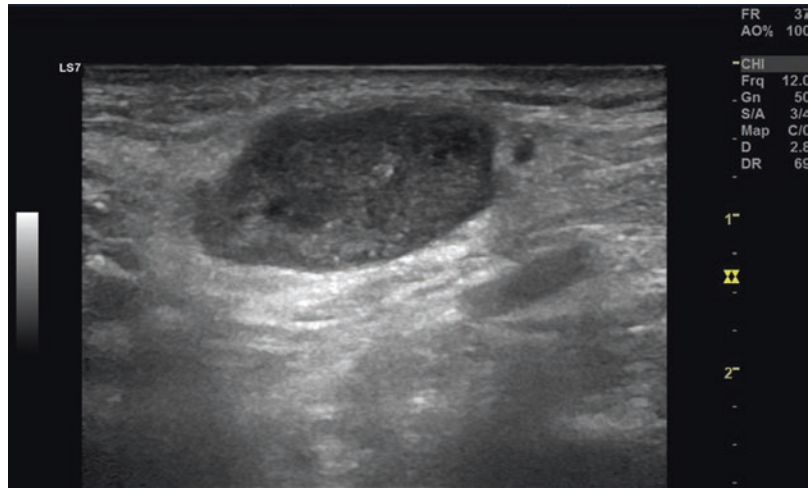

Fig. 12.20 US image of metastatic lymphadenopathy in parotid gland mucoepidermoid carcinoma with minimally irregular contours, effacement of hilum, and areas of cortical necrosis

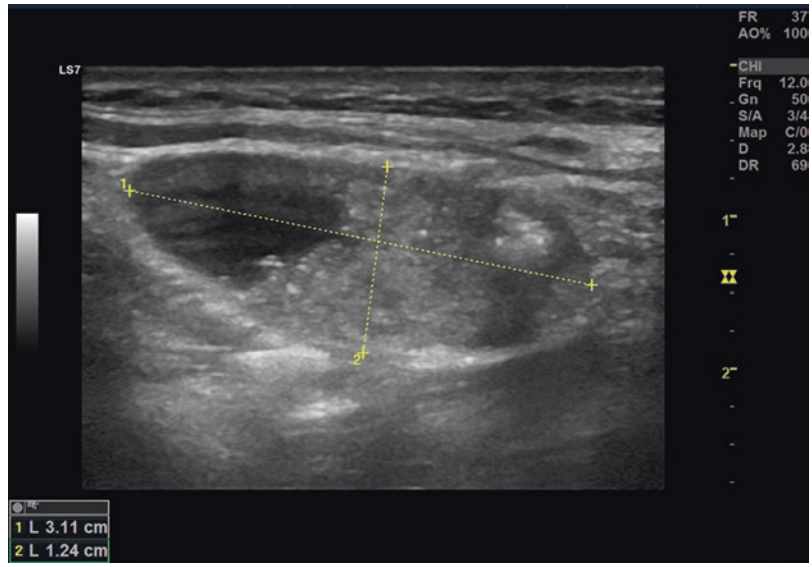

Fig. 12.21 US image of metastatic lymphadenopathy of thyroid gland papillary carcinoma in the cervical region with an effaced hilum and a large area of cortical necrosis

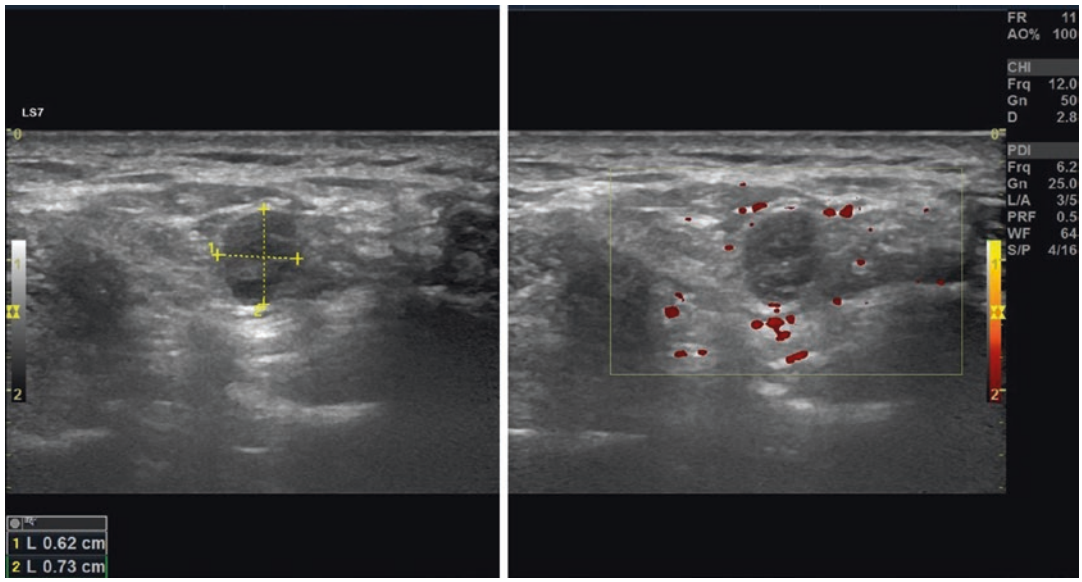

Fig. 12.22 US image of spherical lymphadenopathy in metastatic cervical lymphadenopathy with a transverse/antero-posterior diameter of less than 1 cm in the patient with a history of squamous cell carcinoma (SCC)

12.5 Trauma

The USG, especially B-mode, is being used as a reliable first-line imaging technique in the evaluation of maxillofacial fractures, particularly fractures involving the anterior maxillary walls, orbital walls, nasal bone, and zygomatic complex (Fig. 12.26) [3]. It is also promising in the detection of extracapsular sub-condylar fractures [1]. It can be performed in real-time, allowing 3D, dynamic, and intraoperative ultrasound-guided reduction of fractures during the surgery [3]. The place of the fixation material and success of the repositioning may be checked with USG [8] and it can be performed several times with no significant concerns (i.e., radiation) [3]. However, the clinicians must be aware of USG's limitations in

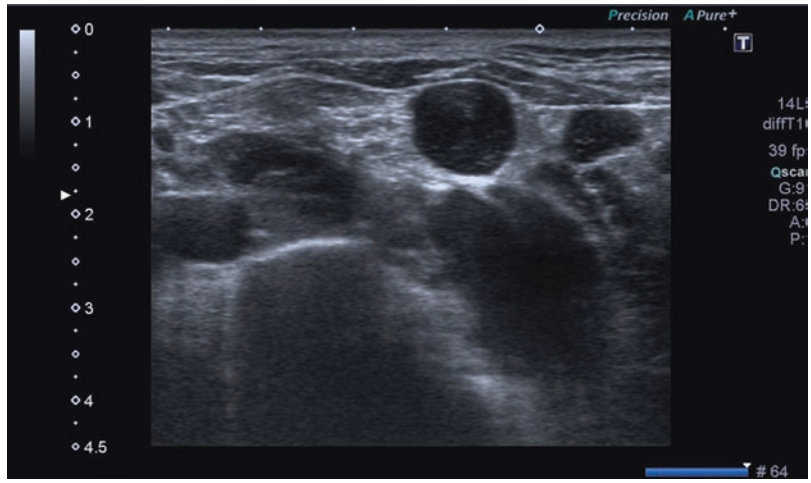

Fig. 12.23 US image of cervical lymphadenopathy in Hodgkin lymphoma shows spherical lymphadenopathy with effaced hilum and hypoechoic cortex in the left submental region

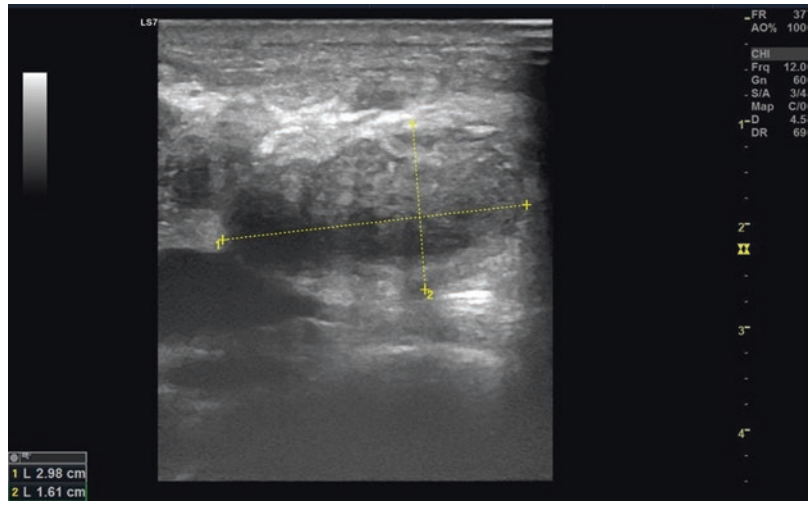

Fig. 12.24 US image of cervical lymphadenopathy in Hodgkin lymphoma (HL) shows conglomerate lymphadenopathy with heterogeneous cortex of a nodular sclerosing type NHL case with an effaced hilum and increased cortical echogenicity in the left cervical region

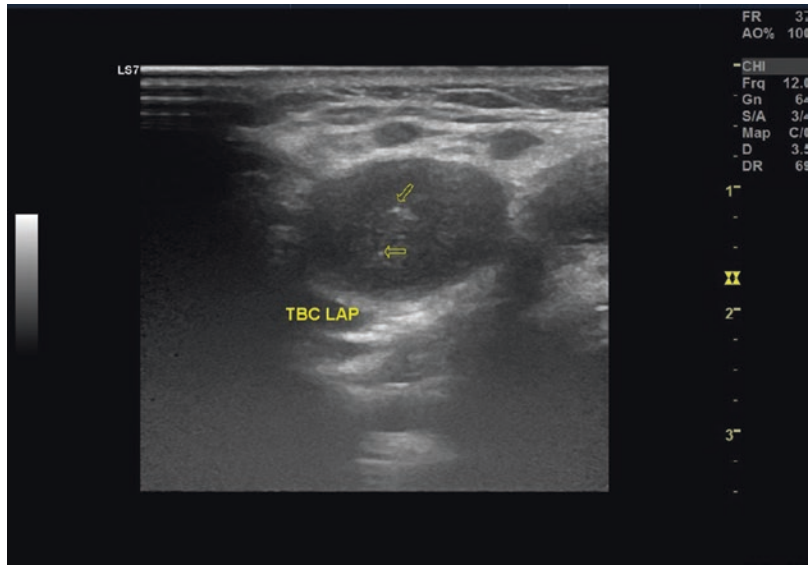

Fig. 12.25 US image of cervical lymphadenopathy in Tuberculosis (TB) shows posttreatment follow-up TB lymphadenopathy (TBC LAP) case with an effaced hilum and several cortical microcalcifications (yellow arrows) in the right anterior cervical lymph nodes

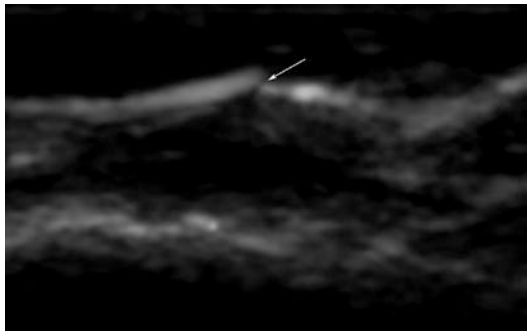

Fig. 12.26 US image shows fracture of the anterior maxilla (white arrow). Case courtesy of Dr. Kaan Orhan

complex maxillofacial fractures (i.e., Le Fort fractures), non-displaced fractures, posterior orbital floor fractures, intracapsular mandibular condyle fractures in addition to the patient's discomfort during the acute phase. Appropriate imaging can be impeded by massive emphysema and edema along with pain and tenderness caused while probing [1].

In the case of a hematoma, post-traumatic swelling with hypoechoic extension is seen in the bruised area [8]. Interruption of homogeneous and continuous total reflections of the bone surface is suggestive of displaced facial skeleton fracture in patients with a history of maxillofacial trauma. For instance, in a displaced fracture, characteristic M-shaped reflection of the bone surface indicates depressed zygomatic arch fracture [21]. Although the eyeball can be examined with USG, it is contraindicated in trauma patients where the eyeball is ruptured [22].

12.5.1 USG Use in Nasal Bone Fractures

One of the most frequently affected bones in facial bone fractures is the nasal bone [23, 24]. USG is one of the recommended methods for isolated nasal bone fractures, along with the advantages of its ability to detect anterior septal cartilage deviation and linear nondepressed nasal bridge fractures [1]. However, it has been suggested to be used with CT in complex fractures [23, 24]. Additionally, the anatomical structure of the nasal region is not suitable for linear probe use during ultrasonographic imaging. Due to their size, the linear probes do not fully fit the anatomical structure of the nose; thus, adequate image formation cannot be achieved due to air remaining between the lateral aspect of the nose and the zygomatic bone [4]. In recent years, hockey stick probes are preferred due to their ergonomic structure in the examination of the midline region, especially in trauma cases, for determination of the fracture line [21]. Small linear probes in the range of 7.5–20 MHz have been found to be successful in detecting fractures as well [21, 22].

12.5.2 USG Use in Zygomatic Arc Fractures

Due to its location and anatomy, zygomatic arch is very prone to local traumas. USG has been successful in detecting zygomatic fractures, but in cases with minor displacement, fracture lines may not be detected [25].

12.5.3 USG Use in Orbital Floor Fractures

USG has been shown as a good alternative for the evaluation of orbital wall and floor fractures. But, the detection capability of USG is not considered sufficient for the fractures located more than 4 cm posterior to the orbital border [1].

12.6 Foreign Bodies

Along with the detection of foreign bodies, the removal of such bodies under USG guidance is among the uses of USG. Foreign bodies show a typical echogenicity that is hyperechoic with distal acoustic attenuation. The high reflectivity of both foreign bodies and metallic needles facilitate the localization process and ultrasound-guided biopsy examinations, respectively [14].

References

1. Adeyemo WL, Akadiri OA. A systematic review of the diagnostic role of ultrasonography in maxillofacial fractures. Int J Oral Maxillofac Surg. 2011;40(7):655–61.
2. Tiedjen KU, Becker E, Heimann KD, Knorz S, Hildmann H. Value of B-image ultrasound in diagnosis of paranasal sinus diseases in comparison with computerized tomography. Laryngorhinootologie. 1998;77(10):541–6.
3. Marotti J, Heger S, Tinschert J, Tortamano P, Chuembou F, Radermacher K, et al. Recent advances of ultrasound imaging in dentistry–a review of the literature. Oral Surg Oral Med Oral Pathol Oral Radiol. 2013;115(6):819–32.
4. ALPÖZ E, KOYUNCU BÖ, TUĞSEL Z. Paranazal Sinüsler ve Orta Yüz Bölgesinin Ultrasonografik Anatomisi. Turkiye Klinikleri Oral Maxillofac Radiol Spec Top. 2016;2(3):85–91.
5. Fufezan O, Asavoaie C, Chereches Panta P, Mihut G, Bursasiu E, Anca I, et al. The role of ultrasonography in the evaluation of maxillary sinusitis in pediatrics. Med Ultrason. 2010;12(1):4–11.
6. Seçil M. Temel Ultrasonografi ve Doppler. 1st ed. Bornova: Meta basım matbaacılık hizmetleri; 2008.
7. Puidupin M, Guiavarch M, Paris A, Caroff P, Boutin JP, Le Bivic T, et al. B-mode ultrasound in the diagnosis of maxillary sinusitis in intensive care unit. Intensive Care Med. 1997;23(11):1174–5.
8. Iro H, Bozzato A, Zenk J. In: Iro H, Bozzato A, Zenk J, editors. Atlas of head and neck ultrasound. 1st ed. New York: Thieme Medical Publishers, Inc.; 2013.
9. Liu JJ, Gao Y, Wu YF, Zhu SY. Sonography for diagnosis of benign and malignant tumors of the nose and paranasal sinuses. J Ultrasound Med. 2014;33(9):1627–34.
10. Dumitru M, Tweedie D, Anghel I, Cergan R, Sarafoleanu C, Costache A. Correlations between morphology and ultrasound exam in cases with nasal and paranasal sinuses pathology. Rom J Rhinol. 2015;5(19):167–72.
11. Reilly JS, Hotaling AJ, Chiponis D, Wald ER. Use of ultrasound in detection of sinus disease in children. Int J Pediatr Otorhinolaryngol. 1989;17(3):225–30.
12. El-Romyssa M, Jakubikova J, Pavlovcinova G. Pilomatrixoma of the head and neck in children. Bratisl Lek Listy. 2010;111(12):666–9.
13. Hwang JY, Lee SW, Lee SM. The common ultrasonographic features of pilomatricoma. J Ultrasound Med. 2005;24(10):1397–402.
14. Oeppen RS, Gibson D, Brennan PA. An update on the use of ultrasound imaging in oral and maxillofacial surgery. Br J Oral Maxillofac Surg. 2010;48(6):412–8.
15. Folkman J. The role of angiogenesis in tumor growth. Semin Cancer Biol. 1992;3(2):65–71.
16. Santamaria G, Velasco M, Farre X, Vanrell JA, Cardesa A, Fernandez PL. Power Doppler sonography of invasive breast carcinoma: does tumor vascularization contribute to prediction of axillary status? Radiology. 2005;234(2):374–80.
17. Takeuchi Y, Suzuki H, Omura K, Shigehara T, Yamashita T, Okumura K, et al. Differential diagnosis of cervical lymph nodes in head and neck cancer by ultrasonography. Auris Nasus Larynx. 1999;26(3):331–6.
18. Ying M, Ahuja A. Sonography of neck lymph nodes. Part I: normal lymph nodes. Clin Radiol. 2003;58(5):351–8.
19. Ahuja AT, Ying M. Sonographic evaluation of cervical lymph nodes. AJR Am J Roentgenol. 2005;184(5):1691–9.
20. van den Brekel MW, Castelijns JA, Stel HV, Golding RP, Meyer CJ, Snow GB. Modern imaging techniques and ultrasound-guided aspiration cytology for the assessment of neck node metastases: a prospective comparative study. Eur Arch Otorhinolaryngol. 1993;250(1):11–7.
21. Friedrich RE, Heiland M, Bartel-Friedrich S. Potentials of ultrasound in the diagnosis of midfacial fractures*. Clin Oral Investig. 2003;7(4):226–9.
22. Köse TE, Özcan İ. Orta Yüz Travmalarında Ultrason Muayenesi. Turkiye Klinikleri Oral Maxillofac Radiol Spec Top. 2016;2(3):11–4.
23. Lee MH, Cha JG, Hong HS, Lee JS, Park SJ, Paik SH, et al. Comparison of high-resolution ultrasonography and computed tomography in the diagnosis of nasal fractures. J Ultrasound Med. 2009;28(6):717–23.
24. Mohammadi A, Ghasemi-Rad M. Nasal bone fracture-ultrasonography or computed tomography? Med Ultrason. 2011;13(4):292–5.
25. Ogunmuyiwa SA, Fatusi OA, Ugboko VI, Ayoola OO, Maaji SM. The validity of ultrasonography in the diagnosis of zygomaticomaxillary complex fractures. Int J Oral Maxillofac Surg. 2012;41(4):500–5.

Ultra-High Frequency Ultrasound in Oral and Maxillofacial Imaging

13

Rossana Izzetti

Contents

R. Izzetti (✉)
Unit of Dentistry and Oral Surgery, Department of Surgical, Medical and Molecular Pathology and Critical Care Medicine, University of Pisa, Pisa, Italy
e-mail: rossana.izzetti@med.unipi.it

K. Orhan (ed.), *Ultrasonography in Dentomaxillofacial Diagnostics*,
https://doi.org/10.1007/978-3-030-62179-7_13

13.1 Introduction

Ultra-high frequency ultrasound (UHFUS) is a recently introduced ultrasonographic technique characterized by the use of ultrasound frequencies between 30 and 100 MHz, yielding improved spatial resolution at the expense of a shallower depth of penetration.

High-frequency techniques include UHFUS, High-frequency ultrasound (HFUS), and ultrasound biomicroscopy (UBM), which were originally introduced in the mid-90s in the preclinical setting for the study of animal models. In particular, preclinical applications have expanded in the last years and currently include the evaluation of developmental changes during embryogenesis, cardiac and brain development, tumor growth patterns and spread of metastases, and pharmacokinetics and pharmacodynamics of antineoplastic therapies in experimental murine models [1, 2].

For what concerns clinical setting, ultra-high frequencies find application in several medical fields, including vascular, musculoskeletal, small parts, and dermatological evaluation [3–6].

In particular, vascular applications include the study of radial artery, venous valves, peripheral vascularization, blood flow characteristics, arterial intima/media thickness, stiffness, and risk assessment of atherosclerosis. Musculoskeletal evaluation includes hand anatomy and planning of hand surgery, superficial joints, tendons and pulleys, medial menisci, carpal and tarsal tunnel, while small parts evaluation is mostly focused on nerves and lymph nodes. In dermatology, ultra-high frequencies are employed for the study and differentiation of cutaneous lesions (including melanoma), skin layers, hair follicles, and identification of foreign bodies [7].

Oral medicine is a recently introduced field of application, due to the possibility of ultra-high frequencies to provide high-resolution images of superficial structures [8–10].

13.2 Principles of UHFUS Imaging

Image generation in ultrasonography is characterized by the production of ultrasound waves and registration of reflected echoes after attenuation related to the passage of the waves inside different tissues. The return echoes are then converted into electric signals, and the signals into images.

Ultrasound wave frequency and depth of penetration are inversely proportional: the higher the frequency, the shallower the depth of penetration. In this sense, the use of ultra-high frequencies allows to image the superficial layers from the point of application of the probe, but on the other hand it allows to obtain micron-sized resolution.

Vevo MD (VisualSonics) is the first UHFUS equipment available for clinical use (Fig. 13.1). For the study of the oral cavity, 48 MHz and 70 MHz frequencies appear suitable to obtain high-resolution imaging of the superficial layers of the oral mucosa. In Table 13.1, the characteristics of 48 MHz and 70 MHz UHFUS probes are summarized.

Considering ultrasound physics, axial resolution is determined by the bandwidth of the pulse, while lateral resolution is the result of the ratio between focal distance and spatial dimension of the transducer multiplied for the wavelength. In this sense, 70 MHz frequencies provide 30 μm axial resolution and 65 μm lateral resolution, at the expense of an increase in attenuation in tissues, with a depth of penetration limited to 10.0 mm.

Ultra-high frequencies appear suitable when small anatomy is investigated. In general, if a region or a lesion to be scanned is <2 cm, 70 MHz can provide adequate detail and imaging of the lesion as a whole. If the area to be scanned is >2 cm, reduction in scanning frequencies is required, with 48 MHz probe allowing to image all the lesion with one scan. However, it is often advisable to perform a double scan regardless of lesions'

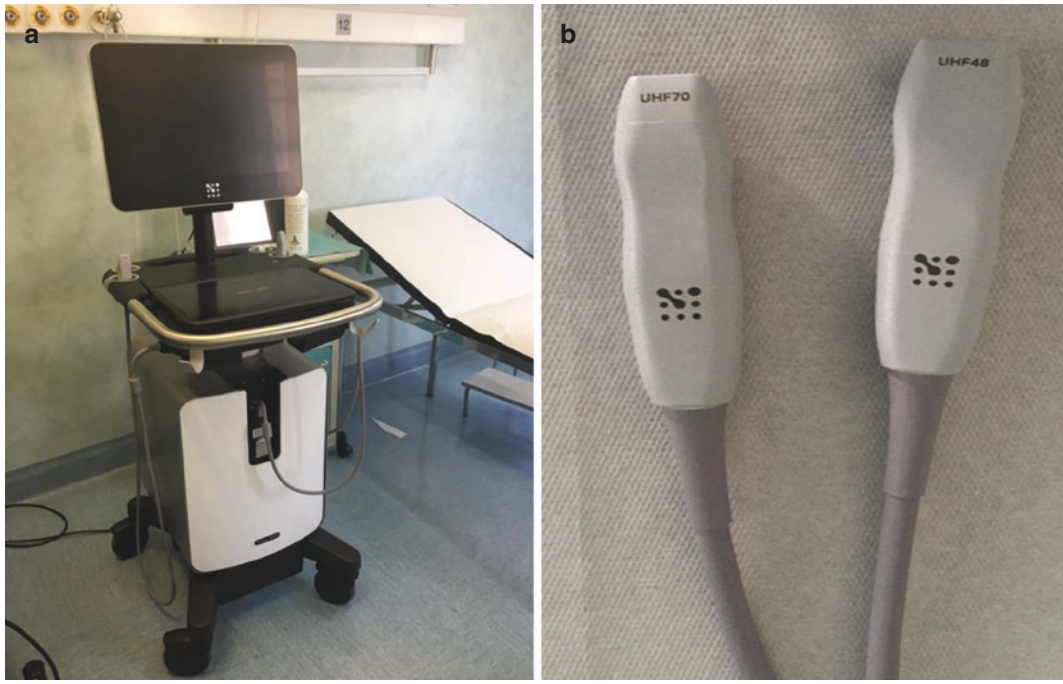

Fig. 13.1 Vevo MD equipment is the first UHFUS system for medical use. (**a**) UHFUS appliance; (**b**) UHFUS probes; on the left, probe reaching frequency of 70 MHz, on the right 48 MHz probe

Table 13.1 Summary of technical characteristics of 48 MHz and 70 MHz UHFUS probes

Probe frequency	70 MHz	48 MHz
Center transmit	50 MHz	30 MHz
Bandwidth	29–71 MHz	20–46 MHz
Axial resolution	30 μm	50 μm
Lateral resolution	65 μm	110 μm
Maximum depth	10.0 mm	23.5 mm
Image width (max)	9.7 mm	15.4 mm
Image depth (max)	10.0 mm	23.5 mm
Focal depth	5.0 mm	9.0 mm

dimensions, as the two frequencies in most cases are complementary in diagnosis performance.

13.3 Components of Image Production

13.3.1 Performance of Intraoral UHFUS Scan

Intraoral UHFUS scan is generally performed with the patient in supine position, providing head stabilization with a headrest. In some cases, UHFUS performance can be chair-side to the dental chair thus improving patient positioning.

Head positioning varies depending on the area to be investigated. In particular, the following positions may be adopted for the following sites:

- Buccal mucosa: the patient's mouth is wide open, and the head is tilted right to image right buccal mucosa and left to image left buccal mucosa. In some cases, in particular, when exophytic lesions are to be investigated, the cheek may be gently stretched and slightly turned outward to contrast probe pressure during the scan. If the fornix is to be scanned, additional divarication may be needed.
- Tongue: the patient's mouth is open, and the tongue is gently pulled outwards with the support of a gauze to avoid sliding during examination. If the tongue dorsum is the object of the investigation, tongue is kept straight, while if the lesion involves tongue margins, the tongue has to be pulled contralaterally to expose the area of investigation. If the ventral aspect of the tongue is to be scanned, the patient can be asked to put the tip of the tongue

against the palate in correspondence with the retroincisal papilla and to keep this position.
- Lips: lip mucosa can be examined by gently pulling outwards the lip. No additional traction is generally required to perform the scan. In this case, the patient's mouth can be kept closed, in order to decrease muscular tension on lip muscles.
- Palate: palate imaging requires wide mouth opening, and head tilted right for the examination of right side of the palate and left for the scan of left palate. The probe is inserted from the contralateral side, to avoid interference with dental arches.
- Mouth floor: mouth floor can be scanned by inserting the probe almost vertically or from the contralateral side. Patient's mouth is wide open, and no additional traction is required. In some cases, in particular, for lesions located deeply in the mouth floor, it may be advisable to apply a gentle pressure extraorally from the submandibular area, in order to raise the mouth floor and to contrast probe pressure.
- Gingiva: to image gingiva gentle divarication of lip or buccal mucosa is required. In general, no additional divarication is necessary.

A coupling medium (gel, saline solution) should be used to facilitate transmission of the ultrasound energy, and create a better interface for the imaging of the mucosal surface. Prior to examination beginning, a thin layer of US gel is applied inside a disposable sheath. Then the sheath is positioned on the UHFUS probe and cable and secured with supplied bands for the management of cross-infections. After protecting the probe, it is important to check for the presence of air bubbles which could affect ultrasound images, and eliminate them from the space between the transducer and the sheath. In some cases, extra application of coupling medium may be necessary to avoid compression of the shallower tissue layers, which could impair image quality.

13.3.2 Setting Image Acquisition Parameters

During the UHFUS examination, several parameters may be adjusted to improve image quality. Image depth depends on the transducer applied, and it corresponds to the total acquired depth of the non-zoomed image.

Gain control may be varied to adjust the visual intensity of the returning signal. In particular, an increase in gain brightens the image, while a decrease leads to darkening. In B-mode images, variations in Time Gain Compensation (TGC) adjust the ultrasound signal to compensate for minor attenuation for the signal returning from deeper situated tissues.

13.3.3 Strengths and Limitations

13.3.3.1 Size and Cost

The main drawback of the use of UHFUS systems is the lack of dedicated probes for intraoral access, which can hinder full mouth examination in patients with limited mouth opening. Acquiring a UHFUS system is relatively costly compared to conventional US systems, although the benefits in terms of image quality and the opportunities for oral mucosa exploration are much higher compared to conventional US equipment.

13.3.3.2 Fast Acquisition

UHFUS acquisition is fast, due to relatively easy accessibility to the oral cavity. The possibility to perform real-time measurements and evaluation of blood flow make the technique suitable for preoperative investigations. Moreover, the repeatability of UHFUS scan makes this technique a valuable tool for performing follow-up after surgical procedures involving the oral mucosa.

13.3.3.3 Submillimeter Resolution

It is known that the higher the ultrasound frequencies, the lower the depth of penetration of the ultrasound wave. However, imaging of the shallower layers of the oral mucosa is also accompanied by higher spatial resolution, which in cases of 70 MHz frequencies can reach up to 30 μm. When dealing with small anatomy as one of the oral cavity, it is of utmost importance to obtain high-resolution images, which could support diagnosis performance. Moreover, oral lesions are in most cases confined to a maximum of 2 cm beneath the surface thus making UHFUS systems ideal for the

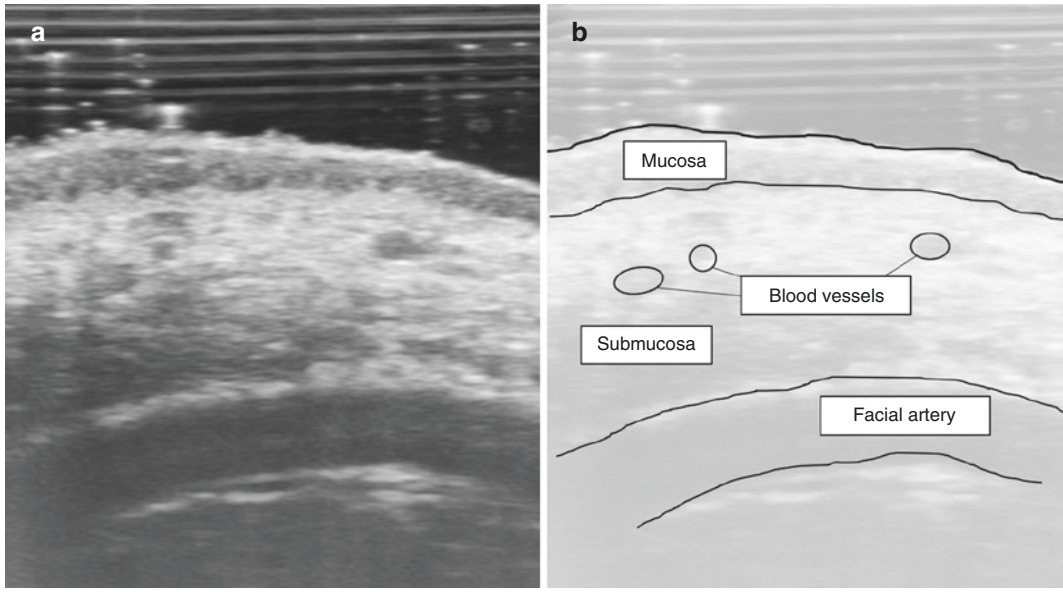

Fig. 13.2 Normal anatomy of the buccal mucosa. (**a**) UHFUS aspect of the buccal mucosa; (**b**) Schematic exemplification of anatomy

study of the majority of oral diseases. Diagnostic imaging is going towards an increasing interest in micron-sized anatomy, and in this sense UHFUS reflects the need for submillimeter imaging of small anatomical parts. The detailed evaluation of oral mucosa therefore represents one of the most promising innovations in this field.

13.4 Normal Anatomy

13.4.1 Buccal Mucosa

UHFUS structure of buccal mucosa is characterized by a thin homogeneously hypoechoic layer corresponding to the mucosa. The submucosa appears as a well-defined, hyperechoic stratum below the mucosa. In the submucosal layer, it is possible to observe vascular structures appearing as roundish hypoechoic structures. In this region, the most important anatomical structure is represented by the facial artery, which on longitudinal scan appears as a linear structure with hypoechoic margins, and is characterized by pulsation and intense blood flow. Doppler mode shows mild vascularity, while intense blood flow is detected in correspondence with the facial artery. (Figs. 13.2 and 13.3).

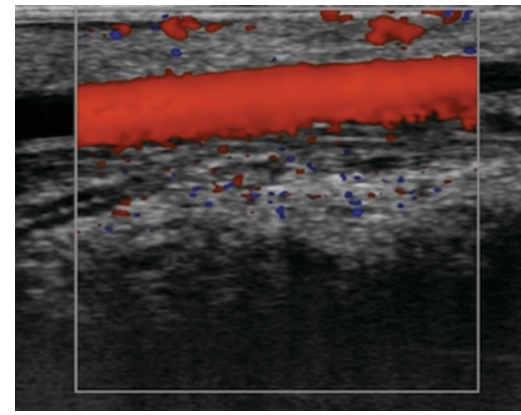

Fig. 13.3 Doppler mode of the buccal mucosa

13.4.2 Tongue

Being tongue a muscular organ, two thin layers representing the mucosa and the submucosa can be observed in the shallower areas of the scan, while deeper only muscular tissue can be seen. In particular, the more superficial layer which is characterized by a regular course of muscular fibers can be related to intrinsic tongue muscles. Larger muscular fibers can be observed below, and correspond to the extrinsic muscles of the tongue. Being tongue extremely rich in blood vessels, Doppler

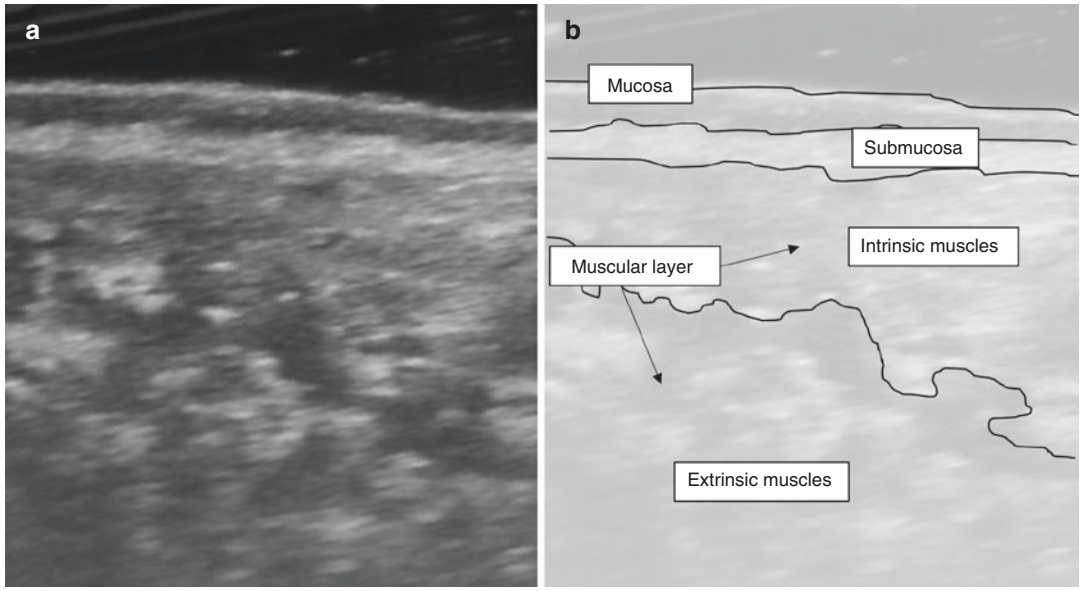

Fig. 13.4 Normal anatomy of the tongue. (**a**) UHFUS aspect of the tongue; (**b**) Schematic exemplification of anatomy

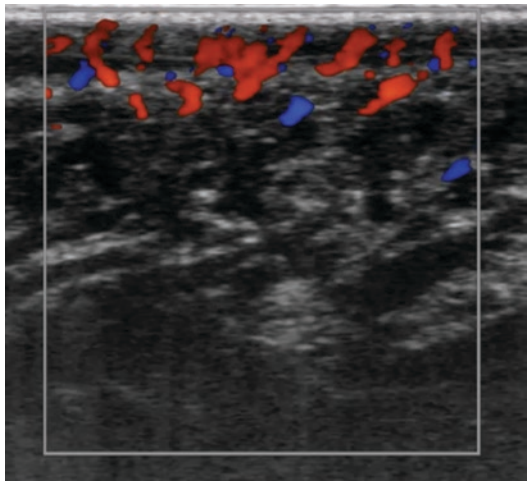

Fig. 13.5 Doppler mode of the tongue

mode shows moderate vascularity, especially in the superficial layers. (Figs. 13.4 and 13.5).

13.4.3 Lips

Lip anatomy on UHFUS is characterized by a thin layer of mucosa and a thick submucosa, where vascular and glandular structures can be observed. In the submucosa, in particular, it is possible to easily recognize minor salivary glands as roundish structures in groups of 3/4 glands. In healthy subjects, minor salivary glands appear as homogeneous structures which present slight hypoechogenicity compared to submucosa. In particular, the ultrasonographic pattern resembles the typical glandular appearance of the thyroid thus making it easy to recognize salivary gland tissue at this level. In some cases, single roundish hypoechoic formations in the glands can be seen, corresponding to glandular ducts. Minor salivary glands can be found more frequently in the lateral compartments of the lip mucosa, while in the central area few glands are generally present. In the submucosal layer, it is also possible to find branches of the labial arteries and veins. Doppler shows mild vascularity, with a more intense signal in correspondence with the labial artery. (Figs. 13.6 and 13.7).

13.4.4 Gingiva

UHFUS structure of gingiva is characterized by the presence of a thin hypoechoic layer (mucosa), followed by a thick hyperechoic layer corresponding to the dense connective tissue favoring the adherence of the mucosa to the underlying

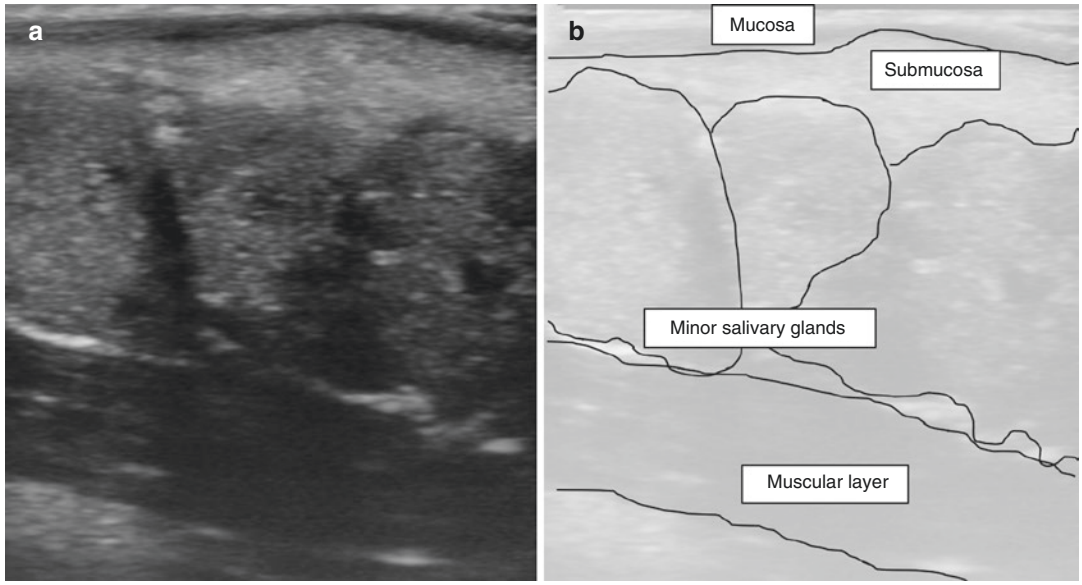

Fig. 13.6 Normal anatomy of the lip. (**a**) UHFUS aspect of the lip; (**b**) Schematic exemplification of anatomy

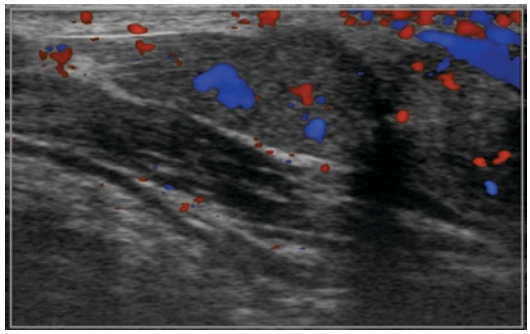

Fig. 13.7 Doppler mode of the lip

periosteum. Further imaging is then hindered by the presence of mineralized tissue (teeth and alveolar bone) which causes ultrasound beam reflection. However, the profile of the teeth and the bone can be clearly recognized. Vascularity is scarce but can be increased in course of inflammation. (Figs. 13.8 and 13.9).

13.4.5 Palate

Similar to the structure of the gingiva, the palate also presents a hypoechoic mucosal layer and a thick hyperechoic layer of connective tissue strongly adherent to the underlying bone. Blood vessels can be frequently spotted in this area, in particular, the palatine artery can be seen when imaging posterior areas of the palate. Doppler mode highlights the presence of blood flow in correspondence with larger blood vessels. (Figs. 13.10 and 13.11).

13.4.6 Mouth Floor

When discussing mouth floor anatomy, it is mandatory to highlight the difficult repeatability of UHFUS examination at this level due to access issues. In patients with limited mouth opening, proper imaging of the mouth floor can be hindered by the presence of the dental arch. Vascularity is more intense in the mucosal and submucosal layers (Figs. 13.12 and 13.13).

13.5 Oral Diseases: A Brief Review of Typical UHFUS Aspect of the Most Frequently Encountered Oral Lesions

13.5.1 Melanocytic Nevus

Oral nevus UHFUS appearance is characterized by the presence of a well-defined, roundish structure. It can be isoechoic or slightly hypoechoic,

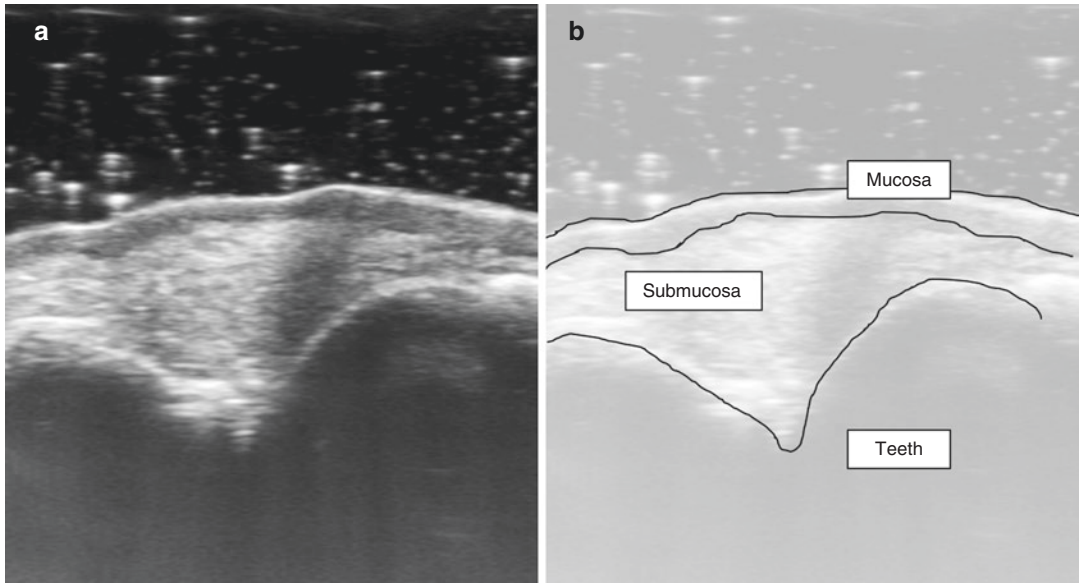

Fig. 13.8 Normal anatomy of the gingiva. (**a**) UHFUS aspect of the gingiva; (**b**) Schematic exemplification of anatomy

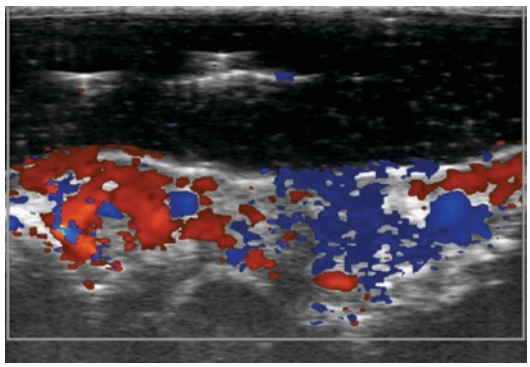

Fig. 13.9 Doppler mode of the gingiva

with a clear hypoechoic margin. The central area can be markedly hypo- or anechoic. Vascularity is generally low and confined to surrounding tissue (Figs. 13.14 and 13.15).

13.5.2 Migratory Glossitis

Migratory glossitis is a recurrent benign form, which is characterized by phases of remission and exacerbation. Due to the nature of the lesion, structural alterations of tongue layering are generally absent. In correspondence with the lesion, a wavy aspect of the mucosa can be present, and a thickening of the mucosal layer can be observed. The transition with the submucosa may present blurred edges, while the underlying muscle appears unchanged. Vascularity is markedly increased, in particular in correspondence with the thick mucosal band. (Figs. 13.16 and 13.17).

13.5.3 Hemangioma

Hemangiomas are typically well-defined hyperechoic lesions, characterized by occasional presence of hypoechoic areas on the inside, corresponding to vascular structures. Doppler mode generally shows peripheral increased vascularity due to the presence of feeding vessels. (Figs. 13.18 and 13.19).

13.5.4 Fibrous Hyperplasia

Fibrous hyperplasia of the oral cavity is generally characterized by the development of an exophytic growth secondary to traumatic and/or inflamma-

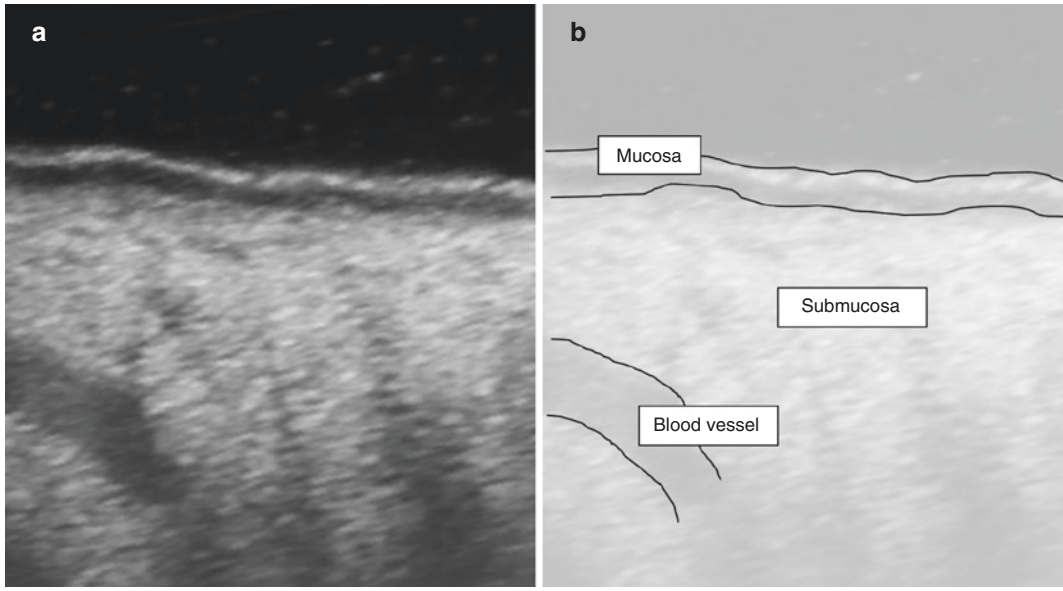

Fig. 13.10 Normal anatomy of the palate. (**a**) UHFUS aspect of the palate; (**b**) Schematic exemplification of anatomy

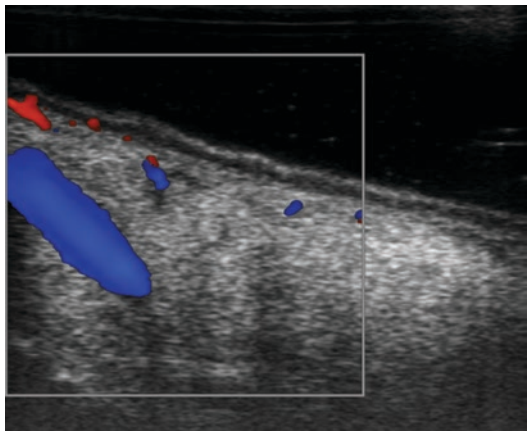

Fig. 13.11 Doppler mode of the palate

tory causes. On UHFUS, fibrous hyperplasia appears as a mass arising from the submucosal layer, in absence of a clear line of demarcation. Continuity of the overlying mucosa can be seen, in absence of changes in the epithelial thickness. The lesion appears homogeneous and slightly hypoechoic compared to the submucosa. In some cases, the lesion can provoke acoustic shadowing. Doppler mode reveals peripheral vascularity. (Figs. 13.20 and 13.21).

13.5.5 Lipoma

Oral lipomas are characterized by a hyperechoic appearance on UHFUS, with occasional tiny hypoechoic areas within. The lesion is delimited by a well-defined thin hypoechoic rim, corresponding to the capsule. No internal vascularity is noted, and also surrounding tissue appears unchanged. (Figs. 13.22 and 13.23).

13.5.6 HPV-Papilloma

HPV infection in the oral cavity is predominantly observed with the development of papilloma lesions, which are characterized by exophytic growth. On UHFUS, the lesion appears to arise from the epithelium of the mucosal layer, consistently with the viral colonization of epithelial cells. A clear demarcation with the submucosa is maintained, in absence of significant modifications. The UHFUS aspect suggests a localization in the shallower layer of the oral mucosa, with underlying strata appearing sound. Increased vascularity is generally associated with the presence of the lesion. (Figs. 13.24 and 13.25).

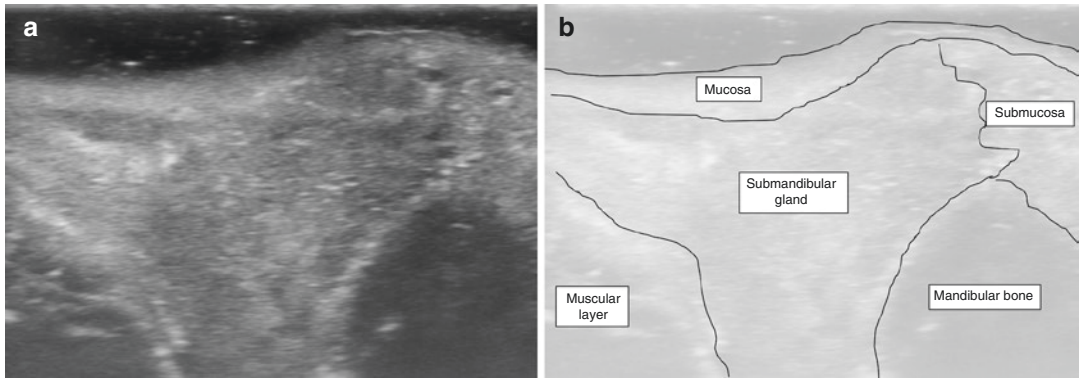

Fig. 13.12 Normal anatomy of the mouth floor. (**a**) UHFUS aspect of the mouth floor; (**b**) Schematic exemplification of anatomy

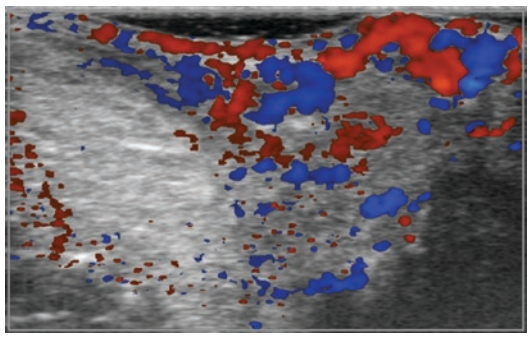

Fig. 13.13 Doppler mode of the mouth floor

13.5.7 Pyogenic Granuloma

These exophytic lesions develop from the connective tissue of the gingival mucosa. UHFUS aspect shows continuity between the basis of the lesion and the gingival tissue thus allowing to detect the papilla from which the lesion originates. Echogenicity is similar to the gingival tissue, although septa and blood vessels at high flow rate can be often observed inside the mass. The lesion is extremely vascular, with intense blood flow and occasional presence of aliasing phenomena. (Figs. 13.26 and 13.27).

13.5.8 Salivary Retention/ Extravasation Cysts

Salivary cysts are a commonly encountered finding especially in the lower lip due to the abundance of minor salivary glands present in this site. Salivary cysts are localized in correspondence with minor salivary glands, in the submucosal layer. The surrounding layers (mucosal layer above and muscular layer below) do not show significant alterations. These cysts, whether pseudocysts or retention cysts, show well-defined margins, are often of round/oval shape, and are characterized by an inhomogeneous echogenicity. In particular, salivary cysts show slightly higher echogenicity compared to surrounding tissue and are often characterized by a central hypo/anechoic area corresponding to mucus collection. In general, these lesions have scarce vascularization. Mild blood flow can be seen on Doppler mode peripheral to the lesion. (Figs. 13.28 and 13.29).

13.5.9 Salivary Ranula

Submandibular ranula aspect on UHFUS shows thin-walled cystic lesions, with anechoic content and posterior enhancement. Vascularity is absent inside the lesion and limited to surrounding tissues in absence of significant variations. (Figs. 13.30 and 13.31).

13.5.10 Sjögren's Syndrome

The alterations of minor salivary glands in course of Sjögren's syndrome are related to the

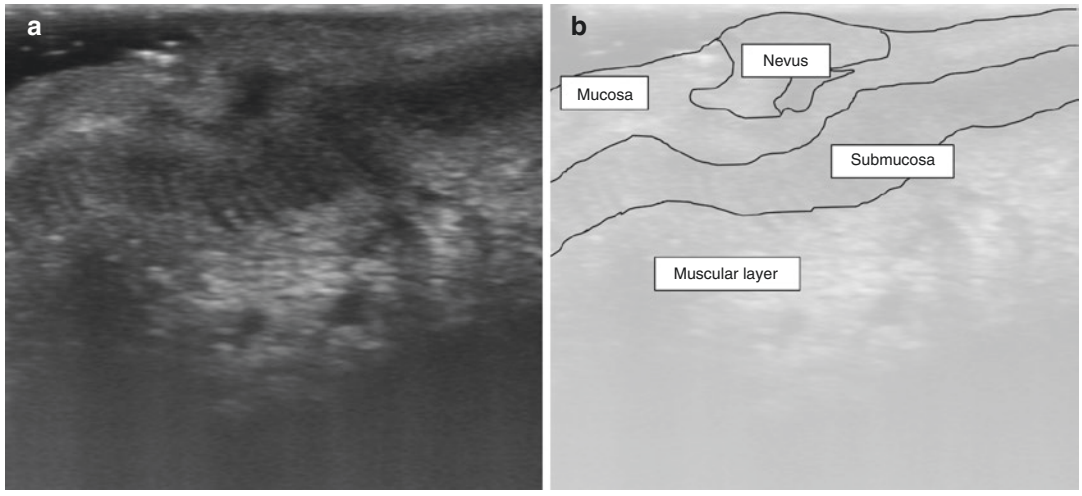

Fig. 13.14 (**a**) UHFUS aspect of a melanocytic nevus of the buccal mucosa; (**b**) Schematic exemplification

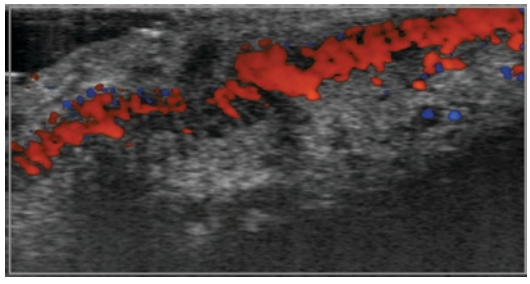

Fig. 13.15 Doppler mode of melanocytic nevus of the buccal mucosa

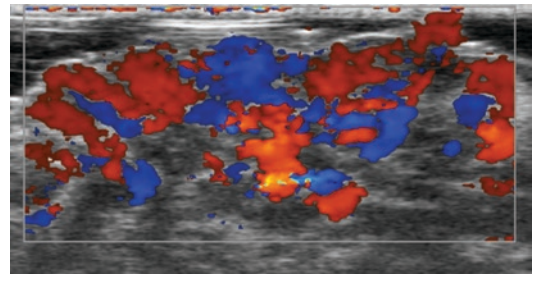

Fig. 13.17 Doppler mode of migratory glossitis

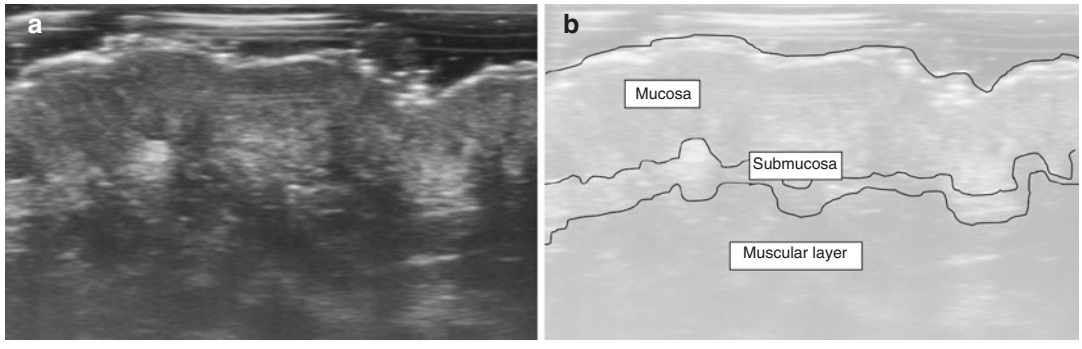

Fig. 13.16 (**a**) UHFUS aspect of migratory glossitis; (**b**) Schematic exemplification

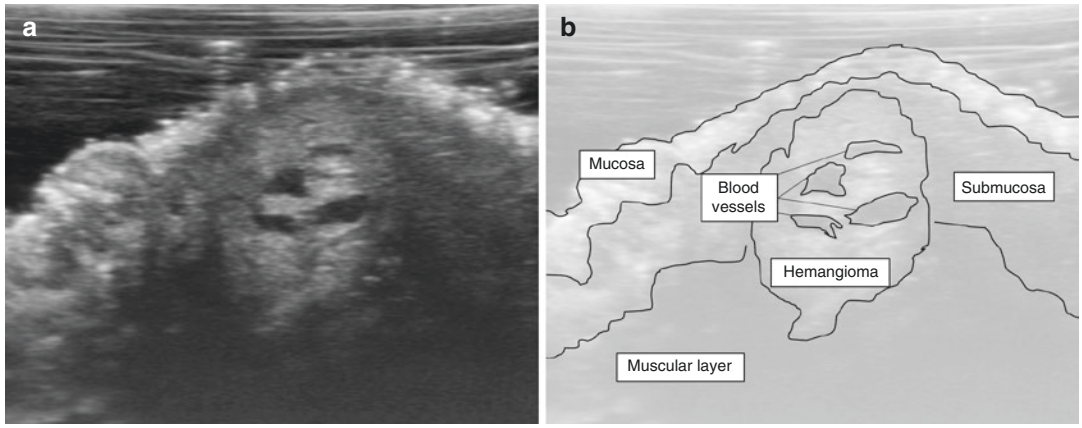

Fig. 13.18 (**a**) UHFUS aspect of hemangioma; (**b**) Schematic exemplification

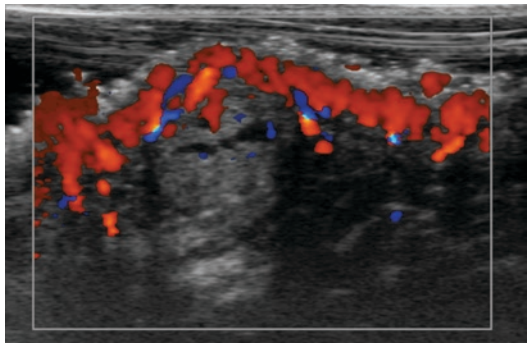

Fig. 13.19 Doppler mode of hemangioma

substitution of glandular tissue with lymphocytic infiltrate causing the development of cystic areas inside the gland. Consistently with the alterations observed in major salivary glands, also minor salivary glands can present the same modifications related to Sjögren's disease. Affected glands thus appear as inhomogeneous, with the development of both hypoechoic and hyperechoic areas. Hypoechoic areas correspond to infiltration and substitution of salivary tissue, while hyperechoic areas are related to a thickening in the epithelial wall of the salivary duct. Such an aspect causes gland structure alteration, which reflects the severity of the disease. Vascularity is generally normal or slightly increased. (Figs. 13.32 and 13.33).

13.5.11 Oral Lichen Planus

Oral lichen planus (OLP) is characterized by a variety of forms of presentation. However, a typical UHFUS pattern in OLP lesions can be always spotted regardless of the clinical form of presentation. UHFUS aspect of OLP is characterized by the presence of a thick hypoechoic stratum localized between the mucosal and submucosal layers. The hypoechoic band is homogeneous, well demarked, linear, and detectable in all the clinical affected areas. The echogenicity is lower compared to the mucosal layer, and in some cases an anechoic demarcation line can be seen between the mucosa and the hypoechoic stratum. The submucosa and the underlying strata appear unaffected, showing normal echogenicity. Vascularity is moderate to intense, especially in the superficial layers of the mucosa, while normal vascularity can be observed in the underlying strata. (Figs. 13.34 and 13.35).

13.5.12 Leukoplakia

The clinical diagnosis of leukoplakia reflects the presence of nonspecific alterations in the mucosal structure, ranging from acanthosis to hyperkeratosis. On UHFUS, leukoplakia appears as a

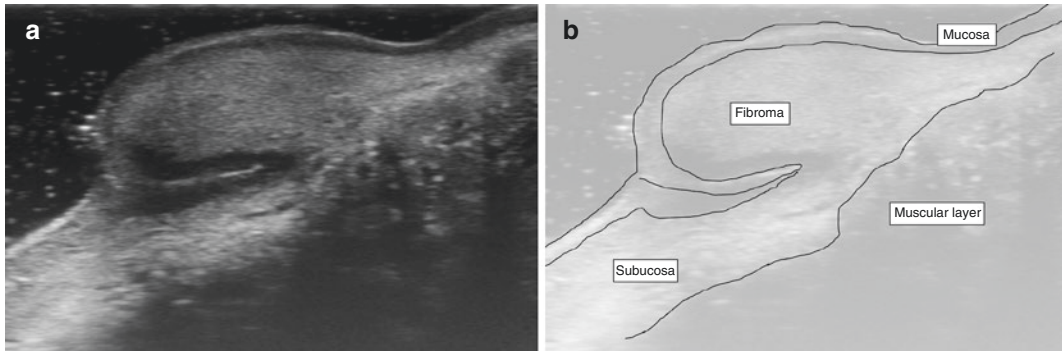

Fig. 13.20 (**a**) UHFUS aspect of fibrous hyperplasia; (**b**) Schematic exemplification

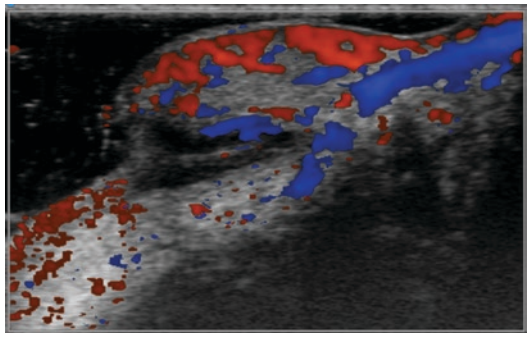

Fig. 13.21 Doppler mode of fibrous hyperplasia

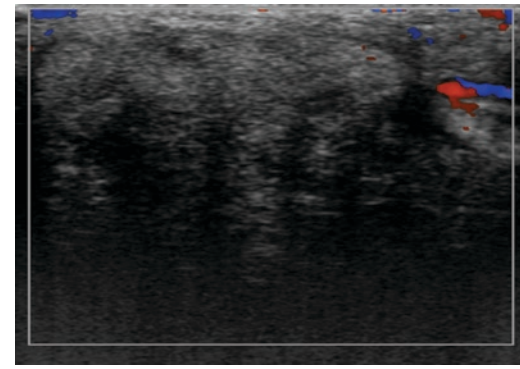

Fig. 13.23 Doppler mode of lipoma

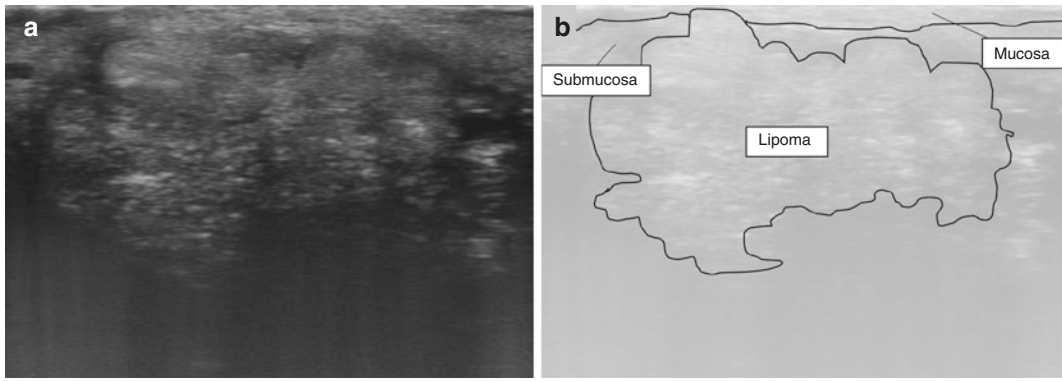

Fig. 13.22 (**a**) UHFUS aspect of lipoma of the buccal mucosa; (**b**) Schematic exemplification

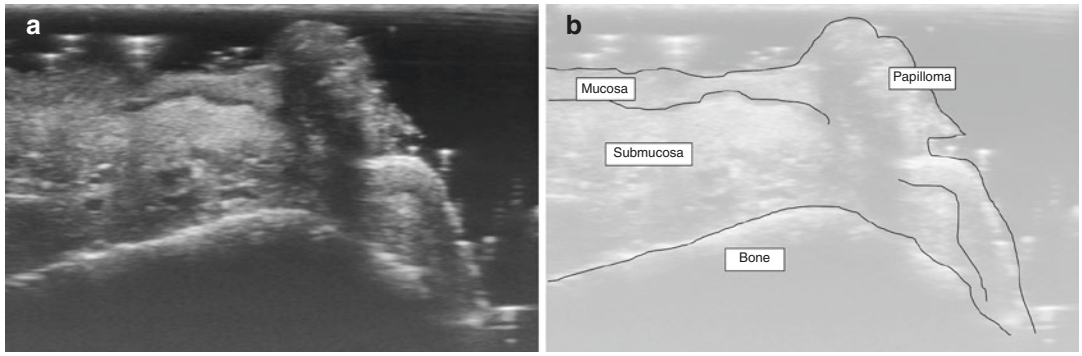

Fig. 13.24 (**a**) UHFUS aspect of papilloma of the palate; (**b**) Schematic exemplification

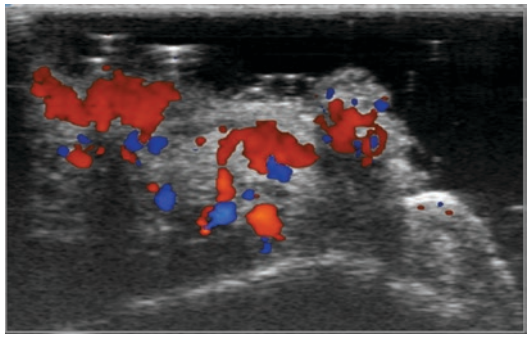

Fig. 13.25 Doppler mode of papilloma

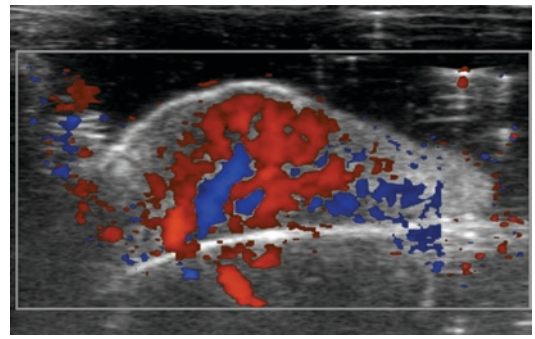

Fig. 13.27 Doppler mode of pyogenic granuloma

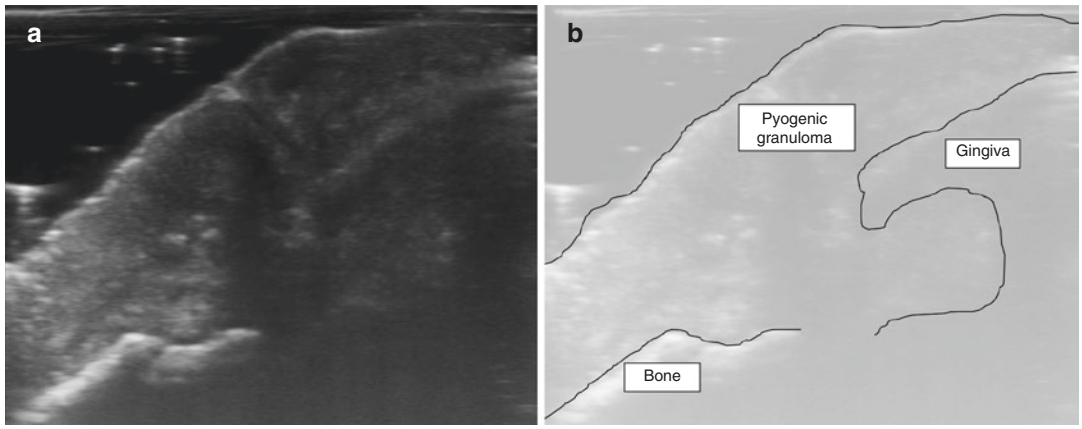

Fig. 13.26 (**a**) UHFUS aspect of pyogenic granuloma of the gingiva; (**b**) Schematic exemplification

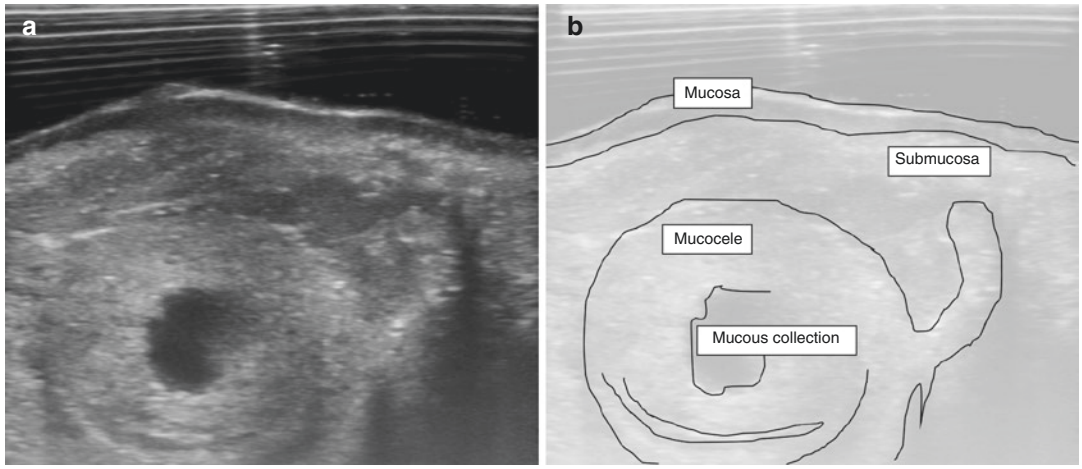

Fig. 13.28 (**a**) UHFUS aspect of salivary cyst of the lower lip; (**b**) Schematic exemplification

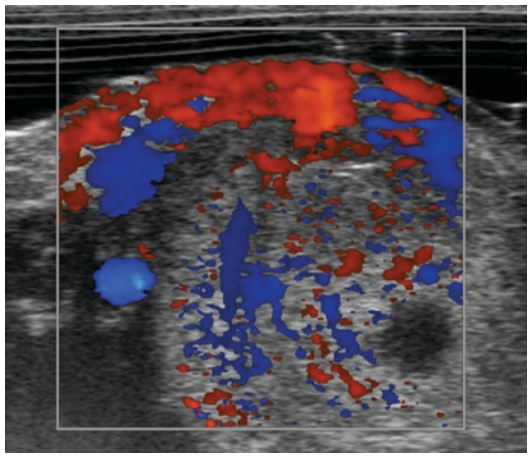

Fig. 13.29 Doppler mode of salivary cyst

markedly hypoechoic area with blurred edges, extending from the mucosa to the submucosa. The hypoechoic area can present characteristics of homogeneity or inhomogeneity associated with the presence of focal hyperechogenicity. It is important to highlight the fact that while in OLP the hypoechoic band can be observed as a continuous, well demarcated line localized beneath the mucosal layer, in leukoplakia the hypoechoic area appears thicker, nonlinear, and with blurred margins. Moreover, the thickness of leukoplakia lesion is variable, while in OLP the hypoechoic layer is almost constant in thickness. Doppler shows moderate vascularity in correspondence with the lesion (Figs. 13.36 and 13.37).

13.5.13 Erythroplakia

Erythroplakia has an extremely variable aspect. In the majority of cases, the lesion can be seen as a markedly irregular area, characterized by the loss of defined demarcation between mucosa, submucosa, and the lesion. An increase in vascularity can be observed, and also in B-mode several enlarged blood vessels can be seen in the submucosa. A typical feature is the nonlinear shape of the lesion, which is characterized by interdigitations with the submucosa. Vascularity is mild to intense. (Figs. 13.38 and 13.39).

13.5.14 Oral Squamous Cell Carcinoma

Oral squamous cell carcinoma causes a totally subverted aspect of the affected mucosa. The typical layering is missed, with a loss of demarcation between epithelial layers. In particular, the submucosa appears altered with the presence of

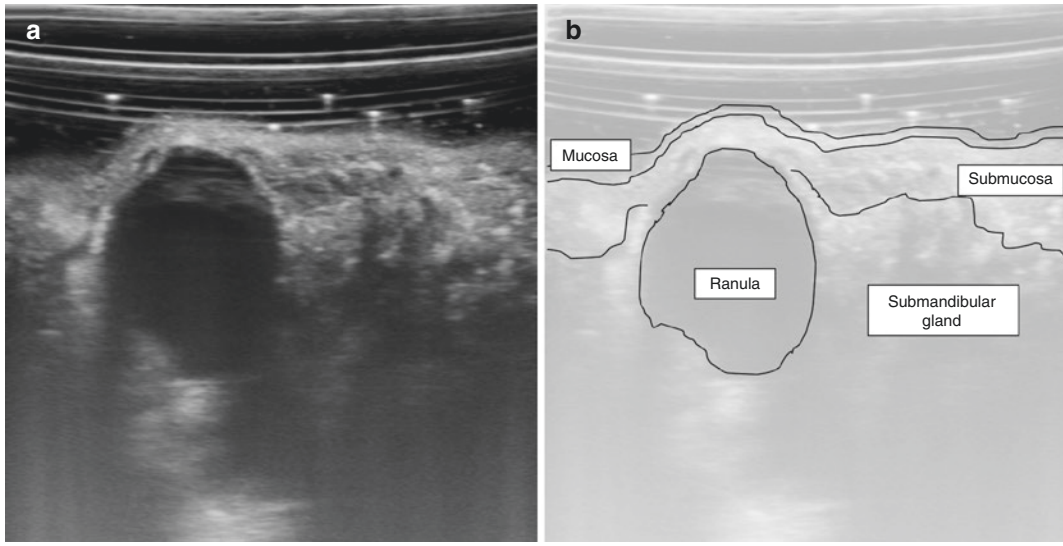

Fig. 13.30 (**a**) UHFUS aspect of salivary ranula of the submandibular gland localized in the mouth floor; (**b**) Schematic exemplification

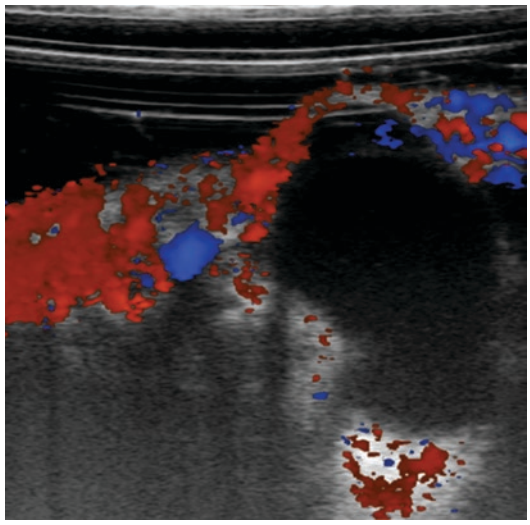

Fig. 13.31 Doppler mode of salivary ranula

an increased number of dilated blood vessels. Echogenicity can vary from hypoechoic areas to hyperechoic structures depending on the pattern of the tumor. In advanced cases, the two aspects coexist in the same lesion. The lesion appears in continuity with the surrounding areas, in absence of clear margins. Infiltration of the underlying tissues (muscular layer or bone) can be present, causing an alteration in the structure of the deeper strata. Doppler shows intense vascularity, with several areas being interested in aliasing phenomena. (Figs. 13.40 and 13.41).

13.6 Patient Protection

13.6.1 ALARA Principle

The "as low as reasonably achievable" criteria is applicable to the proper use of diagnostic ultrasound, in order to keep exposure and biologic effects to a minimum during the examination. It is known that a stationary beam causes a concentrated exposure compared to a scanned beam, which distributes the exposure on a wider area. Exposure depends on frequency, penetration, resolution, and field of view of the transducer, but is also influenced by some intrinsic characteristics of the tissue being scanned (body size, location of the bone relative to the focal point, attenuation in the body, and ultrasound exposure time).

In ultrasonography, the ALARA principle takes into account the limitation of ultrasound application to situations in which it is medically useful and keeping patient exposure to the lowest ultrasound output for the shortest time necessary to achieve acceptable diagnostic results [11].

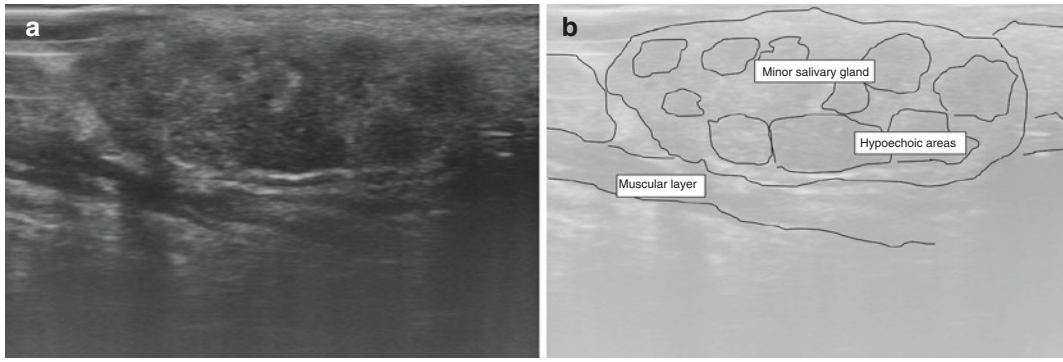

Fig. 13.32 (**a**) UHFUS aspect of minor labial salivary gland in course of Sjögren's syndrome; (**b**) Schematic exemplification

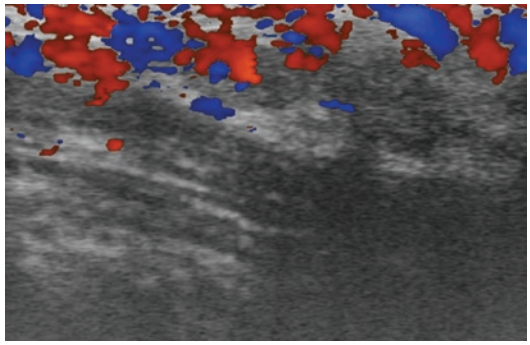

Fig. 13.33 Doppler mode of minor labial salivary gland in course of Sjögren's syndrome

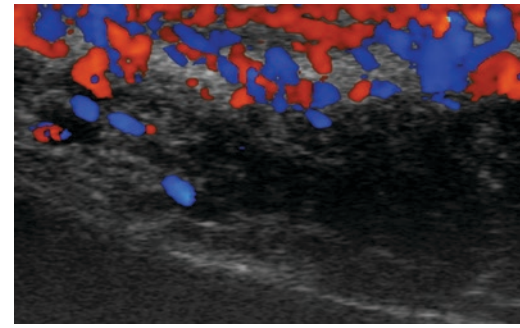

Fig. 13.35 Doppler mode of oral lichen planus

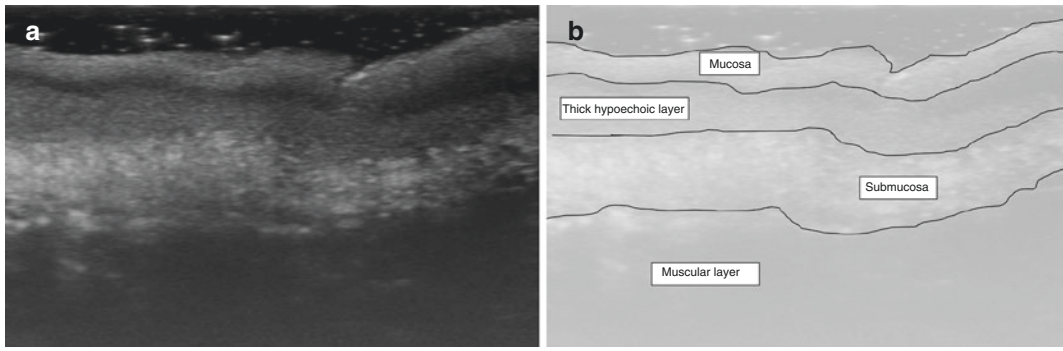

Fig. 13.34 (**a**) UHFUS aspect of oral lichen planus; (**b**) Schematic exemplification

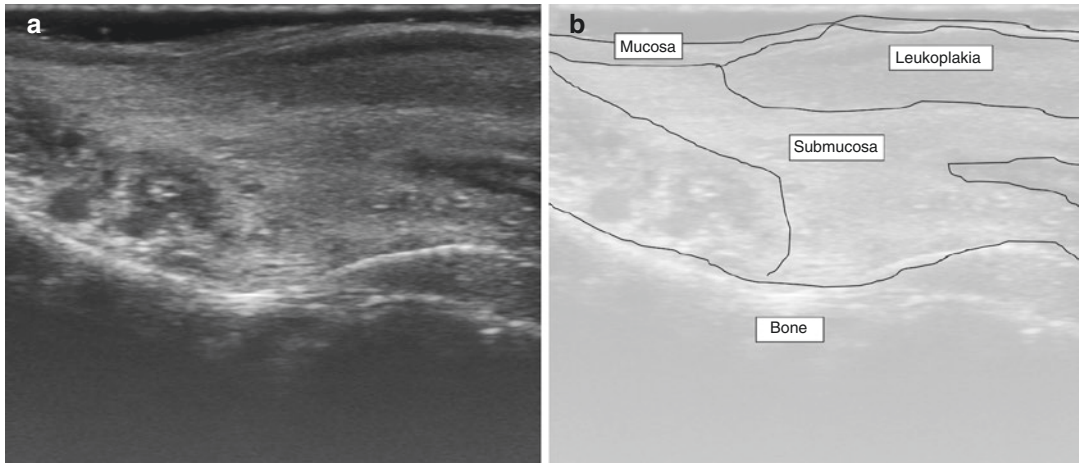

Fig. 13.36 (**a**) UHFUS aspect of leukoplakia of the lower buccal fornix; (**b**) Schematic exemplification

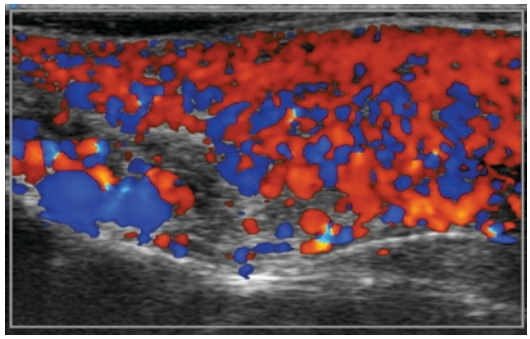

Fig. 13.37 Doppler mode of leukoplakia

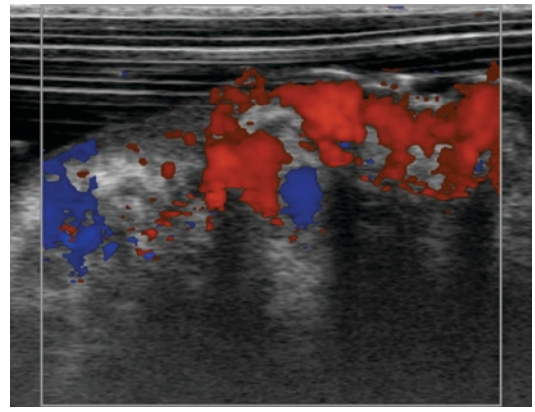

Fig. 13.39 Doppler mode of erythroplakia

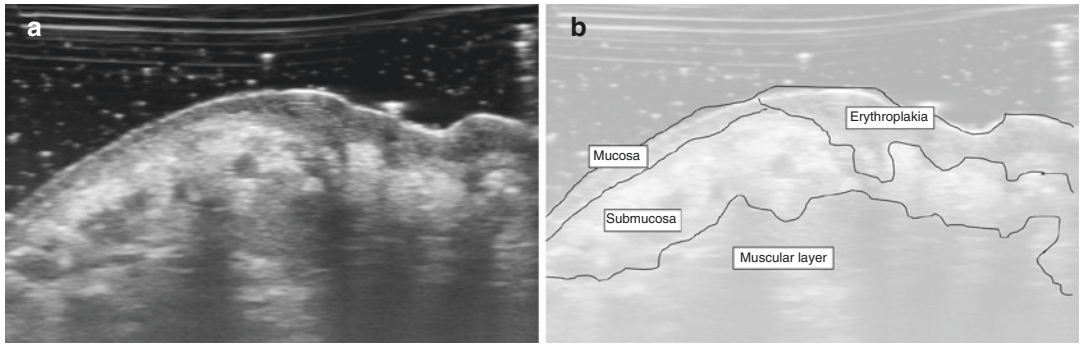

Fig. 13.38 (**a**) UHFUS aspect of tongue erythroplakia; (**b**) Schematic exemplification

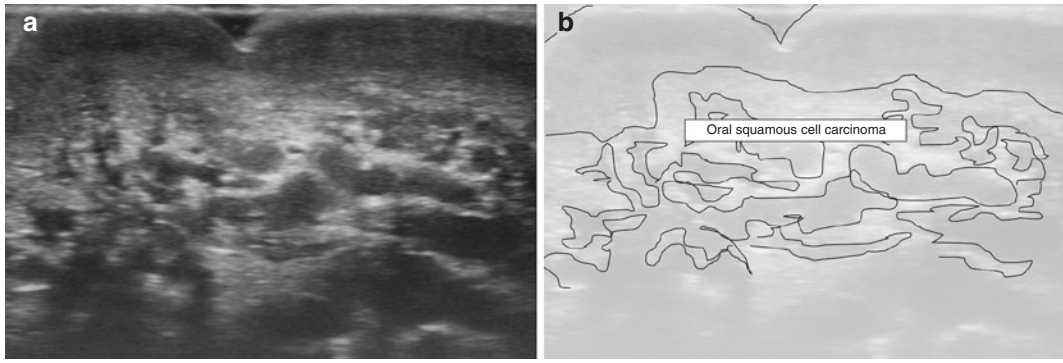

Fig. 13.40 (**a**) UHFUS aspect of oral squamous cell carcinoma of the tongue; (**b**) Schematic exemplification

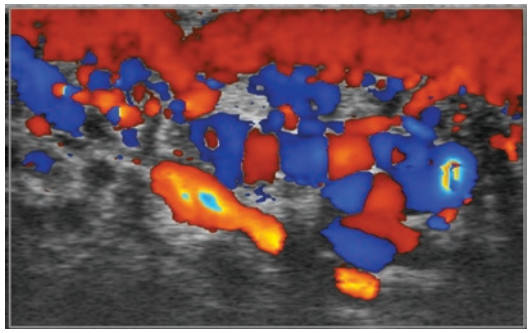

Fig. 13.41 Doppler mode of oral squamous cell carcinoma

The major issue during ultrasound scan performance is related to the potential localized heating of the patient due to transducer surface temperature. When using UHFUS, the estimated temperature in simulated use is reported to be 18 °C both for 48 MHz and 70 MHz transducers, while in still air the transducer can reach temperature limit of 48.6 °C. However, the electrical design of the transducer limits both power supply current and voltage, by controlling the output (directly and indirectly) and the receiver.

Mechanical Index (MI) varies with the adjustment of the focal zone depth, while adjusting the Pulse-Repetition Frequency (PRF), box width, box location, and focal depth will affect the Thermal Index (TI) value.

References

1. Foster FS, Hossack J, Adamson SL. Micro-ultrasound for preclinical imaging. Interface Focus. 2011;1:576–601.
2. Greco A, Mancini M, Gargiulo S, Gramanzini M, Claudio PP, Brunetti A, et al. Ultrasound biomicroscopy in small animal research: applications in molecular and preclinical imaging. J Biomed Biotechnol. 2012;2012:519238. https://doi.org/10.1155/2012/519238.
3. Sarkola T, Redington A, Keeley F, Bradley T, Jaeggi E. Transcutaneous very-high-resolution ultrasound to quantify arterial wall layers of muscular and elastic arteries: validation of a method. Atherosclerosis. 2010;212(2):516–23. https://doi.org/10.1016/j.atherosclerosis.2010.06.043.
4. Cartwright MS, Baute V, Caress JB, Walker FO. Ultrahigh-frequency ultrasound of fascicles in the median nerve at the wrist. Muscle Nerve. 2017;56(4):819–22. https://doi.org/10.1002/mus.25617.
5. Hayashi A, Giacalone G, Yamamoto T, et al. Ultra high-frequency Ultrasonographic imaging with 70 MHz scanner for visualization of the lymphatic vessels. Plast Reconstr Surg Glob Open. 2019;7(1):e2086. https://doi.org/10.1097/GOX.0000000000002086.
6. Oranges T, Vitali S, Benincasa B, Izzetti R, Lencioni R, Caramella D, Romanelli M, Dini V. Advanced evaluation of hidradenitis suppurativa with ultra-high frequency ultrasound: a promising tool for the diagnosis and monitoring of disease progression. Skin Res Technol. 2019; https://doi.org/10.1111/srt.12823.
7. Izzetti R, Vitali S, Aringhieri G, Nisi M, Oranges T, Dini V, Ferro F, Baldini C, Romanelli M, Caramella D,

Gabriele M. Ultra-high frequency ultrasound, a promising diagnostic technique: review of the literature and single-center experience. Can Assoc Radiol J. 2020:846537120940684. https://doi.org/10.1177/0846537120940684.

8. Izzetti R, Vitali S, Aringhieri G, Caramella D, Nisi M, Oranges T, Dini V, Graziani F, Gabriele M. The efficacy of ultra-high frequency ultrasonography in the diagnosis of intraoral lesions. Oral Surg Oral Med Oral Pathol Oral Radiol. 2019; https://doi.org/10.1016/j.oooo.2019.09.012.
9. Izzetti R, Vitali S, Oranges T, Dini V, Romanelli M, Caramella D, Gabriele M. Intraoral ultra-high frequency ultrasound study of oral lichen planus: a pictorial review. Skin Res Technol. 2020;26(2):200–4. https://doi.org/10.1111/srt.12777.
10. Izzetti R, Vitali S, Gabriele M, Caramella D. Feasibility of a combination of intraoral UHFUS and CBCT in the study of peri-implantitis. Oral Surg Oral Med Oral Pathol Oral Radiol. 2019;127(3):e89–94. https://doi.org/10.1016/j.oooo.2018.08.014.
11. Kollmann C, Jenderka KV, Moran C, Draghi F, Jimenez Diaz J, Sande R. EFSUMB clinical safety statement for diagnostic ultrasound (2019 revision). Ultraschall Med. 2019; https://doi.org/10.1055/a-1010-6018.

14 Ultrasonographic Imaging in Periodontology

Kaan Orhan and Revan Birke Koca

Contents

14.1 Periodontium

Periodontium is the tissue integrity that surrounds the teeth and consists of four main components. They are gingiva, periodontal ligament, cementum, and alveolar bone. Each of these periodontal components is different, but all of these components function together as a single unit [1]. The main function of the periodontium is to attach the tooth to the alveolar bone and to maintain the integrity of the surface of the masticatory mucosa of the oral cavity.

This chapter first describes periodontium and periodontal diseases; then discusses the usage areas of ultrasonography in periodontology.

K. Orhan (✉)
Faculty of Dentistry, Department of Dentomaxillofacial Radiology, Ankara University, Ankara, Turkey

R. B. Koca
Faculty of Dentistry, Department of Periodontology, University of Kyrenia, Kyrenia, Cyprus

K. Orhan (ed.), *Ultrasonography in Dentomaxillofacial Diagnostics*,
https://doi.org/10.1007/978-3-030-62179-7_14

14.1.1 Gingiva

14.1.1.1 Anatomy of Gingiva

The gingiva is the part of the masticatory mucosa covering the alveolar process and surrounding the cervical part of the teeth. It consists of an epithelial layer and an underlying layer of connective tissue called lamina propria. The color of the gingiva is coral pink and it has a stippled "orange peel" surface (Fig. 14.1). The gingiva acquires its final shape and texture with the eruption of the teeth. The gingiva is divided anatomically into free gingiva, attached gingiva, and interdental gingiva (Fig. 14.2).

Free Gingiva

The free or marginal gingiva is the most coronal part of the gingiva, coral pink, has a dull surface and a firm consistency. It is clinically about 1 mm wide and forms the soft tissue wall of the gingival sulcus. The free gingival margin is rounded and is located approximately 1.5–2 mm coronal to the cementoenamel junction (CEJ) (Fig. 14.3).

The Attached Gingiva

The attached gingiva is located in the continuation of the free gingiva and is tightly attached to the periosteum underneath. It is separated from the movable alveolar mucosa by the mucogingi-

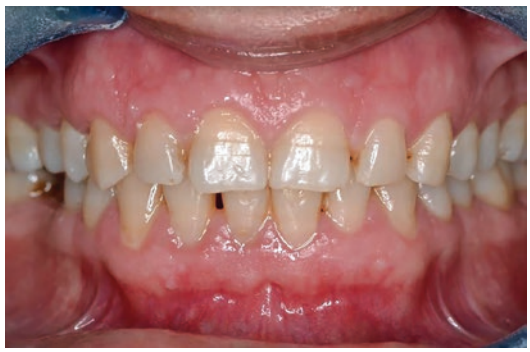

Fig. 14.1 Healthy periodontium

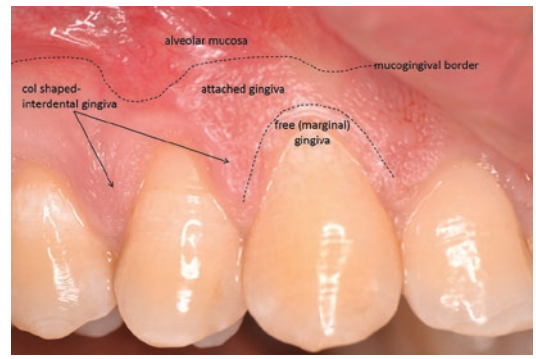

Fig. 14.2 Anatomy of the healthy gingiva

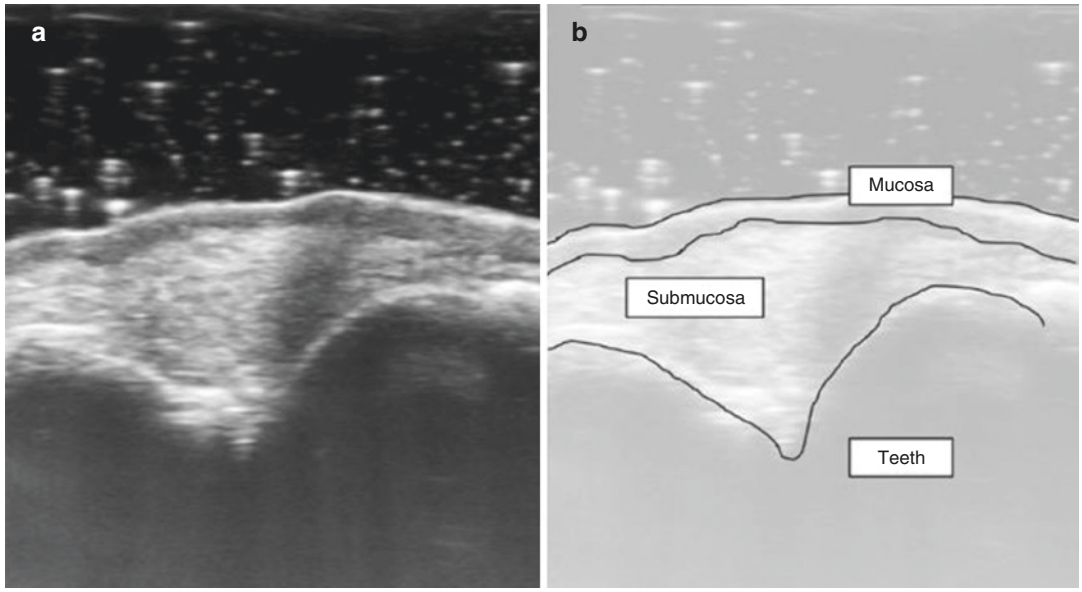

Fig. 14.3 Anatomy of healthy gingiva (**a**) UHFUS aspect of the gingiva; (**b**) Schematic exemplification of anatomy

val border. The distance between the mucogingival border and the gingival sulcus is defined as the width of the attached gingiva and is an important parameter for the health of the periodontium. This width is the largest in the incisor area (3.5–4.5 mm in the maxilla, 3.3–3.9 mm in the mandible), the narrowest in the premolars (1.9 mm in the maxilla, 1.8 mm in the mandible) [2]. The dark red alveolar mucosa (AM) located in the mucogingival junction apical is loosely attached to the periosteum. Alveolar mucosa is seen more reddish than the attached gingiva since it has more blood supply (Fig. 14.4). Therefore, it is mobile unlike the attached gingiva.

The Interdental Gingiva

The interdental gingiva is a pyramid or "col" shaped gingiva covering the interproximal space below the contact area of the teeth. It is not seen between the teeth without contact, it becomes flat.

The Gingival Sulcus

The gingival sulcus is a shallow groove with an epithelium lined with a tooth surface on one side and free gingiva on the other. The depth of the gingival sulcus is a parameter in the periodontium health. This depth is measured with the help of a periodontal probe. In healthy gingiva, the depth of the sulcus is between 0–1 mm clinically and an average 1.8 mm histologically [1].

The Gingival Fluid

In the gingiva sulcus, there is the gingival fluid originating from the subgingival gingiva. In the healthy sulcus, although the amount of gingival fluid is very small, during inflammation, the gingival fluid increases and its composition begins to resemble an inflamed exudate.

14.1.2 Periodontal Ligament

Periodontal ligament is a cellular connective tissue rich in vascularization that surrounds the tooth roots and connects the cement to the inner wall of the alveolar bone [3]. It is continuous with the connective tissue of the gingiva and communicates with the alveolar bone through the vascular channels of the bone.

The periodontal ligament is in the shape of an hourglass and is the narrowest at the middle root level. The average width of the periodontal ligament is about 0.2 mm; however, it decreases in dysfunctional teeth, increases in teeth exposed to hyperfunction [1].

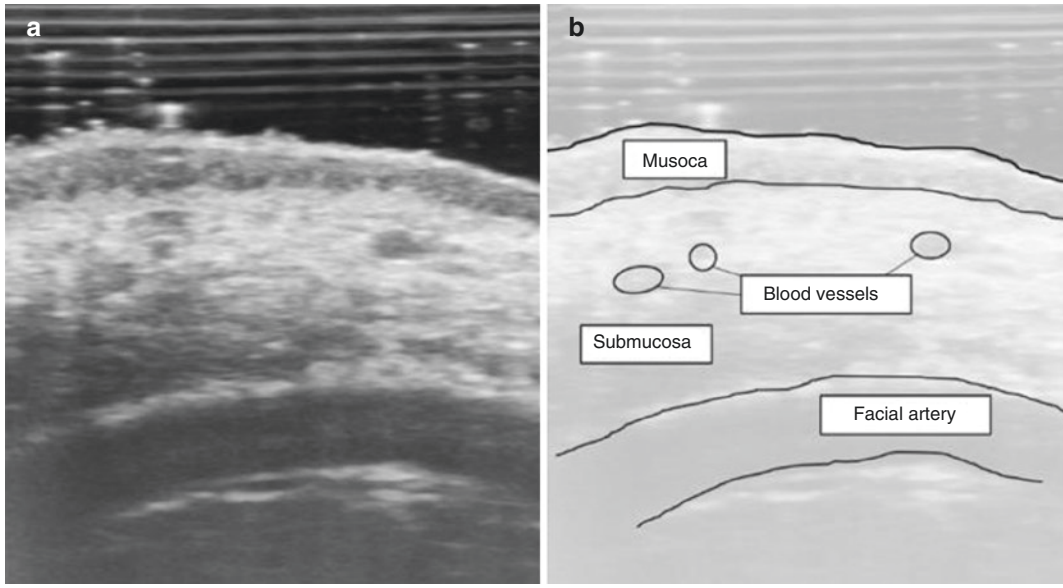

Fig. 14.4 Anatomy of the healthy buccal mucosa, (**a**) UHFUS aspect of the buccal mucosa; (**b**) Schematic exemplification of anatomy

14.1.2.1 Periodontal Ligament Cells

The cells of the periodontal ligament are *undifferentiated mesenchymal cells*, *fibroblasts*, *osteoblasts*, *osteoclasts*, *cementoblasts*, *epithelial cells*, *neurovascular elements,* and *immune system cells* [4].

14.1.2.2 Extracellular Matrix of Periodontal Ligament (ECM)

The periodontal ligament also contains a large amount of ECM that fills the gaps between the fibers and cells. This matrix consists of two main components, such as glycosaminoglycan (hyaluronic acid, proteoglycan, heparan sulfate, dermatan sulfate, chondroitin sulfate) and glycoprotein (fibronectin and laminin) and 70% water [1]. Besides, cells use it for support, water storage, bonding, and intercellular exchange.

14.1.3 Cementum

Cementum is a calcified avascular mesenchymal tissue that covers the root surfaces. Contrary to the bone, the cementum does not contain blood or lymph vessels, has no innervation, moreover it does not have a physiological resorption or remodeling. The cementumt is characterized by continuing to accumulate throughout life.

14.1.3.1 Cementoenamel Junction

There may be three possibilities in cementoenamel combination (Fig. 14.5);

- About 30%, mine-cementum comes to tip.
- 60–65%, cement texture covers the enamel.
- 5–10%, enamel-cement does not combine, dentin tissue remains exposed. In this case, the risk of gingival recession and dentin sensitivity increases.

14.1.3.2 Cementum Resorption

In the regions where cementum resorption is active, multinucleus giant cells and mononuclear macrophages are present. Cementum resorption may be caused by local or systemic factors or may be idiopathic. *Local conditions* that cause cementum resorption include [1];

- Occlusal trauma
- Orthodontic movement [5]

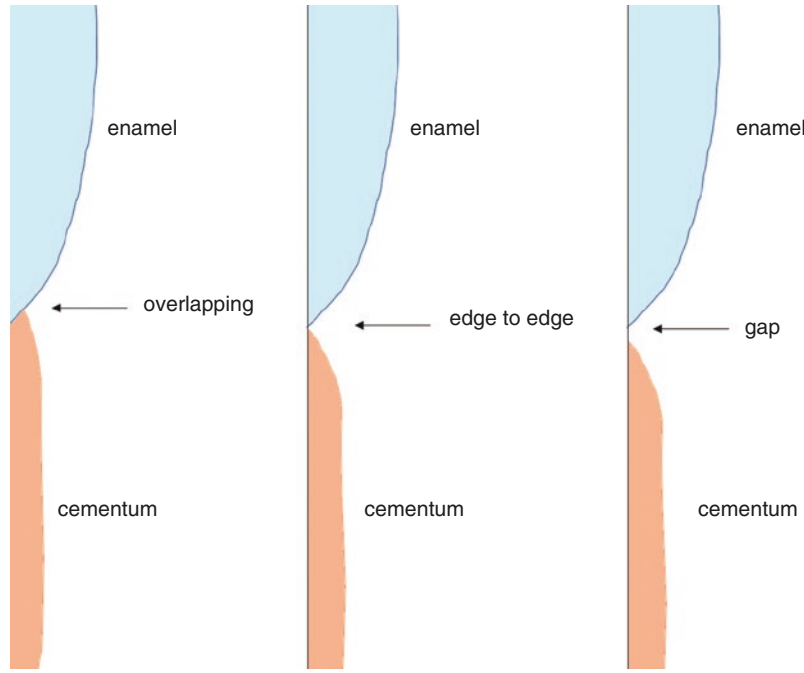

Fig. 14.5 Schematic exemplification of possibilities in cementoenamel combination

- Teeth pressures outside the dental arch
- Cysts or tumors
- Teeth without functional antagonists
- Impacted teeth
- Reimplanted teeth
- Periodontal and periapical diseases

Systemic conditions that predispose the individual to cementum resorption include;

- Calcium deficiency
- Vitamin A and Vitamin D deficiency
- Hypothyroidism [6]
- Hereditary fibrosis osteodystrophy
- Paget's disease
- Tuberculosis
- Pneumonia

Cementum resorption (Fig. 14.6) can extend into the dentin and even the pulp under the resorptive process and is asymptomatic. It is not continuous, repair period may begin with newly formed cementum tissue.

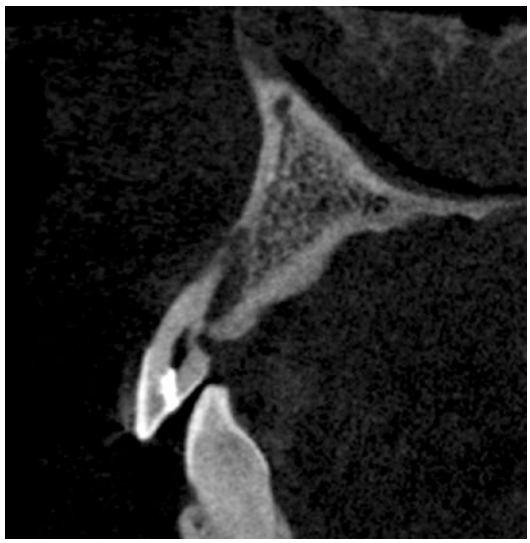

Fig. 14.6 Cementum resorption in the sagittal section of CBCT

14.1.4 Alveolar Process

The alveolar process is the portion of the maxilla and mandible that forms and supports the tooth sockets. The alveolar process extends from the basal bone of the jaws and develops in conjunction with eruption of the teeth, gradually disappears when the tooth is lost [1].

14.1.4.1 Anatomy of Alveolar Process

Alveolar bone proper forms the attachment apparatus of the teeth with the root cementum and periodontal membrane. The main function of the alveolar process is to distribute the masticatory force and other occlusal forces.

The alveolar process consists of the following:

- Cancellous trabeculae between these two compact layers, supporting alveolar bone
- Compact bone on the inner wall of the socket called alveolar bone proper, which is called lamina dura on radiographs
- An external plate of cortical bone formed by Haversian bone canals and compact bone lamellae

The walls of the sockets and the outer walls of the alveolar process are made of cortical bone. The area surrounding the cortical bone walls is occupied by the cancellous bone. Cancellous bone covers most of the interdental septa; however, only a relatively small portion of the buccal and palatal bone walls. Also, the bones of maxilla and mandibula include the basal bone, which is the portion of the jaw located apically but unrelated to the teeth. The cancellous part of the alveolar bone consists of trabeculae surrounding the irregularly shaped bone marrow cavities covered with a thin, flattened endosteal cell layer. Cancellous bone is found mainly in interradicular and interdental spaces. The adult person has more cancellous bones in the maxilla than the mandible.

The bone covering the socket wall usually continues with the compact bone in the lingual and buccal aspects of the alveolar process. In the cheek and lingual aspects of the alveolar process, the thickness of the bone can vary from one area to another. The same is true for teeth. In the incisors and premolar regions, the bone in the buccal directions of the teeth is much thinner than the lingual aspect. In the molar region, the bone is thicker than the buccally and lingually.

A region without bone coverage in the marginal part of the root is called *dehiscence*. If there is a bone in the most coronal part of the buccal bone, but the defect is found more apically, it is called *fenestration*. In areas with such deficiencies, the root is covered only with connective tissue attachment and overlying mucosa.

Periosteum-Endosteum

All bone-forming active sites contain osteoblasts. The outer surface of the bone is covered with a layer called the periosteum. This layer consists of an inner layer surrounded by osteoblasts and an outer layer containing dense vascularization, innervation, and collagen fiber. Blood vessels branch extensively and travel through the periosteum. On the inner surface of the bone, that is, in the bone marrow cavity, there is an endosteum with properties similar to the periosteum. Periosteum regulates bone size for life. A change in bone size is the result of periosteal osteoblastic and osteoclastic activity.

Remodeling

Remodeling provides bone shape changes, resistance to forces, repair of wounds, and regulation of calcium and phosphate metabolism in the body. New bone formation and bone destruction in a constant balance constitute the *main principle of bone*. Remodeling involves coordination between osteoblasts that stimulate new bone formation and osteoclasts that stimulate bone resorption.

In healthy alveolar bone, renewal and remodeling made by osteoblasts are balanced by resorption by osteoclasts. Although the number of osteoblasts decreases with aging, there is no change in the number of osteoclasts. Systemic effects that stimulate bone remodeling are usually caused by hormones such as parathormone, calcitonin, and vitamin D3.

Alveolar bone is constantly renewed depending on functional conditions. The life-long tendency of the teeth to be mesialized requires a continuous remodeling of the alveolar bone.

Resorption

Bone resorption is associated with osteoclastic activity. These cells are large multi-core cells that specialize in the breakdown of matrices and minerals.

Regulation of bone remodeling is a complex process involving hormones and local factors that act in the form of an autocrine and paracrine on the formation and activity of different bone cells. Bone contains 99% of the body's calcium ions. Therefore, it is the main source of calcium release when the level of calcium in the blood drops; it is regulated by the parathormone secreted by the parathyroid gland.

Remodeling of the trabecular bone begins with the resorption of bone surface by osteoclasts.

14.2 Periodontal Diagnosis and Prognosis

14.2.1 Classification of Periodontal and Peri-implant Diseases and Conditions

Classification of diseases affecting the gingiva and periodontium provides a universal assessment of diseases in terms of etiology, pathogenesis, clinical symptoms, radiographic symptoms, medical history, and treatment.

Universal features of gingival diseases include clinical signs and symptoms associated with inflammation, the reversibility of diseases by the elimination of the etiology, the presence of bacterial plaque to initiate or exacerbate the disease.

A classification scheme for periodontal and peri-implant diseases and conditions is essential for clinicians to accurately diagnose and treat patients, as well as for scientists to investigate the

treatment of etiology, pathogenesis, natural history, and diseases and conditions.

So far, many periodontal disease classifications have been introduced such as 1989, 1993, 1996, and 1999. The Classification of Periodontal and Peri-Implant Diseases and Conditions organized by the World Workshop in 2017 is as follows [7]:

14.2.1.1 Classification of Periodontal and Peri-Implant Diseases and Conditions-2017

A. Periodontal Diseases and Conditions
   I. Periodontal Health, Gingival Diseases and Conditions
      1. Periodontal Health and Gingival Health
         (a) Clinical gingival health on an intact periodontium
         (b) Clinical gingival health on a reduced periodontium
            (1) Stable periodontitis patient
            (2) Non-periodontitis patient
      2. Gingivitis–dental biofilm-induced
         (a) Associated with dental biofilm alone
         (b) Mediated by systemic or local risk factors
         (c) Drug-induced gingival enlargement
      3. Gingival diseases–non-dental biofilm-induced
         (a) Genetic/developmental disorders
         (b) Specific infections
         (c) Inflammatory and immune conditions
         (d) Reactive processes
         (e) Neoplasms
         (f) Endocrine, nutritional & metabolic disorders
         (g) Traumatic lesions
         (h) Gingival pigmentations
   II. Forms of Periodontitis
      1. Necrotizing Periodontal Diseases
         (a) Necrotizing Gingivitis
         (b) Necrotizing Periodontitis
         (c) Necrotizing Stomatitis
      2. Periodontitis as Manifestation of Systemic Diseases

         Classification of these conditions should be based on the primary systemic disease according to the International Statistical Classification of Diseases and Related Health Problems (ICD) codes
      3. Periodontitis
         (a) Stages: Based on the severity and complexity of management
            (1) Stage I: Initial periodontitis
            (2) Stage II: Moderate periodontitis
            (3) Stage III: Severe periodontitis with potential for additional tooth loss
         (b) Extent and distribution: localized, generalized; molar-incisor distribution
         (c) Grades: Evidence or risk of rapid progression, anticipated treatment response
            (1) Grade A: Slow rate of progression
            (2) Grade B: Moderate rate of progression
            (3) Grade C: Rapid rate of progression
   III. Periodontal Manifestations of Systemic Diseases and Developmental and Acquired Conditions
      1. Systemic diseases or conditions affecting the periodontal supporting tissues
      2. Other Periodontal conditions
         (a) Periodontal abscesses
         (b) Endodontic-periodontal lesions
      3. Mucogingival deformities and conditions around teeth
         (a) Gingival phenotype
         (b) Gingival/soft tissue recession
         (c) Lack of gingiva
         (d) Decreased vestibular depth
         (e) Aberrant frenum/muscle position
         (f) Gingival excess
         (g) Abnormal color

(h) Condition of the exposed root surface

4. Traumatic occlusal forces
   (a) Primary occlusal trauma
   (b) Secondary occlusal trauma
   (c) Orthodontic forces
5. Protheses and tooth-related factors that modify or predispose to plaque-induced gingival diseases/periodontitis
   (a) Localized tooth-related factors
   (b) Localized dental protheses-related factors

B. Peri-Implant Diseases and Conditions
   I. Peri-implant Health
   II. Peri-implant Mucositis
   III. Peri-implantitis
   IV. Peri-implant Soft and Hard Tissue Deficiencies

14.2.2 Definition and Etiology of Periodontal Diseases

14.2.2.1 Plaque-Induced Gingivitis

The onset of gingival diseases occurs in the presence of microbial dental plaque. If the accumulation of microbial dental plaque increases between the tooth and the marginal gingiva, inflammation and classic clinical gingivitis may develop.

Plaque-induced gingivitis is inflammation of the gingiva resulting from bacteria located at the gingival margin. In gingivitis, the inflammatory lesion is confined to the gingiva. However, when the microbial dental plaque is not eliminated, the infection may spread to deeper tissues and periodontitis may develop. This process varies according to the individual's host response.

Clinical manifestations of gingivitis, bleeding during probing, enlarged gingival contours due to edema or fibrosis are color change to a reddish tone and increased exudate and increased temperature. Clinical attachment levels and radiographic records are needed to establish this diagnosis.

14.2.2.2 Periodontitis

Periodontitis is a common chronic inflammatory disease due to host response caused by subgingival biofilm products characterized by destruction of the periodontal ligament and alveolar bone around the teeth.

Gingivitis precedes periodontitis, but it is clear that not all cases of gingivitis progress to periodontitis. In gingivitis, the inflammatory lesion is confined to the gingiva; however, with periodontitis, the inflammatory processes extend to additionally affect the periodontal ligament and the alveolar bone. The net result of these inflammatory changes is the breakdown of the fibers of the periodontal ligament, resulting in clinical loss of attachment together with resorption of the alveolar bone.

14.2.2.3 Etiology of Periodontal Diseases

Periodontal disease develops as a result of disturbances in the oral microbiota, leading to an immune response of the host thus affecting periodontium protection and support [8]. An understanding of the etiology and pathogenesis of periodontitis is essential for diagnosis and treatment planning.

In some diseases caused by microorganisms such as periodontitis, the symptoms of the disease do not always have to be seen in the presence of a microbial agent. The development of the disease, in addition to the microbial agent, may depend on many additional factors as specific host response, toxic exposures, nutritional deficiencies, systemic status, emotional stress, and social effects.

Alveolar Bone Loss

Alveolar bone destruction can be seen both in clinical examination and radiological examination. Clinical examination is carried out by probing. In the radiological examination, the distance from the interdental area to the crest indicates the level of alveolar bone loss.

The pattern of bone loss also determines the cause of bone loss in some cases. These are also

called local factors. These can be grouped under two headings as gingival inflammation and occlusal trauma.

Bone Destruction Caused by Chronic Inflammation

When periodontal disease is not treated, depending on the type of disease, an average of 0.2 mm/year bone loss is observed. This rate may vary depending on the type of periodontal disease. There are silent and active periods in chronic periodontal diseases. These periods can be followed clinically by examining the bleeding index, exudate amount, and bacterial plaque composition. In the active phase, the periodontal pocket deepens, collagen and alveolar bone loss occur. During bone destruction, bone formation continues. The newly formed osteoid tissue is more resistant to resorption than the old bone.

Bone Destruction Caused by Occlusal Trauma

Occlusal trauma can cause bone destruction even without inflammation. When the forces that cause occlusal trauma are eliminated, tissues can be renewed without bone loss in non-inflammatory cases. If there is severe occlusal trauma, with increased tension and pressure in the periodontal ligament, the necrosis can be seen in periodontal ligament together with resorption in the alveolar bone or tooth. If occlusal trauma is prolonged, it causes funnel-shaped expansion in the coronal part of the periodontal ligament and resorption in the alveolar bone (Fig. 14.7).

Bone Destruction Caused by Systemic Conditions

Local and systemic factors regulate the physiological balance of bone. If there is a tendency to resorption in general, local inflammatory events may increase it. Periodontal bone destruction may also be occurred in relation to following systemic diseases such as; hematological diseases such as leukemia, acquired neutropenia, or genetic diseases such as familial and cyclic neutropenia, Down syndrome, Papillon-Lefèvre syndrome, and hypophosphatasia.

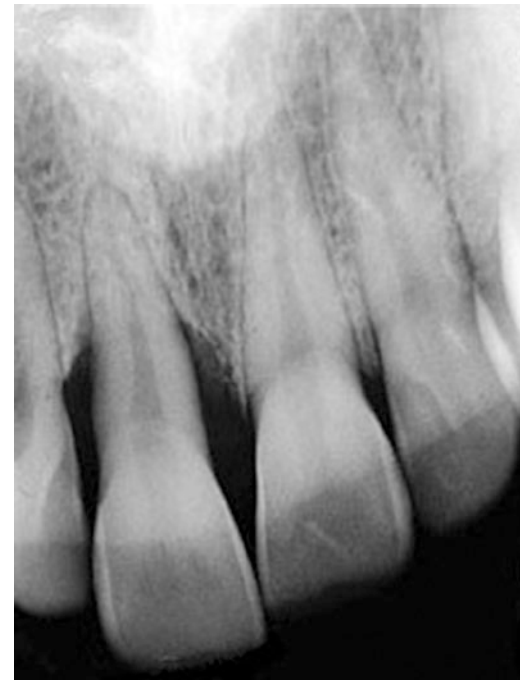

Fig. 14.7 Funnel-shaped resorption in the alveolar bone due to occlusal trauma

Furcations

According to AAP, a furcation involvement exists when periodontal disease has caused resorption of bone into the bi- or trifurcation area of a multirooted tooth [9]. Attachment loss may extend to furcation of multirooted teeth. In this case, there is pathological resorption of the interradicular bone. The examination of furcation involvement in the diagnosis of periodontal disease is determined by special probes such as Nabers probe, carefully probing the root surfaces.

The most common use of the furcation classification is the Glickman [10] classification, the first classification:

Grade I: Early lesion limited by soft tissue, intact interradicular bone. It has no radiological findings.

Grade II: loss of interradicular bone and pocket formation of varying depths into the furcation but not extending through to the opposite side of the tooth. The radiograph may or may not reveal the Grade II furcation involvement.

Grade III: The furcation opening cannot be seen clinically, but it is essentially established as a through tunnel. It may appear on the radiograph as a radiolucent area between the roots.

Grade IV: The interradicular bone is completely destroyed. The gingival tissue is also receded apically so that the furcation opening is clinically visible. The radiographic image is essentially the same as in grade III lesions.

Nonsurgical periodontal therapy and effective plaque control are recommended for Class I furcation defects. However, surgical management is required for root planning in Class II and Class III defects. This includes root surface debridement to support periodontal regeneration. The primary purpose of regenerative treatment of Class II furcation defects is to close the area to prevent furcation entry from the oral environment. Class III furcation defects are generally not suitable for successful regenerative treatment and are usually treated by surgical debridement and apical positioning of the flap to achieve pocket reduction, thereby providing access to the area for effective plaque control [11].

Abscesses of Periodontium

Periodontal abscesses are acute lesions that may result in the very rapid destruction of the periodontal tissues. A periodontal abscess is the accumulation of a localized exudate inside the gingival wall of a periodontal pocket. Etiology of periodontal abscesses includes untreated periodontal disease, food impaction, and pushing the bacterial deposit into deep gingival tissues during periodontal treatment [12]. The most common sign of a periodontal abscess is the presence of an oval rise in the periodontal tissues along the lateral side of the root. The gingiva is edematous and red with a smooth and shiny surface. Usually, suppuration occurs flowing out through a fistula or spontaneously when pressure is applied to the pocket. Symptoms in periodontal abscesses are bleeding on probing, swelling, tenderness or pain in the gingiva, sensitivity to the percussion of the teeth, the sensation of tooth elevation, and increased tooth mobility [12, 13].

Differential Diagnosis

Differential diagnosis of periodontal abscesses should be made with acute infections such as periapical abscesses, lateral periodontal cysts (Fig. 14.8), vertical root fractures, and endo-

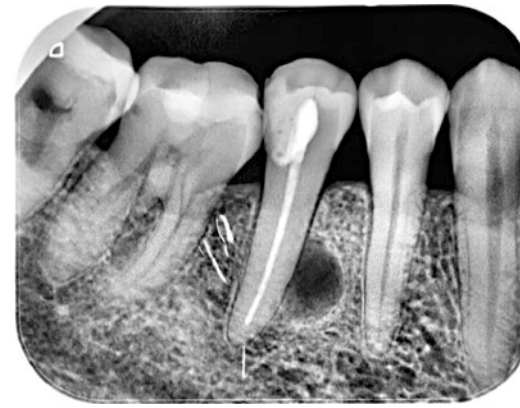

Fig. 14.8 Lateral periodontal cyst in periapical imaging

periodontal lesions. Their images are similar but their etiologies are different.

The history of periodontal disease, suppuration when probed, the presence of deep periodontal pockets, and the vitality of the tooth suggests periodontal abscess. Radiographically, it shows crestal bone loss in the tooth, and generally angular bone defects and furcation lesions.

14.2.3 Bony Defects of Periodontium

14.2.3.1 The Pattern of Bone Loss

Damage from periodontal disease occurs as attachments and alveolar bone loss. Bone loss is classified as "horizontal" or "vertical"; however, destruction usually occurs as a combination of the two.

Horizontal Bone Loss

It is the most common pattern of bone loss in periodontal disease. There is a horizontal loss in the bone and the same level of loss in each area of the tooth, and the loss proceeds perpendicularly to the root (Fig. 14.9). In particular, horizontal losses usually occur in the bone surrounding the teeth in the anterior since the bone is thin in this area.

Vertical Bone Loss (Angular Bone Defects)

In vertical or angular defects, an oblique loss occurs in the bone. The base of the defect is located in the apical of the bone surrounding the tooth. It is usually seen with intrabony pockets. It is examined clinically with careful probing. Radiological examination is also important in the examination of angular defects (Figs. 14.10 and

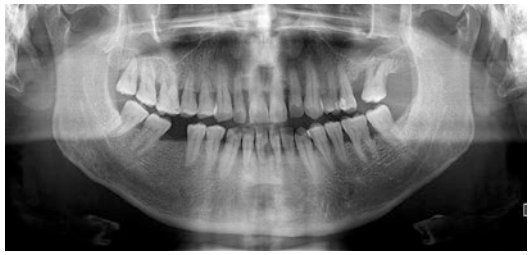

Fig. 14.9 Horizontal bone loss in orthopantomograph

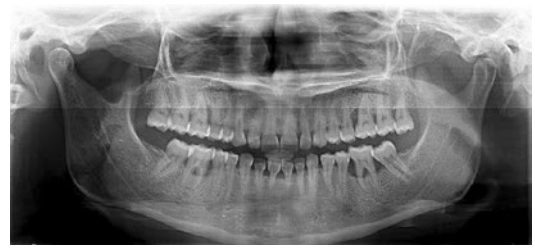

Fig. 14.11 Vertical bone loss in orthopantomograph

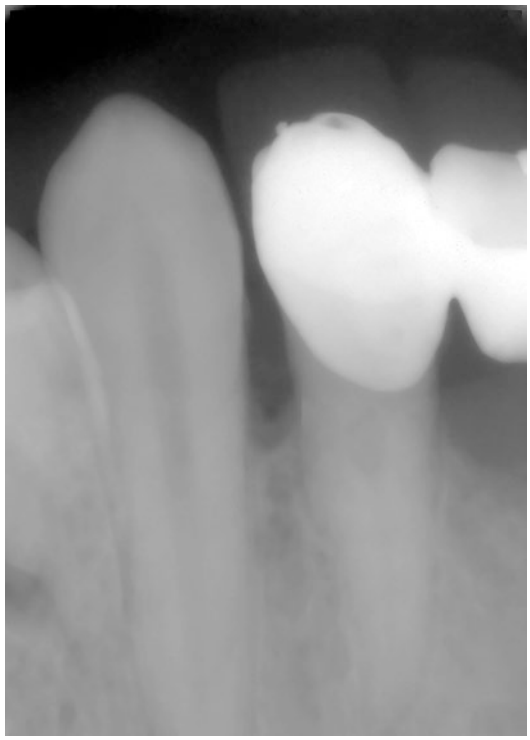

Fig. 14.10 Vertical bone loss in periapical imaging

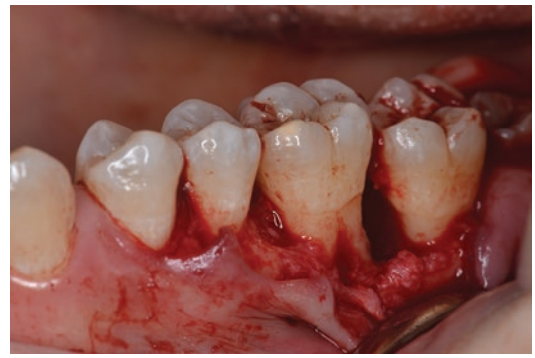

Fig. 14.12 Vertical (angular) bone defect in open flap debridement

14.11). On the radiograph, the bone appears obliquely towards the tooth.

14.2.3.2 Bony Defects

Various types of bone defects occur in periodontal diseases. They are detected both by clinical probing and radiological examination. The classification that Goldman and Cohen categorized angular defects according to the number of bone walls surrounding the defect in 1958 is still the most commonly used classification [14]. According to this classification, angular defects can be one, two, or three-walled. Similar to a groove, defects containing more than one surface of a tooth are called circumferential defects. The number of walls in the apical part of the defect is generally higher than the occlusal part, in which case the term combined defect is used.

Vertical or angular bony defects, including furcation defects, are often responsive to periodontal regeneration. Radiological examination and periodontal probing can provide important diagnostic information to aid the appropriate selection of regenerative therapy for intrabony defects. Vertical defects that appear interdentally can often be seen on radiography, but thick, bony plates can hide them occasionally. Surgical exposure is the only sure way to determine the presence and configuration of vertical bone defects.

Open flap debridement is required in almost all angular defects (Fig. 14.12). When grafting is performed alone, it supports periodontal repair which is characterized by the formation of the long junctional epithelium. Guided tissue regeneration contributes to the bone filling of the defect. However, the surgical method should be chosen according to the type of defect. The most predictable regenerative results are typically achieved in three-walled defects with adequate proximal bone height. Single-wall defects generally do not respond well to regenerative therapy [15].

It has been reported that vertical defects detected radiographically are most common on distal [16] and mesial [17] surfaces. However, three wall defects are more common on the mesial surfaces of the upper and lower molar teeth [18].

14.3 Periodontal Radiology

14.3.1 Intraoral Radiographs (Periapical, Bitewing, Occlusal Radiographs)

Intraoral radiographs, including bitewing (BW) and periapical (PA) images, are considered the gold standard radiographic tools for periodontal diagnosis and treatment planning [19]. Since periodontology also examines early bone changes and diseases that cause local defects in bone, intraoral imaging is frequently used.

Intraoral radiographs are useful scanning images that provide a detailed view of a small area of the alveolar arch or localized pathologies. Also, they are easy and inexpensive to obtain and provide high-resolution images [20]. In intraoral radiographs, bone loss assessments are usually performed by evaluating the presence of intact lamina dura, the width of the periodontal ligament space, bone trabeculation, and the presence of interproximal bone resorption or angular defect. Generally, in cases where the distance between CEJ and the alveolar crest is more than 1.9 mm, bone resorption is accepted [21].

In intraoral images, early inflammatory disease involvement of a furcation usually occurs as an enlarged periodontal ligament space in the furcation. As the disease progresses, a clearer bone defect appears in furcation. It should also be noted that an inflammatory furcation lesion may be originated from accessory pulpal canals, root resorption, or pulp.

The major disadvantages of periapical radiographs are that they do not give any information about the buccal-lingual size of the alveolar ridge and the image is limited to the size of the film or sensor used. This often results in more than one periapical radiography needed when large areas need to be evaluated.

Occlusal radiographs are intraoral projections that provide easy, affordable, low radiation dose, and high-resolution images covering a wider area than periapical imaging. Occlusal radiographs have the same drawbacks as periapical radiographs but can visualize wider alveolar dorsal areas compared to periapical radiographs.

14.3.2 Orthopantomograph (Panoramic Radiograph/OPG)

Orthopantomographs (OPG) are images that are routinely used for examination. It is widely available and easy to use. Despite low-dose radiation, it is very advantageous to be able to view all alveolar areas, foramen, mandibular canal, nasal base, sinuses, and temporomandibular joint (Fig. 14.13). It is frequently used in periodontology to evaluate generalized bone destruction and periodontal disease. It is recommended to detect all bone defects with OPGs, then to evaluate suspicious areas with intraoral radiographs.

The disadvantages of the OPGs are that it is not detailed because of the large area it is seen and its actual size enlarged approximately 30% [22] (Fig. 14.14). In addition, the presence of ghost shadows and the variation of the image with respect to patient positioning errors are among other disadvantages.

OPGs may be used for simple implant cases, but the magnification rate should be known and the bone is measured accordingly. However, 3D imaging should be preferred for complicated implant or augmentation cases with advanced bone destruction.

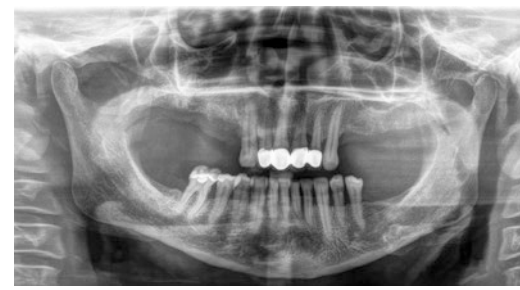

Fig. 14.13 Field of view of orthopantomograph

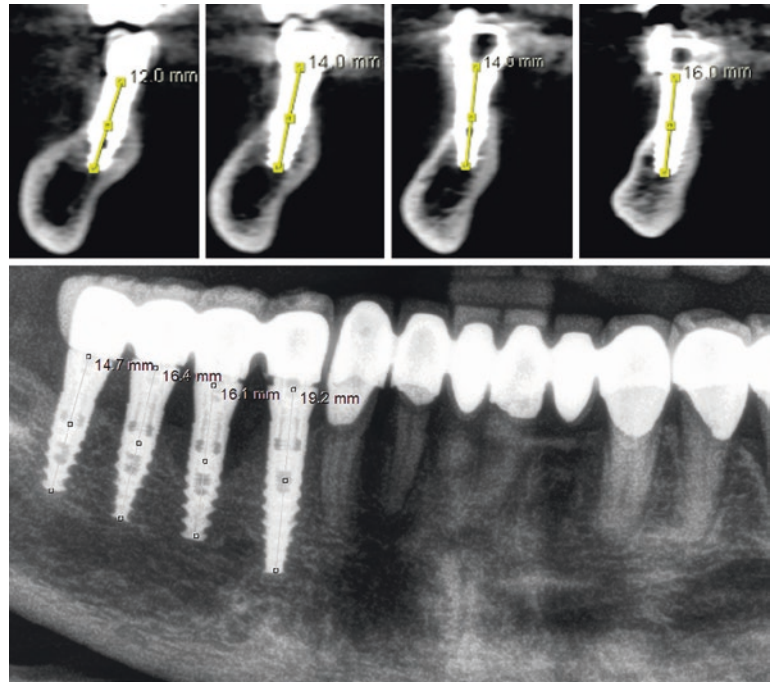

Fig. 14.14 Comparison of implant lengths in OPG and CBCT sections to determine the magnification rate of OPG

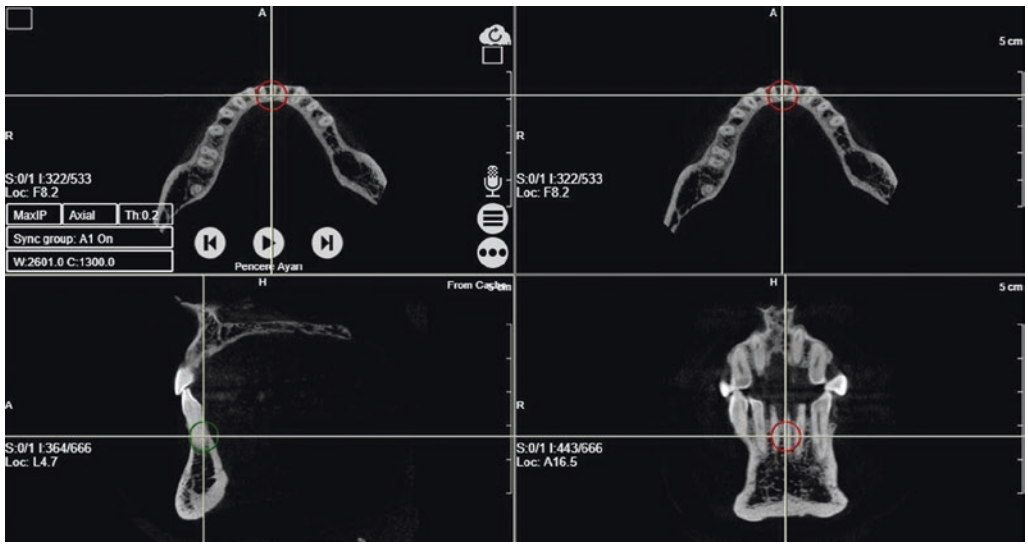

Fig. 14.15 It is possible to view the region evaluated in three different plans with CBCT

14.3.3 Cone-Beam Computed Tomography (CBCT)

In conventional radiographic methods, the periodontal examination was performed using 14 intraoral films and 4 posterior bitewing films before three-dimensional imaging. Determination of the presence and morphology of periodontal defects is best possible with CBCT.

CBCT is used in periodontology to evaluate the integrity of the periodontal ligament space, continuity of the lamina dura, the pattern of bone loss, angular bony defects, osseous craters, fenestrations, dehiscences, furcation defects, and the effectiveness of regenerative periodontal therapy in different plans [23] (Fig. 14.15).

The grading of bone loss forms the basis of regeneration; conventional radiographic meth-

ods are inadequate due to the overlapping of images. Preoperative measurement of bone defect with the help of CBCT can aid in determining the amount of graft material and surgical method required to adequately fill the defect [24].

Although it demonstrates the hard tissue very clearly, its relatively high dose of ionizing radiation and its non-reproducibility necessitated clinically safer methods than CBCT in periodontology.

14.3.4 Ultrasonographic Imaging in Periodontology

In dentistry, diagnoses on lesions in hard tissues have been made for decades with various imaging methods. Despite new technological advances in soft tissue imaging, the diagnosis was made by clinical examination and radiography.

In ultrasonic imaging, high-frequency (2–20 MHz) sound waves (above the range that the human ear can hear) are sent to the human body, and an image is created by converting the sounds coming back from the tissues into electronic impulses with the help of a converter [25]. As a diagnostic tool that does not use real-time, dynamic, noninvasive, and ionizing radiation, ultrasonography plays an increasingly important role in soft tissue evaluation [26].

Especially in periodontal ultrasonography, using a specific and relatively small intraoral transducer is important for more accurate results.

14.3.4.1 Advantages of Ultrasonographic Imaging

Sometimes, failure to see soft tissue on radiographs may lead to errors in diagnosis. Besides, the disadvantage of diagnosing mostly by clinical examination is that it is not possible to obtain a presurgical idea about the biopsy to be performed on the lesion. With the use of ultrasonographic imaging in dentistry, all the disadvantages of ionizing radiation have been eliminated. With the imaging of the soft tissue, an idea was obtained before taking a biopsy regarding the depth, vascularization, and shape of the lesions [27].

Since periapical and panoramic radiographs show soft tissue as radiolucent, in the diagnosis of soft tissue lesions, factors as clinical appearance, color, shape, rigidity, ulceration of lesion, symptoms of infection and age, gender, genetic, and systemic features of a person are taken into consideration, definitive diagnosis is always made with histopathology. It has been stated that the disadvantages of traditional radiographs in periodontology are ionizing radiation, generally two-dimensional image and differentness of the image according to the angle [28].

Ultrasonography has an increasingly important role in detecting pathologies in pediatrics and pregnant women, where X-rays are contraindicated [29]. Besides, being repeatable, practical, dynamic, and portable makes ultrasonography superior.

Since ultrasonic imaging is a repeatable and noninvasive procedure, it is superior to both transgingival probing and endodontic file measurement methods as a measurement tool. In view of the noninvasive nature of the imaging and the avoidance of ionizing radiation, ultrasonography could have a valuable place in periodontal imaging [26].

14.3.4.2 Ultrasonographic Imaging in Periodontology

- ***Periodontal Pocket***

Although pocket measurement with the periodontal probe is still the most practical method used, being invasive and changing the measurement depending on various factors has led to the need for a more precise method in diagnosis. These factors are probe pressure, probe tip size, probing angle, pocket calculus, and inflammation [30]. In the traditional probing system, the distance between the two reference points is measured. However, these points can be misleading. In ultrasonographic imaging, pocket measurement is made between the standard points since the pocket base and alveolar crest can be demonstrated. In addition, ultrasonography is a method that is stated to be superior to probing in periodontal pocket evaluation since it is a real-time and ionized radiation-free imaging system.

- ***Attachment Level***

For periodontal diseases, the radiological examination is important as well as clinical examination. For decades, the most commonly used systems radiologically are orthopantomographs and intraoral radiographs. However, ultrasonography is very advantageous according to these methods, which differ according to the angle. It is possible to measure the level of attachment, which is a parameter in the diagnosis of periodontal disease by ultrasonography.

- ***Alveolar Crest Morphology***

Hard tissue can also be evaluated as soft tissue with ultrasonography imaging. It has been reported in some studies that measurement of alveolar bone level with ultrasound is as accurate as transgingival probing [31, 32].

The first reports of ultrasonographic imaging in periodontology in the literature are studies in which the height of the alveolar crest [33] and morphology [34] of periodontitis patients are determined. Apart from these, animal studies evaluating the width of periodontal ligament [35] and height of the alveolar crest [36] have also been reported and it has been reported that alveolar bone crest will always be determined [37].

- ***Alveolar Bone Loss***

An ultrasonic transducer reflects high-frequency ultrasonic energy between the tooth and gingiva and detects the echoes of the returning wave and converts it into distance [38]. Thus, alveolar crest height, attachment loss (Fig. 14.16), and pocket depth can be measured by measuring the distance between CEJ and alveolar crest.

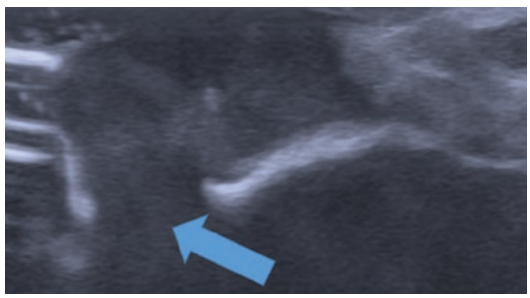

Fig. 14.16 Hypoechoic area with alveolar bone destruction (blue arrow) in US imaging

- ***Tissue Thickness***

Soft tissue grafting is applied clinically in areas around the tooth and implant to increase tissue thickness, reconstruct sufficient width of keratinized tissue, correct mucogingival deformities, and improve esthetics [39].

Free Gingival Graft: A soft tissue graft collected from the palate with the upper epithelium is defined as a free gingival graft (FGG) and applied to increase keratinized gingival tissue in the recipient area.

Subepithelial Connective Tissue Graft: Subepithelial connective tissue graft (CTG) is a mucogingival surgery performed to close gingival pulls around the tooth and implant, increase gingival thickness, and interdental papillary reconstruction.

Ultrasonographic imaging has been used in periodontology for more than 20 years to measure gingival thickness [40]. Gingiva thickness and vascularization are the most important factors affecting the success of soft tissue graft in mucogingival surgery. It has also been used in mucogingival surgeries, such as measuring the gingival thickness before and after root coverage prosedure [41], connective tissue graft thickness [42], and the masticatory mucosa thickness [43]. In addition, it was used to measure gingival thickness after guided tissue regeneration bioabsorbable membranes [44] (Figs. 14.17 and 14.18).

With ultrasonography, the thickness of the keratinized gingival tissue around the implants can also be measured and this is an important value in the diagnosis of inflammatory diseases such as peri-implanter mucositis and peri-implantitis [45].

- ***Tissue Vascularization***

In mucogingival surgery with soft tissue grafting, at least as important as gingiva thickness is to ensure adequate nutrition of the tissue. This nutrition is through vascularization in the recipient and donor areas. From the moment the graft is placed in the recipient area, plasma supply with

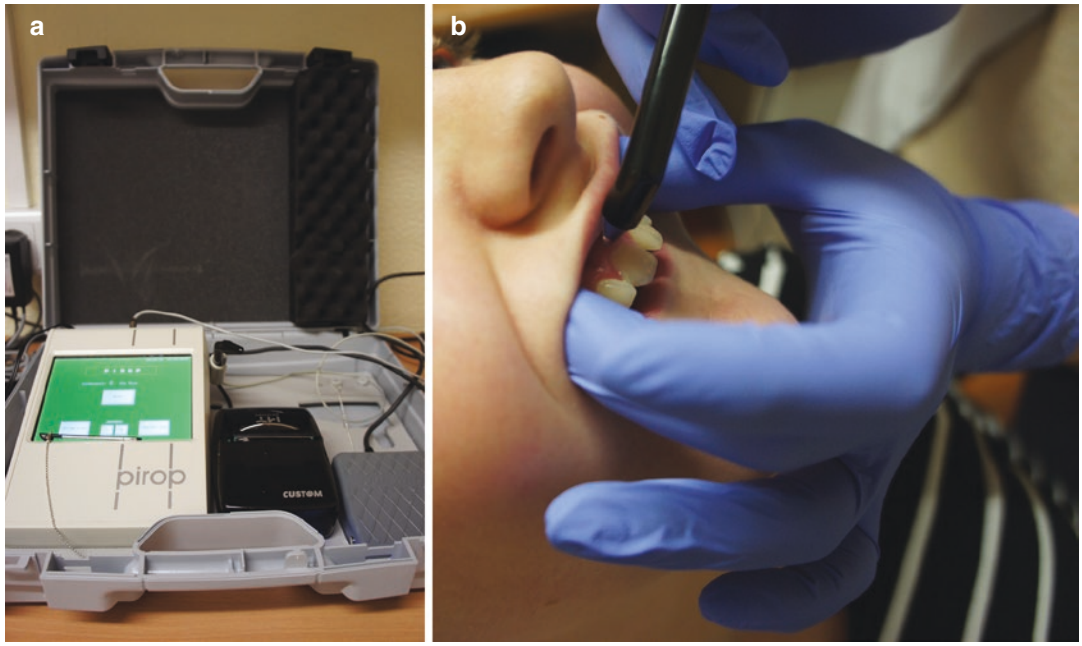

Fig. 14.17 (**a**) An US device which is dedicated to measuring the gingival thickness (**b**) the image showing the application of the device, note that the high-frequency probe for measuring the gingival thickness. Courtesy of the Czelej Editorial House in the 3rd Edition of the book "Współczesna Radiologia Stomatologiczna"

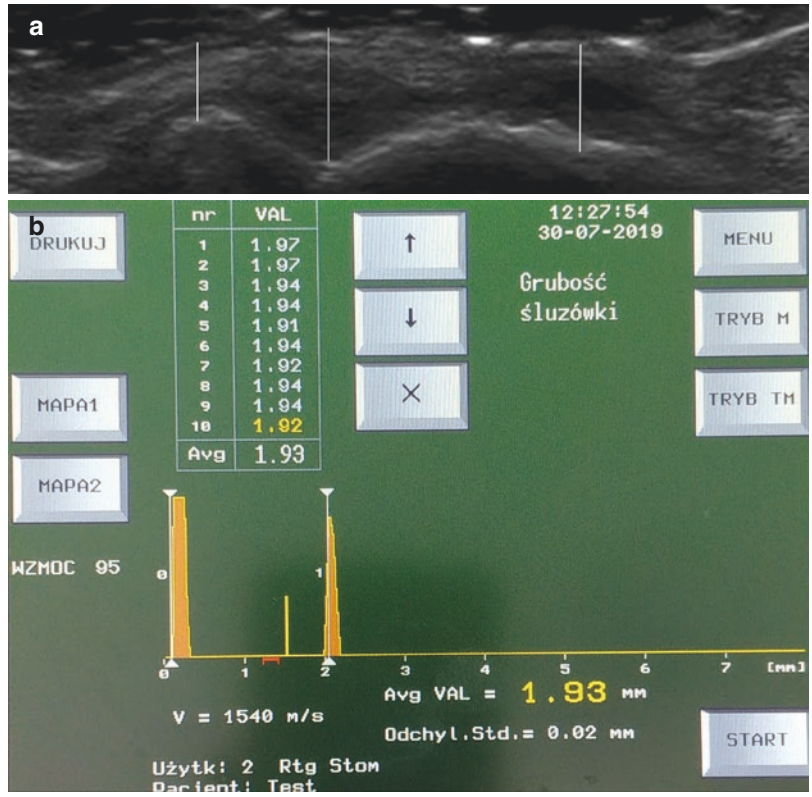

Fig. 14.18 (**a**) US image showing the measurement of the gingival thickness, (**b**) Gingival thickness measurement seen on ultrasonography screen, note that the device measures the average of ten measurements. Courtesy of the Czelej Editorial House in the 3rd Edition of the book "Współczesna Radiologia Stomatologiczna"

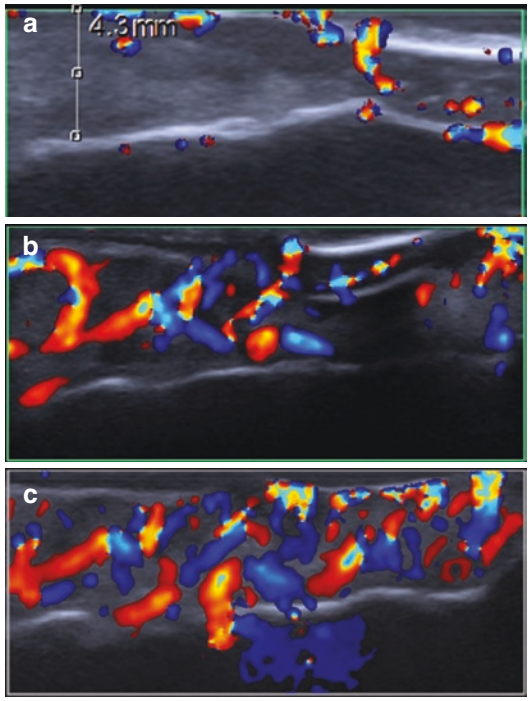

Fig. 14.19 (**a**) US image of donor area in the palate before FGG. (**b**) US image of donor area in the palate 2 weeks after FGG (without PRF placement as a dressing). (**c**). US image of donor area in the palate 2 weeks after FGG (with PRF placement as a dressing). Doppler imaging revealed intensity of vascularization

plasma diffusion and collateral vessels constitute the first stage of healing [46]. Vascularization of both the recipient and the donor site can be measured by ultrasonographic imaging in mucogingival surgeries (Fig. 14.19). Assessment of tissue thickness and vascularity can positively affect the success of the treatment.

Postoperative wound healing depends on the stabilization and organization of the clot formed in the wound area. Increased vascularization in the region indicates the early phase of the wound healing process. In this context, early wound healing can be evaluated with ultrasonography.

- ***Calculus Visualization***

Ultrasonography can demonstrate supragingival and subgingival calculus. In this way, the patient can be informed before the periodontal treatment. Likewise, calculus visualization is possible before and after scaling and root planning to appreciate the quality of the treatment [38].

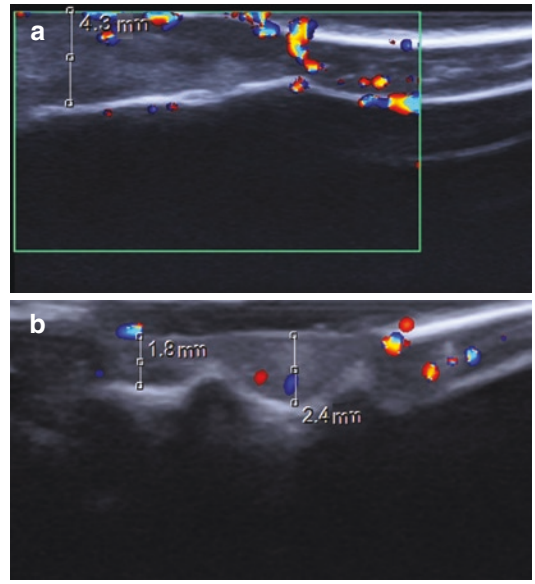

Fig. 14.20 The thickness of the mucosa which implant planned can be measured with US imaging. Comparison of gingival phenotypes of different thicknesses

- ***Implant Planned Mucosa***

Implant planning has been performed according to traditional radiographs for many years. While CBCT is indicated in complicated cases, CBCT only shows hard tissue clearly. However, sometimes the soft tissue may be too thick or too thin. In the toothless areas where the implant is planned, soft and hard tissue heights and widths can be measured before elevating a full-thickness flap by ultrasonography [47] (Fig. 14.20).

- ***Soft and Hard Tissues Around Implants***

Although implant treatment is becoming more and more preferred day by day, the rate of infections around the implant is increasing rapidly.

There are three possibilities for peri-implanter disorders:

Peri-Implant Mucositis: It is a soft tissue infection without bone destruction around the implant. It is similar to gingivitis in natural teeth. When the factor eliminates, it is reversible.

Peri-Implantitis: Marginal bone destruction occurs around the implant. It is similar to periodontitis in natural teeth. It is not reversible and requires surgical intervention to halt bone loss.

Peri-Implant Soft and Hard Tissue Deficiencies: Tissue deficiencies around the implant do not occur due to infection; however, they are predisposing factors for infection. Tissue regeneration is required by surgical intervention.

Fenestration and Dehiscence Around Implants: In periodontium, areas can be seen in which the root is denuded of bone and the root surface is covered only by periosteum and overlying gingiva. If it opens like a window in the apical part of the root, it is named fenestration; if the marginal bone is stripped from its coronal part, it is named dehiscence. This condition can also be seen in the alveolar bone around the implant. These isolated areas where the implant is separated from the bone can be detected by ultrasonography (Figs. 14.21 and 14.22).

Successful implant treatment and diagnosing peri-implant diseases and conditions require a good clinical and radiological examination. These diseases and conditions are usually evaluated by clinical probing and two-dimensional radiographs. However, clinical probing may fail due to excessively contoured implant crowns [48]. While only hard tissue is seen with periapical films, being two-dimensional may cause errors. Being the only form of clinical cross-sectional imaging tool, CBCT provides clinically accurate hard tissue imaging; however, it needs to be used judiciously, due to its reliance on ionizing radiation [49].

The width, height of soft tissue, and marginal bone loss detection around the implant is important for the diagnosis of peri-implant diseases. Also, the use of ultrasonography during the operation in cases that require surgical procedures may prevent some surgical complications.

Implant esthetics is also one of the success criteria. Gingival phenotype directly affects esthetics. The thick gingival phenotype around the implant camouflages metal reflection better than the thin phenotype [50]. Metal reflection and gingival recession can be seen in the thin phenotype, and soft tissue surgery is usually required to correct it. Ultrasonography also determines the gingival phenotype by measuring tissue thickness and vascularization.

- ***Vertical Bony Defects***

Horizontal bone destruction is generally seen in periodontal diseases. However, in some cases, vertical bony defects can also be seen. Such bone losses appear as a hollow pit adjacent to the tooth root. Bony defects are mentioned in the previous sections. Their treatment often requires a surgical approach.

For the correct treatment plan, the location, type, and number of walls of the bone defect should be accurately diagnosed. Making these evaluations correctly is important for proper

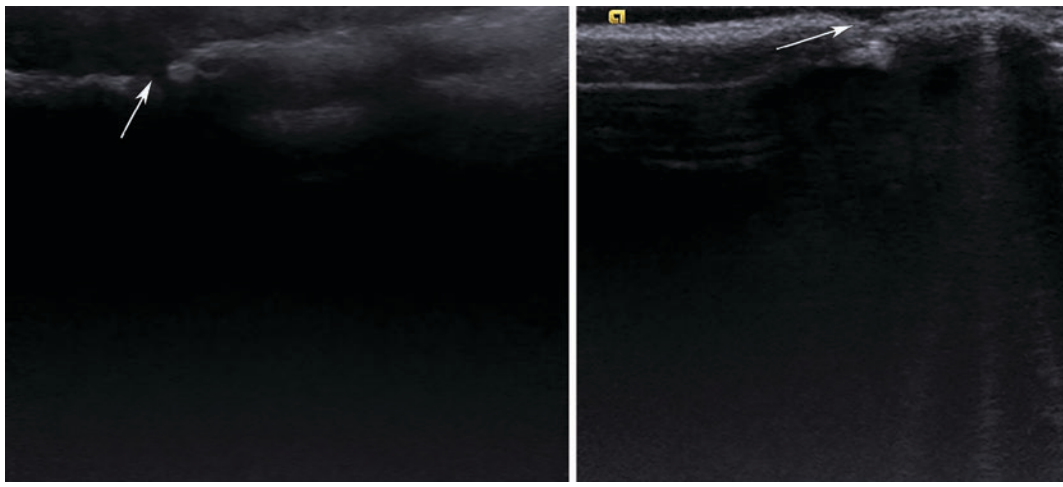

Fig. 14.21 Dehiscence around the implant by US imaging (white arrows indicate the dehiscences)

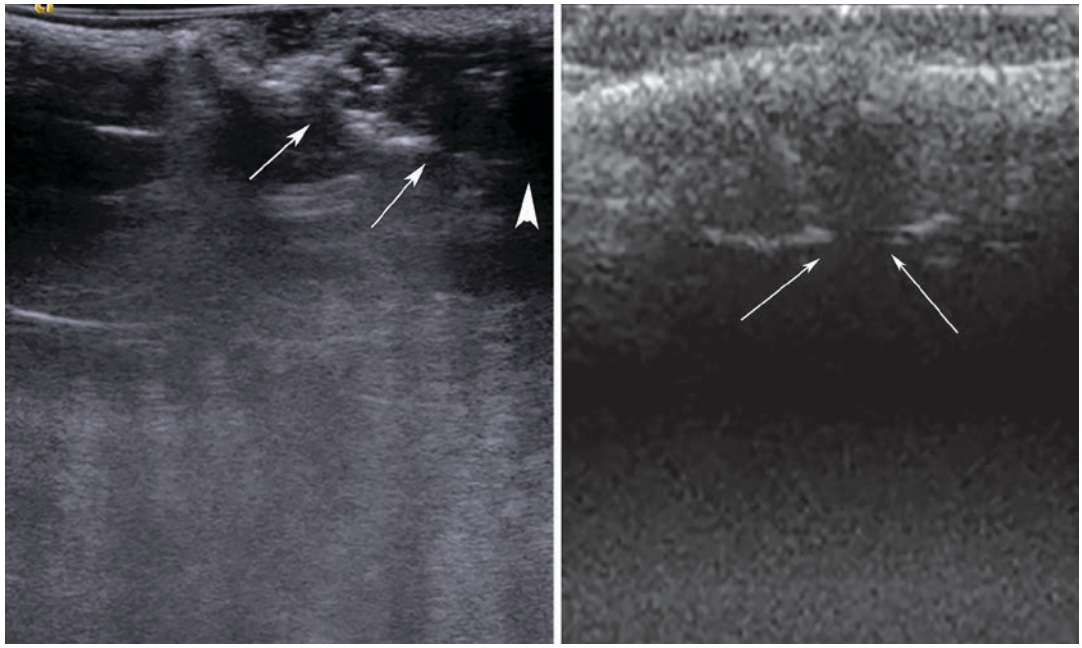

Fig. 14.22 Fenestration around the implant by ultrasonography (big arrow indicates the implant, small arrows indicate fenestrations)

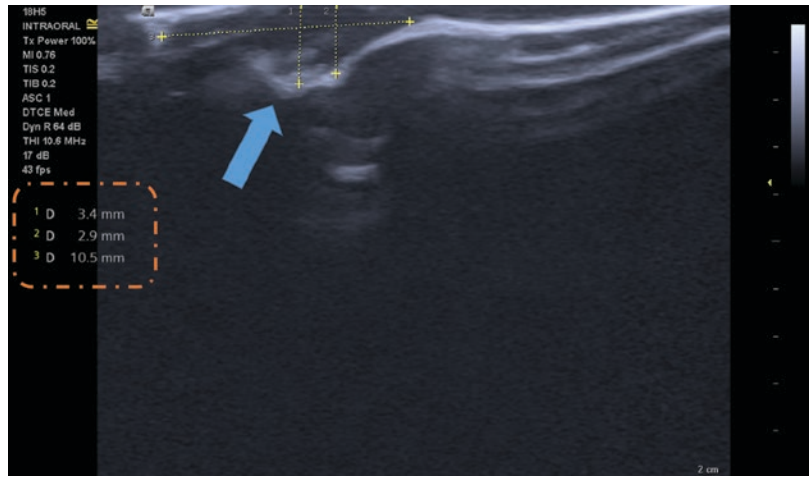

Fig. 14.23 US image of dental plaque-induced gingival enlargement. Continuous hyperechoic well-defined borders (blue arrow) suggest a benign lesion. It is also possible to measure the lesion (orange frame) with US

treatment and maintenance of the tooth. If these defects are not treated properly, there is even a risk of tooth loss.

In the diagnosis of these defects, the radiological examination is as important as a clinical problem. Intraoral radiographs provide a significant amount of information about these periodontal structures. However, these radiographs are able to reveal changes in bone only after 30–50% of the bone mineral has been resorbed [51]. This prevents early diagnosis of defects.

- ***Gingival Lesions***

Neoplasia-like tumors are common in the gingiva and can be of different colors, shapes, and sizes. These proliferations are painless peduncles or sessile masses of different colors, starting from light pink to red. The outer appearance can be changed from non-ulcerated flat to ulcerated mass. The lesion size ranges from almost no millimeter to several centimeters [52] (Fig. 14.23).

Although the hard tissue lesions on the gingiva are evaluated with conventional radiographs, the examination of soft tissue lesions is mostly performed by clinical examination since these techniques are insufficient in soft tissue imaging (Fig. 14.24).

The features of soft tissue lesions such as border, size, depth, elasticity, and vascularization can be determined with ultrasonography (Fig. 14.25). These features are very valuable in terms of preliminary diagnosis.

Many different benign or malignant tumors can be seen on the gingiva (Fig. 14.26). Some locally aggressive benign tumors are similar to malignant tumors clinically (Fig. 14.27). Since definitive diagnosis is made only by histopathological analysis, the biopsy is essential for all lesions. Thanks to the US examination, vascularization can be evaluated during biopsy preparation and possible hemorrhagic complications can be prevented.

Ultrasonography is still a new area for dentists. In order to evaluate ultrasonography, they must have a good knowledge of anatomy, know the device they use, and practice very well. The future of ultrasonography in periodontology is promising for both clinical practice and research.

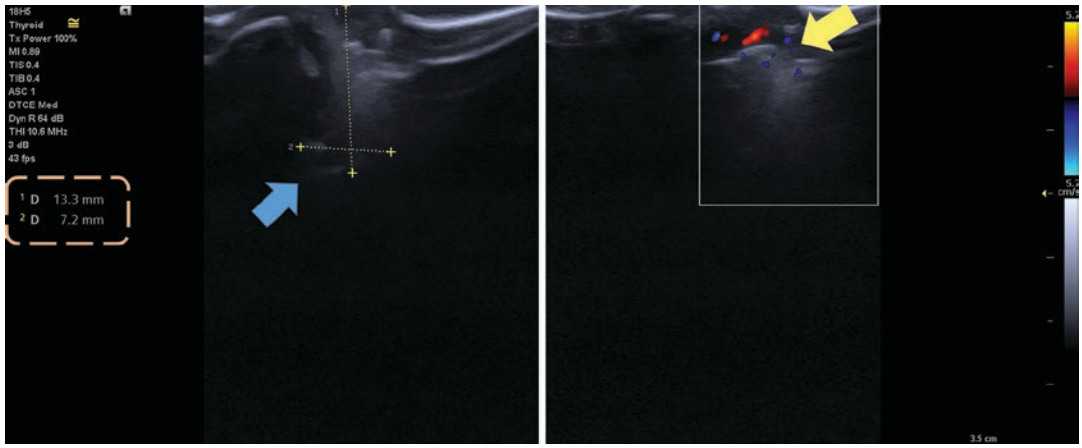

Fig. 14.24 Hyperechoic appearance (blue arrow), limited vascularization (yellow arrow), and continuous well-defined borders indicate a benign and ossified structure. It is also possible to measure the lesion (orange frame) with US. Histopathological diagnosis was peripheral ossifying fibroma

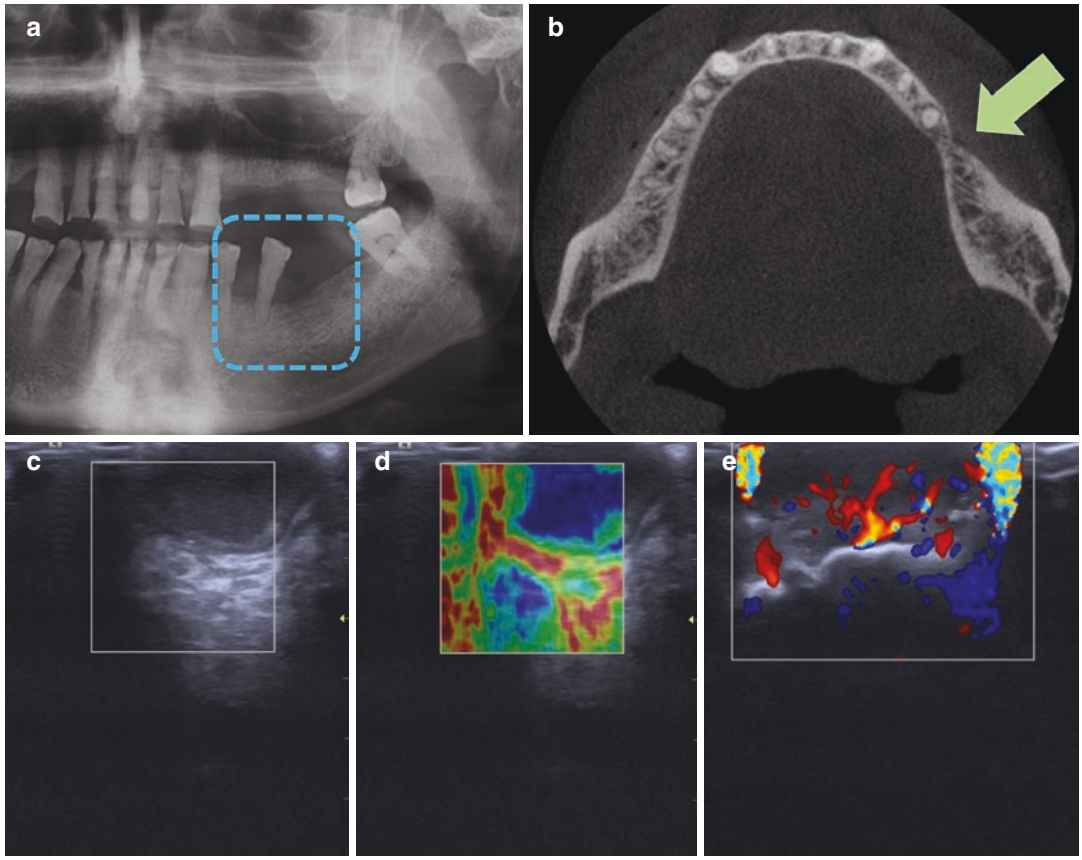

Fig. 14.25 A benign soft tissue lesion in gingiva (**a**) on orthopantomography (mild bone loss in blue frame), (**b**) on axial CBCT slice (mild cortical bone loss with green arrow), (**c**) on US imaging, (**d**) on elastograph, (**e**) with Doppler imaging

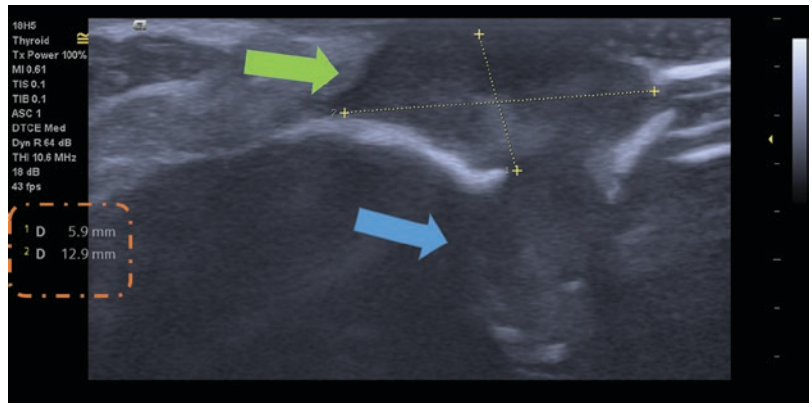

Fig. 14.26 US image of a malignant lesion in gingiva. The figure shows the diameter (orange frame), shape (green arrow), and pedicle (blue arrow) of the lesion

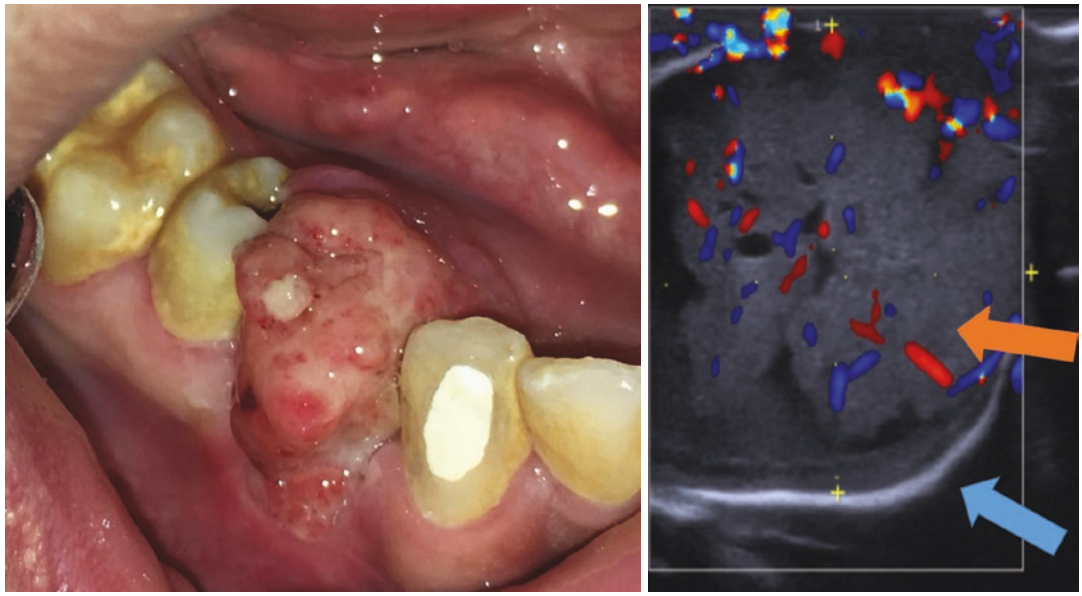

Fig. 14.27 Gingival lesion which has heterogeneous structure with erythematous areas suggesting malignancy. US reveals an unilocular lesion with predominantly hyperechoic internal structure and Doppler imaging reveals moderate vascularization (orange arrow). Continuous hyperechoic well-defined borders (blue arrow) suggest a benign lesion in contrast to clinical appearance. Histopathological diagnosis was ameloblastoma

References

1. Newman MGT, Takei HH, Klokkevold PR, Carranza FA. Newman and Carranza's clinical periodontology. 13th ed. Philadelphia, PA: Elsevier; 2019.
2. Ainamo J, Loe H. Anatomical characteristics of gingiva. A clinical and microscopic study of the free and attached gingiva. J Periodontol. 1966;37(1):5–13.
3. McKee MD, Zalzal S, Nanci A. Extracellular matrix in tooth cementum and mantle dentin: localization of osteopontin and other noncollagenous proteins, plasma proteins, and glycoconjugates by electron microscopy. Anat Rec. 1996;245(2):293–312.
4. Beertsen W, McCulloch CA, Sodek J. The periodontal ligament: a unique, multifunctional connective tissue. Periodontol 2000. 1997;13:20–40.
5. Wehrbein H, Fuhrmann RA, Diedrich PR. Human histologic tissue response after long-term orthodontic tooth movement. Am J Orthod Dentofac Orthop. 1995;107(4):360–71.
6. Becks H. Root resorptions and their relation to pathologic bone formation. Int J Orthod Oral Surg. 1936;22:445.
7. Caton JG, Armitage G, Berglundh T, et al. A new classification scheme for periodontal and peri-implant diseases and conditions - introduction and key changes from the 1999 classification. J Periodontol. 2018;89(Suppl 1):S1–8.
8. Nunn ME. Understanding the etiology of periodontitis: an overview of periodontal risk factors. Periodontol 2000. 2003;32:11–23.
9. Pilloni A, Rojas MA. Furcation involvement classification: a comprehensive review and a new system proposal. Dent J (Basel). 2018;6(3):34.
10. Glickman I. Bifurcation involvement in periodontal disease. J Am Dent Assoc. 1950;40(5):528–38.
11. Carranza FA Jr, Jolkovsky DL. Current status of periodontal therapy for furcation involvements. Dent Clin N Am. 1991;35(3):555–70.
12. Herrera D, Roldan S, Sanz M. The periodontal abscess: a review. J Clin Periodontol. 2000;27(6):377–86.
13. Smith RG, Davies RM. Acute lateral periodontal abscesses. Br Dent J. 1986;161(5):176–8.
14. Goldman HM, Cohen DW. The Infrabony pocket: classification and treatment. J Periodontol. 1958;29(4):272–91.
15. Reynolds MA, Aichelmann-Reidy ME, Branch-Mays GL. Regeneration of periodontal tissue: bone replacement grafts. Dent Clin N Am. 2010;54(1):55–71.
16. Nielsen IM, Glavind L, Karring T. Interproximal periodontal intrabony defects. Prevalence, localization and etiological factors. J Clin Periodontol. 1980;7(3):187–98.
17. Papapanou PN, Tonetti MS. Diagnosis and epidemiology of periodontal osseous lesions. Periodontol 2000. 2000;22:8–21.

18. Larato DC. Intrabony defects in the dry human skull. J Periodontol. 1970;41(9):496–8.
19. Corbet EF, Ho DK, Lai SM. Radiographs in periodontal disease diagnosis and management. Aust Dent J. 2009;54(Suppl 1):S27–43.
20. Jeffcoat MK. Current concepts in periodontal disease testing. J Am Dent Assoc. 1994;125(8):1071–8.
21. Zhang W, Rajani S, Wang BY. Comparison of periodontal evaluation by cone-beam computed tomography, and clinical and intraoral radiographic examinations. Oral Radiol. 2018;34(3):208–18.
22. Kim YK, Park JY, Kim SG, Kim JS, Kim JD. Magnification rate of digital panoramic radiographs and its effectiveness for pre-operative assessment of dental implants. Dentomaxillofac Radiol. 2011;40(2):76–83.
23. Vandenberghe B, Jacobs R, Yang J. Detection of periodontal bone loss using digital intraoral and cone beam computed tomography images: an in vitro assessment of bony and/or infrabony defects. Dentomaxillofac Radiol. 2008;37(5):252–60.
24. Guo YJ, Ge ZP, Ma RH, Hou JX, Li G. A six-site method for the evaluation of periodontal bone loss in cone-beam CT images. Dentomaxillofac Radiol. 2016;45(1):20150265.
25. Kundra P, Mishra SK, Ramesh A. Ultrasound of the airway. Indian J Anaesth. 2011;55(5):456–62.
26. Tsiolis FI, Needleman IG, Griffiths GS. Periodontal ultrasonography. J Clin Periodontol. 2003;30(10):849–54.
27. Natori T, Koga M, Anegawa E, et al. Usefulness of intra-oral ultrasonography to predict neck metastasis in patients with tongue carcinoma. Oral Dis. 2008;14(7):591–9.
28. Jeffcoat MK, Wang IC, Reddy MS. Radiographic diagnosis in periodontics. Periodontol 2000. 1995;7:54–68.
29. Rama Mohan K, Koteswara Rao N, Leela Krishna G, Santosh Kumar V, Ranganath N, Vijaya Lakshmi U. Role of ultrasonography in oral and maxillofacial surgery: a review of literature. J Maxillofac Oral Surg. 2015;14(2):162–70.
30. Highfield J. Diagnosis and classification of periodontal disease. Aust Dent J. 2009;54(Suppl 1):S11–26.
31. Greenberg J, Laster L, Listgarten MA. Transgingival probing as a potential estimator of alveolar bone level. J Periodontol. 1976;47(9):514–7.
32. Ursell MJ. Relationships between alveolar bone levels measured at surgery, estimated by transgingival probing and clinical attachment level measurements. J Clin Periodontol. 1989;16(2):81–6.
33. Spranger H. Ultra-sonic diagnosis of marginal periodontal diseases. Int Dent J. 1971;21(4):442–55.
34. Palou ME, McQuade MJ, Rossmann JA. The use of ultrasound for the determination of periodontal bone morphology. J Periodontol. 1987;58(4):262–5.
35. Lost C, Irion KM, Nussle W. Determination of the facial/oral alveolar crest using RF-echograms. An in vitro study on the periodontium of pigs. J Clin Periodontol. 1989;16(8):539–44.
36. Lost C, Irion KM, Nussle W. Ultrasonic B-scans of the facial/oral periodontium in pigs. J Clin Periodontol. 1989;16(8):534–8.
37. Lost C, Irion KM, Nussle W. Periodontal ultrasonic diagnosis: experiments on thin bony platelets and on a simulated periodontal ligament space. J Periodontal Res. 1988;23(6):347–51.
38. Chifor R, Badea AF, Chifor I, Mitrea DA, Crisan M, Badea ME. Periodontal evaluation using a non-invasive imaging method (ultrasonography). Med Pharm Rep. 2019;92(Suppl 3):S20–32.
39. Zucchelli G, Tavelli L, McGuire MK, et al. Autogenous soft tissue grafting for periodontal and peri-implant plastic surgical reconstruction. J Periodontol. 2020;91(1):9–16.
40. Eger T, Muller HP, Heinecke A. Ultrasonic determination of gingival thickness. Subject variation and influence of tooth type and clinical features. J Clin Periodontol. 1996;23(9):839–45.
41. Muller HP, Eger T, Schorb A. Gingival dimensions after root coverage with free connective tissue grafts. J Clin Periodontol. 1998;25(5):424–30.
42. Muller HP, Stahl M, Eger T. Root coverage employing an envelope technique or guided tissue regeneration with a bioabsorbable membrane. J Periodontol. 1999;70(7):743–51.
43. Muller HP, Schaller N, Eger T, Heinecke A. Thickness of masticatory mucosa. J Clin Periodontol. 2000;27(6):431–6.
44. Muller HP, Stahl M, Eger T. Dynamics of mucosal dimensions after root coverage with a bioresorbable membrane. J Clin Periodontol. 2000;27(1):1–8.
45. Chambrone L, Tatakis DN. Long-term outcomes of untreated buccal gingival recessions: a systematic review and meta-analysis. J Periodontol. 2016;87(7):796–808.
46. Sculean A, Gruber R, Bosshardt DD. Soft tissue wound healing around teeth and dental implants. J Clin Periodontol. 2014;41(Suppl 15):S6–22.
47. Tattan M, Sinjab K, Lee E, et al. Ultrasonography for chairside evaluation of periodontal structures: a pilot study. J Periodontol. 2020;91(7):890–9.
48. Serino G, Turri A, Lang NP. Probing at implants with peri-implantitis and its relation to clinical peri-implant bone loss. Clin Oral Implants Res. 2013;24(1):91–5.
49. Chan HL, Kripfgans OD. Ultrasonography for diagnosis of peri-implant diseases and conditions: a detailed scanning protocol and case demonstration. Dentomaxillofac Radiol. 2020;49(7):20190445.
50. Fu JH, Lee A, Wang HL. Influence of tissue biotype on implant esthetics. Int J Oral Maxillofac Implants. 2011;26(3):499–508.
51. Jeffcoat MK, Reddy MS. A comparison of probing and radiographic methods for detection of periodontal disease progression. Curr Opin Dent. 1991;1(1):45–51.
52. Hunasgi S, Koneru A, Vanishree M, Manvikar V. Assessment of reactive gingival lesions of oral cavity: a histopathological study. J Oral Maxillofac Pathol. 2017;21(1):180.

USG Imaging in Orthodontics

15

Kaan Orhan and Cansu Görürgöz

Contents

K. Orhan (✉)
Faculty of Dentistry, Department of Dentomaxillofacial Radiology, Ankara University, Ankara, Turkey

C. Görürgöz
Faculty of Dentistry, Department of Dentomaxillofacial Radiology, Bursa Uludağ University, Bursa, Turkey

15.1 Introduction

Orthodontics is the art and science that considers harmonizing crowded teeth, jaw relationships, abnormal teeth bites, and circumoral muscles and

K. Orhan (ed.), *Ultrasonography in Dentomaxillofacial Diagnostics*,
https://doi.org/10.1007/978-3-030-62179-7_15

deals with jaw orthopedics in children/adults that may need surgery-assistant prosedures [1].

The understanding of the complex anatomy, correlations, and adjacent structures of the craniofacial skeleton is essential for treatment planning and management. Radiographic scanning is the complementary part of the entire evaluation of the orthodontic cases. In orthodontic practice, the aim of the imaging involves ensuring additional information for the diagnosis of skeletal/dental problems, soft tissues, and their interrelationships [2].

The radiographic findings obtained from conventional diagnostic tools (e.g., panoramic and lateral cephalometric images) have been integrated with clinical data for orthodontic diagnosis and planning, assessment of growth and development, and evaluation of treatment course and outcomes [2].

Every technique has its own advantages, disadvantages, and limitations [3]. However, the potential risks of radiography, some investigators have been directed to the new methodologies [4]. Ultrasonography (USG) has been utilized in the medical field as a diagnostic and therapeutic device [5]. Ultrasound is a recently introduced field of application in dentistry. Since the first study by Baum et al. [6], in dental practice, many different and new usages of Ultrasound imaging have been stated.

The aim of this chapter is to give an overview of the applications of USG in orthodontic clinics and broadening researchers' horizons depending on the recent studies in the literature.

15.2 Evaluation of the Muscles of Mastication

Orthodontic treatment planning is, not to stand completely on biomechanical considerations, but it needs consideration of the maxillofacial muscular component of each case. The craniofacial muscles have assumed to be a great significance in treatment stages, including the etiology and active treatment of occlusal problems and deformation of the jaw, and the stability of treatment [7].

Among imaging modalities, it has been demonstrated that USG has a capability for providing information by displaying muscle structural changing[8] (Fig. 15.1). Ultrasound imaging is usually performed on the superficial tissues in the maxillofacial area, as the hard tissues absorbed the sound waves and the sound beam can not transmit deep tissues [8–10]. Also, the transducer can not always cover the cross-sectional area of the muscle [11, 12]. Despite the disadvantages of the technique, USG offers important advantages, which made it proper for longitudinal researches, especially in children [11–13].

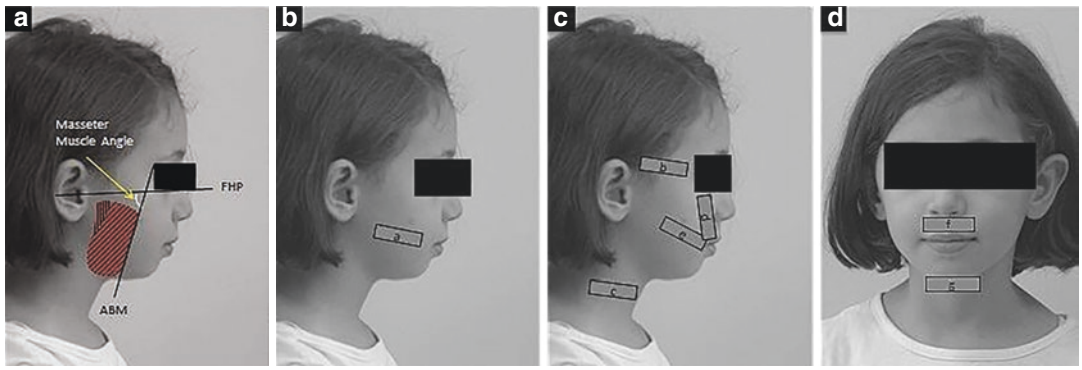

Fig. 15.1 (**a**) Masseter muscle angle is defined as the angle between the FHP (Frankfort Horizontal Plane) and ABM (Anterior Border of Masseter muscle). (**b–d**) Schematic representation of the ultrasound transducer placement on volunteer for the (**a**) masseter, (**b**) anterior portion of temporalis, (**c**) sternocleidomastoid muscle, (d) levator labii superioris, (**e**) zygomaticus major, (**f**) orbicularis oris, and (**g**) anterior digastric muscles

Ultrasound has been represented as a reliable imaging method for accurately measuring the thickness and cross-sectional area of the masticatory muscles and for calculating changes in local cross-sectional parameters of the craniofacial muscle groups in vivo [11–21].

The thickness measurement has been utilized commonly in studies that evaluated Ultrasound imaging of masticatory muscles. Also, the crosssections, transversal areas, and the transverse dimensions have been evaluated [13, 22–24]. The images have obtained unilaterally and bilaterally, in the course of relaxation and/or contraction [25].

15.2.1 Masseter

The masseter was the most common masticatory muscle investigated [25]. The muscle's thickness, cross-sectional area, volume, and length have been used for the morphometric analysis of the masseter (Fig. 15.2). It is possible to make comparisons, as it constitutes objective data [26, 27].

Several studies investigated the measurements of the masseter muscle by USG within different conditions, including correlations between the thickness of masseter and facial morphology [15, 19, 20, 28–33], dental arch width [34, 35], thickness of alveolar process, mandibular symphysis, mandibular inclination [20], and integrated orthodontic treatment/functional appliances outcome [36–39].

USG has been utilized for thickness and/or cross-sections to explore the interactions with temporomandibular joint dysfunction (TMD), muscle palpation pain, facial morphology, bite force, and occlusal factors, specifically of the incisors and molars [15].

It has also evaluated the relationships between the masseter muscle volume and selected cephalometric values with USG [40].

In the literature, we determined the significant inhomogeneity in the published studies' data. The measurement of the masseter muscle with ultrasound imaging is offered in different analyzes as an accurate method, reliable, and reproducible. However, in future researches, to increase the value of the methodology and results of the studies, data may need to be exhibited and analyzed in new hypothesis tests, also taking into account the heterogeneity of the studies.

15.2.2 Temporalis

After the masseter muscle, the most second masticatory muscle studied [25].

A study conducted by Rasheed et al. [41], reported that patients with an open or deep bite in the mixed dentition have a statistically thicker anterior temporalis muscle than patients with

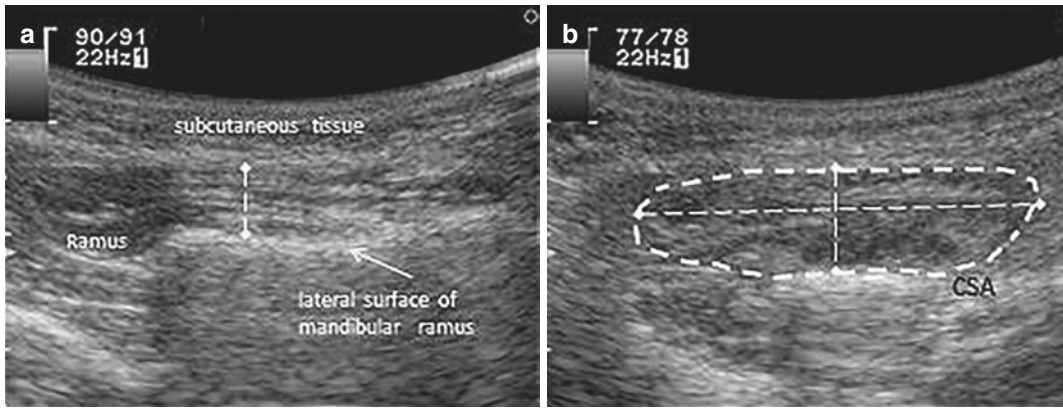

Fig. 15.2 Transverse ultrasound image of (**a**) relaxed and (**b**) contracted left masseter muscle demonstrating the measurement of length (horizontal dotted line), thickness (vertical dotted lines), and cross-sectional area (CSA)

normal occlusion. Castelo et al. [42] compared the normal and crossbite sides, the mixed-crossbite group presented a significantly thicker anterior temporalis muscle at rest for the crossbite side than the normal side.

15.2.3 Other Muscles of the Stomatognathic System

The medial and lateral pterygoid muscles have not been assessed with USG, as they are not superficial muscles, and thus they do not diagnose on the ultrasound imaging, clearly [25].

Raadsheer et al. [43] examined the correlations between bite force (magnitude and directions), facial morphology, and masticatory muscle thickness (masseter, temporalis, and digastric muscle). A preliminary study by Macrae et al. [44] reported that USG is an effective imaging method for the measurement of the anterior belly of the digastric muscle and submental muscle group (Fig. 15.3). In addition, the authors have concluded that on MRI imaging, measuring the cross-sectional area of the geniohyoid muscle and mylohyoid muscle thickness was not possible, as poor border representation.

Şatıroğlu et al. [45] investigated the thickness of the masseter, *levator labii superioris*, and zygomaticus major muscles by USG and evaluated the correlation between facial and masticatory muscle thickness and vertical facial morphology. The authors found that masseter muscle thickness was significantly associated with vertical facial measurements, but the facial muscles were not correlated with the vertical facial morphology.

Several authors explored the relationship between the *orbicularis oris* muscle and malocclusion states [46], treatment outcomes [47, 48], and skeletal and dental variables [49] (Fig. 15.4).

A study by Coclici et al. [50] used ultrasound device for displaying the posttreatment muscular alterations in class II and class III malocclusion patients and measured the length, width, and cross-sectional area of the masseter and suprahyoid muscles (mylohyoid and geniohyoid muscle). Variable adaptive response to orthognathic surgery has been detected in the mandibular muscles.

Impellizzeri et al. [51] aimed to evaluate the association between the masticatory and cervical muscles (temporalis, masseter, and sternocleidomastoid) thickness and facial asymmetries in young individuals (Fig. 15.5). It has been concluded that a significant relationship between facial asymmetries and masticatory and cervical musculature, and there are thinner muscles in the

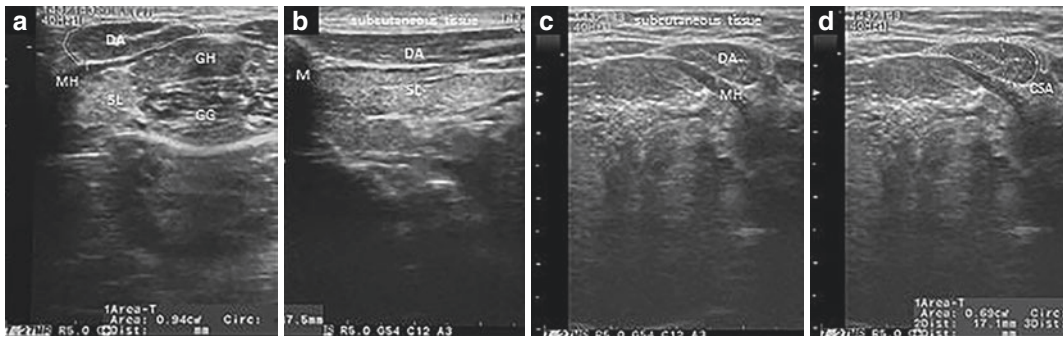

Fig. 15.3 Gray-scale transverse (**a**) and longitudinal (**b**) USG of the right anterior digastric muscle measured using electronic cursors to instantaneously calculate the cross-sectional area. (**a**) Transversal ultrasound image of the left anterior digastric muscle (**c**, **d**). Image demonstrating the measurement of length (horizontal dotted line), thickness (vertical dotted line), and cross-sectional area (CSA) measurement made by manually tracing around the circumference of the muscle with an electronic caliper (**d**). *DA* Anterior belly of Digastrics Muscle, *MH* Mylohyoid Muscle, *GH* Geniohyoid muscle, *GG* Genioglossus muscle, *SL* Sublingual gland, *M* Mandible

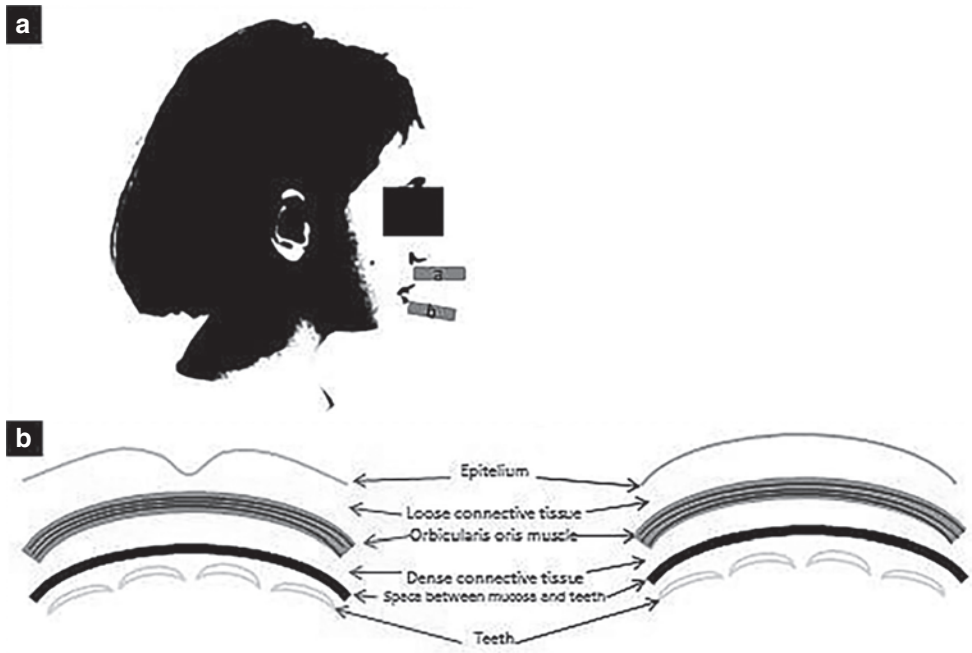

Fig. 15.4 (**a**) Scheme of application of transversal ultrasound transducer on the (a) upper and (b) lower lip. (**b**) Schematic drawing of the transversal image cross-section

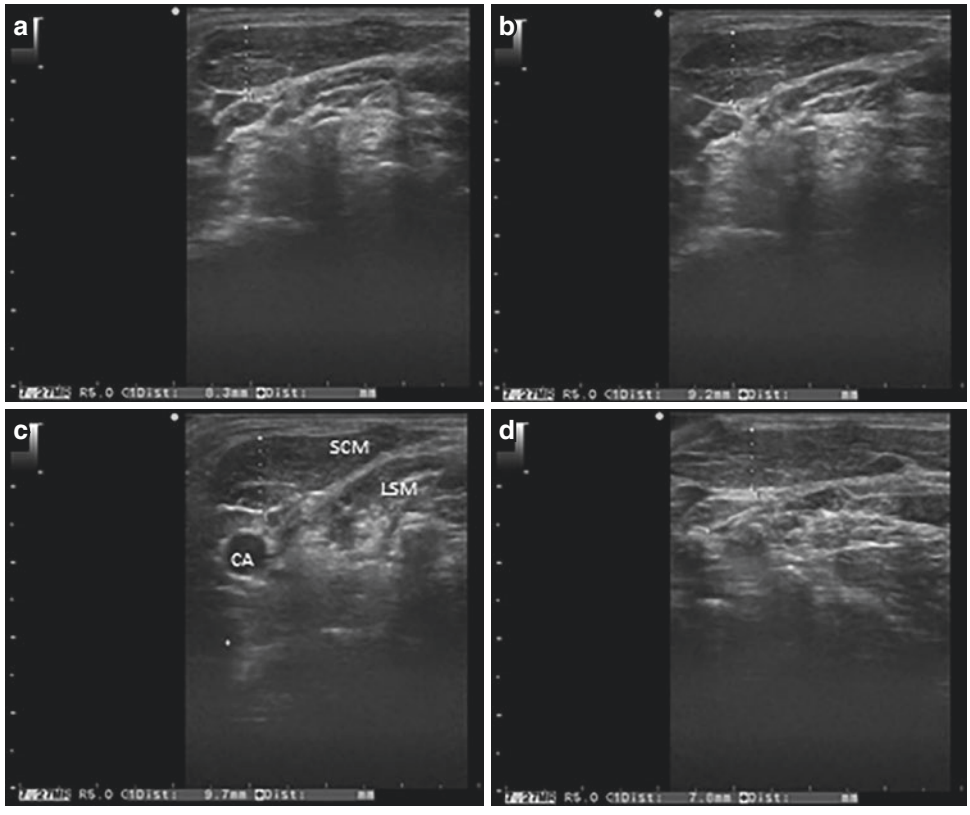

Fig. 15.5 Transverse USG of the left sternocleidomastoid muscle at rest (**a**), during dental clenching (**b**), flexion (**c**), and extension (**d**) of the head; the vertical dotted lines indicate the sites of muscle thickness measurements. *SCM* sternocleidomastoid muscle, *LSM* levator scapulae muscle, *CA* carotid artery

latero-deviation side than in the contralateral normal side, in cases untreated.

Future studies should standardize the methods and parameters for reducing errors and optimizing accuracy with a large-scale population. The use of ultrasound continues a promising option for the study of muscles of mastication.

In addition, Doppler sonography can be helpful for investigating the arteries in and around the masseter muscle and this method has the capability for evaluating pathological alterations in the muscles and arteries [25]. In a study conducted by Ariji et al. [52], the change of muscle thickness immediately after exercise showed a significant correlation with minimum blood-flow velocity.

15.3 Analysis of Tongue, Hyoid, and Swallowing

The tongue is a largely movable muscular organ within the orofacial region and for years, it has been theorized that the tongue size, postures, and functions must have a relationship to the surrounding oral cavity. It is assumed that the tongue size, postures, and functions have great importance for the etiology of malocclusions and dentofacial deformities [53].

Several methods are available for assessment of the tongue's size in vivo: direct measurements [54], different impression techniques [55], and the fluid displacement method [56]. Recently, different imaging methods have been used in tongue volume assessment: cephalometrics [57], computed tomography (CT) [58], cone-beam computed tomography (CBCT) [59], and magnetic resonance imaging (MRI) [60]. However, all techniques have their own clinical indications, advantages, and disadvantages.

Two-dimensional (2D) ultrasound is used for tongue function evaluation such as swallowing [61, 62] and speech [63] as well as for estimating tongue thickness, and tongue volume [64]. Three-dimensional (3D) ultrasound is already performed for the tongue posture assessment [65], as a device for the evaluation of tongue function [66].

15.3.1 Tongue Volume

Wojtczak et al. [64] examined tongue volume that was obtained from the multiplication of the midsagittal cross-sectional images of the tongue by its width in transverse scans, using 2D USG. The correlation between the tongue volume and mandibular arch size [55], vertical facial height, chin position has been demonstrated in clinical studies [67]. Hren ve Barbič [68], aimed to evaluate tongue size and it has been found that tongue volumes are significantly greater in skeletal Class III patients than normal. Also, larger tongues correlate with more severe skeletal Class III malocclusion.

Hren ve Barbic [68] and Barbič et al. [53] have utilized 3D USG for evaluating tongue volume. During USG investigation, each patient sits in upright resting positions and their heads fixed with a strap, so that the Frankfurt horizontal line was parallel to the floor. The 3D convex transducer was positioned on the skin of mouth floor in the midsagittal plane, submentally. The tongue volume evaluation was performed using 4D VIEW program software. The 3D Ultrasound technologies provide a multi-planar image of the region of interest or of certain pathology as well as perform more accurate analyses of them [53].

15.3.2 Tongue Posture

Tongue posture has been described as an etiologic factor in malocclusion development, including anterior open bite and articulation disorders as well as that plays an important role in anterior open bite treatment planning and posttreatment stability [69, 70]. It is believed that the tongue resting posture to be even more important for the dentoalveolar development and dental occlusion than

the tongue function during swallowing or speaking [71].In the view of total time, swallowing and speaking is too short to affect the balance of the forces acting on dentoalveolar development.

In the orofacial region, the tone and pressure of the resting tongue is one of the most important long-acting forces on the adjacent structures represented [72, 73]. Clinical evaluation of the tongue dynamics and resting postures are important parts of functional diagnostics [65]. A study by Kravanja et al. [74], who evaluated the tongue posture in children showed that the 3D ultrasound was found to be the most objective method to identify tongue posture in growing children and it could be an important device in functional diagnostics before, during, and after orthodontic treatment.

15.3.3 Tongue Movement

Tongue movement is related to some disorders, such as dysphagia. A better understanding of tongue movement in detail is important for the diagnosis and treatment of such diseases [75]. The tongue posture and function can be evaluated by clinical examination, including observation of tongue movements with lips apart and palpation of the temporalis and masseter muscles during swallowing. Because of anatomical limitations, these methods are not enough for objective evaluation [62]. Additional techniques have been developed and used for tongue movement evaluation, such as videofluoroscopy [76–78], electromyography [79–81], electromagnetic articulography [82], palatography [83], MRI [84], scintigraphy [85], and tongue pressure measurements [86]. Between these methods, the use of videofluoroscopy, which records the dynamic movement of radiopaque barium through the upper digestive tract by conventional X-rays, is considered as the standard criterion for the deglutition and dysphagia evaluation [87–90]. However, especially the disadvantages of irradiation, repeated evaluations are often avoided.

The advantages of ultrasonography for being noninvasive, detailed, repeatable, and real-time soft tissue scanning makes it superior for deglutitive tongue research [91]. The first time, Shawker et al. [92] used B-mode USG to evaluate tongue movements during swallowing. Peng et al. [93, 94] used M-mode sonography for quantitative and qualitative tongue functions assessment. The tongue was viewed by a hyperechoic line in the M-mode traces and that synchronized with the tongue movements during swallowing [75]. Peng et al. [93], divided the swallowing pattern obtained into five phases (phases I, IIa, IIb, IIIa, and IIIb) based on each turn points determined on the M-mode images (Fig. 15.6). This mode allows recording and successful separation of duration, speed, and range of tongue movements in each phase. Peng et al. [95] used the cushion scanning technique (CST) to manage the problems such as the movement of the transducer during examination and compression of the submental region that resulted in abnormal swallowing patterns. However, there is a conflict with using this technique because that increases the distance between the transducer and the floor of the mouth which could decrease the image resolution.

Cheng et al. [96] found that there are significant correlations between tongue movement during swallowing and dentofacial forms using B + M-Mode sonography combined with the CST, especially in the amplitude of the early final phase. They concluded that as the arch length increased, the duration of swallowing prolonged significantly in the late final phase.

Peng et al. [97] stated that the tongue movements of mature swallowing and tongue-thrust swallowing can be differentiated with USG. Based on this study, Tongue-thrust swallowers had a longer late transport phase than mature swallowers, and the tongue speed was

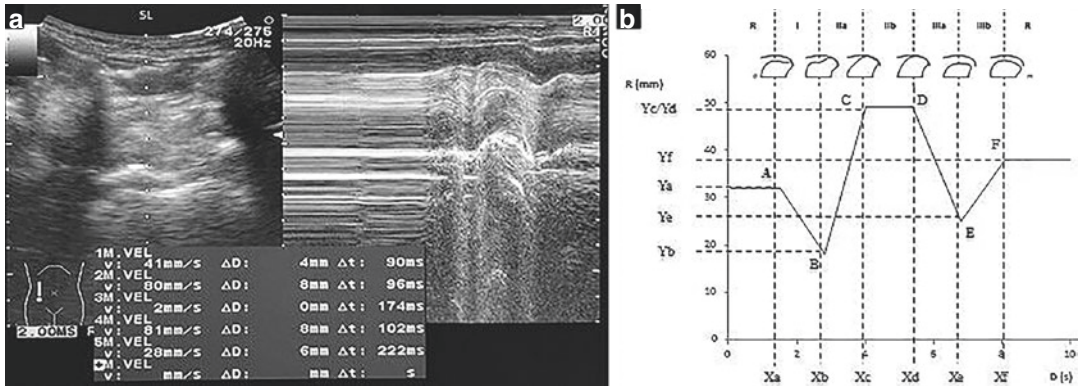

Fig. 15.6 B + M mode ultrasonogram. The left side shows the B-mode image with the scan line (SL) of the ultrasound probe set in the middle of the tongue. The M-mode image (right side) illustrates movements of various anatomic structures along the SL (**a**). Duration and range of tongue movement in each phase were determined graphically. In the rest phase (R), the tongue tip is usually positioned on the lingual surfaces of incisors or is touching the incisive papilla. The swallowing act starts with the shovel phase (I), in which the tongue tip moves cranially, the middle third of the tongue becomes concave and this is reflected in the down-movement of the curve in the M-mode ultrasonogram. In the early transport phase (IIa), the tongue is moving cranially and distally, the middle third of the tongue is approaching the hard palate, and therefore the concavity is disappearing. The late transport phase (IIb) is characterized by minimal vertical movement of the tongue because of the distal transportation of saliva. In the early final phase (IIIa), the curve in the M-mode ultrasonogram drops because of the lowering of the mouth floor. In the late final phase (IIIb), the tongue returns to the rest position and this is reflected as a rise in the M-mode curve [93] (**b**). *R* rest phase; *d* distal, *m* mesial, *D* duration, *R (mm)* Range

faster in the early final phase compared with mature swallowers.

Ardakani et al. [98] investigated the swallowing patterns of the tongue using B-mode Sonography. They concluded that the majority of abnormal or inconsistent swallowing patterns were detected in patients of mandibular prognathism.

Ovsenik et al. [71] compared the swallowing pattern and tongue function during swallowing in children with unilateral posterior crossbite (ULCB) in deciduous dentition by B + M-mode USG. The ultrasound analysis showed that duration, range, and speed of the tongue movements during swallowing significantly differ between children with and without ULCB.

In another study, Vaishnevi et al. [99], investigated the relationship between tongue movement and facial morphology in three types of malocclusion and found that the skeletal class III cases have prolonged duration of tongue movement and greater motion magnitude in the early final phase (III A) of swallowing. Also, there is a decrease in the motion range and duration of swallowing in the skeletal class II individuals.

15.3.4 Hyoid Bone Displacement

The measurements of tongue, hyoid, and laryngeal movements have been used to evaluate swallowing in USG studies [100–107]. The hyoid bone is the point of attachment for muscular and nonmuscular tissues of the floor of the mouth, tongue, and larynx and its movement functions as a marker of the integrity of the hyoid/larynx/epiglottis unit [100]. Under normal physiologic conditions, timely and adequate laryngeal elevation along with hyoid bone movement is an important part of the swallowing movement [108, 109]. The hyoid bone is easily viewed on USG in the sagittal plane as a hyperechoic area with a posterior acoustic.

Shadow (Fig. 15.7). USG allows for detailed evaluation via frame-by-frame images when real-time swallow(s) is acquired. Particularly, the

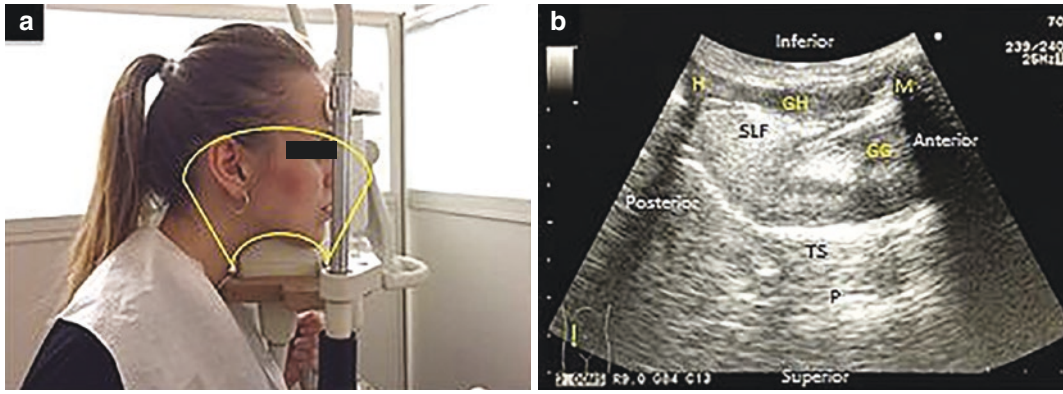

Fig. 15.7 Sagittal view in the submandibular position using a convex transducer between the mentum and the hyoid bone (**a**). The sonogram shows the tongue and the floor of the mouth (**b**). The insets show the transducer position on the skin. *GG* genioglossus, *GH* geniohyoid, *M* Mandible, *H* Hyoid bone, *P* Palate, *SLF* Sublingual fat, and *TS* Tongue surface

hyoid bone displacements during a swallow can be measured [110].

Yabunaka et al. [111] stated that the trajectory of the hyoid bone in the sagittal plane can be a feasible option for detecting some anomalies in swallowing. Similarly, Chen et al. [112] demonstrated that submental USG is a reliable and accurate technique for the hyoid bone movement assessment and that could be an aid in dysphagia screening and evaluation.

Effective bolus flow and pharyngeal clearing need enough hyoid bone movement during swallowing. Feng et al. [113] evaluated the association between the geniohyoid muscle size-function and hyoid bone movement during swallowing. The authors measured the cross-sectional area of the geniohyoid muscle, geniohyoid muscle contraction velocity, and the hyoid bone displacement in healthy young adults. A correlation has been found between the size of the geniohyoid muscle and hyoid bone movement.

15.4 Evaluation of the Airway

Airway obstruction and mouth breathing are among the etiological factors of malocclusion. Therefore, airway evaluation has great importance in clinical practice. The assessment is performed using lateral cephalometric radiography, commonly [114]. Cone-beam Computed Tomography scans can be utilized for assessing the morphology and mechanical behavior of the upper airway bony and soft tissue structures [115]. Also, various methods, including MRI, endoscopic procedures (e.g., fiber-optic, nasopharyngoscopy, fluoroscopy), acoustic reflection, and optical coherence tomography are feasible to display these structures [116–119].

In the literature, there are limited studies with the ultrasound-assisted evaluation of the upper airway. However, it has been demonstrated that USG has great potential for identifying the anatomic structures of the upper airway [120–122]. Bajracharya et al. [123] studied several sonographic parameters (soft tissue thickness at level of hyoid bone, epiglottis and vocal cords, visibility of hyoid bone in sublingual ultrasound, hyomental distance in head-extended position, and hyomental distance ratio) and they suggested the potential use of USG in the airway assessment (Fig. 15.8). Future studies may ensure that the information and understanding of the biomechanics of upper airway structures and their physiology in the different clinical scenarios.

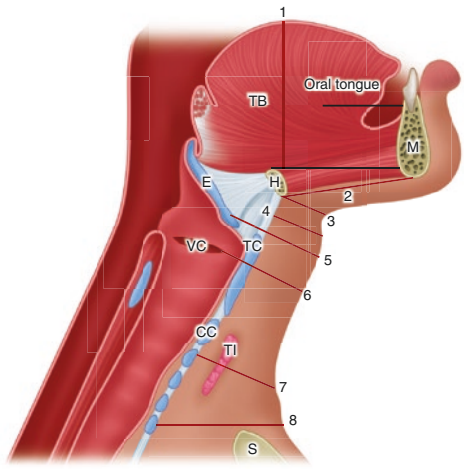

Fig. 15.8 Schematic diagram with USG parameters to evaluate the airway. Ultrasound measurements at various levels, *1* Cross-sectional area at base of tongue. *2* Distance from hyoid bone to mentum. *3* Distance from skin to hyoid bone. *4* Soft tissue thickness at level of thyrohyoid membrane. *5* Distance from skin to epiglottis midway between thyroid cartilage and hyoid bone. *6* Distance from skin to anterior commissure of true vocal cords. *7* Soft tissue thickness at level of thyroid isthmus. *8* Soft tissue thickness at level of suprasternal notch. *TB* Tongue base, *H* Hyoid bone, *M* Mentum, *E* Epiglottis, *TC* Thyroid cartilage, *CC* Cricoid cartilage, *VC* vocal cords, *TI* Thyroid isthmus, *S* manubrium sterni

15.5 The Temporomandibular Joint Evaluation

Temporomandibular joint disorder (TMD) is a general term for disorders affecting the masticatory muscles, temporomandibular joint (TMJ)-related structures, or all [124]. The prevalence of TMD is ranging from 10% to 70%, among the general population [125]. There may be different causes and different specific conditions in the etiology of TMD [126]. The TMDs may cause problems in some of the orthodontic patients, therefore TMJ assessment before, during, and after orthodontic treatment have great significance [127]. There are several methods and techniques used in the diagnosis of TMD, along with the basic clinical examination [126].

Panoramic radiography, conventional (linear or complex motion) tomography, helical or multislice computed tomography (CT), and cone-beam computed tomography (CBCT) are used to view the bony components, and magnetic resonance imaging (MRI) is used to evaluate the soft tissue components (discs) of the TMJ [128]. Bone scintigraphy can help for diagnosis of the osteoarthritis and joint inflammation [129, 130]. However, these methods have advantages and limitations to each.

The diagnosis of TMD can be performed by USG imaging of TMJ and adjacent tissues (Fig. 15.9). A study by Gateno et al. [131], investigated the accuracy of USG to visualize the position of mandibular condylar within the glenoid fossa. They supported that USG can be used as an objective method, during orthognathic surgery for reproducing the condylar position. However, a meta-analysis by Klatkiewicz et al. [126] resulted that there were no standardized procedures for using ultrasound scanning of the temporomandibular joint and further research is needed that should concern both normal and abnormal TMJs.

15.6 Determination of Soft Tissue Thickness at Orthodontic Miniscrew Placement Sites

Loss of anchorage in orthodontic treatments is often an important problem that risks treatment outcomes. Temporary skeletal anchorage instruments have been indicated as a reliable solution for situations where anchorage is critical. The use of orthodontic miniscrews in clinical orthodontics has revolutionized anchorage control, opening a new era [132].

The stability and success of orthodontic miniscrews depend on various factors, including the screw implantation site, the miniscrew angulation, the quality and quantity of cortical bone, the insertion and removal torques, the degree of miniscrew to bone contact, inflammation degree of the peri-orthodontic miniscrew tissues, the soft tissues thickness and mobility,

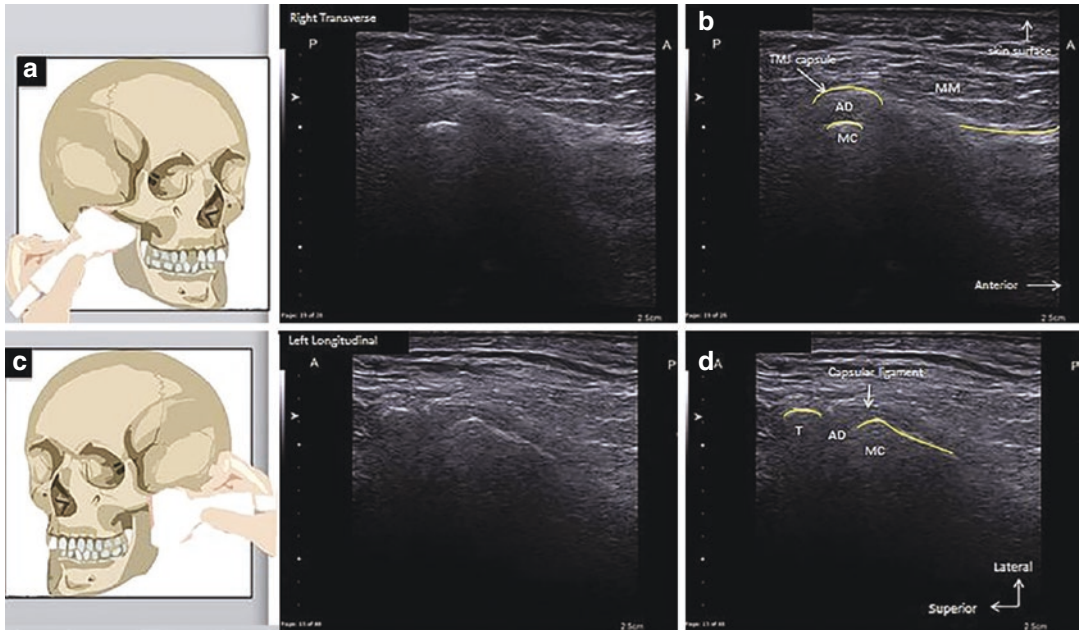

Fig. 15.9 Method of using ultrasound in TMJ. (**a**) *Horizontal positioning*, transverse image of the TMJ, and transverse section of sonography of the right TMJ obtained while the patient was in the closed-mouth position. (**b**) Anatomical landmarks observed in transversal/axial slice. (**c**) *Vertical positioning*, coronal/sagittal image of the TMJ, and coronal section of sonography of the left TMJ obtained while the patient was in the closed-mouth position. (**d**) Anatomical landmarks observed in coronal view. *TMJ* temporomandibular joint, *AD* Articular Disc, *MC* Mandibular condyle, *MM* Masseter muscle, *T* Temporal bone (depending on the angulations of the USG probe)

the patient's craniofacial morphology, and the screw dimensions [133–139].

Risk of failure of orthodontic miniscrews surrounded by nonkeratinized mucosa is higher than for screws surrounded by keratinized mucosa, for the soft tissue component of stability [140]. In the different candidate, areas for screw placement have different soft tissue thicknesses. Therefore, evaluation of the quantitative differences in gingival thickness for miniscrew implantation is one of the significant factors affecting surgical success [141].

Measurements on the thickness of oral mucosa can be acquired by direct methods, such as using a needle or periodontal probe with an endodontic file stopper and biopsy, or indirect measurement using radiographic images. USG is an alternative method that has the potential for providing an evaluation of the soft tissue thickness [142].

Cha et al. [141] evaluated the gingival thickness of potential sites for miniscrew placement in the buccal-attached gingiva and the palatal masticatory mucosa. Mucosal thickness was measured intraorally with an ultrasonic gingival thickness meter (5 MHz).

A study by Parmar et al. [132] aimed to examine the soft tissue thicknesses at potential miniscrew implantation zones and to prescribe a guideline for miniscrew selection in orthodontic clinics. The measurements were performed with A-mode ultrasound device that uses the pulse-echo principle with the frequency was 10 MHz at 10%. The transducer was placed perpendicular to the most gingival surface.

Cha et al. [141] and Parmar et al. [132] concluded that evaluation of the gingival tissues could help in selecting a proper miniscrew in orthodontic practice.

Schulze et al. [142] reported that using B-mode and A-mode ultrasonography is acceptable in various clinical practices for measuring the mucosal thickness accurately. However,

B-mode USG is a capable device for soft tissue diagnostics, that needs a small transducer for measurements in the oral cavity.

Although the quantity and quality of cortical bone greatly influenced the stability of miniscrews, also the width of the attached gingiva on the buccal and palatal surfaces in the interdental areas must be considered before surgery [143]. Maximum retention can be obtained when an adequate length of the screw is placed in areas of thin gingival tissue and thick cortical bone [144].

The validity and reliability of USG were shown for measuring soft tissue thickness in different anatomical locations of the oral cavity [145–149], and that offers great potential in presurgical assessment for placement of orthodontic miniscrew placement.

15.7 Determining Pubertal Growth and Bone Age

In the human beings, skeletal maturation has a great value for the detection of growth and differentiation processes [150, 151]. Bone age is an important indicator of the skeletal and biological maturity of an individual. The knowledge of the skeletal maturation and the stage of growth can provide useful information for many clinical practices as well as in orthodontic procedures such as treatment planning, the timing of treatment, and selection of the treatment method [152].

Radiological indicators have been used for bone age estimation [153]. For this, several techniques are generally utilized based on hand-wrist radiographs. In clinical practice, the Greulich-Pyle (an atlas method which compares the radiograph of the individual with the nearest standard radiograph in the atlas) and Tanner-Whitehouse (a scoring method which focuses on skeletal maturity for each patient hand and wrist bone) methods are preferred commonly [154–156].

In recent years, because of the possible side effects and damages of ionizing radiation, there is an increasing focus on the establishment of nonionizing imaging methods for age estimation [157]. Some researchers have used USG, which has many advantages and as an ionized radiation-free imaging technique, to estimate bone age [157–160].

The bone age estimation by ultrasonography is not a new method. In children, the hip [158], iliac and radius bones [159], and ossification center of the wrist [160] have been used as sonographic landmarks for determination of the skeletal age previously.

Carpenter and Lester [161] stated that there was a significant difference between chronologic age and bone age in the different regions of hand and genders. Also, in children under age 10 years, the entire hand should be taken to consider for evaluation of bone age, maybe with less interest on the carpal bones, they may cause over- and under-estimated results greatly. They concluded that bone age estimation based on the metacarpals and phalanxes more accurate than wrist and carpal bone age readings.

Nessi et al. [160], Bilgili et al. [157], and Hajalioghli et al. [4] have followed the same protocol for ultrasonographic bone age evaluation. These researchers aimed assessment of the ossification centers, which were viewed as hyperechoic foci with acoustic shadowing, in sonographic images of the radius and ulna distal epiphysis, carpal bones, epiphyses of the first and third metacarpals, and epiphysis of the middle phalanx (Fig. 15.10). Schmidt et al. [151] have targeted examining ossification of the distal radial epiphysis and the ossification stages were categorized. Nessi et al. [160] mentioned that USG is a valuable technique for scanning skeletal maturation of the ossification centers of the hand and wrist (sesamoid bone and DP3). Bilgili et al. [157] who aimed to described hand and wrist ultrasonography charts that present all carpal bones, phalangeal, and metacarpal epiphyses by placing the probe in transverse and longitudinal planes for each finger. They reported significant correlations between radiographic and ultrasonographic results in both genders (71.1% of male cases and 84.4% of female cases) and stated that maturity of carpal bones varies greatly. Daneff et al. [162] concluded that conventional USG has the potential for identifying the ossification centers of the hand and wrist and can be preferred as a harmless follow-up method in cases with

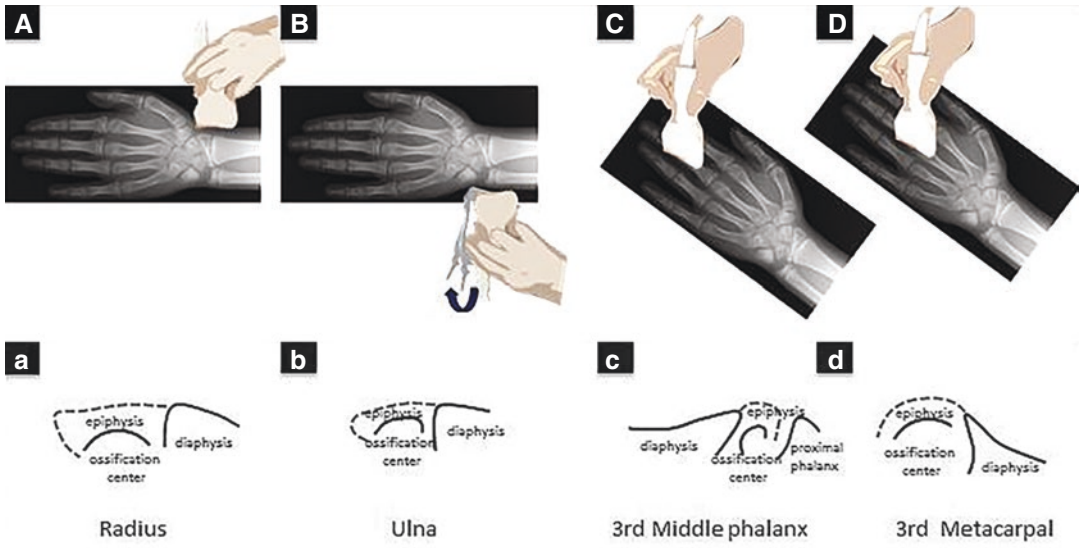

Fig. 15.10 Scanning planes for hand and wrist imaging by ultrasound to examine bone age. (**A**) The probe was set on the radial styloid process in the coronal plane to image the epiphysis of the radius. (**B**) The probe was set on the ulna styloid process in the coronal-to-sagittal plane to image the epiphysis of the ulna. (**C**, **D**) The probe was set on the sagittal plane to image the epiphyses of the third phalanxes and metacarpal. Schematic drawing of the distal radius and ulna, phalanx and metacarpal (**a**–**d**). The *epiphysis* is represented by a dotted line. The hyperechoic surface of the *ossification center* and the *cortex of the diaphysis* are symbolized by solid lines

growth problems. Khan et al. [163], who used an automatic USG device, reported that a low correlation between USG and radiography in their work. In contrast, Hajalioghli et al. [4] reported that conventional radiography can be replaced by USG for bone age estimation. According to a study by Ağırman et al. [152], USG is an alternative method to conventional radiography in the bone age estimation and viewing sesamoid bone and MP3 capping, which is the indicator of pubertal growth.

Although, the reliability of the results of USG examinations largely depends on the experience of each practitioner. It is necessary to study with larger groups to make a standard evaluation of bone age in sonography.

15.8 Evaluation of the Midpalatal Suture

Maxillary transverse constriction is concerning various issues that include posterior crossbite (dental and/or skeletal), occlusal disharmony, dental crowding, pharyngeal airway narrowing, tongue posture alterations, mouth breathing, abnormal muscular function, and esthetic problems [164–166]. The choice of treatment depends on many clinical conditions [167]. Rapid palatal expansion (RPE) is a routine orthodontic treatment that aims to increase the transversal width with the midpalatal suture and the circummaxillary sutural system separation. RPE corrects that by stretching of collagenous fibers and the local formation of a new bone [168]. However, in patients with a midpalatal suture opening, RPE has been recommended, but the surgically assisted rapid maxillary expansion (SARME) has been needed in patients with a full midpalatal suture ossification [167, 169].

The midpalatal suture is one of the critical areas for maxillary expansion as the zygomatic buttress and the pterygomaxillary junction [170]. Oral radiographs and CT are imaging methods used for the evaluation of palatal suture maturation, commonly. However, radiography/CT involves ionizing radiation. In the orthopedic literature, it is reported that USG is accurate and reliable method to assess distraction osteogenesis wounds in long bones [171, 172].

Examination of the midpalatal suture has been performed from outside the mouth on the skin overlying (probe has been placed in the region between the nasal columella–labial junction and the upper lip), and the ultrasound beam was oriented perpendicular to the bone surface [173]. To the best of our knowledge, there are two published studies of sutural expansion with USG in RPE and SARPE patients [170, 173].

Sumer et al. [170] evaluated sutural mineralization at five-time points during the SARME and retention protocol for three patients, scoring each patient's callus formation via semiquantitative bone fill scores (0–3).

Gumussoy et al. [173] utilized the USG examination in 29 RPE patients, and they measured the amount of sutural expansion as mesiodistal length at every stage (immediately after appliance practice, 10 turns, and 20 turns). They reported that the surfaces of the bone segments were easily viewed, and examination in the expansion area could be performed accurately during the active phase of the expansion. The expansion zone was identified by a nonhomogeneous and hyperechoic, sharply demarcated area (Fig. 15.11). Also, they mentioned that the system is not enough for viewing of the whole anatomy, as the field of view depends on the linear probe and scanning angle. Therefore, it was stated that the scoring system used by Sumer et al. [170] is not suitable.

Overall, these studies did not present solid evidence of their validity for the accurate determination of the maturation of the palatal suture. However, when we think about the disadvantages and limitations of other imaging modalities, further evaluations can show the accuracy of ultrasonography examinations for this purpose.

15.9 Ultrasonographic Evaluation of Periodontal Changes During Orthodontic Tooth Movement

The periodontal tissue reaction to tooth movement by orthodontic forces consists of remodeling changes in the periodontal ligament, alveolar bone, and gingiva [174]. Real-time, in vivo visualization of the alterations induced by orthodontic tooth movement in the morphology of the anatomical structures of the periodontium, would be helpful for managing the treatment plan and assessment of the tissue response to orthodontic forces [175]. Previous studies concluded that USG is suitable for evaluating the cortical bone, periodontal space, sulcular depth, the characteris-

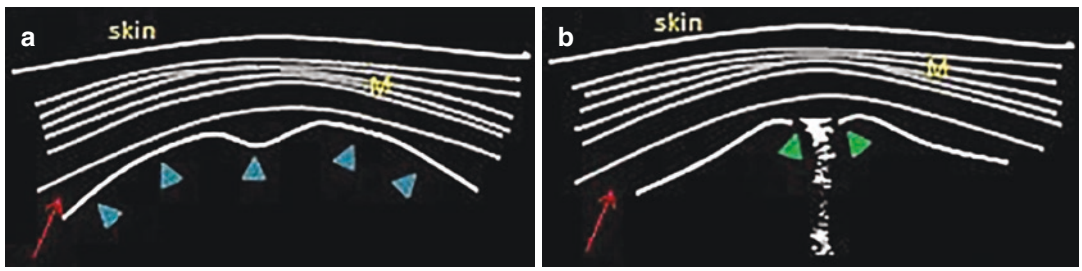

Fig. 15.11 Schematic transverse ultrasound image of normal anatomical structures at (**a**) pre-expansion and (**b**) during treatment. *M* superior orbicularis oris muscle, *red* arrows show vestibulum oris, *blue* arrowheads show border maxillary cortical bone, and *green* arrowheads show sutural expansion

tics of the gingiva, and length of the anatomical crown [176, 177].

A study by Zimbran et al. [175] aimed to examine whether changes that appear, induced by the orthodontic canine retraction, in periodontal tissues can be diagnosed by USG. Sonographic scans were performed from outside the mouth on the skin overlying, in three different areas of the canines buccal surface (mesial, middle, and distal) and three times (before, during, and after retraction). The transducer (40 MHz frequency pulses) was placed in a longitudinal plane. Four different distances were measured, including depth of the sulcus, thickness of the gingiva, length of the supracrestal fibers, width of periodontal space. The authors found significant results for sulcus depth measurement and distance between marginal gingiva and alveolar crest, immediately after force application on the middle and mesial area of the canine. They concluded that high-resolution USG has the potential to reveal changes in periodontium during orthodontic tooth movement (Fig. 15.12) (Fig. 15.13).

15.10 Effect of Low-Intensity Pulsed Ultrasound (LIPUS) on Tooth Movement and Root Resorption

Orthodontically induced root resorption (OIRR) is an undesirable outcome of orthodontic treatment [178]. The prevalence of OIRR is higher than 90% [179], and from minor to severe, the incidence of OIRR ranges from 94% to 6.6%, respectively [180]. Lund et al. [180] reported that 6.6% of the orthodontic patients had at least one tooth with OIRR more than 4 mm. Mirabella and Artun [181] indicated that about 4% of orthodontic patients with generalized resorption of the six anterior teeth of greater than 3 mm. During treatment, several studies have mentioned that probably about 5% of adults and only 2% of adolescents show at least one tooth with severe resorption of greater than 5 mm.

Several etiologic reasons have been reported that can influence OIRR, including biological (susceptibility, genetics, and systemic factors),

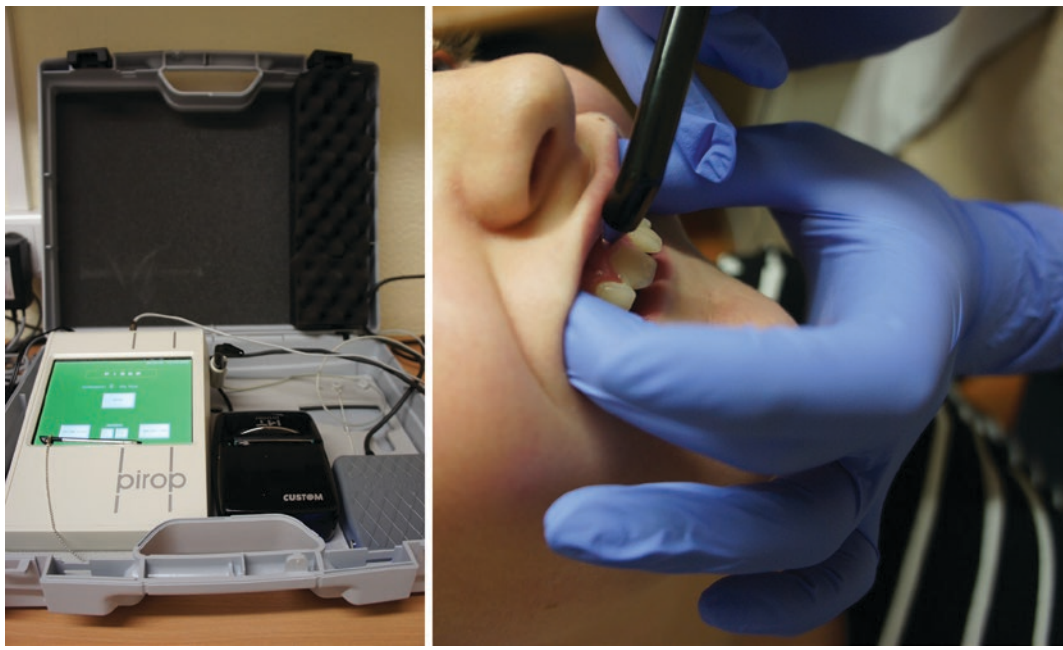

Fig. 15.12 (**a**) An USG device which is dedicated to measure the gingival thickness, (**b**) the image showing the application of the device, note that the high frequency probe for measuring gingival thickness. Courtesy of the Czelej Editorial House in the 3rd Edition of the book "Współczesna Radiologia Stomatologiczna"

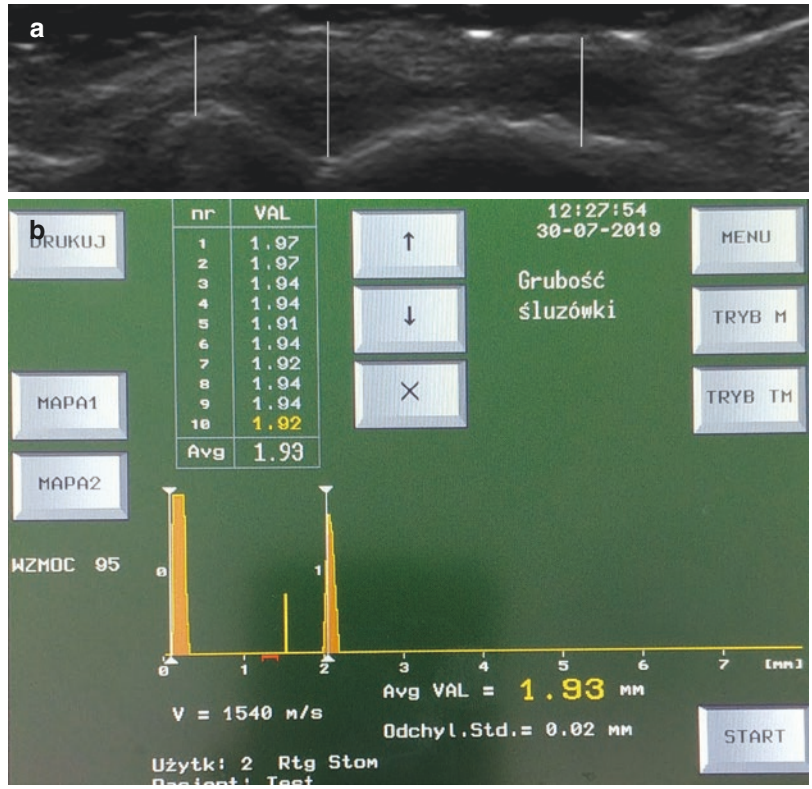

Fig. 15.13 (**a**) USG image showing the measurement of gingival thickness, (**b**) Note that the device measures the average of the app. 10 measurements. Courtesy of the Czelej Editorial House in the 3rd Edition of the book "Współczesna Radiologia Stomatologiczna"

mechanical, and combined factors [182]. However, the relationship between severe OIRR and the possible etiologic factors is unclear [1]. Sasaki [183] reported that osteoprotegerin (OPG)/RANK/Receptor activator of nuclear factor kappa-B ligand (RANKL) pathway that controls the osteoclastogenesis and odontoclastogenesis exist in physiologic root resorption in deciduous teeth [1]. Some studies indicated that OPG and RANKL levels increase during the application of heavy forces and severe root resorption [182, 184–186]. Also, it has been detected that increased RANKL production and low OPG expression, which stimulated the formation of osteoclast, in PDL cells from severe OIRR patients [186].

Several methods have been used in OIRR treatment, including the bisphosphonate application to rats' teeth [187]; allowing for self-healing for 70 days [179] or after retention [188]; topical corticosteroid [189]; calcium hydroxide root canal treatment [190]; and recently low-intensity pulsed ultrasound (LIPUS-acoustic pressure waves) in humans [191, 192], and in experimental animals [193–196]. Previous reports concluded that LIPUS modulates the OPG/RANK/RANKL balance, so it minimizes and shows a suppressive effect on osteoclastogenesis. In studies in experimental animals and in humans, it has been detected that LIPUS increased cementum formation and predentine/dentine [191, 195–199].

Accelerated tooth movement has received increasing attention by clinicians for minimizing possible OIRR, shortening treatment duration, saving patient compliance, and reducing side effects of prolonged orthodontic treatment such as enamel decalcification, periodontitis, and psychological impact [1]. Several techniques have been previously reported to reduce treatment periods, including pulsed electromagnetic fields [200], electrical currents [201], corticotomy [202], distraction osteogenesis [203], mechanical vibration [204], photobiomodulation [205], low-level laser therapy [206], and LIPUS.

The 30 mW/cm^2 output signal of LIPUS device (1.5 MHz, pulse 200 μs, delivered at 20% duty cycle, 30 mW/cm2, 20 min daily) has been

approved for clinical use [207]. LIPUS device has been used in bone regeneration and fracture healing approved by the U.S. FDA (Food and Drug Administration) for bone regeneration and fracture healing [208].

In addition, a pilot study, within the limitations, reported that LIPUS combined with functional appliances can be used for treating enhancing mandibular growth in children with hemifacial microsomia [197].

However, LIPUS use in these treatments is still controversial because of inconsistency among all trials [209], adverse effects [210], underlying mechanisms remain unclear partly. Therefore, a proper understanding of the complete mechanism of LIPUS stimulation needs further research.

References

1. El-Bialy T. Application of LIPUS in orthodontics. In: Therapeutic ultrasound in dentistry. Cham: Springer; 2018. p. 63–9.
2. Harrell WE, Scarfe WC, Pinheiro LR, Farman AG. Applications of CBCT in orthodontics. In maxillofacial cone beam computed tomography. Cham: Springer; 2018. p. 645–714.
3. Dhiman S, Maheshwari S, Verma SK. Assessment of maturity in orthodontics: a review. J Adv Clin Res Insights. 2015;2(2):100–3.
4. Hajalioghli P, Tarzamni MK, Arami S, Fouladi DF, Ghojazadeh M. The utility of ultrasonographic bone age determination in detecting growth disturbances; a comparative study with the conventional radiographic technique. Skelet Radiol. 2015;44(9):1351–6.
5. Sharma S, Rasila D, Singh M, Mohan M. Ultrasound as a diagnostic boon in dentistry a review. Int J Sci Stud. 2014;2:70–6.
6. Baum G, Greenwood I, Slawski S, Smirnow R. Observation of internal structures of teeth by ultrasonography. Science. 1963;139:495–6.
7. Pepicelli A, Woods M, Briggs C. The mandibular muscles and their importance in orthodontics: a contemporary review. Am J Orthod Dentofac Orthop. 2005;128(6):774–80.
8. Ariji E, Ariji Y, Yoshiura K, Kimura S, Horinouchi Y, Kanda S. Ultrasonographic evaluation of inflammatory changes in the masseter muscle. Oral Surg Oral Med Oral Pathol. 1994;78:797–801.
9. Martin AO. Can ultrasound cause genetic damage? J Clin Ultrasound. 1984;12:11–20.
10. Stewart HF, Moore RM. Development of the health risk evaluation data for diagnostic ultrasound. J Clin Ultrasound. 1984;12:493–500.
11. Raadsheer MC, Van Eijden TM, Van Spronsen PH, Van Ginkel FC, Kiliaridis S, Prahl-Andersen B. A comparison of human masseter muscle thickness measured by ultrasonography and magnetic resonance imaging. Arch Oral Biol. 1994;39:1079–84.
12. Raadsheer MC, Kiliaridis S, Van Eijden TM, Van Ginkel FC, Prahl-Andersen B. Masseter muscle thickness in growing individuals and its relation to facial morphology. Arch Oral Biol. 1996;41:323–32.
13. Close PJ, Stokes MJ, L'Estrange PR, Rowell J. Ultrasonography of masseter muscle size in normal young adults. J Oral Rehabil. 1995;22:129–34.
14. Wilson IR, Crocker EF. An introduction to ultrasonography in oral surgery. Oral Surg Oral Med Oral Pathol. 1985;59:236–41.
15. Bakke M, Tuxen A, Vilmann P, Jensen BR, Vilmann A, Toft M. Ultrasound image of human masseter muscle related to bite force, electromyography, facial morphology and occlusal factors. Scand J Dent Res. 1992;100:164–71.
16. Bertram S, Rudisch A, Bodner G, Emshoff R. The short-term effect of stabilization-type splints on the local asymmetry of masseter muscle sites. J Oral Rehabil. 2001;28:1139–43.
17. Bertram S, Brandlmaier I, Rudisch A, Bodner G, Emshoff R. Crosssectional characteristics of the masseter muscle: an ultrasonographic study. Int J Oral Maxillofac Surg. 2003;32:64–8.
18. Emshoff R, Bertram S. The short-term effect of stabilization-type splints on local cross-sectional dimensions of muscles of the head and neck. J Prosthet Dent. 1998;80:457–61.
19. Kiliaridis S, Kälebo P. Masseter muscle thickness measured by ultrasonography and its relation to facial morphology. J Dent Res. 1991;70:1262–5.
20. Kubota M, Nakano H, Sanjo I, Satoh K, Sanjo T, Kamegai T, Ishikawa F. Maxillofacial morphology and masseter muscle thickness in adults. Eur J Orthod. 1998;20:535–42.
21. Sano K, Ninomiya H, Sekine J, Pe MB, Inokuchi TJ. Application of magnetic resonance imaging and ultrasonography to preoperative evaluation of masseteric hypertrophy. J Craniomaxillofac Surg. 1991;19:223–6.
22. Emshoff R, Bertram S. The ultrasonic value of local muscle hypertrophy in patients with temporomandibular joint disorders. J Prosthet Dent. 1995;73:373–6.
23. Emshoff R, Bertram S, Strobl H. Ultrasonographic cross-sectional characteristics of muscles of the head and neck. Oral Surg Oral Med Oral Pathol Oral Radiol Endod. 1999;87:93–106.
24. Emshoff R, Bertram S, Brandlmaier I, Scheiderbauer G, Rudisch A, Bodner G. Ultrasonographic assessment of local cross-sectional dimensions of masseter muscle sites: a reproducible technique? J Oral Rehabil. 2002;29:1059–62.
25. Serra MD, Gavião MBD, dos Santos Uchôa MN. The use of ultrasound in the investigation of the muscles of mastication. Ultrasound Med Biol. 2008;34(12):1875–84.

26. Smith MW, Faulkner A. Perceptual adaptation by normally hearing listeners to a simulated "hole" in hearing. J Acoust Soc Am. 2006;120(6):4019–30.
27. Oliveira JHPD, Dourado Filho MGD, Melo TMA, Lima NSD, Marcelino Filho M, Silva HJD. Evidence of measures of normalcy for thickness of masseter muscle evaluated with ultrasound: a review study. Revista CEFAC. 2015;17(1):238–52.
28. Uchida Y, Motoyoshi M, Shigeeda T, Shinohara A, Igarashi Y, Sakaguchi M, et al. Relationship between masseter muscle size and maxillary morphology. Eur J Orthod. 2011;33:654–9.
29. Benington PC, Gardener JE, Hunt NP. Masseter muscle volume measured using ultrasonography and its relationship with facial morphology. Eur J Orthod. 1999;21:659–70.
30. Satiroğlu F, Arun T, Işik F. Comparative data on facial morphology and muscle thickness using ultrasonography. Eur J Orthod. 2005;27:562–7.
31. Ngom PI, Ly BA, Diagne F, Diouf JS, Chakib O, Hennequin M. Masseter muscle thickness in relation to craniofacial morphology. Int Orthod. 2008;6:251–67.
32. Rani S, Ravi MS. Masseter muscle thickness in different skeletal morphology: an ultrasonographic study. Indian J Dent Res. 2010;21:402–7.
33. Rohila AK, Sharma VP, Shrivastav PK, Nagar A, Singh GP. An ultrasonographic evaluation of masseter muscle thickness in different dentofacial patterns. Indian J Dent Res. 2012;23:726–31.
34. Kiliaridis S, Georgiakaki I, Katsaros C. Masseter muscle thickness and maxillary dental arch width. Eur J Orthod. 2003;25(3):259–63.
35. Tircoveluri S, Singh JR, Rayapudi N, Karra A, Begum M, Challa P. Correlation of masseter muscle thickness and intermolar width-an ultrasonography study. J Int Oral Health. 2013;5(2):28.
36. Trawitzki LV, Dantas RO, Mello-Filho FV, Elias-Júnior J. Effect of treatment of dentofacial deformity on masseter muscle thickness. Arch Oral Biol. 2006;51(12):1086–92.
37. Kiliaridis S, Mahboubi PH, Raadsheer MC, Katsaros C. Ultrasonographic thickness of the masseter muscle in growing individuals with unilateral crossbite. Angle Orthod. 2007;77(4):607–11.
38. Kiliaridis S, Mills CM, Antonarakis GS. Masseter muscle thickness as a predictive variable in treatment outcome of the twin-block appliance and masseteric thickness changes during treatment. Orthod Craniofac Res. 2010;13(4):203–13.
39. Trawitzki LV, Dantas RO, Elias-Júnior J, Mello-Filho FV. Masseter muscle thickness three years after surgical correction of class III dentofacial deformity. Arch Oral Biol. 2011;56(8):799–803.
40. Naser-Ud-Din S, Thoirs K, Sampson WJ. Ultrasonography, lateral cephalometry and 3D imaging of the human masseter muscle. Orthod Craniofac Res. 2011;14:33–43.
41. Rasheed SA, Prabhu NT, Munshi AK. Electromyographic and ultrasonographic observations of masseter and anterior temporalis muscles in children. J Clin Pediatr Dent. 1996;20:127–32.
42. Castelo PM, Gavião MBD, Pereira LJ, Bonjardim LR. Masticatory muscle thickness, bite force, and occlusal contacts in young children with unilateral posterior crossbite. Eur J Orthod. 2007;29(2):149–56.
43. Raadsheer MC, Van Eijden TMGJ, Van Ginkel FC, Prahl-Andersen B. Contribution of jaw muscle size and craniofacial morphology to human bite force magnitude. J Dent Res. 1999;78(1):31–42.
44. Macrae PR, Jones RD, Myall DJ, Melzer TR, Huckabee ML. Cross-sectional area of the anterior belly of the digastric muscle: comparison of MRI and ultrasound measures. Dysphagia. 2013;28(3):375–80.
45. Şatıroğlu F, Arun T, Işık F. Comparative data on facial morphology and muscle thickness using ultrasonography. Eur J Orthod. 2005;27(6):562–7.
46. Prabhu NT, Munshi AK. Ultrasonographic observation of the circumoral musculature: an in vivo study. J Clin Pediatr Dent. 1995;19:195–203.
47. Anupam Kumar T, Kuriakose S. Ultrasonographic evaluation of effectiveness of circumoral muscle exercises in adenotonsillectomized children. J Clin Pediatr Dent. 2005;29(1):49–55.
48. Das UM, Beena JP. Effectiveness of circumoral muscle exercises in the developing dentofacial morphology in adenotonsillectomized children: an ultrasonographic evaluation. J Indian Soc Pedod Prev Dent. 2009;27(2):94.
49. Barbosa TDS, Gavião MBD, Pupo LS, Castelo PM, Pereira LJ. Associations between orbicularis oris thickness and skeletal and dental variables in mixed dentition. Rev Odontol UNESP. 2012;41(6):402–7.
50. Coclici A, Hedeşiu M, Bran S, Băciuţ M, Dinu C, Rotaru H, Roman R. Early and long-term changes in the muscles of the mandible following orthognathic surgery. Clin Oral Investig. 2019;23:3437–44.
51. Impellizzer A, Serritella E, Putrino A, Vizzielli G, Polimeni A, Galluccio G. Assessment of masticatory and cervical muscles' thickness by ultrasonography in patients with facial asymmetry. Clin Ter. 2019;170(4):e272–7.
52. Ariji Y, Sakuma S, Kimura Y, Kawamata A, Toyama M, Kurita K, Ito Y, Ariji E. Colour Doppler sonographic analysis of blood-flow velocity in the human facial artery and changes in masseter muscle thickness during low-level static contraction. Arch Oral Biol. 2001;46:1059–64.
53. Barbič U, Verdenik I, Mušič MM, Hren NI. Three-dimensional ultrasound evaluation of tongue volume. Slov Med J. 2016;85(4) https://doi.org/10.6016/ZdravVestn.1477.
54. Oliver RG, Evans SP. Tongue size, oral cavity size and speech. Angle Orthod. 1986;56(3):234–43.
55. Tamari K, Shimizu K, Ichinose M, Nakata S, Takahama Y. Relationship between tongue volume and lower dental arch sizes. Am J Orthod Dentofac Orthop. 1991;100(5):453–8.
56. Bandy HE, Hunter WS. Tongue volume and the mandibular dentition. Am J Orthod. 1969;56(2):134–42.

57. Cuccia AM, Campisi G, Cannavale R, Colella G. Obesity and craniofacial variables in subjects with obstructive sleep apnea syndrome: comparisons of cephalometric values. Head Face Med. 2007;3:41. https://doi.org/10.1186/1746-160X-3-41.
58. Roehm EG. Computed tomographic measurement of tongue volume relative to its surrounding space. Am J Orthod. 1982;81(2):172. https://doi.org/10.1016/0002-9416(82)90044-6.
59. Uysal T, Yagci A, Ucar FI, Veli I, Ozer T. Cone-beam computed tomography evaluation of relationship between tongue volume and lower incisor irregularity. Eur J Orthod. 2013;35(5):555–62. https://doi.org/10.1093/ejo/cjr054.
60. Iida-Kondo C, Yoshino N, Kurabayashi T, Mataki S, Hasegawa M, Kurosaki N. Comparison of tongue volume/oral cavity volume ratio between obstructive sleep apnea syndrome patients and normal adults using magnetic resonance imaging. J Med Dent Sci. 2006;53(2):119–26.
61. Casas MJ, Seo AH, Kenny DJ. Sonographic examination of the oral phase of swallowing: bolus image enhancement. J Clin Ultrasound. 2002;30:83–7.
62. Ovsenik M, Volk J, Marolt MM. A 2D ultrasound evaluation of swallowing in children with unilateral posterior crossbite. Eur J Orthod. 2014;36:665–71.
63. Shawker TH, Sonies BC. Tongue movement during speech: a real-time ultrasound evaluation. J Clin Ultrasound. 1984;12:125–33.
64. Wojtczak JA. Submandibular sonography: assessment of hyomental distances and ratio, tongue size, and floor of the mouth musculature using portable sonography. J Ultrasound Med. 2012;31(4):523–8.
65. Volk J, Kadivec M, Music MM, Ovsenik M. Three-dimensional ultrasound diagnostics of tongue posture in children with unilateral posterior crossbite. Am J Orthod Dentofac Orthop. 2010;138(5):608–12.
66. Bressmann T, Thind P, Uy C, Bollig C, Gilbert RW, Irish JC. Quantitative three-dimensional ultrasound analysis of tongue protrusion, grooving and symmetry: data from 12 normal speakers and a partial glossectomee. Clin Linguist Phon. 2005;19(6–7):573–88.
67. Yoo E, Murakami S, Takada K, Fuchihata H, Sakuda M. Tongue volume in human female adults with mandibular prognathism. J Dent Res. 1996;75(12):1957–62.
68. Hren NI, Barbič U. Tongue volume in adults with skeletal class III dentofacial deformities. Head Face Med. 2016;12(1):12.
69. Johnson NCL, Sandy JR. Tooth position and speech - is there a relationship? Angle Orthod. 1999;69:306–10.
70. Farronato G, Giannini L, Riva R, Galbiati G, Maspero C. Correlations between malocclusions and dyslalias. Eur J Paediatr Dent. 2012;13:13–8.
71. Ovsenik M. Incorrect orofacial functions until 5 years of age and their association with posterior crossbite. Am J Orthod Dentofac. 2009;136:375–81.
72. Proffit WR. Equilibrium theory revisited: factors influencing position of the teeth. Angle Orthod. 1978;48:175–86.
73. Stahl F, Grabowski R, Gaebel M, Kundt G. Relationship between occlusal findings and orofacial myofunctional status in primary and mixed dentition- part II: prevalence of orofacial dysfunctions. J Orofac Orthop. 2007;68:74–90.
74. Kravanja SL, Hocevar-Boltezar I, Music MM, Jarc A, Verdenik I, Ovsenik M. Three-dimensional ultrasound evaluation of tongue posture and its impact on articulation disorders in preschool children with anterior open bite. Radiol Oncol. 2018;52(3):250–6.
75. Li C, Li J, Zhang C, Cao X, Li N, Song D, Yu T. Application of B+ M-mode ultrasonography in assessing deglutitive tongue movements in healthy adults. Med Sci Monit. 2015;21:1648.
76. Avdiunina IA, Popova LM, Dokuchaeva NV, et al. Videofluoroscopy study of swallowing in neurogenic dysphagia. Anesteziol Reanimatol. 2000;4:64–8. [in Russian]
77. Rivelsrud MC, Osten PE, Conradi S, et al. Videofluoroscopy in the examination of swallowing disorders. A useful method for evaluation of rehabilitation. Tidsskr Nor Laegeforen. 1995;115(10):1241–3. [in Norwegian]
78. Olszewska E, Rutkowska J, Czajkowska A, et al. Selected surgical managements in snoring and obstructive sleep apnea patients. Med Sci Monit. 2012;18(1):CR13–8.
79. Vaiman M, Eviatar E, Segal S. Surface electromyographic studies of swallowing in normal subjects: a review of 440 adults. Report 2. Quantitative data: amplitude measures. Otolaryngol Head Neck Surg. 2004;131(5):773–80.
80. McNamara JAJ, Moyers RE. Electromyography of the oral phase of deglutition in the rhesus monkey (Macaca mulatta). Arch Oral Biol. 1973;18(8):995–1002.
81. Vaiman M, Krakovski D, Haitov Z. Oxycodone and dexamethasone for pain management after tonsillectomy: a placebo-controlled EMG assessed clinical trial. Med Sci Monit. 2011;17(10):PI25–31.
82. Steele CM, Van Lieshout PH. Use of electromagnetic midsagittal articulography in the study of swallowing. J Speech Lang Hear Res. 2004;47(2):342–52.
83. Chi-Fishman G, Stone M. A new application for electropalatography: swallowing. Dysphagia. 1996;11(4):239–47.
84. Hartl DM, Albiter M, Kolb F, et al. Morphologic parameters of normal swallowing events using single-shot fast spin echo dynamic MRI. Dysphagia. 2003;18(4):55–62.
85. Valenza V, Galli J, Romano L, et al. Oropharyngoesophageal scintigraphy in the evaluation of swallowing disorders after surgery for oral cancer. Clin Nucl Med. 2001;26(12):1054–7.
86. Ono T, Hori K, Nokubi T. Pattern of tongue pressure on hard palate during swallowing. Dysphagia. 2004;19(4):259–64.
87. Logemann JA. Swallowing physiology and pathophysiology. Otolaryngol Clin N Am. 1988;21(4):613–23.

88. Logemann JA. Approaches to management of disordered swallowing. Baillieres Clin Gastroenterol. 1991;5(2):269–80.
89. Logemann JA. Dysphagia: evaluation and treatment. Folia Phoniatr Logop. 1995;47(3):140–64.
90. Kujawski K, Stasiak M, Rysz J. The evaluation of esophageal stenting complications in palliative treatment of dysphagia related to esophageal cancer. Med Sci Monit. 2012;18(5):CR323–9.
91. Tamburrini S, Solazzo A, Sagnelli A, et al. Amyotrophic lateral sclerosis: sonographic evaluation of dysphagia. Radiol Med. 2010;115(5):784–93.
92. Shawker TH, Sonies B, Stone M, Baum BJ. Real-time ultrasound visualization of tongue movement during swallowing. J Clin Ultrasound. 1983;11:485–90.
93. Peng CL, Jost-Brinkmann PG, Lin CT. Classification and interpretation of the oral swallowing phase with BM mode ultrasound. Radiologe. 1995;35:747–52.
94. Peng CL, Jost-Brinkmann PG, Miethke RR, Lin CT. Ultrasonographic measurement of tongue movement during swallowing. J Ultrasound Med. 2000;19:15–20.
95. Peng CL, Jost-Brinkmann PG, Miethke RR. The cushion scanning technique: a method of dynamic tongue sonography and its comparison with the transducer-skin coupling scanning technique during swallowing. Acad Radiol. 1996;3(3):239–44.
96. Cheng CF, Peng CL, Chiou HY, Tsai CY. Dentofacial morphology and tongue function during swallowing. Am J Orthod Dentofac Orthop. 2002;122(5):491–9.
97. Peng CL, Jost-Brinkmann PG, Yoshida N, Chou HH, Lin CT. Comparison of tongue functions between mature and tongue-thrust swallowing—an ultrasound investigation. Am J Orthod Dentofac Orthop. 2004;125(5):562–70.
98. Ardakani FE. Evaluation of swallowing patterns of the tongue using real-time B-mode sonography. J Contemp Dent Pract. 2006;7(3):67–74.
99. Vaishnevi NT, Rajasekharan A, Aravind D, Kumar A. The assessment of relationship between facial morphology and tongue function during swallowing-an ultrasound study. J Dent Med Sci. 2014;13(9):49–58.
100. Chi-Fishman G, Sonies BC. Effects of systematic bolus viscosity and volume changes on hyoid bone kinematics. Dysphagia. 2002;17:278.
101. Chi-Fishman G, Sonies BC. Kinematic strategies for hyoid movement in rapid sequential swallowing. J Speech Lang Hear Res. 2002;45:457.
102. Frattali CM, Sonies BC, Chi-Fishman G, et al. Effects of physostigmine on swallowing and oral motor functions in patients with progressive supranuclear palsy: a pilot study. Dysphagia. 1999;14:165.
103. Kuhl V, Eicke BM, Dieterich M, et al. Sonographic analysis of laryngeal elevation during swallowing. J Neurol. 2003;250:333.
104. Shawker TH, Sonies B, Stone M, et al. Real time ultrasound visualization of tongue movement during swallowing. J Clin Ultrasound. 1983;11:485.
105. Shawker TH, Sonies B, Hall TE, et al. Ultrasound analysis of tongue, hyoid, and larynx activity during swallowing. Investig Radiol. 1984;19:82.
106. Soder N, Miller N. Using ultrasound to investigate intrapersonal variability in durational aspects of tongue movement during swallowing. Dysphagia. 2002;17:288.
107. Sonies BC, Parent LJ, Morrish K, et al. Durational aspects of the oral-pharyngeal phase of swallow in normal adults. Dysphagia. 1988;3:1.
108. Logemann JA. Evaluation and treatment of swallowing disorders. Nerang, QLD: Pro-Ed Australia; 1983.
109. Ekberg O. The normal movements of the hyoid bone during swallow. Investig Radiol. 1986;21:408e10.
110. Scarborough DR, Waizenhofer S, Siekemeyer L, Hughes M. Sonographically measured hyoid bone displacement during swallow in preschool children: a preliminary study. J Clin Ultrasound. 2010;38(8):430–4.
111. Yabunaka K, Sanada H, Sanada S, Konishi H, Hashimoto T, Yatake H, et al. Sonographic assessment of hyoid bone movement during swallowing: a study of normal adults with advancing age. Radiol Phys Technol. 2011;4(1):73–7.
112. Chen YC, Hsiao MY, Wang YC, Fu CP, Wang TG. Reliability of ultrasonography in evaluating hyoid bone movement. J Med Ultrasound. 2017;25(2):90–5.
113. Feng X, Cartwright MS, Walker FO, Bargoil JH, Hu Y, Butler SG. Ultrasonographic evaluation of geniohyoid muscle and hyoid bone during swallowing in young adults. Laryngoscope. 2015;125(8):1886–91.
114. Miles PG, Vig PS, Weyant RJ, Forrest TD, Rockette HE Jr. Craniofacial structure and obstructive sleep apnea syndrome: a qualitative analysis and meta-analysis of the literature. Am J Orthod Dentofac Orthop. 1996;109:163–72.
115. Mah JK, Yi L, Huang RC, Choo H. Advanced applications of cone beam computed tomography in orthodontics. Semin Orthod. 2011;17:57–71.
116. Schwab RJ. Upper airway imaging. Clin Chest Med. 1998;19:33–54.
117. Schwab RJ, Goldberg AN. Upper airway assessment: radiographic and other imaging techniques. Otolaryngol Clin N Am. 1998;31:931–68.
118. Stuck BA, Maurer JT. Airway evaluation in obstructive sleep apnea. Sleep Med Rev. 2008;12:411–36.
119. Kuo GP, Torok CM, Aygun N, Zinreich SJ. Diagnostic imaging of the upper airway. Proc Am Thorac Soc. 2011;8:40–5.
120. Singh M, Chin KJ, Chan VW, Wong DT, Prasad GA, Yu E. Use of sonography for airway assessment: an observational study. J Ultrasound Med. 2010;29(1):79–85.
121. Kristensen MS. Ultrasonography in the management of the airway. Acta Anaesthesiol Scand. 2011;55(10):1155–73.

122. Osman A, Sum KM. Role of upper airway ultrasound in airway management. J Intensive Care. 2016;4(1):52.
123. Cata JP. Ultrasound-assisted evaluation of the airway in clinical anesthesia practice: past, present and future. Int J. 2015;1(1):2.
124. Salemi F, Shokri A, Maleki FH, Farhadian M, Dashti G, Ostovarrad F, Ranjzad H. Effect of field of view on detection of condyle bone defects using cone beam computed tomography. J Craniofac Surg. 2016;27(3):644–8.
125. Kundu H, Basavaraj P, Kote S, Singla A, Singh S. Assessment of TMJ disorders using ultrasonography as a diagnostic tool: a review. J Clin Diagn Res. 2013;7:3116–20.
126. Klatkiewicz T, Gawriołek K, Radzikowska MP, Czajka-Jakubowska A. Ultrasonography in the diagnosis of temporomandibular disorders: a meta-analysis. Med Sci Monit. 2018;24:812–7.
127. Svensson B, Adell R, Kopp S. Temporomandibular disorders in juvenile chronic arthritis patients. A clinical study. Swed Dent J. 2000;24:83–92.
128. Barghan S, Tetradis S, Mallya SM. Application of cone beam computed tomography for assessment of the temporomandibular joints. Aust Dent J. 2012;57(s1):109–18.
129. Bag AK, Gaddikeri S, Singhal A, et al. Imaging of the temporomandibular joint: an update. World J Radiol. 2014;28:567–82.
130. Petscavage-Thomas JM, Walker EA. Unlocking the jaw: advanced imaging of the temporomandibular joint. Am J Roentgenol. 2014;203:1047–58.
131. Gateno J, Miloro M, Hendler BH, Horrow M. The use of ultrasound to determine the position of the mandibular condyle. J Oral Maxillofac Surg. 1993;51(10):1081–6.
132. Parmar R, Reddy V, Reddy SK, Reddy D. Determination of soft tissue thickness at orthodontic miniscrew placement sites using ultrasonography for customizing screw selection. Am J Orthod Dentofac Orthop. 2016;150(4):651–8.
133. Deguchi T, Takano-Yamamoto T, Kanomi R, Hartsfield JK Jr, Roberts WE, Garetto LP. The use of small titanium screws for orthodontic anchorage. J Dent Res. 2003;82:377–81.
134. Miyawaki S, Koyama I, Inoue M, Mishima K, Sugahara T, Takano-Yamamoto T. Factors associated with the stability of titanium screws placed in the posterior region for orthodontic anchorage. Am J Orthod Dentofac Orthop. 2003;124:373–8.
135. Cheng SJ, Tseng IY, Lee JJ, Kok SH. A prospective study of the risk factors associated with failure of mini-implants used for orthodontic anchorage. Int J Oral Maxillofac Implants. 2004;19:100–6.
136. Kim JW, Ahn SJ, Chang YI. Histomorphometric and mechanical analyses of the drill-free screw as orthodontic anchorage. Am J Orthod Dentofac Orthop. 2005;128:190–4.
137. Cho HJ. Clinical applications of mini-implants as orthodontic anchorage and the peri-implant tissue reaction upon loading. J Calif Dent Assoc. 2006;34:813–20.
138. Park HS, Jeong SH, Kwon OW. Factors affecting the clinical success of screw implants used as orthodontic anchorage. Am J Orthod Dentofac Orthop. 2006;130:18–25.
139. Kuroda S, Sugawara Y, Deguchi T, Kyung HM, Takano-Yamamoto T. Clinical use of miniscrew implants as orthodontic anchorage: success rates and postoperative discomfort. Am J Orthod Dentofac Orthop. 2007;131:9–15.
140. Park HS, Kwon TG, Sung JH. Non-extraction treatment with microscrew implants. Angle Orthod. 2004;74:539–49.
141. Cha BK, Lee YH, Lee NK, Choi DS, Baek SH. Soft tissue thickness for placement of an orthodontic miniscrew using an ultrasonic device. Angle Orthod. 2008;78(3):403–8.
142. Schulze RK, Ćurić D, d'Hoedt B. B-mode versus A-mode ultrasonographic measurements of mucosal thickness in vivo. Oral Surg Oral Med Oral Pathol Oral Radiol Endod. 2002;93(1):110–7.
143. Cacciafesta V, Bumann A, Cho JH, Graham JW, Paquette DE, Park HS, et al. Skeletal anchorage: part I. J Clin Orthod. 2009;43:303–17.
144. Kim HJ, Yun HS, Park HD, Kim DH, Park YC. Soft-tissue and cortical-bone thickness at orthodontic implant sites. Am J Orthod Dentofac Orthop. 2006;130:177–82.
145. Muller HP, Barrieshi-Nusair KM, Kononen E. Repeatability of ultrasonic determination of gingival thickness. Clin Oral Investig. 2007;11:439–42.
146. Muller HP, Kononen E. Variance components of gingival thickness. J Periodontal Res. 2005;40:239–44.
147. Tzoumpas M, Mohr B, Kurtulus-Waschulewski I, Wahl G. The use of high-frequency ultrasound in the measurement of thickness of the maxillary attached gingiva. Int J Prosthodont. 2015;28:374–82.
148. Furtak A, Leszczynska E, Sender-Janeczek A, Bednarz W. The repeatability and reproducibility of gingival thickness measurement with an ultrasonic device. Dent Med Probl. 2018;55:281–8.
149. Rajpoot N, Nayak A, Nayak R, Bankur PK. Evaluation of variation in the palatal gingival biotypes using an ultrasound device. J Clin Diagn Res. 2015;9:ZC56–60.
150. Pelsmaekers B, Loos R, Carels C, Derom C, Vlietinck R. The genetic contribution to dental maturation. J Dent Res. 1997;76:1337–40.
151. Schmidt S, Schibor M, Pfeiffer H, Schmeling A, Schulz R. Age dependence of epiphyseal ossification of the distal radius in ultrasound diagnostics. Int J Legal Med. 2013;127(4):831–8.
152. Torenek Ağırman K, Bilge OM, Miloğlu Ö. Ultrasonography in determining pubertal growth and bone age. Dentomaxillofac Radiol. 2018;47(7):20170398.
153. Roche AF. A study of skeletal maturation in a group of Melbourn children. Aust Paediatr J. 1967;3:123–7.

154. Paesano PL, Vigone MC, Siragusa V, Chiumello G, Maschio AD, Mora S. Assessment of skeletal maturation in infants: comparison between 2 methods in hypothyroid patients. Pediatr Radiol. 1998;28:622–6.
155. Tanner JM, Whitehouse RH, Marshall WA, Healy MJR, Goldstein H. Assessment of skeletal maturity and prediction of adult height (TW method). 2nd ed. London: Academic Press; 1983.
156. Greulich WW, Pyle SI. Radiographic atlas of skeletal development of the hand and wrist. 2nd ed. Stanford, CA: Stanford University Press; 1959.
157. Bilgili Y, Hizel S, Kara SA, Sanli C, Erdal HH, Altinok D. Accuracy of skeletal age assessment in children from birth to 6 years of age with the ultrasonographic version of the Greulich-Pyle atlas. J Ultrasound Med. 2003;22(7):683–90.
158. Castriota-Scanderbeg A, Sacco MC, Emberti-Gialloreti L, Fraracci L. Skeletal age assessment in children and young adults: comparison between a newly developed sonographic method and conventional methods. Skelet Radiol. 1998;27(5):271–7.
159. Wagner UA, Diedrich V, Schmitt O. Determination of skeletal maturity by ultrasound: a preliminary report. Skelet Radiol. 1995;24(6):417–20.
160. Nessi R, Garattini G, Bazzini E, Zaffaroni R, Lazzerini F. Ultrasonography assessment of ossification foci of the wrist and pubertal growth spurt. La Radiol Med. 1997;94(1–2):43–6.
161. Carpenter CT, Lester EL. Skeletal age determination in young children: analysis of three regions of the hand/wrist film. J Pediatr Orthop. 1993;13(1):76–9.
162. Daneff M, Casalis C, Bruno CH, Bruno DA. Bone age assessment with conventional ultrasonography in healthy infants from 1 to 24 months of age. Pediatr Radiol. 2015;45:1007–15.
163. Khan KM, Sarafoglou K, Somani A, Frohnert B, Miller BS. Can ultrasound be used to estimate bone mineral density in children with growth problems? Acta Paediatr. 2013;102(9):e407–12.
164. Aloufi F, Preston CB, Zawawi KH. Changes in the upper and lower pharyngeal airway spaces associated with rapid maxillary expansion. ISRN Dent. 2012;2012:290964.
165. Vidya VS, Sumathi FA. Rapid maxillary expansion as a standard treatment for obstructive sleep apnea syndrome: a systematic review. J Dent Med Sci. 2015;14(2):51–5.
166. Jang HI, Kim SC, Chae JM, Kang KH, Cho JW, Chang NY, et al. Relationship between maturation indices and morphology of the midpalatal suture obtained using cone-beam computed tomography images. Kor J Orthod. 2016;46(6):345–55.
167. Suri L, Taneja P. Surgically assisted rapid palatal expansion: a literature review. Am J Orthod Dentofac Orthop. 2008;133(2):290–302.
168. McNamara JA, Brudon WL. Orthodontics and dentofacial orthopedics. Ann Arbor: Needham Press; 1995. p. 211e2.
169. Silva Filho OG, Magro AC, Capelozza FI. Early treatment of the class III malocclusion with rapid maxillary expansion and maxillary protraction. Am J Orthod Dentofac Orthop. 1998;113(2):196–203.
170. Sumer AP, Ozer M, Sumer M, Danaci M, Tokalak F, Telcioglu NT. Ultrasonography in the evaluation of midpalatal suture in surgically assisted rapid maxillary expansion. J Craniofac Surg. 2012;23(5):1375–7.
171. Maffulli N, Hughes T, Fixsen JA. Ultrasonographic monitoring of limb lengthening. J Bone Joint Surg. 1992;74:130Y132.
172. Derbyshire ND, Simpson AH. A role for ultrasound in limb lengthening. Br J Radiol. 1992;65:576Y580.
173. Gumussoy I, Miloglu O, Bayrakdar IS, Dagistan S, Caglayan F. Ultrasonography in the evaluation of the mid-palatal suture in rapid palatal expansion. Dentomaxillofac Radiol. 2014;43(8):20140167.
174. Rygh P, Brudvik P. The histological responses of the periodontal ligament to horizontal orthodontic loads. In: Berkovitz BB, Moxham BJ, Newman HN, editors. The periodontal ligament in health and disease. St Louis: Mosby; 1995.
175. Zimbran A, Dudea D, Gasparik C, Dudea S. Ultrasonographic evaluation of periodontal changes during orthodontic tooth movement-work in progress. Clujul Med. 2017;90(1):93.
176. Zimbran A, Dudea S, Dudea D. Evaluation of periodontal tissues using 40 MHz ultrasonography. Preliminary report. Med Ultrason. 2013;15(1):6–9.
177. Chifor R, Hedeşiu M, Bolfa P, Catoi C, Crişan M, Serbănescu A, et al. The evaluation of 20 Mhz ultrasonography, computed tomography scans as compared to direct microscopy of periodontal system assessment. Med Ultrason. 2011;13(2):120–6.
178. Tsesis I, Fuss Z, Rosenberg E, Taicher S. Radiographic evaluation of the prevalence of root resorption in a Middle Eastern population. Quintessence Int. 2008;39:e40–4.
179. Harry MR, Sims MR. Root resorption in bicuspid intrusion. A scanning electron microscope study. Angle Orthod. 1982;52:235–58.
180. Lund H, Gröndahl K, Hansen K, Gröndahl H-G. Apical root resorption during orthodontic treatment. A prospective study using cone beam CT. Angle Orthod. 2012;82:480–7.
181. Mirabella AD, Artun J. Risk factors for apical root resorption of maxillary anterior teeth in adult orthodontic patients. Am J Orthod Dentofac Orthop. 1995b;108:48–55.
182. Kaley J, Philips C. Factors related to root resorption in edgewise practice. Angle Orthod. 1991;61:125–32.
183. Sasaki T. Differentiation and functions of osteoclasts and odontoclasts in mineralized tissue resorption. Microsc Res Tech. 2003;61:483–95.
184. Reitan K. Biomechanical principals and reactions. In: Vanarsdall RL, Graber TM, editors. Orthodontics: current principals and techniques. Saint Louis, PA: Mosby; 1985. p. 101–92.

185. Hoeve T, Mulie MR. The effect of antero-posterior incisor repositioning on the palatal cortex as studied with laminography. J Clin Orthod. 1976;10:802–22.
186. Sharpe W, Reed B, Subtelny JD, Polson A. Orthodontic relapse, apical root resorption, and crestal alveolar bone levels. Am J Orthod Dentofac Orthop. 1987;91:252–8.
187. Igarashi K, Adachi H, Mitani H, Shinoda H. Inhibitory effect of the topical administration of a bisphosphonate (risedronate) on root resorption incident to orthodontic tooth movement in rats. J Dent Res. 1996;75:1644–9.
188. Owman-Moll P, Kurol J, Lundgren D. Repair of orthodontically induced root resorption in adolescents. Angle Orthod. 1995;65:403–8. Discussion 409–410
189. Keum K-Y, Kwon O-T, Spängberg LS, Kim C-K, Kim J, Cho M-I, et al. Effect of dexamethasone on root resorption after delayed replantation of rat tooth. J Endod. 2003;29:810–3.
190. Aqrabawi J, Jamani K. Severe external root resorption arrested by conventional endodontic treatment. Dent Update. 2005;32:224–6.
191. El-Bialy T, El-Shamy I, Graber TM. Repair of orthodontically induced root resorption by ultrasound in humans. Am J Orthod Dentofac Orthop. 2004;126:186–93.
192. Raza H, Major PW, Dederich D, El-Bialy T. Effect of low-intensity pulsed ultrasound on orthodontically induced root resorption caused by torque: A prospective double-blind controlled clinical trial. Angle Orthod. 2016;35(2):349–58.
193. Al-Daghreer S, Doschak MR, Sloane AJ, Major PW, Heo G, Scurtescu C, Tsui YY, El-Bialy T. Effect of LIPUS on orthodontically induced root resorption in beagle dogs. Ultrasound Med Biol. 2014;40(6):1187–96.
194. Inubushi T, Tanaka E, Rego EB, Ohtani J, Kawazoe A, Tanne K, Miyauchi M, Takata T. Low-intensity ultrasound stimulation inhibits resorption of the tooth root induced by experimental force application. Bone. 2013;53:497–506.
195. Liu Z, Xu J, E L, Wang D. Ultrasound enhances the healing of orthodontically induced root resorption in rats. Angle Orthod. 2012;82:48–55.
196. Rego EB, Inubushi T, Miyauchi M, Kawazoe A, Tanaka E, Takata T, Tanne K. Ultrasound stimulation attenuates root resorption on rat replanted molars and impairs TNF-α signaling in vitro. J Periodontal Res. 2011;46:648–54.
197. El-Bialy T, Hassan AH, Alyamani A, Albaghdadi T. Treatment of hemifacial microsomia by therapeutic ultrasound and hybrid functional appliance. A non-surgical approach. J Clin Trials. 2010;2:29–36.
198. Inubushi T, Tanaka E, Rego EB, Kitagawa M, Kawazoe A, Ohta A, Okada H, Koolstra JH, Miyauchi M, Takata T, Tanne K. Effects of ultrasound on the proliferation and differentiation of cementoblast lineage cells. J Periodontol. 2008;79:1984–90.
199. El-Bialy TH, Zaki AE, Evans CA. Effect of ultrasound on rabbit mandibular incisor formation and eruption after mandibular osteodistraction. Am J Orthod Dentofac Orthop. 2003;124:427–34.
200. Showkatbakhsh R, Jamilian A, Showkatbakhsh M. The effect of pulsed electromagnetic fields on the acceleration of tooth movement. World J Orthod. 2010;11:52–6.
201. Kim DH, Park YG, Kang SG. The effects of electrical current from a micro-electrical device on tooth movement. Kor J Orthod. 2008;38:337.
202. Hassan AH, Al-Fraidi AA, Al-Saeed SH. Corticotomy-assisted orthodontic treatment: review. Open Dent J. 2010;13:159–64.
203. Işeri H, Kişnişci R, Bzizi N, Tüz H. Rapid canine retraction and orthodontic treatment with dentoalveolar distraction osteogenesis. Am J Orthod Dentofac Orthop. 2005;127:533–41.
204. Nishimura M, Chiba M, Ohashi T, Sato M, Shimizu Y, Igarashi K, Mitani H. Periodontal tissue activation by vibration: intermittent stimulation by resonance vibration accelerates experimental tooth movement in rats. Am J Orthod Dentofac Orthop. 2008;133:572–83.
205. Ojima K, Dan C, Kumagai Y, Schupp W. Invisalign treatment accelerated by photobiomodulation. J Clin Orthod. 2016;50:309–17.
206. Yamaguchi M, Hayashi M, Fujita S, Yoshida T, Utsunomiya T, Yamamoto H, Kasai K. Low-energy laser irradiation facilitates the velocity of tooth movement and the expressions of matrix metalloproteinase-9, cathepsin K, and alpha(v) beta(3) integrin in rats. Eur J Orthod. 2010;32:131–9.
207. Wijdicks CA, Virdi AS, Sena K, Sumner DR, Leven RM. Ultrasound enhances recombinant human BMP-2 induced ectopic bone formation in a rat model. Ultrasound Med Biol. 2009;35:1629–37.
208. Qamruddin I, Alam MK, Khamis MF, et al. Minimally invasive techniques to accelerate the orthodontic tooth movement: a systemic review of animal studies. Biomed Res Int. 2015;2015:608530.
209. Lou S, Lv H, Li Z, Tang P, Wang Y. Effect of low-intensity pulsed ultrasound on distraction osteogenesis: a systematic review and meta-analysis of randomized controlled trials. J Orthop Surg Res. 2018;13(1):205.
210. Maung WM, Nakata H, Miura M, Miyasaka M, Kim YK, Kasugai S, Kuroda S. Low-intensity pulsed ultrasound stimulates osteogenic differentiation of periosteal cells in vitro. Tissue Eng Part A. 2020; https://doi.org/10.1089/ten.TEA.2019.0331. [Epub ahead of print]

Ultrasonography Imaging in Endodontics

16

Kaan Orhan and Hakan Eren

Contents

16.1 Introduction

Etiology of the dental infections can be broadly classified into mechanical including trauma, fractures, bruxism, and thermal changes; chemical including various acidic substances; and bacterial including caries, microleakage or periodontal infections [1]. Although the periapical region is an area where lesions are commonly seen, most of these lesions are of inflammatory origin [2]. Dental pulp consists of vascular connective tissue and various factors like physical, chemical, or bacterial factors can affect it resulting in the onset of the inflammatory process leading to apical lesions.

Periapical radiographs together with clinical examination as a gold standard are often sufficient without the need for CBCT imaging in the diagnosis, treatment, and follow-up of inflammatory lesions [3–5]. Inflammatory process not only describes periapical bone loss but also consists of all the dynamic host responses to the infection, and conventional radiographs are not able to provide information about these variables [6, 7]. Thus, there is a need for an extra imaging modality in the diagnosis, treatment, and follow-up stages to monitorize the content of the lesion, tissue architecture, vascularity, and mineralization.

Ultrasonography (USG) is a real-time, noninvasive, and nonionizing imaging method that is able to collect information about content, vascularity, and more by obtaining images of apical lesions as an assistive imaging procedure to conventional radiographs [8, 9]. Besides, in order for an inflammatory process to be imaged by ultrasonography, it must cause changes in periapical tissues or lead to buccal cortical resorption. Therefore, reversible or irreversible pulpitis can not be imaged by ultrasonography unless they

K. Orhan (✉) · H. Eren
Faculty of Dentistry, Department of Dentomaxillofacial Radiology, Ankara University, Ankara, Turkey

K. Orhan (ed.), *Ultrasonography in Dentomaxillofacial Diagnostics*,
https://doi.org/10.1007/978-3-030-62179-7_16

cause any severe changes in periapical tissues, after which they become periapical infections. Eventually, USG has over 95% accuracy and very high sensitivity and specificity in diagnosing periapical lesions as compared to conventional and digital radiography [10].

Periapical lesions are classified into six main groups:

- Normal periapical tissues,
- Symptomatic (acute) apical periodontitis,
- Asymptomatic (chronic) apical periodontitis,
- Condensing osteitis,
- Acute apical abscess,
- Chronic apical abscess.

Lesions associated with significant symptoms, such as pain or swelling, are referred to as acute or symptomatic, whereas those with mild or no symptoms are identified as chronic or asymptomatic [11].

Condensing osteitis is usually asymptomatic variation of apical infection, and is characterized by an increase of bone trabeculation related with persistent irritant factor. Therefore, if there is no secondary infection in soft tissue, it cannot be visualized by USG.

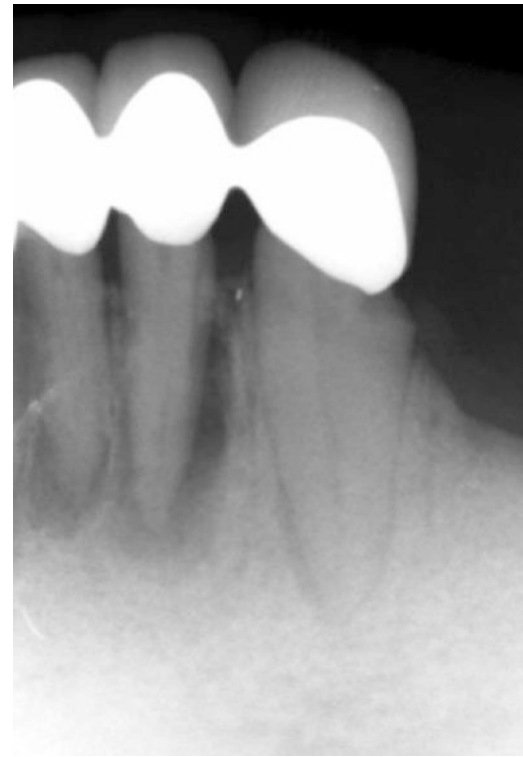

Fig. 16.1 Periapical radiograph of acute (Symptomatic) apical periodontitis detected in periapical region of tooth #33 related with inappropriate dental restoration. There is a slight resorption medially in lamina dura

16.2 Acute Apical Periodontitis

Acute apical periodontitis is a painful inflammation of periodontium arising from trauma, irritation, or pulpal infection. It is an acute condition that occurs when inflammation spreads rapidly to the periradicular region for the first time. It is generally located around the apex of the root. Normally buccal cortical resorption is not expected, but periosteal reaction can be seen. Thus, changes in periapical tissues can be displayed in USG examination if cortical resorption occurs or periosteal reaction develops. Also, increased blood supply can be seen around the related region (Figs. 16.1, 16.2, and 16.3).

16.3 Chronic Apical Periodontitis

Chronic or asymptomatic apical periodontitis develops after pulp necrosis and it usually remains as a sequel of symptomatic apical paradontitis. These lesions are mostly detected on routine radiographic examination, and sometimes previously performed root canal treatment in the relevant tooth can be present. Buccal cortical resorption can allow the lesion to be visualized by USG. Vascularity is an important finding in the differentiation of cystic and granular lesions in high compatibility with histopathological examination (Figs. 16.4, 16.5, and 16.6) [12].

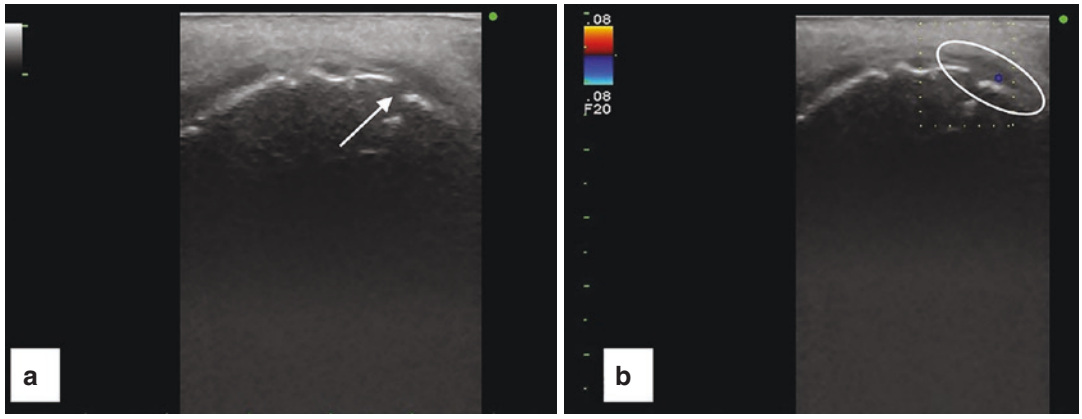

Fig. 16.2 USG images of the same patient in transversal position. Buccal cortical resorption can be clearly seen (white arrow) as an anechoic interruption of hyperechoic buccal cortex in periapical region of tooth #33, also periosteal reaction (white ring) can be noticed as uncertain bordered hypoechoic dome-like appearance in the related buccal area with a slightly increased blood supply distally

Fig. 16.3 Intraoral clinical appearance of the patient. There is no swelling or fistula related to tooth #33. Besides, incompatibility in prosthetic restoration can be noticed

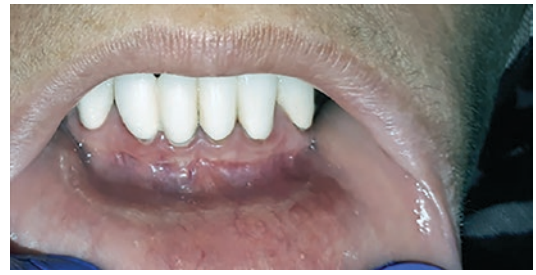

Fig. 16.4 Chronic apical paradontitis detected in tooth #24 without any clinical signs or symptoms (white arrow). Root canal treatment has been performed previously in the relevant tooth

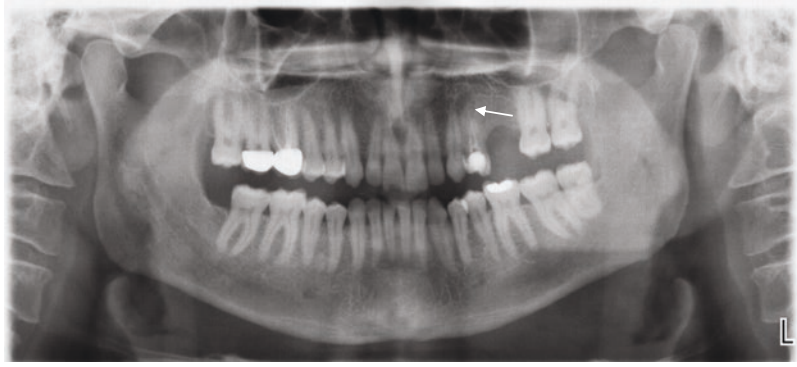

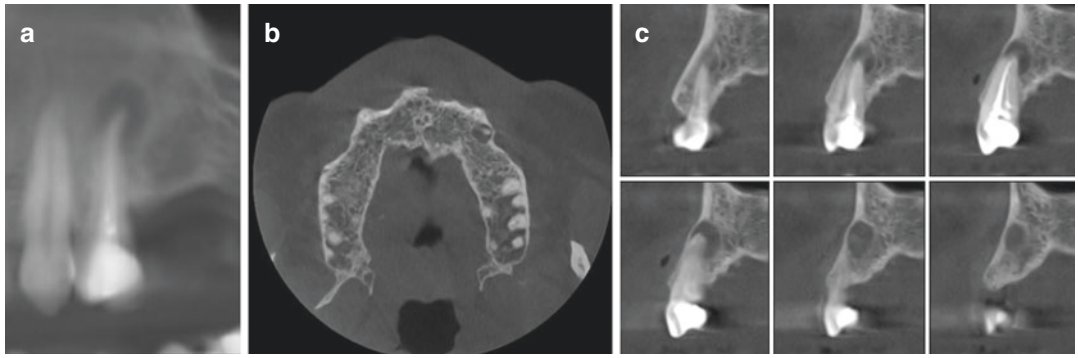

Fig. 16.5 Cone beam CT examination of the same patient. Panoramic (**a**), axial (**b**), and cross-sectional images are showing a well-defined radiolucent apical lesion with previously treated tooth. It is observed in cross-sectional sections that the buccal cortex still maintains its continuity

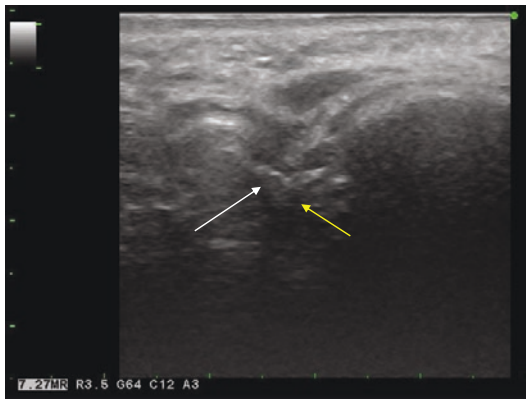

Fig. 16.6 Transversal USG image is showing a slight hypoechoic area (white arrow) around the apex of tooth #24 (yellow arrow) appearing as hyperechoic. Although the buccal cortex is not completely resorbed, the lesion hidden behind it can be visualized with USG because of the thinning of cortical bone. However, it does not give a very clear picture

16.4 Acute Apical Abscess

Acute abscess is a diffused or localized lesion of the tooth in the alveolar bone that causes destruction of periradicular tissues and provokes acute severe inflammatory response to the necrotic pulp as the origin of the infection. The term "abscess" is not only used when infection destroys the periradicular tissues and can cause swelling of the face but also it generally has systemic manifestations such as elevated temperature, malaise, and leukocytosis with or without swelling. Radiographic features of acute abscess range from no changes to the widening of the PDL space to an obvious radiolucent lesion.

Abscess can be displayed as a hypoechoic pattern with well-defined or ill-defined borders by USG [13–15]. Increased vascularity is generally observed in color Doppler examination. Also, periosteal reaction can be seen in USG sections (Figs. 16.7, 16.8, 16.9, and 16.10).

16.5 Chronic Apical Abscess

The chronic apical abscess is a longstanding inflammatory lesion of pulpal origin. Tissue overlaying an abscess may become inflated from the pressure of underlying pus and it can rupture. The pus comes out in an opening after the rupture of the tissue (mucosal or skin surface). This process is called chronic abscess. Chronic lesions are generally asymptomatic because of the drainage. Clinical and radiographic features of a chronic abscess are similar to an acute abscess except having a fistula in mucosa or skin surface.

USG findings are also the same as an acute abscess (a hypoechoic area over the hard tissue with or without a hyperechoic thin layer of periosteal reaction sign), but sometimes sinus tract can be displayed as a hypoechoic duct (Figs. 16.11, 16.12, and 16.13).

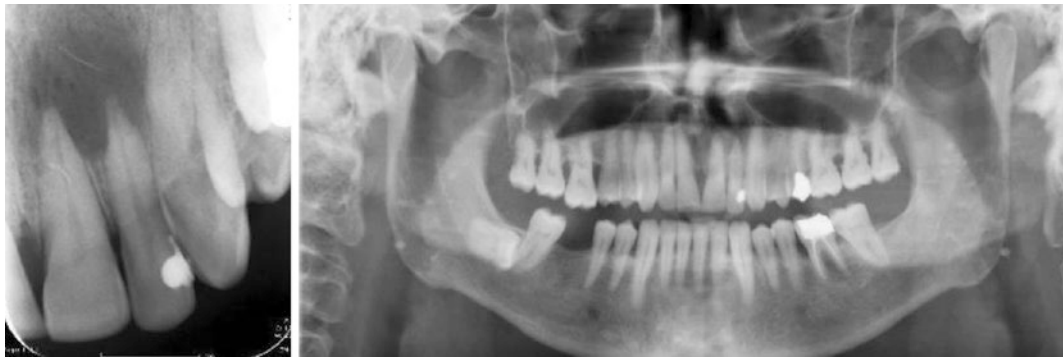

Fig. 16.7 Periapical and panoramic radiographs of the patient are showing the lesion of an acute apical abscess. An ill-defined lesion is localized at the apex of tooth #22

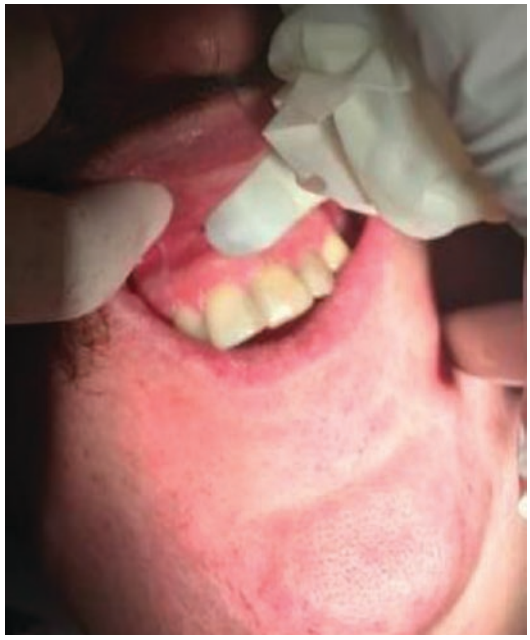

Fig. 16.8 Intraoral appearance of the same patient during the USG examination. There is a swelling in the buccal sulcus adjacent to the related tooth

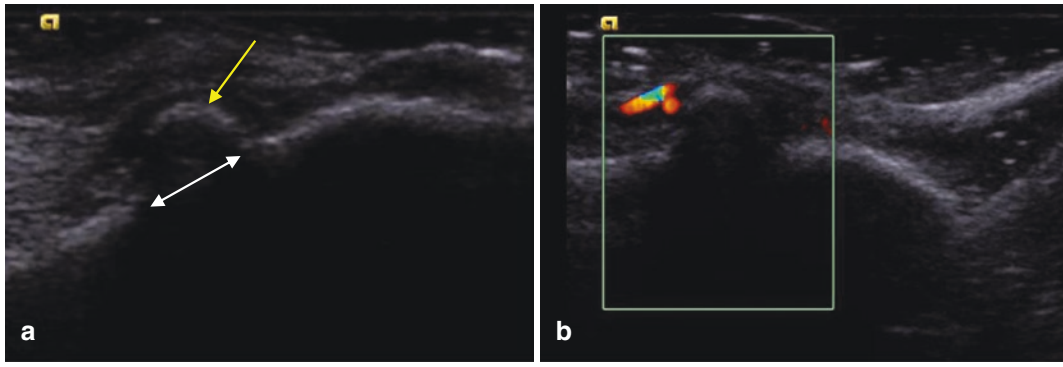

Fig. 16.9 Transversal USG examination of the same patient shows a buccal cortical resorption adjacent to the related tooth (white arrow) with periosteal reaction (yellow arrow) seen as a hyperechoic layer over the hypoechoic abscess area (**a**). Increased vascularity can be seen in the color Doppler examination (**b**)

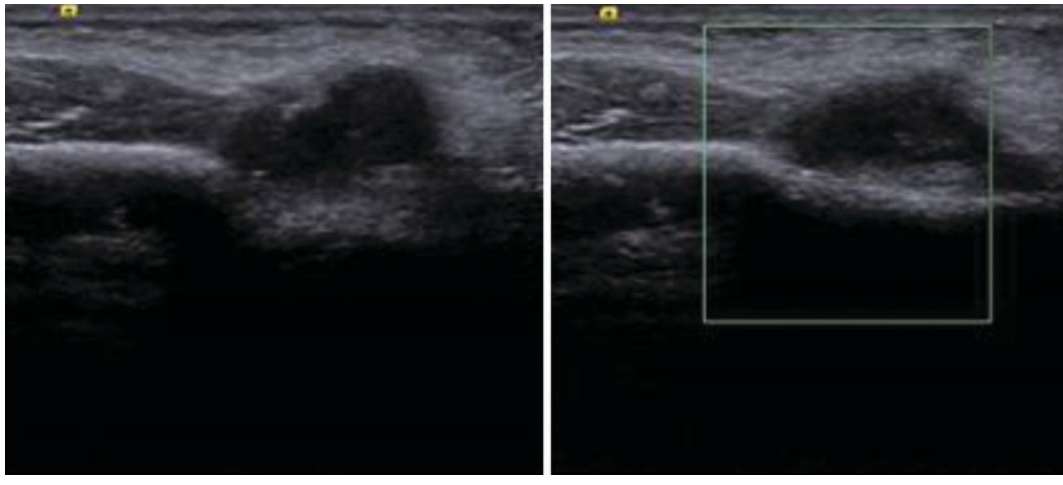

Fig. 16.10 Transversal USG examination is showing a case of antibiotoma; a pus-filled localized hard swelling in the soft tissue which occurs after long-term antibiotic use without draining an abscess. It is seen as a hypoechoic echo pattern and it does not have very pronounced borders without increased vascularity in the color Doppler examination

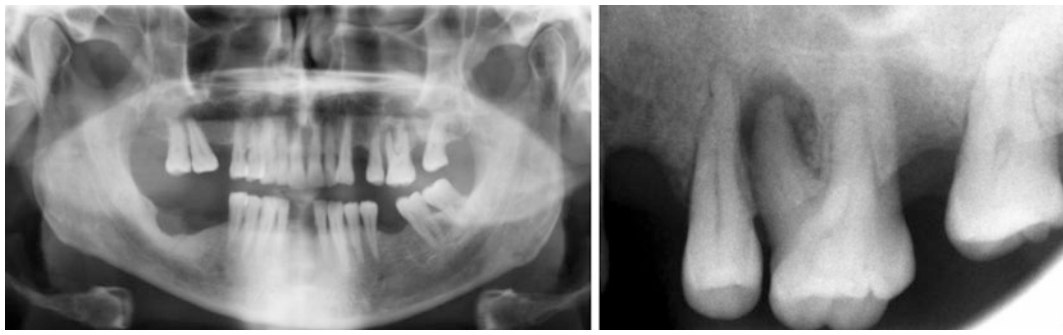

Fig. 16.11 Periapical and panoramic radiographs are showing a well-defined radiolucent lesion located all over the roots of tooth #26. It is noteworthy that there are no caries on the tooth. The lesion is due to periodontal infection

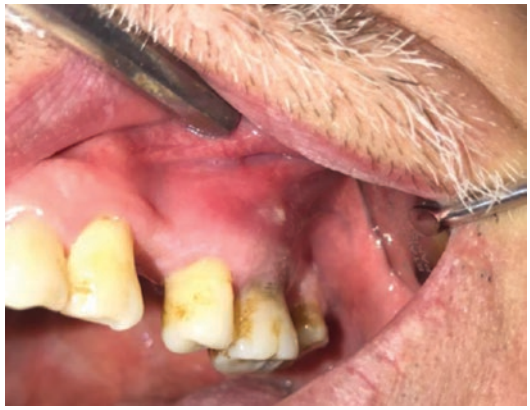

Fig. 16.12 Intraoral view of the same patient shows a fistula related to the mesial root of tooth #26 without any other clinical symptoms

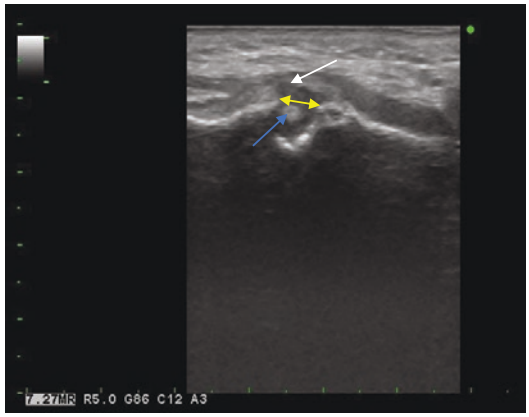

Fig. 16.13 Transversal USG image of the same patient shows a hypoechoic lesion around the mesial root of tooth #26 (blue arrow). Buccal cortical resorption can be clearly seen (yellow arrow) and fistula is observed as a hypoechoic duct that pierces the mucosa (white arrow)

References

1. Garg N, Garg A. Pathologies of pulp and periapex, Chapter 3. In: Textbook of endodontics. 3rd ed. New Delhi: Jaypee Brothers Medical Publishers; 2014. p. 22–50.
2. MacDonald D. Lesions of the jaws presenting as radiolucencies on cone-beam CT. Clin Radiol. 2016;71:972–85.
3. Torabinejad M, Rice DD, Maktabi O, Oyoyo U, Abramovitch K. Prevalence and size of periapical radiolucencies using cone-beam computed tomography in teeth without apparent intraoral radiographic lesions: a new periapical index with a clinical recommendation. J Endod. 2018;44:389–94.
4. European Society of Endodontology. Quality guidelines for endodontic treatment: consensus report of the European Society of Endodontology. Int Endod J. 2006;39:921–30.
5. AAE & AAOMR. American Association of Endodontists and American Academy of Oral & Maxillofacial Radiology joint position statement: use of cone beam computed tomography in endodontics update. J Endod. 2015;41:1393–6.
6. Nair PN. Apical periodontitis: a dynamic encounter between root canal infection and host response. Periodontol 2000. 1997;13:121–48.
7. Abbott PV. The periapical space: a dynamic interface. Aust Endod J. 2002;28:96–107.
8. Martin K. Basic equipment, components and image production. In: Allan PL, Baxter GM, Weston MJ, editors. Clinical ultrasound. 3rd ed. Edinburg: Churchill Livingstone; 2011. p. 16–30.
9. Cotti E, Campisi G, Garau V, Puddu G. A new technique for the study of periapical bone lesion: ultrasound real time imaging. Int Endod J. 2002;35:148–52.
10. Cotti E, Campisi G, Ambu R, Dettori C. Ultrasound real time imaging in differential diagnosis of periapical lesions. Int Endod J. 2003;36:556–63.
11. Torabinejad M, Shabahang S. Pulp and periapical pathosis, Chapter 4. In: Torabinejad M, Walton RE, Fouad AF, editors. Endodontics principles and practice. 5th ed. St. Louis, MO: Elsevier Saunders; 2015. p. 48–67.
12. Khambete N, Kumar R. Ultrasound in differential diagnosis of periapical radiolucencies: a radiohistopathological study. J Conserv Dent. 2015;18(1):39–43.
13. Zope SR, Talathi AA, Kamble A, et al. Efficiency of ultrasonography in swellings of orofacial region. Niger J Surg. 2018;24(2):82–9.
14. Saeed SS, Ibraheem UM, Alnema MM. The efficiency of ultrasound and Dopplor ultrasound in differential diagnosis of periapical lesions in Iraqi populations. Int J Enhanc Res Sci Technol Eng. 2014;3:72–9.
15. Chandak R, Degwekar S, Bhowte RR, Motwani M, Banode P, Chandak M, et al. An evaluation of efficacy of ultrasonography in the diagnosis of head and neck swellings. Dentomaxillofac Radiol. 2011;40:213–21.

17 Applications of Ultrasonography in Maxillofacial/Intraoral Inflammatory and Cystic Lesions

Kaan Orhan and Gürkan Ünsal

Contents

K. Orhan (✉)
Faculty of Dentistry, Department of Dentomaxillofacial Radiology, Ankara University, Ankara, Turkey

G. Ünsal
Faculty of Dentistry, Department of Dentomaxillofacial Radiology, Near East University, Nicosia, Cyprus

Near East University, DESAM Institute, Nicosia, Cyprus

17.1 Inflammatory Odontogenic Cysts

17.1.1 Radicular Cyst

Radicular cysts are the inflammatory odontogenic cysts associated with a non-vital tooth. A residual radicular cyst, which is often referred as

K. Orhan (ed.), *Ultrasonography in Dentomaxillofacial Diagnostics*,
https://doi.org/10.1007/978-3-030-62179-7_17

residual cyst, is also a radicular cyst that remains following the extraction of the associated tooth. Periapical cyst and apical periodontal cyst are also synonyms of the radicular cyst [1–3].

Radicular cysts represent 55% of all odontogenic cysts which makes them the most common cyst of the jawbones. They mostly occur due to dental caries which cause pulpal necrosis [1].

They are mostly located at the apex of the teeth but radicular cysts that occur at the apex of lateral root canals are also reported and they are known as "lateral radicular cysts" [2].

The most important differential diagnosis tool for radicular cysts is they are always associated at the apex or lateral of a non-vital tooth; thus, vitality test plays a crucial role [2, 3].

Unless they cause expansions they are detected incidentally on routine radiographs as round or oval, well-defined, unilocular radiolucent lesions at the apex of a non-vital tooth. Residual radicular cysts have the same radiographical features with radicular cyst; however, they are located at previously extracted teeth sites. Eventhough they are inflammatory odontogenic cysts, they can get secondarily infected and cause destructions at buccal and lingual cortical plates [1–3]. (Figs. 17.1 and 17.2). See also Chap. 16 for more detailed information on periapical diseases.

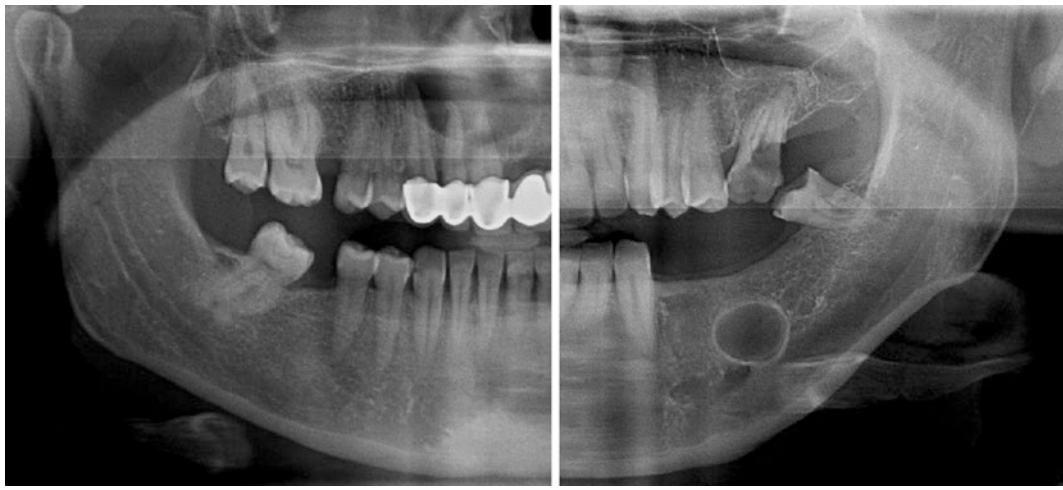

Fig. 17.1 A: Radicular Cyst/B: Residual Cyst. A: OPG reveals unilocular radiolucent lesion with a cortical well-defined border at maxillary anterior site. Roots of three teeth with crowns are seen in relation to the lesion. B: Unlike Fig. 17.2A, a unilocular radiolucent lesion with a corticated well-defined border is seen in the edentulous mandibular left posterior site

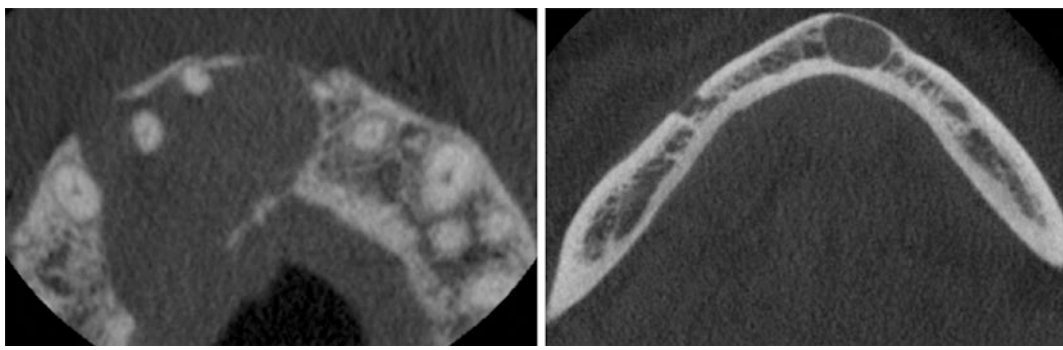

Fig. 17.2 A: Secondarily Infected Radicular Cyst/B: Residual Cyst. A: Axial CBCT slice reveals the destruction of the buccal and palatal cortical plates of the maxilla. Although odontogenic cysts cause expansion instead of destruction, secondarily infected cystic lesion cause more aggressive lytic patterns. B: Axial CBCT slice reveals unilocular hypodense lesion with hyperdense corticated well-defined border at edentulous site

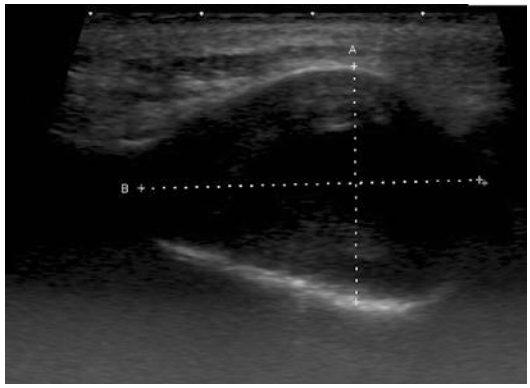

Fig. 17.3 Radicular Cyst. US reveals unilocular homogeneous anechoic lesion with a well-defined hyperechoic oval border. Acoustic enhancement is not clearly visible although the appearance suggests a cystic lesion

Common sonographic features of radicular cysts are (Fig. 17.3):

- Lesions without bone perforation or destruction at cortical plate or any bone dehiscences may not have ultrasonography findings due to artifacts such as acoustic shadowing.
- Internal Structure: Homogeneous anechoic internal structure is generally seen without any hyperechoic focis.
- Peripheral Structure: Well-defined hyperechoic oval or round borders are generally seen.

17.1.2 Inflammatory Collateral Cysts

Inflammatory collateral cysts are two entities which were known as buccal bifurcation cysts and paradental cysts. They account for 5% of odontogenic cysts. Most of the paradental cysts are associated with mandibular third molars and most of the buccal bifurcation cysts are associated with mandibular first molars [1].

Paradental cysts are well-defined, unilocular, radiolucent lesions which have similar features with dentigerous cyst. Paradental cysts are associated with partial unerupted teeth while dentigerous cysts are associated with complete unerupted teeth. Paradental cysts and pericoronitis share some clinical and radiographic features and WHO stated that "Paradental cysts are usually associated with a history of longstanding pericoronitis." [1].

Buccal bifurcation cysts are also well-defined, unilocular, radiolucent lesions and they have a characteristic clinical feature called "tilting." The crowns of the affected teeth are tilted buccally due to the lesion. They are generally painless swellings [1–3].

17.2 Developmental Odontogenic Cysts

17.2.1 Dentigerous Cyst

Dentigerous cyst is an odontogenic cyst that is attached to the cervical region of an unerupted tooth and envelops the crown. Eruption cyst is a variant of dentigerous cyst found in the soft tissues overlying an erupting tooth [1].

Dentigerous cysts are developmental odontogenic cysts which are attached to the cementoenamel junction of an unerupted tooth. "Follicular cyst" is the synonym of the dentigerous cysts [2–4]. They cover the crown portion of the tooth. Dentigerous cysts which are located in the soft tissues are known as eruption cysts and they are not frequent since they only account for less than 2% of the cases [1].

Dentigerous cysts are the second most common cyst in the jaws and they represent 20% of the odontogenic cysts [1]. The most common teeth which are associated with dentigerous cysts are the mandibular third molars. Mandibular third molars represent 75% of the dentigerous cysts. Maxillary canines and maxillary third molars are the most frequent associated teeth after mandibular third molars [1–3] (Fig. 17.4).

As the other developmental cysts, small lesions are generally asymptomatic; however, they can reach great sizes and cause expansions at cortical bones (Fig. 17.5). Secondarily infected dentigerous cysts may cause pain and swellings [2].

Radiographically, OPG reveals a corticated well-defined periphery structure and a unilocular radiolucent internal structure that is attached to

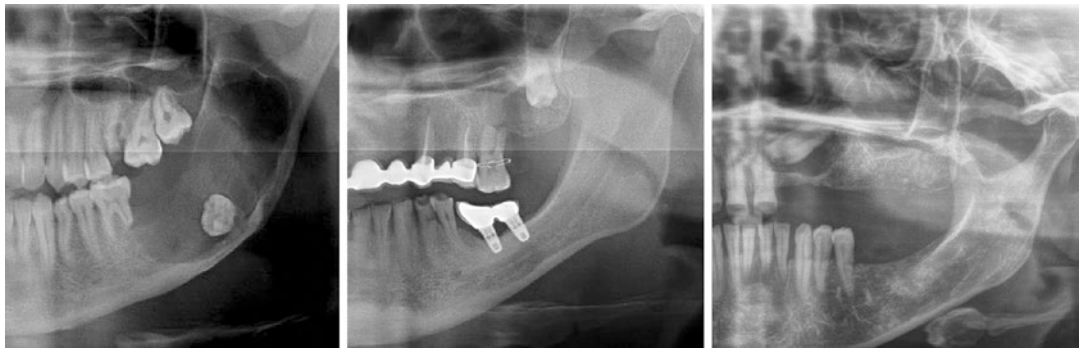

Fig. 17.4 Dentigerous Cysts of three different cases. A: OPG reveals a unilocular radiolucent lesion with well-defined borders attached to the molar tooth's crown. The lesion extends from the left coronoid process of the mandible to the mandibular left molar site. B: OPG reveals a unilocular radiolucent lesion with well-defined borders attached to the cementoenamel junction of a vertical impacted molar tooth. C: OPG reveals a unilocular radiolucent lesion with well-defined borders which seem like surrounding the whole teeth. Circumferential type dentigerous cysts appear as they contain within although they are also attached to the cementoenamel junction of a tooth. CBCT is useful while evaluating lesions with relevant radiographic features

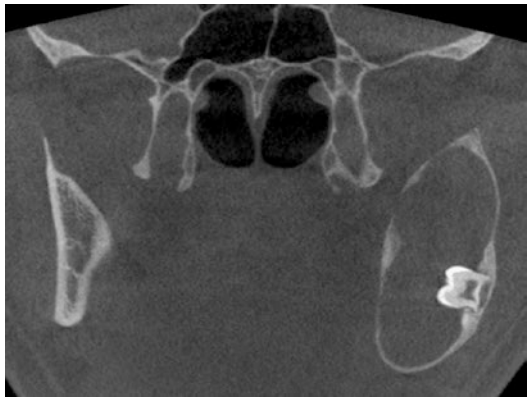

Fig. 17.5 Dentigerous Cyst. Coronal CBCT slice of the of Fig. 17.5A. Lesion's attachment to the cementoenamel junction and the expansions of the buccal and lingual cortical plates are seen

the cementoenamel junction of an unerupted tooth. The lesion envelops the crown portion of the tooth. CBCT reveals expansion at buccal and lingual cortical borders and inferior displacement of the mandibular canal/superior displacement of maxillary sinus floor for larger lesions [2–4].

Common sonographic features of dentigerous cysts are (Fig. 17.6):

- Lesions without bone perforation or destruction at the cortical plate or any bone dehiscences may not have ultrasonography findings due to artifacts such as acoustic shadowing.

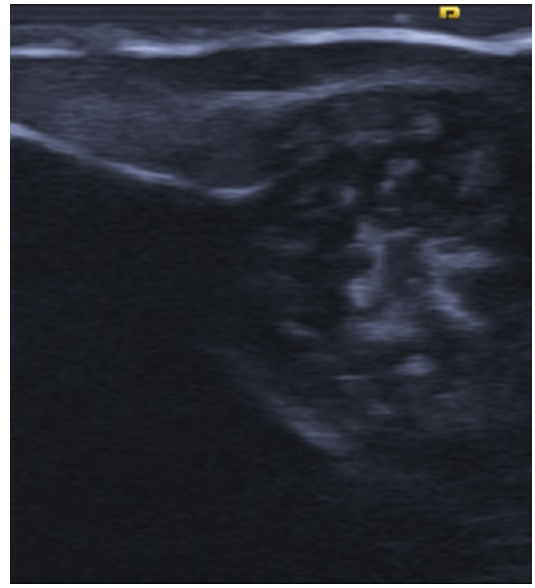

Fig. 17.6 Dentigerous Cyst. US reveals unilocular heterogeneous mixed internal structure with "snow-flake" radiographic appearance. Deep portions of the lesion are not clearly seen with US since the lesion is an intraosseous lesion which did not cause thinning or perforation at the cortical plate

- Internal Structure: Heterogeneous hyperechoic and hypoechoic areas one within each other which creates an appearance of "snow-flakes internal structures" which is common for dentigerous cysts.

- Peripheral Structure: Well-defined/moderately-defined borders can be seen. Since dentigerous cysts are intraosseous lesions deep portions of the lesion are not detectable with US.

17.2.2 Odontogenic Keratocyst

With the novel 2017 WHO classification, odontogenic keratocyst (OKC) was reclassified as an odontogenic cyst [1, 5, 6]. OKC is an odontogenic cyst characterized by a thin, regular lining of parakeratinized stratified squamous epithelium with palisading hyperchromatic basal cells. OKCs represent 10–20% of odontogenic cysts and following the radicular cyst and dentigerous cyst they are the most common odontogenic cyst. 5% of all OKCs are associated with Gorlin-Goltz Syndrome (Nevoid Basal Cell Carcinoma) and multiple OKCs are seen with this syndrome [1].

Mandibular posterior site and mandibular ramus are the most common localization for the OKCs as the lesion at these localization accounts for 80% of all OKC cases [1, 7]. Instead of causing expansion at buccal and lingual cortical plates, OKCs grow in anterior-posterior direction. Since they do not cause expansion or cause only minimal expansion they are mostly seen in routine radiographic examinations. Small lesions can be completely asymptomatic; however, large lesions can even displace the orbits [1–4, 7].

Radiographically, OPG reveals corticated well-defined radiolucent lesions. They can be multilocular or unilocular. Additional to OPG images, CBCT reveals the minimal-expansive or non-expansive nature of the lesions (Figs. 17.7 and 17.8) [1–4, 7]. Since those lesions do not tend to expand or destroy the cortical plates US imaging of OKCs are limited. If OKCs get secondarily infected they can also cause destructions at cortical plates.

Common sonographic features of odontogenic keratocysts are (Fig. 17.9):

- Lesions without bone perforation or destruction at cortical plate or any bone dehiscences may not have ultrasonography findings due to artifacts such as acoustic shadowing.

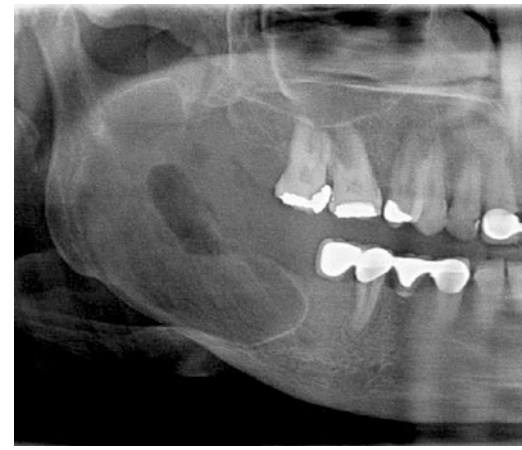

Fig. 17.7 Odontogenic Keratocyst. OPG reveals a unilocular radiolucent lesion with well-defined borders which extends from the right coronoid process of the mandible to the mandibular right molar site. Note the mandibular canal which is dislocated inferiorly due to the lesion (red arrow). Due to the extraction of the mandibular right third molar, a more radiolucent area is seen at the post-molar site (turquoise arrow)

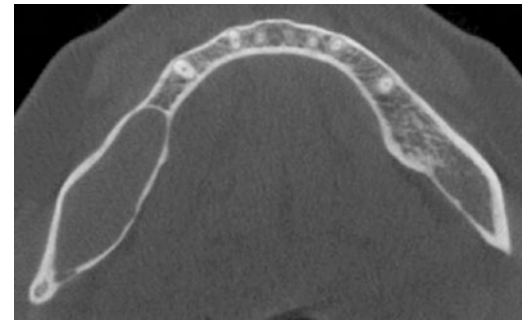

Fig. 17.8 Odontogenic Keratocyst: Axial CBCT slice of Fig. 17.8 reveals a minimal expansive lesion despite extending from coronoid process to molar region which is one of the key radiographic features of odontogenic keratocyst

- Internal Structure: Homogeneous anechoic internal structure is generally seen without any hyperechoic focis. If foci present, the appearance turns to be heterogeneous hyperechoic and hypoechoic areas one within each other which creates an appearance of "snowflakes internal structures."
- Peripheral Structure: Well-defined hyperechoic oval or round borders are seen.

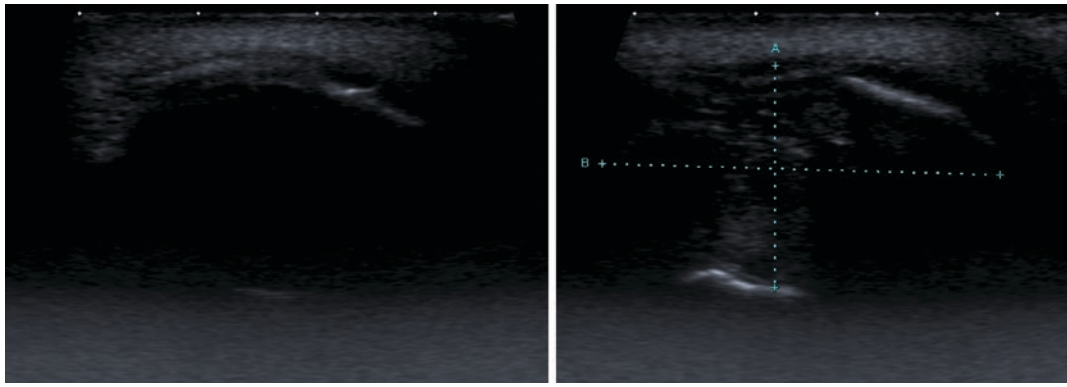

Fig. 17.9 Odontogenic Keratocyst. US reveals a unilocular anechoic internal structure (A) and a unilocular heterogeneous mixed internal structure of two cases. While acoustic enhancement is seen in Fig. 17.7B it is not visible in Fig. 17.7A. Since odontogenic keratocysts do not cause perforations or destructions at cortical plates it is possible that US examination might not demonstrate the internal structure of the lesion clearly

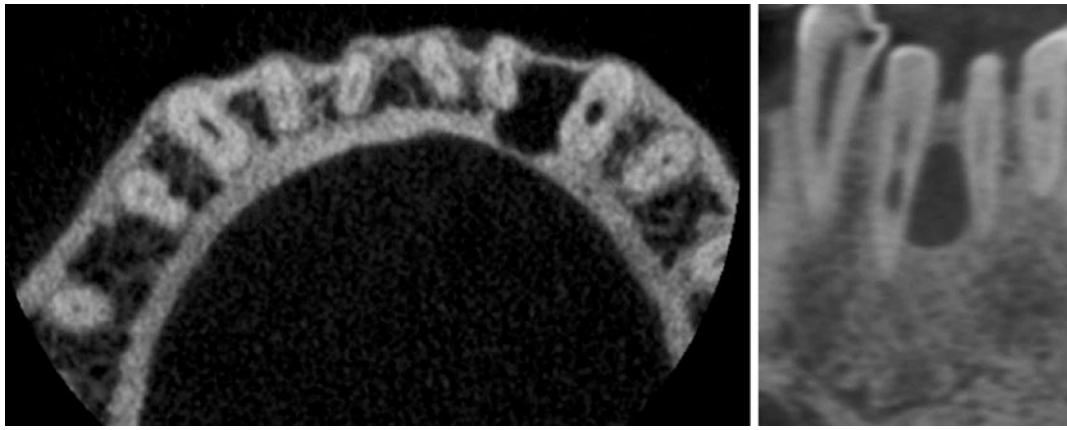

Fig. 17.10 Lateral Periodontal Cyst. A: CBCT Axial slice reveals a unilocular hypodense lesion with well-defined borders at the lateral site of the roots without any expansions at cortical plates. B: CBCT Panoramic reconstruction reveals the lateral localization of the lateral periodontal cyst

17.2.3 Lateral Periodontal Cyst and Botryoid Odontogenic Cyst

Lateral Periodontal Cyst and Botryoid Odontogenic Cyst are developmental odontogenic cysts which are located at the lateral of the erupted teeth's roots. They are both detected as incidental findings on routine radiographs due to their asymptomatic nature. While lateral periodontal cyst is a unilocular cyst, botryoid odontogenic cyst is a multilocular cyst. Both of these cysts usually have a cortical well-defined periphery structure and radiolucent internal structures on OPGs [1–4] (Fig. 17.10).

Common sonographic features of lateral periodontal cysts are (Fig. 17.11):

- Lesions without bone perforation or destruction at cortical plate or any bone dehiscences may not have ultrasonography findings due to artifacts such as acoustic shadowing.
- Internal Structure: Homogeneous anechoic internal structure is generally seen without any hyperechoic focis.
- Peripheral Structure: Well-defined borders are generally seen.

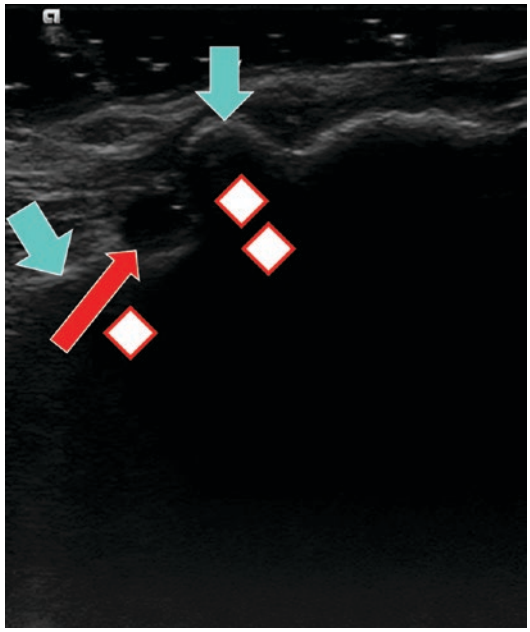

Fig. 17.11 Lateral Periodontal Cyst. US reveals a lateral periodontal cyst (red arrow) located between the dental roots (turquoise arrow). Red diamonds represent the crowns of the relevant teeth

17.2.4 Gingival Cyst

Gingival cysts (GC) are developmental odontogenic cysts which are located in soft tissues. They are mostly found in the alveolar mucosa. Gingival cysts have two different variants as "gingival cysts of the adults" and "gingival cysts of the infants." While GCs of the adults only account for less than 0.5% of odontogenic cysts, GCs of the infants are very common in infants younger than 3 months. GCs of the infants are rarely seen after 3 months and they regress spontaneously almost for every case; thus, no treatment is required [1–4]. GCs can be solitary or multiple and they are mostly asymptomatic [1, 8].

GCs are painless, small (<2 mm diameter), blister-like soft tissue lesions that are attached to the gingiva. They have the dome-shaped clinical appearance as most of the soft tissue lesions appear as light-blue. Since they are not intraosseous lesions they do not have any radiographic features on OPGs; however, CBCT may reveal surface erosions at buccal cortical plate without demonstrating the lesion. In this case, US can clearly visualize for GCs [1–4].

Common sonographic features of gingival cysts are:

- Internal Structure: Homogeneous anechoic internal structure is generally seen.

17.2.5 Glandular Odontogenic Cyst

Glandular odontogenic cysts are developmental odontogenic cysts which have glandular differentiation. They are also known as sialo-odontogenic cysts and they only represent less than 1% of the odontogenic cysts. They are mostly located in mandible (75%) and maxillary anterior site [1, 9].

Clinically, a painless swelling is seen for early lesions; however, they can reach greater sizes and cause root resorptions or teeth displacements [1–4, 9].

OPG and CBCT reveal a well-defined radiolucent/hypodense lesion with scalloped or regular borders which is generally located near the tooth apices. Greater lesions can cross the midline [1, 2] (Fig. 17.12).

Common sonographic features of glandular odontogenic cysts are (Fig. 17.13):

- Internal Structure: Since glandular odontogenic cysts have glandular differentiation, their internal structures have solid hyperechoic components and anechoic cystic structure.
- Peripheral Structure: Well-defined scalloped hyperechoic borders are generally seen.

17.2.6 Calcifying Odontogenic Cyst

WHO defines calcifying odontogenic cysts (COC) as "Simple cyst lined by ameloblastoma-like epithelium, which contains focal accumulations of ghost cells." Previously known as calcified cystic odontogenic tumor, with the novel classification of odontogenic tumours in 2017, it is thought to be a developmental cyst rather than a neoplasm [1, 5].

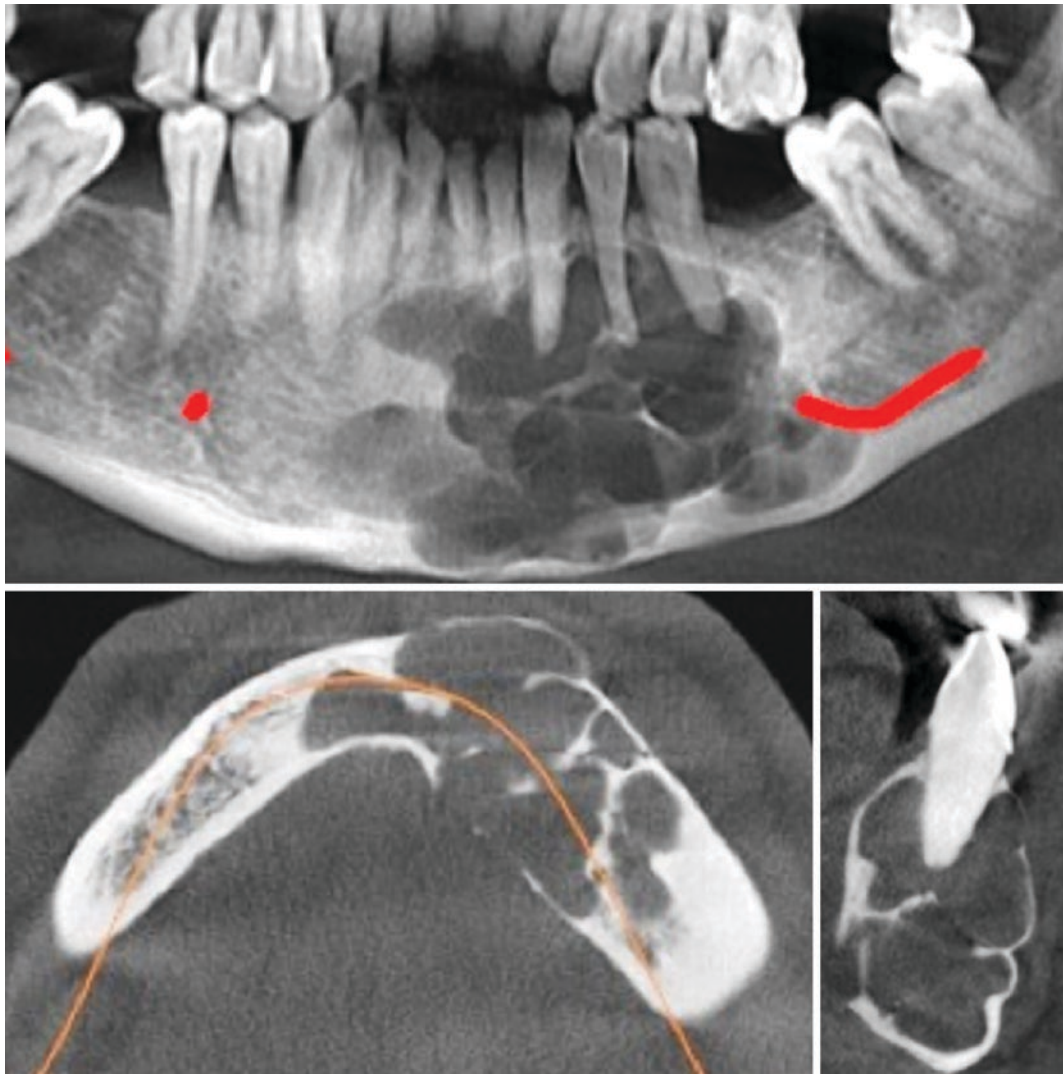

Fig. 17.12 Glandular Odontogenic Cyst. A: CBCT panoramic reconstruction image reveals a multilocular hypodense lesion which is in relation to the roots of mandibular anterior teeth. B: CBCT axial slice reveals a multilocular hypodense lesion with buccal and lingual cortical plate expansions at mandibular anterior region. C: CBCT cross-sectional image reveals expansion and thinning at buccal and lingual cortical plates without any appearance of lamina dura and periodontal ligament space. The associated tooth has the "floating-teeth" appearance even though Glandular Odontogenic Cyst is a benign lesion

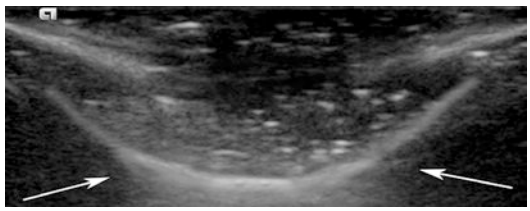

Fig. 17.13 Glandular Odontogenic Cyst. CBCT axial slice reveals a multilocular hypodense lesion with buccal and lingual cortical plate expansions at mandibular anterior region

COCs represent less than 1% of all odontogenic cysts and they can be located in either jaw. Usually, the lesion is associated with an odontoma in the anterior regions of the jaws. They are mostly intraosseous; however, 10% of COCs are extraosseous [1].

Clinically, a painless expansive lesion of the jaws is seen as a swelling. OPG and CBCT reveal a well-defined generally unilocular, radiolucent/hypodense lesion which may cause root resorp-

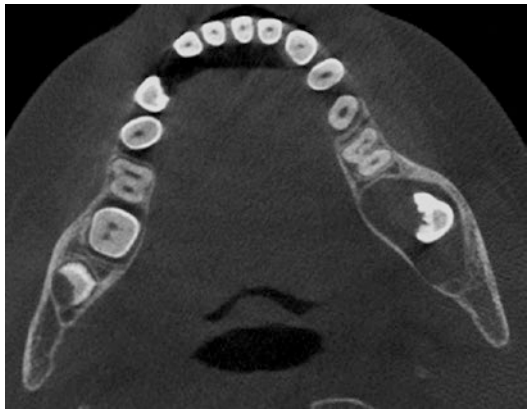

Fig. 17.14 Orthokeratinized Odontogenic Cyst. Axial CBCT slice reveals a unilocular hypodense lesion with minimal expansion. Unlike dentigerous cyst, the lesion is not attached to the cementoenamel junction of the tooth but contains the tooth

tion or displacement. Extraosseous COCs do not have any distinguished clinical or radiographic features as they are gingival swellings with tenderness [1–4, 10].

17.2.7 Orthokeratinized Odontogenic Cyst

Orthokeratinized Odontogenic Cyst (OOC) was known as a variant of odontogenic keratocyst; however, with the novel 2017 WHO classification, OOC is recognized as a new entity. Since it is recognized as a new entity for just 3 years, the prevalence of OOC is not certain. WHO stated that "OOCs probably account for about 1% of all odontogenic cysts overall." [1].

As odontogenic keratocysts, OOCs are also generally located in mandibular posterior site. For differential diagnosis, it should be known that almost half of the OOC is associated with an impacted tooth and unlike odontogenic keratocysts there is no relation between the OOCs and Gorlin-Goltz syndrome (Fig. 17.14). OOCs with an impacted tooth may resemble an appearance like dentigerous cysts. OPG and CBCT reveal the same radiographic appearances with odontogenic keratocysts [1, 11, 12].

17.3 Developmental Non-odontogenic Cysts and Cyst-Like Lesions

17.3.1 Nasopalatine Duct Cyst

Nasopalatine duct cyst, also known as incisive canal cyst, is a developmental non-odontogenic cyst that is located in the midline of the maxillary anterior site. It is the most common non-odontogenic cyst, representing 80% of them and they account for 5% of all cysts in the jawbones [1, 13].

Clinically, painless swelling which is located posterior to the maxillary anterior teeth is seen. Teeth in relation to the lesion is vital as a differential diagnosis with radicular cysts [1–3, 13].

Periapical radiographs reveal intact and unaffected periodontal ligament spaces of the maxillary anterior teeth with an expansive lesion in nasopalatine channel. Due to the superposition of the spina nasalis anterior, nasopalatine duct cysts appear as a heart-shaped lesion (Figs. 17.15 and 17.16). CBCT reveals well-defined, hypodense lesions which are located in the midline of the hard palate [1–3, 13].

Normal nasopalatine canals can have 6 mm diameter but if the nasopalatine canal is measured wider than 6 mm and if the affected teeth are vital without any symptoms, the nasopalatine canal cyst should be in the differential diagnosis [1–3].

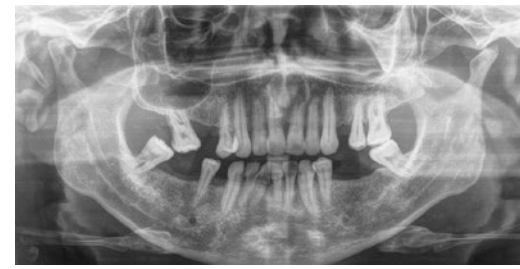

Fig. 17.15 Nasopalatine Canal Cyst. OPG reveals an expanded nasopalatine canal which suggests a nasopalatine canal cyst. The lesion appears as a heart-shaped lesion since the anterior nasal spine is superimposed on the lesion

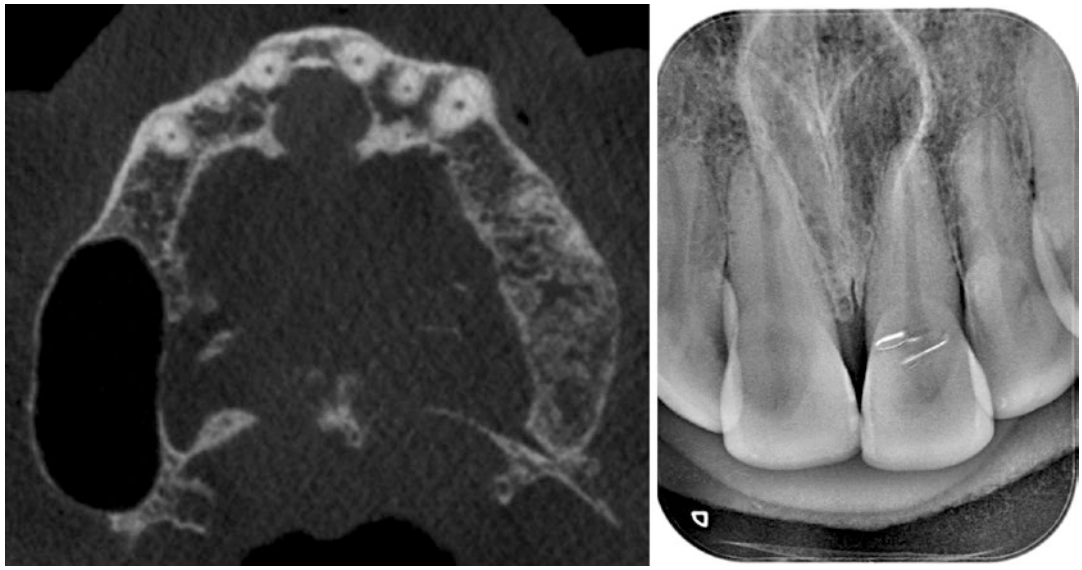

Fig. 17.16 Nasopalatine Canal Cyst. A: CBCT axial slice reveals expanded nasopalatine canal without any cortical bone destruction. B: Periapical radiograph reveals expanded nasopalatine canal

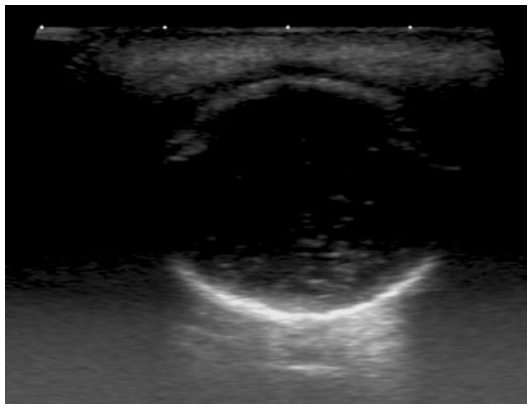

Fig. 17.17 Nasopalatine Canal Cyst. US reveals superficial, round-shaped, well-defined, unilocular anechoic lesion with acoustic enhancement

Common sonographic features of nasopalatine canal cysts are (Fig. 17.17):

- Internal Structure: Homogeneous anechoic internal structure is generally seen without any hyperechoic focis. Some cysts are hyperechoic due to cholesterol crystals in the internal structure.
- Peripheral Structure: Well-defined hyperechoic oval or round borders are seen. Since cysts are fluid-filled lesions, they attenuate the ultrasounds less and an "acoustic enhancement" is seen at the bottom of the lesion. Since the (figure) has calcification inside a comet-tail artifact is also seen.

17.3.2 Nasolabial Cyst

Nasolabial cyst, also known as nasoalveolar cyst, is a developmental non-odontogenic cyst which is located at the maxillary anterior region and sublabial area [1].

Clinically, the lesion is generally asymptomatic slowly enlarging unilateral swelling at the nasolabial fold. If left untreated, the lesion may get larger and it may cause obstruction in nasal cavity, distortion at nostrils, and swelling at the upper lip. Nasolabial cysts may drain into the nasal cavity if they get secondarily infected.

Infected nasolabial cyst may appear as a dental abscess; thus, vitality test should be performed for differential diagnosis [1–4, 13].

Periapical radiographs, OPG and CBCT are unable to demonstrate the lesion since it is a soft tissue lesion. Some cases may have an erosion at the buccal cortical plate underneath the nasola-

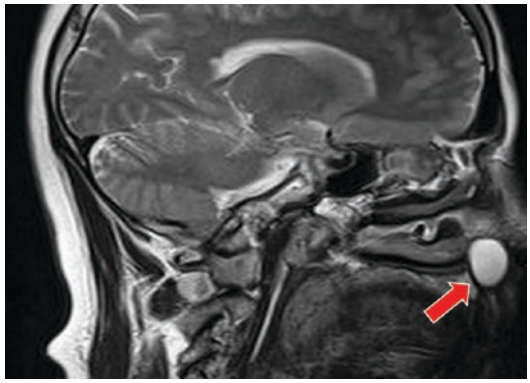

Fig. 17.18 Nasolabial Canal Cyst. T2-weighted MRI reveals a unilocular, hyperintense lesion with well-defined borders and superficial erosion at the buccal cortical plate (red arrow)

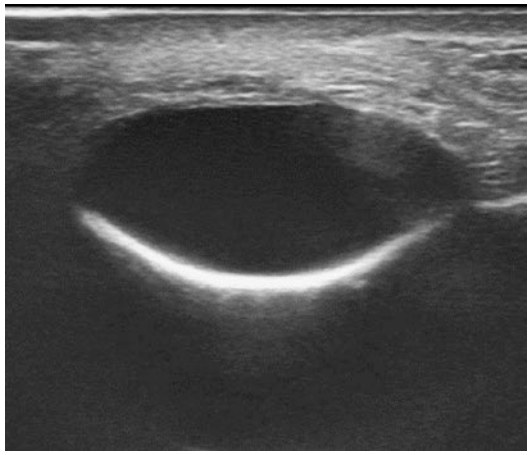

Fig. 17.19 Nasolabial Canal Cyst. US reveals an oval-shaped, unilocular, anechoic lesion with well-defined borders and acoustic enhancement

bial cyst. CT reveals a homogeneous hypodense internal structure with well-defined borders while MRI T2-sequences reveal a hyperintense cystic lesion with well-defined borders [1–4, 13] (Fig. 17.18).

Common sonographic features of nasolabial cysts are (Fig. 17.19):

- Internal Structure: Homogeneous anechoic internal structure is generally seen without any hyperechoic focis.
- Peripheral Structure: Well-defined hyperechoic oval borders are seen. Like the other cystic lesions, they frequently have an acoustic (posterior) enhancement.

17.3.3 Dermoid Cyst

A dermoid cyst is a cyst containing ectoderm- and mesoderm-derived tissues. It has three histological variants as "true dermoid," "epidermoid," and "teratoid." True dermoid cysts are cavities lined with epithelium with keratinization and skin appendages in cyst wall. Epidermoid cysts do not show skin appendages [1].

Dermoid cysts are common in the jaws since only 7% of dermoid cysts are located in the head and neck region. More than half of the patients are younger than 5 years and the common localizations are nasolabial fold, lateral third of the eyebrow, and midline nose-neck. Clinically, a non-pulsative and asymptomatic mass is seen and since dermoid cysts are soft tissue lesions OPG and CBCT cannot reveal their features [1–4, 13].

Common sonographic features of dermoid cysts are (Fig. 17.20):

- Internal Structure: Unlike other cysts and cystic lesions their internal structure is predominantly hyperechoic. Doppler imaging may reveal moderate vascularization.
- Peripheral Structure: Well-defined non-hyperechoic oval borders are seen. Since their internal structure is not composed of cystic fluids, acoustic enhancement is frequently not seen.

17.3.4 Ranula

Ranulas are non-odontogenic cystic lesions which usually occur after a trauma to an excretory salivary gland. Ranulas are mostly associated with the sublingual salivary glands [1].

There are two types of ranulas: simple ranulas and deep ranulas. Simple ranulas are located on the floor of the mouth and associated with sublingual salivary gland. Deep ranulas are located in the neck region due to dissection of the extravasated mucin from the mouth floor to the neck. Both simple ranulas and deep ranulas are painless lesions and they are frequently unilateral [1, 13–17].

Common sonographic features of ranulas are (Fig. 17.21):

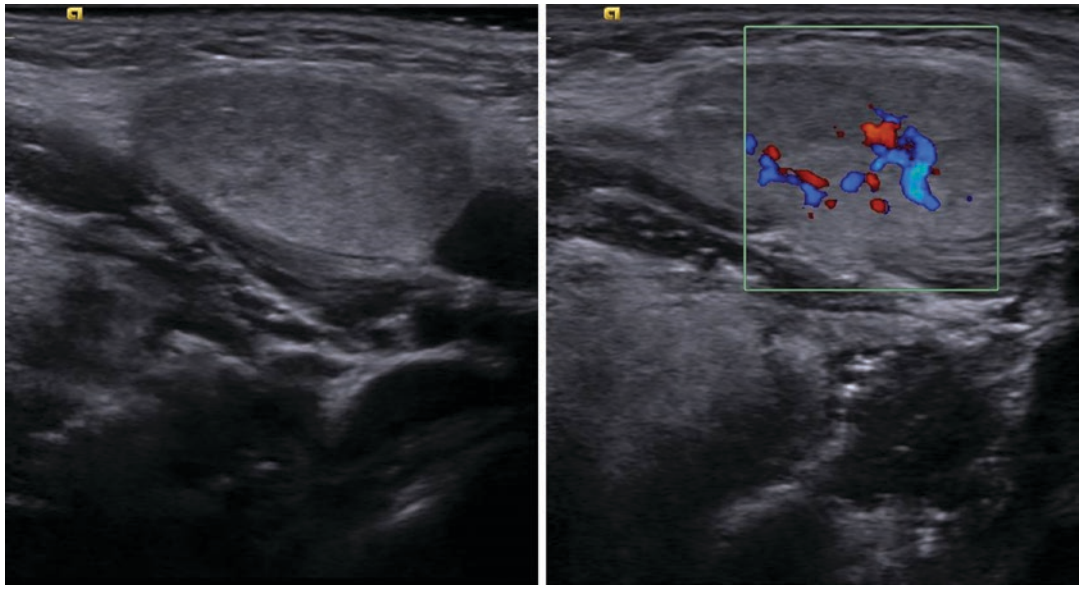

Fig. 17.20 Dermoid Cyst. US reveals a superficial, oval-shaped, unilocular, isoechoic lesion with well-defined borders and mild vascularization on Doppler image

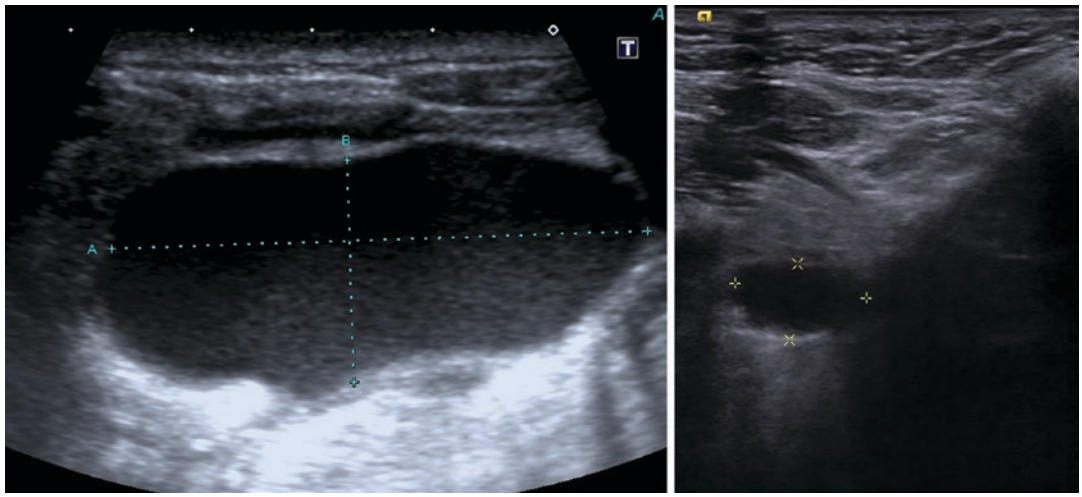

Fig. 17.21 Ranula of the two different cases. A: Simple Ranula. US reveals a superficial, unilocular, anechoic lesion with well-defined borders and acoustic enhancement. B: Deep Ranula. US reveals unilocular, anechoic lesion with well-defined borders, a mild acoustic enhancement which is located in the neck region

- Internal Structure: Both simple and deep ranulas have homogeneous anechoic internal structures.
- Peripheral Structure: Well-defined non-corticated oval borders are seen. Since simple ranulas are located more superficial to deep ranulas, the acoustic enhancement of the simple ranulas is more hyperechoic than deep ranulas.

17.3.5 Thyroglossal Duct Cyst

Thyroglossal Duct Cysts (TDC) are the persistent thyroglossal duct's cystic dilations. Among the lesions which are located in the neck TDC is the most common lesion. Their characteristic localization is between the infrahyoid and suprahyoid level and midline neck [1, 18–20].

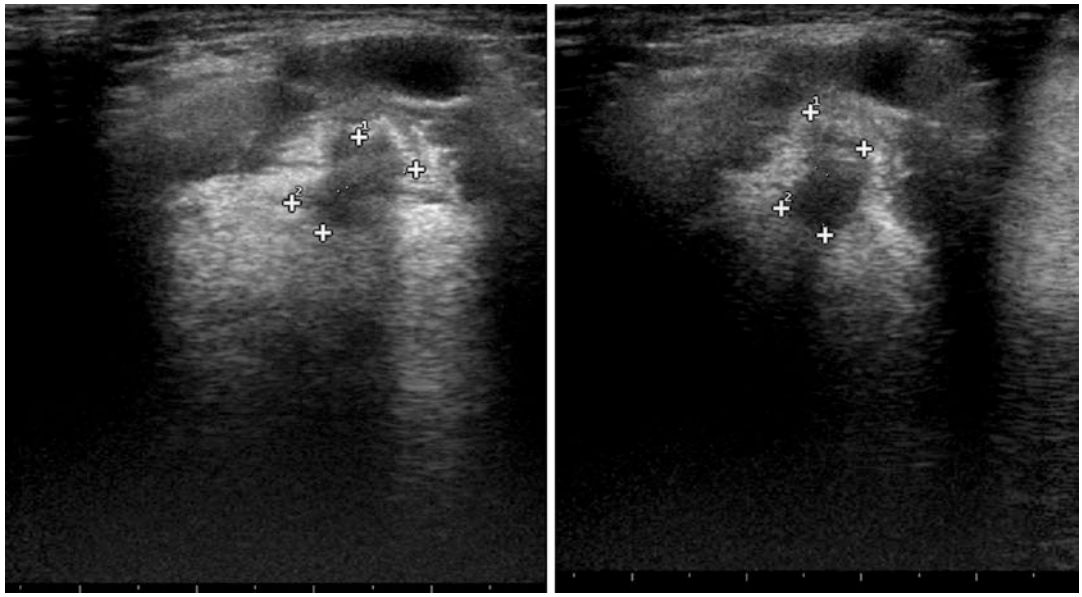

Fig. 17.22 A thyroglossal duct cyst laying deep adjacent to the hyoid bone

Clinically a swollen asymptomatic mass which moves while swallowing is seen. Radiographically, ultrasonography is a reliable technique to demonstrate the TDCs as they can demonstrate the thyroid gland [1, 18–20] (See Chap. 8, Sect. 8.3).

Common sonographic features of thyroglossal duct cysts are (Figs. 17.22 and 17.23)

- Internal Structure: A heterogeneous hypoechoic mass is seen. Low to moderate vascularization may be seen with Doppler imaging.
- Peripheral Structure: Ill-defined lesions which are located inside the hyperechoic thyroid tissue is seen.

17.3.6 Branchial Cleft Cyst

Branchial Cleft Cysts (BCC), also known as cervical lymphoepithelial cyst, are cystic lesions which are located at lateral neck. Most of the cases are derived from the remnants of the second branchial apparatus [1].

BCCs represent 90% of the lateral cervical cysts and they are mostly seen in patients who are 20–40 years old. Although they can be located between the suprasternal notch and hyoid bone, they are usually located near the mandibular angle and along the anterior border of musculus sternocleidomastoideus [1, 21–24].

Clinically, a unilateral painless swelling at the cervical region which may cause dysphagia, dyspnoea, and dysphonia is seen. Cases with bilateral involvement suggest syndromes or familial association. Purulent drainage to the pharynx or skin can be seen in BCCs with spontaneous ruptures [1, 21–24].

Upon ultrasonographic examination, the lesion is usually seen as a well-marginated anechoic mass with a thin, well-defined wall (See Chap. 8).

17.4 Pseudo-Cysts of the Jaws

17.4.1 Stafne Bone Cavity

Stafne Bone Cavity (SBC), also known as Lingual Mandibular Bone Depression, Static Bone Cavity, and Latent Bone Cyst, is the deep depression of the submandibular or sublingual salivary gland to the lingual cortical plates sur-

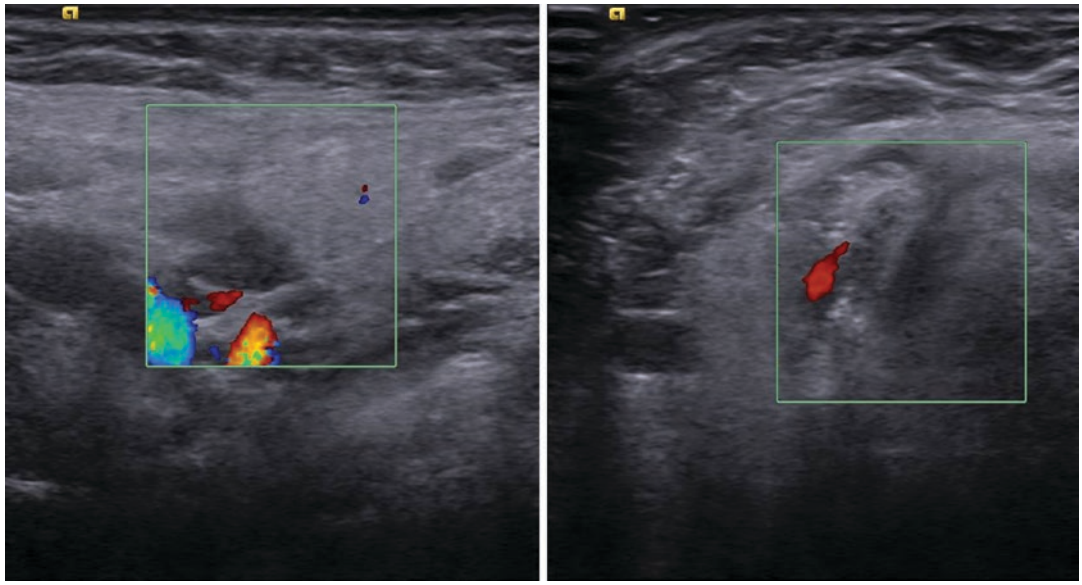

Fig. 17.23 A thyroglossal duct cyst characteristically anechoic mass close to thyroid tissue

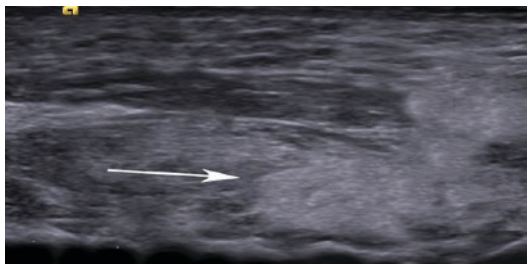

Fig. 17.24 Stafne Bone Cavity. US reveals salivary gland tissue with heterogeneous echogenicity in the lingual depression area

face. Their incidence is less than 1% and since they are asymptomatic, no clinical findings are present [1, 25].

Radiographically, a well-defined, ovoid or round unilocular radiolucency is seen. The posterior variants of Stafne Bone Cavity are located anterior to the mandibular angulus and below the mandibular canal. The anterior variants are located at the apex of the mandibular premolars since they are associated with the sublingual salivary gland. Posterior variants have more corticated borders than anterior variants. MRI is the best option for Stafne Bone Cavity since they can reveal the features of all salivary glands [1–4, 25].

Some reports showed salivary gland neoplasms developing in the defect; thus, they should be monitored after the diagnosis [2].

Common sonographic features of Stafne bone cavity are (Fig. 17.24):

- Internal Structure: A heterogeneous hyperechoic area which has a similar echogenicity with the relevant salivary gland is seen.
- Peripheral Structure: Stafne bone cavities are not cystic lesions; thus, they do not have corticated well-defined borders. Since these lesions are the extensions of the submandibular or sublingual salivary gland, an isthmus is seen where the extension caused cortical destruction.

17.4.2 Aneurysmal Bone Cyst

See Chap. 18 (Figs. 18.28 and 18.30) (Benign Tumors of Maxillofacial Region → Giant Cell Lesions and Simple Bone Cyst).

17.4.3 Simple Bone Cavity

See Chap. 18 (Fig. 18.37) (Benign Tumors of Maxillofacial Region → Giant Cell Lesions and Simple Bone Cyst).

Acknowledgments Figures 17.6, 17.7, 17.14, 17.15, 17.16, and 17.19B are courtesy of Prof. Dr. İlknur Özcan and Dr. Hülya Çakır Karabaş, Istanbul University, Department of Dentomaxillofacial Radiology".

Figure 17.12 is courtesy of Prof. Dr. İlknur Özcan and Dr. Sedef Ayşe Taşyapan, Istanbul University, Department of Dentomaxillofacial Radiology.

Figures 17.3, 17.9, 17.17, 17.18, 17.19A, and 17.21A are courtesy of Assoc. Prof. Dr. İbrahim Şevki Bayrakdar, Eskişehir Osmangazi University, Department of Dentomaxillofacial Radiology.

References

1. El-Naggar, A. K., Chan, J. K. C., Rubin, G. J., Takata, T., Slootweg, P. J., International Agency for Research on Cancer. WHO classification of head and neck tumours; 2017.
2. White SC, Pharoah MJ. Oral radiology: principles and interpretation. St. Louis, MO: Mosby/Elsevier; 2014.
3. Ozcan I. Diş Hekimliğinde Radyolojinin Esasları: Konvansiyonelden Dijitale. İstanbul: İstanbul Tıp Kitapevi; 2017.
4. Koenig LJ. Diagnostic Imaging. Philadelphia, PA: Elsevier; 2017.
5. Soluk-Tekkeşin M, Wright J. The World Health Organization classification of odontogenic lesions: a summary of the changes of the 2017 (4th) edition. Turk J Pathol. 2013;34 https://doi.org/10.5146/tjpath.2017.01410.
6. Slusarenko da Silva Y, Naclério-Homem M. A systematic review on the expression of bcl-2 in the nonsyndromic odontogenic keratocyst: should it be considered a cyst or a tumor? Oral Maxillofac Surg. 2020; https://doi.org/10.1007/s10006-020-00856-5.
7. Sarvaiya B, Vadera H, Sharma V, Bhad K, Patel Z, Thakkar M. Orthokeratinized odontogenic cyst of the mandible: a rare case report with a systematic review. J Int Soc Prevent Communit Dent. 2014;4(1):71–6. https://doi.org/10.4103/2231-0762.131265.
8. Siponen M, Neville BW, Damm DD, Allen CM. Multifocal lateral periodontal cysts: a report of 4 cases and review of the literature. Oral Surg Oral Med Oral Pathol Oral Radiol Endod. 2011;111(2):225–33. https://doi.org/10.1016/j.tripleo.2010.09.072.
9. Chrcanovic BR, Gomez RS. Glandular odontogenic cyst: an updated analysis of 169 cases reported in the literature. Oral Dis. 2018;24(5):717–24. https://doi.org/10.1111/odi.12719.
10. de Arruda JAA, Schuch LF, Abreu LG, et al. A multicentre study of 268 cases of calcifying odontogenic cysts and a literature review. Oral Dis. 2018;24(7):1282–93. https://doi.org/10.1111/odi.12906.
11. Macdonald-Jankowski DS. Orthokeratinized odontogenic cyst: a systematic review. Dentomaxillofac Radiol. 2010;39(8):455–67. https://doi.org/10.1259/dmfr/19728573.
12. Mahdavi N, Taghavi N. Orthokeratinized odontogenic cyst of the maxilla: report of a case and review of the literature. Turk Patoloji Derg. 2017;33(1):81–5. https://doi.org/10.5146/tjpath.2014.01273.
13. Philbert RF, Sandhu NS. Nonodontogenic cysts. Dent Clin N Am. 2020;64(1):63–85. https://doi.org/10.1016/j.cden.2019.08.006.
14. Pouzoulet P, Collet C, Foletti JM, Guyot L, Chossegros C. Ranulas à expression cervicale. Mise au point [Plunging ranula. Review]. Rev Stomatol Chir Maxillofac Chir Orale. 2016;117(2):84–8. https://doi.org/10.1016/j.revsto.2015.10.007.
15. Packiri S, Gurunathan D, Selvarasu K. Management of Paediatric Oral Ranula: a systematic review. J Clin Diagn Res. 2017;11(9):ZE06–9. https://doi.org/10.7860/JCDR/2017/28498.10622.
16. Pontes FSC, de Souza LL, Pedrinha VF, Pontes HAR. Congenital Ranula: a case report and literature review. J Clin Pediatr Dent. 2018;42(6):454–7. https://doi.org/10.17796/1053-4625-42.6.9.
17. Date AS, Padhye M, Desai R, Hire A. Simultaneous bilateral ranula in an edentulous patient. Rare presentation with a brief review of the literature. Stomatologija. 2016;18(4):133–6.
18. Sturniolo G, Vermiglio F, Moleti M. Thyroid cancer in lingual thyroid and thyroglossal duct cyst. Endocrinol Diabetes Nutr. 2017;64(1):40–3. https://doi.org/10.1016/j.endonu.2016.07.010.
19. Fujii NJ, Gibson TM, Satheesh KM, Cobb CM. Thyroglossal duct cyst: abbreviated review and case report. Compend Contin Educ Dent. 2017;38(2):97–102.
20. Amos J, Shermetaro C. Thyroglossal duct cyst. In: StatPearls. Treasure Island, FL: StatPearls Publishing; 2020.
21. Coste AH, Lofgren DH, Shermetaro C. Branchial cleft cyst. In: StatPearls. Treasure Island, FL: StatPearls Publishing; 2020.
22. Meng F, Zhu Z, Ord RA, Zhang T. A unique location of branchial cleft cyst: case report and review of the literature. Int J Oral Maxillofac Surg. 2019;48(6):712–5. https://doi.org/10.1016/j.ijom.2018.11.014.
23. Quintanilla-Dieck L, Penn EB Jr. Congenital neck masses. Clin Perinatol. 2018;45(4):769–85. https://doi.org/10.1016/j.clp.2018.07.012.
24. Hosokawa T, Takahashi H, Miyasaka Y, et al. Ultrasound evaluation of dermal sinuses/fistulas in pediatric patients. J Ultrasound Med. 2019;38(12):3107–22. https://doi.org/10.1002/jum.15016.
25. Ünsal G, Karapınar G, Özcan I, Koca RB, Olgaç V, Orhan K. Stafne bone cavity with expansion at posterior mandible: a case report and review of the literature. Oral Maxillofac Surg Cases. 2020;6(1):100132.

18 Applications of Ultrasonography in Maxillofacial/Intraoral Benign and Malignant Tumors

Kaan Orhan and Gürkan Ünsal

Contents

K. Orhan (✉)
Faculty of Dentistry, Department of Dentomaxillofacial Radiology, Ankara University, Ankara, Turkey

G. Ünsal
Faculty of Dentistry, Department of Dentomaxillofacial Radiology, Near East University, Nicosia, Cyprus

Near East University, DESAM Institute, Nicosia, Cyprus

K. Orhan (ed.), *Ultrasonography in Dentomaxillofacial Diagnostics*,
https://doi.org/10.1007/978-3-030-62179-7_18

18.1 Benign Tumors of Maxillofacial Region

18.1.1 Epithelial Odontogenic Tumors

18.1.1.1 Ameloblastoma

Ameloblastomas are the most common epithelial odontogenic tumors which have the ability to grow progressively. It may cause huge expansions if not removed entirely and has a tendency for local recurrence. Initial clinical features are slow-growing painless expansions however bigger lesions can cause malocclusion, paresthesia, trismus, facial asymmetries, and even airway obstruction [1–6].

Ameloblastomas have four different subtypes as solid, unicystic, peripheral, and metastasizing ameloblastoma. Unicystic ameloblastomas occur as a single cavity while solid ameloblastomas are multilocular lesions. Peripheral ameloblastomas are extraosseous that occur in soft tissues and metastasizing ameloblastomas are benign odontogenic tumors which have the ability to metastasize [1–6].

Unless cortical destruction or thinning is present, intraosseous cystic lesions and tumors cannot be visualized, since the sonographic waves cannot penetrate the cortical plates. Similar to their radiological appearances in CBCT, MRI, and 2D Imaging techniques, solid ameloblastomas have multilocular appearances (Figs. 18.1, 18.2, and 18.3) at US images and unicystic ameloblastomas have unilocular appearances (Fig. 18.4).

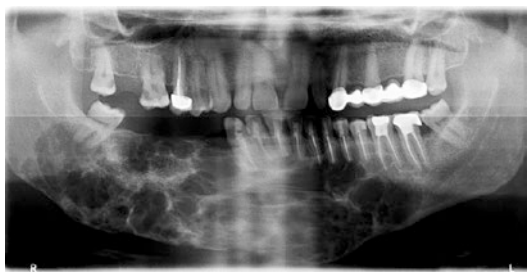

Fig. 18.1 Solid ameloblastoma. OPG reveals a multilocular well-defined predominantly radiolucent lesion with curved and thick septa formations which is characteristic of ameloblastomas

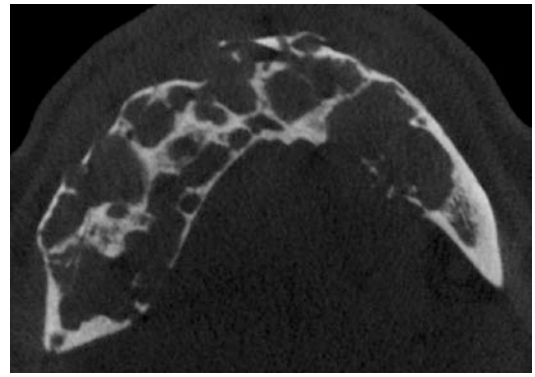

Fig. 18.2 Solid ameloblastoma. CBCT axial slice of Fig. 18.1 reveals buccal and lingual cortical plate expansion and perforations

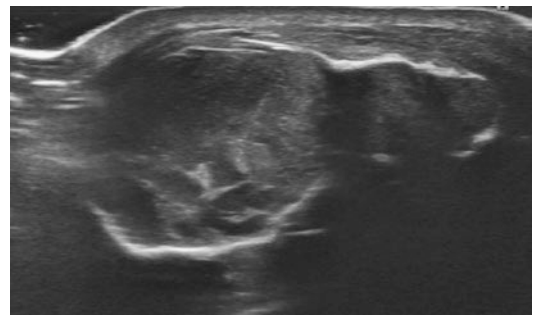

Fig. 18.3 Solid ameloblastoma. US image of Fig. 18.1 reveals a solid, predominantly hyperechoic internal structure with well-defined multilocular borders and hyperechoic septa formations

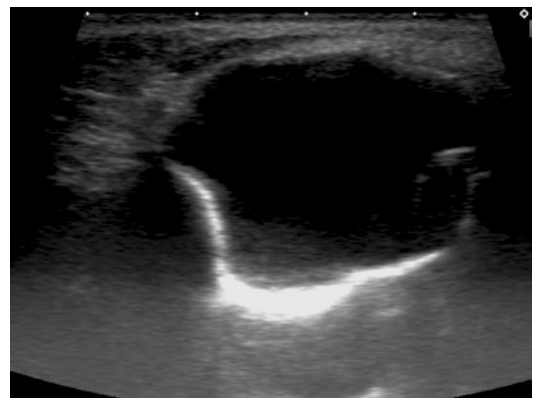

Fig. 18.4 Unicystic ameloblastoma. US reveals predominantly hypoechoic internal structure with well-defined unilocular borders. Acoustic enhancement is seen

Common sonographic features of ameloblastomas are:

- Internal Structure: Hyperechoic internal structure is seen with solid contents. Minimal or moderate vascularization is seen on Doppler examination. Solid ameloblastomas appear multilocular while unicystic ameloblastomas appear unilocular. Honeycomb appearance can be also seen. Internal bony septas may present and they appear as hyperechoic linings.
- Peripheral Structure: If no secondary infection is involved, cortical boundaries of the lesion usually appear as clear continuous hyperechoic linings. If destructions at cortical bones are present, disrupted hyperechoic linings can be seen. Acoustic enhancement is usually present.

18.1.1.2 Squamous Odontogenic Tumor

Squamous odontogenic tumors (SOT) are extremely rare cases with just <200 cases published. SOTs show terminal squamous differentiations and they have an asymptomatic, slow-growing nature. Most cases appear as unilocular radiolucencies however multilocular SOT cases were also reported. Unlike ameloblastoma, they may not have cortication in their margins. Their characteristic radiological appearance is triangular, with the base of the triangle located at the apical region, radiolucent area which causes root divergence [1, 7].

18.1.1.3 Calcifying Epithelial Odontogenic Tumor

Calcifying epithelial odontogenic tumor (CEOT), also known as Pindborg tumor is a benign epithelial odontogenic tumor which has a characteristic amyloid protein that has a tendency to calcify. They only represent less than 1% of the odontogenic tumors. CEOTs usually grow slowly and asymptomatically until they cause facial asymmetries. 3/4 of the CEOTs are unilocular and generally they have well-defined borders. More than half of the CEOTs are associated with unerupted teeth and 2/3 of CEOTs are mixed lesions with radiopaque focis [1–4, 8]

18.1.1.4 Adenomatoid Odontogenic Tumor

Adenomatoid odontogenic tumors (AOT) are epithelial benign tumors which show duct-like structures histopathologically. They account for less than 5% of odontogenic tumors and they are mostly seen in the first three decades. Less than 5% of the AOTs are extraosseous and 60% of all cases are associated with an unerupted canine (Figs. 18.5 and 18.6). Expansion may not be present since this tumor has a limited growth potential and is considered as a hamartoma by some authorities. Radiographically this lesion may have small foci of radiopacity which is present in 2/3 of cases. They tend to localize at the apically to cementoenamel junction which is a

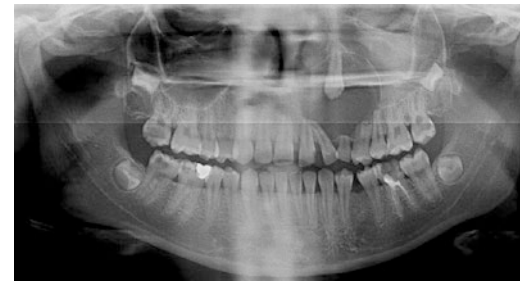

Fig. 18.5 Adenomatoid odontogenic tumor. OPG reveals a unilocular well-defined radiolucent lesion which is on the crown of impacted canine. Note that the lesion is attached apical to cemento-enamel junction which eliminates dentigerous cyst possibility

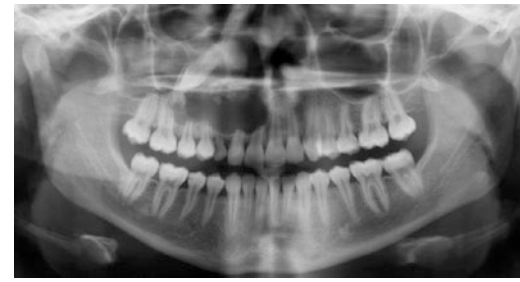

Fig. 18.6 Adenomatoid odontogenic tumor. OPG reveals a unilocular well-defined radiolucent lesion which is on the crown of impacted canine. Internal radiopaque focis are present

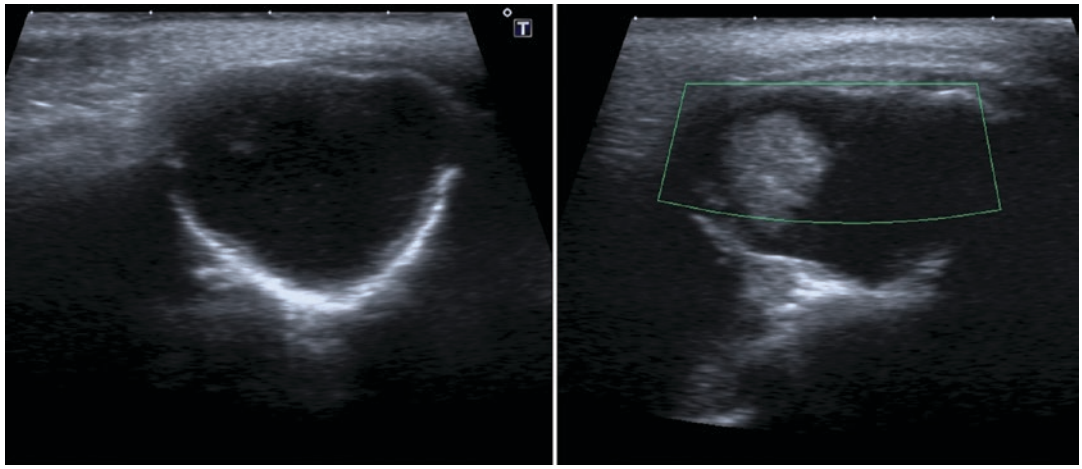

Fig. 18.7 Adenomatoid odontogenic tumor. US images of Fig. 18.6. (**a**) US reveals a unilocular, well-defined anechoic lesion with hyperechoic internal calcified foci (turquoise arrow). (**b**) Doppler US reveals no vascularization with hyperechoic internal calcified foci (turquoise arrow)

diagnostic feature to differentiate from dentigerous cysts [1–5, 9, 10]

Common sonographic features of adenomatoid odontogenic tumors are (Fig. 18.7):

- Internal Structure: Hypoechoic internal structure is seen with some hyperechoic calcified masses. Minimal or moderate vascularization is seen on Doppler examination. Since they are unilocular lesion a single hyperechoic lining will surround the lesion.
- Peripheral Structure: If no secondary infection is involved, cortical boundaries of the lesion usually appear as clear continuous hyperechoic linings. If destructions at cortical bones are present, disrupted hyperechoic linings can be seen. Acoustic enhancement is usually present.

18.1.2 Mixed Odontogenic Tumors

18.1.2.1 Ameloblastic Fibroma

Ameloblastic fibroma (AF) is a benign mixed tumor and constitute 1.5–6.5% of all odontogenic tumors. 80% of AFs occur in patients younger than 22 years. AFs locate at posteriors of the jaws (82%) and mandible (74%). They are usually painless slow-growing tumors and most of the time they will not cause facial deformity. 80% of AFs are associated with an impacted tooth (Figs. 18.8 and 18.9) [1–3, 11, 12]

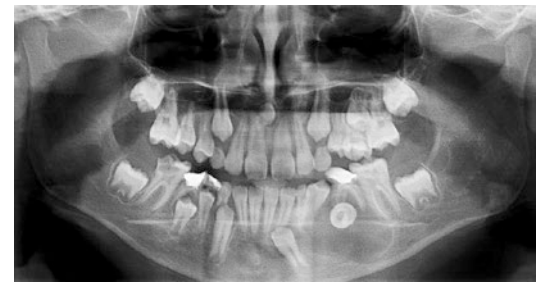

Fig. 18.8 Ameloblastic fibroma. OPG reveals a unilocular, well-defined radiolucent lesion with an impacted canine tooth at mandibular left premolar region

18.1.2.2 Primordial Odontogenic Tumor

Primordial odontogenic tumor is a benign mixed tumor and only 7 cases (6 in mandible, 1 in maxilla) were reported. Age range is 3–19 years. All reported cases were well-defined, radiolucent intraosseous lesions which were associated with an unerupted tooth. They are usually asymptomatic until they cause expansion at the cortical plates [1, 2]

18.1.2.3 Odontoma

Odontomas are mixed tumor-like hamartomas composed of soft tissues and dental hard tissues. Odontomas have two variants as compound odontoma and complex odontoma. Odontomas are the most common odontogenic tumors. Complex odontomas are usually found in the mandibular posterior site whereas complex odontomas are usually found in maxillary anterior site. They are usually asymptomatic and generally associated with unerupted teeth. Unless they cause expansion, impaction, malocclusion, diastema, aplasia, and malformation they are generally asymptomatic and detected on routine radiographs. Radiographically, early odontomas appear as a radiolucent lesion with radiopaque calcification areas. As the lesion maturates a well-defined radiopacity which is surrounded by a thin soft tissue lining and corticated bone is observed. Complex odontomas consist of disorganized radiopaque calcified masses (Fig. 18.10) whereas compound odontomas consist of multiple tooth-like radiopaque structures (Fig. 18.11) [1–5, 13, 14].

- Internal Structure: The images are similar to calcified structures and osteomas. Since they are composed of hard tooth-like structures, their internal structure is mostly anechoic. Acoustic shadowing is prominent.

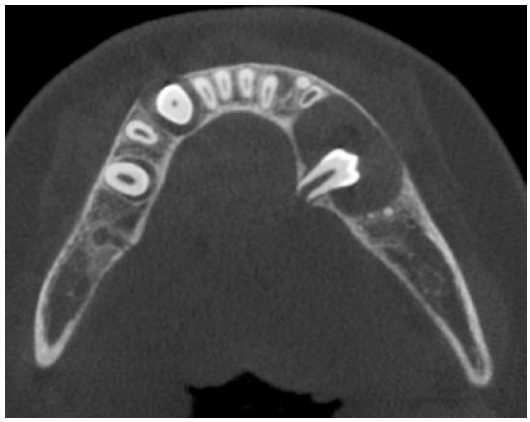

Fig. 18.9 Ameloblastic fibroma. CBCT axial slice of Fig. 18.8 reveals minimal expansive unilocular lesion which is attached apical to cemento-enamel junction of a premolar tooth

18.1.2.4 Dentinogenic Ghost Cell Tumor

Dentinogenic ghost cell tumor (DGCT) is a benign but locally infiltrating neoplasm of odontogenic epithelium. DGCT is the rarest of all ghost cell cases. Less than 50 cases have been reported. Both intraosseous and extraosseous variants are present and DGCTs are mostly localized at the posterior of the jaws. Extraosseous variants are usually located in the gingiva and alveolar mucosa. DGCTs are mostly unilocular and have a mixed internal structure with well-defined borders. DGCTs with ill-defined borders are also reported as 32%. Almost half of the cases are symptomatic. DGCTs associated with an odontoma is also reported [1, 2, 15]

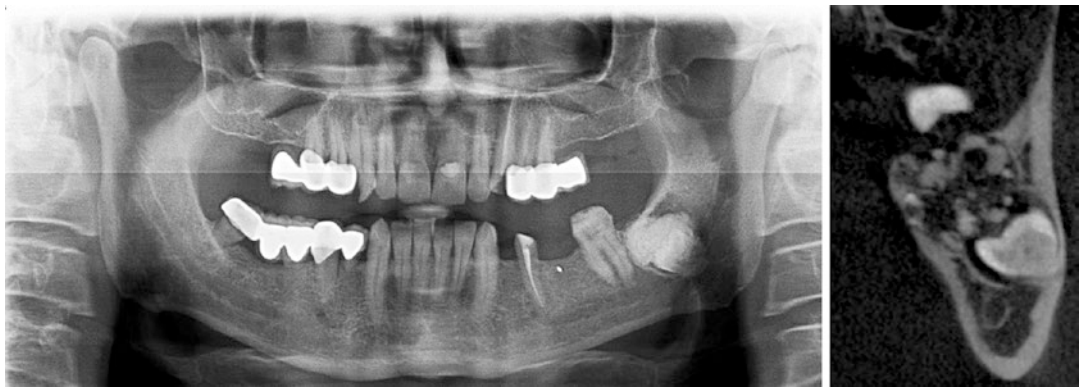

Fig. 18.10 Complex odontoma. (**a**) OPG reveals a calcified radiopaque mass which is located on the crown of impacted mandibular left third molar tooth. (**b**) CBCT coronal slice of (**a**) reveals unorganized hyperdense

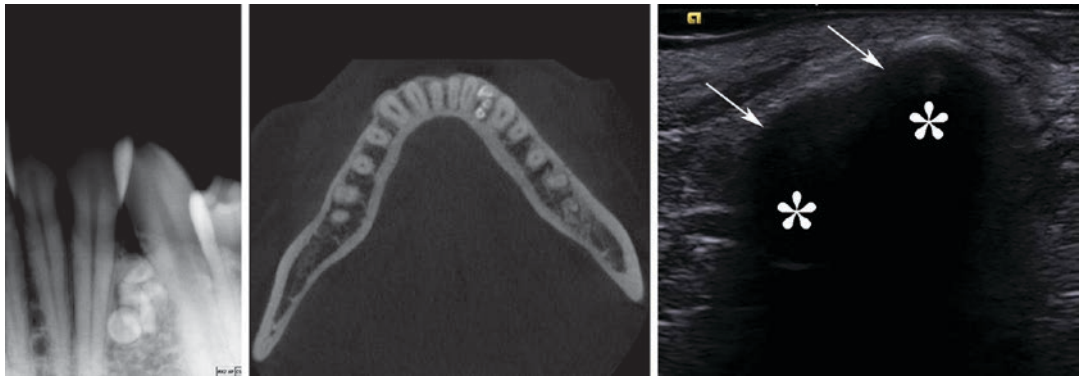

Fig. 18.11 Compound odontoma. (**a**) Periapical radiograph reveals multiple tooth-like radiopaque structures between mandibular left second incisor and mandibular left canine. (**b**) CBCT axial slice of (**a**) reveals non-expansive multiple tooth-like hyperdense structures with root-canal-like formations between mandibular left second incisor and mandibular left canine. (**c**) USG images showing an extensive acoustic shadowing due to odontoma (arrows and stars)

18.1.3 Mesenchymal Odontogenic Tumors

18.1.3.1 Odontogenic Fibroma

Odontogenic fibroma (OF) is a rare neoplasm which has intraosseous and extraosseous variants. Extraosseous variant is more common. OF occurs almost equally in the mandible and maxilla. Small OFs are generally asymptomatic; however, the bigger OFs can cause facial asymmetries and loosening of teeth. While smaller intraosseous OFs are generally well-defined, unilocular, radiolucencies, it may be also multilocular. Well-defined corticated borders are often present in intraosseous OFs. Extraosseous odontogenic fibromas (EOF) usually develop slowly with an intact mucosal surface and locate at gingiva [1–5, 16, 17]

Common sonographic features of extraosseous odontogenic fibromas are (Fig. 18.12):

- Internal Structure: Hyperechoic internal structure is seen with indistinct calcified hyperechoic contents. No vascularization pattern is expected to be visualized with Doppler examination. They are mostly unilocular.
- Peripheral Structure: If no secondary infection is involved, EOFs generally have smooth borders.

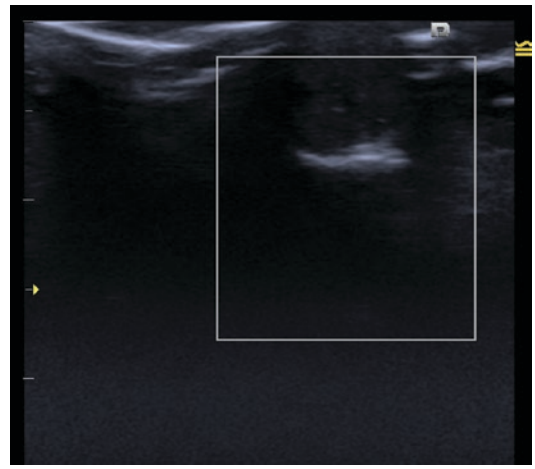

Fig. 18.12 Odontogenic fibroma. US reveals a unilocular, well-defined anechoic lesion without any cortical perforation or acoustic enhancement at gingiva. Doppler US reveals no vascularization

18.1.3.2 Odontogenic Myxoma/Myxofibroma

Odontogenic myxoma is a benign odontogenic neoplasm characterized by stellate and spindle-shaped cells dispersed in an abundant myxoid extracellular matrix. When a greater amount of collagen is evident, the term "odontogenic myxofibroma" may be used. Odontogenic Myxomas (OM) are the third most frequent odontogenic tumors following odontomas and ameloblasto-

mas. OMs are benign odontogenic tumors characterized by spindle-shaped and stellate cells scattered in a myxoid extracellular matrix. Odontogenic myxofibroma term is used when the amount of collagen is greater [1, 2, 18, 19]

OMs are usually located in mandibular molar regions. Maxillary sinus obliteration is common in OMs which is located in the maxilla. Extraosseous form is unique but there are reports especially located in the gingiva. Radiographically, OMs usually have characteristic tennis-racket trabeculations in multilocular lesions; however, they can be unilocular too (Figs. 18.13 and 18.14). Painless expansion is common and occasionally cortical plate perforation may develop. Margins of the OMs are usually a misleading feature in orthopantomographs since the actual borders of OMs are relatively diffuse and defined better in CT/MRI images [1, 3–5, 20]

18.1.3.3 Cementoblastoma

Cementoblastoma (CB) is a benign odontogenic tumor that is associated with the roots of teeth. It is characterized by the formation of cementum-like tissue on a tooth root. CB is a relatively rare tumor, accounting for less than 7% of all odontogenic tumors. Majority of the CBs locate at mandibular premolar-molar site. Pulpitis-like pain with expansion at buccal-lingual/palatal cortical plates are the most common clinical findings. A well-defined radiopaque calcified mass with a thin radiolucent surrounding zone appearance is almost pathognomonic. CBs relatively grow slowly and they can reach quite big sizes if they left untreated [1–5, 21]

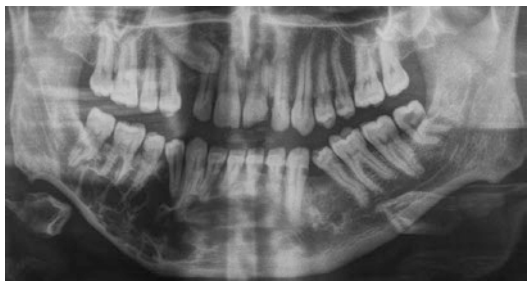

Fig. 18.13 Odontogenic myxoma. OPG reveals a multilocular, predominantly radiolucent lesion with non-corticated borders at mandibular right premolar-molar region which extends to mandibular basis. Note the thin and sharp septa formations which are characteristic of odontogenic myxomas

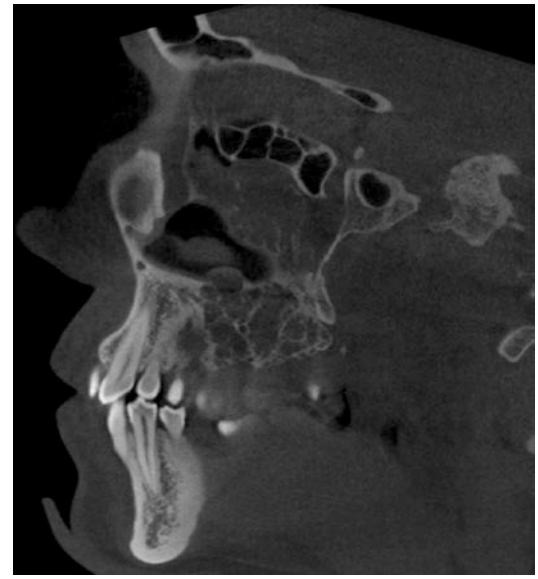

Fig. 18.14 Odontogenic myxoma. CBCT sagittal slice reveals a multilocular, predominantly radiolucent lesion with non-corticated borders at maxillary left premolar region which extends to the floor of maxillary sinus. Note the thin and sharp septa formations which are characteristic of odontogenic myxomas

18.1.3.4 Cemento-Ossifying Fibroma

See Sect. 18.1.5.1.

18.1.4 Benign Maxillofacial Bone and Cartilage Tumors

18.1.4.1 Chondroma

Chondromas are the benign mesenchymal tumor of hyaline cartilage which arise in the trabecular cavity of mandible/maxilla. If the tumor has malignant features "chondrosarcoma" is the term that should be used. They are very rare in the dentomaxillofacial region. MRI and CT are useful imaging modalities to visualize chondromas and MRI is superior in defining the extension of the tumor. Chondromas are seen as well-defined hypodense tumors with some internal calcifications [1–5]

18.1.4.2 Osteoma

Osteomas are benign tumors composed of mature bone. Their main localization is craniofacial bones. They are more common in mandible (especially mandibular condyle) than in the maxilla (Fig. 18.15). There are two variants of osteomas as surface osteomas and central osteomas. Surface osteomas are usually painless swellings which are located on the cortical surface of the bone (Fig. 18.16). Central osteomas are well-defined calcified hyperdense masses that are mostly smaller than 2 cm in size [1–5, 22, 23].

Common sonographic features of bone and cartilage tumors are (Fig. 18.17):

- Internal Structure: Since they are calcified structures their internal structure is mostly anechoic. Acoustic shadowing is prominent.

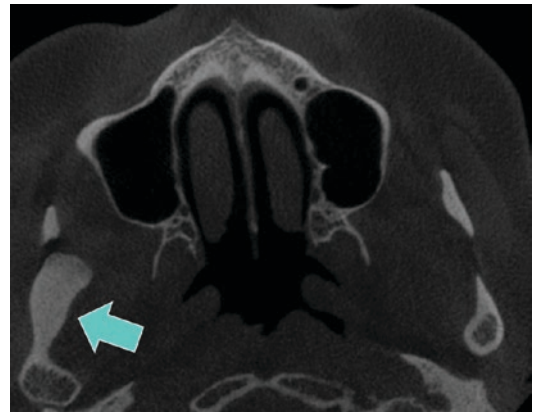

Fig. 18.15 Peripheral osteoma. CBCT axial slice reveals a unilocular well-defined calcified hyperdense lesion which is located at right mandibular notch. Note that there is no lining between the healthy bone of right mandibular condyle and the lesion

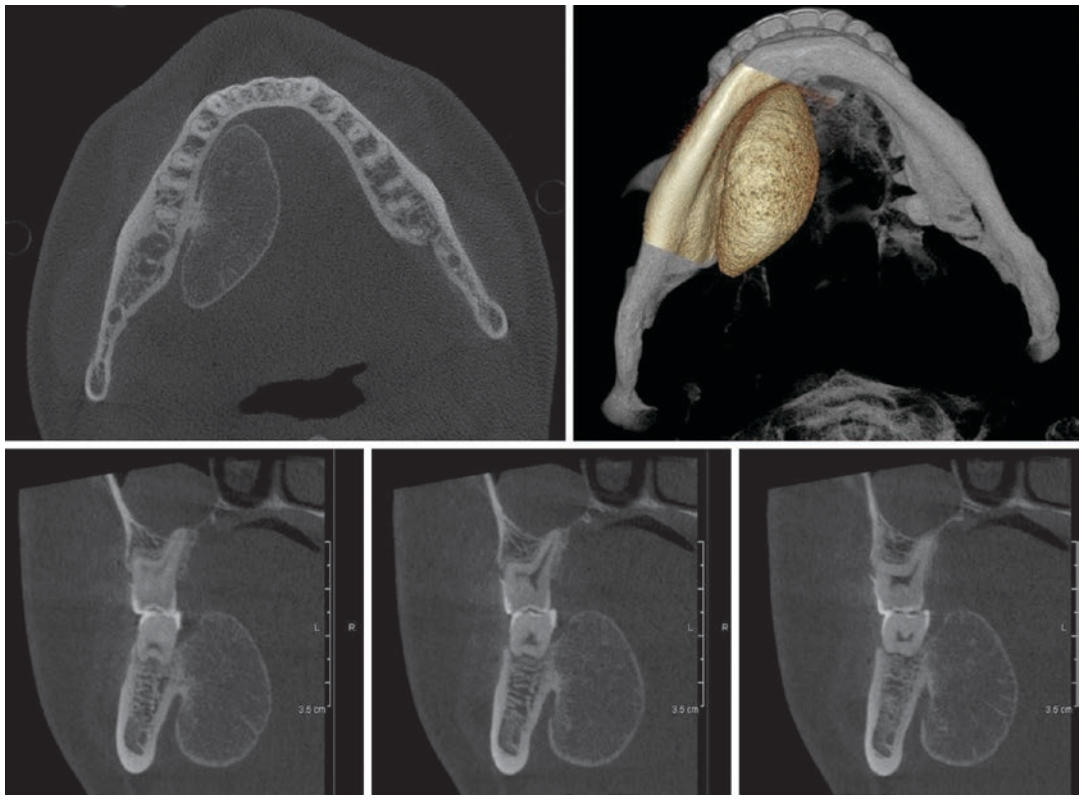

Fig. 18.16 Peripheral osteoma. CBCT axial and cross-sectional images reveal a unilocular well-defined calcified hyperdense peduncled lesion which is attached to mandibular lingual cortical plate

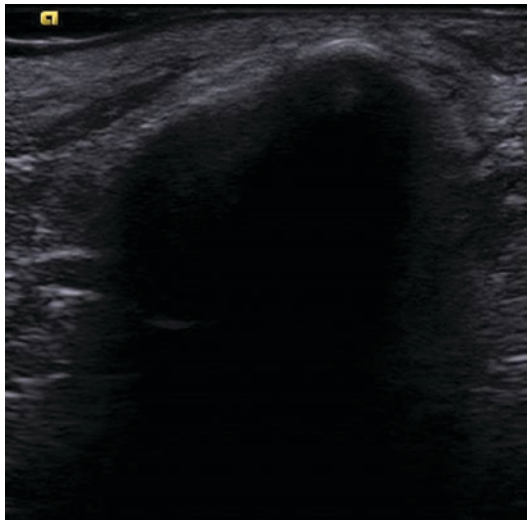

Fig. 18.17 Osteoma. USG image showing extensive acoustic shadowing due to osteoma

No vascularization is expected in osteomas; thus, Doppler examination will not reveal any vascularization. They are mostly unilocular

- Peripheral Structure: If no secondary infection is involved, cortical boundaries of the lesion usually appear as well-defined.

18.1.4.3 Melanocytic Neuroectodermal Tumor of Infancy

Melanocytic neuroectodermal tumor of infancy (MNTI) is a rare tumor which is defined by WHO as "locally aggressive, rapidly growing tumour consisting of a biphasic population of small neuroblast-like and larger melanin-producing epithelioid cells." The most common localization is maxilla which accounts for more than 50% of all MNTI. 90% of MNTIs were reported in infants. Clinically a sessile, black-blue colored lesion which grows rapidly is seen. Radiographically, an aggressive lesion which causes destruction at cortical and trabecular bone is seen [1].

18.1.4.4 Chondroblastoma

Chondroblastoma is a benign chondroid-producing tumor which is composed of chondroblasts. They are very unique at maxillofacial region. Chondroblastomas which are localized in maxillofacial region is mostly seen in temporomandibular joint [1].

18.1.4.5 Chondromyxoid Fibroma

Chondromyxoid fibroma is a rare benign cartilaginous tumor and around 5% of cases are associated with maxillofacial bones [1].

18.1.4.6 Osteoid Osteoma

Osteoid Osteoma is a very rare benign bone-forming tumor with limited growth potential. Most of the cases have diameters less than 2 cm and pain is common. Radiographically a mixed lesion with cortical radiopaque/hyperdense periphery and radiolucent/hypodense internal structure is seen [1, 24].

18.1.4.7 Osteoblastoma

Osteoblastoma is a rare benign bone-forming tumor which has local aggressive features. They are mostly seen in spinal column and around 10% of osteoblastomas are seen in craniofacial bones. Their differential diagnosis with osteoid osteomas is made with lesion's diameter since osteoblastomas have diameters more than 2 cm while osteoid osteomas are relatively small and less aggressive. Radiographic features of osteoblastomas may resemble a malignant tumor and a predominantly radiolucent/hypodense lesion is seen [1, 25].

18.1.4.8 Desmoplastic Fibroma

Desmoplastic fibromas (DF) are locally aggressive myofibroblastic lesions of the bone. About 86% of the DFs occur in mandible and they are generally localized in the mandibular ramus and mandibular angulus region. Clinically DFs are generally painless slow-growing lesions. DFs are seen as well-defined hypodense lesions without any calcified structure at the internal structure. They may cause destruction at the mandibular angulus site which may have a malignant lesion appearance (Fig. 18.18) [1–5, 26, 27].

Sonographic features of desmoplastic fibromas are (Fig. 18.19):

- Internal Structure: DFs have heterogeneous internal structure, mostly hypoechoic to the surrounding soft tissue and muscles. Minimal

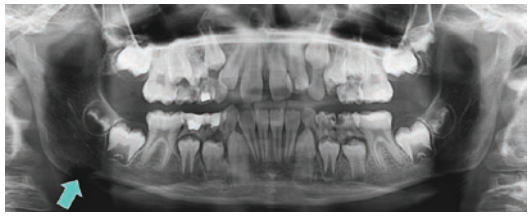

Fig. 18.18 Desmoplastic fibroma. OPG reveals an ill-defined unilocular radiolucent lesion which is located at right mandibular angulus region and below the mandibular canal. This localization is characteristic of desmoplastic fibromas

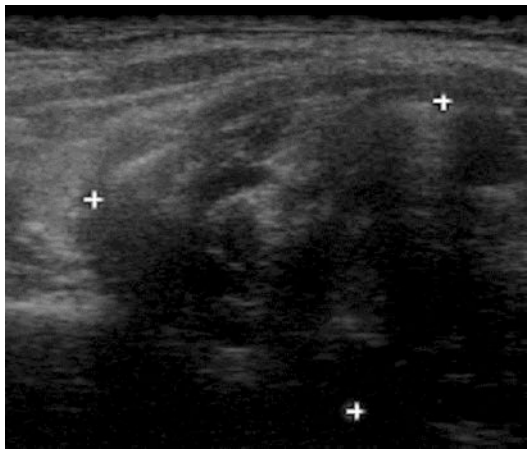

Fig. 18.19 Desmoplastic fibroma. B-mode USG showing lobulated margins with predominantly anechoic areas of a desmoplastic fibroma in the mandible

or moderate vascularization is seen on Doppler examination.

- Peripheral Structure: DFs do not have corticated capsules; thus, no hyperechoic lining surrounds the lesion. Their periphery has smooth and occasionally lobulated margins.

18.1.5 Fibro-Osseous and Osteochondromatous Lesions

18.1.5.1 Ossifying Fibroma

Ossifying fibromas (OF) are benign fibro-osseous neoplasms affecting both the craniofacial skeleton and jawbones. There are three different variants of OFs as juvenile ossifying fibroma (JOF), juvenile psammomatoid ossifying fibroma (JPOF), and cemento-ossifying fibroma (COF) the ossifying fibroma of odontogenic origin. COF is usually seen in the third and fourth decades; whereas, JOF is usually seen in children and adolescents. JPOF has a relatively wide age range since there are cases which have been reported in 3-month-old patients and a 72-year-old patient. COF is generally seen in the tooth-bearing areas of the jawbones and predominantly in mandibular premolar/molar site (Figs. 18.20 and 18.21). Although OFs which were located outside of the jawbones were reported, they are extremely rare. COFs are generally painless intraosseous expan-

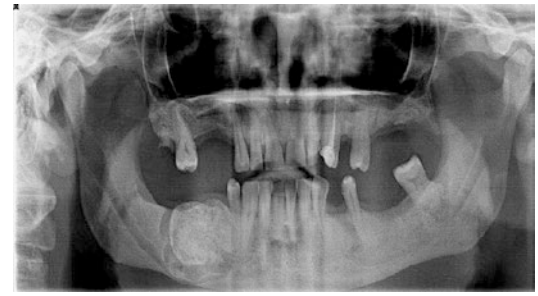

Fig. 18.20 Cemento-ossifying fibroma**.** OPG reveals a well-defined radiopaque calcified mass at mandibular right premolar region. Note the epicentric growth appearance which is a characteristic feature for ossifying fibromas

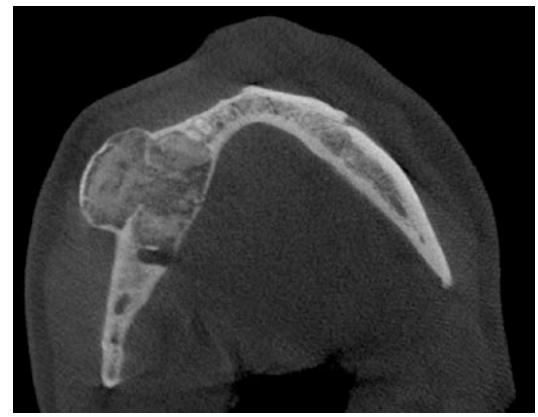

Fig. 18.21 Ossifying fibroma. CBCT axial slice of Fig. 18.20 reveals a well-defined hyperdense lesion with a round shape and gross buccal cortical plate expansion

sive lesions which may elevate the floor of the maxillary sinus and expand the basis mandibularis. Initial COF lesions are radiolucent/hypodense and as they progressively maturate they become radiopaque/hyperdense calcified structures [1–5, 28–31].

18.1.5.2 Familial Gigantiform Cementoma

Familial gigantiform cementoma (FGC) is a rare form of fibro-osseous lesion which is only seen in jawbones. They are characterized by the facial deformities caused by multifocal expansive lesions. Sporadic, familial, and autosomal dominant inheritance cases were reported. Radiographically, radiopaque calcifications in a radiolucent lesion with well-defined expansive borders are seen in CT images. Most of the time these lesions are bilateral and bimaxillar [1, 32].

18.1.5.3 Fibrous Dysplasia

Fibrous dysplasia (FD), as defined in the WHO Classifications of Head and Neck Tumours guide, is a skeletal anomaly in which normal bone is replaced and distorted by poorly organized and inadequately mineralized immature bone and fibrous tissue. FD is caused by mutations in the GNAS gene. FDs present 7% of all benign bone tumors and initial diagnoses are mostly in children. There are three different involvements of the FD as follows:

- Monostotic FD: involving a single bone or adjacent craniofacial bones (Craniofacial FD)
- Polyostotic FD: involving multiple bones
- McCune-Albright Syndrome: FDs are present with cafe-au-lait skin pigmentation and endocrine abnormalities [1, 3–5, 33, 34].

Polyostotic and Monostotic FDs usually occur in femur and craniofacial bones but every single bone can have FDs. FDs are more common in maxilla than in the mandible [3–5].

FDs are characterized with painless expansive lesion of the jawbones which may lead to malocclusion. Clinical findings of the advanced and extensive lesions are visual loss, headache, nasal obstruction, and hearing loss. Radiographically, FDs appear radiolucent in early lesions and progressively they become sclerotic. "Ground-glass appearance" is a characteristic radiographical finding for FDs with ill-defined borders and radiopaque internal structure which is indistinct from the surrounding healthy trabecular bone [3–5, 35, 36] (Figs. 18.22 and 18.23).

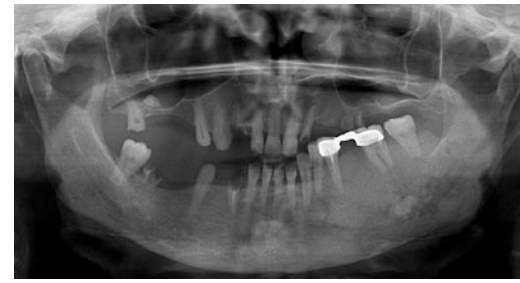

Fig. 18.22 Fibrous dysplasia. OPG reveals an ill-defined radiopaque calcified mass at mandibular left posterior site with gross expansion

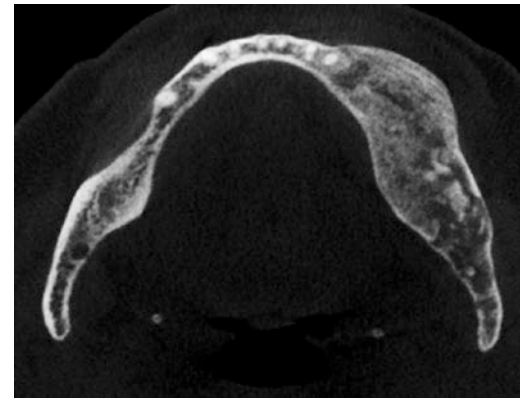

Fig. 18.23 Fibrous dysplasia. CBCT axial slice of Fig. 18.22 reveals an ill-defined hyperdense mass with buccal and lingual cortical plate expansion

18.1.5.4 Cemento-Osseous Dysplasia

Cemento-osseous dysplasia (COD) is the most common fibro-osseous lesions of the jaws which is mostly seen in middle-aged women. WHO defines this lesion as "a non-neoplastic fibro-osseous lesion of the tooth-bearing regions of the gnathic bones" [1].

It can be localized at three different anatomical locations [3–5].

- Periapical COD: Apical region of the mandibular incisor teeth
- Focal COD: Single tooth or quadrant involvement
- Florid COD: Multiquadrant involvement

Only florid CODs can cause expansive and pain but periapical CODs and focal CODs are generally asymptomatic and may only be detected on routine radiographic examinations (Figs. 18.24 and 18.25). Anterior teeth that are associated with periapical CODs are vital. Regardless of their location, they initiate as homogenous radiolucent lesions and as they maturate calcified areas in the central portion of the lesion occur. Advanced or maturated lesions can have a completely radiopaque internal structure with a thin radiolucent rim [3–5, 37–39].

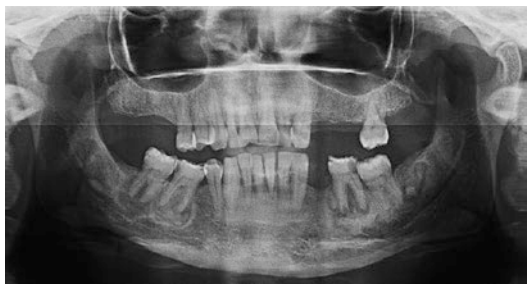

Fig. 18.24 Florid cemento-osseous dysplasia. OPG reveals multiple well-defined mixed lesions which are located at the apex of mandibular molar teeth. Note the different calcification rates of each lesion

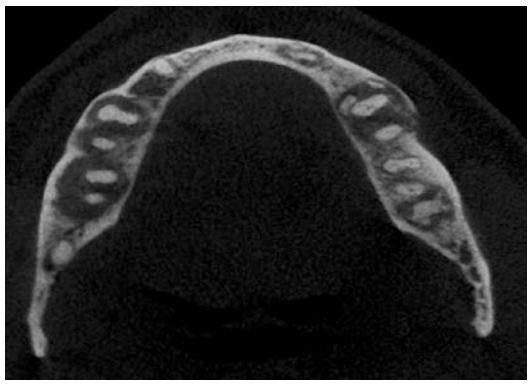

Fig. 18.25 Florid cemento-osseous dysplasia. CBCT axial slice of Fig. 18.24 reveals multiple mixed lesions at the apex of mandibular teeth with buccal and lingual cortical plate expansion. Since the lesion is matured the lesions appear predominantly hypodense

18.1.5.5 Osteochondroma

Osteochondromas are rare benign neoplasms and less than 1% of the cases are located in the head and neck region. It is mostly found in the axial skeleton since it generally occurs where endochondral ossification exists. Skull base, zygomatic bone, mandibular coronoid process and mandibular condyle, and maxillary sinus are the most common reported sites in the head and neck region. Common clinical features are malocclusion, pain, asymmetry, and trismus for the lesions that are located in mandible. Radiographically a thin cartilaginous cap and a lobulated bone growth is seen within the cortical or trabecular area of the relevant bone [1, 3–5, 40, 41].

Common sonographic features of fibro-osseous and osteochondromatous lesions are (Fig. 18.26):

- Internal Structure: Since these lesions are known for their calcified features, maturated lesions will have a complete anechoic internal structure with extensive acoustic shadowing.
- Peripheral Structure: These lesions generally have smooth borders; however, no hyperechoic lining is visible surrounding the lesions periphery.

18.1.6 Giant Cell Lesions and Simple Bone Cyst

18.1.6.1 Central Giant Cell Granuloma

Central giant cell granulomas (CGCG) are occasionally aggressive benign osteolytic lesions of the jawbones that account for 10% of the benign tumors in mandible/maxilla. It was previously known as "reparative giant cell granuloma"; however, as the WHO stated, this synonym is obsolete. Majority of CGCG are found in patients younger than 20 years and in females. Most frequent localization of this lesion is mandibular

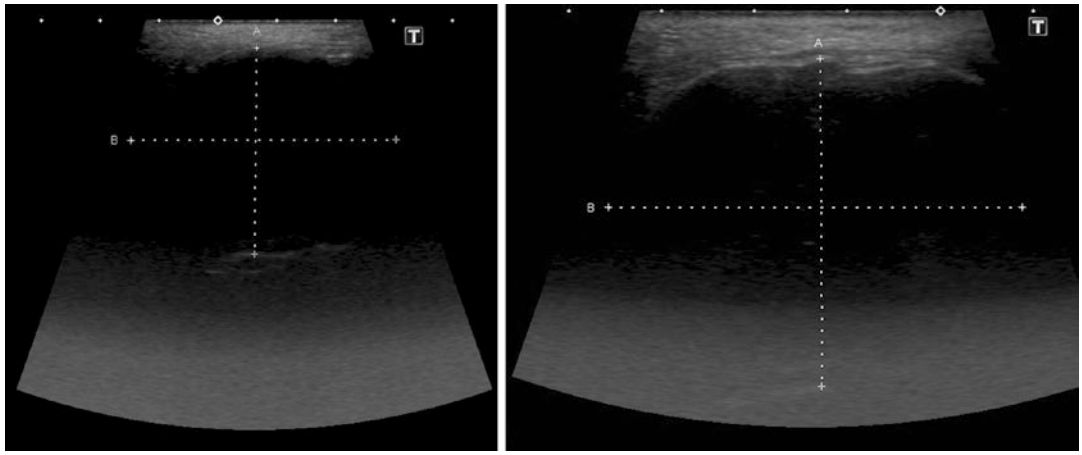

Fig. 18.26 Cemento-ossifying fibroma. US reveals the characteristic of fibro-osseous and osteochondromatous lesions. Since the lesions in this subtype has calcified internal structure an acoustic shadowing is mostly seen inside the lesion. The most superficial portion of the lesions can be examined

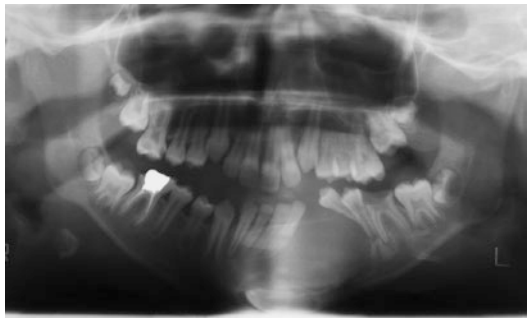

Fig. 18.27 Central giant cell granuloma. OPG reveals an expansive radiolucent lesion which caused teeth displacement and impaction of mandibular left canine

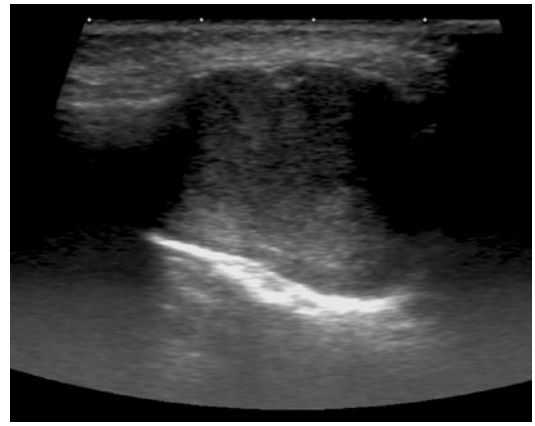

Fig. 18.28 Central giant cell granuloma. US image of Fig. 18.27 reveals a well-defined unilocular lesion with hypoechoic internal structure. Acoustic enhancement is present and no cortical plate perforation is seen

anterior region. Syndromes such as Noonan syndrome and Neurofibromatosis Type I should be considered in cases with multiple CGCG [1, 3–5, 42, 43].

CGCGs are generally asymptomatic but less than half of the CGCG may present pain, cortical perforation, invasion of surrounding tissues, and tooth resorption. Radiographically, expansive, well-defined hypodense/radiolucent lesions can be seen in CBCT images and MRI-CT images can demonstrate the soft tissue involvement of the CGCGs. They are mostly unilocular. PET-CT images are helpful in detecting multicentric lesions [1, 3–5, 42, 43] (Fig. 18.27).

Common sonographic features of central giant cell granulomas are (Fig. 18.28):

- Internal Structure: Hypoechoic/anechoic internal structure is mostly seen. Moderate to advanced vascularization is seen on Doppler examination. They are mostly unilocular but advanced cases can be multilocular.
- Peripheral Structure: If no secondary infection is involved, well-defined cortical boundaries

of the lesion usually appear as clear continuous hyperechoic linings. If destructions at cortical bones are present, disrupted hyperechoic linings can be seen. Acoustic enhancement is usually present.

18.1.6.2 Peripheral Giant Cell Granuloma

Peripheral giant cell granulomas (PGCG) are the most common giant cell lesion that affects the oral tissues. They are localized in alveolar mucosa or gingiva. Mechanism of the lesion is described by the WHO as "As a result of local irritation of the muco-periosteum or the coronal part of the periodontal ligament by dental calculus deposits or other types of chronic irritation." PGCGs are frequently seen in the mandibular gingiva and mandibular edentulous alveolar ridges. Clinically, a purple-blue lesion with an ulcerated or papillomatous surface is seen. CBCT images may reveal a recess at the surface of the adjacent cortical plate (Fig. 18.29) [1, 44, 45]

Common sonographic features of peripheral giant cell granulomas are (Figs. 18.30 and 18.31):

- Internal Structure: Hypoechoic internal structure is mostly seen. An advanced vascularization is frequently seen in Doppler examination. They are mostly unilocular. Elastography will demonstrate a harder tissue than the surrounding soft tissues.
- Peripheral Structure: If no secondary infection is involved, the lesion has usually well-defined boundaries. If perforations on the surface are present, the well-defined periphery structure may disappear. Acoustic enhancement is usually present.

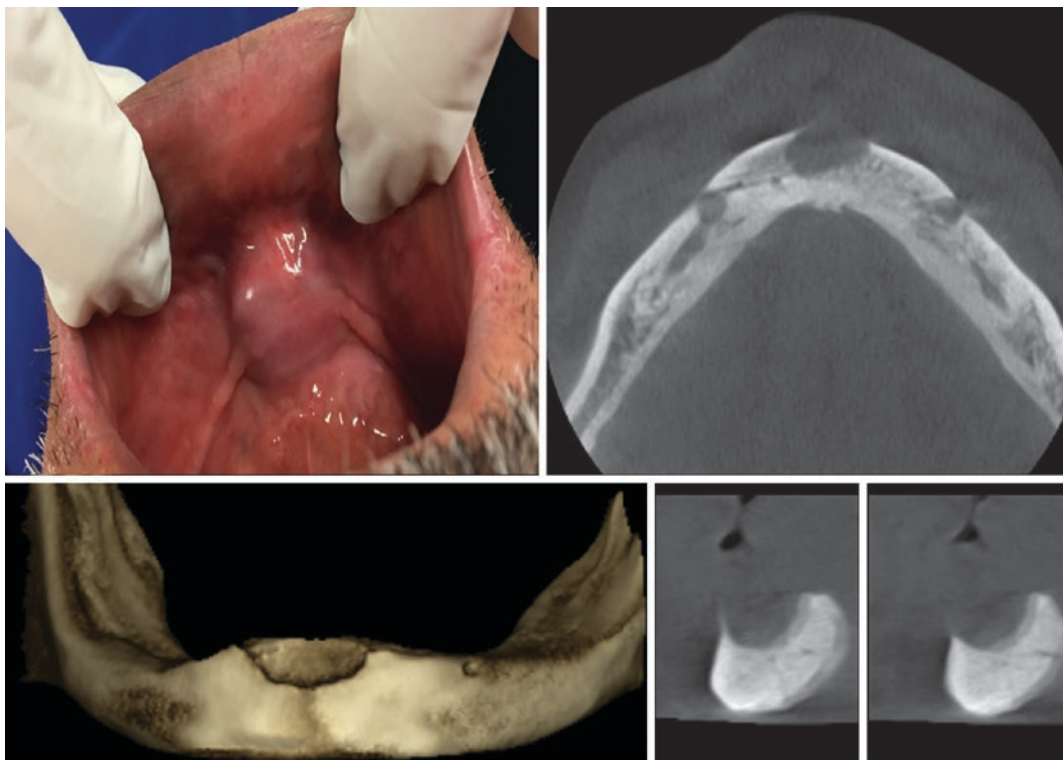

Fig. 18.29 Peripheral giant cell granuloma. (**a**) Intraoral swelling is seen at edentuluos mandibular anterior site. (**b**) CBCT axial slice reveals a unilocular, well-defined non-corticated hypodense lesion with buccal cortical plate destruction. (**c**) CBCT 3D Reconstruction of the patient. (**d**) Cross-sectional slices reveal a unilocular, well-defined non-corticated hypodense lesion with buccal cortical plate destruction

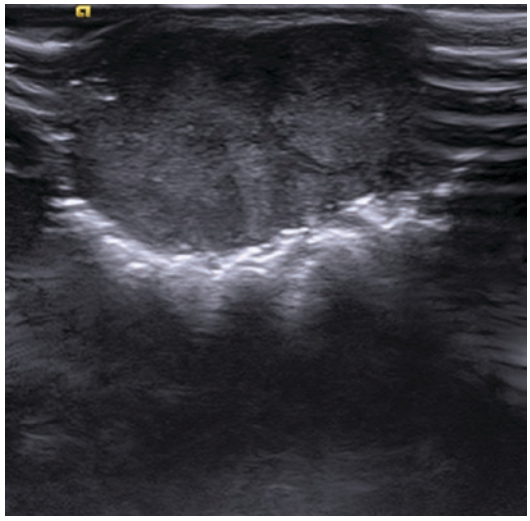

Fig. 18.30 Peripheral giant cell granuloma**.** US reveals a unilocular, well-defined lesion with heterogeneous echogenicity. Acoustic enhancement is seen

18.1.6.3 Aneurysmal Bone Cyst

WHO defines Aneurysmal Bone Cyst (ABC) as "cystic or multicystic expansile osteolytic neoplasm composed of blood-filled spaces separated by fibrous septa containing osteoclast-type giant cells." ABCs account for 1.5% of all lesions in the mandible and maxilla; however, they can be seen in the craniofacial complex structures [1].

They are frequently seen in the mandibular posterior region since the ABCs in mandible account for more than 60% of all cases. Clinically, a painful swelling is present which may cause tooth displacement and root resorption. Mandibular ABCs are rather safer since ABCs in maxilla can affect the orbits, paranasal sinuses, and nasal fossa. Radiographically, CBCT reveals a well-defined, unilocular or multilocular hypodense lesion with an expansion or a perforation in the cortical plates. Extension of ABCs may not be visible with CBCT in cases with cortical perforation; thus, CT and MRI should be performed (Figs. 18.32 and 18.33) [1, 3–5, 46, 47].

MRI reveals the fluid-fluid level in ABCs; however, this imaging feature is not unique for the ABCs and can be found in the other giant cell tumors, chondroblastoma, and telangiectatic osteosarcomas.

Common sonographic features of aneurysmal bone cysts are (Fig. 18.34):

- Internal Structure: A heterogeneous hyperechoic internal structure with or without a fluid-fluid level is seen. Doppler imaging may reveal mild vascularity.
- Peripheral Structure: Cases without perforations or destruction reveal well-defined hyperechoic borders; however, cases with cortical destruction reveal ill-defined borders with an extension of the ABC to the adjacent soft tissue.

18.1.6.4 Simple Bone Cyst

Simple Bone Cyst (SBC), also known as traumatic bone cyst and hemorrhagic bone cyst, is an intraosseous cavity without any epithelial surroundings. SBCs may have hematic fluid inside their cavity and also they may represent empty cavities. SBCs are frequently seen in the metaphysis of long bones and the most common localization in the head and neck region is the mandibular body [1, 3–5, 48, 49].

Most of the SBCs are asymptomatic; however, some cases with a pathological fracture were also reported.

Radiographically, OPG and CBCT reveal well-defined, generally unilocular, radiolucent/hypodense lesions which extend between the roots at the relevant area. Root resorption or tooth displacement is not seen (Figs. 18.35 and 18.36) [1, 3–5, 48, 49].

Common sonographic features of simple bone cyst are (Fig. 18.37):

- Internal Structure: Homogeneous anechoic internal structure is generally seen without any hyperechoic focis.
- Peripheral Structure: Well-defined oval or round borders are seen. SBCs with hematic fluid may have an acoustic enhancement; however, SBCs with empty cavities may not have an acoustic enhancement.

18.1.6.5 Cherubism

Cherubism is an autosomal dominant inherited genetic condition that affects mandible and max-

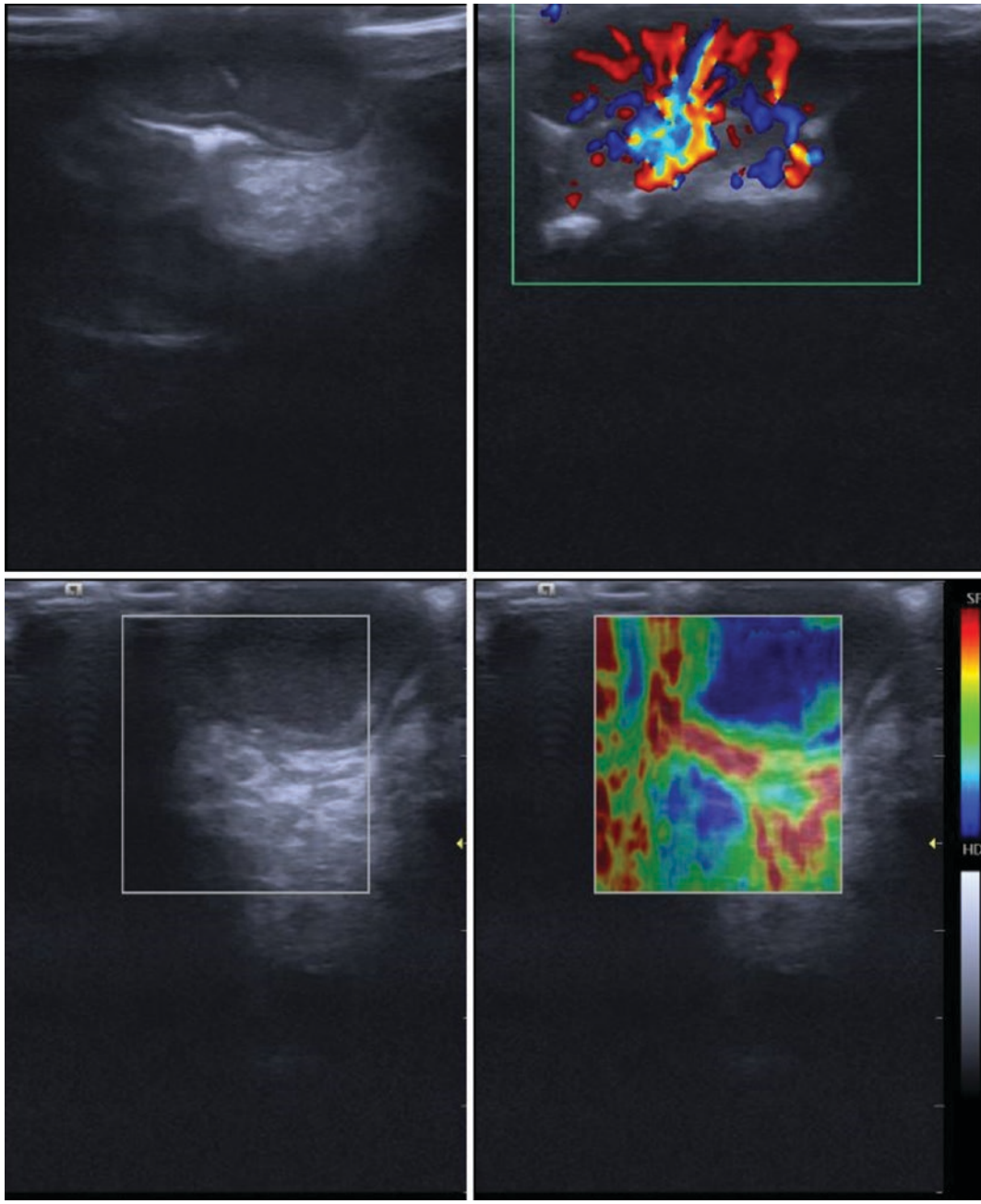

Fig. 18.31 Peripheral giant cell granuloma. (**a**) US reveals a unilocular, well-defined lesion with a predominantly hypoechoic internal structure. Heavy acoustic enhancement is seen. (**b**) Doppler US reveals increased hypervascularity. (**c**, **d**) Elastography reveals the density of lesion comparing to the surrounding soft tissues. Note that the lesion is denser than adjacent tissues

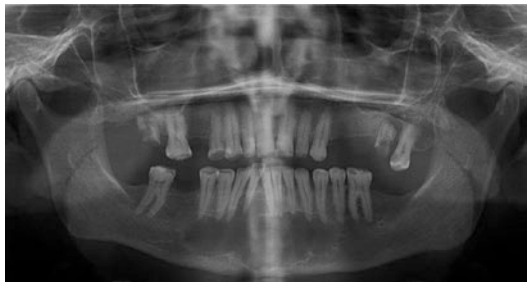

Fig. 18.32 Aneurysmal bone cyst. OPG reveals a unilocular radiolucent lesion with lobulated well-defined borders which extends between mandibular left premolar region to mandibular right premolar region

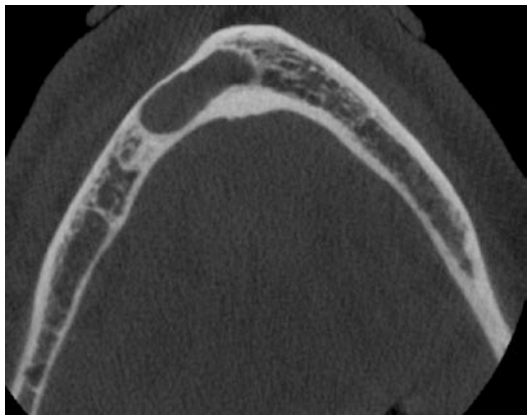

Fig. 18.33 Aneurysmal bone cyst. CBCT reveals a unilocular, non-expansive, hypodense lesion with well-defined non-corticated borders

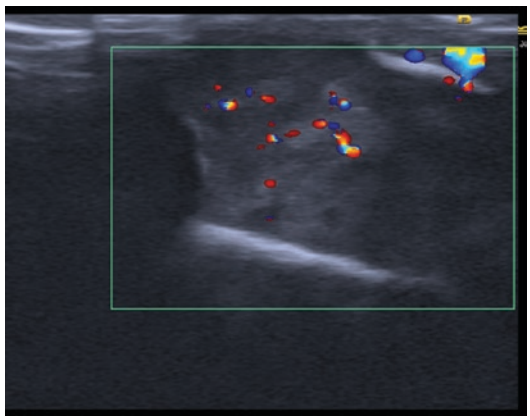

Fig. 18.34 Aneurysmal bone cyst. US reveals a unilocular, well-defined lesion with heterogeneous internal structure. Minor acoustic enhancement is seen. Doppler US reveals mild vascularization

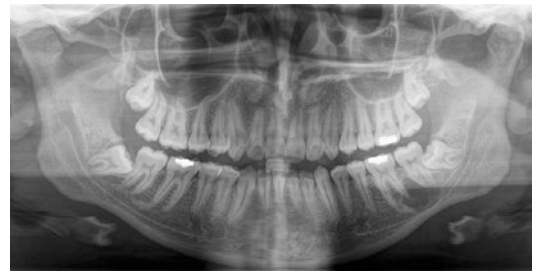

Fig. 18.35 Simple bone cavity. OPG reveals a unilocular radiolucent lesion with well-defined non-corticated scalloped borders at mandibular left molar region

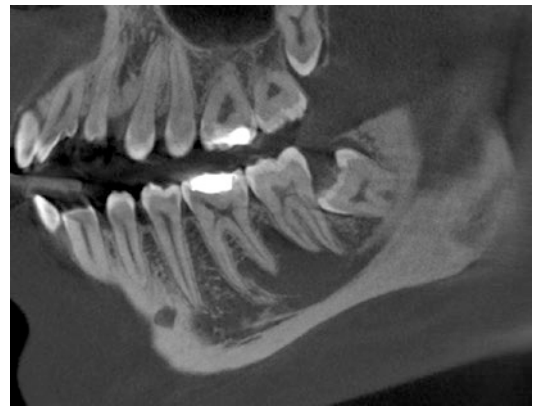

Fig. 18.36 Simple bone cavity. CBCT sagittal slice of Fig. 18.35 reveals the extension of the lesion with non-corticated borders to the interdental area

illa. They are usually seen before age of 6 years and followed by complete or partial regression after. Clinically, slow-growing, bilateral, symmetrical expansive lesions which are located at the posterior sites of the jaw is seen. These cyst-like giant cell lesions cause retraction of the facial skin, which causes the characteristic appearance which is falsely known as cherubs. The appearance is actually similar to the "putti" facial appearance [1, 3–5, 50, 51].

Radiographically, bilateral symmetrical expansive lesions are seen starting from the tuberosity of maxilla and first molar region of the mandible. These expansive lesions are multilocular radiolucent/hypodense lesions which may cause thinning at cortical plates, malocclusion, tooth displacement, and loosening of the teeth.

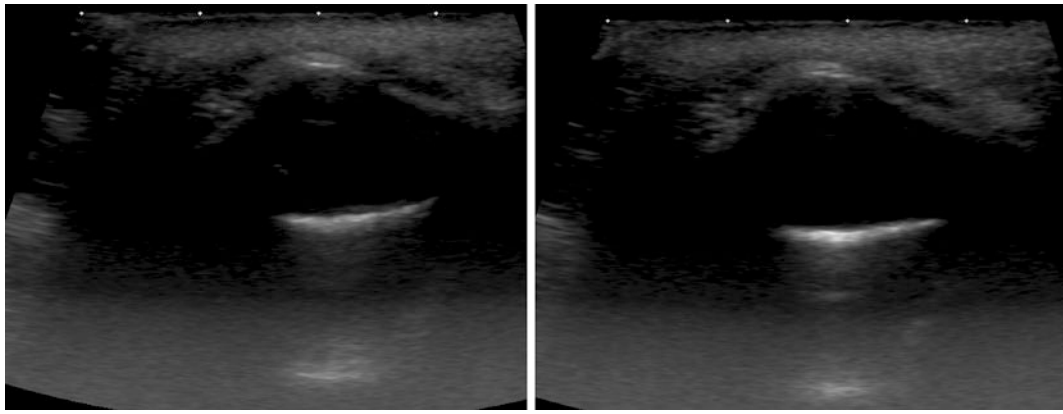

Fig. 18.37 Simple bone cavity. US reveals a unilocular, well-defined anechoic lesion with minor acoustic enhancement

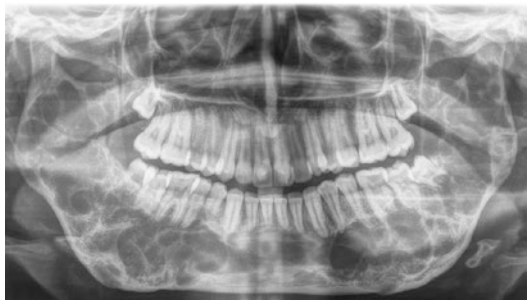

Fig. 18.38 Cherubism. OPG reveals bilateral multilocular expansive lesions in mandible. No lesion at maxilla is seen

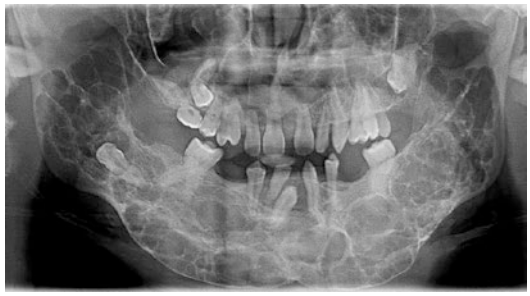

Fig. 18.39 Cherubism. OPG reveals bilateral multilocular expansive lesion in maxilla and mandible. Note the advanced teeth displacement

As the giant cell lesions have regression, lytic cherubism lesions are replaced by sclerotic new bone [3–5, 50, 51]. (Figs. 18.38, 18.39, and 18.40).

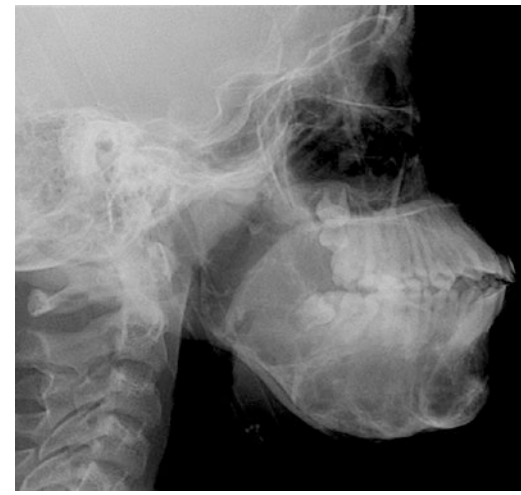

Fig. 18.40 Cherubism. CBCT Scout image of Fig. 18.38 reveals expansive lesions in mandible

18.1.7 Hematolymphoid Tumors

18.1.7.1 Solitary Plasmacytoma of Bone (SPB)

Solitary plasmacytoma of bone (SPB) is the only tumor that is classified under the "hematolymphoid tumors" section. WHO defines SPBs as "a localized proliferation of monoclonal plasma cells involving bone." SPBs are rare and they only represent around 4% of plasma cell neoplasms. They are usually seen in the axial skeleton; however, rare cases are reported in the head

and neck region. SPBs in the head and neck region are more common in the mandible than in the maxilla and they are usually located in the mandibular body, mandibular ramus, and mandibular angulus. Those areas were more affected since they are marrow rich areas in the head and neck region [1, 3, 52].

Clinically, hemorrhage and expansion of the jaw are seen with the pain in the jaws and teeth. Some cases with multiple teeth migration were also reported. Radiographically, a well-defined, multilocular hypodense/radiolucent lesion with or without septas is seen mostly in the mandible. The anteroposterior extension of the lesion may resemble an odontogenic keratocyst which should be included in the differential diagnosis [1].

Common sonographic features of the solitary plasmacytoma of bone are (Fig. 18.41):

- Internal Structure: A mix (Hypo and Hyperechoic internal structure) usually be seen. Moderate vascularization is seen on Doppler examination. The lesions may appear multilocular with septas. In the case of internal bony septas, hyperechoic linings can be present.
- Peripheral Structure: Cortical boundaries of the lesion usually appear as clear continuous hyperechoic linings. If destructions at cortical bones are present, a disrupted hyperechoic linings can be seen.

18.1.8 Other Benign Tumors of Maxillofacial Region

18.1.8.1 Hemangioma

Hemangioma is a benign vascular tumor characterized by the proliferation of hyperplastic endothelial cells and pericytes. Hemangiomas are divided into two classes according to their diameters as cavernous and capillary hemangiomas. While capillary hemangiomas have thin-walled relatively small vessels, cavernous hemangiomas have large cavities which are filled with blood. Mixed hemangiomas were also reported. At the maxillofacial region, salivary glands of infants are very common site for hemangiomas and they represent 50% of all parotid tumors.

Clinically, a purple-red or pink soft tissue mass with smooth or lobulated borders is seen with various diameters. Hemangiomas give positive diascopy test; however, this test is not always reliable with capillary hemangiomas. Hemorrhages may be seen after minor traumas or spontaneously [1, 3–5, 53–55].

Radiographically, OPG and CT may not reveal the tumor but the erosion and destruction at the cortical and trabecular bones may be seen (Fig. 18.42). MRI reveals low-intermediate signal in T1-W images and high signal in T2-W images. Signal void areas which are seen in T2-W images are characteristic of hemangiomas which shows peripheral and central vessel flows. Internal calcifications may be seen in T2-W and fat-suppressed images [56, 57] (Fig. 18.43).

Common sonographic features of the hemangiomas are:

- Internal Structure: Heterogeneous internal structure is seen with possible calcified hyperechoic structures. Doppler US demonstrates mild-high internal vascularity inside the lesion. Cavernous hemangiomas have higher vascularization pattern than capillary hemangiomas in Doppler US images (Fig. 18.44).
- Peripheral Structure: Lobulated or smooth well-defined borders are seen. If calcifications are present in the lesion, comet-star artifact can be seen.

18.1.8.2 Lipoma

Lipomas are benign soft tissue tumors of mature adipocytes. Although lipomas are uncommon in the maxillofacial region, they are the most frequent soft tissue tumor and they are present in around 2% of the population. Clinically, lipomas are painless soft tissue swellings and they may get affected with changes in weight. They are mostly seen in torso and proximal extremities. Most common sites for oral lipomas are parotid region, lip, buccal mucosa, submandibular region, and tongue [58–62].

Radiographically, CT images reveal hypodense superficial lesions with minimal inter-

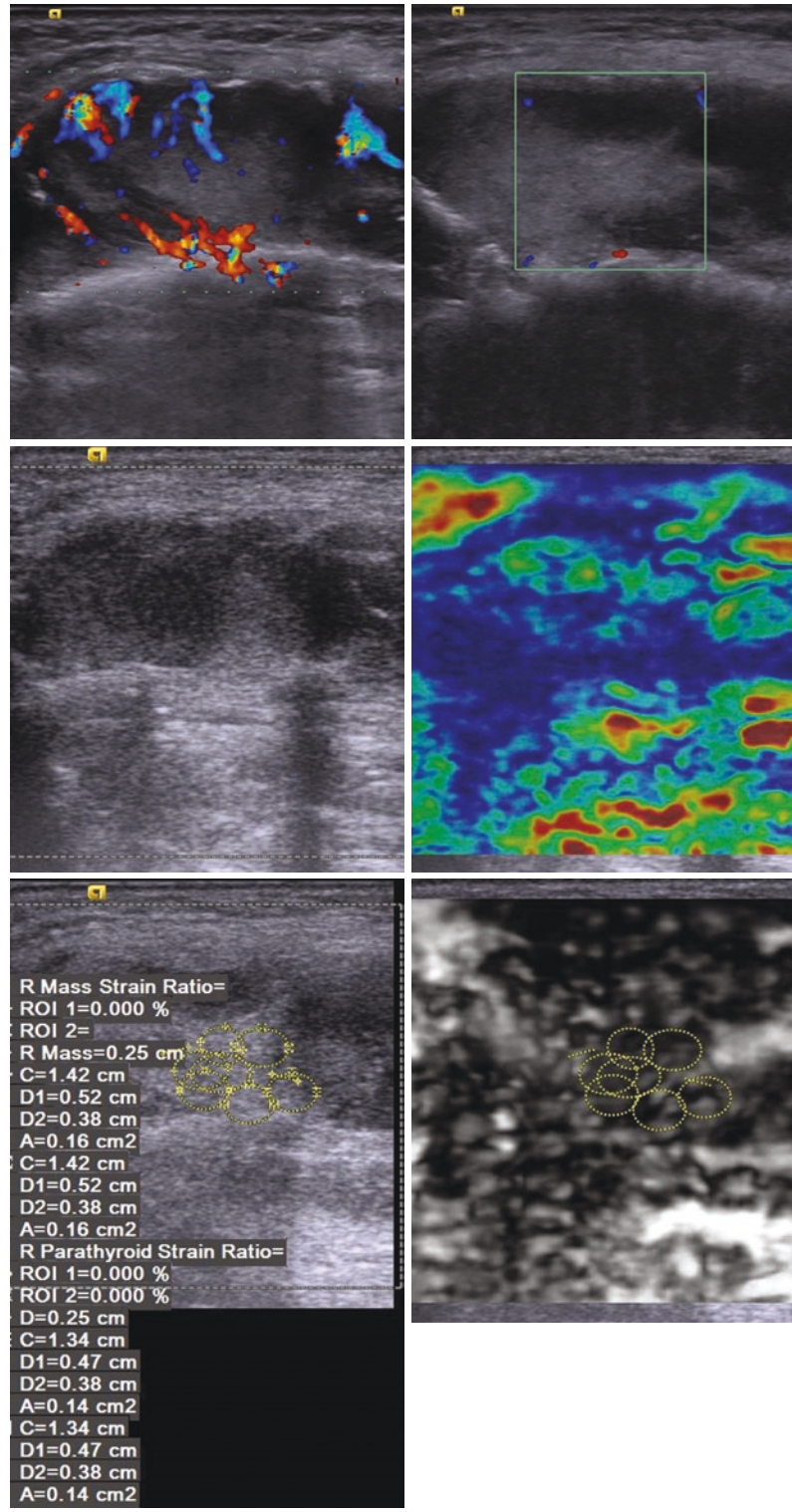

Fig. 18.41 Plasmacytoma. Doppler USG image showing a moderate vascular lesion with hyperechoic solid content. The lesion disrupted hyperechoic linings due to internal septas. Colored strain elastography showing a moderate stiff lesion

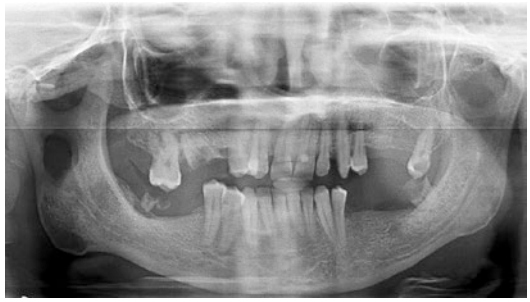

Fig. 18.42 Intraosseous hemangioma. OPG reveals well-defined non-corticated borders of a unilocular radiolucent lesion at mandibular right ascending ramus

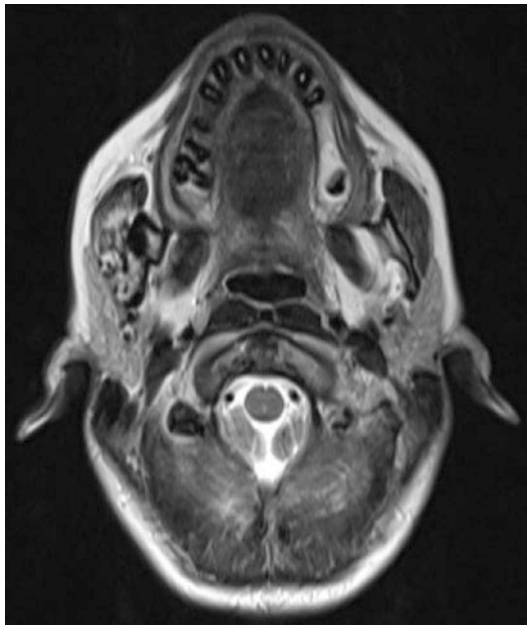

Fig. 18.43 Cavernous hemangioma. MRI T2-W image of Fig. 18.42 reveals heterogeneous signal with signal-void areas which is characteristic for intraosseous cavernous hemangiomas

nal soft tissue component and low HU value. Lipomas which are intramuscular may invade and adhere to the relevant muscle. MRI reveals hyperintense lesions with no or minimal enhancement and saturation at FAT-SAT sequences in T1-W images and T2-W image [1–5, 63–65].

Common sonographic features of the hemangiomas are (Figs. 18.45, 18.46, and 18.47):

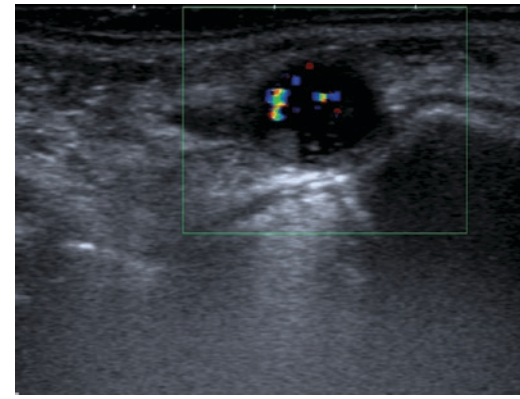

Fig. 18.44 Capillary hemangioma. Doppler US reveals unilocular well-defined predominantly anechoic lesion with mild vascularization. Since capillary hemangiomas are less vascularized than cavernous hemangiomas, the vascularization appereance can be diminished. Note the hyperechoic internal calcification areas as Phleboliths

- Internal Structure: Their echogenicity varies since there are reports with hyperechoic, isoechoic, and hypoechoic internal structures. Encapsulated lipomas are harder to visualize and diagnose. Doppler US images reveal no-low vascularization and mild-high vascularization suggests liposarcoma.
- Peripheral Structure: Capsulated lipomas have hyperechoic well-defined borders while non-capsulated lipomas may confuse with surrounding soft tissues. Acoustic shadowing is uncommon.

18.1.8.3 Lymphangioma

Lymphangiomas are congenital lymphatic vessel malformations which are generally diagnosed in infancy. Most common localization for lymphangiomas are subcutaneous tissue and skin of the head and neck region. Intraoral lymphangiomas are relatively uncommon and they are mostly seen on tongue, palate, and buccal mucosa. Clinically, a fast-growing or regressed lesion is seen which can be sessile or pedunculated [1].

Radiographically, MRI reveals a high signal in T2-W images and US reveals internal septas with cystic contents. Doppler US may reveal arterial/venous flow [66] (Fig. 18.48).

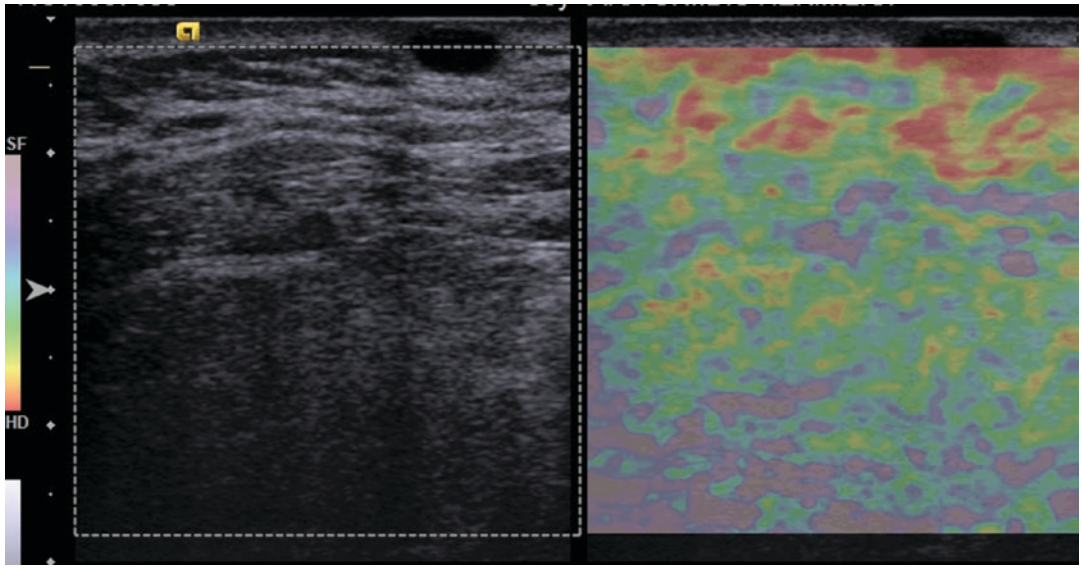

Fig. 18.45 Lipoma. US Elastography reveals a lesion which is isoechoic with adjacent soft tissues

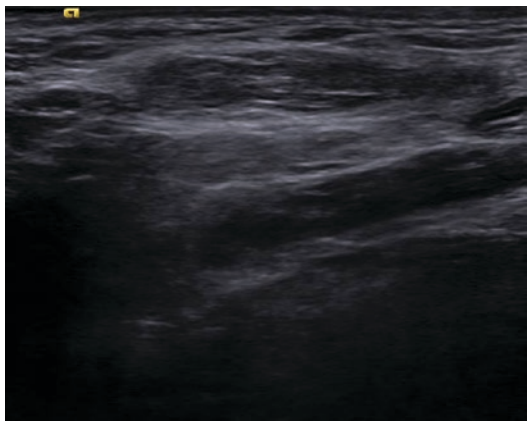

Fig. 18.46 Lipoma. US image showing a lesion, solid with linear internal strands, compressible. No calcification or cystic changes

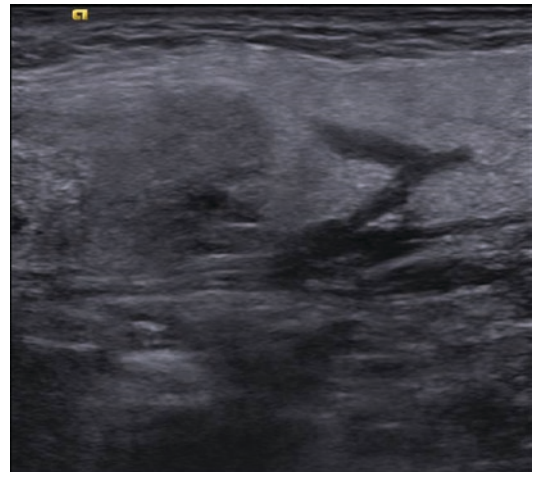

Fig. 18.47 Lipoma. US image showing a lesion on the floor of the mouth with linear incomplete internal striations

Common sonographic features of the lymphangiomas are:

- Internal Structure: Multilocular cystic masses, internal septa of varying thickness. If there are cystic contents: the apperance is usually anechoic or hyperechoic the debris inside of the lesion may show high lipid concentration, infection or hemorrhage. There are also wide variations such as solid areas, or mostly solid with cystic foci. In Doppler USG there is also arterial or venous flow in the septa.

18.1.8.4 Neurofibroma and Schwannoma

Schwannomas are benign nerve sheath tumors of Schwann cells and neurofibromas are benign nerve sheath tumors of fibroblasts, axons, Schwann cells, and perineurial cells. Clinically, a generally symptomatic, slow-growing mass is seen at submucosa. They are mostly seen in tongue, palate, and buccal mucosa. If multiple neurofibromas are found neurofibromatosis type I should be included in the differential diagnosis [1, 3–5, 67–70].

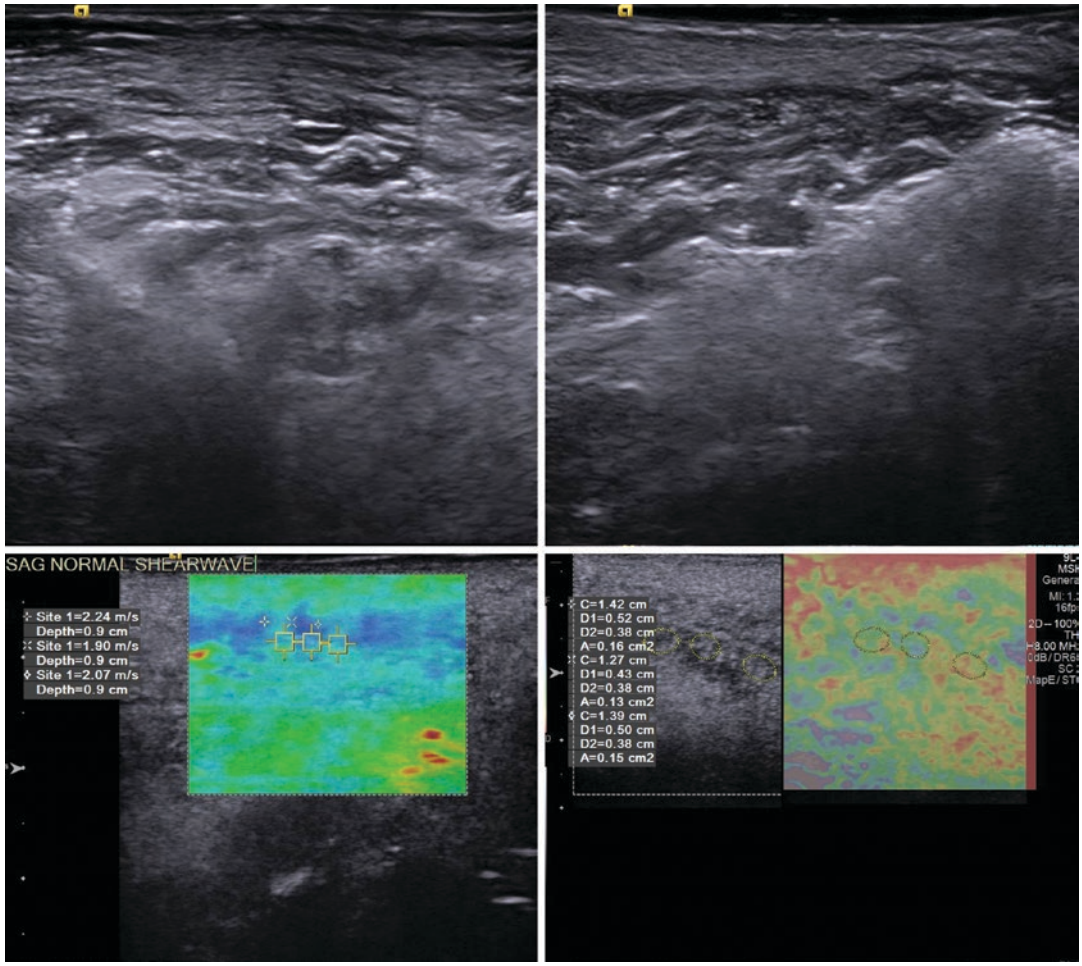

Fig. 18.48 Lymphangioma. US image showing a lymphangioma in the tongue tissue with internal anechoic cystic degenerations. The elastography in this case was not helpful to differentiate the lesion

Radiographically, OPG reveals well-defined radiolucent lesions (Fig. 18.49). Both neurofibroma and schwannoma demonstrate "target-sign" with a hyperintense periphery and hypointense internal structure in T2-W MRI images. CT images reveal well-defined hypodense lesions with no or mild contrast enhancement [67–70].

Sonographic features of the neurofibroma (Fig. 18.49).

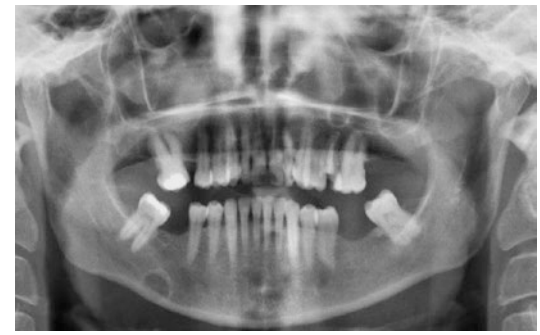

Fig. 18.49 Neurofibroma. US image showing a well-defined hypo/hyperechoic vascularized oval-shaped mass with benign characteristics that proved to be a neurofibroma

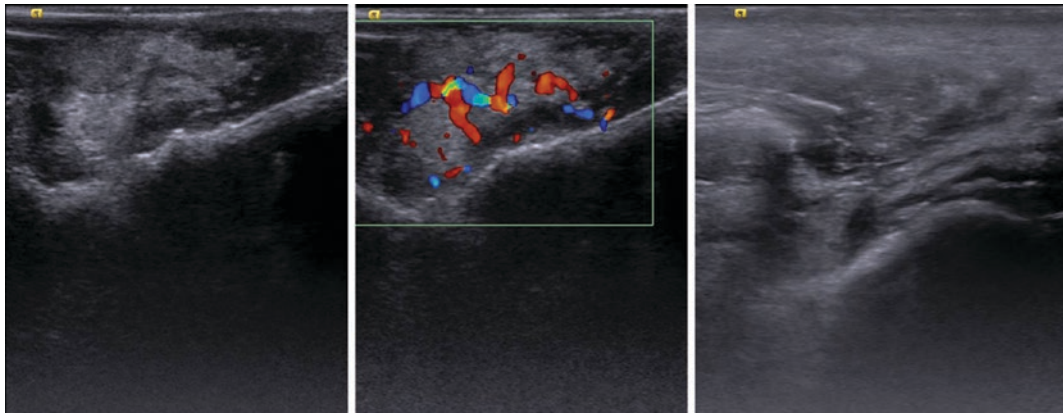

Fig. 18.50 Schwannoma. An OPG showing a radiolucent area in the level of mandibular canal in continuation with mandibularis

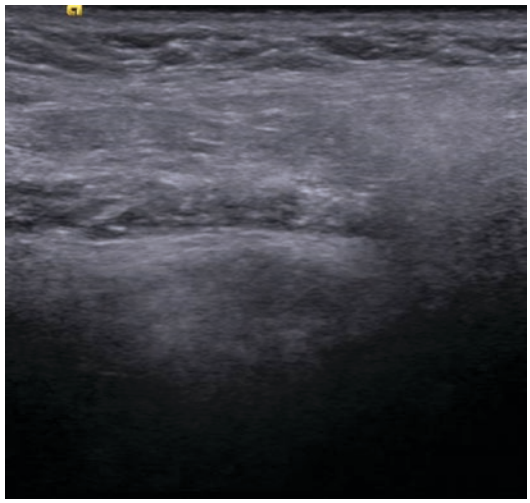

Fig. 18.51 Schwannoma. A Well-defined hypoechoic mass in continuation with a nerve that was scanned intraorally that biopsy proved to be a schwannoma

- Internal Structure: Commonly well-defined hypoechoic soft tissue masses
- Peripheral Structure: Commonly Well-defined hypoechoic vascularized oval-shaped mass with benign characteristics.

Sonographic features of the neurofibroma schwannoma are (Figs. 18.50 and 18.51):

- Internal Structure:
- Peripheral Structure:

18.1.8.5 Pleomorphic Adenoma

Pleomorphic Adenomas (PA) are the most common benign tumor of salivary glands and they are generally found in parotid gland. Submandibular gland and minor salivary glands at the palate are also common sites for PAs. Clinically, asymptomatic and slow-growing tumors are seen but painful cases with nerve problems may suggest a malignant transformation. PAs are generally well-defined mobile lesions with gray or pale brown color [1, 3–5].

Radiographically, T1-W MRI images reveal hypointense lesions while T2-W MRI images reveal hyperintense lesions with relatively hypointense rim which represents fibrous capsule of the lesion. T1 + C MRI images reveal homogeneous enhancements [71].

Common sonographic features of the pleomorphic adenomas are (Fig. 18.52):

- Internal Structure: A heterogeneous structure is predominant, internal fluid areas can also be present. Acoustic enhancement was present in most pleomorphic adenomas.
- Peripheral Structure: Commonly, pleomorphic adenomas were well-defined, with sharp borders. The presence of lobulated contours are indicative of these lesions.

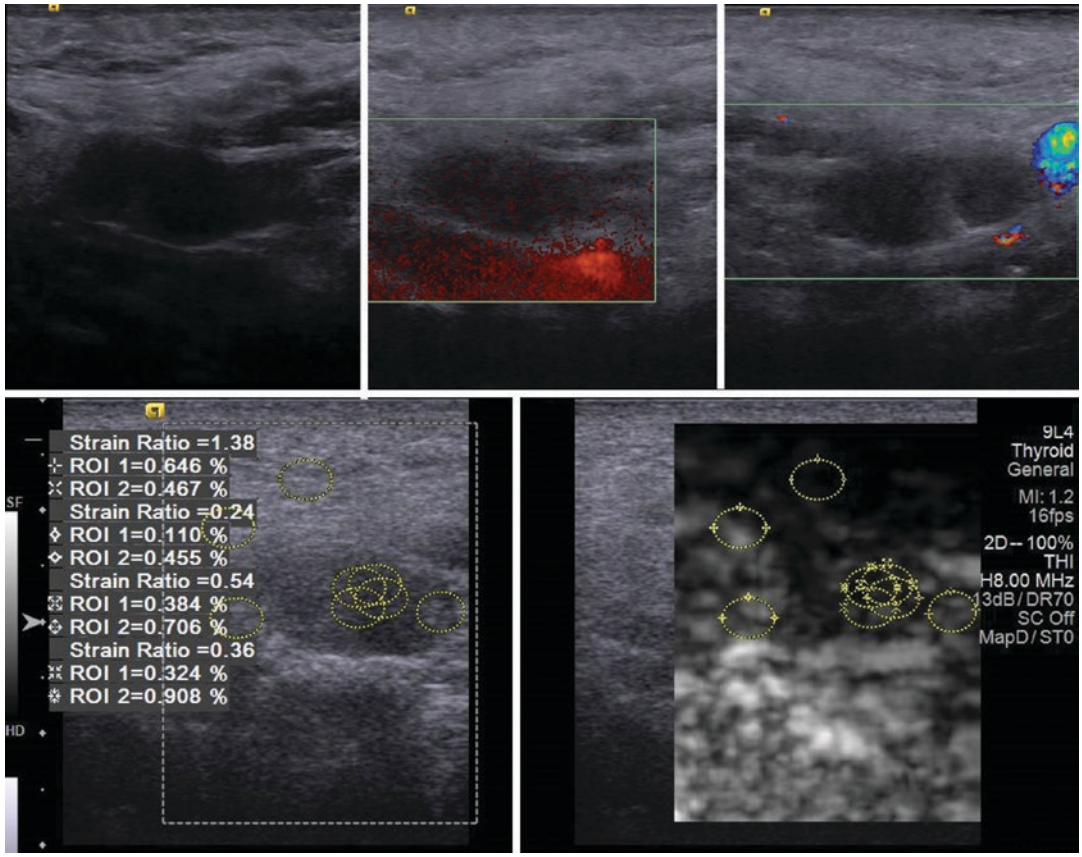

Fig. 18.52 Pleomorphic adenoma. Pleomorphic adenoma with a well-defined hypoechoic vascularized mass in the parotid gland. Elastrography showing mild to moderate stiff lesion

18.1.8.6 Lobular Capillary Hemangioma (Pyogenic Granuloma)

Pyogenic Granuloma or Lobular Capillary Hemangioma is a benign soft tissue tumor which is generally associated with hormonal factors or trauma [72–74]. It is also known as pregnancy tumor [72] since a significant number of cases were found in pregnant patients [73, 74]

Common sonographic features of lobular capillary hemangiomas are (Figs. 18.53 and 18.54):

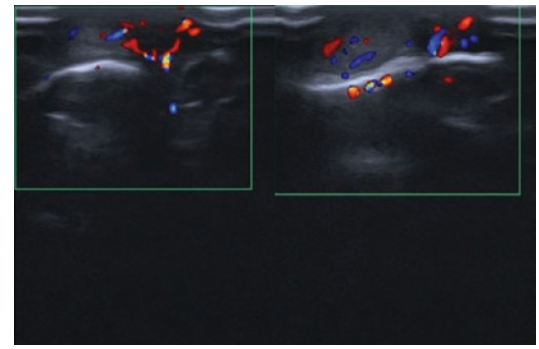

Fig. 18.53 Capillary lobulary hemangioma (pyogenic granuloma). Doppler US reveals a well-defined superficial soft tissue lesion with moderate vascularization

- Internal Structure: Commonly unilocular hypoechoic superficial soft tissue lesion is seen. Doppler US reveals moderate to high vascularity.
- Peripheral Structure: A well-defined lesion is seen without any cortical perforation. Mild acoustic enhancement may be seen.

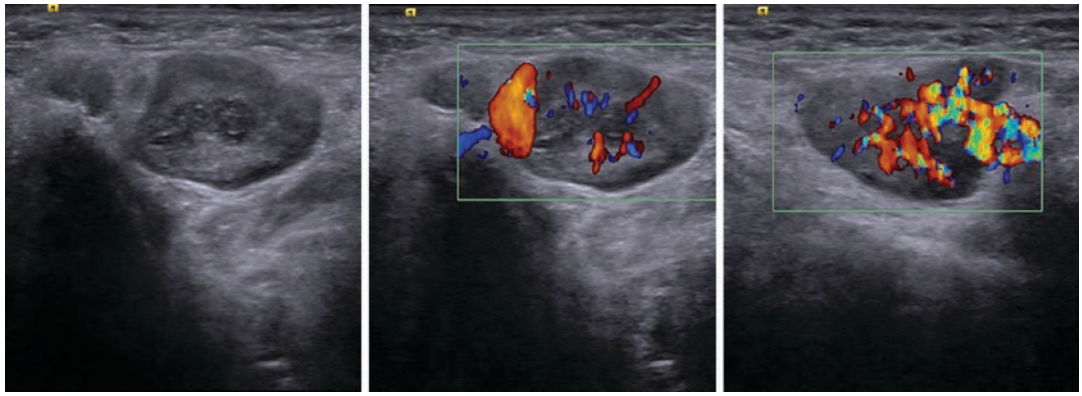

Fig. 18.54 Capillary lobulary hemangioma. Gray-scale US image shows a well-defined mass (arrow), which is a mix hypo/hyperechoic appearance. It is delineated by a hyperechoic margin, which appears to arise from the surrounding tissue

18.2 Malign Tumors of Maxillofacial Region

18.2.1 Odontogenic Carcinomas

18.2.1.1 Ameloblastic Carcinoma

Ameloblastic Carcinoma (AC) is the counterpart of ameloblastoma. As ameloblastoma, it also mainly affects male patients who are older than 45 years. Mandibular posterior site is the most common localization of intraosseous ACs and a few peripheral AC cases have been reported in the literature [1].

Radiographically, the imaging features of AC are not different than other malignant tumors with soft tissue infiltration to adjacent anatomical structures, cortical destruction with ill-defined peripheral and radiolucent internal structure. Several cases with cortical expansion mimicking benign tumors have also been reported [1, 75, 76] (Fig. 18.55):

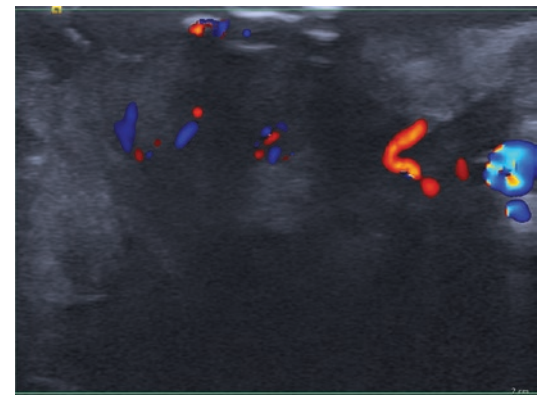

Fig. 18.55 Ameloblastic carcinoma. Intraoral US reveals heterogeneous internal structure with hypoechoic and hyperechoic areas in mandibular posterior site. Doppler imaging reveals mild vascularization. Due to the destruction of cortical plates no hyperechoic zone suggesting hard tissues are seen

18.2.1.2 Primary Intraosseous Carcinoma (NOS)

Primary intraosseous carcinoma NOS (PIOC) is also known as primary intraosseous squamous cell carcinoma. "NOS" means nonspecific since PIOCs cannot be categorized in any other carcinoma classification. PIOC can arise in odontogenic cysts since they can arise from odontogenic epithelium. Squamous cell carcinomas which arise in the oral mucosa and then infiltrate the bone have to be excluded since those lesions are not "primary" intraosseous carcinoma. Also, metastatic oral tumors have to be excluded too. In order to differentiate metastatic tumors and PIOC the localization plays a great role. Any lesion with its epicenter below mandibular canal should be evaluated as a metastatic tumor rather than PIOC [1–3].

They are usually seen in patients at 55–60 years and show male predilection. PIOCs are mostly localized in mandibular posterior region and

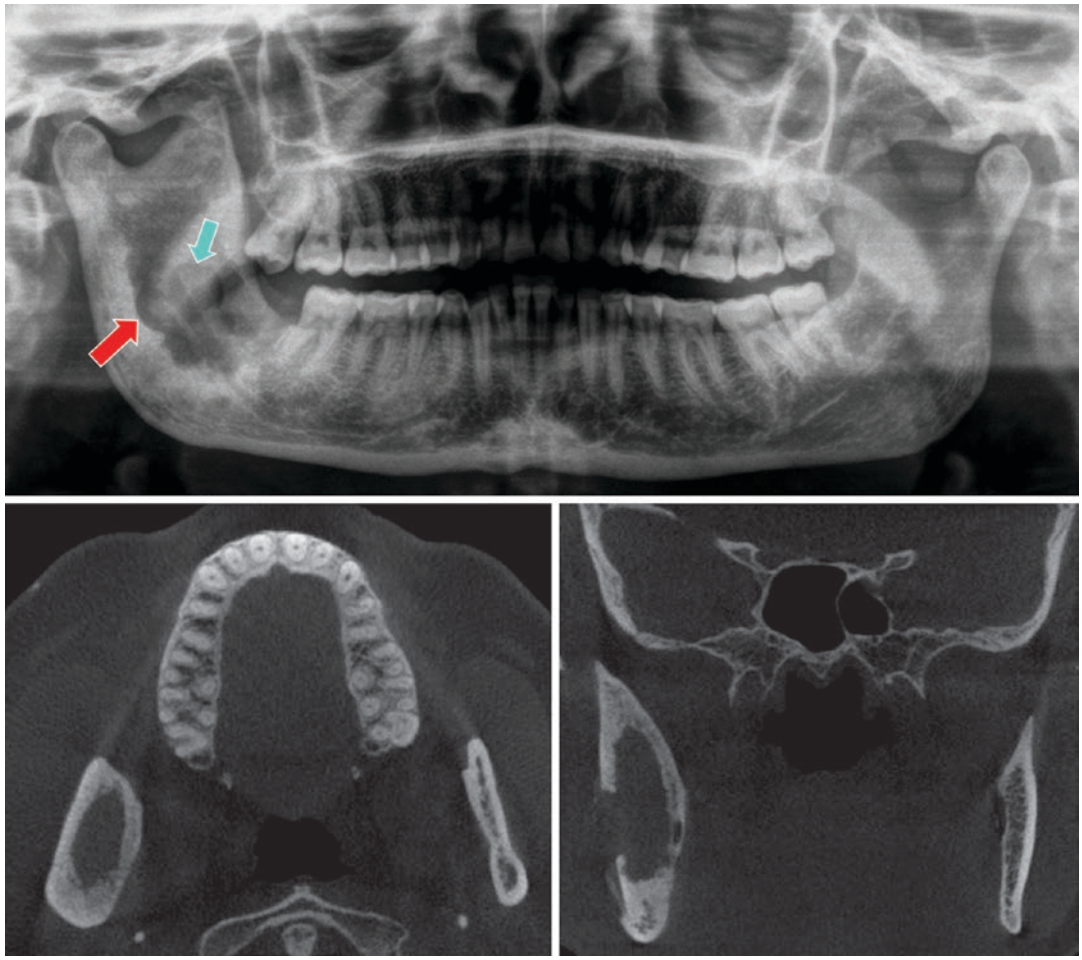

Fig. 18.56 Primary intraosseous carcinoma in odontogenic keratocyst. (**a**) OPG reveals a lesion with ill-defined scalloped borders and radiolucent internal structure (red arrow) at mandibular right ascending ramus. Another round-shaped area with lower density is seen inside the lesion suggesting cortical destruction (turquoise arrow). (**b**) Coronal CBCT slice of Fig. 18.2 reveals buccal and lingual cortical plate expansion and buccal cortical plate destruction in mandibular right mandibular ramus with aggressive periosteal reaction. (**c**) Axial CBCT slice of Fig. 18.2 reveals buccal and lingual cortical plate expansion and trabecular bone destruction in mandibular right mandibular ramus with aggressive periosteal reaction. Histopathological diagnosis is primary intraosseous carcinoma in odontogenic keratocyst

mandibular ramus. Maxillary anterior region is the most affected site in maxilla [1, 2]

PIOCs usually arise in radicular cysts, dentigerous cysts, and odontogenic keratocysts (Figs. 18.56 and 18.57). Since the primary lesion is benign, early radiographic features of PIOC resemble a benign lesion while advanced PIOCs are seen with cortical plate perforations, pain, ulceration, non-healed extraction sockets, nerve findings, root resorptions, and pathological fractures. As the other malignancies advanced, PIOCs are seen with non-corticated ill-defined radiolucent/hypodense lesions [1–3]

18.2.1.3 Sclerosing Odontogenic Carcinoma

Sclerosing Odontogenic Carcinoma (SOC) is a unique tumor with fewer than 10 cases in the literature. SOC is an odontogenic primary intraosseous carcinoma and histopathologic features of

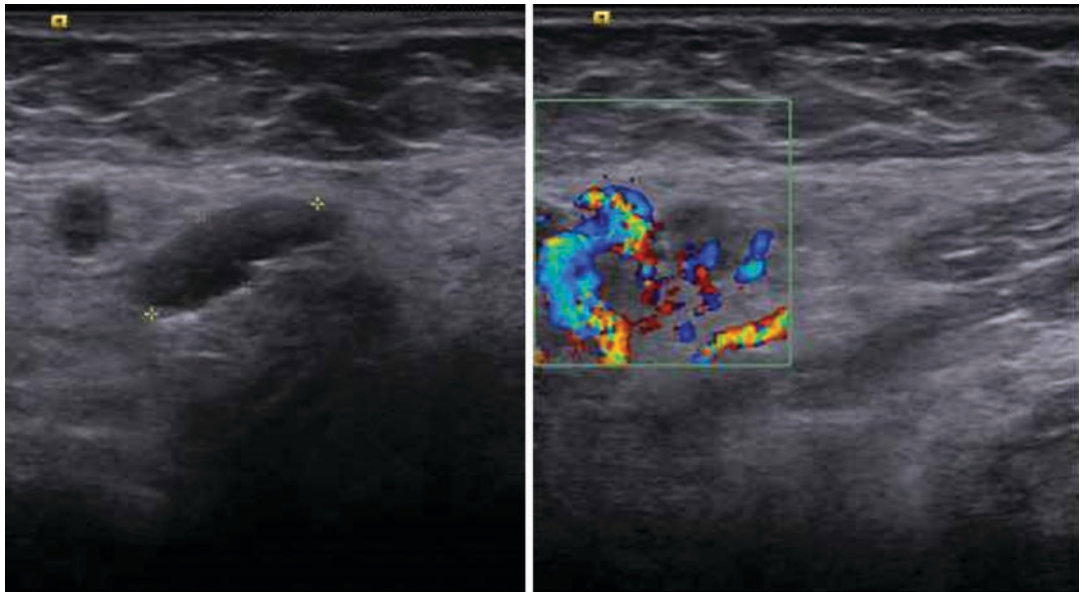

Fig. 18.57 Primary intraosseous carcinoma. (**a**) USG shows fusiform shape in submandibular lymph nodes. (**b**) Color Doppler reveals peripheral vascularity of the lymph node which can be a precursor for metastasis

SOC are characteristic with its sclerotic stroma and aggressive infiltration [1, 77, 78].

Clinically, a swelling with nerve signs can be seen. Radiographically, an ill-defined non-corticated bordered lesion with radiolucent/hypodense internal structure is seen. Root resorption, trabecular, and cortical plate destruction with invasive extensions are frequently seen [1, 77, 78].

18.2.1.4 Clear Cell Odontogenic Carcinoma

Clear cell odontogenic carcinoma (CCOC) is a unique tumor with around 100 cases reported in the literature. CCOC is an odontogenic primary intraosseous carcinoma and histopathological features of CCOC are characteristic with islets of lacunar and clear cells. It is commonly located in mandibular posterior site and mandibular ramus [1, 2, 79–81]

Clinically, slow-growing mass with various symptoms such as pain, ulceration, and nerve signs is seen.

Radiographically, an ill-defined non-corticated radiolucent lesion with root resorptions is seen [1, 80]

18.2.1.5 Ghost Cell Odontogenic Carcinoma

Ghost cell odontogenic carcinoma (GCOC) is a unique tumor with around 40 cases reported in the literature. It only represents less than 5% of all ghost cell lesions. GCOC is an odontogenic primary intraosseous carcinoma and histopathological features of GCOC is characteristic with dentinoid deposition and atypical ghost cell keratinization. Non-peripheral GCOC is reported and the most common localization of GCOCs is maxilla. It can develop in other benign ghost cell tumors such as calcifying odontogenic cyst [1, 82, 83]

Clinically, slow-growing mass with various symptoms such as pain, ulceration, and nerve signs is seen.

Radiographically, an ill-defined non-corticated radiolucent lesion with root resorptions and displacements is seen. Due to "dentinoid deposition" inside GCOCs, around half of the cases may be seen with radiopaque/hyperdense focis [1, 82, 83].

18.2.2 Odontogenic Carcinosarcomas

Odontogenic carcinoma is a unique tumor with malignant mesenchymal and malignant epithelial components. Only 9 cases were reported [84]. The most common localization for odontogenic carcinosarcomas is mandibular posterior site [1].

Clinically, a swelling which is associated with a numbness of the lips may be seen. Radiographically, an ill-defined non-corticated expansive and extensive radiolucent/hypodense lesion is seen with root resorption and cortical plate destruction/perforation [1, 84].

18.2.3 Odontogenic Sarcomas

Odontogenic sarcoma is a unique tumor with malignant mesenchymal components and benign epithelial components. They can arise in ameloblastic fibro-dentinoma and ameloblastic fibro-odontoma. Most common localization for odontogenic sarcomas are mandibular posterior site and maxillary posterior site [1, 2]

Clinically, an expansive mass with nerve deficit is seen mimicking any low-grade tumor. Radiographically, OPG and CBCT reveals ill-defined radiolucent or predominantly radiolucent mixed lesions [1, 2, 85]

18.2.4 Malignant Maxillofacial Bone and Cartilage Tumors

18.2.4.1 Osteosarcoma

Osteosarcomas are malignant bone tumors with bone producing neoplastic cells. Conventional, periosteal and parosteal osteosarcomas are the three subtypes of osteosarcomas with conventional being the most aggressive high-grade subtype and parosteal being the low-grade subtype. Jawbones represent 6% of all osteosarcomas as being the fourth most common site following the femur, tibia, and humerus. Mandibular osteosarcomas are more common than maxillary osteosarcomas [1–3, 86]

Clinically, nonspecific findings are present such as swelling, loosening of teeth, and pain. Radiographically, OPG and CBCT reveal mixed lesions with cortical perforations and characteristic sunburst periosteal reaction. Widening of the periodontal ligament space may be also seen (Fig. 18.58). MRI reveals high signal intensity at non-mineralized component area and low signal intensity at mineralized component area [1, 3, 86].

Common sonographic features of osteosarcomas are:

- Peripheral Structure: Osteosarcoma can be detected especially with periosteal reaction with irregular vascularization.

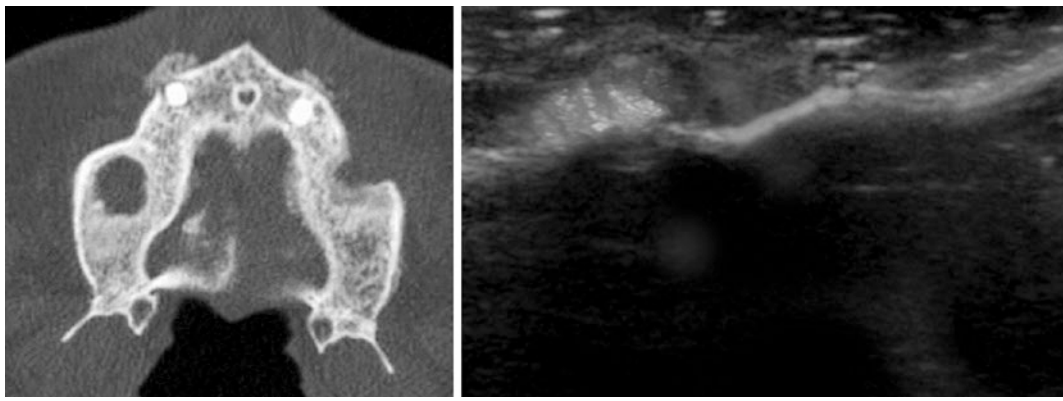

Fig. 18.58 Osteosarcoma. Axial CBCT and USG slice reveal bilateral spicular periosteal reaction at buccal cortical plate of maxillary anterior region which is characteristic of osteosarcomas

18.2.4.2 Chondrosarcoma

Chondrosarcoma NOS (nonspecific) is a malignant bone tumor that produces cartilaginous

matrix. Chondrosarcoma represents 25% of all primary malignant bone tumors but less than 4% of chondrosarcomas are found in the maxillofacial bones. Maxilla is more commonly involved than the mandible [1, 87, 88]

Clinically, nonspecific findings such as pain are present. Radiographically, OPG/CBCT and CT reveal radiopaque/hyperdense matrix calcification and cortical destruction with a soft tissue mass. MRI reveals very high intensity in T2-W images at the areas without calcifications [87, 88]

18.2.4.3 Mesenchymal Chondrosarcoma

WHO defines Mesenchymal chondrosarcoma as "a biphasic malignant tumor composed of small round blue cells and islands of differentiated hyaline cartilage." Intraosseous mesenchymal chondrosarcomas represent around 75% of all mesenchymal chondrosarcomas and the mandible and maxilla are the most common localizations [1, 89].

18.2.5 Non-odontogenic Malign Tumors of Maxillofacial Region

18.2.5.1 Oral Squamous Cell Carcinoma

Oral Squamous Cell Carcinomas (OSCC) arising in soft tissues are the most common malign tumor of the oral cavity. The malignant epithelial cells of the OSCCs spread to deeper tissues as soft tissues, neighboring bone, lymph nodes, and distant sites (metastasis). They account for 90% of all oral malignancies and the most common site for soft tissue OSCCs are lateral border of the tongue and floor of the mouth [1–3]

Clinically, irregular patchy red-white lesions are seen on the surface of the affected area with or without pain. Soft tissue mass, trismus, fetor, paresthesia, anesthesia, dysesthesia, and hemorrhage can be seen. Fatigue and weight loss are very common among patients with OSCC [1, 3–5].

Radiographically, OPG and CBCT may reveal no radiographic finding if the OSCC did not reach and cause any destruction at hard tissues. Advanced OSCC lesions are seen as ill-defined non-corticated radiolucent lesions with cortical plate destruction, destruction of mandibular canal and maxillary sinus floor, finger-like invasive extension to adjacent regions, and pathological fractures [1, 3–5] (Fig. 18.59).

Early lesions can be examined with US imaging and deep lesions can be examined with both MRI and US. MRI is useful in determining the tumor infiltration and OSCCs have intermediate-low signal in T1-W images, intermediate-high signal in T2-W images, and enhanced appearance especially in contrasted T1-W images with fat saturation [5, 90, 91]. Each tumor type had a characteristic vascular pattern The blood vessels do not determine the growth of tumors on the contrary the tumor determines the growth pattern of blood vessels. Color Doppler ultrasonography (CD-USG) has been used for detecting blood flow signals in vessels of malignant tumors by means of continuous pulsed-wave Doppler and color flow mapping techniques. Vessels with low-

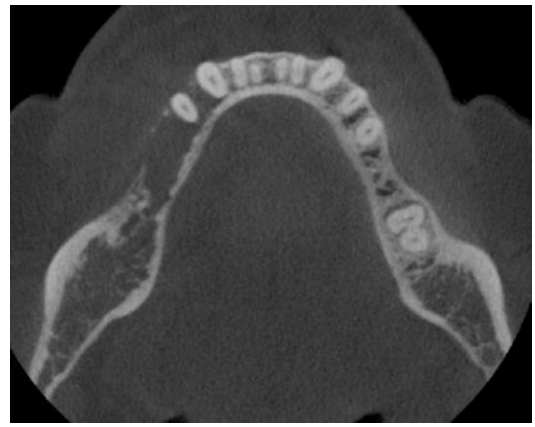

Fig. 18.59 Oral squamous cell carcinoma. Axial CBCT slice reveals an ill-defined hypodense lesion with finger-like extensions and buccal cortical plate destruction at mandibular right premolar site. It should be remembered that Oral Squamous Cell Carcinoma arises in soft tissues and may invade inside the bone structure; thus, OSCC is a different entity from Primary Intraosseous Carcinoma

impedance flow have low pulsatility indices (PIs) and resistivity indices (RIs). Studies have also revealed that this low-impedance tumor flow is helpful in differentiating malignant from benign tumors, as also the changes in blood flow in malignant tumors have some value in predicting the tumor response to chemotherapy.

Common sonographic features of oral squamous cell carcinomas are (Figs. 18.60, 18.61, and 18.62):

- Internal Structure: Heterogeneous predominantly hypoechoic areas are seen with high vascularity in Doppler imaging.
- Peripheral Structure: Ill-defined, non-corticated peripheral structures with invasion to adjacent tissues and destruction at adjacent hard tissues are seen.

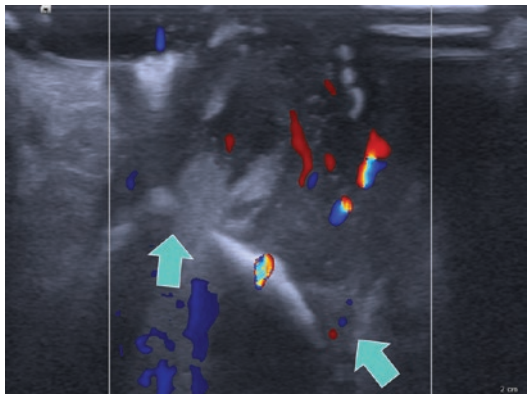

Fig. 18.60 Oral squamous cell carcinoma. US image of Fig. 18.5. US reveals a soft tissue lesion with heterogeneous predominantly hypoechoic internal structure and ill-defined borders. Note the cortical bone destruction (turquoise arrow) and soft tissue infiltration of the lesion

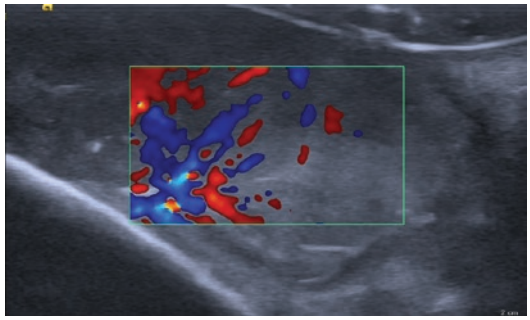

Fig. 18.61 SCC. Color Doppler of a soft tissue SCC

18.2.5.2 Adenoid Cystic Carcinoma

Adenoid cystic carcinoma (AdCC) is a histological subtype of adenocarcinoma and they account for around 10% of salivary gland tumors and 1% of all head and neck malignancies. It is the most common minor salivary gland malignant tumor and also common in major salivary glands. AdCCs can also be located in paranasal sinuses, larynx, trachea, and lacrimal glands [1, 92]

Clinically, a slow-growing mass with pain and ulceration is seen. AdCCs in parotid can cause facial nerve dysfunction and perineural invasion is common. Nasal obstruction, epistaxis, and deep facial pain can be seen in paranasal and nasal AdCCs while oro-antral fistula can be seen with AdCCs in palate. Radiographically, AdCCs in salivary glands appear hypointense/isointense in T1-W images, slightly hyperintense in T2-W images, and contrasted T1-W images have homogeneous enhancement. However, AdCCs in lacrimal glands show moderate enhancement in contrasted T1-W images [1, 92–94].

Early AdCCs does not have any imaging features in OPG and CT images; however, hard tissue destruction can be seen in advanced AdCCs (Figs. 18.63 and 18.64).

Common sonographic features of Adenoid cystic carcinomas are (Fig. 18.65):

- Internal Structure: Heterogeneous hyperechoic area with mild vascularization in Doppler images are seen. Echogenicity of the lesion is similar to salivary gland tissue.
- Peripheral Structure: Relatively well-defined hyperechoic borders are seen. Due to cystic component in the lesion, acoustic enhancement may be present.

18.2.5.3 Mucoepidermoid Carcinoma

Mucoepidermoid Carcinoma (MeC) is the most common salivary gland malignant tumor. It is frequently seen in parotid glands, minor salivary glands of the palate, submandibular salivary gland and sublingual salivary glands, respectively. Although rare intraosseous mucoepidermoid carcinomas of the jaws were also reported [1]

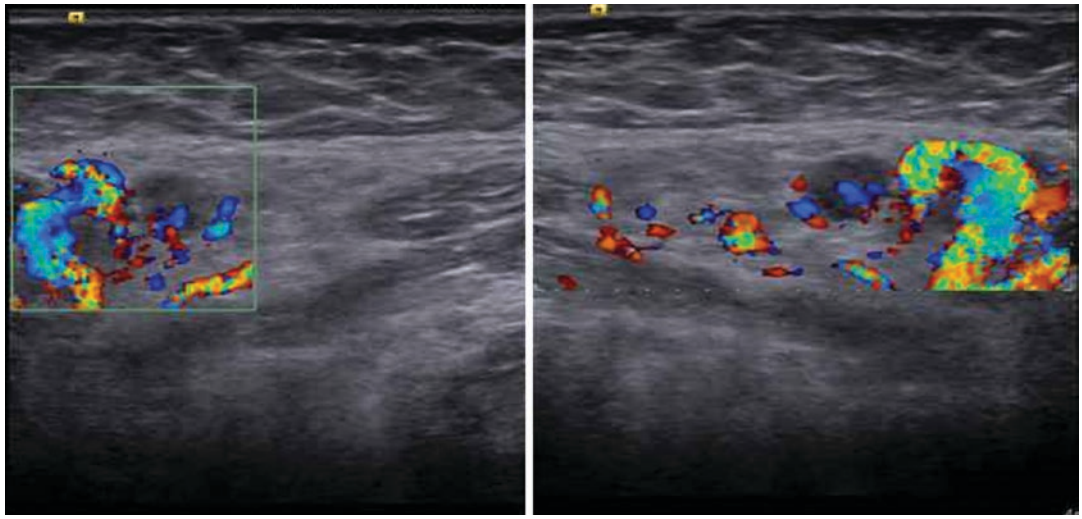

Fig. 18.62 SCC. Color Doppler reveals peripheral vascularity of the lymph node which can be a precursor for metastasis

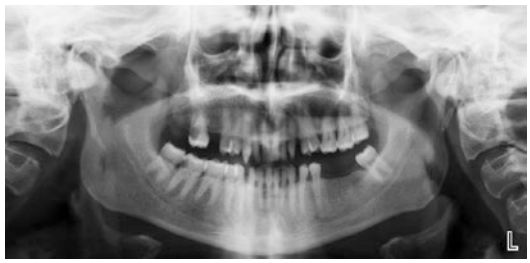

Fig. 18.63 Adenoid cystic carcinoma. OPG reveals a relatively radiolucent area at maxillary left premolar-molar region

Radiographically, CT images reveal low-grade MeCs as the benign tumors with well-defined expansions and calcifications (Figs. 18.66 and 18.67); however, high-grade tumors are seen with ill-defined borders and infiltrative features. MR images also vary due to the MeCs grade; since low-grade tumors have high signal in T2-W while high-grade tumors have intermediate-low signal (Fig. 18.68) [1, 91, 95].

Common sonographic features of Mucoepidermoid carcinomas are:

- Internal Structure: Heterogeneous hypoechoic lesion with partial or complete cystic areas.
- Peripheral Structure: Low-grade MeCs appear with well-defined borders while high-grade MeCs appear with ill-defined borders.

18.2.5.4 Non-Hodgkin Lymphoma

Non-Hodgkin's lymphoma (NHL) affects lymph nodes in 76% of the cases; however, extranodal localizations can be also affected. Frequent extranodal localizations of NHL are gastrointestinal tract, skin, bones, and Waldeyer's ring. Only 5% of the NHLs occur in bones and mandible represents 0.6% of all NHL [1, 4, 5, 90, 96].

Radiographically, diffuse or local ill-defined radiolucent lesions are seen in OPG and CBCT images. CBCT may reveal cortical plate destruction in advanced cases; however, no specific radiographic finding is present [4, 5, 90, 96]

Common sonographic features of Mucoepidermoid carcinomas are (Fig. 18.69):

- Internal Structure: Heterogeneous hyperechoic lesion with mild vascularization on Doppler imaging may be seen.
- Peripheral Structure: Since advanced NHL lesions cause cortical plate destruction, ill-defined noncontinuous bone borders can be seen with soft tissue infiltration to adjacent structures.

18.2.5.5 Malignant Melanoma

Oral Malignant Melanomas (OMM) are very rare comparing to cutaneous malignant melanomas since all OMMs are mucosal malignant melanomas. Mucosal melanomas represent 1.3% of all

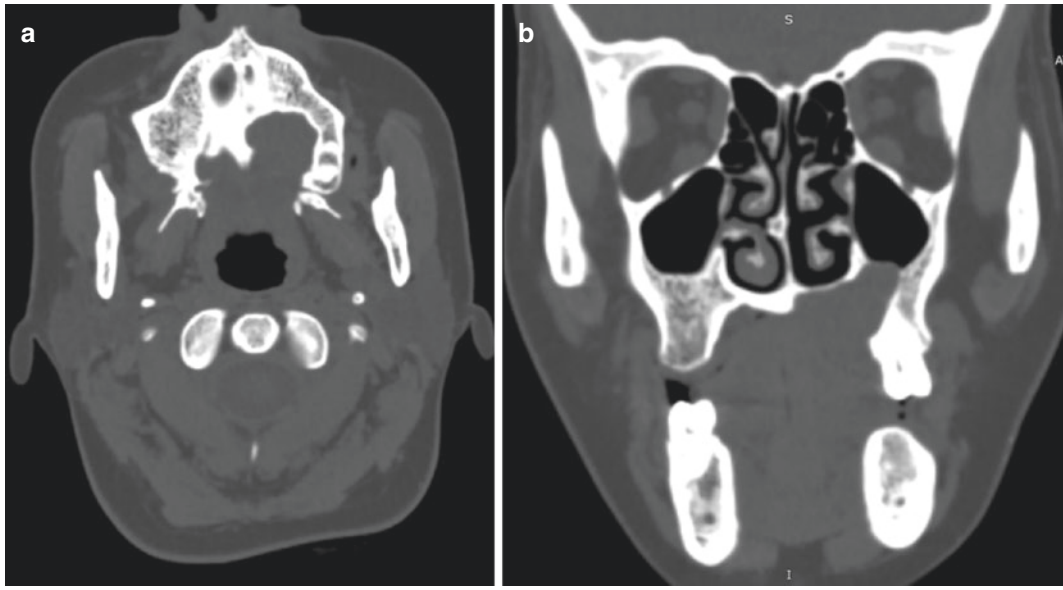

Fig. 18.64 Adenoid cystic carcinoma. (**a**) Axial CT slice reveals a well-defined hypodense lesion at maxillary left premolar site and hard palate. (**b**) Coronal CT slice reveals a well-defined invasive hypodense lesion which caused destruction at maxillary left premolar site, erosion at nasal floor and maxillary sinus infiltration

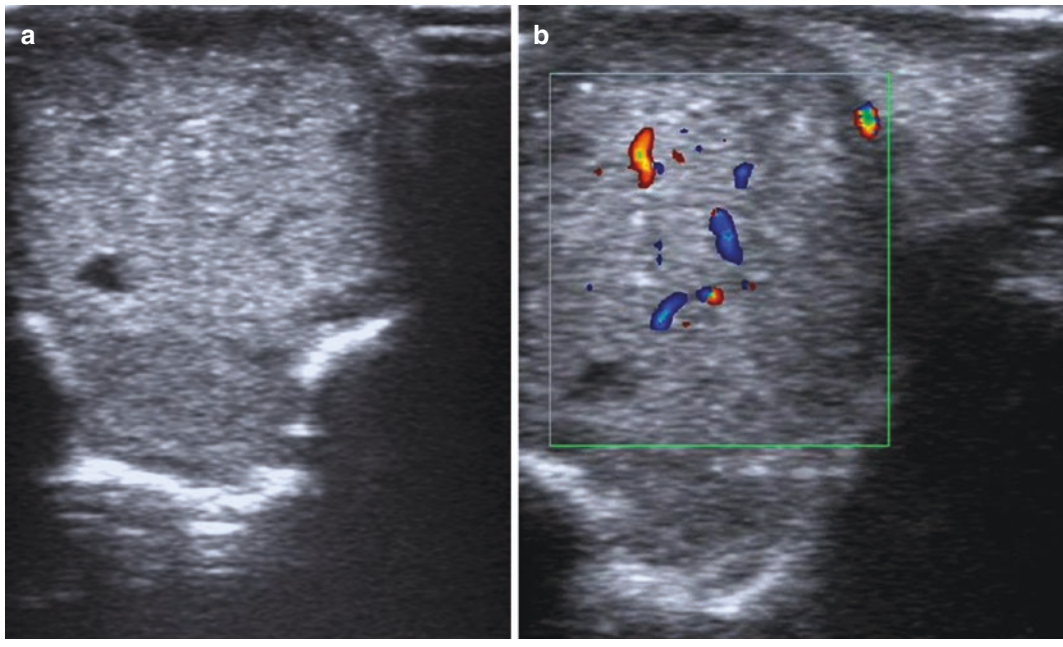

Fig. 18.65 Adenoid cystic carcinoma. (**a**) US reveals predominantly hyperechoic internal structure with some anechoic cystic components. The lesion has well-defined hyperechoic borders and acoustic enhancement is seen. (**b**) Doppler imaging reveals mild vascularization

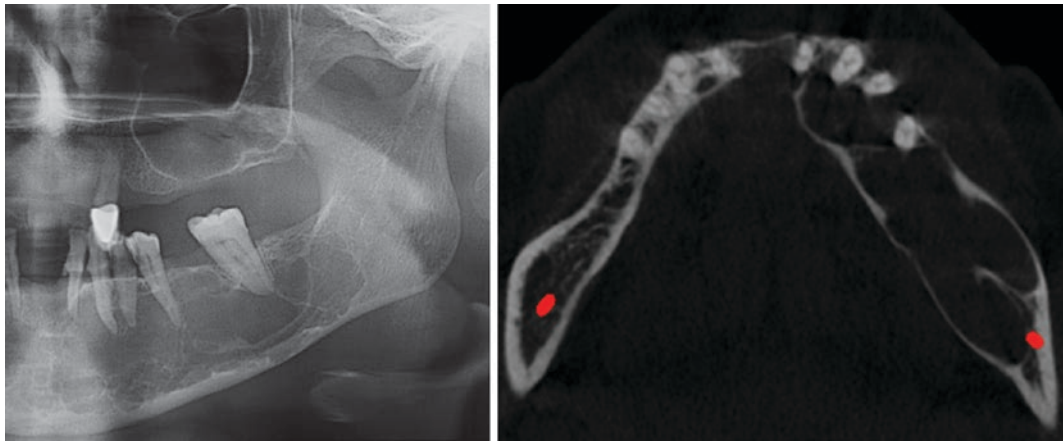

Fig. 18.66 Mucoepidermoid carcinoma. (**a**) Cropped OPG reveals a well-defined multilocular lesion extending between mandibular midline to mandibular right postmolar site. Thin septa formations are seen. (**b**) CBCT Axial Slice reveals a well-defined multilocular lesion extending between mandibular midline to mandibular right postmolar site with minimal buccal and lingual cortical plate expansion and trabecular bone destruction

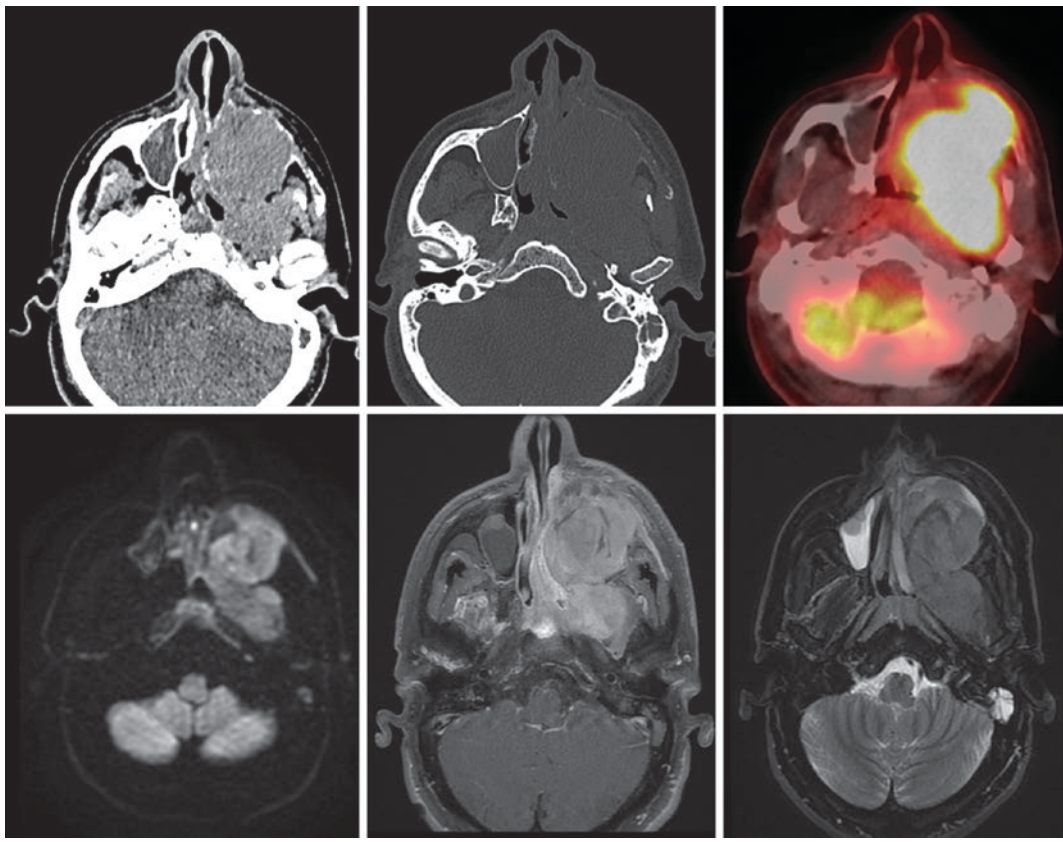

Fig. 18.67 Mucoepidermoid carcinoma. (**a**) Soft tissue level CT reveals perforated cortical borders of a well-defined lesion with an ill-defined soft tissue extension to adjacent structures at the posterior region. (**b**) Bone level CT reveals destruction at maxillary sinus cortical borders. (**c**) PET/CT reveals high radionuclide. (**d**) Diffusion MR image reveals hyperintense lesion at the left maxillary sinus. (**e**) T1-W + C image reveals hyperintense lesion at left maxillary sinus with mild enhancement. (**f**) T2-W image reveals iso-intense lesion at left maxillary sinus

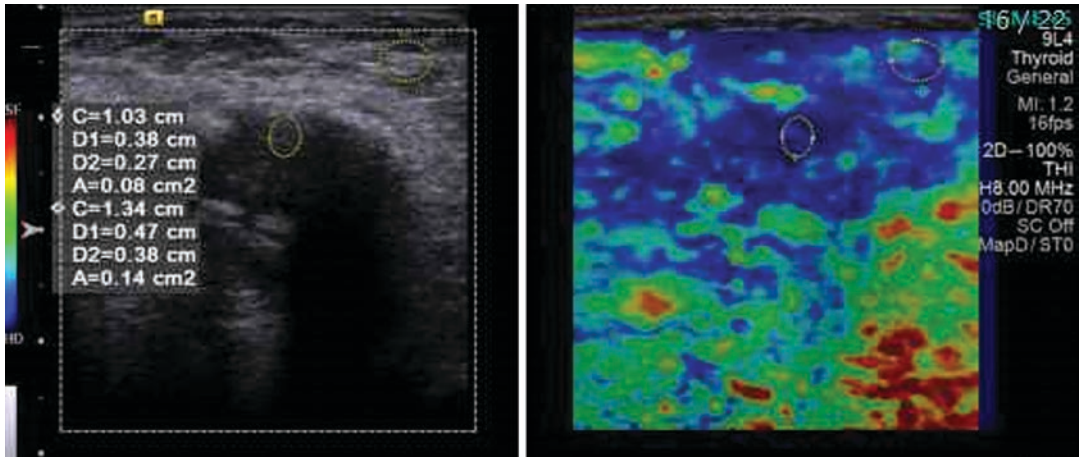

Fig. 18.68 Mucoepidermoid carcinoma strain and shear wave elastography of the same patient. The lesion was coded as low to medium to high stiffness

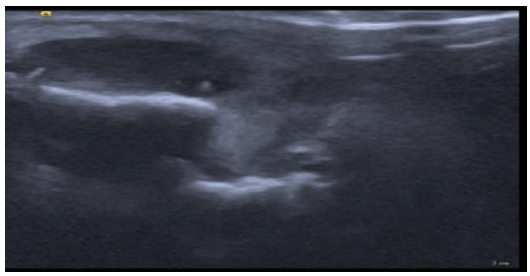

Fig. 18.69 Non-Hodgkin lymphoma. US reveals a soft tissue lesion inside an extraction socket with heterogeneous echogenicity and ill-defined borders infiltrating intraosseous structures. Cortical destruction is seen at the lateral aspect of the extraction socket

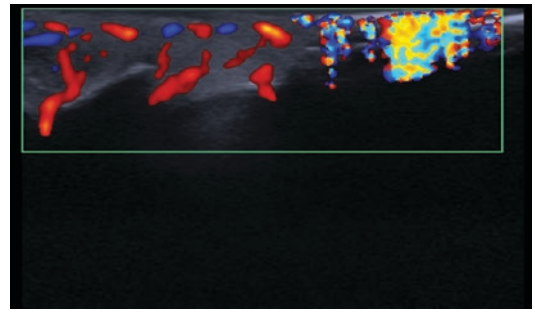

Fig. 18.70 Oral malignant melanoma. Doppler US reveals a mucosal malignant melanoma with hyperechoic internal structure and high vascularity

melanomas and 55% of mucosal malignant melanomas are in the head and neck region. Among the head and neck mucosal malignant melanomas only 25% are located in the oral mucosa. Oral mucosal melanomas represent less than 0.5% of oral malignancies. OMMs have aggressive clinical behavior; thus, they have a poor prognosis [97–101]

OMMs are characteristic melanin pigmentation; however, around 2% of all malignant melanomas do not have melanin pigmentation. These malignant melanomas are known as amelanotic malignant melanomas and they also have the same clinical features as swelling, pain, bleeding, ulceration, and cortical plate destruction [99]

Their most common localizations are maxillary gingiva and palate. Since they grow without any symptoms and rapidly they, unfortunately, get diagnosed when they already metastasize to lymph nodes. OMMs are superficial lesions which make US imaging an ideal tool for them [97–101].

Common sonographic features of oral malignant melanomas are (Figs. 18.70 and 18.71):

- Internal Structure: Early lesions may not reach to bone; so, cortical plate destruction may be absent. Advanced lesions are heterogeneous hypoechoic lesions with high vascularization on Doppler imaging.
- Peripheral Structure: OMMs are ill-defined non-capsulated aggressive lesions which cause cortical plate destruction and invasion to the adjacent tissues.

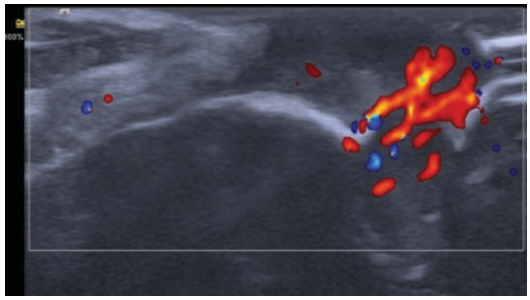

Fig. 18.71 Oral malignant melanoma. Doppler US reveals a mucosal malignant melanoma with predominantly hypoechoic echogenicity and cortical plate destruction. Note the high vascularity and thick vascular structures inside the lesion

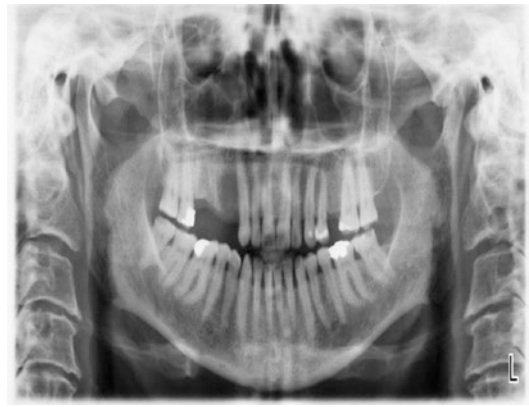

Fig. 18.72 Multiple myeloma. OPG reveals a non-corticated well-defined radiolucent lesion located at the maxillary canine region

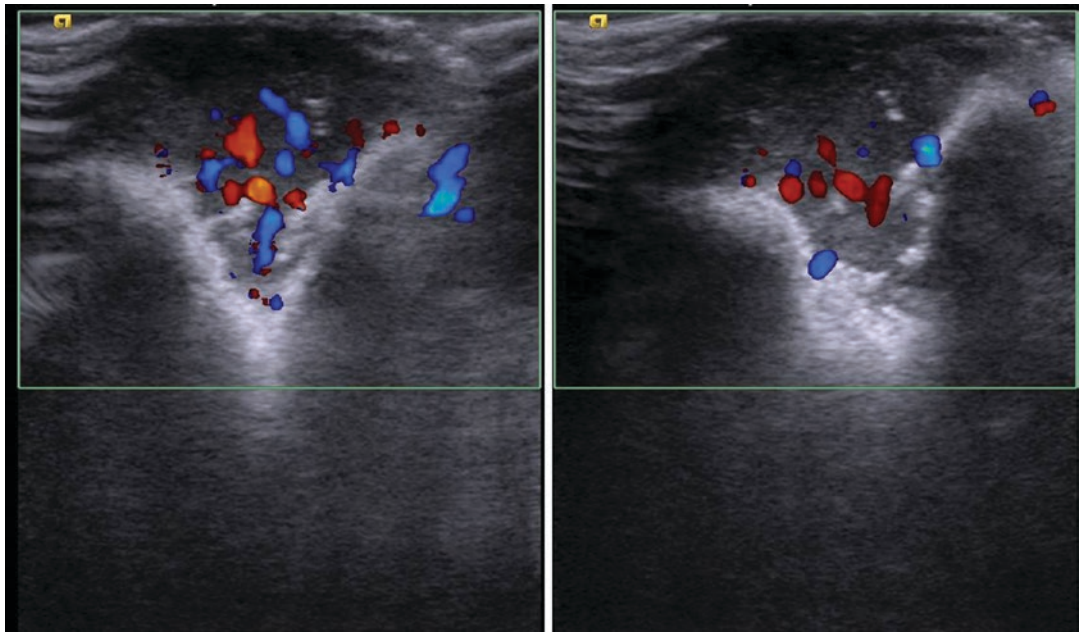

Fig. 18.73 Multiple myeloma. USG image showing heterogeneous hypoechoic lesions with high vascularization on Doppler image

18.2.5.6 Multiple Myeloma

Multiple myeloma is the malignancy of the plasma cells and the most common malignancy of the bones in adult patients. Jaws are affected in 30% of multiple myeloma cases and the most common sites are mandibular posterior region and mandibular ramus [2, 102, 103]

Clinically, weight loss, bone pain, fever, and fatigue are seen. Some patients have Bence-Jones proteins in their urine with a foamy structure. Patients with amyloidosis and hypercalcemia were also reported. Advanced Multiple myelomas affect the trabecular and cortical bone by altering the structure to radiolucent areas. No oral findings can be present but the most common oral findings are swelling, paresthesia, dysesthesia, hemorrhage, and tooth pain. Radiographically, well-defined but non-corticated radiolucent lesions are seen (Figs. 18.72 and 18.73). Multiple punched-out lesions are present on the skull and

lesions located near the tooth apex may mimic a periapical infection. Lesions in mandible can cause thinning in cortical plates while advanced lesions in maxilla can cause destruction at maxillary sinus floor and hard palate [1, 2, 102, 103].

Common sonographic features of multiple myelomas are (Fig. 18.72):

- Internal Structure: Mixed heterogeneous, predominantly hypoechoic lesions with high vascularization on Doppler imaging.

18.2.5.7 Metastatic Tumors

Metastatic tumors are new focis of malignancy from a malignant tumor of distant organ by lymphatic way or blood vessels. Metastatic Tumours at mandible and maxilla represent 1% of metastases and the most frequent primary sites are breast, kidney, and lung. They are mostly seen at mandibular posterior sites and maxillary sinuses. Clinically, atypical dental pain, pathologic fractures, numbness, paresthesia, and hemorrhage are seen [3–5].

Radiographically, a radiolucent lesion with polymorphous ill-defined borders is seen mostly below the mandibular canal. Invasive margins with non-corticated and non-encapsulated borders are characteristic of metastatic tumors. Occasionally lesions which are located in the periodontal ligament space are seen which may cause false diagnosis. Floating teeth appearance is another characteristic appearance of metastatic tumors due to the destruction of bony support [3–5].

US is superior to clinical palpation examination while examining lymph nodes. Common radiographic features of metastatic lymph nodes are ill-defined nodes with central necrosis (Fig. 18.74)

18.3 Pseudo-Tumors of Maxillofacial Regions

18.3.1 Masson's Hemangioma (Intravascular Papillary Endothelial Hyperplasia)

Intravascular papillary endothelial hyperplasia (IPEH) or Masson's hemangioma is a benign reactive proliferation which is most common at mucosa, subcutaneous tissue, and skin. It represents 2% of vascular proliferation of subcutaneous tissues and skin, and head and neck region is the most common site for IPEHs [104].

Clinically, a bluish-reddish solid nodule is located submucosally in the oral cavity (Fig. 18.75). OPG and periapical radiographs may reveal soft tissue thickening especially at edentulous areas but US is superior to those imaging techniques since IPEHs are superficial soft tissue lesions (Fig. 18.76).

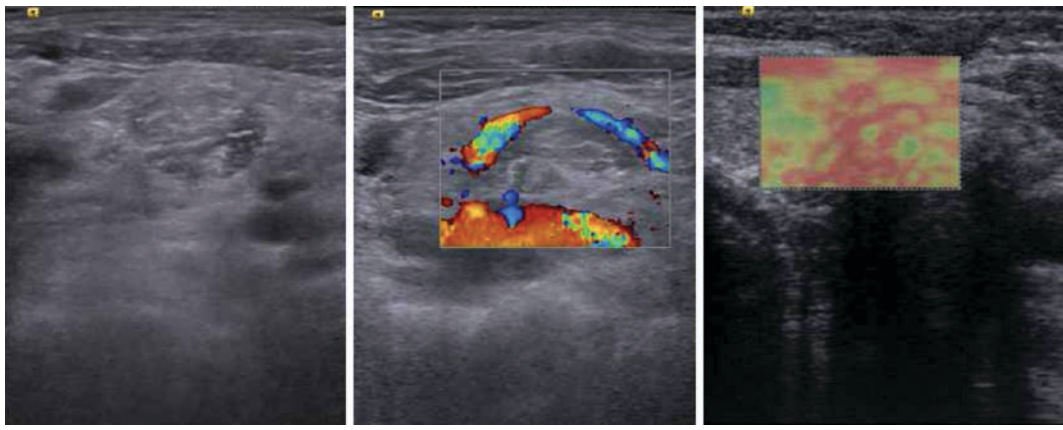

Fig. 18.74 A 38-year-old woman with breast CA. USG image showing metastatic lymph node in the neck. Ultrasound image shows loss of degeneration of hilum and ovoid change. Color-coded strain elastography shows stiff lesion which was then confirmed as malignant cells by cytology results

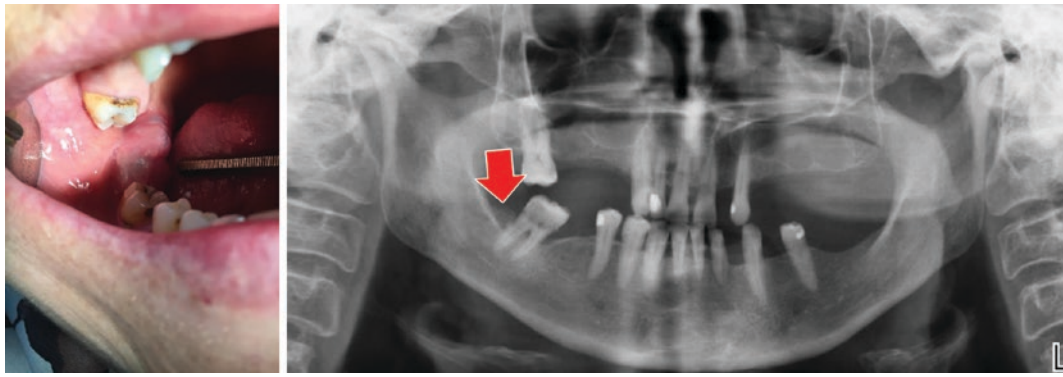

Fig. 18.75 IPEH. (**a**) Intraoral photo showing a bluish-reddish solid nodule is located submucosally in the oral cavity. (**b**) OPG image was nonrelevant for soft tissue imaging

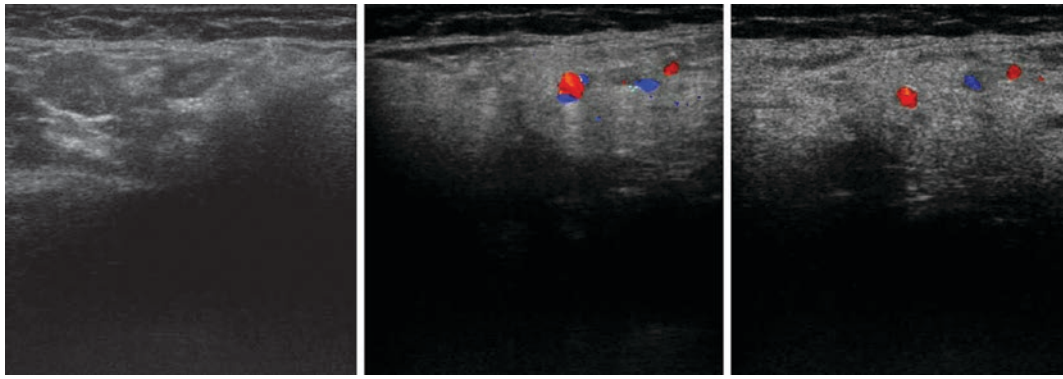

Fig. 18.76 IPEH. (**a**) A gray-scale US showing a small, well-defined, oval, heterogeneously hypoechoic mass with an internal septum-like structure. (**b**) Oblique transverse color Doppler US showing moderate vascularity with one or more, both central and peripheral color signals. (**c**) Note the vascular stalk of the affected vessel (arrow) continuing to the lesion

18.3.2 Caliber Persistent Artery

Caliber persistent artery (CPA) is a vascular lesion which is generally located at the submucosal area, especially in lips, without loss of caliber. Generally, they have an abnormal larger diameter than healthy arteries in the relevant region. Clinically, a bluish mass with pulsation is palpated at the lips. Presence of surface ulceration may mimic a squamous cell carcinoma of the lips and bleeding may occur as a major surgical complication; thus, US evaluation is crucial in order to prevent misdiagnosis (Fig. 18.77) [105, 106].

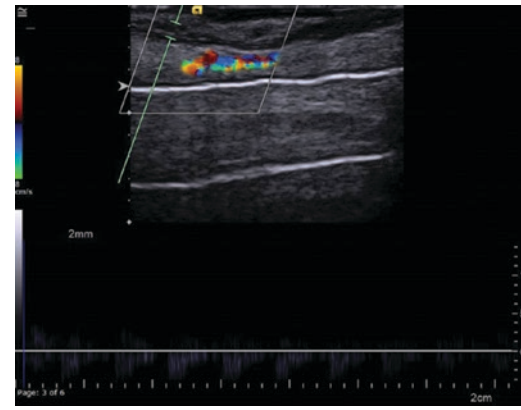

Fig. 18.77 Spectral and color analysis using Doppler ultrasound shows resistance flow in labial artery looks like a loop

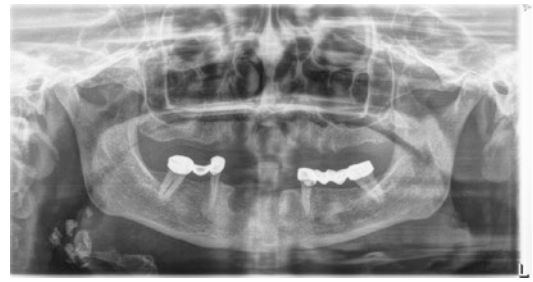

Fig. 18.78 Calcified lymph node. OPG reveals radiopaque calcified masses at soft tissue area below mandibular right angulus

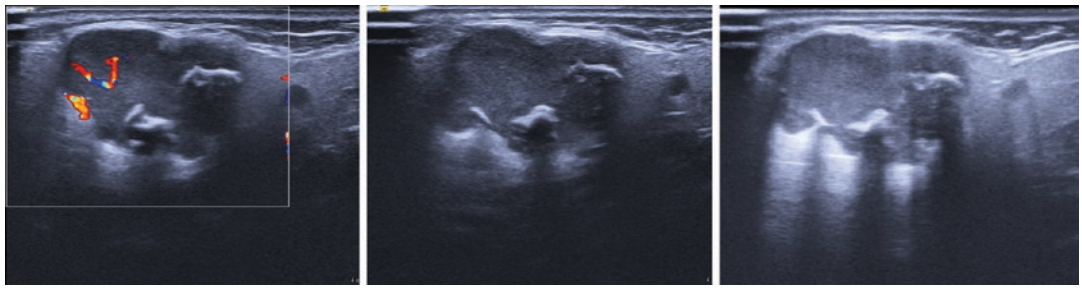

Fig. 18.79 Calcified lymph node. USG images show inhomogeneous enlarged submandibular lymph node with calcifications caused by mycobacterium

18.3.3 Lymph Node Calcification

Dystrophic calcification of cervical lymph nodes generally occurs following a granulomatous disorder.

Sarcoidosis, tuberculosis, rheumatoid arthritis, fungal infections, radiation therapy of lymphoma, and metastatic thyroid carcinomas are the most common pathologies [3, 4, 107–109]

Clinically, asymptomatic, firm, and round lymph nodes are palpated. Radiographically, OPG reveals incidental calcifications generally around the submandibular area (Fig. 18.78). Those radiopaque calcified areas can be single node or multiple node. Multiple calcified lymph nodes have a characteristic cauliflower appearance which is important in differential diagnosis with other calcifications [3, 4]. USG images show inhomogeneous enlarged lymph node representing irregular hypoechoic mass with calcifications (Fig. 18.79) caused by mycobacterium.

Acknowledgments Figures 18.3, 18.15, 18.16, 18.22, 18.23, 18.31, 18.34, 18.39, 18.56, 18.67, and 18.79 are courtesy of Prof. Dr. İlknur Özcan, Dr. Hülya Çakır Karabaş, Dr. Sedef Ayşe Taşyapan, and Dr. Ahmet Faruk Ertürk, Istanbul University, Department of Dentomaxillofacial Radiology.

Figures 18.6, 18.7, 18.17, 18.26, 18.27, 18.28, 18.37, 18.44, 18.64, 18.65, and 18.66 are courtesy of Assoc. Dr. İbrahim Şevki Bayrakdar, Eskişehir Osmangazi University, Department of Dentomaxillofacial Radiology.

We would like to thank Prof. Dr. İlknur Özcan, Dr. İbrahim Şevki Bayrakdar, Dr. Merva Soluk Tekkeşin, Dr. Fatma Nihan Aksakallı, Dr. Vakur Olgaç, Dr. Hülya Çakır Karabaş, Dr. Sedef Ayşe Taşyapan, and Dr. Ahmet Faruk Ertürk for their helpful advices and contributions.

References

1. El-Naggar AK, Chan JKC, Rubin GJ, Takata T, Slootweg PJ, International Agency for Research on Cancer. WHO classification of head and neck tumours. Lyon: IARC; 2017.
2. Wright JM, Soluk Tekkesin M. Odontogenic tumors: where are we in 2017? J Istanbul Univ Fac Dent. 2017;51(3 Suppl 1):S10–30. Published 2017 Dec 2
3. White SC, Pharoah MJ. Oral radiology: principles and interpretation. St. Louis, Mo: Mosby/Elsevier; 2014.
4. Ozcan I. Diş Hekimliğinde Radyolojinin Esasları: Konvansiyonelden Dijitale. İstanbul: İstanbul Tıp Kitapevi; 2017.
5. Koenig LJ. Diagnostic Imaging. Philadelphia, PA: Elsevier; 2017.

6. Cadavid AMH, Araujo JP, Coutinho-Camillo CM, et al. Ameloblastomas: current aspects of the new WHO classification in an analysis of 136 cases. Surg Exp Pathol. 2019;2:17. https://doi.org/10.1186/s42047-019-0041-z.
7. Chrcanovic BR, Gomez RS. Squamous odontogenic tumor and squamous odontogenic tumor-like proliferations in odontogenic cysts: an updated analysis of 170 cases reported in the literature. J Craniomaxillofac Surg. 2018;46(3):504–10. https://doi.org/10.1016/j.jcms.2017.12.023.
8. Chrcanovic BR, Gomez RS. Calcifying epithelial odontogenic tumor: an updated analysis of 339 cases reported in the literature. J Craniomaxillofac Surg. 2017;45(8):1117–23. https://doi.org/10.1016/j.jcms.2017.05.007.
9. Philipsen HP, Khongkhunthiang P, Reichart PA. The adenomatoid odontogenic tumour: an update of selected issues. J Oral Pathol Med. 2016;45(6):394–8. https://doi.org/10.1111/jop.12418.
10. Naidu A, Slater LJ, Hamao-Sakamoto A, Waters P, Kessler HP, Wright JM. Adenomatoid odontogenic tumor with peripheral cemento-osseous reactive proliferation: report of 2 cases and review of the literature. Oral Surg Oral Med Oral Pathol Oral Radiol. 2016;122(3):e86–92. https://doi.org/10.1016/j.oooo.2015.12.003.
11. Peters SM, Bergen MS, Philipone EM, Yoon AJ. Ameloblastic fibro-Odontoma in an adolescent: a case report and review of literature. J Clin Pediatr Dent. 2018;42(6):458–60. https://doi.org/10.17796/1053-4625-42.6.10.
12. Darling MR, Daley TD. Peripheral ameloblastic fibroma. J Oral Pathol Med. 2006;35(3):190–2. https://doi.org/10.1111/j.1600-0714.2006.00353.x.
13. Singer SR, Mupparapu M, Milles M, Rinaggio J, Pisano D, Quaranta P. Unusually large complex odontoma in maxillary sinus associated with unerupted tooth. Report of case and review of literature. N Y State Dent J. 2007;73(4):51–3.
14. Altay MA, Ozgur B, Cehreli ZC. Management of a Compound Odontoma in the primary dentition. J Dent Child (Chic). 2016;83(2):98–101.
15. Konstantakis D, Kosyfaki P, Ebhardt H, Schmelzeisen R, Voss PJ. Intraosseous dentinogenic ghost cell tumor: a clinical report and literature update. J Craniomaxillofac Surg. 2014;42(5):e305–11. https://doi.org/10.1016/j.jcms.2013.10.011.
16. Correa Pontes FS. Lacerda de Souza L, Paula de Paula L, de Melo Galvão Neto E, Silva Gonçalves PF, Rebelo Pontes HA. Central odontogenic fibroma: an updated systematic review of cases reported in the literature with emphasis on recurrence influencing factors. J Craniomaxillofac Surg. 2018;46(10):1753–7. https://doi.org/10.1016/j.jcms.2018.07.025.
17. Heithersay GS, Musu D, Cotti E. External tooth resorption associated with a peripheral odontogenic fibroma: review and case report. Aust Dent J. 2017;62(4):516–22. https://doi.org/10.1111/adj.12544.
18. Noffke CE, Raubenheimer EJ, Chabikuli NJ, Bouckaert MM. Odontogenic myxoma: review of the literature and report of 30 cases from South Africa. Oral Surg Oral Med Oral Pathol Oral Radiol Endod. 2007;104(1):101–9. https://doi.org/10.1016/j.tripleo.2007.01.026.
19. Hammad HM, Hasen YM, Odat AA, Mikdadi AM, Safadi RA. Odontogenic myxoma with diffuse calcifications: a case report and review of a rare histologic feature. Oral Surg Oral Med Oral Pathol Oral Radiol. 2016;122(4):e116–24. https://doi.org/10.1016/j.oooo.2015.12.009.
20. Kaffe I, Naor H, Buchner A. Clinical and radiological features of odontogenic myxoma of the jaws. Dentomaxillofac Radiol. 1997;26(5):299–303. https://doi.org/10.1038/sj.dmfr.4600261.
21. Chrcanovic BR, Gomez RS. Cementoblastoma: an updated analysis of 258 cases reported in the literature. J Craniomaxillofac Surg. 2017;45(10):1759–66. https://doi.org/10.1016/j.jcms.2017.08.002.
22. Ostrofsky M, Morkel JA, Titinchi F. Osteoma of the mandibular condyle: a rare case report and review of the literature. J Stomatol Oral Maxillofac Surg. 2019;120(6):584–7. https://doi.org/10.1016/j.jormas.2019.01.013.
23. Sayan NB, Uçok C, Karasu HA, Günhan O. Peripheral osteoma of the oral and maxillofacial region: a study of 35 new cases. J Oral Maxillofac Surg. 2002;60(11):1299–301. https://doi.org/10.1053/joms.2002.35727.
24. Deferm JT, Steens SCA, Vriens D, Bekers EM, Kalaykova SI, Borstlap WA. Chronic temporomandibular joint pain: two cases of osteoid osteoma and a review of the literature. Int J Oral Maxillofac Surg. 2017;46(9):1130–7. https://doi.org/10.1016/j.ijom.2017.03.036.
25. Alvares Capelozza AL, Gião Dezotti MS, Casati Alvares L, Negrão Fleury R, Sant'Ana E. Osteoblastoma of the mandible: systematic review of the literature and report of a case. Dentomaxillofac Radiol. 2005;34(1):1–8. https://doi.org/10.1259/dmfr/24385194.
26. Shekhar MG, Reddy RS, Ravikanth M, Lavanya R, Kumar M. Desmoplastic fibroma of the mandible: case report and review of literature. Prim Dent Care. 2011;18(3):115–8.
27. Said-Al-Naief N, Fernandes R, Louis P, Bell W, Siegal GP. Desmoplastic fibroma of the jaw: a case report and review of literature. Oral Surg Oral Med Oral Pathol Oral Radiol Endod. 2006;101(1):82–94. https://doi.org/10.1016/j.tripleo.2005.03.034.
28. Triantafillidou K, Venetis G, Karakinaris G, Iordanidis F. Ossifying fibroma of the jaws: a clinical study of 14 cases and review of the literature. Oral Surg Oral Med Oral Pathol Oral Radiol. 2012;114(2):193–9. https://doi.org/10.1016/j.tripleo.2011.07.033.

29. MacDonald-Jankowski DS. Ossifying fibroma: a systematic review. Dentomaxillofac Radiol. 2009;38(8):495–513. https://doi.org/10.1259/dmfr/70933621.
30. Chrcanovic BR, Gomez RS. Juvenile ossifying fibroma of the jaws and paranasal sinuses: a systematic review of the cases reported in the literature. Int J Oral Maxillofac Surg. 2020;49(1):28–37. https://doi.org/10.1016/j.ijom.2019.06.029.
31. Figueiredo LM, de Oliveira TF, Paraguassú GM, de Hollanda Valente RO, da Costa WR, Sarmento VA. Psammomatoid juvenile ossifying fibroma: case study and a review. Oral Maxillofac Surg. 2014;18(1):87–93. https://doi.org/10.1007/s10006-013-0400-y.
32. Mainville GN, Turgeon DP, Kauzman A. Diagnosis and management of benign fibro-osseous lesions of the jaws: a current review for the dental clinician. Oral Dis. 2017;23(4):440–50. https://doi.org/10.1111/odi.12531.
33. Ricalde P, Magliocca KR, Lee JS. Craniofacial fibrous dysplasia. Oral Maxillofac Surg Clin North Am. 2012;24(3):427–41. https://doi.org/10.1016/j.coms.2012.05.004.
34. MacDonald-Jankowski D. Fibrous dysplasia: a systematic review. Dentomaxillofac Radiol. 2009;38(4):196–215. https://doi.org/10.1259/dmfr/16645318.
35. MacDonald-Jankowski D. Fibrous dysplasia in the jaws of a Hong-Kong population: radiographic presentation and systematic review. Dentomaxillofac Radiol. 1999;28(4):195–202. https://doi.org/10.1038/sj/dmfr/4600440.
36. Pereira TDSF, Gomes CC, Brennan PA, Fonseca FP, Gomez RS. Fibrous dysplasia of the jaws: integrating molecular pathogenesis with clinical, radiological, and histopathological features. J Oral Pathol Med. 2019;48(1):3–9. https://doi.org/10.1111/jop.12797.
37. Zhang PY, Xiao C. Zhonghua Kou Qiang Yi Xue Za Zhi. 2018;53(4):280–3. https://doi.org/10.3760/cma.j.issn.1002-0098.2018.04.013.
38. Senia ES, Sarao MS. Periapical cemento-osseous dysplasia: a case report with twelve-year follow-up and review of literature. Int Endod J. 2015;48(11):1086–99. https://doi.org/10.1111/iej.12417.
39. Mangala M, Ramesh DN, Surekha PS, Santosh P. Florid cemento-osseous dysplasia: review and report of two cases. Indian J Dent Res. 2006;17(3):131–4. https://doi.org/10.4103/0970-9290.29875.
40. Patel R, Obeid G. Osteochondroma of the zygomatic arch: a case report and review of the literature. J Oral Maxillofac Surg. 2018;76(9):1912–6. https://doi.org/10.1016/j.joms.2018.03.038.
41. Peroz I. Osteochondroma of the condyle: case report with 15 years of follow-up. Int J Oral Maxillofac Surg. 2016;45(9):1120–2. https://doi.org/10.1016/j.ijom.2016.04.005.
42. de Lange J, van den Akker HP, van den Berg H. Central giant cell granuloma of the jaw: a review of the literature with emphasis on therapy options. Oral Surg Oral Med Oral Pathol Oral Radiol Endod. 2007;104(5):603–15. https://doi.org/10.1016/j.tripleo.2007.04.003.
43. Jadu FM, Pharoah MJ, Lee L, Baker GI, Allidina A. Central giant cell granuloma of the mandibular condyle: a case report and review of the literature. Dentomaxillofac Radiol. 2011;40(1):60–4. https://doi.org/10.1259/dmfr/85668294.
44. Chrcanovic BR, Gomes CC, Gomez RS. Peripheral giant cell granuloma: an updated analysis of 2824 cases reported in the literature. J Oral Pathol Med. 2018;47(5):454–9. https://doi.org/10.1111/jop.12706.
45. Boffano P, Benech R, Roccia F, Gallesio C, Garzaro M, Pecorari G. Review of peripheral giant cell granulomas. J Craniofac Surg. 2013;24(6):2206–8. https://doi.org/10.1097/SCS.0b013e31829a8316.
46. Zadik Y, Aktaş A, Drucker S, Nitzan DW. Aneurysmal bone cyst of mandibular condyle: a case report and review of the literature. J Craniomaxillofac Surg. 2012;40(8):e243–8. https://doi.org/10.1016/j.jcms.2011.10.026.
47. Hebbale M, Munde A, Maria A, Gawande P, Halli R. Giant aneurysmal bone cyst of the mandible. J Craniofac Surg. 2011;22(2):745–8. https://doi.org/10.1097/SCS.0b013e31820871b8.
48. Philbert RF, Sandhu NS. Nonodontogenic cysts. Dent Clin N Am. 2020;64(1):63–85. https://doi.org/10.1016/j.cden.2019.08.006.
49. Sabino-Bezerra JR, Santos-Silva AR, Jorge J Jr, Gouvêa AF, Lopes MA. Atypical presentations of simple bone cysts of the mandible: a case series and review of literature. J Craniomaxillofac Surg. 2013;41(5):391–6. https://doi.org/10.1016/j.jcms.2012.11.002.
50. Sidorowicz W, Kubasiewicz-Ross P, Dominiak M. Familial cherubism: clinical and radiological features. Case report and review of the literature. Eur J Paediatr Dent. 2018;19(3):213–7. https://doi.org/10.23804/ejpd.2018.19.03.8.
51. Holley TJ, Giannini PJ, Narayana N, Desa VP. Early detection of cherubism with eventual bilateral progression: a literature review and case report. Oral Surg Oral Med Oral Pathol Oral Radiol. 2019;127(3):e77–83. https://doi.org/10.1016/j.oooo.2018.08.011.
52. Agostini T, Sacco R, Bertolai R, Acocella A, Lazzeri D. Solitary plasmacytoma of the jaw. J Craniofac Surg. 2011;22(6):e2–e10. https://doi.org/10.1097/SCS.0b013e31822ec79a.
53. Jain S, Singaraju S, Singaraju M. Central hemangioma: a case report and review of literature. J Indian Soc Pedod Prev Dent. 2016;34(1):87–91. https://doi.org/10.4103/0970-4388.175525.
54. Gómez Oliveira G, García-Rozado A, Luaces Rey R. Intraosseous mandibular hemangioma. A case report and review of the literature. Med Oral Patol Oral Cir Bucal. 2008;13(8):E496–8.

55. Cortese A, Pantaleo G, D'Alessio G, Garzi A, Amato M. Hemangiomas of the maxillofacial area: case report, classification and treatment planning. Open Med. 2015;10(1):529–34. https://doi.org/10.1515/med-2015-0066.
56. Ciurea ME, Bondari S, Stoica LE, Gheonea IA. Role of MRI in the diagnosis and evaluation of cavernous hemangioma of the arm. J Med Life. 2014;7(1):46–50.
57. Masand P. Radiographic findings associated with vascular anomalies. Semin Plast Surg. 2014;28(2):69–78. https://doi.org/10.1055/s-0034-1376266.
58. Cakarer S, Selvi F, Isler SC, Soluk M, Olgac V, Keskin C. Intraosseous lipoma of the mandible: a case report and review of the literature. Int J Oral Maxillofac Surg. 2009;38(8):900–2. https://doi.org/10.1016/j.ijom.2009.03.712.
59. MA F-SJC, Childers EL. Lipoma of the oral and maxillofacial region: site and subclassification of 125 cases. Oral Surg Oral Med Oral Pathol Oral Radiol Endod. 2004;98(4):441–50. https://doi.org/10.1016/j.tripleo.2004.02.071.
60. Sohn WI, Kim JH, Jung SN, Kwon H, Cho KJ. Intramuscular lipoma of the sternocleidomastoid muscle. J Craniofac Surg. 2010;21(6):1976–8. https://doi.org/10.1097/SCS.0b013e3181f502cd.
61. Rehal SS, Alibhai M, Perera E. Lipoma of the parotid gland after trauma: a case report and review. Br J Oral Maxillofac Surg. 2017;55(1):e5–6. https://doi.org/10.1016/j.bjoms.2016.06.003.
62. Tehranzadeh J. Musculoskeletal Imaging Cases. New York: McGraw-Hill Professional; 2008. ISBN: 0071465421
63. Murphey MD, Carroll JF, Flemming DJ, et al. From the archives of the AFIP: benign musculoskeletal lipomatous lesions. Radiographics. 2004;24(5):1433–66. https://doi.org/10.1148/rg.245045120.
64. Inampudi P, Jacobson JA, Fessell DP, et al. Soft-tissue lipomas: accuracy of sonography in diagnosis with pathologic correlation. Radiology. 2004;233(3):763–7. https://doi.org/10.1148/radiol.2333031410.
65. DiDomenico P, Middleton W. Sonographic evaluation of palpable superficial masses. Radiol Clin N Am. 2014;52(6):1295–305. https://doi.org/10.1016/j.rcl.2014.07.011.
66. Bansal AG, Oudsema R, Masseaux JA, Rosenberg HK. US of pediatric superficial masses of the head and neck. Radiographics. 2018;38(4):1239–63.
67. Pilavaki M, Chourmouzi D, Kiziridou A, et al. Imaging of peripheral nerve sheath tumors with pathologic correlation: pictorial review. Eur J Radiol. 2004;52(3):229–39.
68. Hassell DS, Bancroft LW, Kransdorf MJ, Peterson JJ, Berquist TH, Murphey MD, Fanburg-Smith JC. Imaging appearance of diffuse neurofibroma. Am J Roentgenol. 2008;190(3):582–8. https://doi.org/10.2214/AJR.07.2589.
69. Kransdorf MJ, Murphey MD. Imaging of soft tissue tumors. Philadelphia: W. B. Saunders; 1997. ISBN: 9780781747714
70. Skolnik AD, Loevner LA, Sampathu DM, et al. Cranial nerve schwannomas: diagnostic Imaging approach. Radiographics. 2016;36(5):150199. https://doi.org/10.1148/rg.2016150199.
71. Moonis G, Patel P, Koshkareva Y, et al. Imaging characteristics of recurrent pleomorphic adenoma of the parotid gland. AJNR Am J Neuroradiol. 2007;28(8):1532–6.
72. SM GA, Chole R. Oral pregnancy tumor. Contemp Clin Dent. 2010;1(3):190–2. https://doi.org/10.4103/0976-237X.72792.
73. Rachappa MM, Triveni MN. Capillary hemangioma or pyogenic granuloma: A diagnostic dilemma. Contemp Clin Dent. 2010;1(2):119–22. https://doi.org/10.4103/0976-237X.68593.
74. Kamal R, Dahiya P, Puri A. Oral pyogenic granuloma: various concepts of etiopathogenesis. J Oral Maxillofac Pathol. 2012;16(1):79–82. https://doi.org/10.4103/0973-029X.92978.
75. Ram H, Mohammad S, Husain N, Gupta PN. Ameloblastic carcinoma. J Maxillofac Oral Surg. 2010;9(4):415–9. https://doi.org/10.1007/s12663-010-0169-.
76. Simko EJ, Brannon RB, Eibling DE. Ameloblastic carcinoma of the mandible. Head Neck. 1998;20(7):654–9. https://doi.org/10.1002/(SICI)1097-0347(199810)20:7<654::AID-HED14>3.0.CO;2-4.
77. Hanisch M, Baumhoer D, Elges S, Fröhlich LF, Kleinheinz J, Jung S. Sclerosing odontogenic carcinoma: current diagnostic and management considerations concerning a most unusual neoplasm. Int J Oral Maxillofac Surg. 2017;46(12):1641–9. https://doi.org/10.1016/j.ijom.2017.05.024.
78. Todorovic E, Berthelet E, O'Connor R, et al. Sclerosing odontogenic carcinoma with local recurrence: case report and review of literature. Head Neck Pathol. 2019;13(3):371–7. https://doi.org/10.1007/s12105-018-0975-6.
79. Loyola AM, Cardoso SV, de Faria PR, et al. Clear cell odontogenic carcinoma: report of 7 new cases and systematic review of the current knowledge. Oral Surg Oral Med Oral Pathol Oral Radiol. 2015;120(4):483–96. https://doi.org/10.1016/j.oooo.2015.06.005.
80. Ferreira S, Faverani LP, Santos GMD, Martins EP, Garcia Júnior IR. Clear cell odontogenic carcinoma of the mandible: a treatment strategy. J Appl Oral Sci. 2018;26:e20160645. https://doi.org/10.1590/1678-7757-2016-0645.
81. Swain N, Dhariwal R, Ray JG. Clear cell odontogenic carcinoma of maxilla: a case report and mini review. J Oral Maxillofac Pathol. 2013;17(1):89–94. https://doi.org/10.4103/0973-029X.110681.
82. Park SY, Park J, Kwon DH, et al. Ghost cell odontogenic carcinoma on right mandible and its respective surgical reconstruction: a case report. J Korean Assoc Oral Maxillofac Surg. 2017;43(6):415–22. https://doi.org/10.5125/jkaoms.2017.43.6.415.
83. Martos-Fernández M, Alberola-Ferranti M, Hueto-Madrid JA, Bescós-Atín C. Ghost cell odontogenic carcinoma: a rare case report and review of litera-

ture. J Clin Exp Dent. 2014;6(5):e602–6. https://doi.org/10.4317/jced.51809.
84. Schuch LF, de Arruda JAA, Silva LVO, Abreu LG, Silva TA, Mesquita RA. Odontogenic carcinosarcoma: A systematic review. Oral Oncol. 2018;85:52–9. https://doi.org/10.1016/j.oraloncology.2018.08.017.
85. Atarbashi-Moghadam S, Lotfi A, Mokhtari S. A mixed odontogenic sarcoma: A challenging histopathologic. J Oral Maxillofac Pathol. 2018;22:S29–34.
86. Murphey MD, Robbin MR, Mcrae GA, et al. The many faces of osteosarcoma. Radiographics. 1997;17(5):1205–31.
87. Geirnaerdt MJ, Hogendoorn PC, Bloem JL, et al. Cartilaginous tumors: fast contrast-enhanced MR imaging. Radiology. 2000;214(2):539–46.
88. Murphey MD, Walker EA, Wilson AJ, et al. From the archives of the AFIP: imaging of primary chondrosarcoma: radiologic-pathologic correlation. Radiographics. 2003;23(5):1245–78. https://doi.org/10.1148/rg.235035134.
89. Xu J, Li D, Xie L, Tang S, Guo W. Mesenchymal chondrosarcoma of bone and soft tissue: a systematic review of 107 patients in the past 20 years. PLoS One. 2015;10(4):e0122216. https://doi.org/10.1371/journal.pone.0122216.
90. Harrison LB, Sessions RB, Hong WK, editors. Head and neck Cancer. London: Lippincott Williams & Wilkins; 2008. ISBN: 0781771366
91. Som PM, Curtin HD. Head and neck imaging – 2, volume set. 5th ed. St Louis, MO: Mosby; 2011.
92. Qin W, Chong R, Huang X, Liu M, Yin ZQ. Adenoid cystic carcinoma of the lacrimal gland: CT and MRI findings. Eur J Ophthalmol. 2012;22(3):316–9. https://doi.org/10.5301/ejo.5000015.
93. Dubergé T, Bénézery K, Resbeut M, Azria D, Minsat M, Ellis S, Teissier E, Zaccariotto A, Champetier C, Cowen D. Carcinomes adénoïdes kystiques ORL: étude rétrospective multicentrique de 169 cas. Cancer/Radiothérapie. 2012;16(4):247–56.
94. Coca-Pelaz A, Rodrigo JP, Bradley PJ, et al. Adenoid cystic carcinoma of the head and neck–an update. Oral Oncol. 2015;51(7):652–61. https://doi.org/10.1016/j.oraloncology.2015.04.005.
95. Yousem DM, Kraut MA, Chalian AA. Major salivary gland imaging. Radiology. 2000;216(1):19–29.
96. Adouani A, Bouguila J, Jeblaoui Y, et al. B-cell lymphoma of the mandible: a case report. Clin Med Oncol. 2008;2:445–50. https://doi.org/10.4137/cmo.s366.
97. Brandwein-Weber MS. Textbook of Head and neck pathology, vol. 1. New York: Springer; 2016.
98. Padhye A, D'souza J. Oral malignant melanoma: A silent killer? J Indian Soc Periodontol. 2011;15(4):425–8. https://doi.org/10.4103/0972-124X.92587.
99. Koca RB, Ünsal G, Soluk-Tekkeşin M, Kasnak G, Orhan K, Özcan İ, Fıratlı E. A review with an additional case: amelanotic malignant melanoma at mandibular gingiva. Int Cancer Conf J. 2020;9:175–81. https://doi.org/10.1007/s13691-020-00425-3.
100. Manigandan T, Sagar GV, Amudhan A, Hemalatha VT, Babu NA. Oral malignant melanoma: a case report with review of literature. Contemp Clin Dent. 2014;5(3):415–8. https://doi.org/10.4103/0976-237X.137978.
101. Mellouli N, Sioud S, Garma M, Chokri A, Hamdi H, Selmi J. Oral malignant melanoma: history of malignant degeneration of a pigmented lesion. J Oral Med Oral Surg. 2019;25(2):19. https://doi.org/10.1051/mbcb/2019003.
102. Ali IK, Parate AR, Kasat VO, Dora A. Multiple myeloma with primary manifestation in the mandible. Cureus. 2018;10(3):e2265. https://doi.org/10.7759/cureus.2265.
103. Ramaiah KK, Joshi V, Thayi SR, Sathyanarayana P, Patil P, Ahmed Z. Multiple myeloma presenting with a maxillary lesion as the first sign. Imaging Sci Dent. 2015;45(1):55–60. https://doi.org/10.5624/isd.2015.45.1.55.
104. Fernandes D, Travassos DC, Ferrisse TM, et al. Oral intravascular papillary endothelial hyperplasia associated with an organizing Thrombus: case report and Immunohistochemical analysis. Case Rep Pathol. 2016;2016:1908767. https://doi.org/10.1155/2016/1908767.
105. Awni S, Conn B. Caliber-persistent labial artery: a rarely recognized cause of a lower lip swelling-report of 5 cases and review of the literature. J Oral Maxillofac Surg. 2016;74(7):1391–5. https://doi.org/10.1016/j.joms.2016.01.015.
106. Santagata M, Maglione M, Colella G, D'Amato S. Calibre persistent labial artery: clinical features and immunohistochemistry diagnosis. J Maxillofac Oral Surg. 2015;14(3):845–7. https://doi.org/10.1007/s12663-014-0740-7.
107. Koyama T, Ueda H, Togashi K, Umeoka S, Kataoka M, Nagai S. Radiologic manifestations of sarcoidosis in various organs. Radiographics. 2004;24(1):87–104. https://doi.org/10.1148/rg.241035076.
108. Ozgul MA, Cetinkaya E, Kirkil G, et al. Lymph node characteristics of sarcoidosis with endobronchial ultrasound. Endosc Ultrasound. 2014;3(4):232–7. https://doi.org/10.4103/2303-9027.144541.
109. Wei X, Wang M, Wang X, et al. Prediction of cervical lymph node metastases in papillary thyroid microcarcinoma by sonographic features of the primary site. Cancer Biol Med. 2019;16(3):587–94. https://doi.org/10.20892/j.issn.2095-3941.2018.0310.

The Thyroid Gland and Ultrasound Applications

19

Rose Ngu

Contents

Normal appearance of the thyroid gland is of a butterfly in the midline of anterior neck. It has two lobes connected by an isthmus. 40% of people would have a pyramidal lobe arising from the isthmus towards the hyoid bone.

The echotexture of the normal thyroid gland parenchyma is homogeneous throughout, higher

R. Ngu (✉)
Department of Dental Maxillofacial Imaging; Head Neck and Thyroid Imaging, Department of Radiology, Guy's and St Thomas' Hospitals NHS Foundation Trust, London, UK

King's College London Dental Institute, London, UK
e-mail: rose.ngu@kcl.ac.uk

K. Orhan (ed.), *Ultrasonography in Dentomaxillofacial Diagnostics*,
https://doi.org/10.1007/978-3-030-62179-7_19

in echogenicity than the overlying strap muscles. It is similar to the echotexture of a normal parotid gland parenchymal.

It borders by several muscles as seen in the ultrasound image in Fig. 19.1.

Anterior: Strap muscles; Sternothyroid and sternohyoid muscles.

Lateral: Sternocleidomastoid muscles, Superior belly of omohyoid, Common carotid artery (CCA).

Posterior: Oesophagus tends to be on the left, rarely on the right, longus colli, parathyroid gland (only seen if this is enlarged). Some level VI nodes can be visualized.

Medial to the lobe is the trachea.

Blood supply: Superior and inferior arteries; superior, middle, and inferior thyroid veins.

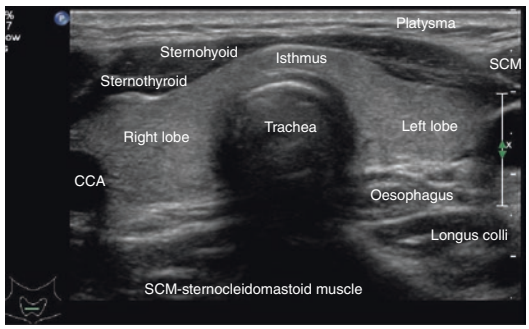

Fig. 19.1 Normal anatomy of the thyroid gland

19.1 Size of the Thyroid Gland

Size of the thyroid is normally measured in volume with measurement taken in three dimensions. It is easier to use a probe which is larger than a 6 cm linear probe. This would enable to scan the thyroid lobe in its maximum dimension. Remember to freeze the US image before measuring. The three dimensions to measure are width, depth, and length. It is not compulsory to measure the thyroid if the gland appears to be of normal size and echotexture. Size is important when there are nodules or if the thyroid is seen to be pathological.

The transverse dimension (width-W) and anterior-posterior (depth- D) dimension is approximately 2 cm (Fig. 19.2).

The length (L) of the lobes is 4–5 cm. Measured longitudinally (Fig. 19.2).

A quick way to check for enlargement is the look at the width of the isthmus. Any enlargement of >0.5 cm generally indicates enlargement of the thyroid gland.

A more detailed consistent way to assess the thyroid size is by measuring the volume. The volume is measured using $\pi/6$ (W × D × L). Most US machine has an onboard computer to calculate this when capturing the measurements [1]. The isthmus is normally ignored when calculating the volume unless there is a large nodule present within the isthmus. The normal size is approximately 10 ml (Fig. 19.3).

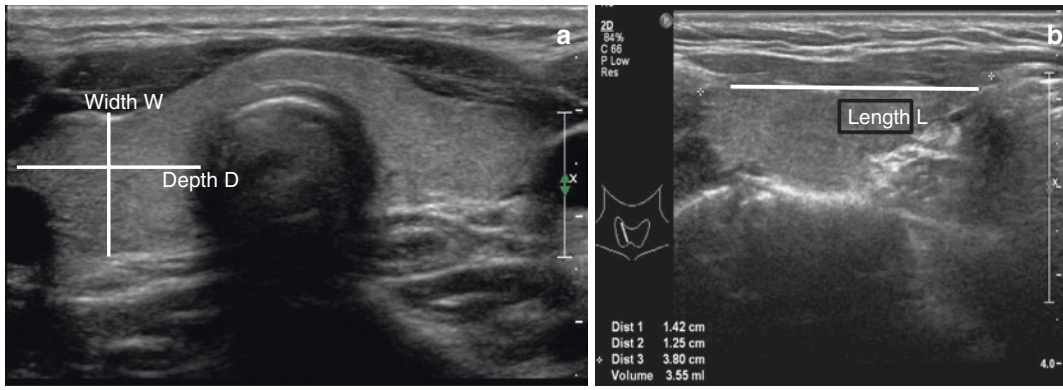

Fig. 19.2 Measuring the volume of the thyroid-transverse for width and depth (**a**) and longitudinally for length (**b**)

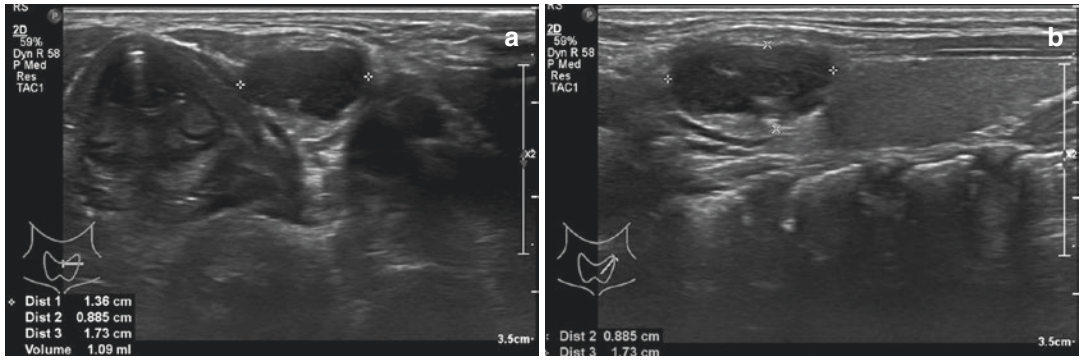

Fig. 19.3 Measuring a thyroid nodule-transverse for width and depth (**a**) and longitudinally for length (**b**)

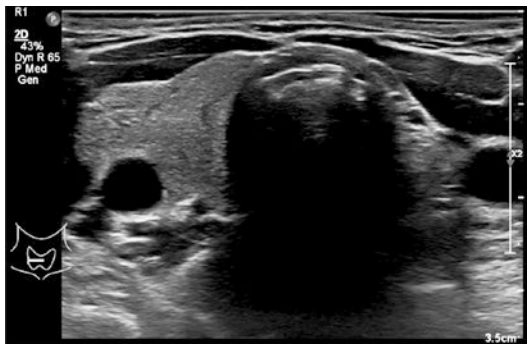

Fig. 19.4 Hemigenesis of the thyroid gland showing a missing left lobe of thyroid

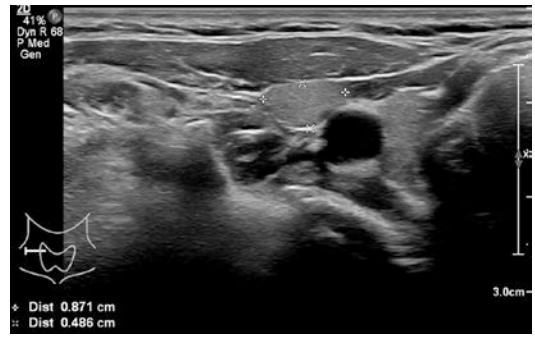

Fig. 19.5 Aberrant/ectopic thyroid: Incidental findings of a lesion in right level 3 in a 60-year-old patient. Hyperechoic tissue found lateral to the carotid artery, it has the same echogenicity as the right thyroid. FNA performed to confirm this is thyroid tissue. On US there is no connection to the thyroid gland which lies in level 6 and is separated by the carotid artery

19.2 Thyroid Anomalies

19.2.1 Hemigenesis

The incidence is 1:2500 with 96% involving hemigenesis of the left lobe [1]. It is a benign condition and often is an incidental finding when scanning for something else (Fig. 19.4). Double check that patient has no surgical scar present in the vicinity.

19.2.2 Aberrant Thyroid

Thyroid developed and descend from the base of the tongue. It descends below the larynx, which bifurcates into two lobes connected with an isthmus [1]. Several scenarios can occur. There may be an incomplete descend, disruption to the descend, or descend into the mediastinum. There may also be a lateral aberrant thyroid tissue in the neck. It is important to evaluate this to rule out a metastatic lymph node from a thyroid origin (Fig. 19.5).

19.3 Masses in the Midline Level 6

19.3.1 Thyroglossal Duct Cyst

Arises from embryonic tissue from the foramen caecum at the base of the tongue to the larynx. Portion of the duct near the isthmus may persist as a pyramidal lobe of the thyroid. This may be filled with proteinaceous material secreted by the lining epithelium (Fig. 19.6). Malignancy changes can occur in long standing Thyroglossal duct cyst, this is said to be approximately 1%.

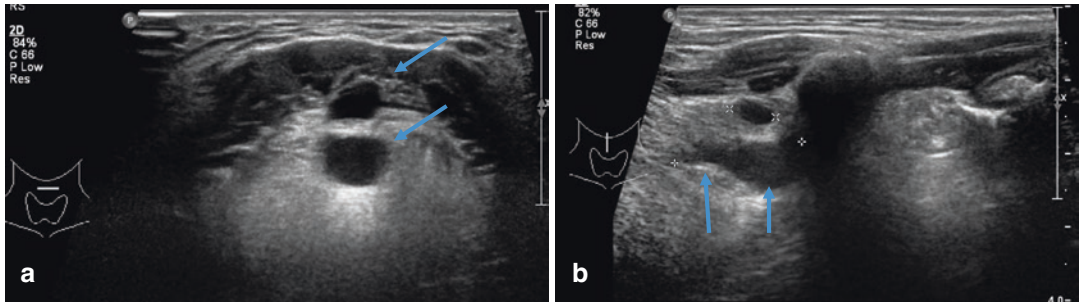

Fig. 19.6 A 42-year-old male presented with a lump in the anterior neck. This shows a track from the tongue (**a**) to the hyoid bone (**b**). On US and FNA this was proven to be a thyroglossal duct cyst

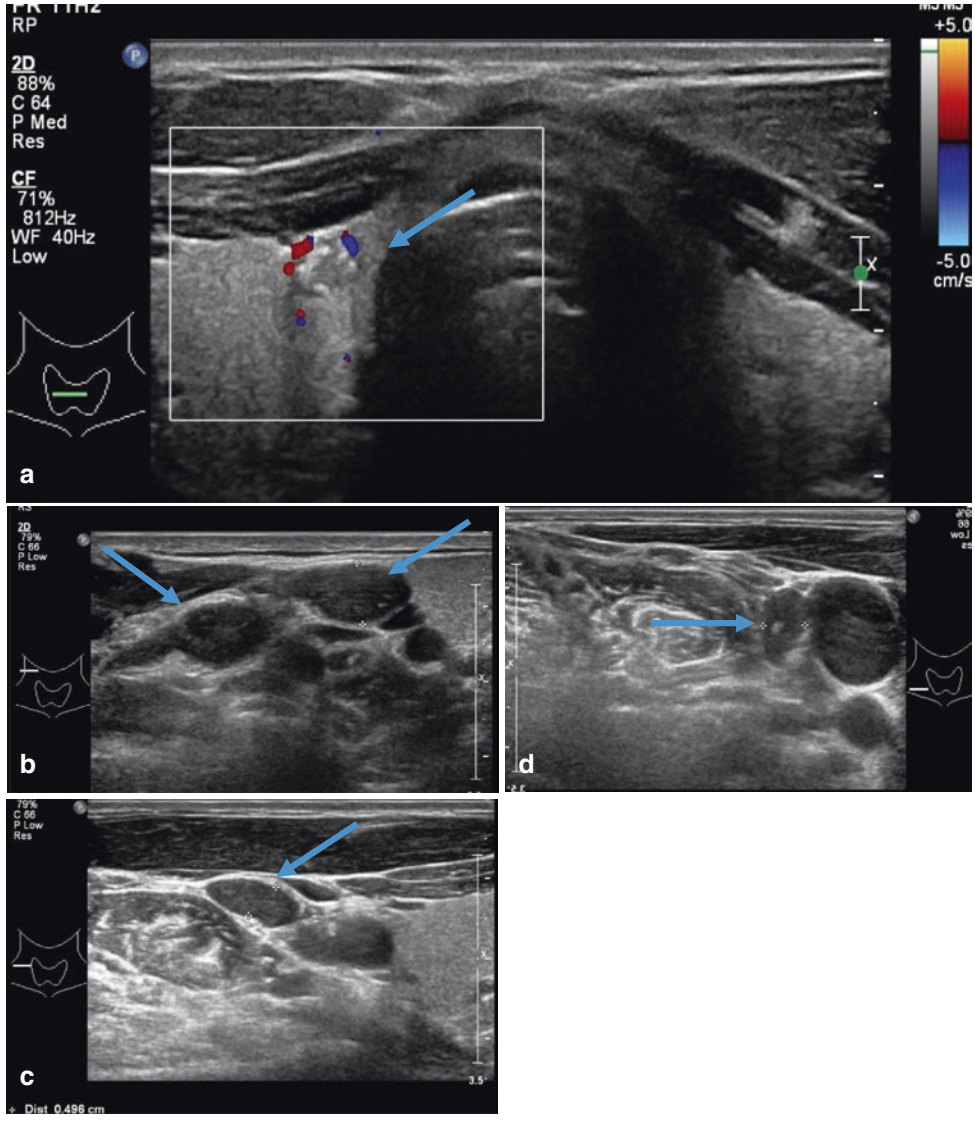

Fig. 19.7 46-year-old patient presented with papillary thyroid cancer in the right thyroid lobe (arrow in **a**). Multiple lymph nodes in the neck from right level II to IV which appears abnormal (**b–d**). These nodes were not metastatic thyroid cancer. On FNAC, these were found to be due to sarcoidosis

19.3.2 Lymph Nodes

Enlarged inflammatory lymph nodes are frequently seen on ultrasound. This may be reactive nodes due to variety of causes (Fig. 19.7).

19.3.3 Malignant Masses

Most frequently found are metastasis from occult primary cancer of head and neck, the commonest is squamous cell carcinoma followed by lymphoma.

If any abnormal mass is found in the neck, ultrasound-guided fine needle aspiration cytology (FNAC) is highly recommended for definitive diagnosis (Fig. 19.8).

19.3.4 Parathyroid Cyst

This is rare. More commonly found in female and can range from 1–6 cm. This is fluid-filled sac that can be located posterior or inferior to the thyroid gland or in the mediastinum. Patient may or may not be symptomatic (Fig. 19.9a, b, c).

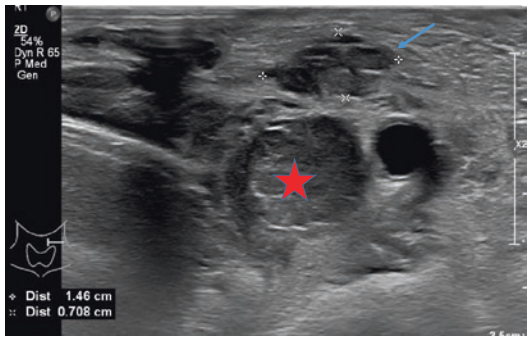

Fig. 19.8 A 54-year-old male found with abnormal node (blue arrow) on US with a solid indeterminate nodule in the left thyroid lobe (red star). On FNAC, the node was found to be a metastatic squamous cell carcinoma (SCC). The "nodule" in the left thyroid was an invasion of SCC into the left thyroid lobe (red star) on FNAC

19.3.5 Parathyroid Adenoma

Parathyroid adenoma can be found in patient who has primary hyperparathyroidism, MEN1 and MEN2a syndromes, and chronic renal failures. On US this appears to be hypoechoic with heterogeneous echotexture, some with cystic degeneration. This may have internal vascularity (to differentiate from a node)—but not always. (Fig. 19.10a, b) The best investigations to confirm a parathyroid adenoma are a combination of Tc99m Sestamibi and US, together with a positive serology of increased calcium level and parathyroid hormone (PTH). US is extremely good for precise localization of the parathyroid adenoma. The advantages of the usage of US for localization are the ease of availability and safety of US, lack of ionizing radiation, patient's comfort, short imaging appointment time, and cost-effective to the patient and the health system. The disadvantages includes operator experience and limitations.

Positioning of the patient is very important when scanning for parathyroid adenoma. At least a pillow or two should be placed underneath the upper body and shoulders of the patient to allow the head to be tilted back and to fully extend the neck. It may not be possible to do this with a patient who suffers from ankylosing spondylosis or if they have neck problems.

Parathyroid adenoma may be located superior or inferior to the thyroid lobe, within the thyroid gland, along the tracheoesophageal groove or intrathoracic, it is important to be able to US the neck by turning the patient's head from side-to-side and by asking the patient to hold their breath or cough.

19.3.6 Parathyroid Carcinoma

This tends to be hypoechoic and tends to be inferior to the thyroid lobe. This can also be found within the thyroid gland. It is indistinguishable from a parathyroid adenoma. It tends to have a thicker capsule.

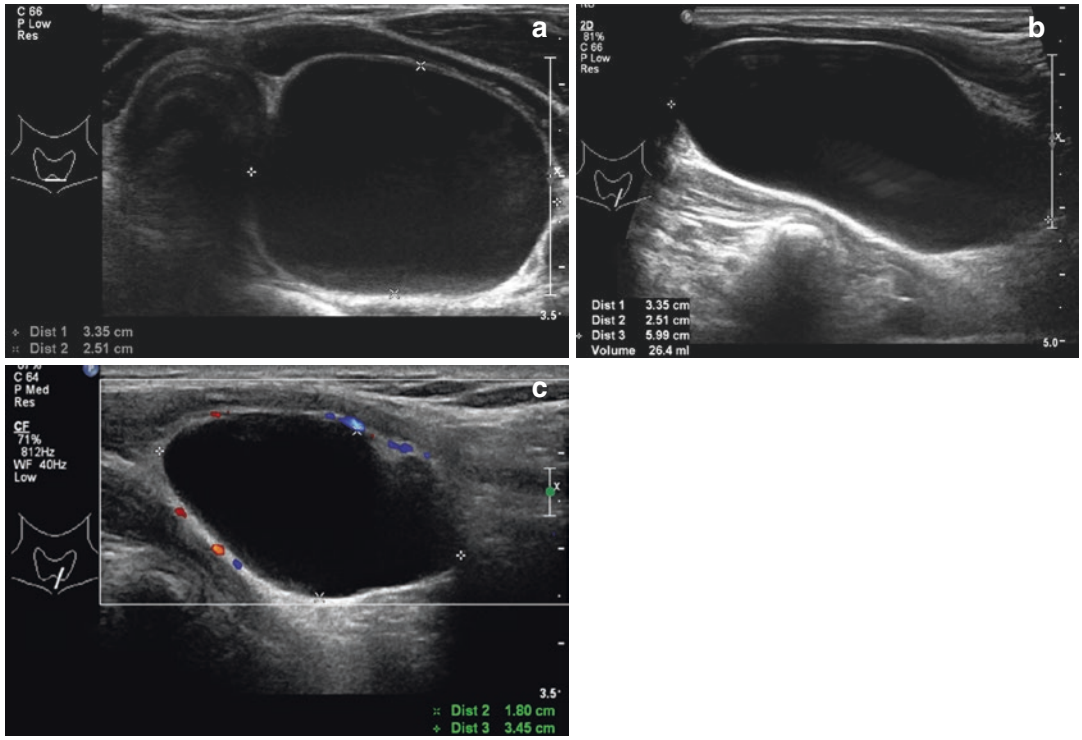

Fig. 19.9 Young male aged 27 presented with incidental finding of a large well-defined anaechoic nodule, inferior to the left thyroid lobe. This lesion presented with post acoustic enhancement and avascular in the inferior level VI/VII. This is likely to be a parathyroid cyst

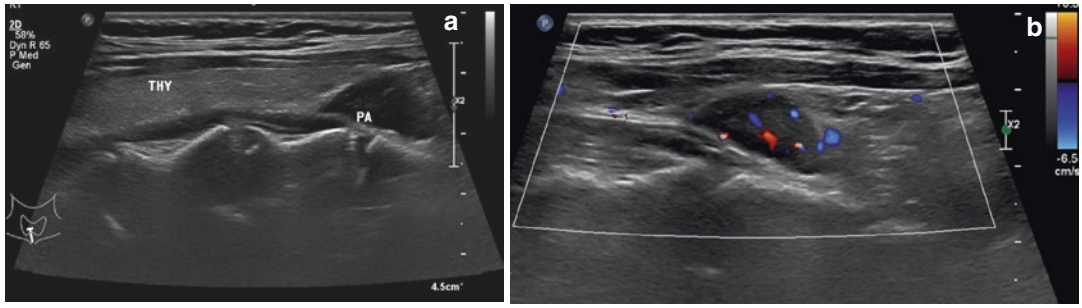

Fig. 19.10 A solid lesion found inferior to the right thyroid lobe (**a**). This has internal vascularity (**b**). This is likely to be a parathyroid adenoma

19.4 Fourth Branchial Cleft Cyst/ Cervical Thymic Cyst

The fourth branchial cleft cysts are very rare. They can form a sinus from the apex of the piriform fossa to the anterior upper pole of the left thyroid lobe. They appear to run parallel to the recurrent laryngeal nerve. 80% of cyst appears on the left (Fig. 19.11).

19.5 Thyroiditis

Chronic autoimmune thyroiditis and Graves' disease are two forms of autoimmune thyroid disease (AITD). Hashimoto thyroiditis and Graves' disease have been commented as being the same autoimmune thyroid disease but at the different end of the spectrum. Their appearance in US are similar. The typical difference is Graves' disease displayed

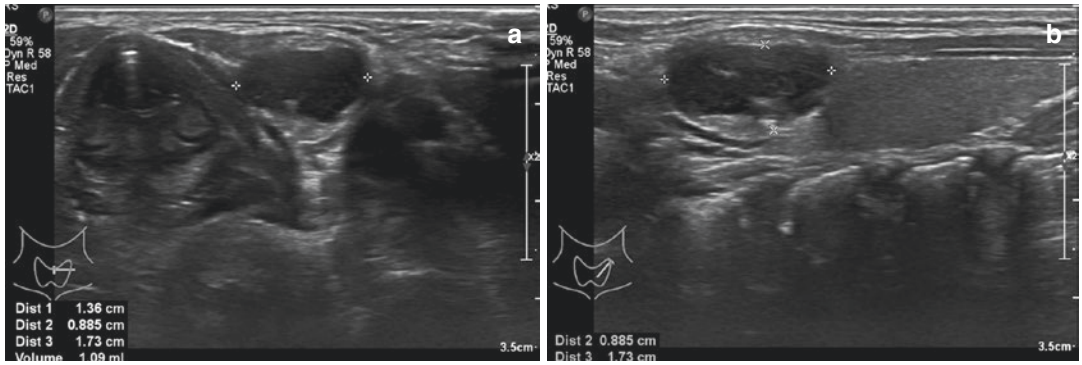

Fig. 19.11 Fourth Branchial cleft cyst: 4-year-old boy presented with a cyst in the superior left thyroid lobe. FNA shows this is a fourth Branchial cleft cyst

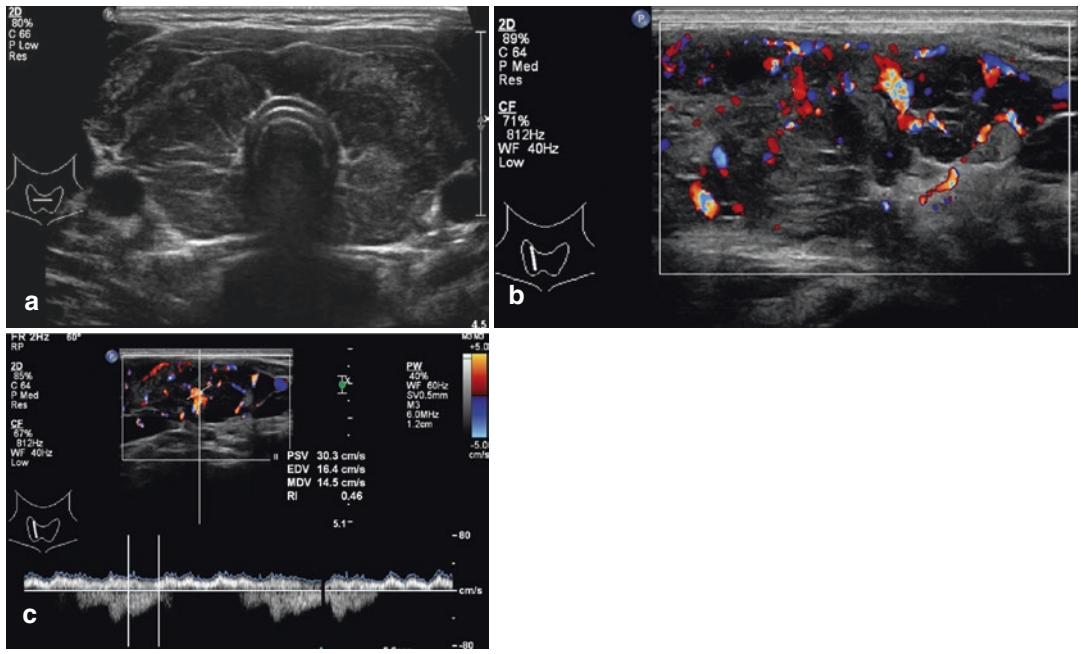

Fig. 19.12 (**a**) An enlarged hypoechoic thyroid gland. The appearance is suggestive of chronic autoimmune thyroiditis—Hashimoto thyroiditis. (**b**) The same thyroid as (**a**), showing hypervascularity throughout the gland. (**c**) Color Doppler with increased peak systolic volume higher than normal but lower than Grave's disease

hypervascularity with power Doppler analysis. The vascularity of Hashimoto thyroiditis is variable and can range from avascular to hypervascular; however, the peak systolic velocity (PSV) tends to be below that of Graves' disease. It has been suggested that if PSV for the superior thyroid artery is >50.5cm/s, this is more likely to be for Graves' disease (Figs. 19.12, 19.13, and 19.14).

19.6 Thyroid Nodules

US is an extremely sensitive imaging modality to detect thyroid nodules which can be as small as 2–3 mm. The prevalence of detecting nodules are 50–60% in comparison to palpation [2] Mazzaferri. There is a steady increased rise in the detection of thyroid nodules due to increased sen-

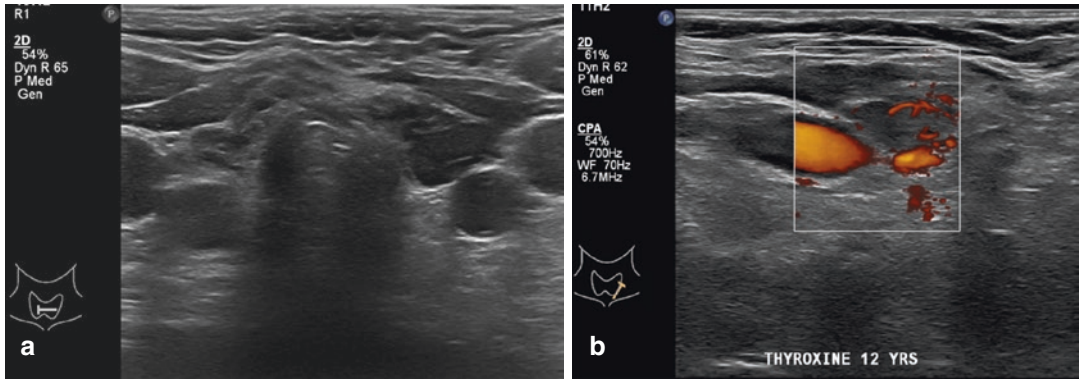

Fig. 19.13 (**a**, **b**) Chronic autoimmune thyroiditis Hashimoto thyroiditis at the end-stage. The thyroid lobe has atrophied. This patient has Hashimoto thyroiditis and has been on thyroxine for 12 years

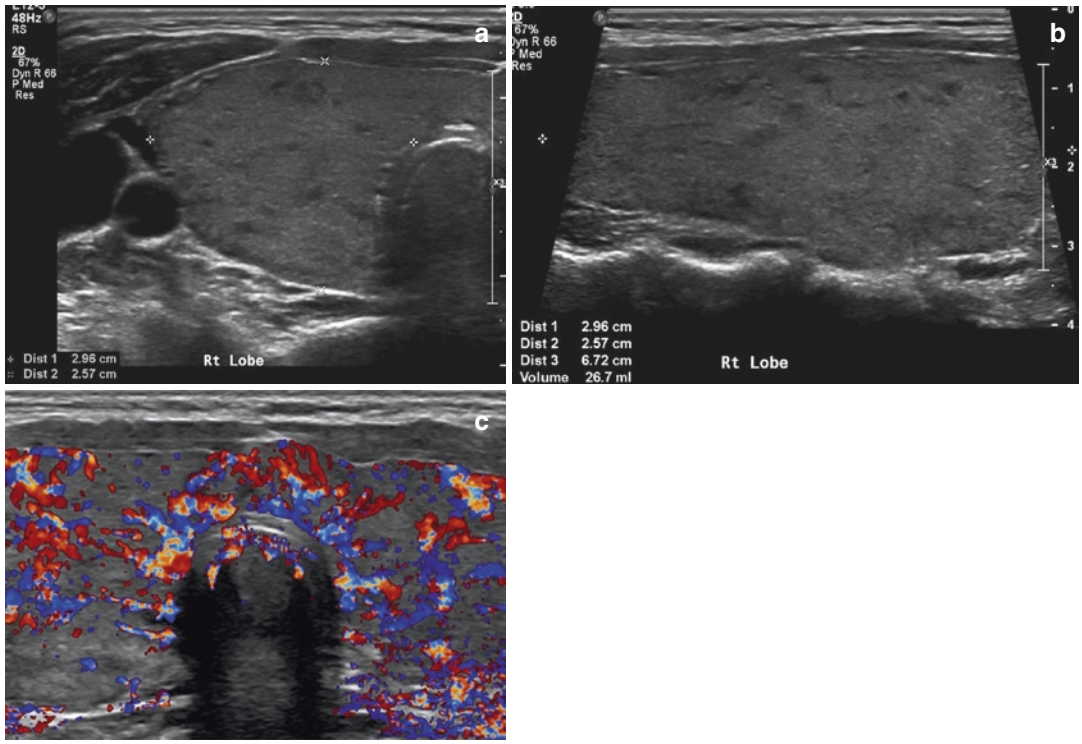

Fig. 19.14 (**a**, **b**, **c**) Graves' disease: 33-year-old female with enlarged thyroid gland throughout with mild heterogeneous echotexture changes and with hypervascularity throughout the lobe (**c**). Courtesy of Dr. Paul Carroll, Consultant Endocrinologist UK

sitivity of our imaging modalities since 1980s with widespread use of US, and in 1990s with increased use of CT and MRI. More sub centimeter nodules are being detected and investigated; however, the mortality from thyroid cancer has not changed since 1980s. It is very important to be able to characterize and recognize a benign thyroid nodule from a malignant nodule. There are several thyroid guidelines produced by eminent thyroid associations around the world and readers are recommended to consult them. As more US studies are being published, certain US features and characteristics have been proven to be helpful in differentiating a malignant nodule

from a benign one. With this, come several risk stratifications purposed by various thyroid associations.

19.7 US Characteristics of Thyroid Nodules: What to Look for and What to Include in Our US Thyroid Report

1. **Size**: Measurement of volume of a nodule is as described in Fig. 19.3. Recording the size helps us to monitor the growth rate of the nodule as well as staging the nodule.
2. **Outline of the nodule**: can be described as well-defined (Figs. 19.9 and 19.11), diffuse, irregular and ill-defined margin (Fig. 19.16a), microlobulated/lobulated (Fig. 19.16b), or spiculated (Fig. 19.15a). High risks nodule tend to have a diffuse, irregular, ill-defined, microlobulated, or spiculated margin.
3. **Echogenicity**: this relates to the brightness of the nodule in comparison to the normal thyroid parenchyma. A normal thyroid parenchyma is similar to a normal parotid gland and appears brighter in comparison to the adjacent strap muscles.

   A nodule that is solid can be characterized as hypo-, iso, and hyperechoic.

   Hypoechoic nodule is a nodule that is slightly darker in comparison to the rest of the thyroid parenchyma as can be seen in Figs. 19.16b and 19.17.

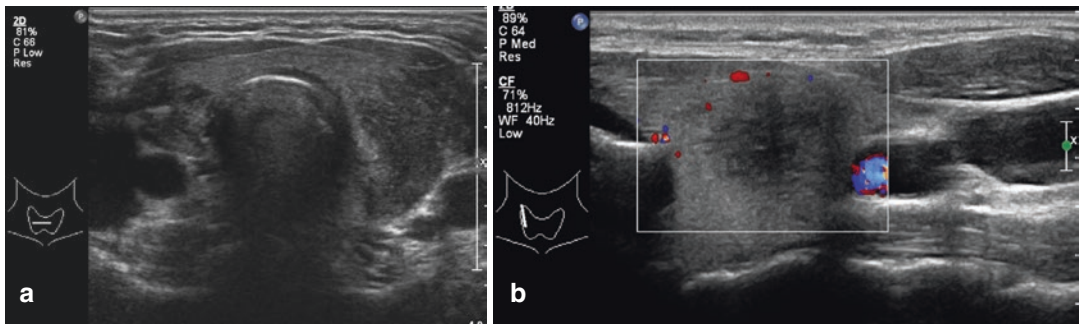

Fig. 19.15 (**a**) and (**b**) Subacute thyroiditis-De Quervain's thyroiditis. A 40-year-old female patient presented with severe pain in the right neck. She developed further pain in the left neck 2 months later. Prior to this, she had flu-like symptoms. US shows hyperechoic changes with irregular margins in both the right and left lobes. Spiculated margin can be seen in the left lobe. There are no hypervascularity within the gland. These area completely resolves 9 months later

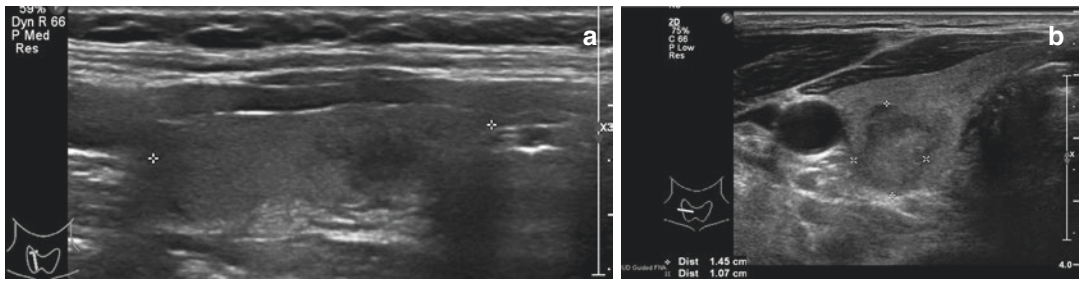

Fig. 19.16 (**a**) Diffused, irregular, ill-defined nodule. (**b**) An abnormal shape, hypoechoic solid nodule that appears to have a lobulated margin. It also displayed tall rather than wide features. On FNAC, this was proven to be papillary thyroid cancer

4. A cystic nodule may be anechoic. This means there are no internal features. This allows through the transmission of sound waves and presented with posterior acoustic enhancement. True cysts over 1.5 and 2 cm are rare, represent <2% of all lesions. These tend to be benign [3].

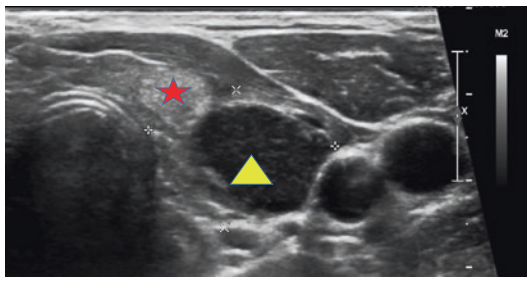

Fig. 19.17 There are two nodules seen in the left thyroid lobe. In the left isthmus, nodule shown here with the red star is brighter than the surrounding parenchyma. This is called hyperechoic echotexture. The larger nodule noted by the yellow triangle is much darker than the strap muscles. This appearance of the nodule is known as "marked hypoechoic" echotexture

Often cystic nodule may contain very bright foci with "comet tail reverberation." These artifacts may be due to sound wave interaction with condensed colloid protein [4] (Fig. 19.18).

Complex nodules may be found which have predominantly cystic but may have a varying amount of solid component within. This may be due to degeneration or hemorrhage. It is important to US and analyze the solid tissue to ensure there are no suspicious features (Fig. 19.9).

5. "Spongiform"/"honeycomb" nodules: these are mixed echogenicity nodules with minute <5 mm cystic areas separated by thin septation mixed within solid tissue. These nodules tend to be benign and the nodule is often found in benign hyperplastic nodule [5].

Important to differentiate from a complex nodule with discrete cystic areas which is iso or hyperechoic as this may be a true neoplastic growth of either follicular or Hürthle cell. This would need histology to discriminate

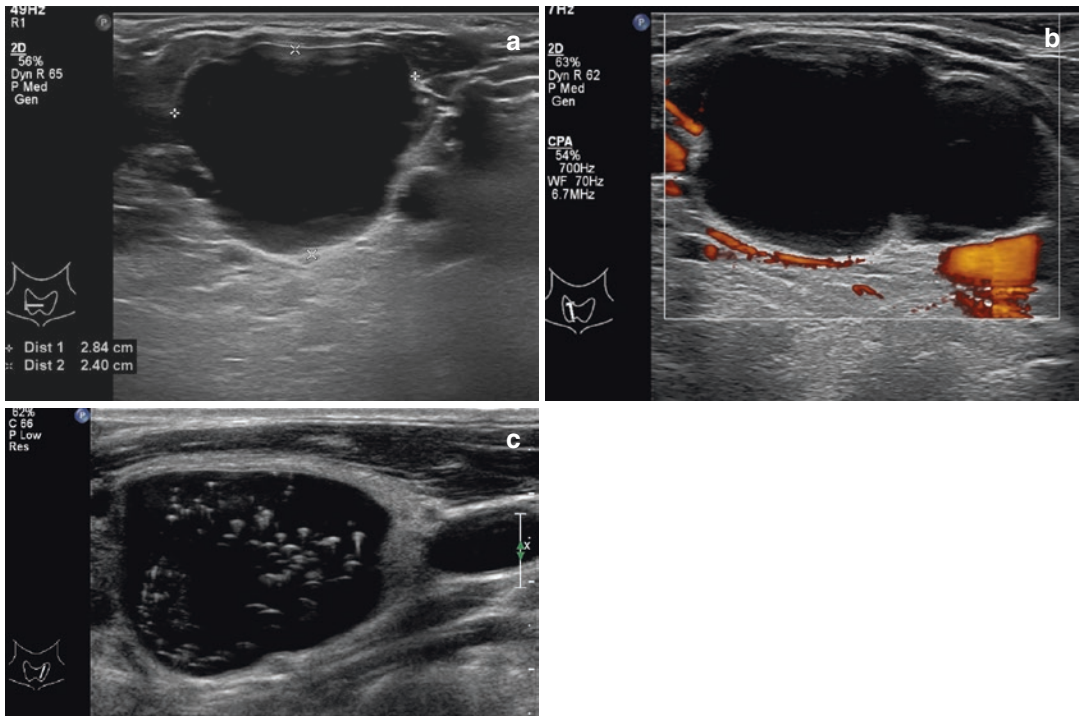

Fig. 19.18 (**a**) This is a large cyst which is nearly 90% pure cyst with post acoustic enhancement and is avascular (**b**). It has very small debris which accounts for 10%. On aspiration, dark-stained fluid obtained indicates a thyroid hemorrhagic cyst. (**c**) Colloid cyst. A well-defined hypoechoic cystic nodule with numerous hyperechoic structures within the cyst with a "comet tail reverberation". These are colloids and are known to be benign

between benign and malignant. Complex nodules harbored 3% risk of malignancy (Fig. 19.19) [3].

6. Calcifications: This can be divided into three types.
   (a) Microcalcification–smaller than 1 mm. It has echogenic foci without post acoustic shadowing (Fig 19.20a). This tends to be associated with thyroid cancer. The calcification is thought to be aggregates of psammoma bodies, a spherical concretions characteristic of most papillary cancers but also found in benign nodules and Hashimotos' thyroiditis [6]. Microcalcifications has a sensitivity of 40% and specificity of 90% of malignancy [7].
   (b) Coarse/dense/dystrophic/macro calcifications are larger than 2 mm and produce posterior acoustic shadowing (Fig 19.20b). These are presented in areas of fibrosis and tissue degeneration and necrosis. These calcifications if presented in the center of a hypoechoic nodule tend to be a concern for malignancy [3, 8].
   (c) Peripheral or egg-shell calcification. A complete rim calcification is thought to be benign (Fig. 19.20c). An incomplete rim calcification with herniation of tissue is suspicious of cancer invasion.
7. Halo: a sonographic hypoechoic lucent rim surrounding the nodule which is thought to be compressed blood vessels as the nodule increases in size. This can be found in half of the benign nodule but less common in thyroid cancer.

   When the halo is irregularly thickened and avascular this may represent a fibrous capsule surrounding a neoplastic nodule, e.g., follicular or Hürthle cell (Figs. 19.19a, b, 19.21).
8. Vascularity: Color flow Doppler can help to detect the vascularity within the nodule. This can be characterized into three types (Fig. 19.22):

   Type I: absent of any vascularity.

   Type II: Perinodular vascularity around the nodule.

   Type III: Perinodular and intranodular vascularity.

   Power Doppler (PD) is more sensitive for detection of flow in small vessels that would not be detected by color flow Doppler (CFD) and is independent of the angle of the probe, sound beam, and noise. Recommend that this should be used more than CFD for assessing thyroid vascularity.
9. Shape of the nodule: the shape of the nodule optimizes exposure of the tumor cells to receive nutrient. Oval shape defined as long to short axis ratio of >2.5 were found to be benign [9], as seen in Fig. 19.21.

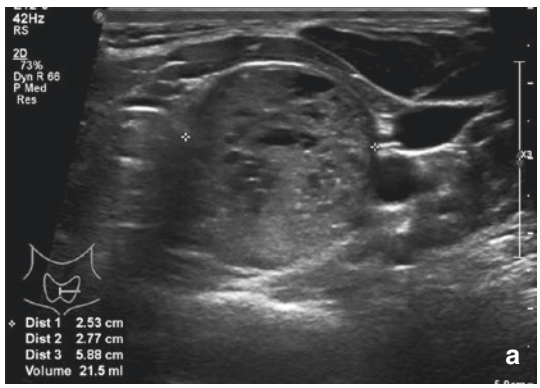

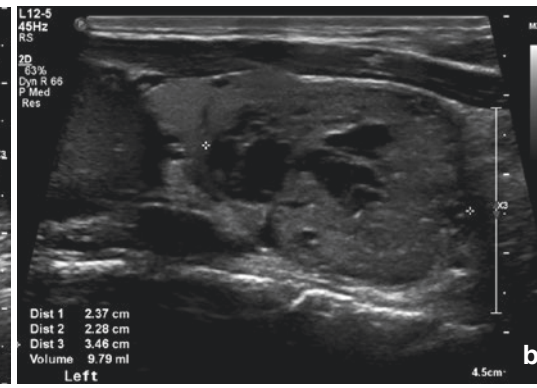

Fig. 19.19 (**a**, **b**) A large complex cyst with spongiform area with some discrete cystic and semisolid area within the nodule with numerous comet tail reverberation within. This was found in a 14-year-old boy. Due to the size, this was confirmed on FNAC to be benign and consists of colloid

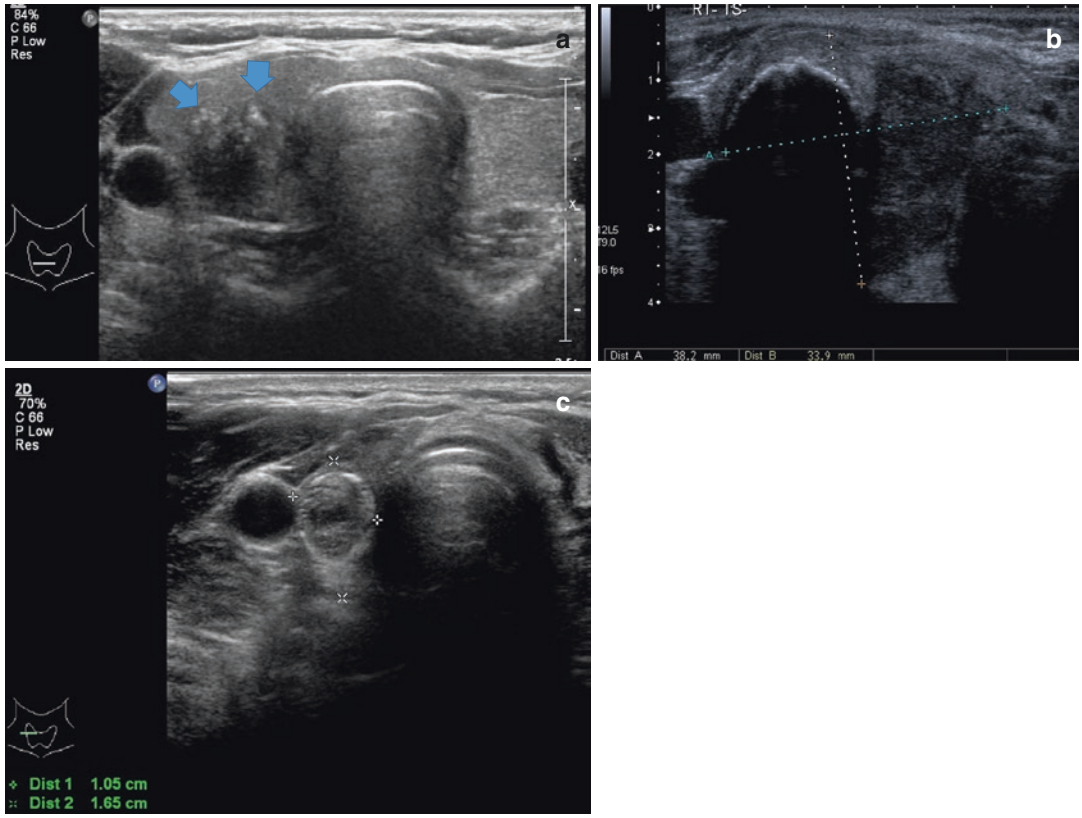

Fig. 19.20 (**a**) A marked hypoechoic ill defined nodule within the right lobe of thyroid with numerous microcalcifications were noted within the lobulated superior border showing a high risk nodule. On FNAC this was proven to be a papillary thyroid carcinoma. (**b**) Dystrophic calcification: A large dystrophic calcification of nearly 2 cm with post acoustic shadowing. It was noted adjacent to a solid marked hypoechoic nodule with tall rather than wide feature and irregular margin. This part of the nodule was suspicious. On FNA this was an anaplastic carcinoma. (**c**) Well-defined complete peripheral rim calcification with no tissue herniation is thought to be benign

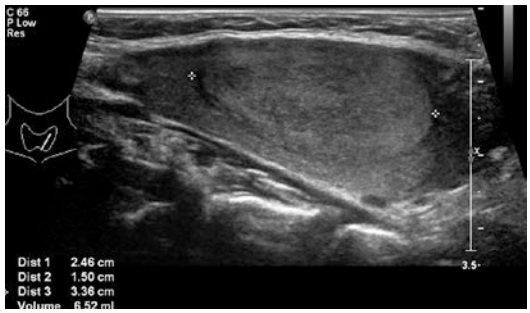

Fig. 19.21 Sonographic rim or a well-defined, uniform hypoechoic width surrounding an oval-shaped nodule

Taller rather than wide: Anterior-posterior measurement to transverse diameter (A/T > = 1) or if this is seen in the longitudinal section. It has higher sensitivity (84%) and specificity (82%) for the detection of cancer (Fig 19.16b).

10. Elastography: it is a noninvasive technique of evaluating thyroid nodules. This can be used to estimate tissue stiffness of the nodule. It is deemed that malignant tissue tends to be associated with increased stiffness. This may be a helpful tool for indeterminate nodule however it does not conclusively discriminate a benign from a malignant nodule. It uses supersonic shear wave imaging and acoustic radiation force impulse with real-time tissue elastography. There are two types currently in use: shear wave and strain elastography (Fig. 19.23).

11. **Extrathyroidal extension**: This can be seen with invasion of the surrounding structures,

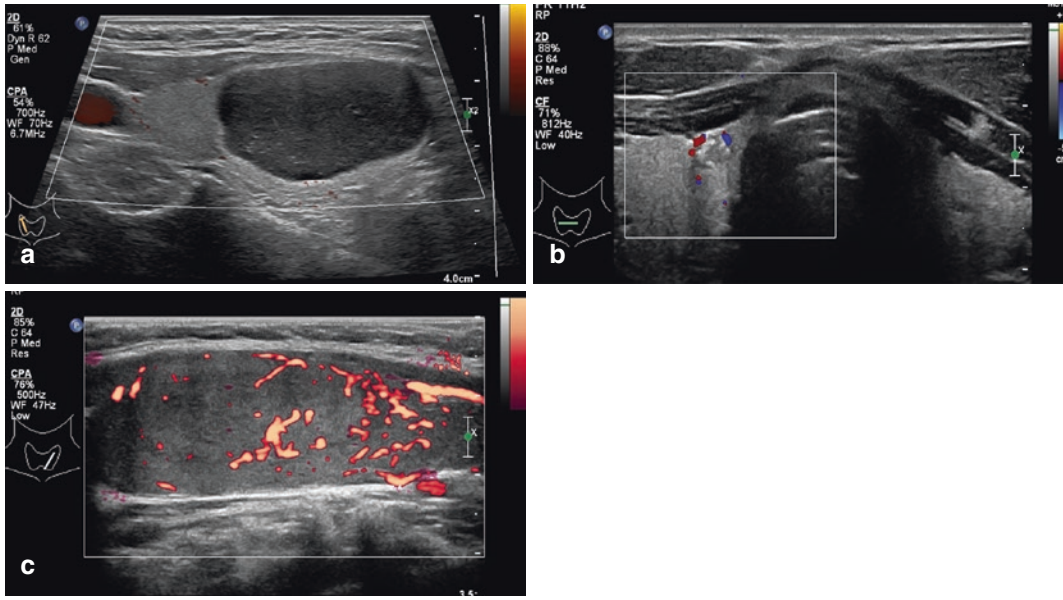

Fig. 19.22 (**a**) Type I vascularity: Absence of any vascularity. (**b**) Type II vascularity: Perinodular vascularity. (**c**) This is the same patient as Fig. 19.21, showing a nodule with Type III vascularity both perinodular and intranodular vascularity

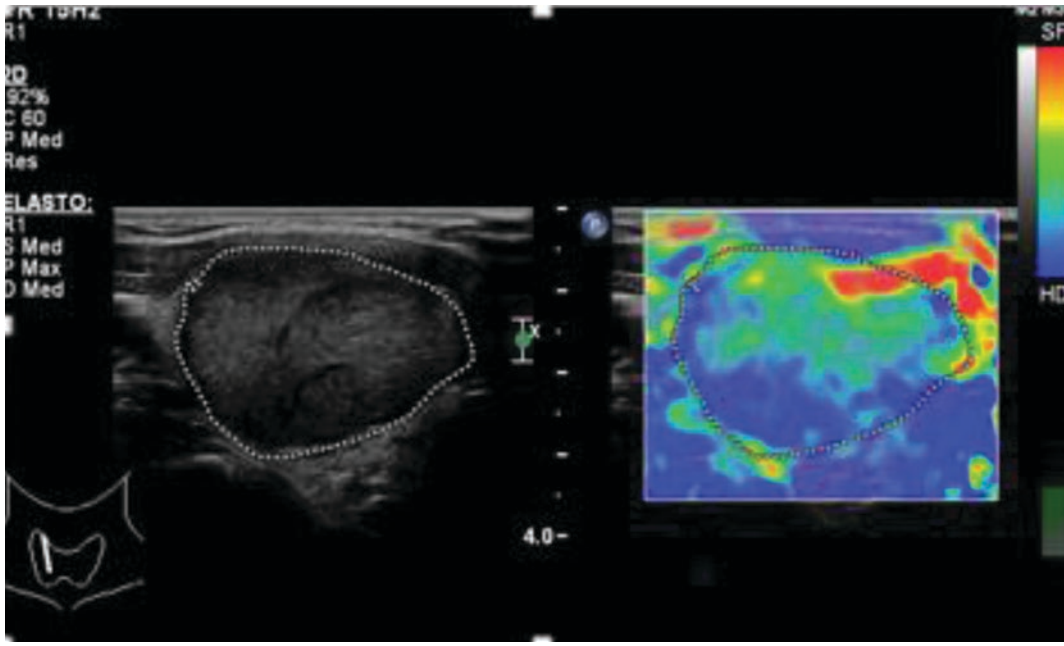

Fig. 19.23 Elastography: This is a visual scale shear wave elastography showing an indeterminate stiffness overall. On FNAC this nodule was shown to be an anaplastic carcinoma

e.g., strap/longus colli muscles or the trachea (Fig. 19.24).

12. **Size of the nodule**: A reasonable yearly growth of a nodule is considered as 20% increase of 2 of the 3-nodule measurement of at least 2 mm. This would mean a resulting at least 44% of the nodule volume is acceptable. This was proposed by America Thyroid Association ATA. Refer to the case in Fig. 19.30 and 19.31.

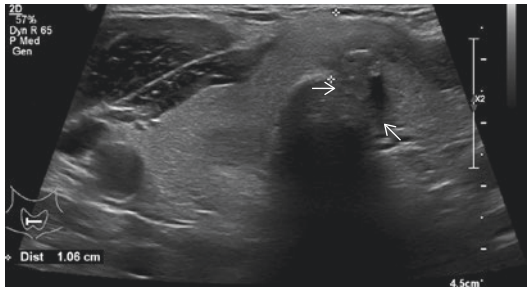

Fig. 19.24 A suspicious left isthmus nodule showing extracapsular spread with a trachea invasion (shown here with the arrows)

13. **Lymph nodes:** the presence of abnormal nodes with similar features to the thyroid nodule are highly suspicious of metastasis. Some can be found even when the lesion in the thyroid is missed or very ill-defined. Refer to Figs. 19.25 and 19.26.

Below are several interesting cases (Figs. 19.27, 19.28, 19.29, 19.30, 19.31, and 19.32):

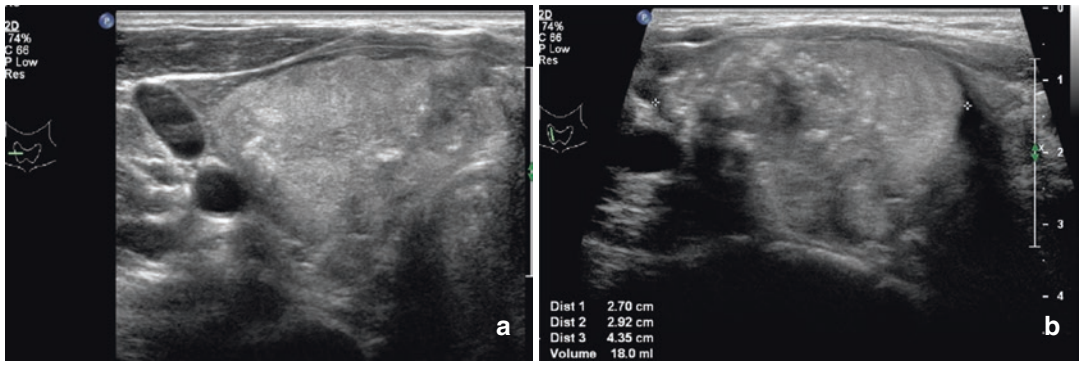

Fig. 19.25 (**a**, **b**) A young 28-year-old pregnant woman presented with lumps in her neck. Ill-defined lesion in the right lobe of thyroid in the transverse and longitudinal views. Multiple punctate and dystrophic calcifications detected in this very ill defined lesion

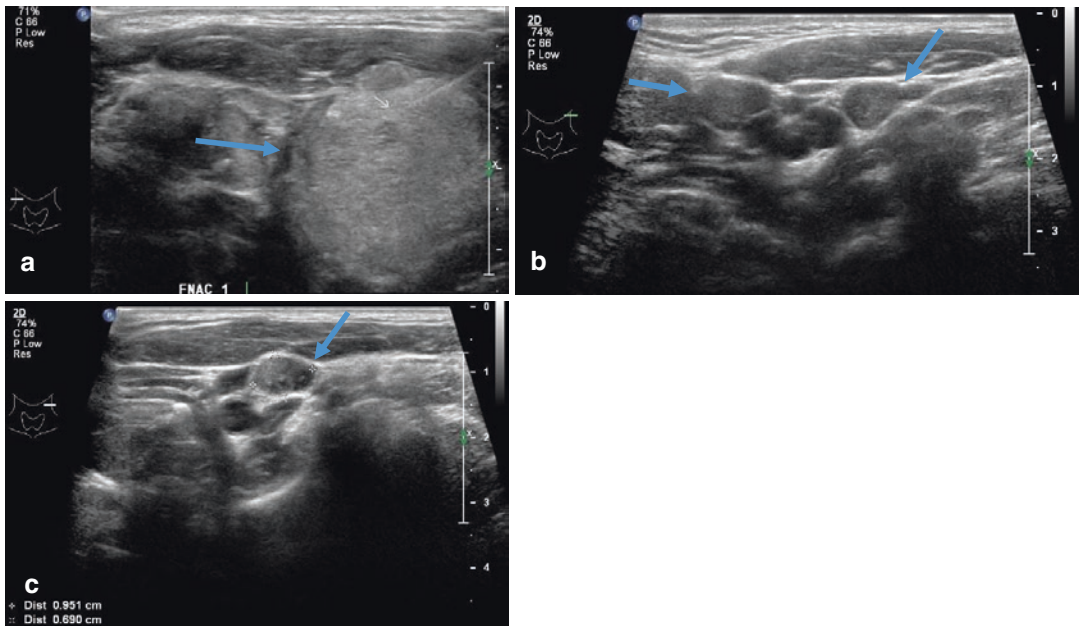

Fig. 19.26 (**a–c**) Same patient as Fig. 19.25, presented with abnormal metastatic nodes (blue arrows) in right L2 (FNA needle shown in **a**), left L2 (**b**), and Left L3 (**c**). FNA confirmed multifocal papillary thyroid cancer with metastatic nodes to bilateral neck

There is not a single sonographic feature that can positively identify all malignant nodules. Risks stratification, using a combination of several of the above appearances, has been used by various thyroid guidelines around the world to attempt to predict malignancy and benignity. Using both US features and FNA is the only way to validate the diagnosis of a nodule. Nodules that are deemed to indeterminate or suspicious of malignancy should be FNA for diagnosis. Any rapidly growing nodule is suspicious until proven otherwise. Where there is discrepancy between US features and cytology, repeating US FNA or US surveillance is vital. It is also important to take into account any patient risk factors, e.g., genetic predisposition, radiation exposure, and family history.

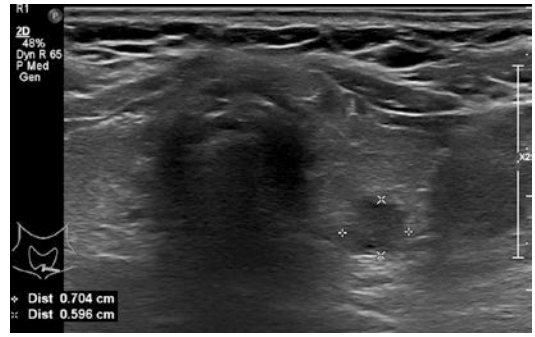

Fig. 19.28 An irregular, hypoechoic nodule in the left thyroid. On FNA, this is a renal metastasis to the left thyroid lobe

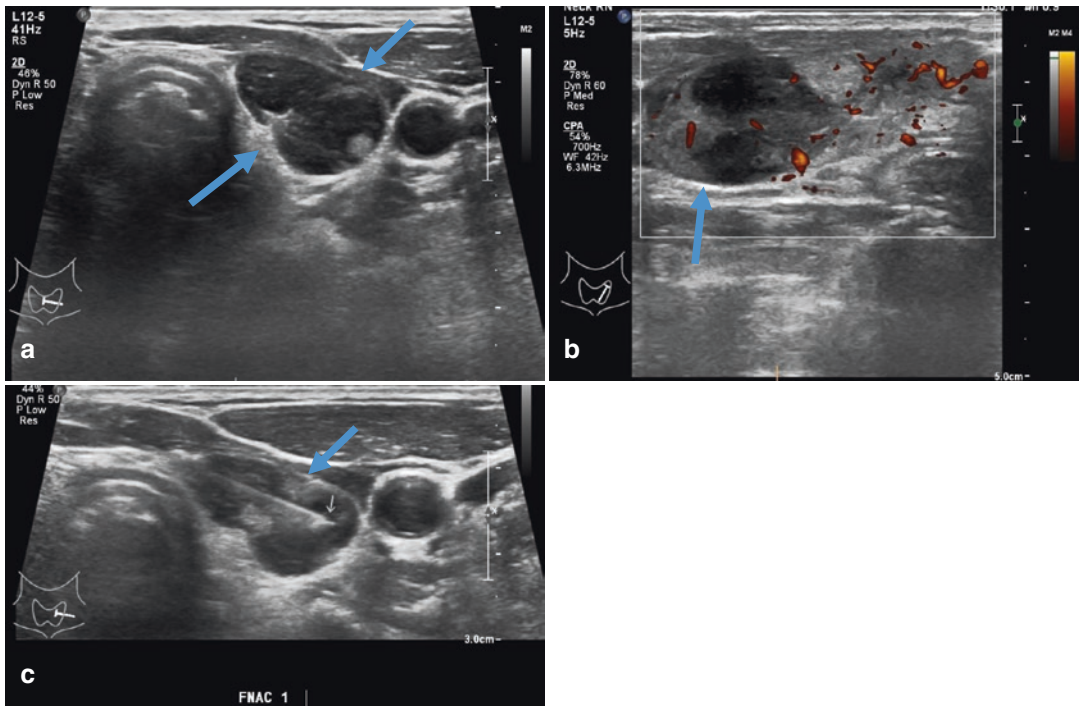

Fig. 19.27 (**a–c**) A 59-year-old male with marked hypoechoic nodule in the left thyroid (**a**). It has type I vascularity (**b**). FNA performed to the left lobe as shown in (**c**). Cytology confirmed this is lymphoma in the left thyroid lobe

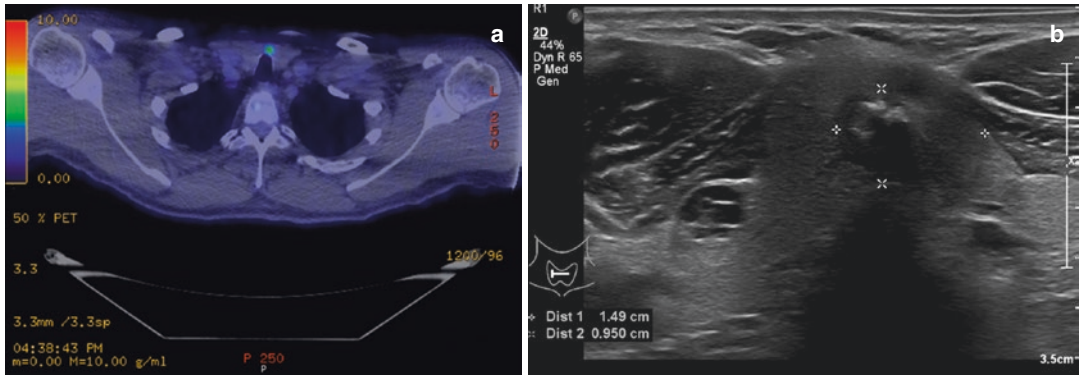

Fig. 19.29 (**a**) CT-PET avid thyroid nodule has a positive predictive value of 34.8–41.7% of malignancy. SUVmax of 6.9 for malignancy [10–12]. Every PET avid nodule should have a US assessment and FNA for diagnosis. A thyroid nodule was detected in the isthmus on US of the same patient. (**b**) This was proven to be papillary thyroid cancer on FNAC

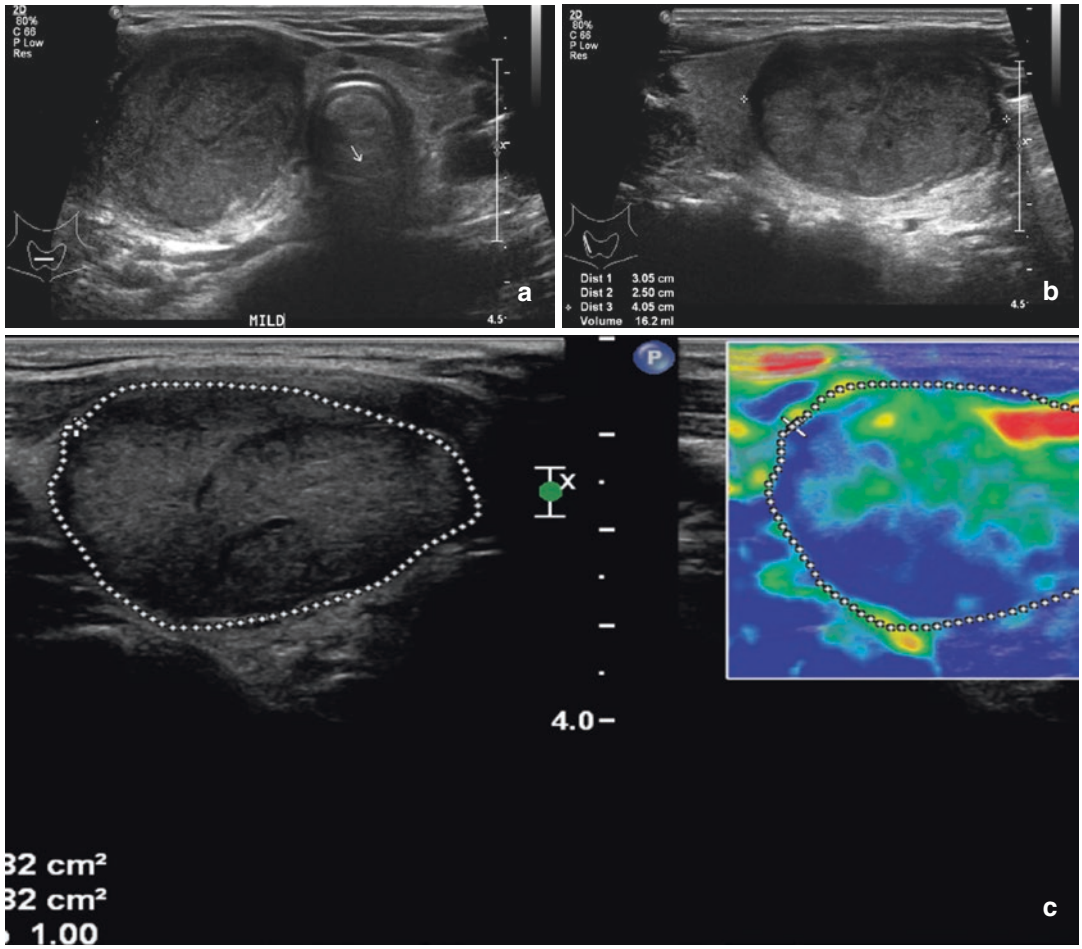

Fig. 19.30 (**a–c**) 36-year-old female presented with an indeterminate nodule, They 3f nodule, a follicular neoplasm cannot be excluded in the right lobe with mild trachea deviation in 2015 (**a**). It is hypoechoic and well-defined measuring up to 4.1 cm (**b**). It has indeterminate stiffness on elastography

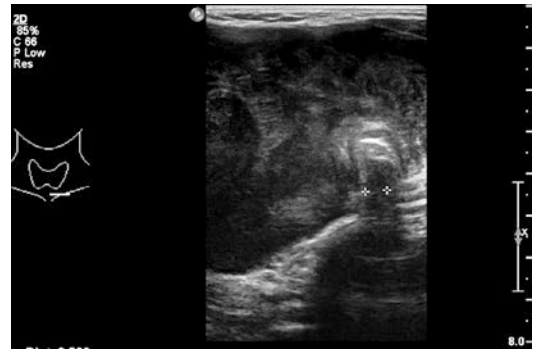

Fig. 19.31 The same patient as seen in Fig. 19.30, by 2018, the nodule in the right thyroid has suddenly grown rapidly. The full extend of the thyroid gland is no longer possible to be visualized on US. It was >8 cm and causes trachea narrowing (calipers). On core biopsy, the nodule has differentiated into an anaplastic carcinoma. It is vital to have an active surveillance on a patient who refuses surgery to avoid a tragic outcome as happened in this patient

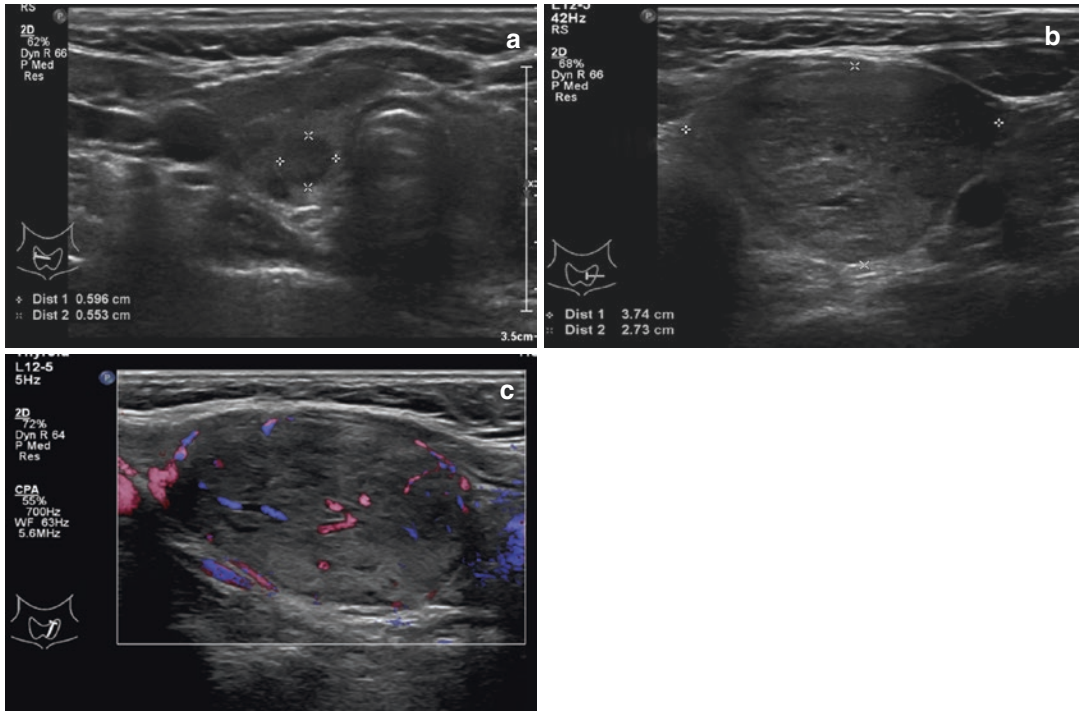

Fig. 19.32 (**a–c**) Several nodules with indeterminate features seen in both lobes of the thyroid (**a**, **b**) and type 3 vascularity in 3.7 cm nodule in the left lobe. This was seen in an 11-year-old patient. He was later tested for Cowden's syndrome. Cowden's syndrome is an autosomal dominant characterized by benign overgrowth hamartomas which can be developed into benign and malignant tumors. It commonly affects breast, uterus, thyroid, gastrointestinal tract, and skin. In the oral cavity, this can cause fibro-epithelial polyps, nodular gingival hyperplasia, high-arched palate, fissure and lobulated tongue, rampant caries, periodontal disease, and squamous cell carcinoma. Cowden's syndrome patients are at an increased risk of approximately 20% of developing differentiated thyroid carcinoma and have a younger age of onset [13]

References

1. Jack Baskin H, et al. Thyroid ultrasound and ultrasound-guided FNA. 2nd ed. New York: Springer; 2008.
2. Mazzaferri EL. Management of a solitary thyroid nodule. N Engl J Med. 1993;328(8):553–9.
3. Frates MC, et al. Prevalence and distribution of carcinoma in patients with solitary and multiple thyroid nodules on sonography. J Clin Endocrinol Metab. 2006;91(9):3411–7.
4. Ahuja A, et al. Clinical significance of the comet-tail artifact in thyroid ultrasound. J Clin Ultrasound. 1996;24(3):129–33.
5. Bonavita John A, et al. Pattern recognition of benign nodules at ultrasound of the thyroid: which nodules can be left alone? Am J Roentgenol. 2009;193(1):207–13.
6. Taki S, Terahata S, Yamashita R, et al. Thyroid calcification s: sonographic patterns and incidence of cancer. Clin Imag. 2004;28(5):368–71.
7. Hoang J, et al. US features of thyroid malignancy: pearls and pitfalls. Radiographics. 2007;27:847–65.
8. Reading CC, et al. Sonography of thyroid nodules: a "classic pattern" diagnostic approach. Ultrasound Q. 2005;21(3):157–65.
9. Alexander EK, et al. Thyroid nodule shape and prediction of malignancy. Thyroid. 2004;14(11):953–8.
10. Chun AR, et al. Risks of malignancy in thyroid incidentalomas identified by FDG-PET. Endocrinol Metab (Seoul). 2015;30(1):71–7.
11. Soelberg KK, et al. Risk of malignancy in thyroid incidentalomas detected by FDG-PET: a systematic review. Thyroid. 2012;22(9):918–25.
12. Agrawal K, Weaver J, Ngu R, Krishnamurthy Mohan H. Clinical significance of patterns of incidental thyroid uptake at (18)F-FDG PET/CT. Clin Radiol. 2015;70:536–43.
13. Yamashita et al. Occurrence and natural history of thyroid cancer in patients with Cowden syndrome. Eur Thyroid J 2020;9(5):243–46.

Recommended Reading List

14. Jack Baskin H, et al. Thyroid ultrasound and ultrasound-guided FNA. 2nd ed. New York: Springer; 2008.
15. Ahuja AT. Diagnostic ultrasound head and neck. 2nd ed. New York: Elsevier; 2019.
16. American thyroid association guidelines: Thyroid nodules and differentiated thyroid cancer guidelines 2015.
17. Russ G, et al. European thyroid association guidelines for ultrasound malignant risk stratification of thyroid nodules in adults: The EU-TIRADS. Eur Thyroid J. 2017;6(5):225–37.
18. The Revised 2016 Korean Thyroid Association Guidelines for Thyroid Nodules and Cancers.

Intervention with US

20

Rose Ngu

Contents

US-guided procedures are extremely helpful in many areas. It helps to identify anatomy and it can help to guide in several situations, e.g.

1. Locating a fragment of the foreign body for surgical removal, e.g., fish bone in the oral mucosa, fragment tooth that embedded in the lips, wood splinter in soft tissue.
2. Botox/steroid injection into the salivary gland or any soft tissue safely.
3. Identify small recurrence or metastatic lymph nodes for removal.
4. Abscess drainage.
5. Fine needle aspiration cytology (FNAC).
6. Core biopsy.
7. Basket retrieval of a stone from a salivary duct.
8. Balloon ductoplasty of a salivary duct.
9. Steroid injection.
10. Guidance aid during a sialoendoscopy of a salivary duct.

20.1 US-Guided Fine Needle Aspiration Cytology (FNAC)

US is extremely helpful to guide a needle into a lump in the head and neck area for cell aspiration or drainage of a fluid collection. Understanding the anatomy is vital as to the structures in the surrounding area to avoid complications. It is important to have a sterile technique to avoid infection.

The FNA tray preparation is as shown below Fig. 20.1 on sterile sheet.

The equipment that is needed depends on the lump and the site of the lump. The needles that are used are normally nonsafety needles. This allow for easy handling when performing the FNAC pro-

R. Ngu (✉)
Department of Dental Maxillofacial Imaging; Head Neck and Thyroid Imaging, Department of Radiology, Guy's and St Thomas' Hospitals NHS Foundation Trust, London, UK

King's College London Dental Institute, London, UK
e-mail: rose.ngu@kcl.ac.uk

K. Orhan (ed.), *Ultrasonography in Dentomaxillofacial Diagnostics*,
https://doi.org/10.1007/978-3-030-62179-7_20

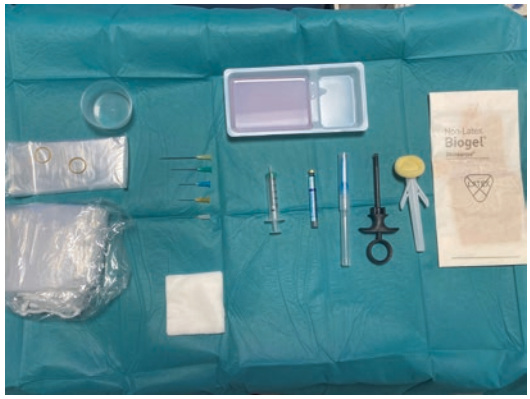

Fig. 20.1 FNAC tray: from top left clockwise: small sterile pot to receive the needle, tray with chlorohexidine solution, sterile surgical glove, chlorohexidine 3% prep stick, syringe handle, disposable local anesthetic applicator 27G needle tip, 22G spinal needle, 27G needle on a 5 ml syringe, gauze, Lignospan@ - a dental local anesthetic cartridge, sterile probe cover and rubber bands. All these have been placed on a sterile green sheet cover

cedure, slide preparation and also for needle washing in a stadardised specimen pot. The needle sizes range from 19G to 27G. Some of the needle sizes are shown in Fig. 20.2. For majority of the lumps, a 27G and 25G needles are recommended for FNAC. If the lesion is very deep, the spinal needle is useful as it is one of the longest needle available.

Patient Preparation:

1. Prior to FNAC or core biopsy, it is very important to know the patient's medical history and if there are any contraindication factors to the patient having a FNAC, e.g., bleeding disorder, anticoagulation medication, e.g., warfarin, heparin, rivaroxaban, etc., steroid medication and any drug allergies.
2. Patient's consent: In the UK, it is vital to have a patient's consent for any intervention procedure. Depending on your local hospital policy, this may be verbal or written consent. Patient should be informed of the expected risks and complications that may arise from the procedure. This includes pain, swelling, bruising, bleeding, possible damage to the nerve giving rise to nerve palsy, infection, abscess/tumor tracking through the needle track, scar formation and non diagnostic sampling. In any patient who has a history of keloid scar formation or whom form scar easily, a skin incision should be avoided where possible eg during the insertion of a core biopsy needle.
3. Prior to inserting the needle, it is very important to wipe the skin of any US gel contamination. As this can cause artifacts on the slide. It is also important to disinfect the skin with an antiseptic solution. During the FNAC, instead of the US gel, chlorhexidine solution can be used as a lubricant (Figs. 20.3 and 20.4). Skin that has not been cleaned or usage of non sterile needle may cause abscess formation.
4. There are two techniques for US-guided FNAC: (1) Using parallel technique or (2) perpendicular technique (Figs. 20.5, 20.6, and 20.7). These images have been taken from [1].

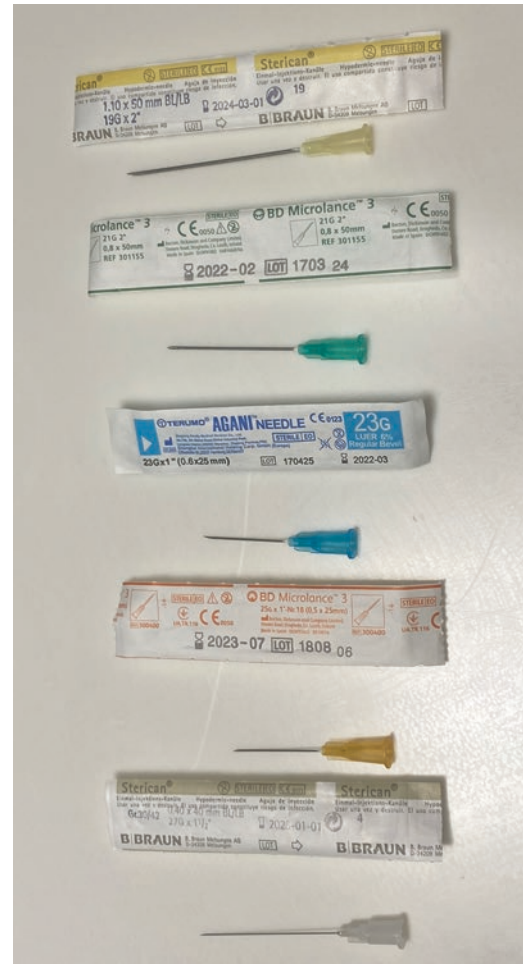

Fig. 20.2 Variety of diameter (19–27G) needles can be used with variety of length size (25–50mm). From top row: 19G (white needle), 21G (green needle), 23G (blue needle), 25G (orange needle), and 27G (white needle)

Fig. 20.3 US machine and patient positioning are very important. It is vital to have a direct vision with the US screen when performing an intervention procedure. This photo shows a US FNA procedure of a lump in the soft palate using a hockey stick probe. This was taken during COVID pandemic in 2020 in which the operator is wearing a full personnel protection gear with an FFP3 mask, full-face visor, sterile probe cover and sterile gloves. On completion of the procedure, a full wipe down to disinfect the US machine and probe were performed

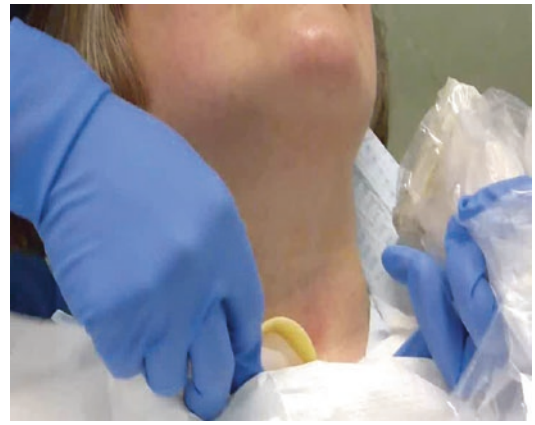

Fig. 20.4 Cleaning the skin for the site of FNA with antiseptic 3% chlorhexidine stick

FNAC can be performed without local anesthetic if the needles is fine and the patient is willing. It is also dependant on the operation skill and experience. It is important for the patient to be comfortable and where several passes are deemed

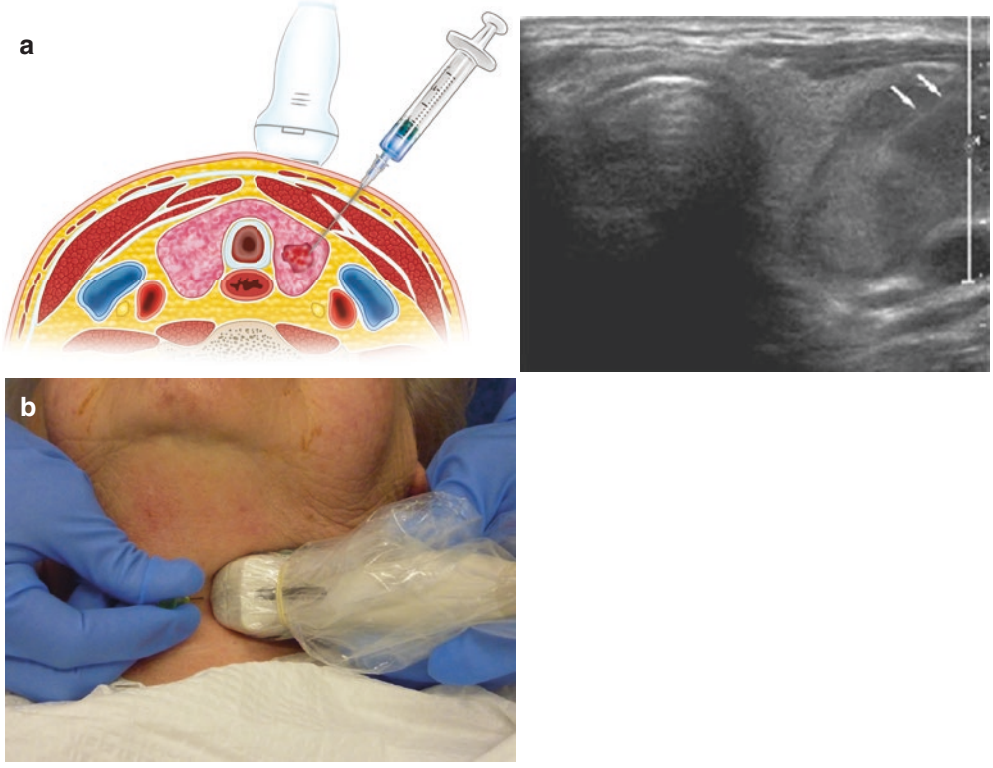

Fig. 20.5 (**a**) Parallel approach (Picture taken from [1]). The needle is inserted midline at the side of the US probe. This allows the tip of the needle to be seen at all times [1]**.** (**b**) Needle is inserted at the side of the probe in the middle. The operator should only advance the needle if they can fully visualised the tip of the needle. This technique is also recommended for core biopsy needle

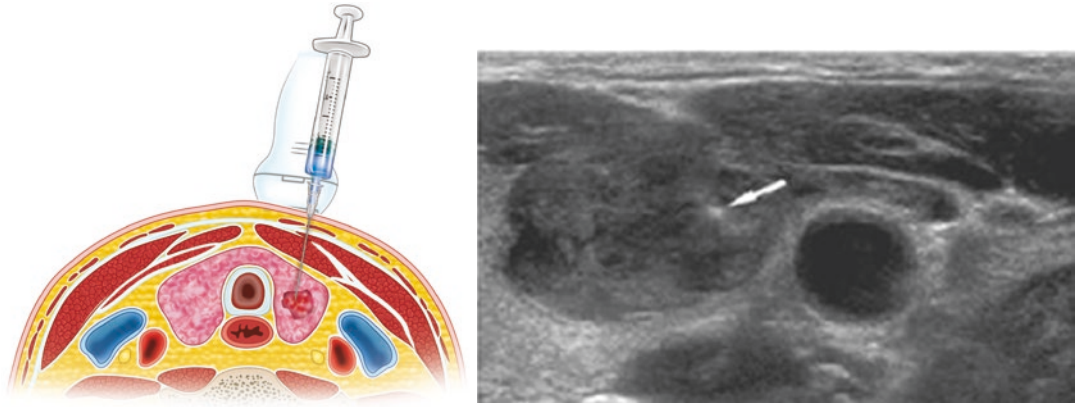

Fig. 20.6 Perpendicular approach (Picture taken from [1]). The needle is inserted in middle of the linear probe as seen below. This allows the needle to go deeper but it is more difficult to see the entire length of the needle or the tip accurately [1]

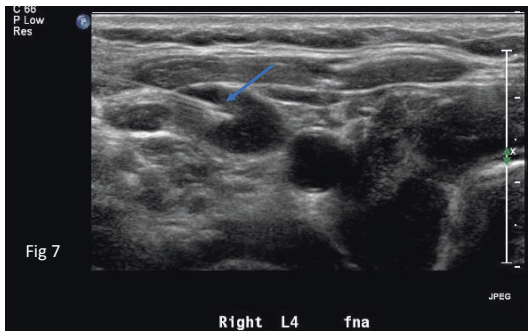

Fig. 20.7 FNA using a perpendicular approach. The needle can be seen through out the entire procedure while FNA in a RL4 node as indicated by the arrow

necessary, local anesthetic would be of great help to ensure a painless procedure. As for core biopsy, local anaesthetic is always advisable.

The number of passes that should be taken depends on the lump. Would recommend at least two passes to different part of the lump. A maximum of 5 passes. Once the needle is in the lump, the needle can be moved backwards and forward within the lump, and rotate with a core motion. This should be a free hand aspiration without negative pressure. Where possible, the needle should not be in the lump longer than 20 secs. This is to avoid clot within the needle which may cause difficulty to get the aspirate through the needle shaft and on to the slides. For each needle pass, one air dried and one fixed slide should be made. If the cytology technician is present, the needle is handed to the technician for slide prepartion. Once prepared, they can view the slides under the microscope to check for cells adequacy. Where needed, further passes could be performed. This is to avoid nondiagnostic specimen due to inadequate sampling. Where there is a need of making a cell block from needle washing or for flow cytometry is needed, a few more needle passes into the needle wash are important (Fig. 20.8). As you can see in the photo a good slide preparation required only a small drop of material. The slide should not be overwhelmed by the material when spreading the slide i.e. this should not reach the edges of the slide. Having a consultant cytopathologist present to perform a rapid onsite assessment (ROSE) can also be extremely helpful as the results can be known immediately. Where necessary a core biopsy can be advised and this can be performed in the one sitting. This arrangement, avoid the need of multiple appointments, avoid anxiety to the patient for needing to return for a second appointment and avoiding too many core biopsy to be performed unnecessarily. This has been known to reduce diagnostic time and play a crucial role in reducing the number of days for patient especially if the patient is within the cancer pathway. In the UK, the pathway time starts from receiving the referral from the patient's doctor to the treatment of cancer, which is 62 days. For some cancer, this has been reduced to 31 days in 2020. It is therefore

Fig. 20.8 (**a, b**) On-site cytology technician and cytopathologist are vital to ensure good slide preparation (**a**) and adequate samples are taken. Rapid on-site examination (ROSE) of the slide by a cytopathologist has been shown to increase diagnostic yield to nearly 99% (author's own audit data)

crucial for any lump to have important for urgent diagnosis. Several other tests could be performed from the needle washing e.g. flow cytometry to aid lymphoma diagnosis and test to identify the presence of P16, which is a marker for HPV. This helps to avoid having to take tissue samples from the patient, which in some cases have to be done under general anaesthesia. During the COVID pandemic, where theatre time is precious, with minimum operating time and space available as most theatres were converted into ITU/ICU for COVID patients. It was also compulsory for COVID patients to be isolated prior to their surgery i.e. to be COVID free for any operations, thus taking a biopsy under general anaesthesia became more challenging. FNAC and core biopsy became an important investigations that can be performed as an outpatient procedures to aid diagnosis.

5. A US-guided core biopsy is very similar to the FNAC needle approach. Highly recommend to use the parallel technique. Depending on the core biopsy needle, some do have a very sharp tip and this could be inserted straight into the skin. If this is not the case, a small little skin incision can be made with a scalpel. (In patient who has high risk of keloid scar, surgical skin incision should be avoided). Due to its invasive nature, a parallel approach is recommended in the head and neck. The size of the needle and length of the core sample depend on the size of the lesion. Where possible, gaining the largest tissue sample is an advantage, e.g., 16G vs 20G. Most commonly used are sized 16 g and 18G (Figs. 20.9, 20.10, and 20.11).

This is important especially after core biopsy in the parotid gland and at Level 4 neck to check for nerve injury or lung perforation. Patient should be informed if this happened (Fig. 20.12).

As the head and neck area is full of blood vessels and nerves, automatic core biopsy needle should be avoided unless in the hand of an experienced operator (Fig. 20.13).

6. It is important to dress the core biopsy site with a sterile dressing to avoid infection. If an incision has been made, putting steristrip on (if available) is useful. Allowing the patient to recover for 20–30 mins in the waiting room post core biopsy is advisable. We normally advised the patient to take analgesia for pain as necessary.

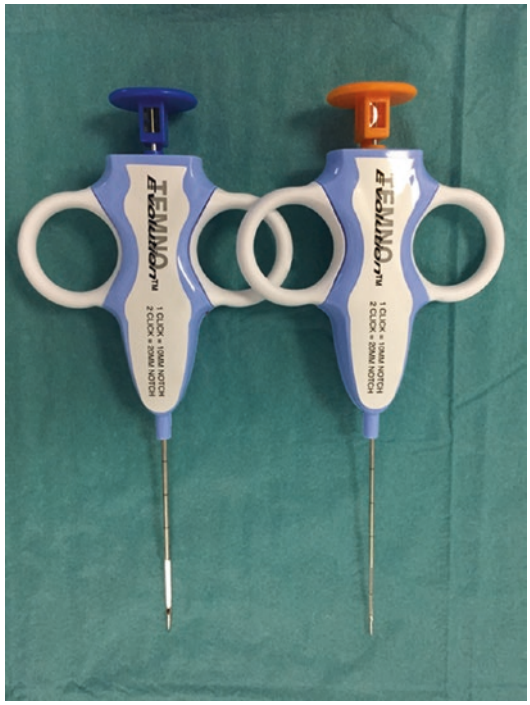

Fig. 20.9 Semi-automatic Temno Evolution ® core biopsy needle with a 2 cm and 1 cm gate (arrow). They come in various sizes and lengths. Below are 16G (blue) and 18G needle (orange), 6 cm in length. For the head and neck region, a 6 cm needle length is preferable for good control

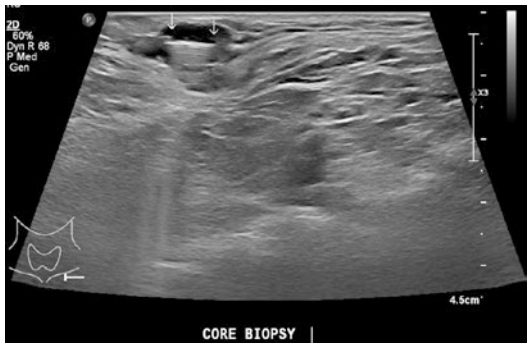

Fig. 20.10 Core biopsy performed to the mass by the left clavicle. It is important to mark the site of the core needle on the body marker or annotate the site of the biopsy on to the US image capture. US image showed the gates of where the tissue was taken from

7. Complications that can arise most commonly are bruising and hematoma. A rare complication is tumor tracking up the needle track. It is important to use the smallest gauge possible. Infection especially TB can do the same (Fig. 20.14 and 20.15).

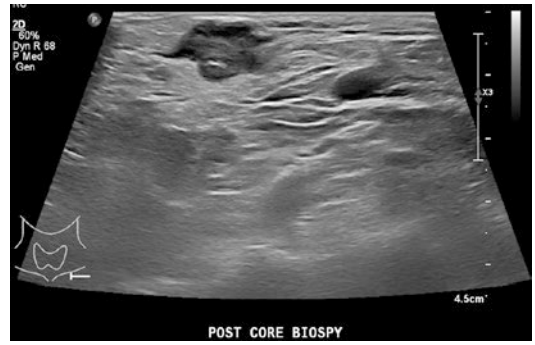

Fig. 20.11 Important to always check that there is no hematoma/hemorrhage or complications after the core biopsy has been performed

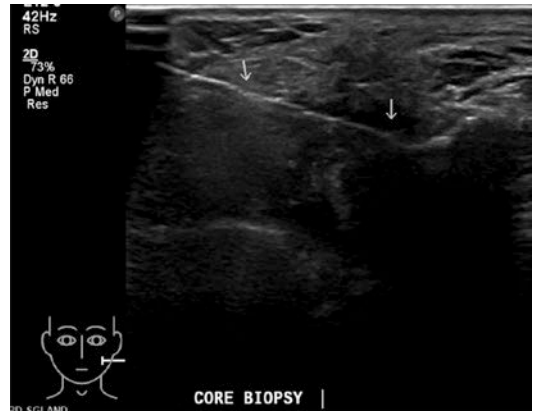

Fig. 20.12 The length of the core biopsy depends on the lesion, this is a 2 cm core length of an ill-defined mass in the left parotid gland

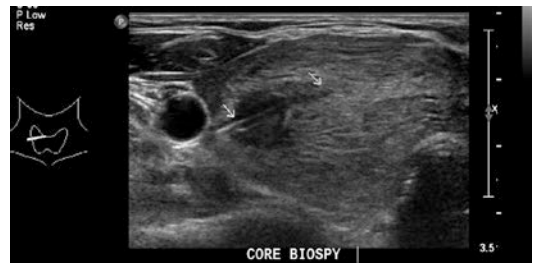

Fig. 20.13 Important to know the anatomical structure. Here the tip of the core biopsy needle is just inferior to the right common carotid artery, to avoid hitting the carotid artery. Important to use a non advancing core biopsy needle. As the image showed, an advancing automatic biopsy needle if incorrectly aim, may perforate the carotid artery and this can cause challenging complication such has heavy bleeding. The gates of the needle must be visible to the operator prior to firing. It is important to ensure the patient stays in the recovery area post core biopsy procedure for at least 20–30 mins. Any complications can may arise such as re-bleeding, haematoma or patient feeling unwell would be identified and managed prior to patient leaving the hospital

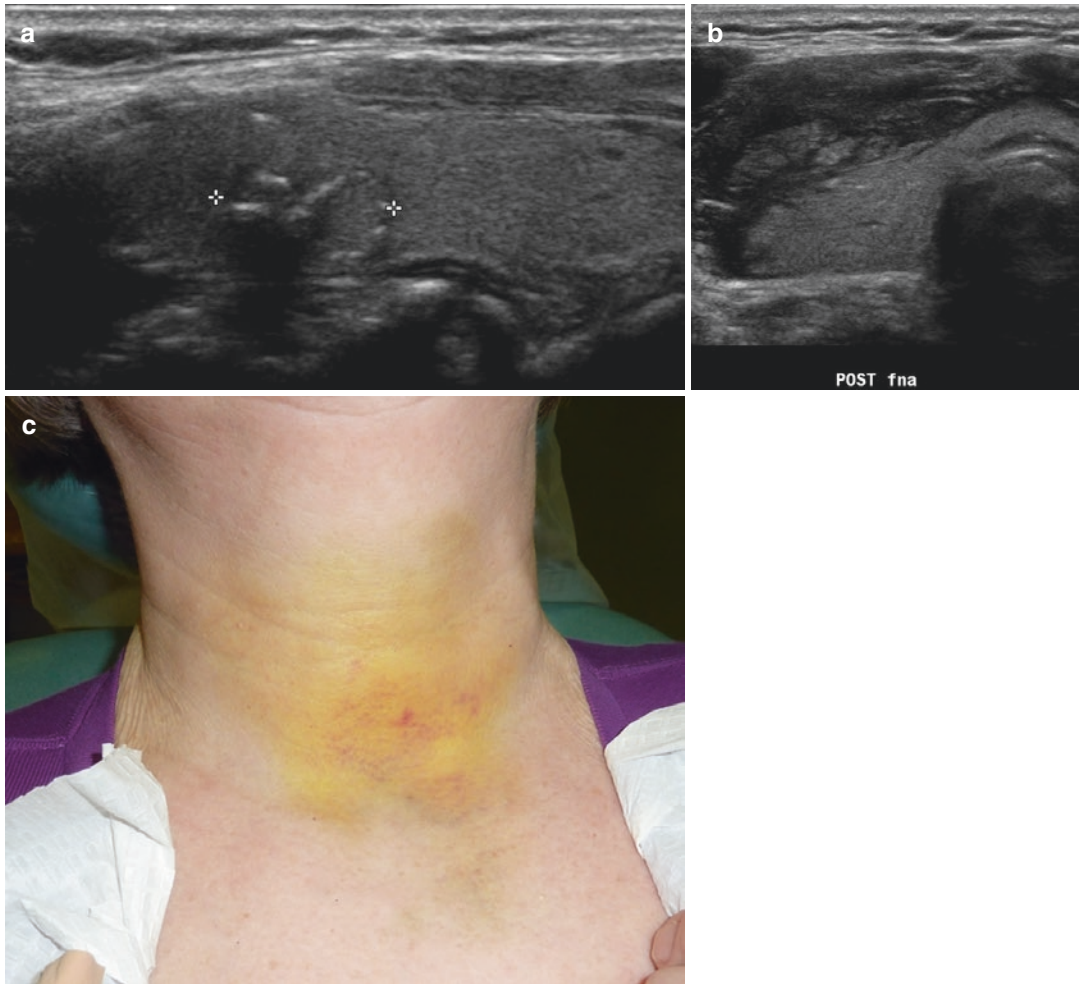

Fig. 20.14 (**a**) Prior to the FNA, (**b**) post FNA, hematoma formation, (**c**) bruising on the skin a week later. It is important to inform the patient of any complications that can occur

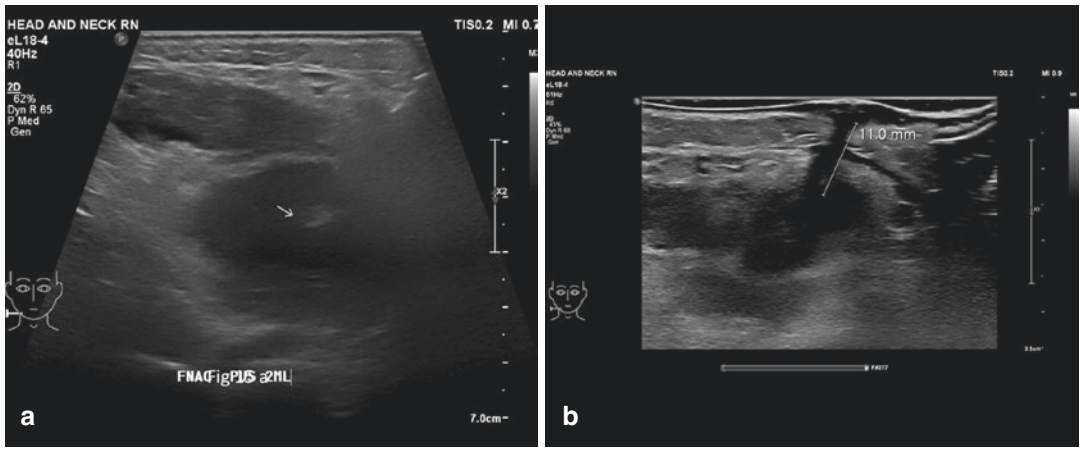

Fig. 20.15 (**a**) Deep-seated abscess with atypical cells that was aspirated with US guidance. A few days later, the patient was noted to have discharge on her skin. US shows the pus with abnormal cells has track up through the needle track to the dermis (**b**). It is highly suspicious of malignancy. Important to use a small gauge needle e.g. 27G or 25G to avoid cells tracking up the needle track in a suspected malignant mass

It is important to use aseptic technique to clean the skin to avoid an infection post biopsy.

8. Various sites that US can be helpful to guide a biopsy needle are as shown below. This may have to make diagnostic procedures easier and avoid the need for general anesthesia which has its own complications and risks to the patients. This was extremely beneficial at the time of the COVID pandemic. (Fig. 20.16 and 20.17).

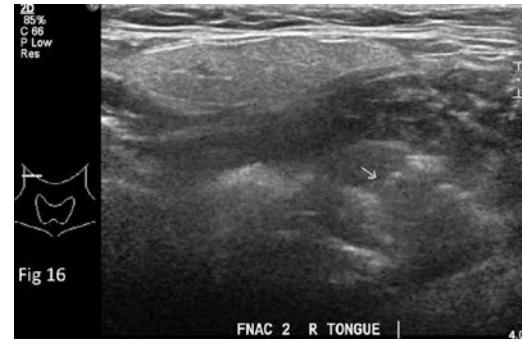

Fig. 20.16 FNA can be performed to the base of the tongue for diagnosis and HPV testing

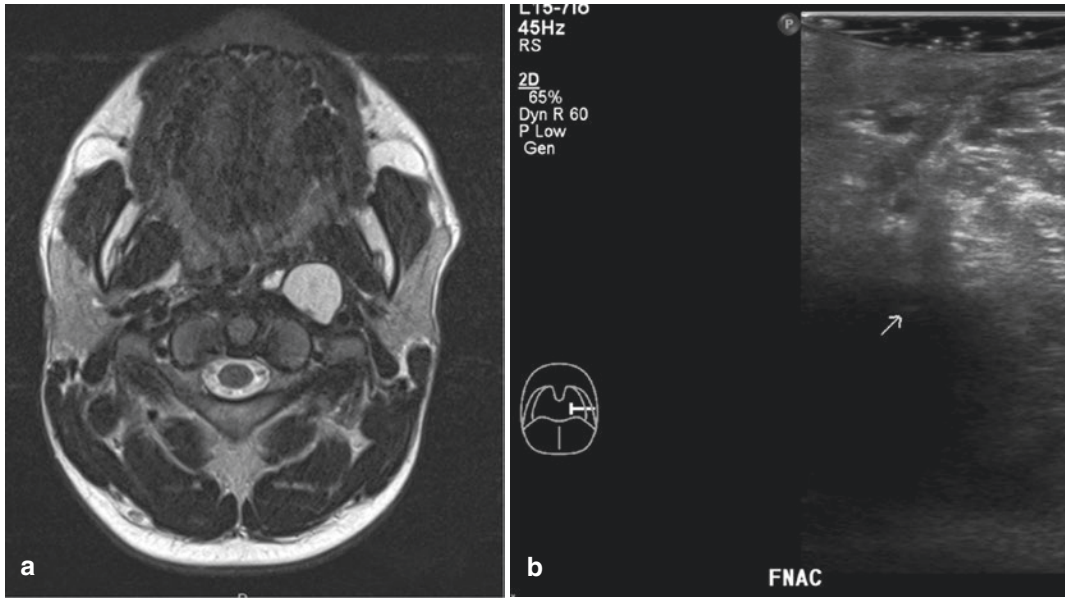

Fig. 20.17 (**a**) A mass was found in the left parapharyngeal space on the MRI scan.US guided FNA was performed to the parapharyngeal mass as this is close to the oropharynx using a hockey stick probe to guide the needle (**b**)

20.2 Salivary Gland Intervention

The most common cause of benign salivary gland obstruction is due to stones (73.2%), followed by strictures (22.6%). 7% of the patients were known to have bilateral parotid stenosis [2].

Minimal invasive techniques in the management of salivary stones have been shown to be successful in 80.5% of the cases [3]. This can be performed as a day case or as an outpatient appointment and avoiding surgical removal of the salivary gland.

Salivary duct stricture treated with balloon dilatation have shown to be successfully treated in 82% of the cases [4]. Balloon ductoplasty is an effective treatment for salivary duct stenosis.

Please note there are several method for treatment of ductal narrowing and stone removal. The method described in this chapter is limited to those performed using ultrasound. Salivary gland intervention to remove a stone or balloon ductoplasty is normally performed with a sialography under fluoroscopy guidance. However, US can also be used instead of fluo-

roscopy for salivary intervention. This can reduce radiation dose to the patient and may be particularly helpful if the patient is allergic to iodine contrast medium.

Salivary stones are occasionally seen in the salivary glands. It is more common in the submandibular glands than all the other glands. The traditional method previously used to treat salivary stone is surgical removal of the salivary gland. This however can cause postsurgical complication such as nerve damage or persistent symptoms with the stone still in situ in the duct. Basket retrieval of calculus using minimal interventional procedures with US/sialoendoscopy or fluoroscopy guidance can aid in salivary stone removal. It has low morbidity, quick and less invasive than traditional surgery. It is most effect in retrieving mobile stones in the extraglandular parotid and submandibular ducts [5].

The criteria for stone retrieval by dormia basket from a salivary duct are:

1. The stone must be mobile within the ductal system.
2. The stone must be smaller or not larger than the distal duct diameter that it has to come through.
3. The stone should measure 0.5 cm or less, preferably with no obstruction or narrowing to the distal portion of the duct (Figs. 20.18, 20.19, 20.20, 20.21, and 20.22).

The disadvantages of using US in comparison to using fluoroscopy for salivary gland interventional procedure are:

1. It is very operator dependant.
2. It does take longer to perform the procedure as one constantly has to stop the intervention, to perform the US scan of the duct or needing two radiologists to be present at the same time.
3. It is more challenging if there are numerous strictures along the duct.

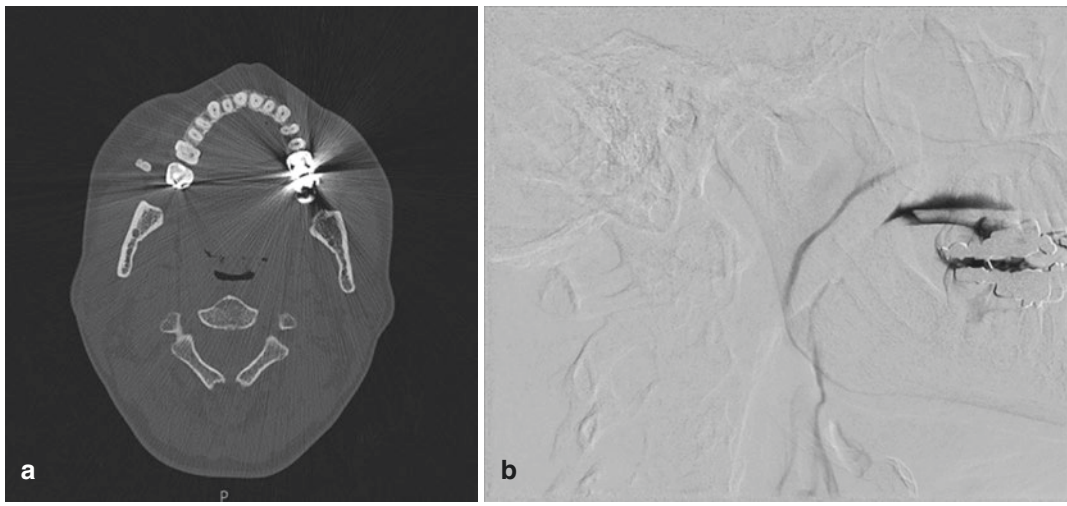

Fig. 20.18 (**a**) A 30-year-old patient was found to have regular meal time symptoms to the right parotid gland and a 0.5 cm stone was found near the ductal opening on CT. Sialography was attempted but due to the stone proximity to the ductal opening, this created a constant reflux when the contrast was introduced (**b**). (**c**) US confirmed the stone (blue arrow) in the anterior third of the duct (orange arrow) which is mobile and causes a proximal dilatation to the hilum. (**d**) Dormia basket (arrow) introduced into the duct, going past the stone, proximally. (**e**) Dormia basket fully open, proximal to the stone. (**f**) Dormia basket successfully captured the stone and this was released with a small relieving incision at the ductal opening. (**g**) US shows the stone has successfully been removed and no further stone is present. (**h**) Sialography performed confirmed no further stones and the duct successfully emptied on massage (**i**)

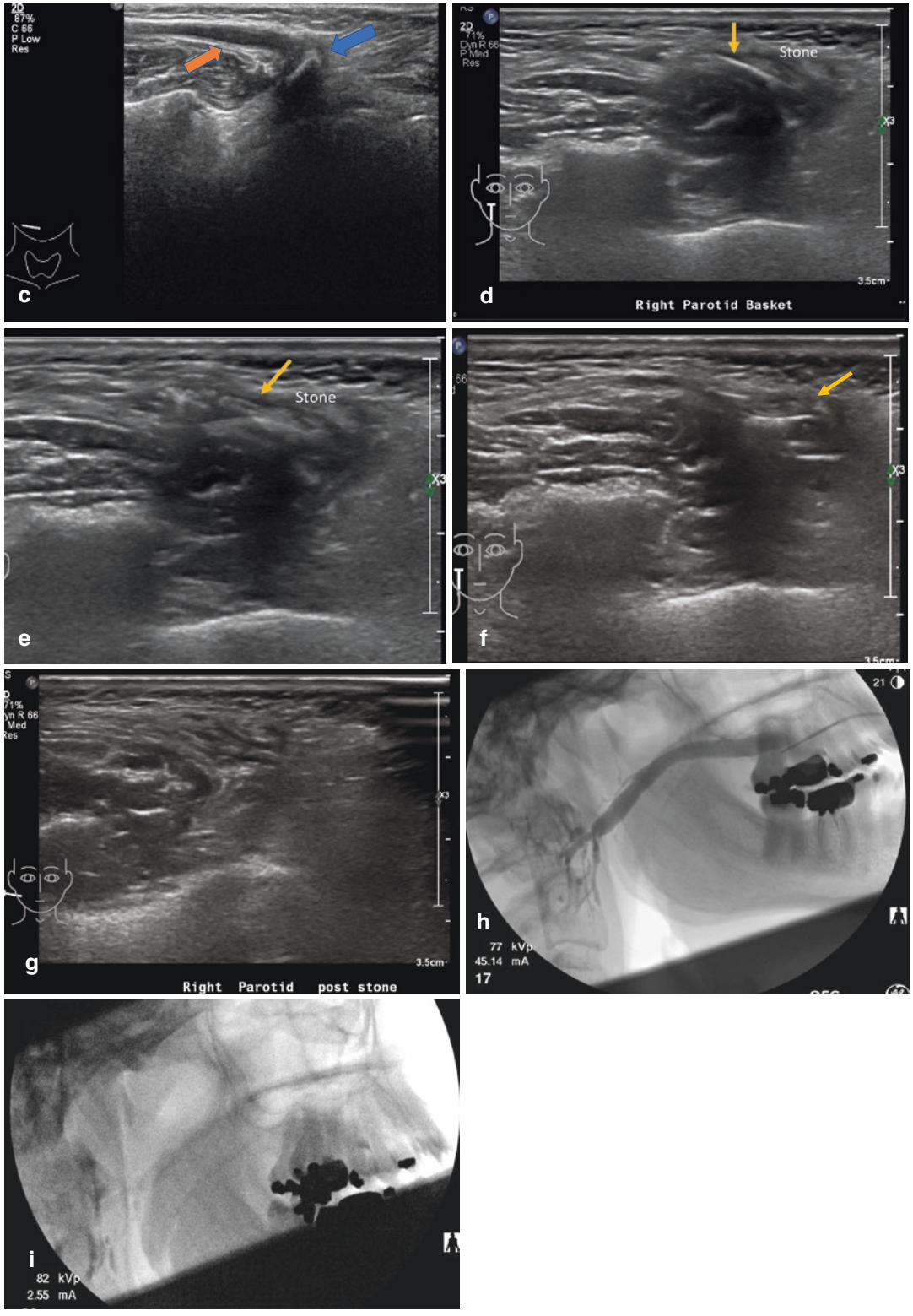

Fig. 20.18 (continued)

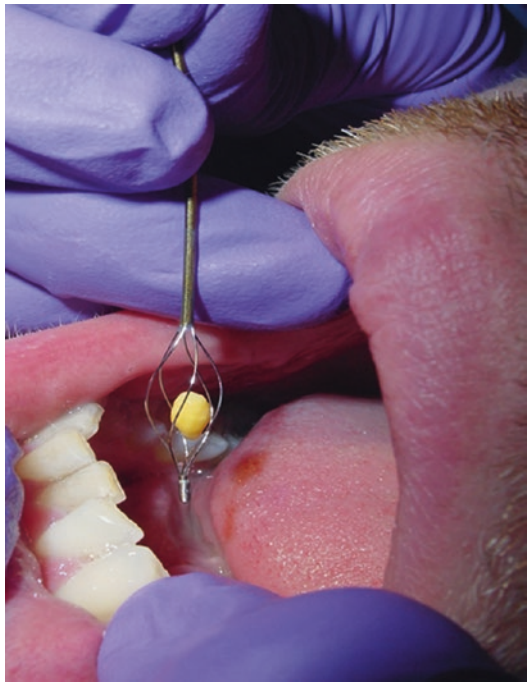

Fig. 20.19 Stone captured in the dormia basket and removed with a small relieving incision. The choice of basket depend on the size of the stone as well as the site of the stone in the ductal system

The advantages of minimal invasive salivary gland intervention technique using US are:

1. Able to identify the narrowest strictures.
2. US is useful to help guide the wire and balloon goes through the correct branch if there is superimposition with other stricture and to ensure this is fully dilated.
3. No ionizing radiation dose to the patient and the procedure can be repeated if necessary.

The above is some of the routine intervention procedures that are performed daily in a dental maxillofacial radiology department. It is important to fully explain the risks and complications to the patient and to gain verbal or written consent as appropriate prior to carrying out any of these procedures. US has been shown to be a very useful tool to aid intervention procedure both intra- and extraorally.

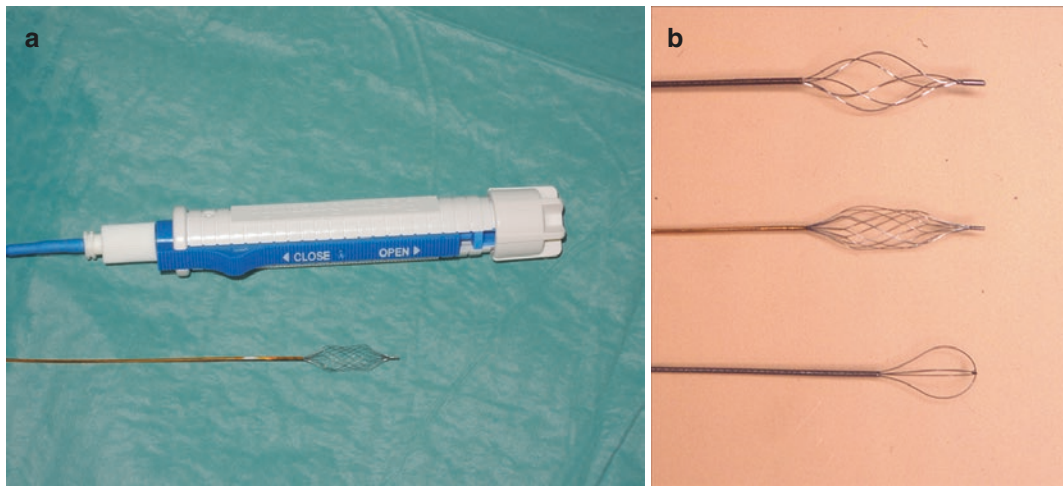

Fig. 20.20 (**a**) Boston Scientific ® 12 wire basket. (**b**) Various dormia baskets: from top to bottom—Cook ®: 5 wire captura, Boston Scientific ®: 12 wires, Cook ®: Nitinol tipless. The choice of basket depend on the size of the stone as well as the site of the stone in the ductal system

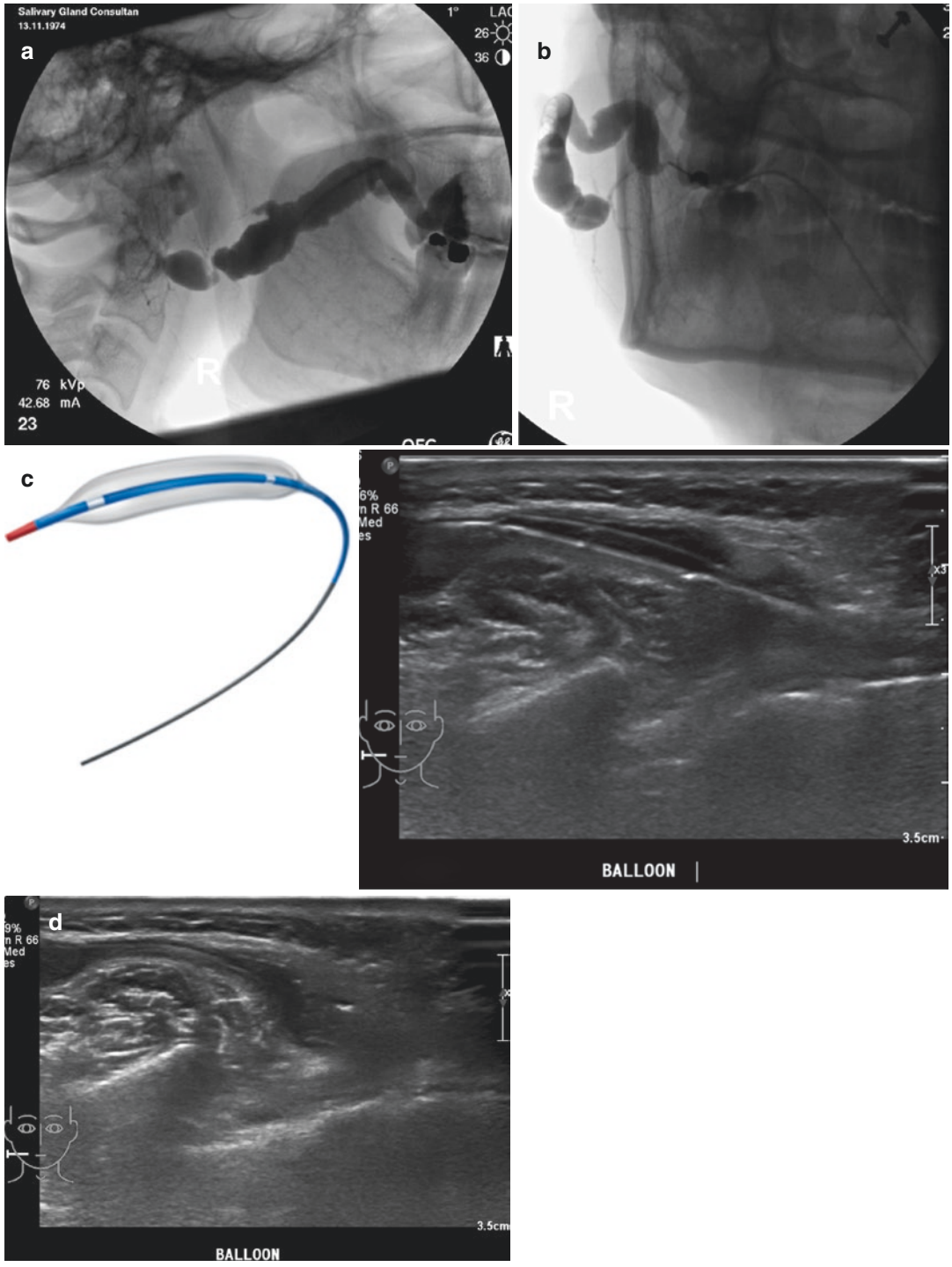

Fig. 20.21 (**a, b**) Right parotid sialography shows dilatation of the duct throughout the whole length of the main duct with a sign of sialodechitis and very narrowed anterior ductal opening, shown on a lateral view (**a**) and OM view (**b**). (**c**) 2.5 mm balloon (Boston Scientific ® angioplasty balloon) was inserted and inflated to dilate the stricture near the ductal opening. (**d**) Post balloon dilatation US, showing the duct emptying out

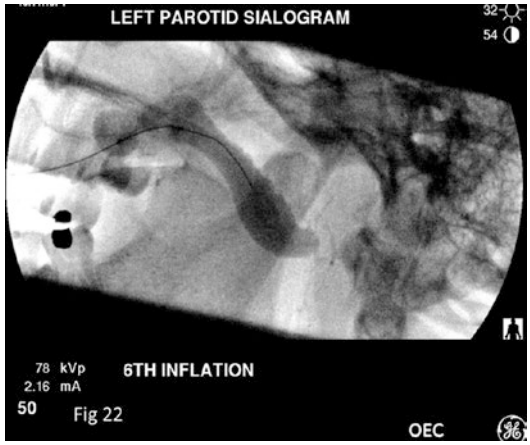

Fig. 20.22 Comparison to the same procedure that was done on the left parotid gland of the same patient using sialography under fluoroscopy

References

1. Kim MJ, Kim EK, Park SI, et al. US-guided fine-needle aspiration of thyroid nodules: indications, techniques, results. Radiographics. 2008;28(7):1869–87.
2. Ngu RK, Brown JE, Whaites EJ, Drage N, Ng SY, Makdissi J. Salivary duct strictures – nature and incidence in benign salivary obstruction. Dentomaxillofacial radiology (Dentomaxillofacial). Radiology. 2007;36(2):63–7.
3. Iro H, Zenk J, Escudier MP, Nahlieli O, Capaccio P, Katz P, Brown J, McGurk M. Outcome of minimally invasive management of salivary calculi in 4,691 patients. Laryngoscope. 2009;119(2):263–8.
4. Drage NA, Brown JE, Escudier MP, Wilson RF, McGurk M. Balloon dilatation of salivary duct strictures: report on 36 treated glands. Cardiovasc Intervent Radiol. 2002;25:356–9.
5. Brown JE, Drage NA, Escudier MP, Wilson RF, McGurk M. Minimally invasive radiologically guided intervention for the treatment of salivary calculi. Cardiovasc Intervent Radiol. 2002;25(5):352–5.

Reading List

Modern Management Preserving the Salivary Glands-Nahlieli, Iro, McGurk, Zenk. Isradon Publishing House.

USG Imaging in Physiotherapy of Dentomaxillofacial Region

21

Gokhan Yazici, Nihan Kafa, Mehmet Eray Kolsuz, and Kaan Orhan

Contents

21.1 Introduction

Most internal derangements can be resolved with conservative treatment, and physiotherapy is increasingly being recognized as an important part of this treatment. With this feature, physiotherapy is a wide-ranging profession with opportunities to work in many different areas. The interrelationship between dentistry and physiotherapy helps in early diagnosis and improves the therapeutic interventions' effectiveness especially in temporomandibular disorders (TMDs), sleep bruxism, and dentomaxillofacial region postural problems.

The diagnosis in these pathologies generally depends on a subjective assessment by patients and clinicians; therefore, there is a need for objective assessment for effective treatment. Soft tissues in the body have high water content and are virtually incompressible thus sophisticated equipment is necessary to detect small tissue changes. Elastography-based imaging techniques have received great interest in recent years for noninvasive assessment of musculoskeletal soft tissue mechanical properties. These techniques take advantage of changing soft tissue elasticity in different pathologies to provide qualitative and quantitative information that can be used for diagnostic purposes and follow-up evaluations during rehabilitation [1]. There are currently two main elastography methods in general clinical usage, namely compression/strain elastography and shear-wave elastography [2].

G. Yazici (✉) · N. Kafa
Faculty of Health Sciences, Department of Physiotherapy and Rehabilitation, Gazi University, Ankara, Turkey

M. E. Kolsuz · K. Orhan
Faculty of Dentistry, Department of Dentomaxillofacial Radiology, Ankara University, Ankara, Turkey

K. Orhan (ed.), *Ultrasonography in Dentomaxillofacial Diagnostics*,
https://doi.org/10.1007/978-3-030-62179-7_21

21.2 Role of Physiotherapy (Applications) in Dentomaxillofacial Region Problems

Temporomandibular disorders (TMD) are a complicated and heterogeneous group of pathologies affecting the temporomandibular joint (TMJ) and muscles of mastication, resulting in pain and disability [3]. Epidemiological studies of TMD report a prevalence of 82% in the general population with 48% of them presenting muscle tenderness and difficulty in mouth opening. TMD are thought to be the most common orofacial pain conditions of non-dental origin [4]. In connection with this problem, another pathology seen in 8–20% of the population is Sleep Bruxism (SB) [5]. Bruxism is a common clinical presence defined as "a repetitive jaw muscle activity characterized by clenching or grinding of the teeth and/or by bracing or thrusting of the mandible." [6].

Studies claim that 85–90% of the general population experience episodes of bruxism during their lives. Therefore, it is important to find an effective treatment for these dentomaxillofacial region pathologies [5]. Because of the symptoms as muscle pain, muscle activity alterations, limitation of mouth opening, anxiety, stress, depression, poor sleep, and oral health quality in TMD and Bruxism, treatment using an interdisciplinary professional team including dentists and physiotherapists is important [5]. Physiotherapy is the preferred conservative approach for treating TMD and Bruxism, as it facilitates multimodal treatment that addresses patient-specific impairments [7].

Recently, actual treatment procedures include the framework of a conservative "multiple-P" approach (i.e., physiotherapy, plates, pep talk, pills, psychology) [5]. Applications of oral orthoses and physiotherapy modalities (such as exercises, thermal agents, or massage) are usually performed prior to medical drug regimens and invasive procedures. Among these methods, the most commonly used one is the occlusal splint (OS) application especially for Sleep Bruxism treatment. However, OS may not be effective in some patients and has limited use for patients who have elevated gag reflex or higher risk of airway obstruction (due to epilepsy, etc.) and who use dental brackets. Thus, there is a need for an alternative treatment method that can replace OS [8].

Treatment methods used in physiotherapy include electrotherapy, therapeutic exercises, muscle relaxation techniques, postural awareness, acupuncture, manual therapy, and cognitive behavioral therapy techniques. However, the effectiveness of all these approaches on the signs and symptoms of TMD and Bruxism is still questionable and continues to be studied [5].

In the literature, there are lots of studies investigating the effectiveness of physiotherapy modalities in patients with bruxism and TMDs. The majority of them investigated the effectiveness of electrotherapy techniques, one of the most used ones is Transcutaneous Electrical Nerve Stimulation (TENS). The results of studies especially showed that electrotherapeutic resources decrease masseter muscle activity and pain and improve oral health in individuals with Bruxism and TMD especially in short term [5, 7, 9, 10]. Massage therapy is another most used treatment approach. In studies, occlusal splint was generally compared with massage therapy. As a general result of studies, it was concluded that massage therapy and the use of an occlusal splint did not lead to changes in the activity of the masseter and anterior temporal muscles. However, the combination of therapies let a reduction in the intensity of the signs and the symptoms of TMD and Bruxism [11–14]. In addition, although there is limited evidence, soft tissue release and strengthening exercises for the muscles of mastication in patients with TMD, provide a reduction in pain and disability. Also, joint mobilization and manipulation to the temporomandibular joint and/or upper cervical articulations, and dry needling or acupuncture to the lateral pterygoid muscle and posterior periarticular connective tissue are considered as the most evidence-based approaches for conservatively treating TMD [7]. Apart from all of these modalities, new different techniques are also being sought. One of the new approaches for bruxism is

Kinesio taping (KT) method. Keskinguzar et al.'s study demonstrated that 5 weeks of treatment with occlusal splint and KT showed similar efficacy for sleep bruxism therapy. They also concluded that KT can be used as a routine technique in patients with Sleep Bruxism as an alternative to occlusal splint especially in patients with nausea, with risk of swallowing or aspiration of the splints (such as an epileptic crisis), or with braces in the teeth for orthodontic treatment [8].

In conclusion, it can be said that physiotherapy interventions are effective for the treatment of bruxism and TMD. Most of the studies have poor methodological quality and very low-quality evidence [5]. Therefore, there is still a need for well-designed randomized controlled trials examining physiotherapy interventions for Bruxism and TMDs.

21.3 USG Imaging Usage in Musculoskeletal System Structures

Chronic or acute musculoskeletal system pathologic conditions are common in the population and generally painful and debilitating. Physiotherapy applications to these pathologies affect the injured area which is generally musculoskeletal soft tissue including muscle, tendon, ligament, and nerve. Mechanical function or physical properties of the injured area may also be affected through these physiotherapy interventions which is difficult to assess particularly under in vivo conditions.

Increased collagen content and stiffness are seen in numerous musculoskeletal pathologies [15]. Ultrasound modalities (US) are being increasingly used not only in the diagnosis of musculoskeletal injuries in an attempt to localize involved structure as well as the extent and severity of the injury but also in the evaluation of intervention effectiveness. The main advantages of US include multiplanar imaging capability, quantification of soft tissue abnormalities, high resolution, direct correlation of clinical symptoms, and imaging findings and the unique possibility of dynamic imaging allows diagnoses that cannot be made with other modalities [16]. Ultrasound represents great utility in evaluating the underlying architecture of more superficial tissues, and a variety of techniques have been used to evaluate stiffness [17, 18], but, until recently, ultrasound has been purely qualitative [15].

Ultrasound elastography (EUS) is a recently developed ultrasound-based method, which allows both the qualitative visual and quantitative assessments of the mechanical properties of tissue [19–21]. The technique was first introduced in vitro in the early 1990s and subsequently evolved into a real-time tool for in vivo imaging of the distribution of tissue strain and elastic modulus [19]. EUS provides information on tissue stiffness, which complements and is independent of the acoustic impedance and vascular flow information provided by B-mode and Doppler imaging [19–21]. It has provided a quantifiable spatial representation of elasticity (or hardness or stiffness) in the form of an elastogram [22, 23].

The basic principle that EUS is based on is that stress applied to the tissue causes tissue differentiation. Preliminary data indicate that ultrasound elastography (EUS) may even be more sensitive than MRI or gray-scale ultrasound in detecting subclinical changes of muscle and tendon, and therefore could be valuable for early diagnosis and during the rehabilitation process. EUS could be used as a research tool to provide insight into the biomechanics and pathophysiology of musculotendinous diseases [19–21]. Over the years of research on elasticity, there have been several types of EUS, resulting in different methods, depending on the way of tissue stress application and the used method to state and set an image of tissue displacement [19]. EUS can be divided into strain elastography, which measures tissue strain, and shear-wave elastography (SWE), which measures the shear-wave speed. Shear-wave elastography can be further classified into transient elastography, point SWE, and multidimensional SWE (2-dimensional [2D] SWE and 3-dimensional SWE) [24].

21.3.1 Technical Considerations and Limitations of Ultrasound Elastography

21.3.1.1 Technical Considerations and Limitations of Sonoelastography in Muscle–Tendon Evaluation

Skeletal muscle is anisotropic, nonlinearly viscoelastic, deformable and active tissue [25] which consists of a very particular and well-described arrangement of muscle fibers. These muscle fibers are also associated with connective tissue network of collagen within the extracellular matrix (ECM) [26]. Elasticity/stiffness is thought as a critical determinant of muscle performance and force; therefore, its measurement in vivo can help to increase the understanding of muscle functions [16, 25]. As skeletal muscles are active tissues, an ideal technique would be capable of the real-time measurement to quantify tissue stiffness throughout functional range. Such a technique should be sensitive to detect small changes in stiffness and capable of determining material properties of relevant and often complex skeletal muscle architecture. Also, in tendon imaging, while using conventional ultrasonography differentiation of tendon alterations might be difficult since edema, hemorrhage, mucoid degeneration, or partial tears present as isoechoic alterations [27]. Therefore, reliable, noninvasive, quantitative techniques for evaluating musculoskeletal stiffness are necessary not only to advance our understanding of the mechanism and effects of altered musculoskeletal stiffness but also to improve diagnosis and treatment following injury [15].

During sonoelastography imaging, the normal relaxed muscle appears as a heterogeneous mosaic of intermediate or increased stiffness with scattered less stiff and stiffer areas, especially at the boundaries of the muscle [19]. Strain elastography has been used to assess many muscle pathologies, including muscular dystrophy, cerebral palsy, myositis, patellofemoral pain syndrome, intramuscular hemorrhage, fibrosis, etc. [19]. In addition, for dentomaxillofacial region, both strain and shear-wave elastography have been used to evaluate masseter muscle in patients with facial pain. In these studies, patients with facial pain and temporomandibular joint dysfunction have been shown to have a greater stiffness in masseter muscle compared with healthy controls. This correlates with the clinical finding of altered stiffness of masseter muscle in symptomatic patients with facial pain thus ultrasound elastography could become a useful technique in the assessment of these patients in both diagnosis and treatment effectiveness [2]. However, there is still no consensus in stiffness imaging differences between asymptomatic and symptomatic tendons. Although suggested potential role of sonoelastography for the assessment of a variety of traumatic and degenerative disorders of tendons, there is little evidence-based published data available for these assessments.

In sonoelastography, data acquisition and interpretation are largely operator dependent, which is the major limitation of this imaging system. While using sonoelastoraphy, a wide variety of techniques could be used to display elastographic images, and therefore the findings as well as the artifacts or limitations may be highly dependent on the technique. A major issue associated with sonoelastography is determining the correct amount of pressure to be applied on the tissue. The pressure should be moderate, described as the level of pressure that maintains contact with skin and for which the association between pressure and strain is proportional. Very high or low pressure should be avoided because the elastic properties of tissue become nonlinear. Fortunately, most sonoelastography systems now provide software, which gives feedback of the amount of pressure as a visual indicator/bar displayed on the screen alongside sonographic images. During evaluation, to minimize intraobserver variation and avoid transient temporal fluctuations, measurements in the elastograms should be based on examination of entire cine loops instead of single static images [19, 28].

Another important limitation in the use of sonoelastography is the size of the elastogram. The elastogram demonstrates the elasticity of each tissue relative to the remaining tissue within

it. Therefore, the amount and level of stiffness of the surrounding tissue influence the appearance of the tissue of interest. This is not a major limitation in tissues such as the breast where the surrounding tissue is fairly homogeneous (fat and glandular tissue); however, in musculoskeletal sonoelastography, the elastogram may include tissues with wide stiffness differences (fat, tendon, bone, muscle), leading to a wider distribution in the acquired elasticity data [19]. In addition, if a skeletal muscle is evaluated with this type of elastography, the examination transducer should be perpendicular to the tissue to avoid anisotropy, as the B-mode ultrasound appearance influences the quality of the elastogram. Also, although tendon images could be taken in both transverse and longitudinal planes, longitudinal images represent better quality [19].

During measurement, another standardization problem is the distance between the probe and the tissue of interest. In many musculoskeletal applications, the tissue of interest is very superficial or even lies directly under the skin (e.g., Achilles tendon). In most ultrasound systems a minimum distance from the skin (usually 1.2 mm) is needed to place the box of the elastogram, so in thin people the use of gel pads or probe adaptors is necessary to increase the distance between the skin and probe [19]. On the contrary, the use of standoff devices for sonoelastography of the superficial structures does not influence the elastogram (a minimum necessary distance between transducer and lesion is 3 mm). However, in tendon evaluation, using too much gel within the region of interest should be avoided which may mask minimal differences [29].

In addition, there are also limitations and difficulties related to the anatomy of the area examined. Sonoelastography is especially problematic in cases of superficial protuberant masses and in areas with prominent adjacent bony structures [19, 28]. When a solid structure is delimited by an incompressible tissue, sonoelastography analysis of the internal structure is limited (the eggshell effect). Due to the tissue shifting, low stiffness lines may be seen at the interfaces between tissues, around calcifications, behind bone, or at the superficial edge of a homogeneous lesion. For instance, fluctuant changes at the borders of the Achilles tendon in an axial elastogram can be seen due to varying contact with the skin [29].

21.3.1.2 Technical Considerations and Limitations of Shear-Wave Elastography

(a) Muscles

Although SWE provides reliable stiffness measurements under proper conditions [30], several technical parameters should be known that influence the measurements and need to be taken in account. Cortez et al. assessed intra- and inter-operator reproducibility of SWE for a specific site in normal skeletal muscles and concluded as fair to good ICC values (0.40–0.78) [47]. The wide range of these ICC values can be interpreted as there are too many factors affecting muscle stiffness measurements. Since no guideline on the use of SWE in medical practice exists yet, the anatomy of the studied muscle, the basic muscular biomechanical concepts (in particular the role of anisotropy), and the limits of the SWE method should be known before using SWE on skeletal muscle.

First, the major technical parameter that influences stiffness measurement is *the anisotropic physical properties of the skeletal muscle*. The anisotropic physical properties are responsible for the fact that shear waves travel faster along the direction of the fibers than they do when perpendicular to them. If technical challenges are understood, more effective algorithms could be developed to identify the anisotropic properties of muscles. For each technique, muscle and joint positioning, material setup, acoustic wave frequency, rheologic fit need to be clarified to harmonize measurements [25]. Stiffness measurements are sensitive to the angle between the probe axis and the orientation of the muscular fibers. Shear modulus measurements using SWE are correlated with Young's modulus only if the probe is oriented parallel to the muscle fibers [25]; thus, it could be said

that orientation of the ultrasound transducer plays a key role to obtain meaningful results. Genisson et al. found that shear waves propagate much more readily along muscle fibers longitudinally, as compared to perpendicularly or any interval of rotation therein. Same investigators reported that parallel transducer orientations obtained the most reliable measures of muscle elasticity [31]. Therefore, it can be said that SWE is partly operator-dependent especially in complex and large muscles. However, intra- and inter-observer reliabilities remain good to excellent if performed by a skilled senior and if the angle between the probe axis and the orientation of the muscular fibers is inferior to 20° [25, 32]. Another point that effect the reliability of measurements is the difficulty in assessing muscles with complex anatomy. Multipennate, conic, triangular, or fusiform anatomy causes a technical difficulty in visualizing the orientation of fibers. Therefore, this technical difficulty requires careful knowledge of muscle anatomy before using SWE. Because of the different pennation of the muscle fibers, during imaging, some elastography signal may be lost [33].

The second parameter concerns *the viscoelastic properties of skeletal muscles*. Muscle behaves as a combination of viscous and elastic properties, which together compose the shear modulus^ (G). Also, the viscoelastic properties are nonlinear, i.e., stiffness changes are relative to the characteristics of the applied stress such as the frequency of the shear wave. Moreover, given the contractile and stretching properties of muscle, muscle viscoelasticity is active.

Third, skeletal muscle is a *deformable tissue*; thus, SWE measurements are sensitive to transducer pressure. Therefore, the pressure applied to the tissue should be as low as possible. In a study, two different manually applied pressures were compared (1.5–3.0 kPa), and it was concluded that there was a significant difference in shear-wave speed values. Therefore, in the present conditions and system, an amount of couplant should be applied onto the tissue surface instead of applying the pressure manually through the probe. When the tested tissue depth is within 0.2 cm, it is not suitable to apply the couplant of more than 10 mm and also if the acquisition depth reaches 30 mm, the couplant should not be used with more than 20 mm [34]. To summarize, during SWE measurements, a generous amount of coupling gel needs to be applied onto the surface of the skin not to compress the muscles. When measuring superficial soft tissues, to give an average amount, approximately 1–5 mm of gel was generally used and thought enough for reliability. In addition, another important point in this regard is the most suitable measurement depth. When measuring the shear-wave speed of muscles, the suitable measurement depth is recommended to be within 3–5 cm that would be feasible or ideal in the present conditions and system. When depth increased to 6 cm, the shear wave failed to be detected with the use of a linear probe (SL10–2 linear probe). If more deeper tissue (>6 cm) is desired to be evaluated, lower frequency convex probe is recommended [34]. However, the subcutaneous adipose tissue also effects the depth of muscle. Thick superficial fat layers and greater BMI also effect the propagation of the shear waves and create artifacts as “holes” or areas of very high/low stiffness in the elastogram. A consequence of this is that the stiffness value might depend on the ROI size and position [25, 35].

Stiffness values also depend on the transducers and machines from the different vendors, presets, acoustic methods and calculation formulas use. The yield curve of increased stiffness during contraction differs between muscles and depends on the intensity of the force and torque as well as on fascicle length. Significant stiffness differences are observed between various muscles. In humans, reported shear modulus values at rest range between 3.1 kPa in the biceps brachii and 42.8 kPa in the masseter in vivo [36, 37]; thus, it can be said that stiffness values of muscles are case-specific. Furthermore,

muscle contraction is one of the major factors affecting stiffness. At higher contraction levels, stiffness can not always be measured as shear waves in more rigid tissues because it may propagate too fast for some ultrasound systems to be properly tracked. Above a certain stiffness threshold, which depends on the performances of the equipment (maximal value v: 16 m/s or G = 266 kPa or E = 800 kPa), the measurement quality deteriorates and SWE cannot properly measure tissue stiffness. After an intense eccentric contraction, stiffness continues to increase for several days as a consequence of muscle damage. Especially during contraction diffuse heterogeneities were reported as well as stiffness differences along the longitudinal axis of muscles. This heterogeneous pattern of stiffness probably reflects the non-synchronization of motor units. Heterogeneity in the transversal axis of muscle have also been observed but showed some inconsistencies: both higher and lower stiffness was found in the deep part of the muscle than in the superficial. SWE measurements decrease with increasing depth and presence of bone below the area measured which makes it difficult to establish cut-off values (Table 21.1) [33].

(b) Tendons

The current literature suggests that shear waves propagate faster in healthy tendons than in those that are tendinopathic, and faster in contracted tendons than in those that are relaxed. In addition, shear waves propagate faster along the long axis of healthy tendons than along the short axis [38]. In tendons, it was found that elasticity has reduced during contraction, which has varying degrees of response, depending on patient position during examination (in supine or standing). Moreover, when tendons degenerate, the collagen fibers break down and it is proposed that tendons become softer; thus a change in their elasticity can be detected with elastography. Tendinous rupture zones appear at USE more "soft" compared with the average elasticity of normal tendon. Conversely, after surgery, tendon characteristics may change and during postoperative evaluation fibrosis scar areas may be seen. If tendon repairs with fibrosis, this may be seen as a hardening of the tendon substance, with a stiffer elastographic picture [29]. Furthermore, like muscles, different values of shear-wave velocity or elastic modulus were obtained depending on the machine used, tendon position, or plane of imaging. With age, a significant decrease in shear-wave velocity values was detected, with SWE having the capacity to

Table 21.1 Current potential clinical applications of SWE in the evaluation of musculoskeletal tissues and expected findings for shear-wave velocity and shear modulus [38]

Examined structure	Shear-wave velocity (c_s)	Shear modulus (G)
Normal relaxed tendon	Intermediate	High
Normal contracted tendon	Increased	High
Tendinopathy (compared with normal tendon)	Lower	Lower
Partial-thickness tendon tear (compared with normal tendon)	Signal void	Signal void
Normal muscles in relaxed state	Low	Low
Contracted muscle (compared with relaxed)	Increased	Higher
Myopathy (compared with normal muscle)	Variable (higher or lower)	Variable (higher or lower)
Torn muscle (compared with normal muscle)	Lower	Lower
Normal fascia in relaxed state	Intermediate	High
Contracted fascia (compared with relaxed)	High	Higher
Torn fascia (compared with normal)	Lower	Lower
Normal nerve	Low	Low
Neuropathy (compared with normal nerve)	Higher	Higher
Normal ligament	Intermediate	High
Thickened ligament (compared with normal)	Increased	Hİgher

detect aging tendons before morphologic abnormalities were observed on B-mode ultrasound. Therefore, it can be concluded that physiological factors (age, sex, muscle performance, fatigue, or training) and pathological changes (trauma, degeneration, or neuromuscular disease) influence muscle and also tendon elasticity [29].

(c) Ligaments, Fascia

Compared to normal muscle and fascia, acute muscle and fascial tears in the same anatomic location show lower shear-wave speeds. In normal ligaments in the relaxed state have intermediate shear-wave speeds; however, in stretched position, stiffness is increased [38]. It is also suggested that SWE may be valuable in detecting aging tendons before visible abnormalities are seen by conventional US techniques since older tendons have lower shear-wave speeds [39].

(d) Nerves

If there is nerve entrapment or degeneration in nerve structures, increased stiffness was attributed to nerve fibrosis or edema. However, like other musculoskeletal structures the joints and limb position and the patients' age should be taken into consideration during SWE examination [40, 41].

21.4 USG Imaging of Masseter Muscle after Physiotherapy Applications

Chewing muscles are one of the main major muscle groups, a group of muscles associated with TMJ movements. There are four chewing muscles that are masseter, temporalis, medial pterygoid, and lateral pterygoid. Masseter muscle is an important muscle of the chewing system. It pulls the mandible upwards, allowing the mouth to close, and is actively used in functions such as speech and chewing. Myofascial pain is the most common cause of chronic orofacial pain. Previous studies have shown that 85% of myofascial pain is associated with masseter muscle [42]. Bruxism or other parafunctional habits may cause dropsical modification in the masseter muscle due to muscle overactivity, this may cause a change in the appearance of the masseter's internal echogenicity [43].

Diagnostic imaging is necessary for documentation, establishing the diagnosis before treatment and after therapy [44]. Studies have shown that a physical examination alone is inaccurate in determining the status of the joint with a clinical diagnostic accuracy for the specific status of the joint of only 50–60%. Ultrasonography is used as an alternative method that can depict the morphology of masseter and other muscles superficially placed in the bone structures in the head and neck [45].

Only a few studies emphasize the use of ultrasonography in evaluating the effect of splint treatment for the masseter muscle of TMD patient. In these studies, it was emphasized that the thickness after treatment decreased compared to the pretreatment [46]. For such measurements, the subjects should be placed in an upright position with the head in a natural position. Both sides of the masseter muscle should be scanned perpendicularly to the anterior border of the muscle and the surface of the mandibular ramus, approximately 2.5 cm above the lower border of the mandible, with the minimum pressure to achieve the muscle image as thick as possible. Measurements should be made in at least three different point regions so the mean value can be achieved (Figs. 21.1, 21.2, 21.3, and 21.4).

One of the most common findings in TMD is myofascial pain. Myofascial pain is diagnosed on the basis of the anamnesis taken from the patient and the presence of pain and tenderness with palpation performed by the physician. The diagnosis is based on a subjective assessment by patients and clinicians; therefore, it is difficult to assess irregularity. Myofascial pain is often associated with regional pain in sensitive areas known as trigger points expressed in skeletal muscle and stretched bands of the tendon. A clear objective

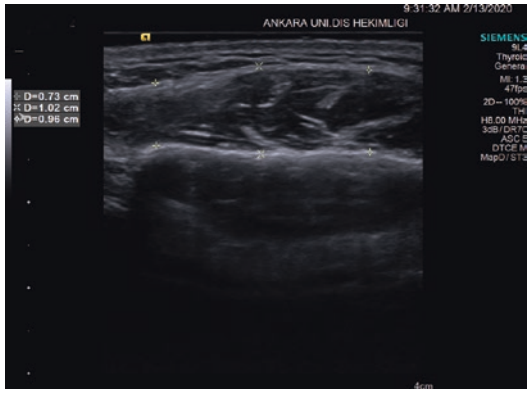

Fig. 21.1 Right masseter muscle USG linear measurements of a patient before treatment

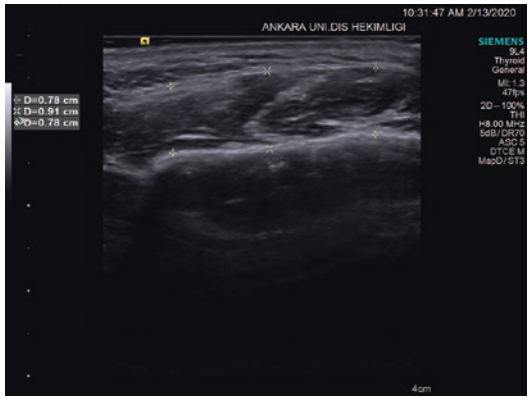

Fig. 21.2 Right masseter muscle USG linear measurements of a patient after treatment

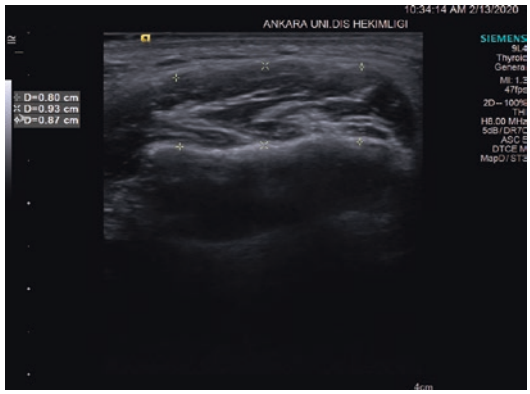

Fig. 21.3 Left masseter muscle USG linnear measurements of a patient before treatment

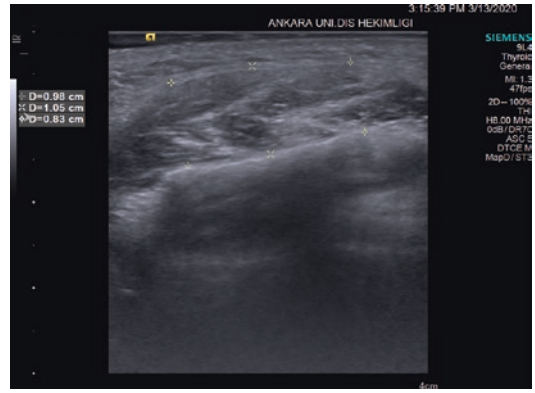

Fig. 21.4 Left masseter muscle USG linnear measurements of a patient after treatment

assessment of chewing muscle stiffness has not yet been performed in patients with myofascial pain [47, 48].

Shear-wave elastography (SWE) is a recently developed type of ultrasound elastography that uses shear wave propagation velocity, measured in m/s, to quantify tissue stiffness. This technology is widely used worldwide to diagnose liver fibrosis in hepatitis C patients. However, recent studies show that shear wave elostography has started to be used clinically in determining the elasticity of chewing muscles in TMD patients. Takashima M. et al., in their study, compared the elasticity between the patients with TMD and healthy people's masseter muscles using shear wave elastography. As a result of the study, masseter stiffness was found to be two times higher in individuals with TMD than healthy individuals [49]. The SWE which provides a semi-transparent color-coded image displaying the shear-wave velocity (m/sec) can be measured in different systems, below in the figures an example of SWE measurements from ten different points of the masseter muscle is given. The average of the ten measurements should be taken and analyzed before and after treatment of the bilateral masseter muscles which can play an active role in the diagnosis of muscle elasticity and its follow-up (Figs. 21.5, 21.6, 21.7, and 21.8).

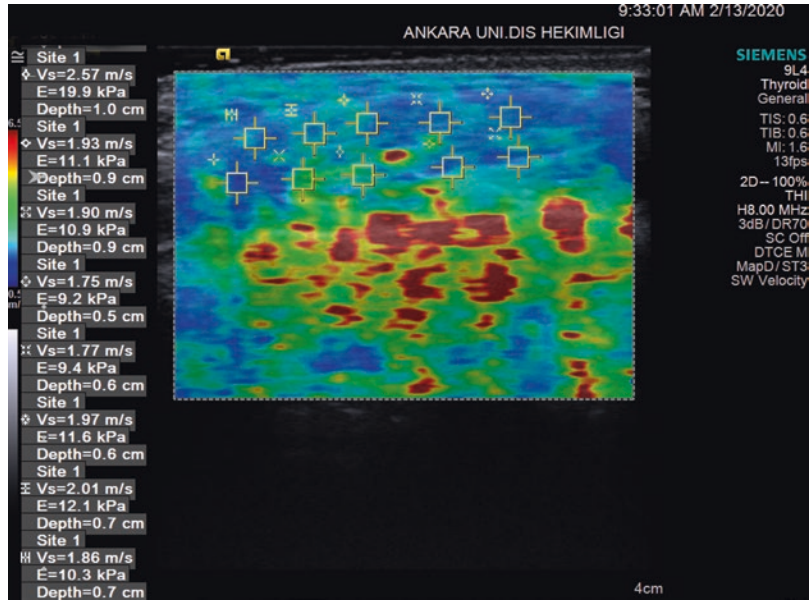

Fig. 21.5 Right masseter muscle USG SWE measurements of a patient before treatment

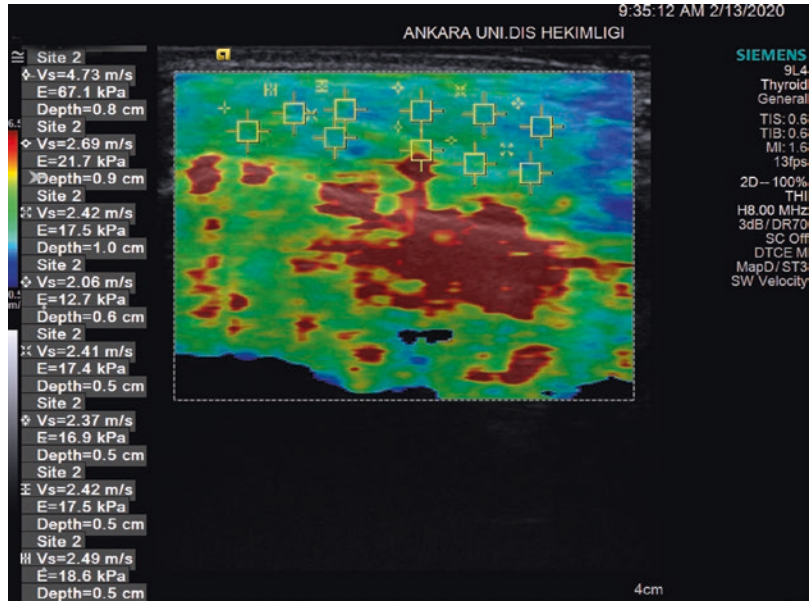

Fig. 21.6 Right masseter muscle USG SWE measurements of a patient after treatment

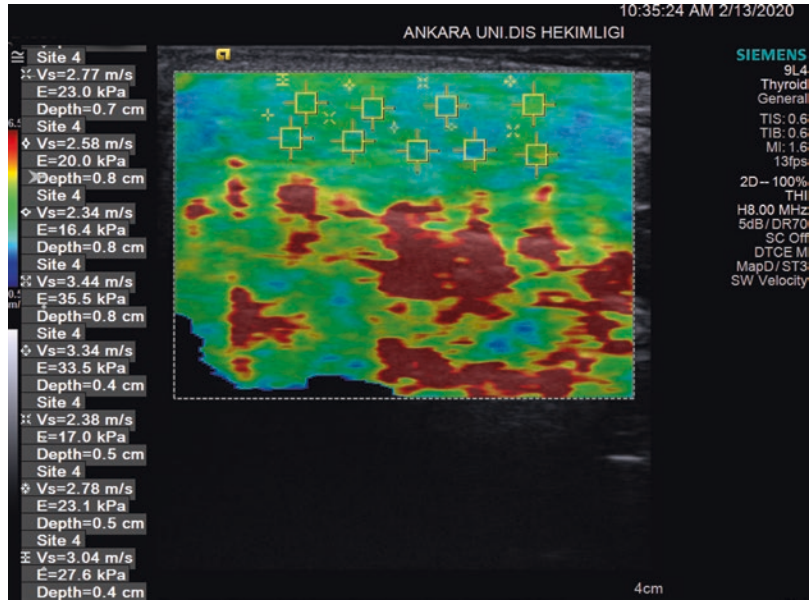

Fig. 21.7 Left masseter muscle USG SWE measurements of a patient before treatment

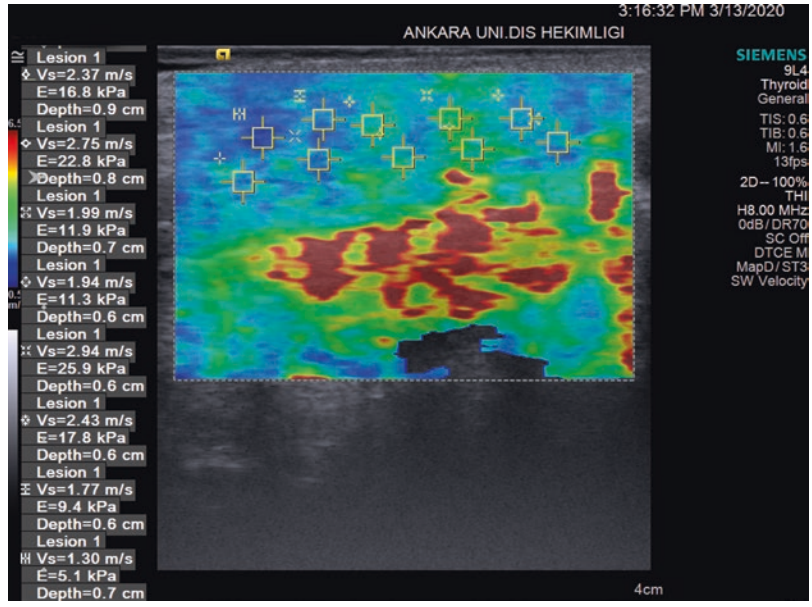

Fig. 21.8 Left masseter muscle USG SWE measurements of a patient after treatment

References

1. Sigrist RMS, et al. Ultrasound Elastography: review of techniques and clinical applications. Theranostics. 2017;7(5):1303–29.
2. Winn N, Lalam R, Cassar-Pullicino V. Sonoelastography in the musculoskeletal system: current role and future directions. World J Radiol. 2016;8(11):868–79.
3. Butts R, et al. Pathoanatomical characteristics of temporomandibular dysfunction: where do we stand? (narrative review part 1). J Bodyw Mov Ther. 2017;21(3):534–40.
4. Saranya B, et al. Comparison of transcutaneous electric nerve stimulation (TENS) and microcurrent nerve stimulation (MENS) in the management of masticatory muscle pain: a comparative study. Pain Res Manag. 2019;2019:8291624.

5. Amorim CSM, et al. Effect of physical therapy in bruxism treatment: a systematic review. J Manip Physiol Ther. 2018;41(5):389–404.
6. Lobbezoo F, et al. Bruxism defined and graded: an international consensus. J Oral Rehabil. 2013;40(1):2–4.
7. Butts R, et al. Conservative management of temporomandibular dysfunction: a literature review with implications for clinical practice guidelines (narrative review part 2). J Bodyw Mov Ther. 2017;21(3):541–8.
8. Keskinruzgar A, et al. Comparison of kinesio taping and occlusal splint in the management of myofascial pain in patients with sleep bruxism. J Back Musculoskelet Rehabil. 2019;32(1):1–6.
9. Awan KH, Patil S. The role of transcutaneous electrical nerve stimulation in the Management of Temporomandibular Joint Disorder. J Contemp Dent Pract. 2015;16(12):984–6.
10. Rajpurohit B, et al. Effectiveness of transcutaneous electrical nerve stimulation and microcurrent electrical nerve stimulation in bruxism associated with masticatory muscle pain--a comparative study. Indian J Dent Res. 2010;21(1):104–6.
11. Capellini VK, de Souza GS, de Faria CR. Massage therapy in the management of myogenic TMD: a pilot study. J Appl Oral Sci. 2006;14(1):21–6.
12. Miernik M, et al. Massage therapy in myofascial TMD pain management. Adv Clin Exp Med. 2012;21(5):681–5.
13. Gomes CA, et al. Effects of massage therapy and occlusal splint usage on quality of life and pain in individuals with sleep bruxism: a randomized controlled trial. J Jpn Phys Ther Assoc. 2015;18(1):1–6.
14. Gomes CA, et al. Effects of massage therapy and occlusal splint therapy on electromyographic activity and the intensity of signs and symptoms in individuals with temporomandibular disorder and sleep bruxism: a randomized clinical trial. Chiropr Man Ther. 2014;22(1):43.
15. Eby SF, et al. Validation of shear wave elastography in skeletal muscle. J Biomech. 2013;46(14):2381–7.
16. Pedersen M, Fredberg U, Langberg H. Sonoelastography as a diagnostic tool in the assessment of musculoskeletal alterations: a systematic review. Ultraschall Med. 2012;33(5):441–6.
17. Botar Jid C, et al. Musculoskeletal sonoelastography. Pictorial essay. Med Ultrason. 2012;14(3):239–45.
18. Park GY, Kwon DR. Application of real-time sonoelastography in musculoskeletal diseases related to physical medicine and rehabilitation. Am J Phys Med Rehabil. 2011;90(11):875–86.
19. Drakonaki EE, Allen GM, Wilson DJ. Ultrasound elastography for musculoskeletal applications. Br J Radiol. 2012;85(1019):1435–45.
20. Garra BS. Imaging and estimation of tissue elasticity by ultrasound. Ultrasound Q. 2007;23(4):255–68.
21. Garra BS. Elastography: current status, future prospects, and making it work for you. Ultrasound Q. 2011;27(3):177–86.
22. Cosgrove D, et al. EFSUMB guidelines and recommendations on the clinical use of ultrasound elastography. Part 2: clinical applications. Ultraschall Med. 2013;34(3):238–53.
23. Bamber J, et al. EFSUMB guidelines and recommendations on the clinical use of ultrasound elastography. Part 1: basic principles and technology. Ultraschall Med. 2013;34(2):169–84.
24. Ozturk A, et al. Principles of ultrasound elastography. Abdom Radiol (NY). 2018;43(4):773–85.
25. Creze M, et al. Shear wave sonoelastography of skeletal muscle: basic principles, biomechanical concepts, clinical applications, and future perspectives. Skelet Radiol. 2018;47(4):457–71.
26. Frontera WR, Ochala J. Skeletal muscle: a brief review of structure and function. Calcif Tissue Int. 2015;96(3):183–95.
27. Klauser AS, Peetrons P. Developments in musculoskeletal ultrasound and clinical applications. Skelet Radiol. 2010;39(11):1061–71.
28. Klauser AS, Faschingbauer R, Jaschke WR. Is sonoelastography of value in assessing tendons? Semin Musculoskelet Radiol. 2010;14(3):323–33.
29. Saftoiu A, et al. The EFSUMB guidelines and recommendations for the clinical practice of Elastography in non-hepatic applications: update 2018. Ultraschall Med. 2019;40(4):425–53.
30. Cortez CD, et al. Ultrasound shear wave velocity in skeletal muscle: a reproducibility study. Diagn Interv Imaging. 2016;97(1):71–9.
31. Gennisson JL, et al. Viscoelastic and anisotropic mechanical properties of in vivo muscle tissue assessed by supersonic shear imaging. Ultrasound Med Biol. 2010;36(5):789–801.
32. Miyamoto N, et al. Validity of measurement of shear modulus by ultrasound shear wave elastography in human pennate muscle. PLoS One. 2015;10(4):e0124311.
33. Ewertsen C, et al. Evaluation of healthy muscle tissue by strain and shear wave elastography - dependency on depth and ROI position in relation to underlying bone. Ultrasonics. 2016;71:127–33.
34. Wang X, et al. Effect of acquisition depth and precompression from probe and couplant on shear wave elastography in soft tissue: an in vitro and in vivo study. Quant Imaging Med Surg. 2020;10(3):754–65.
35. Shin HJ, et al. Comparison of shear wave velocities on ultrasound elastography between different machines, transducers, and acquisition depths: a phantom study. Eur Radiol. 2016;26(10):3361–7.
36. Seo JB, Yoo JS, Ryu JW. Sonoelastography findings of biceps tendinitis and tendinosis. J Ultrasound. 2014;17(4):271–7.
37. Ariji Y, et al. Shear-wave sonoelastography for assessing masseter muscle hardness in comparison with strain sonoelastography: study with phantoms and healthy volunteers. Dentomaxillofac Radiol. 2016;45(2):20150251.

38. Taljanovic MS, et al. Shear-wave Elastography: basic physics and musculoskeletal applications. Radiographics. 2017;37(3):855–70.
39. Hsiao MY, et al. Reduced patellar tendon elasticity with aging: in vivo assessment by shear wave Elastography. Ultrasound Med Biol. 2015;41(11):2899–905.
40. Andrade RJ, et al. Non-invasive assessment of sciatic nerve stiffness during human ankle motion using ultrasound shear wave elastography. J Biomech. 2016;49(3):326–31.
41. Kantarci F, et al. Median nerve stiffness measurement by shear wave elastography: a potential sonographic method in the diagnosis of carpal tunnel syndrome. Eur Radiol. 2014;24(2):434–40.
42. Laskin DM, Block S. Diagnosis and treatment of myofacial pain-dysfunction (MPD) syndrome. J Prosthet Dent. 1986;56:75–84.
43. Azlag Pekince K, Caglayan F, Pekince A. Imaging of masseter muscle spasms by ultrasonography: a preliminary study. Oral Radiol. 2020;36(1):85–8. https://doi.org/10.1007/s11282-019-00383-4.
44. Liao L-J, et al. High-resolution sonographic measurement of Normal temporomandibular joint and masseter muscle. J Med Ultrasound. 2012;20(2):96–100.
45. Larheim TA, et al. Temporomandibular joint disk displacement: comparison in asymptomatic volunteers and patients. Radiology. 2001;218(2):428–32. https://doi.org/10.1148/radiology.218.2.r01fe11428.
46. Ariji Y, Sakuma S, Izumi M, et al. Ultrasonographic features of the masseter muscle in female patients with temporomandibular disorder associated with myofascial pain. Oral Surg Oral Med Oral Pathol Oral Radiol Endod. 2004;98(3):337–41. https://doi.org/10.1016/j.tripleo.2004.06.068.
47. Dworkin SF, Huggins KH, LeResche L, et al. Epidemiology of signs and symptoms in temporomandibular disorders: clinical signs in cases and controls. J Am Dent Assoc. 1990;120(3):273–81. https://doi.org/10.14219/jada.archive.1990.0043.
48. Aksu Ö, Pekin Doğan Y, Sayıner Çağlar N, Şener BM. Comparison of the efficacy of dry needling and trigger point injections with exercise in temporomandibular myofascial pain treatment. Turk J Phys Med Rehabil. 2019;65(3):228–35.
49. Takashima M, Arai Y, Kawamura A, Hayashi T, Takagi R. Quantitative evaluation of masseter muscle stiffness in patients with temporomandibular disorders using shear wave elastography. J Prosthodont Res. 2017;61(4):432–8.